STRENGTH AND STIFFNESS OF SHEAR WALL-FLOOR SLAB CONNECTIONS

Thesis submitted in accordance with the requirements
of the University of Glasgow
for the Degree of Doctor of Philosophy

by

Mahmood Memon

January 1984.

SUMMARY

This thesis presents an analytical and experimental study of the strength of shear wall-slab junctions subjected to gravity and wind loading.

The experimental investigation consisted of testing fourteen 'large scale' models of the reinforced concrete shear wall-slab junction area. The major parameters included in the study are

(i) Wall width (W_w).

(ii) Gravity load/wind load ratio (V_g/V_w).

(iii) Moment due to wind load/shear due to wind load ratio ($^{M_w}/_{V_w}$)

(iv) Moment due to gravity load/shear due to gravity load ratio ($^{M_g}/_{V_g}$)

(v) Percentage of flexural reinforcement (ϱ).

The range of parameters included was that likely to be met in practice.

The theoretical study was carried out by performing nonlinear analysis with the aid of a two dimensional finite element programme and employing a four noded layered element with five degrees of freedom at each node.

Based on the results of the study a procedure has been proposed for estimating the strength of wall-slab junction in a laterally loaded shear wall-structure.

Finally, conclusions of the different investigations and recommendations for further work have been given.

ACKNOWLEDGEMENTS

The work reported in this thesis was carried out in the Department of Civil Engineering of Glasgow University and author wishes to express his thanks to Professor H.B. Sutherland, Cormack Professor and Head of the Department of Civil Engineering, for making the facilities available in this regard.

The author is grateful to Professor A. Coull, Regius Professor of Civil Engineering, University of Glasgow, for his continuous help, invaluable advice and encouragement.

The author is indebted to and wishes to express his sincere gratitude to Dr. P. Bhatt, Lecturer Department of Civil Engineering, University of Glasgow, for his supervision and encouragement during the course of study.

The author would like to thank all the members of teaching staff of Civil Engineering, University of Glasgow, for their cooperation.

Acknowledgement is due to the staff of the Concrete Laboratory, in particular, Mr. J. Love, Mr. J. Thompson, Mr. I. Todd and Mr. J. Coleman.

Thanks are due to Mrs. J. Lawn for her neat and diligent typing of the manuscript.

The author is grateful to the Government of Pakistan for the financial support without which this work would not have been possible.

Finally, the author is very much thankful to his parents for their patience and support.

CONTENTS

LIST OF NOTATIONS

A_o = Area of the rectangle defined by the longitudinal bars in the corners of the hoops.

A_1 , A_2 = Cross sectional areas of piers 1 and 2.

A_{cp} = Area of the critical perimeter for shears.

A_s = Area of steel.

A_t = Total area of longitudinal steel.

A_w = Cross sectional area of the bar from which the hoops are made.

$\{a\}$ = Vector of twenty unknown constants a_1 to a_{20}.

$\{B\}$ = Strain matrix.

B_w = Width of an opening in a box core shear wall.

b = Breadth of a section.

b' = Clear span of connecting beams in a shear wall structure.

b_o = Column perimeter.

b_p = The length of a perimeter at a distance 1.5h from column faces.

b_x , b_y = Dimensions of a column in x and y-direction, respectively.

$[C]$ = Constant of integration in the expression for the integral shear force in the connecting laminae.

C = 20 x 20 matrix depending on nodal coordinates.

C_b = Compression due to bending.

C_{cr} = Initial crack width.

C_m = One third of cube crushing strength of concrete.

D = Flexural rigidity of the plate.

$[D]$ = Constitutive matrix of elasticity for isotropic materials.

D_w = Depth of lintel beam in a box core shear wall with openings.

$[D']$ = Equivalent constitutive matrix for layered element.

$[D^*]$ = Constitutive matrix of cracked concrete.

d = Effective depth of the slab.

$\{d\}$ = Deformation vector.

d_b = The effective depth to centroid of bottom reinforcement for positive moment.

d_n = Depth to the neutral axis.

d_t = The effective depth to centroid of top reinforcement. for negative moment.

E = Modulus of elasticity.

E_c = Modulus of elasticity of concrete.

E_i = Instantaneous modulus of concrete.

E_s = Modulus of elasticity of steel.

E_{se} = Secant modulus of steel.

e = Eccentricity of loading.

F^{ex} = Pseudo or out of balance force.

f'_c = Cylinder crushing strength of concrete.

f_{cc} = Intermediate yield stress.

f_{cu} = Cube crushing ultimate compressive stress of concrete.

f_d = The equivalent compressive strength under biaxial compression.

f_t = Ultimate tensile stress of concrete.

f_{ty}, f_{wy} = Yield strengths of longitudinal steel and hoop steel, respectively.

f_y = Yield stress of steel.

G = Modulus of rigidity.

H = Height of a building.

$\bar{H}$ = Height of shear wall including the height of the column on the ground floor.

h = Overall thickness of slab.

h' = Floor to floor height.

h_p = Depth of the connecting beam.

I_1, I_2 = Moment of inertia of piers 1 and 2.

I_p, I_{po} = The reduced and original moments of inertia of a connecting beam, respectively.

J_c = A property of the critical perimeter analogous to polar moment of inertia.

$[K]$ = Stiffness matrix.

K_1, K_2 = Non dimensional moment factors.

K_q = Shear modification factor.

K^*_{x1},K^*_{x2}, K^*_{x3},K^*_{xc} = Design moments in x-direction in different regions of a slab due to lateral leads.

K^*_{y1},K^*_{y2}, K^*_{y3},K^*_{yc} = Design moments in y-direction in different regions of a slab due to lateral load.

K_θ , K_δ = Nondimensional factors for rotational and translational stiffness respectively.

L = Longer span in flat slab-column structure.

L_w = Corridor opening width.

l = The distance between the centroid of the cross sections of the piers.

l_a = Lever arm.

l_n = Smaller span.

M = Moment.

M_1 , M_2 = Bending moments in the piers 1 and 2 of the shear wall due to lateral loads.

M_a = Maximum average bending moment in a connecting slab.

M_f = Fraction of total unbalanced moment transferred directly from slab to the column at the inner face of critical section.

M_g = Moment due to gravity load.

M_n = Normal moment.

M^*_n = Normal resisting moment.

M_r = Moment of resistance of a concrete section.

M_s = Fraction of unbalanced moment transferred from slab to column through its sides by eccentricity of shear.

M' = Fraction of unbalanced moment transferred from slab to column through its sides by torsion.

M_u = Ultimate moment.

M_w = Moment induced in a connecting beam or slab due to wind load.

M_x = Moment acting in x-direction (Transverse direction).

M^*_x = Design moments in x-direction.

$\bar{M}_x$, $\bar{M}_y$ = Bending moment factors.

M_y = Moment acting in y-direction (windward direction)

M^*_y = Design moments in y-direction.

M_{xy} = Twisting moments.

N_x, N_y, N_{xy} = Inplane stress resultants.

P = Concentrated lateral load acting at the top of the building.

P_{cr} = Cracking load.

Q_i = Shear Force in a connecting beam from T-diagram at floor level i.

Q_{max} = Maximum shear due to lateral load.

Q_w = Total positive shear induced at the wall-slab junction due to wind load.

Q_x, Q_y = Vertical shear per unit width acting along x and y axis, respectively.

q = Intensity of the applied load.

q' = Bond force applied to the flexural reinforcement per unit length.

$[R]$ = Transformation matrix.

R_w = Total positive idealised reaction at the wall, due to lateral load.

S = Spacing of hoops.

S_b = The spacing of bottom reinforcement for negative moment.

S_t = The spacing of top reinforcement for negative moment.

T = Integral shear force in the connecting laminae.

T' = Shear Force per unit height in the connecting laminae.

$[T]$ = Transformation matrix.

T_b = Total tension due to bending.

t_w = Thickness of a planner shear wall.

U = Peripheral distance from the wall.

u_o = Perimeter of the area A_o.

u, v = In plane deformations in x and y directions respectively.

$V_{aggregate}$ The vertical components of inclined shear stresses transmitted across the inclined crack by means of interlocking of the aggregate.

V_{app} = Applied shear.

V_c = Shear force transmitted through the compression zone of concrete.

V_{cal} = Calculated ultimate wind load of a model.

V_{design} = Design ultimate load of a model.

V_{dowel} = Shear force transmitted across the crack by the flexural reinforcement by dowel action.

$V_{exp.}$ = Experimental ultimate wind load of a model.

V_f = Shear transmitted directly at the inner face of critical section.

$V_{F.E.}$ = Ultimate wind load of a model predicted by finite element analysis.

V_g = Shear due to gravity load.

Vu = Ultimate shear transfer capacity of a connection.

V_w = Uneven shear due to wind load.

v_{add} = Increase in the value of critical shear stress due to increase of ratio of flexural steel above 1%.

v_c = Critical shear stress.

v_{crs} = Shear stress which can be transferred through the cracked concrete.

v_{ct} = Critical torsional shear stress.

v_g = Shear stress induced along critical section due to gravity load.

v_i = Shear stress induced along critical section.

v_{max} = Maximum shear stress induced due to transfer of both, shear and unbalanced moment.

v_{sm} = Shear stress induced due to transfer of unbalanced moment alone.

v_u = Shear stress induced along the sides of the wall due to direct shear.

v_{ui} = Shear stress at the inner face of critical section predicted by finite element analysis at a theoretical load equal to experimental ultimate load of the model.

W_{eff} = Effective wall width.

W_w = Wall width.

w = Vertical deflection.

w' = Intensity of lateral load per unit height.

X_w = Overall width of a shear wall building.

x_o , y_o = Width and depth respectively, making area A_o.

Y_e = Effective width of connecting slab.

Y_{max} = For a slab-column connection subjected to unbalanced moments and uneven shears, the distance from the centre of the twist to the section where v_{max} stress acts.

Y_w = Bay width of connecting slab

z = The distance of the layer from the mid plane of the plate.

z_w = Width of the flange of a shear wall.

α_i = Fraction of unbalanced moment transferred from slab to column by torsion and eccentricty of shear.

β = Shear retention factor.

Δ = Shear displacement.

Δx, dx = Distance between two consecutive sampling points along x-axis within the same finite element.

Δy, dy = Distance between two consecutive sampling points along y-axis within the same finite element.

Δz, dz = Thickness of a layer.

δ = Displacement.

δd = Iteration deformation vector.

$\{\delta\}^e$ = Elemental displacement vector.

$\{\varepsilon\}$ = Vector of total inplane strain in a layer.

ε_1, ε_2 = Principal strains.

ε_c = Strain in concrete.

ε_{max} = Maximum principal strain.

ε_p = .0025 strains.

ε_s = Strain in steel.

ε_x, ε_y = Strain in x and y direction respectively.

θ = Angle of rotation.

θ_{cr} = The actual crack direction.

$\theta_x = \frac{\partial w}{\partial y}$ = The rotation about x-axis.

$\theta y = \frac{\partial w}{\partial x}$ = The rotation about y-axis.

λ_m = Factor of safety.

ν = Poisson's ratio.

ζ_s = CP110 Code's emperical depth factor for flat slabs.

ρ = Percentage of flexural steel.

$\{\sigma\}$ = Stress vector in a layer.

σ_o = Mean nominal stress.

σ_1 , σ_2 = Principal stresses.

σ_p = f_{cu} for uniaxial compression.

σ_x , σ_y = Stresses in x and y directions respectively.

τ = Torsional moment.

τ_{oct} = Octahedral shear stress.

τ_u = The strength of a spandrel in combined torsion and shear.

τ_{xy}, τ_{xz} τ_{yz} = Shear stresses acting in xy, xz and yz planes, respectively.

C H A P T E R O N E

INTRODUCTION

1.1 SHEAR WALL STRUCTURES

Increase in population, shortage of space to build and consequently high cost of land in urban areas has led to the construction of high rise buildings. One major structural characteristic of tall buildings is that the effect of wind and seismic loads . becomes more pronounced with the increase in the height of the building. The traditional system of providing lateral stiffness to buildings is essentially one of an extension of rigid structural frames with infills serving the purpose of dividing the space. This form of construction suffers from the following disadvantages.

(i) It is an inefficient form of providing lateral stiffness.

(ii) As the lateral forces vary with the height of the building, the member sizes also need to be varied. This, apart from preventing the exploitation of repetition, architecturally restricts flexibility of internal planning.

(iii) Leads to complications at the joints.

(iv) The deep beams at lower levels can only be concealed with the use of a false ceiling which adds considerably to the volume and cost of the building.

Search for more economical methods of construction and types of structures resulted in the development of a type of tall buildings called shear wall structures. These buildings consist of load bearing walls and slabs. A structure in which the walls (which includes core walls, facade walls or combination of these) carry both/

gravity as well as the lateral loading, is called a shear wall structure. In this structural form the floor slabs act as diaphragms distibuting the horizontal loads to the vertical shear walls. Since no fals ceiling is required to hide the beams etc. the storey height can be kept to a minimum. . A perspective view of a typical building is shown in Fig. 1.1 .

1.2 WALL CONFIGURATION

Ideal situation occurs when shear walls not only have the structural function of carrying vertical and horizontal loads but also the non-structural function of dividing and enclosing the space as well. This leads to the system of cross-wall construction as shown in Fig. (1.2). This arrangement results in parallel assemblies of division walls running perpendicular to the face of the building, with intersecting longitudinal walls along the corridor and facade enclosing the living spaces. The cross-walls are employed as load bearing walls in addition to serving architectural requirements. The longitudinal corridor and facade walls are provided with openings for access to the living areas and balconies, and these longitudinal walls act as flanges for the primary cross-walls. Shear walls are also used to enclose lift shafts and stairwells to form partially open section box structures. . Thus, in practice, shear walls of various shapes, planar, flanged or box shaped, may be coupled together in cross-wall structures. Different wall configurations are shown in Fig. (1.3).

1.3 EFFECT OF LATERAL LOADS

In designing tall buildings special consideration must be given/

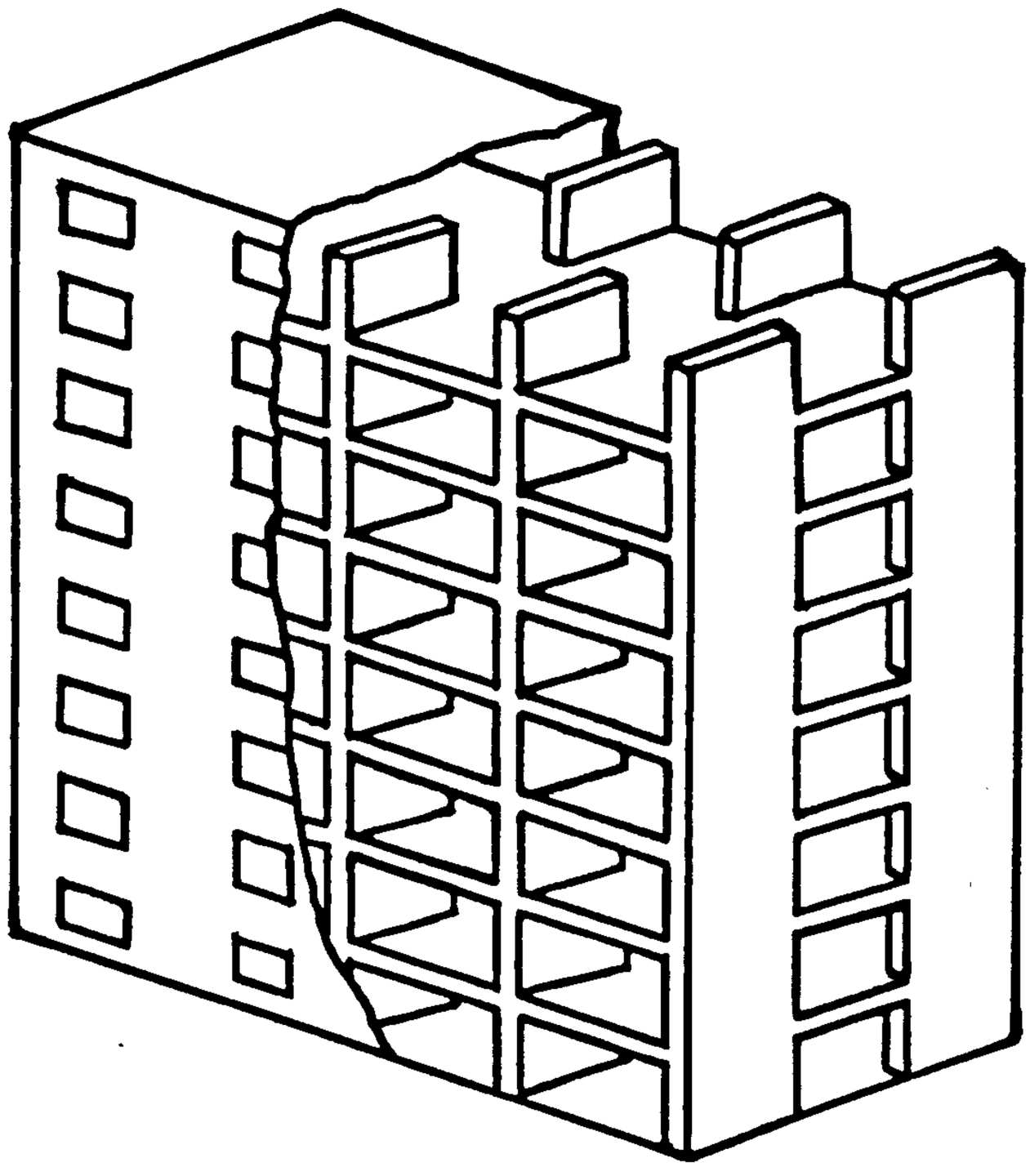

Figure (1.1) : Perspective view of a shear wall building.

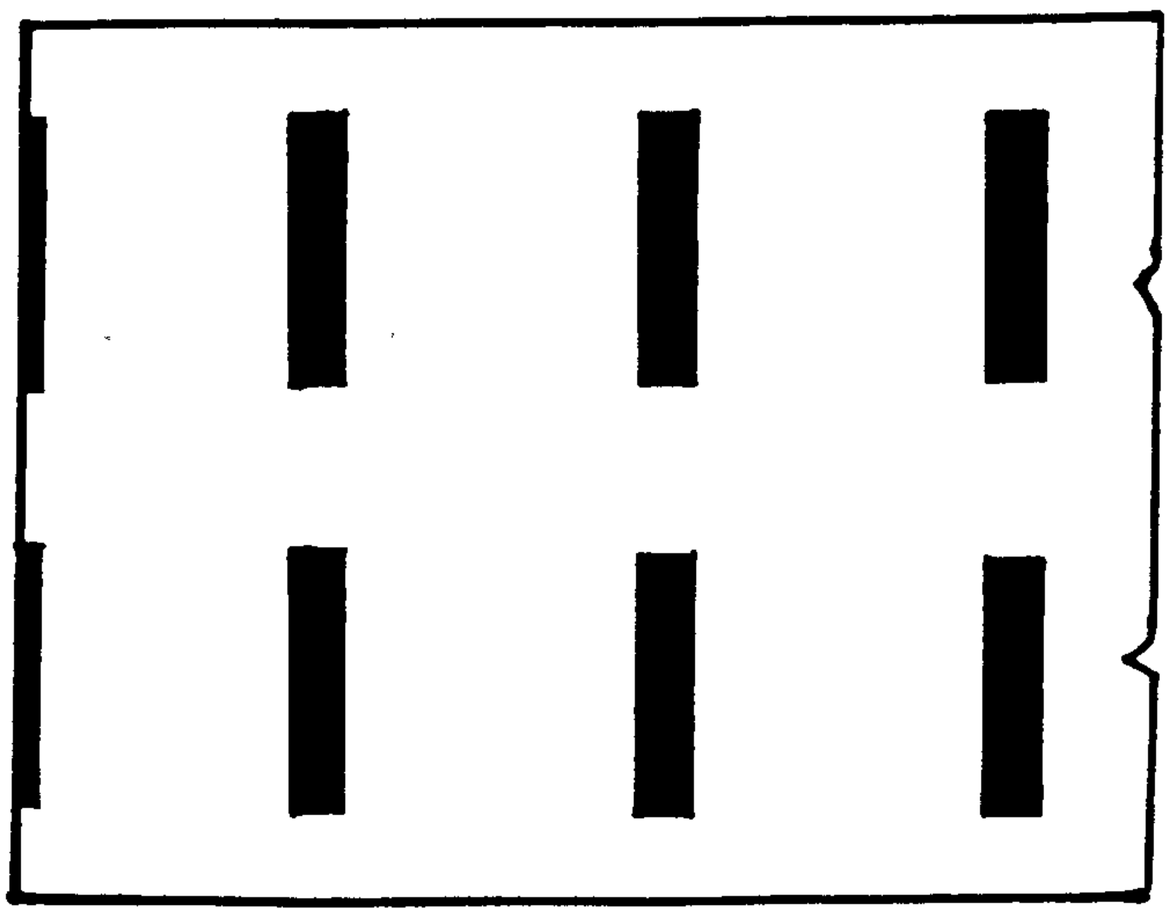

Figure (1.2) : Plan of a typical shear wall building.

to providing sufficient stability in all directions against lateral forces due to wind, earthquake or blast .. These forces produce critical stresses in the structure, set up vibrations in the structure and cause lateral sway of the building which could reach a point of discomfort to the occupants.

The shear walls resist the lateral loads on the structure by cantilever bending action, which results in rotations of the wall cross-sections. The free bending of a pair of shear walls is resisted by the floor slab, which is forced to rotate and bend out of plane where it connects rigidly to the walls(Fig. (1.4)). Due to the large depth of the wall, considerable differential shearing action is imposed on the connecting slab, which develops transverse reactions to resist the wall deformations(Fig. (1.5)),and induces axial forces, (tensile and compressive) in the walls. As a result of the large lever arm involved, relatively small axial forces can give rise to substantial moments of resistance, thereby substantially reducing the wind moments in the walls and the resultant tensile stresses at the windward edges. The lateral stiffness of the structure is as a consequence considerably increased.

1.4 PURPOSE OF THIS STUDY

The design of tall buildings consisting of shear walls and slabs subjected to lateral loads in addition to gravity loads has been a field of active research for over three decades. Methods have been proposed for the determination of moments and shears in walls and connecting slabs in shear wall structures for different support conditions at the base①. However one of the most important aspects of the problem pertaining to the design of such type of structure /

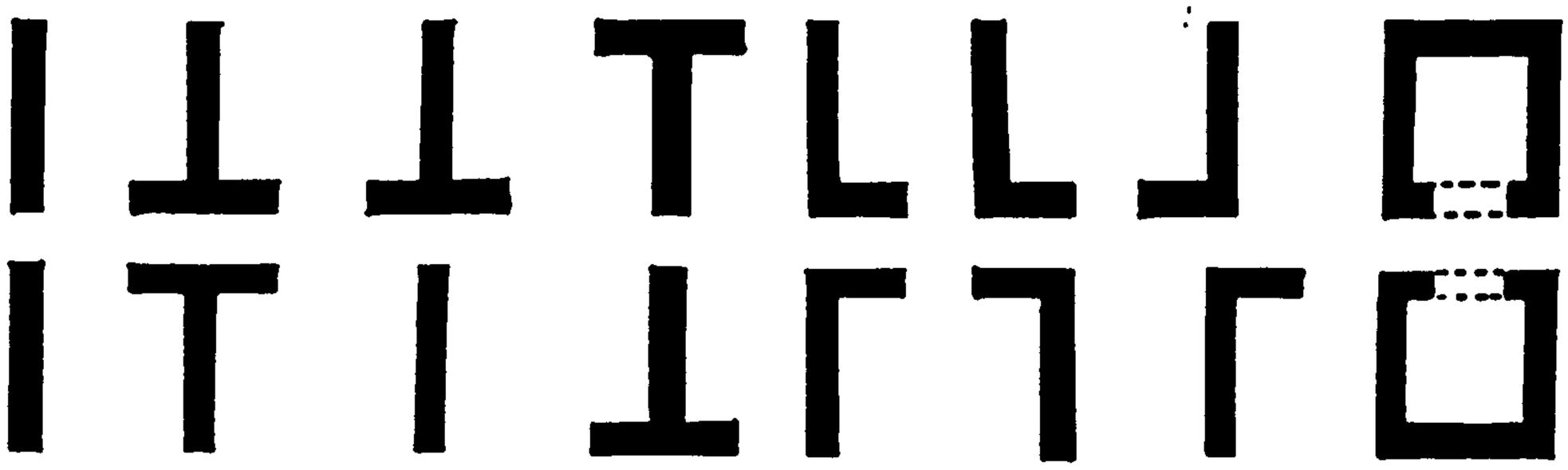

Figure (1.3) : Different wall configurations

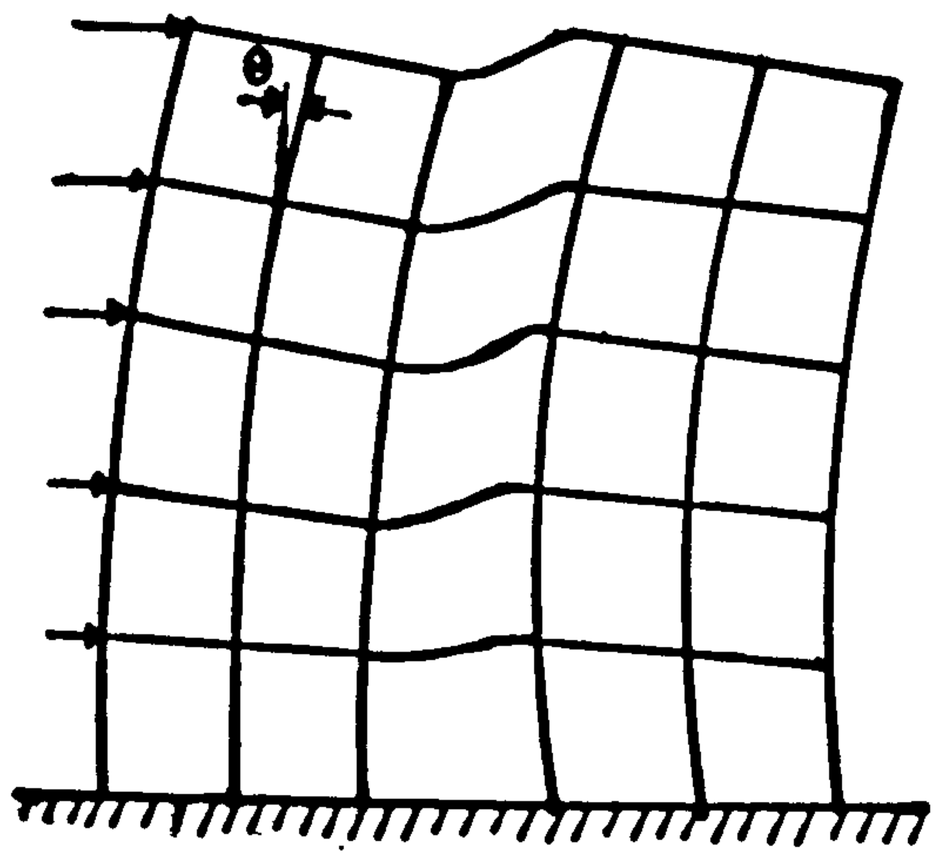

Figure (1.4) : Deflected shape of a typical shear wall - slab structure subjected to lateral loads.

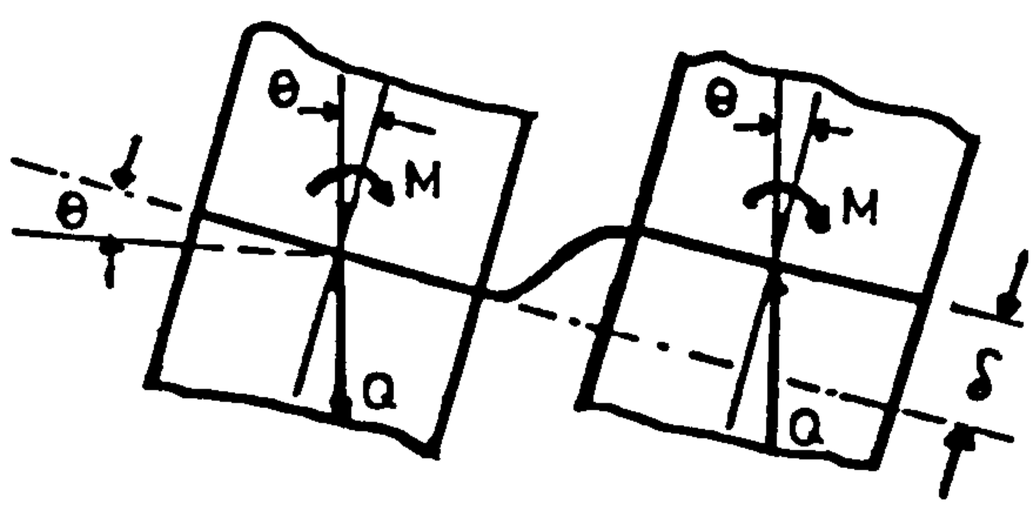

Figure (1.5) : Deflected shape of the connecting slab in a shear wall structure.

is the strength and stiffness of wall-slab connection. Based on elastic analysis, methods have been proposed for this purpose(9,10). However, in actual practice cracking of concrete is bound to occur and consequently due to redistribution of forces at later stages of loading, behaviour of a real wall-slab connection will be different from that predicted by elastic analysis. Although the problem bears some resemblance to strength of slab-column junction in flat slab structures, the main difference arises from the length of the wall which probably will considerably increase the line of failure (shear perimeter) in shear wall structure. The aim of this investigation is therefore to study the behaviour of wall-slab connections in a shear wall - slab structure subjected to wind load in addition to gravity load and based on extensive theoretical and experimental results develop a comprehensive and satisfactory procedure for the design of these connections. The problem is tackled experimentally by testing real concrete models of relatively large scale and thoretically by using non-linear finite element analysis.

C H A P T E R T W O

LITERATURE REVIEW

2.1 GENERAL

The analysis and design of the floor slab-wall junctions of shear wall structures connected by slabs only can be divided into four steps.

(a) Analysis of the shear wall as a 2-D or 3-D structure to determine the forces due to lateral loads e.g. wind, earthquake.

(b) If the shear wall is idealized as a two dimensional structure with slab acting as connecting beams, then an effective slab width which has the same shear stiffness as the whole slab.

(c) The determination of moments, torsion, shear around the junction.

(d) Design of the junction.

Considerable work has been done on the first two aspects of the problem in the last two decades. A review of this work is presented here with the intention of giving an account of the state of the art and to determine areas where more information is needed.

2.2 ANALYSIS OF SHEAR WALL AS A TWO-DIMENSIONAL STRUCTURE

Shear wall structures are normally analysed by the following two methods.

(1) Wide column method.

(2) The continuous connection method.

Wide column-frame method:- The shear wall shown in Figure (2.1) is replaced by a frame whose columns have the conventional axial and flexural stiffness as the wall panels in the shear wall and the connecting beams (or slabs) an equivalent flexural and shear stiffness corresponding to that of the actual slabs. To allow for the large slab-column joint area, the outer parts of the horizontal beams are regarded rigid as shown in Figure (2.2). The wide column-frame is analysed by the matrix displacement method (normally using a computer programme). The output will give the bending moment, shear force and the axial force in the members of the frame (42).

The continuous connection method:- This is an approximate method for the analysis of walls subjected to wind loading. The discrete connecting beams (or slabs) are replaced by a continuous shear medium.made up of beam elements as shown in Figure (2.3). This continuous connection has the same stiffness from storey to storey as the connecting beam. Under horizontal loading the beam elements are assumed to deform with a point of contraflexure at the centre. The continuously distributed vertical shear stresses (Figure (2.3)) in the beam elements at the point of contraflexure (or the integral of these continuously distributed shear stresses) is taken as unknown. It is possible to set up a second order differential equation in terms of this integral shear force which can be solved for different load and boundary conditions and the forces and deflections in the structure can be calculated.

Based on this method Rosman (1) developed a solution for walls with one and two symmetric bands of openings, with various conditions of support at the lower end as shown in Figure (2.4).

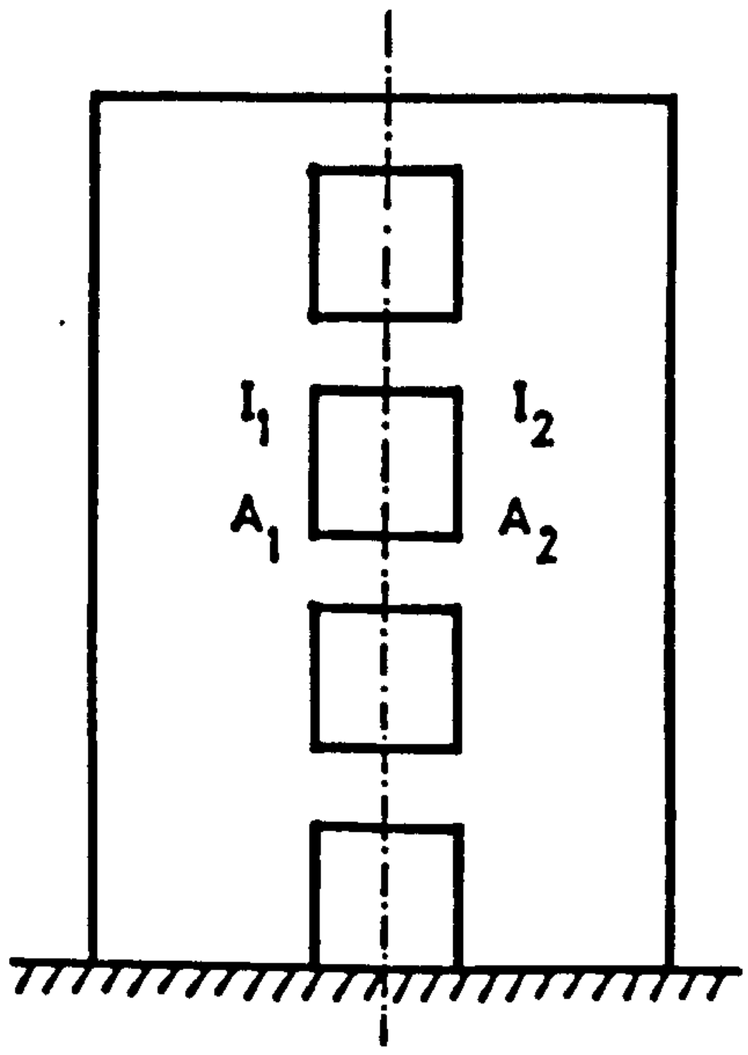

Figure (2.1) : A typical shear wall with openings.

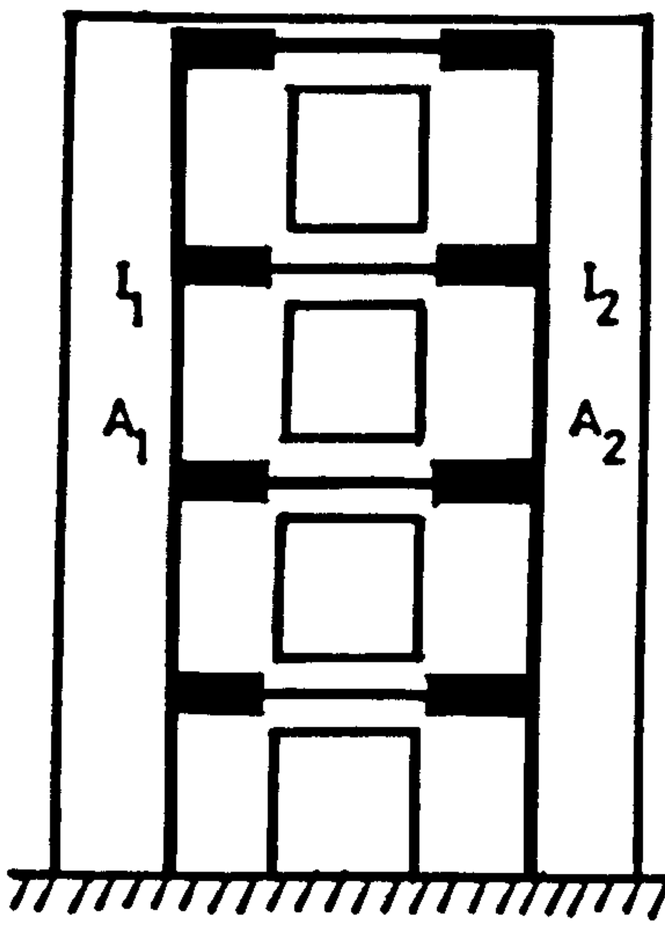

Figure (2.2) : An idealized frame replacing a shear wall containing openings.

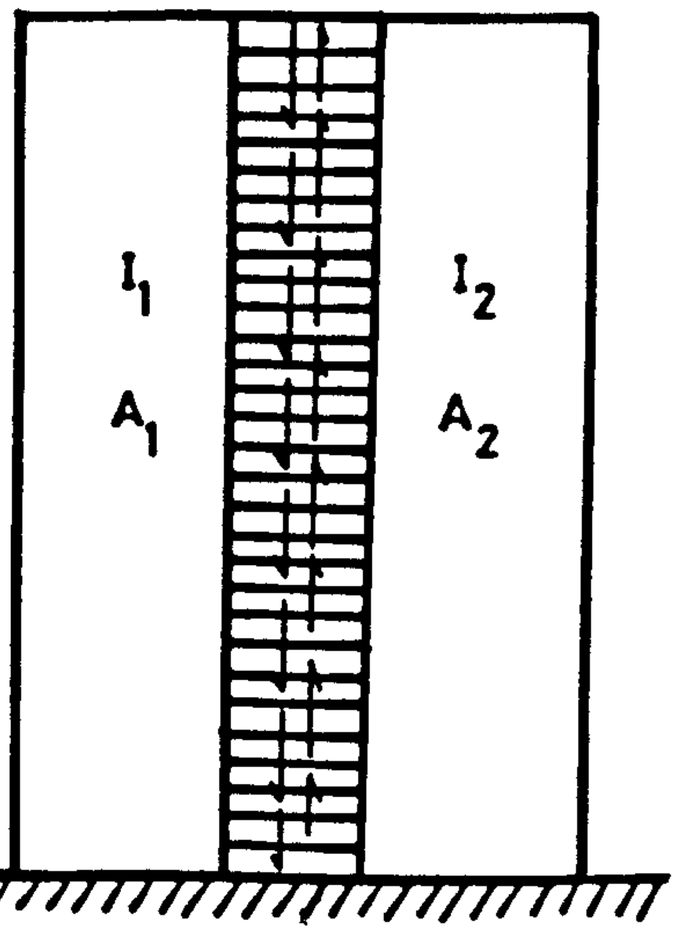

Figure (2.3) : Shear wall with idealized continuous connection or laminae.

The work was based on the following assumptions:

(i) The values of structural parameters h', b', ℓ, A_1, A_2, I_1, I_2, h_p and E are assumed to be constant throughout the whole height H where (See Fig.2.4a)

h' = floor to floor height.

b' = clear span of connecting beams

ℓ = the distance between the centroid of the cross-sections of the piers

I_1, I_2 = moment of inertia of piers 1 and 2.

A_1, A_2 = cross sectional area of piers 1 and 2 .

h_p = the depth of the connecting beam.

(ii) The 'roof beam' has one-half the moment of inertia of the 'storey connection beam'.

(iii) Walls weakened by one band of openings are not necessarily symmetric. Walls with two bands of openings are assumed to be symmetric.

(iv) The points of contraflexure are assumed to be at midspan of the connecting beams.

(v) The usual assumptions of structural theory concerning elasticity are assumed to be valid.

(vi) The perforated wall can be considered to be built up of piers and spanderal elements, the former undergoing bending and axial deformations, while the later only bending and shear deformations.

The continuous connections can be imagined as laminae of height/

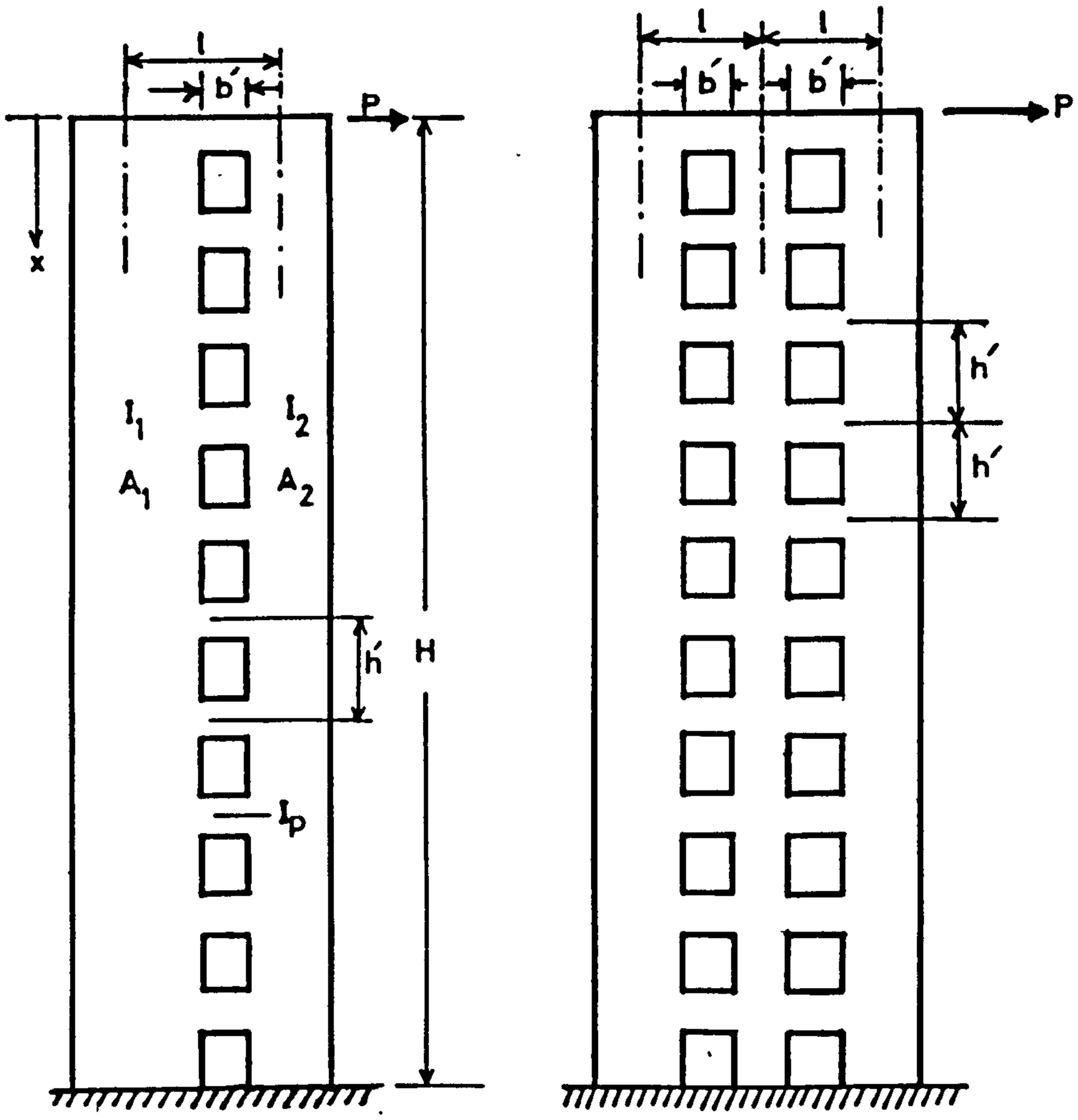

Figure(2.4a): Schemes of walls containing single and double bands of openings.

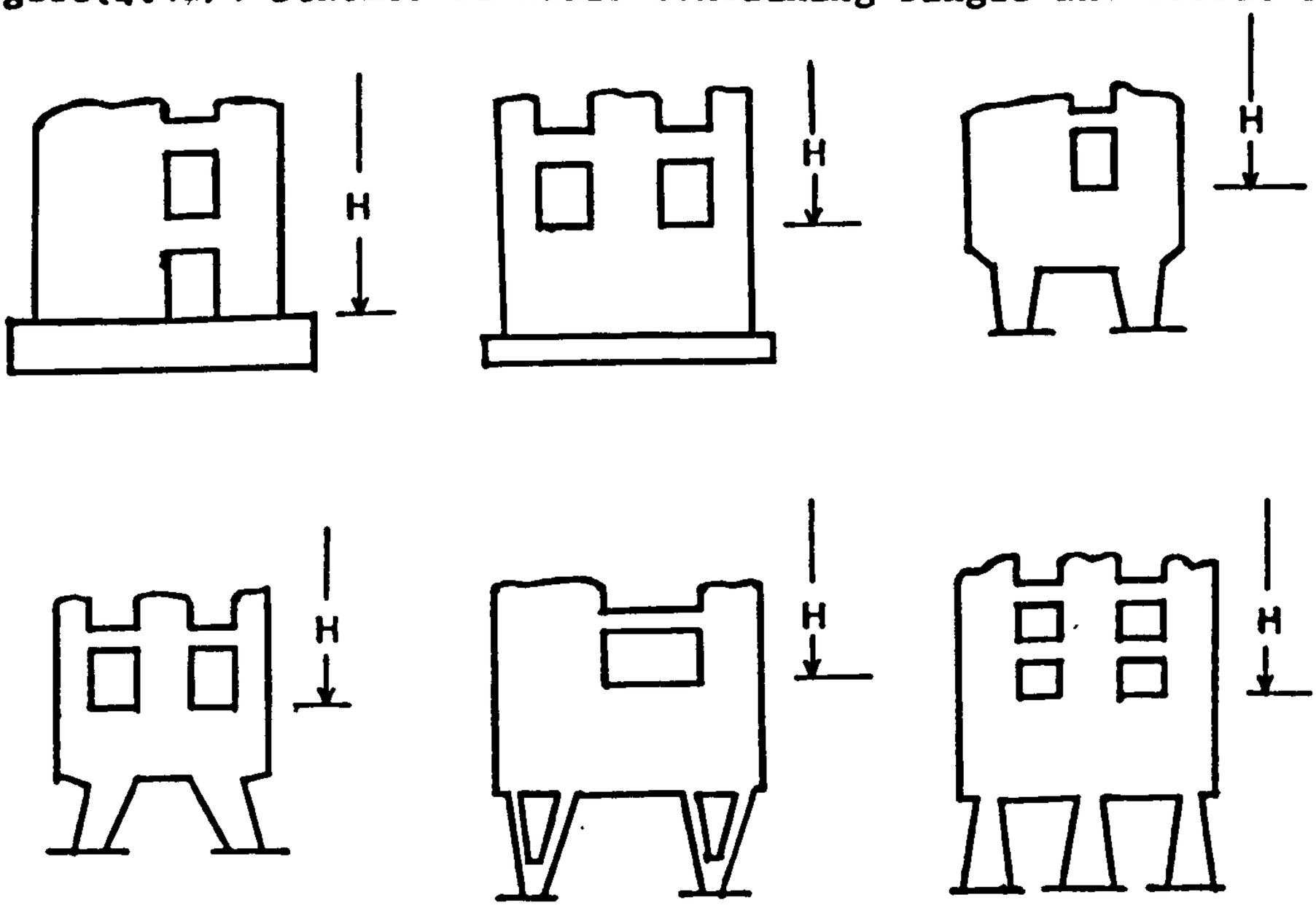

Figure(2.4b) :Different support conditions for shear walls at base.

dx and stiffness $I_p \frac{dx}{h'}$, continuously distributed along the whole height H. Under horizontal loading the walls deflect, inducing shear forces T' per unit height in the laminae. The integral shear force $T = \int_0^x T'dx$ is a statically indeterminate function. The origin of x-axis is at the upper edge of the wall.

The influence of the shear deformation in the connecting beams can be taken into account by using the reduced moments of inertia of the connecting beams, given by:

$$I_p = \frac{I_{po}}{1 + 2.4\ (h_p/b)^2} \qquad (2.1)$$

where I_p and I_{po} are the reduced and original moments of intertia of a connecting beam respectively.

If the laminae are considered to be cut at the middle of the opening (through their assumed points of contraflexure) then, by considering their deformation (Fig.(2.5))due to integral shear force T, equating it to that due to bending of the wall due to applied horizontal load P and assuming that there is a rigid support at the bottom, so that there is no deformation due to settlement of base, we obtain:

$$\frac{hb'^3}{12EI_p}\ T' + \frac{1}{E}\left(\frac{l^2}{I_1 + I_2} + \frac{1}{A_1} + \frac{1}{A_2}\right) \int_x^H T dx = \frac{Pl}{E(I_1 + I_2)} \int_x^H x\ dx \qquad (2.2)$$

For a wall containing one band of openings.

Introducing abbreviations,

$$T' + \alpha^2 \int_x^H T dx = \gamma \int_x^H x\ dx \qquad (2.3)$$

$$\text{where } \alpha^2 = \left(\frac{l^2}{I_1 + I_2} + \frac{1}{A_1} + \frac{1}{A_2}\right) \frac{12\ I_p}{hb'^3} \qquad (2.4)$$

$$\text{and } \gamma = \frac{Pl}{I_1 + I_2} \cdot \frac{12\ I_p}{hb'^3} \qquad (2.5)$$

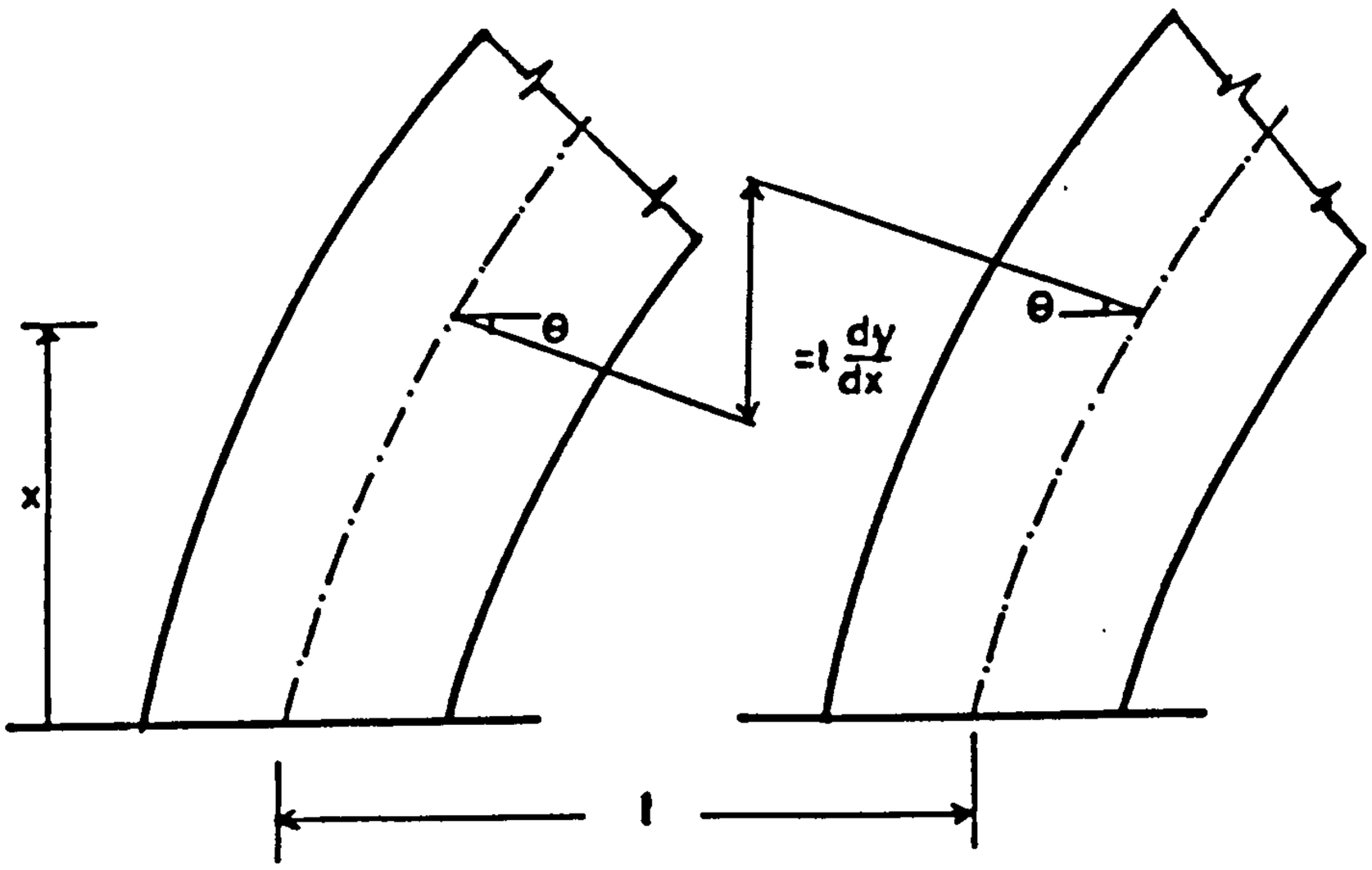

Figure (2.5a) : Displacement due to bending of walls.

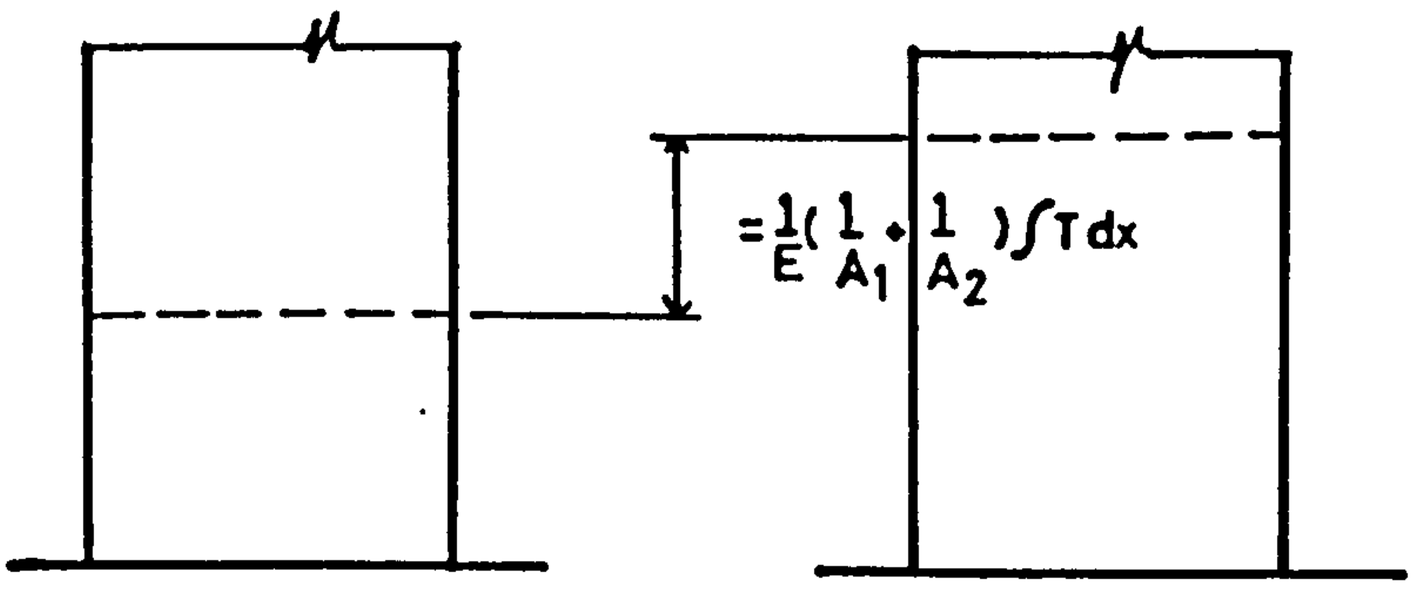

Figure (2.5b) : Displacement due to relative axial deformation of wall.

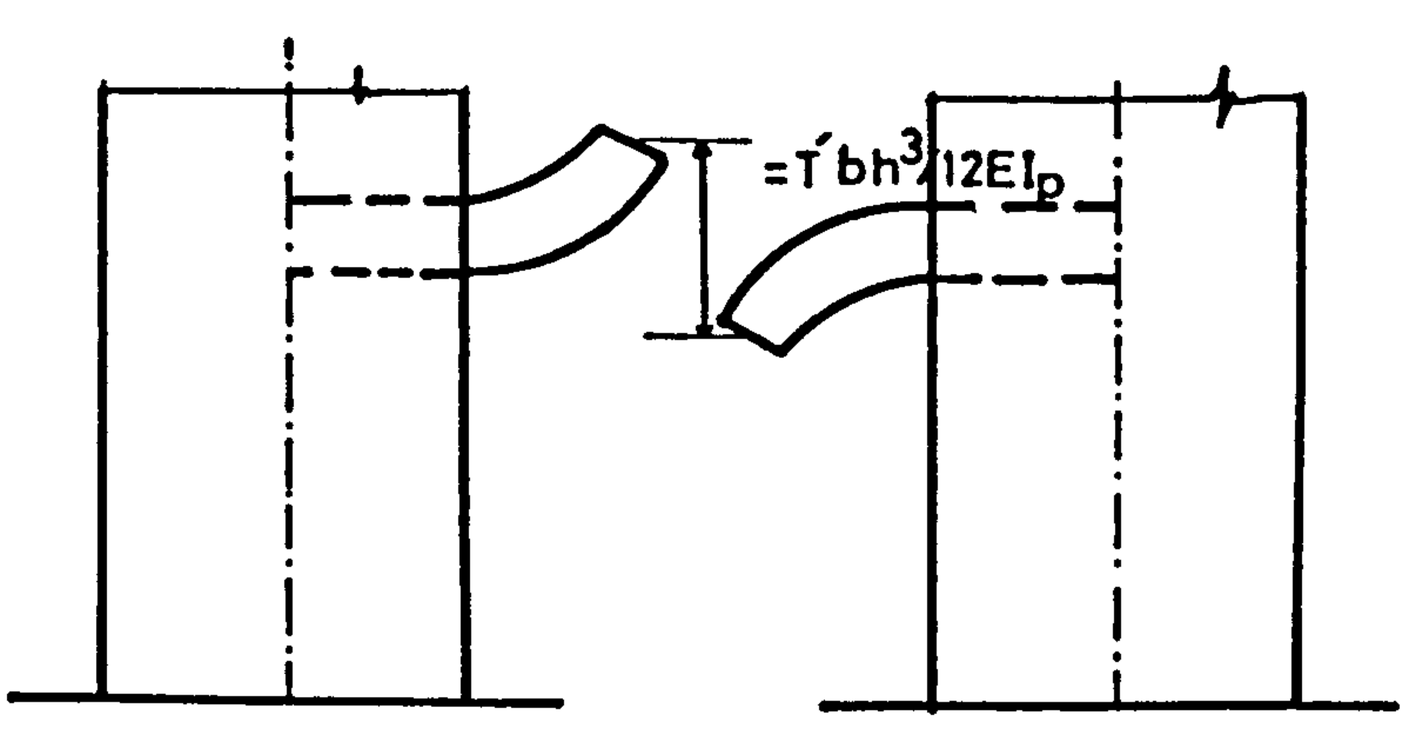

Figure (2.5c) : Displacement due to bending laminae.

After differentiation and using well-known relations:

$$\frac{d}{dx}\left(\int_x^H T\,dx\right) = -T \quad \text{and} \quad \frac{d}{dx}\left(\int_x^H x\,dx\right) = -x,$$

equation 2.3 becomes $\frac{d^2T}{dx^2} - \alpha^2 T = -\gamma x$ (2.6)

Equation 2.6 is also valid for walls containing two bands of openings. In this case the coefficients of the differential equation are found to be:

$$\alpha^2 = \left(\frac{2\ell^2}{2I_1 + I_2} + \frac{1}{A_1}\right) \frac{12\,Ip}{Hb^3} \tag{2.7}$$

$$\text{and } \gamma = \frac{P\ell}{2I_1 + I_2} \frac{12\,Ip}{Hb^3} \tag{2.8}$$

At the top of the wall no restraint against a mutual vertical translation of the piers is imposed. In this case the function T should vanish i.e. $T = 0$ (2.9)

Similarly when the supporting structure completely restrains the ends of the piers against a mutual rotation and translation, we obtain : $\left(\frac{dT}{dx}\right)_H = 0$ (2.10)

The problem is to determine the function T which is a solution differential equation (2.6) within the domain $0 \leq x \leq H$ and satisfying the boundary conditions at the top and the bottom of the wall.

From known mathematical procedures, the general solution can be written as: $T = C \sinh \alpha x + D \cosh \alpha x + \frac{\gamma}{\alpha^2} x$ (2.11)

The integration constants C and D have to be determined from the boundary conditions.

At top i.e. at $x = 0$, $T = 0$, $D = 0$.

The governing equation then takes the form:

$$T = C \sinh \alpha x + \frac{r}{\alpha^2} x \qquad (2.12)$$

For different boundary conditions shown in Figures (2.4b, 2.6, 2.7a and 2.7b) at the bottom of the wall, Rosman evaluated constant C respectively as:

$$C = -\frac{r}{\alpha^3 \cosh \alpha H}$$

$$C = \frac{r_B - \frac{r}{\alpha^2}(1 + \alpha^2{}_B H)}{\alpha^2{}_B \sinh \alpha H + \alpha \cosh \alpha H} \qquad (2.13)$$

$$C = \frac{r_R - r/\alpha^2 (1 + \alpha^2{}_R H)}{\alpha^2{}_R \sinh \alpha H + \alpha \cosh \alpha H}$$

$$C = \frac{1}{\sinh \alpha H} \left(\frac{P\bar{H}}{2\ell} - \frac{r_H}{\alpha^2}\right)$$

where $\bar{H}$ is the height of the wall including the height of the columns on the ground floor.

Once the value of T is known, the shear forces Q_i ($i = 0....x$) of the connecting beams can be read from the T-diagram as shown in Figure (2.8).

The bending moments of the connecting beams can be found from:

$$M_w = \frac{1}{2} Q_i \, b' \qquad (2.14)$$

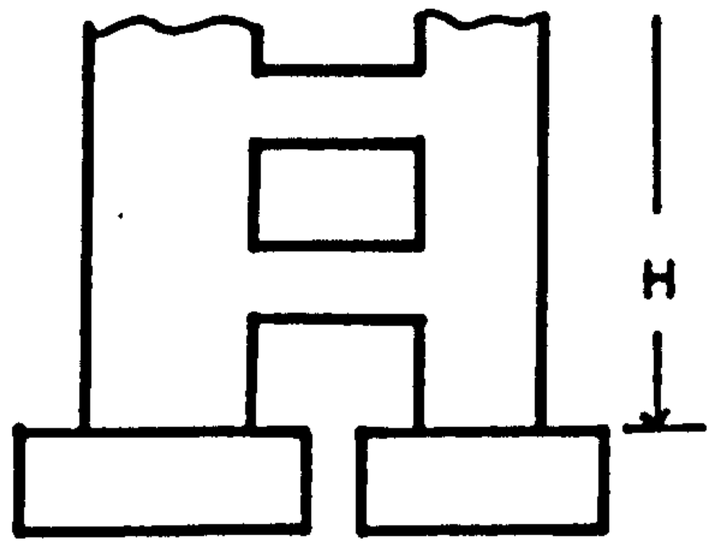

Figure (2.6) : Wall whose piers are fixed in separate foundation.

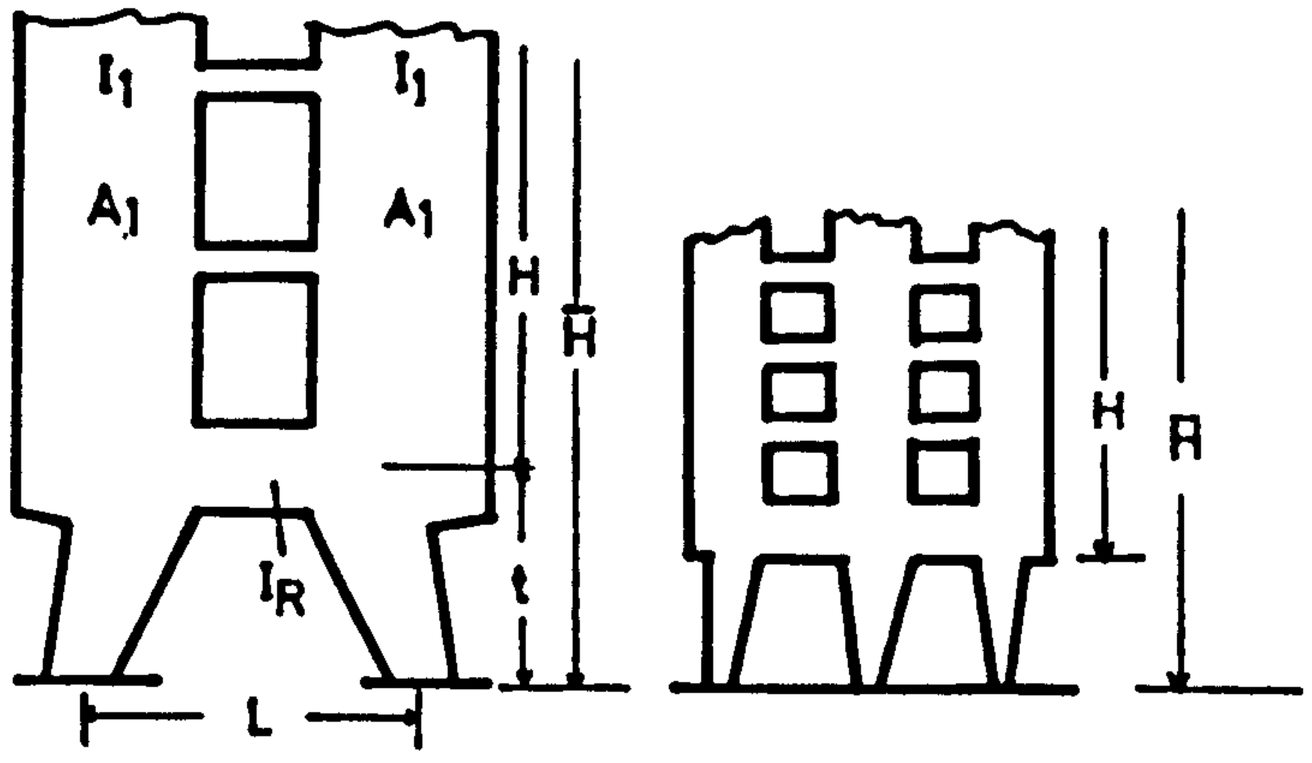

Figure (2.7) : Walls whose lower end beam has a stiffness much different from the stiffness of the upper beam.

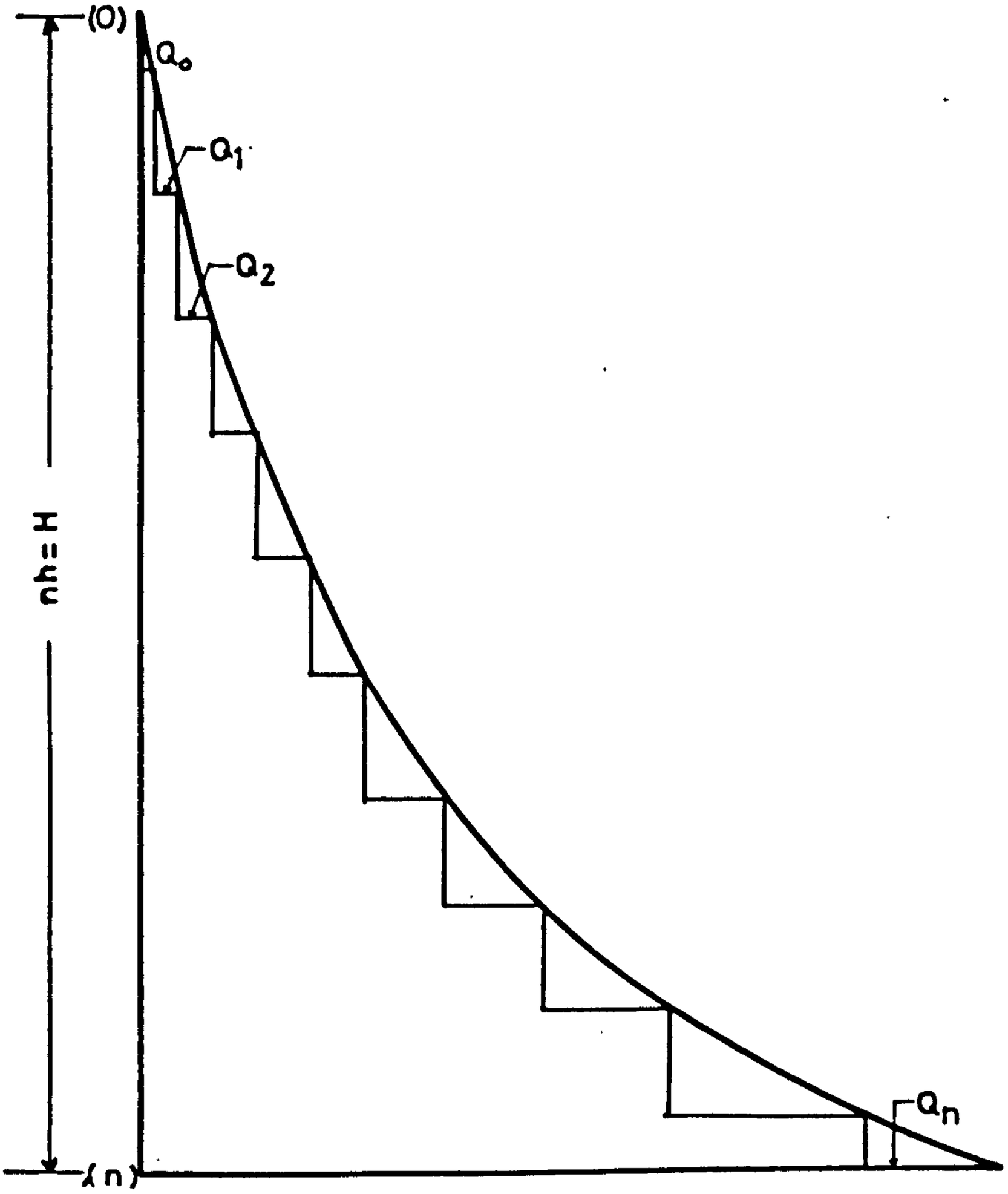

Figure (2.8) : Diagram of the integral shear force.

The total bending moment at an arbitrary cross-section of the wall is given by:

$$M = Px - T\ell \quad \text{or} \quad M = Px - 2T\ell \tag{2.15}$$

for walls weakened by one or two bands of opening respectively.

The bending moments of the walls are equal to

$$M_1 = \frac{I_1}{I_1 + I_2} M \,, \quad M_2 = \frac{I_2}{I_1 + I_2} M \tag{2.16}$$

for walls containing one band of opening and

$$M_1 = \frac{I_1}{2I_1 + I_2} M \,, \quad M_2 = \frac{I_2}{2I_1 + I_2} M \tag{2.17}$$

for two bands of openings.

Similarly for a uniformly distributed lateral load along the whole height H of wall:

$$\beta = \frac{.5w'\ell}{I_1 + I_2} \frac{12 I_p}{Hb^3} \tag{2.18}$$

$$\beta = \frac{.5w'\ell}{2I_1 + I_2} \frac{12 I_p}{Hb^3}$$

where w′ is the intensity of lateral load per unit height.

Equation of the integral shear force:

$$T = C\,\text{Sinh}\,\alpha x - \frac{2\beta}{\alpha^4}(\text{Cosh}\,\alpha x - 1) + \frac{\beta}{\alpha^2} x^2 \tag{2.19}$$

$$\text{where } C = \frac{1}{\text{Cosh}\,\alpha H} \frac{2\beta}{\alpha^3}\left(\frac{\text{Sinh}\,\alpha H}{\alpha} - H\right) \tag{2.20}$$

for walls of Figure (2.4b).

The total bending moment at an arbitrary cross-section of the wall can be found from:

$$M = T\ell - \frac{1}{2} \acute{w} x^2 \qquad M = 2T\ell - \frac{1}{2} \acute{w} x^2 \qquad (2.21)$$

Design curves were presented by Coull & Irwin (2) for the direct evaluation of the maximum shear force in any connecting beam of a coupled shear wall system and supplementary tables yield the actual position of the most highly stressed beam. For triangularly distributed load, the maximum shear can be calculated from

$$Q_{max} = \acute{w} \frac{\mu^2 H^2}{\alpha^2} K$$

where $$\alpha^2 = \mu^2 \left[\ell + \frac{(A_1 + A_2)(I_1 + I_2)}{A_1 A_2 \ell} \right]$$

and $$\mu^2 = \frac{12\ell}{b'^3 h'} \cdot \frac{I_p}{I_1 + I_2}$$

The value of K can be obtained from Figure (2.9).

2.3 EFFECTIVE WIDTH OF SLAB

The wide frame-column or the continuous connection methods are two-dimensional models which assume that the walls are connected by beams. However when the walls are connected solely by slabs the true stiffness of an equivalent beam is less than the total stiffness of the slab considering the entire width. For the sake of convenience it may be assumed that only a small portion of slab called 'effective width', with stiffness equal to the equivalent connecting beam is effective in resisting the effects of lateral loads. To evaluate the effective width for different sets of circumstances, several investigators have studied the nature of interaction between laterally loaded walls and coupling slabs, both experimentally and analytically.

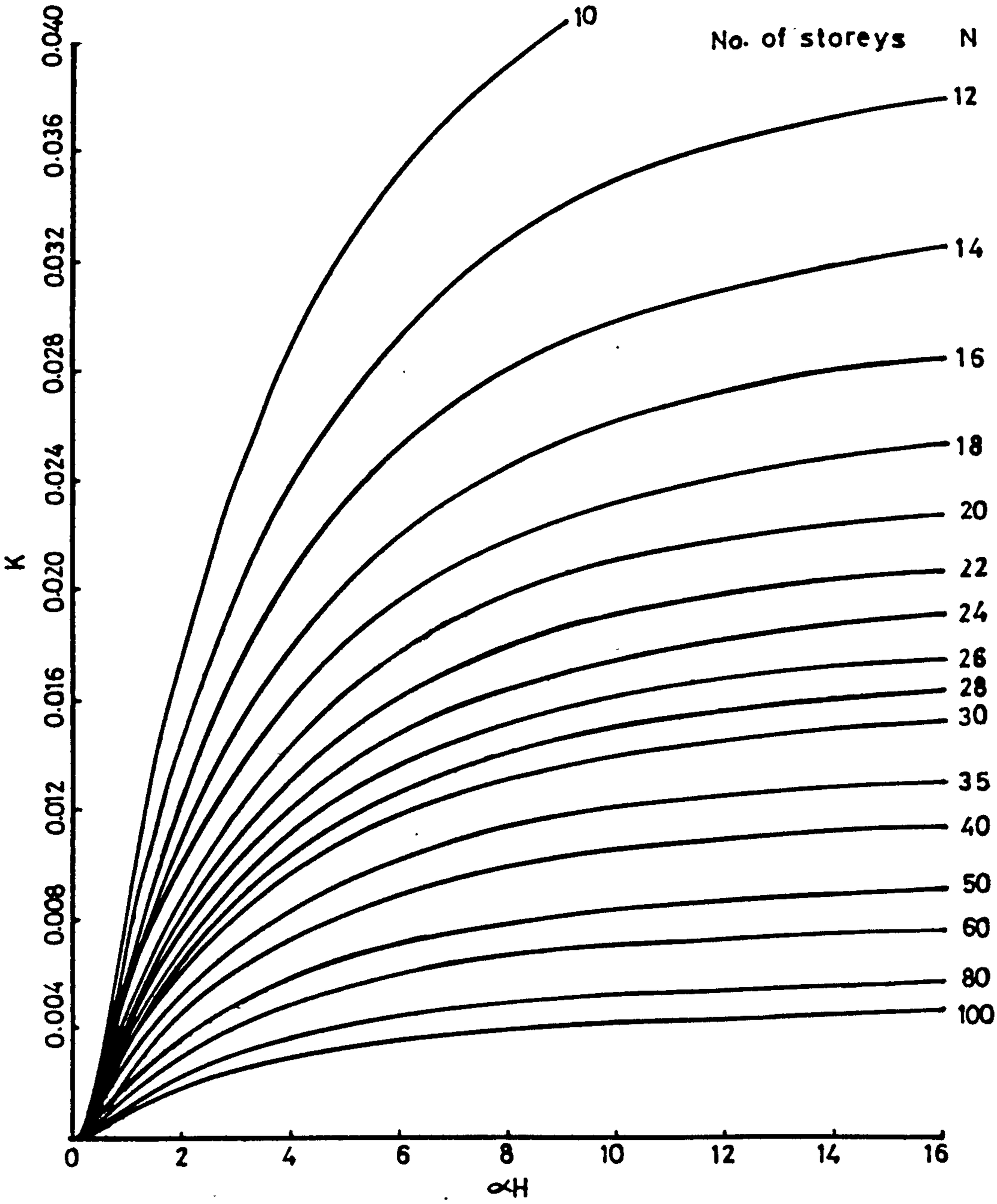

Figure (2.9) : Coefficient of maximum shear force K (triangular load).

2.3.1 Theorétical Investigations

The first paper concerning the effective width of the slab based on comprehensive investigations was by Qadeer and Stafford Smith (3). They discussed the interaction between walls and slabs in cross wall structures, considering planar, parallel, cross wall structures as shown in Figure (2.10). The bending of the slab along the lines of the walls was examined by the finite difference method. They analysed the slab as an elastic plate represented by well known fourth order differential equation:

$$\frac{\partial^4 w}{\partial x^4} + \frac{2\partial^4 w}{\partial x^2 \partial y^2} + \frac{\partial^4 w}{\partial y^4} = q/D \qquad (2.22)$$

where w = Vertical deflection

q = Intensity of the applied load

D = Flexural rigidity of the plate

The resistance of the floor slab against the displacement imposed by the shear walls is a measure of its coupling stiffness, which can be defined in terms of the displacements at its ends and the forces producing them. Thus referring to Figure (2.11), the stiffness of the slab may be defined either as a rotational stiffness M/θ or as a translational stiffness Q/δ, since the two are related. For convenience, the rotational and translational slab stiffnesses can be expressed in the form of non-dimensional stiffness factors K_θ and K_δ given by:

$$K_\theta = \frac{M}{\theta} \cdot \frac{1}{D} \quad \text{and} \quad K_\delta = \frac{Q}{\delta} \cdot \frac{L_w^2}{D} \qquad (2.23)$$

where D is the flexural rigidity of the plate and L_w is the clear opening between walls. It may be assumed that a strip of slab/

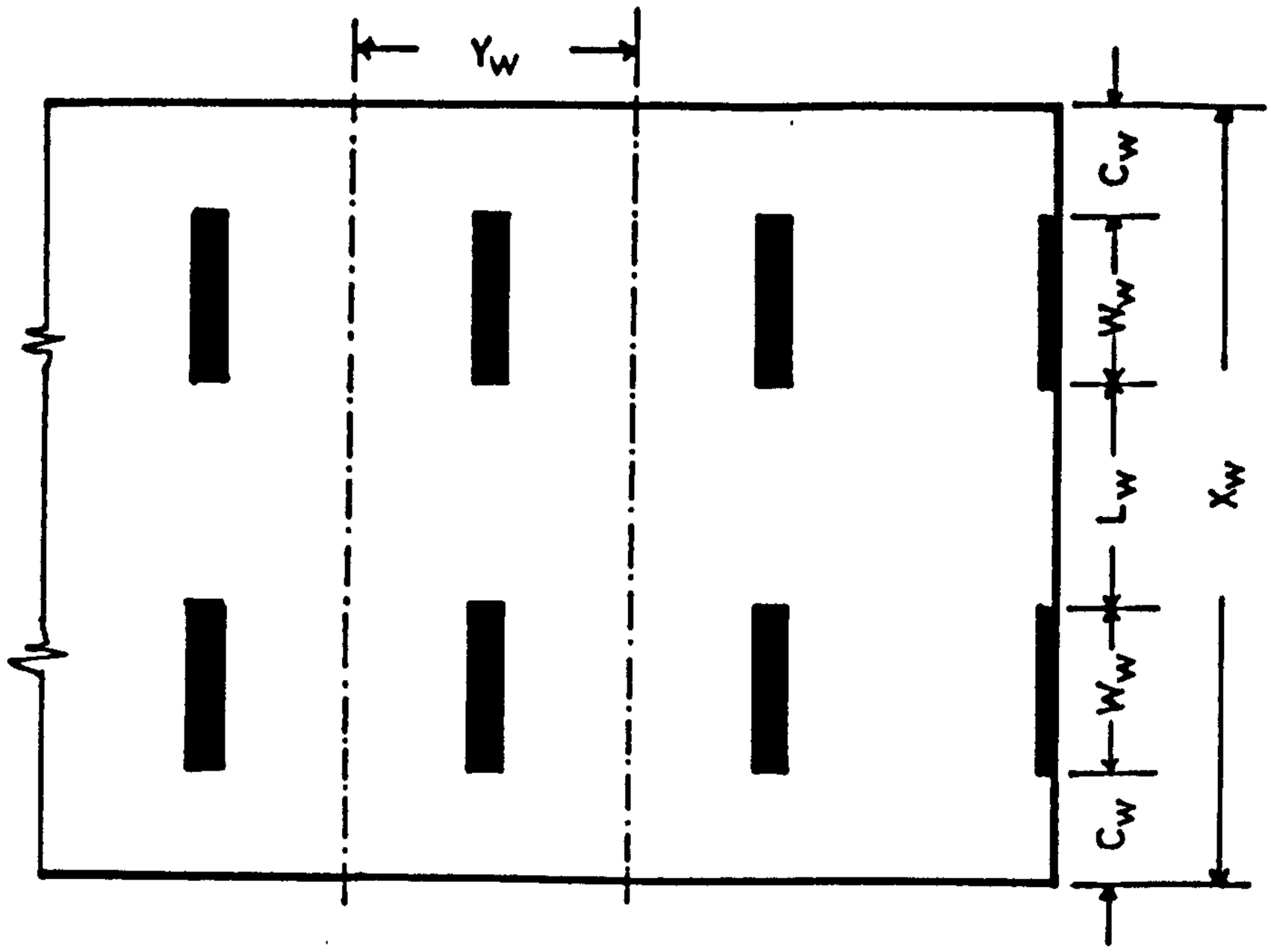

Figure (2.10) : Plan of a typical shear wall structure consisting of plannar walls and slabs.

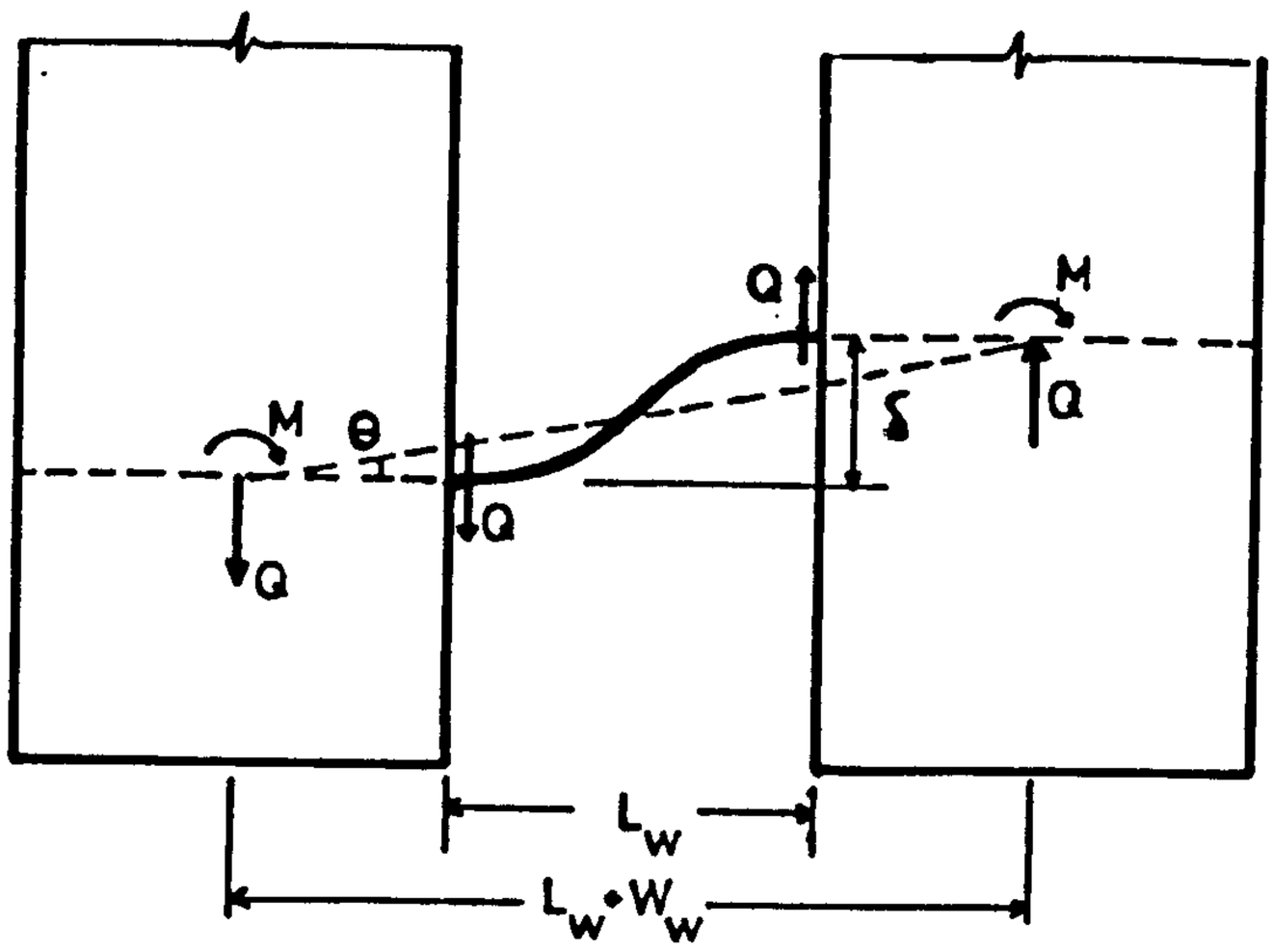

Figure (2.11) : Bending of a connecting slab in a laterally loaded shear wall structure.

acts effectively as a beam in coupling a pair of walls. The effective stiffness of the slab may then be defined simply in terms of the geometric and material characteristics of the equivalent beam. The effective width of slab can be established by equating the translational stiffnesses of the slab to those of the equivalent beam, which may be written as:

$$\frac{Q}{\delta} = \frac{12\ EI}{L^3_w} \qquad (2.24)$$

where $I = Y_e\ h^3/12$ is the second moment of area of the beam, of effective width Y_e and thicknesses h.

For establishing a similar relationship in terms of rotational stiffness, referring to Figure (2.11),

$$2M = Q\ (L_w + W_w) \text{ and } \theta = \frac{\delta}{(L_w + W_w)}$$

$$\therefore \quad \frac{M}{\theta} = \frac{Q}{\delta} \cdot \frac{1}{2}\ (L_w + W_w)^2$$

By using equation (2.24) in above equation,

$$\frac{M}{\theta} = \frac{6\ EI}{L_w 3}\ (L_w + W_w)^2 \qquad (2.25)$$

The effective width can then be expressed in terms of the rotational and translational form as (5),

$$\frac{Y_e}{Y_w} = \frac{K_\theta}{6(1-\nu^2)}\ (\frac{L_w}{Y_w})\ \ (\frac{L_w}{L_w + W_w})^2 \qquad (2.26)$$

or

$$\frac{Y_e}{Y_w} = \frac{K_\delta}{12(1-\nu^2)}\ (\frac{L_w}{Y_w}) \qquad (2.27)$$

where L_w, W_w, Y_w are as shown in Figure (2.10) and ν is Poisson's ratio.

Tso & Mahmood (4) and Coull & Wong (5) in their study used finite element method to obtain the stiffness of the slab coupled shear wall systems. The configurations of shear wall systems analysed by them include slab coupled plannar walls, T-section walls and box section core walls. For all these wall configurations, Tso & Mahmoud (4) took the overall dimensions constant and equal to X_w and Y_w as shown in Figure (2.12) and the results were presented in the form of design curves for wall thickness equal to zero, 228.6 mm (9") and 304.8 mm (12").

The results of their study④ can be summarized as follows:

(i) The values of effective width obtained by finite element are higher than those of Qadeer and Stafford Smith which were obtained by finite differences, indicating that the mesh used for finite difference was probably too coarse.

(ii) Finite thickness of wall has a significant effect on the effective width, particularly when wall opening ratio L_w/X_w is small.

(iii) The portions of slab cantilevering outside the walls (marked as C_w in Figure (2.10)have a negligible effect on the effective width.

(iv) For end bays, if the thickness of end walls is same as that of interior walls, the stiffness of bay is 54% of that of typical interior bay. However with end bay having thickness equal to/

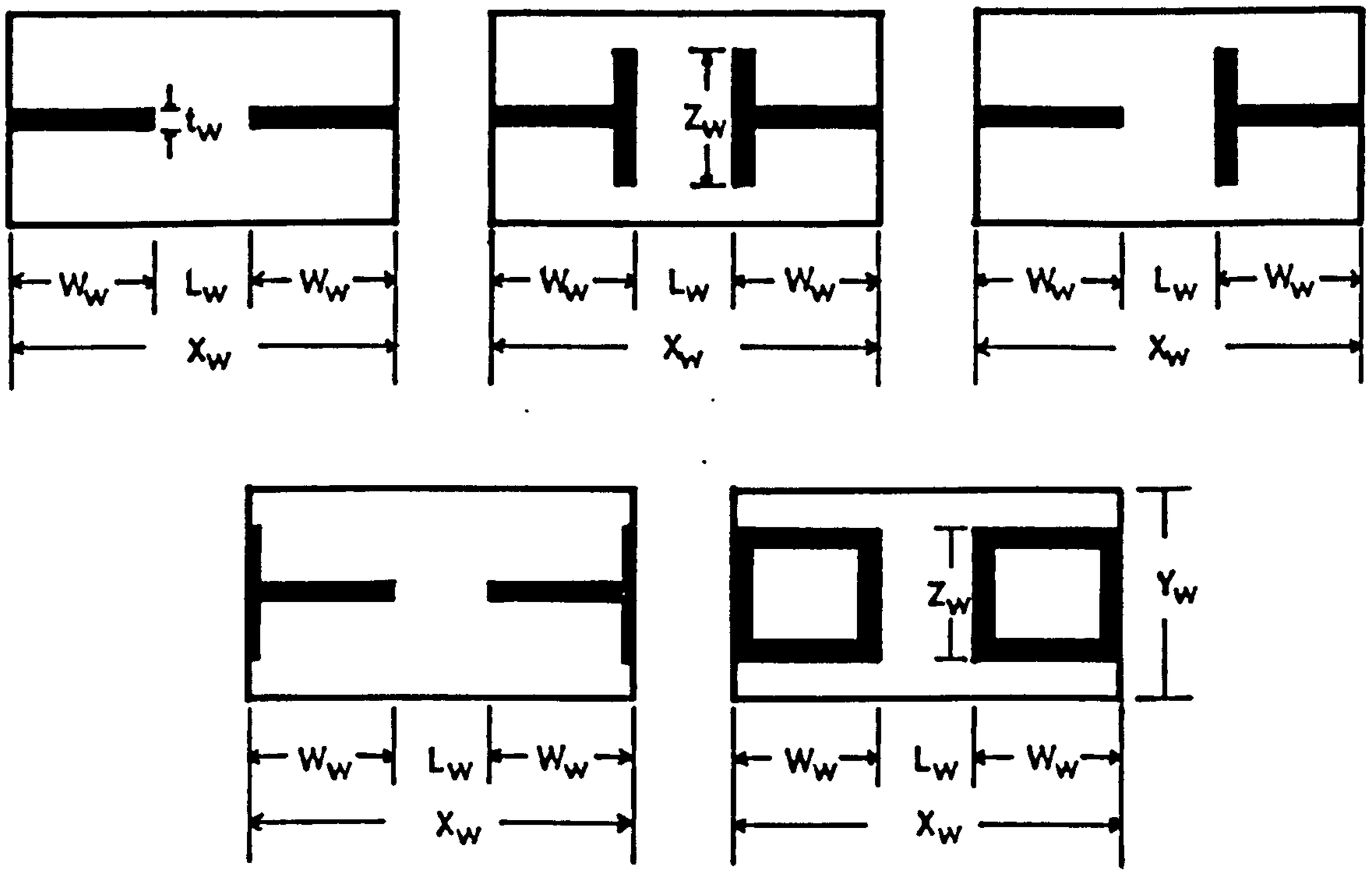

Figure (2.12) : Different configurations of shear walls considered by Tso and Mahmoud.

half of that of the interior walls, the stiffness of end bay is about 42% of that of the typical interior bay.

(v) For shear walls of T-section comparing the theoretically calculated values based on finite element analysis with the experimental results of Coull & El-Hag (6) (see section 2.3.2), it was observed that good agreement between the theoretical and experimental results was possible only when half the flange width was used in the calculation instead of the full width.

(vi) For plannar and T-section as shown in Figure (2.12), the stiffness of the slab is affected somewhat by the flange width but beyond a certain critical width, the stiffness of the system becomes insensitive to any further increase of the flange width of the T-section wall. The empirical rules of using half the flange width in the calculation is applicable in this case also.

(vii) Flanges on the outer edges of walls have negligible effect on the effective width of slabs.

(viii) The effective width for coupled box core walls differ by only 3% from the corresponding value of T-section walls.

(ix) As a general observation it was noticed that the effect of coupling is small when the wall opening ratio L_w/X_w (Figure (2.10)) is larger than 0.3. However when the wall opening ratio is too small, very large elastic forces exist at the inner edge of the wall causing some local deformation in the wall which is not taken into account in the theoretical work, therefore results obtained in such a case may become inaccurate. The general range of interest lies between wall opening ratios of say 0.1 to .3.

Design charts produced by Coull & Wong (5) for rapid determination of effective width of slab for plannar walls with different non-dimensional structural parameteric ratios, $\frac{L_w}{X_w}$ and $\frac{Y_w}{X_w}$ are shown in Figure (2.13).

Coull and Wong (5) concluded that:

(a) The effect of variations in the absolute wall lengths is negligible.

(b) The effect of dissimilar wall lengths in a pair of coupled walls can also be neglected if the ratio of the length of the shorter wall to that of the corridor opening is greater than about 0.5.

They also analysed three different configurations of L-shaped walls, shown in Figure (2.14). With the help of numerical study they have suggested that the effective width for the first and second wall configurations may be obtained directly from the curves presented for coupled T-shaped walls while for the third they have proved that although the flanges are not directly cross coupled, they have a considerable influence on the slab stiffness as a result of their restraining action and for the same total flange width, the effective slab width in this wall configuration and in the plannar wall configuration are practically identical for any corresponding set of wall slab ratios $\frac{L_w}{X_w}$, $\frac{Y_w}{X_w}$ and $\frac{Z_w}{Y_w}$ where L_w, Y_w, Z_w are the different dimensions as shown in Figure (2.12).

Tso and Mahmoud (4) analysed the box core wall configuration without opening but in practice openings do occur for providing access in to the space bounded by these walls as shown in Figure (2.15). In such/

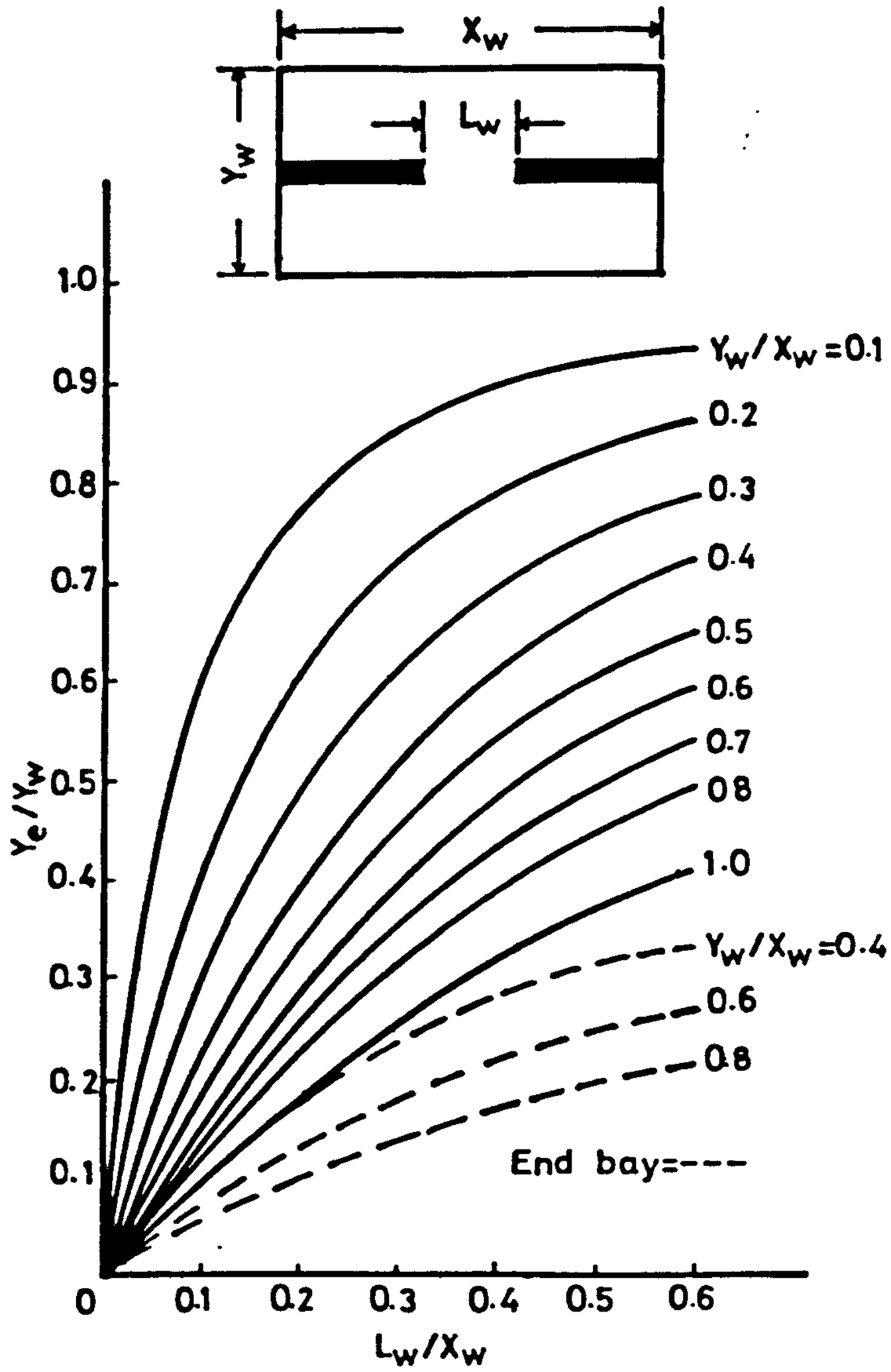

Figure (2.13) : Design chart for rapid determination of effective width of slab coupling plannar walls.

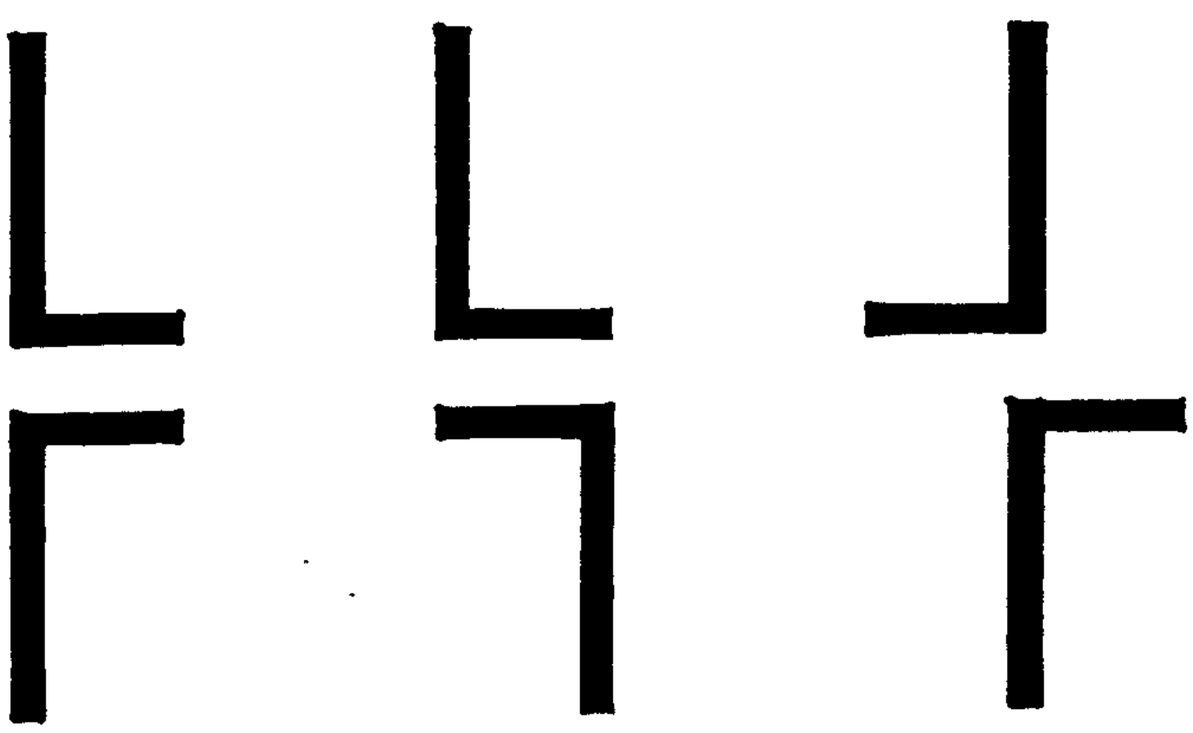

Figure (2.14) : Different L-shaped configuration of shear walls.

a case the stiffness of the connecting slab will be influenced both by the size of opening and the flexibility of lintel beams provided at each storey level. Coull & Wong (5) have dealt with this case also and effective widths Y_e have been evaluated by them for slabs of various aspect ratios $\frac{Y_w}{X_w}$, coupling a pair of square cores with various access opening ratios $\frac{B_w}{Z_w}$ and lintel beam depth ratio D_w/Z_w, for fixed $\frac{L_w}{X_w}$ and $\frac{Z_w}{X_w}$ ratios as shown in Figure (2.15). It is apparent from their investigations that the influence of a core opening is relatively more significant when the core opening width $\frac{B_w}{Z_w}$ is less than 0.5. With a full core opening ($B_w/Z_w = 1$, $D_w/Z_w = 0$), the effective width of the worst affected slab is reduced by about 25% by the presence of opening.

2.3.2 Experimental Investigations

Qadeer and Stafford Smith (3) performed experiments on asbestos sheet slab models to check the accuracy of their work. However a more comprehensive experimental study was conducted by Coull & El-Hag (6).

Under lateral loads the shear walls rotate. This rotation produces relative displacement, δ, between the ends of the connecting beam. Since the effective stiffness of the floor slab can be defined by the relationship between this relative displacement, δ, and the forces producing it, an apparatus was designed to simulate this type of relationship to be measured directly. The walls were simulated by two steel plates of dimensions 152.4 x 76.2 x 6.35 mm which pivoted freely on ball races carried on 12.7 mm diameter steel rods. The steel rods were supported in slots cut in the side of a heavy channel. The slabs were cut from perspex sheet usually/

4.76 mm thick. This testing arrangement is shown in Figure (2.16). The results were presented as curves showing variation of slab stiffness factor and effective width with wall opening for combinations of plane and flanged walls.

A number of perspex models were tested by Wong (7), to check the accuracy of his theoretical results. Generally there was a good agreement between theoretical and experimental results.

2.3.3 Effect of nonlinearity

It is obvious from the previous discussion that the work on the effective width of slab was confined to elastic casesonly. To the best of author's knowledge, to date the only paper published about the experimental behaviour of a real concrete slab coupling shear walls is that of Schwaighofer and Collins (8). Only one reinforced concrete model shown in Figure (2.17), representing to one-third scale, a particular shear wall structure was tested by them. In the test hydraulic jacks were used for loading the model and the effect of lateral load was simulated by relative vertical displacement of one portion of the model with respect to the other. The elevation and testing arrangement of the model is shown in Figure (2.18). The model consisted of only one slab. Strains in steel along section K-K and L-L (Figure (2.17))were measured. From the force-displacement plot they showed that within the elastic range the results of effective width of slab were in good agreement with those obtained earlier by different investigations. They suggested that the flexural strength of the coupling slab could be predicted by using a slab width equal to the corridor opening plus/

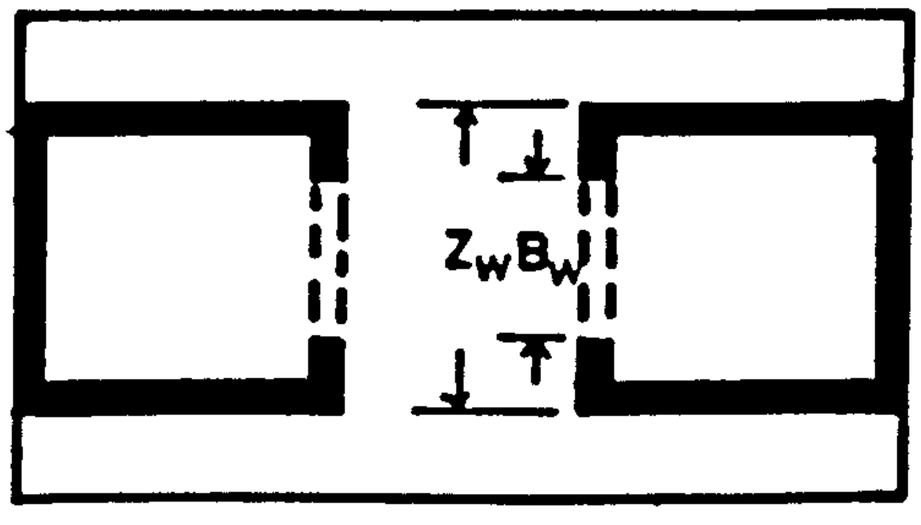

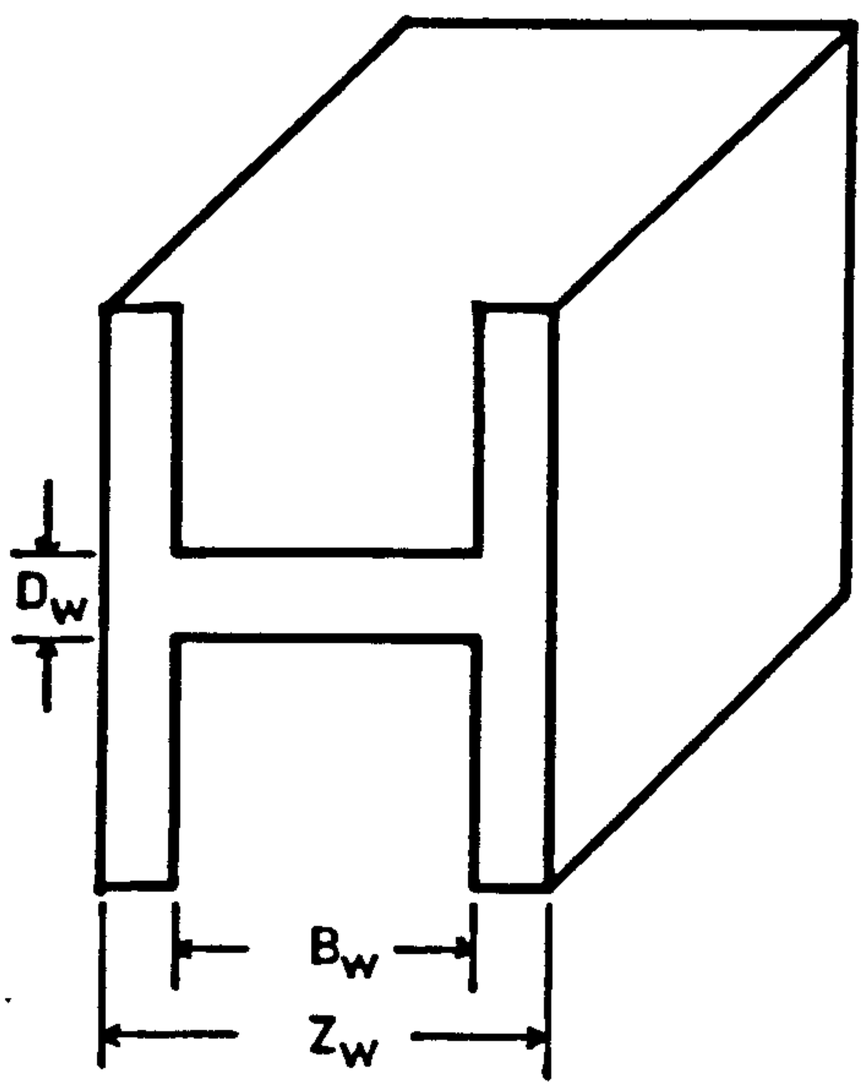

Figure (2.15) : Box core shear walls with openings.

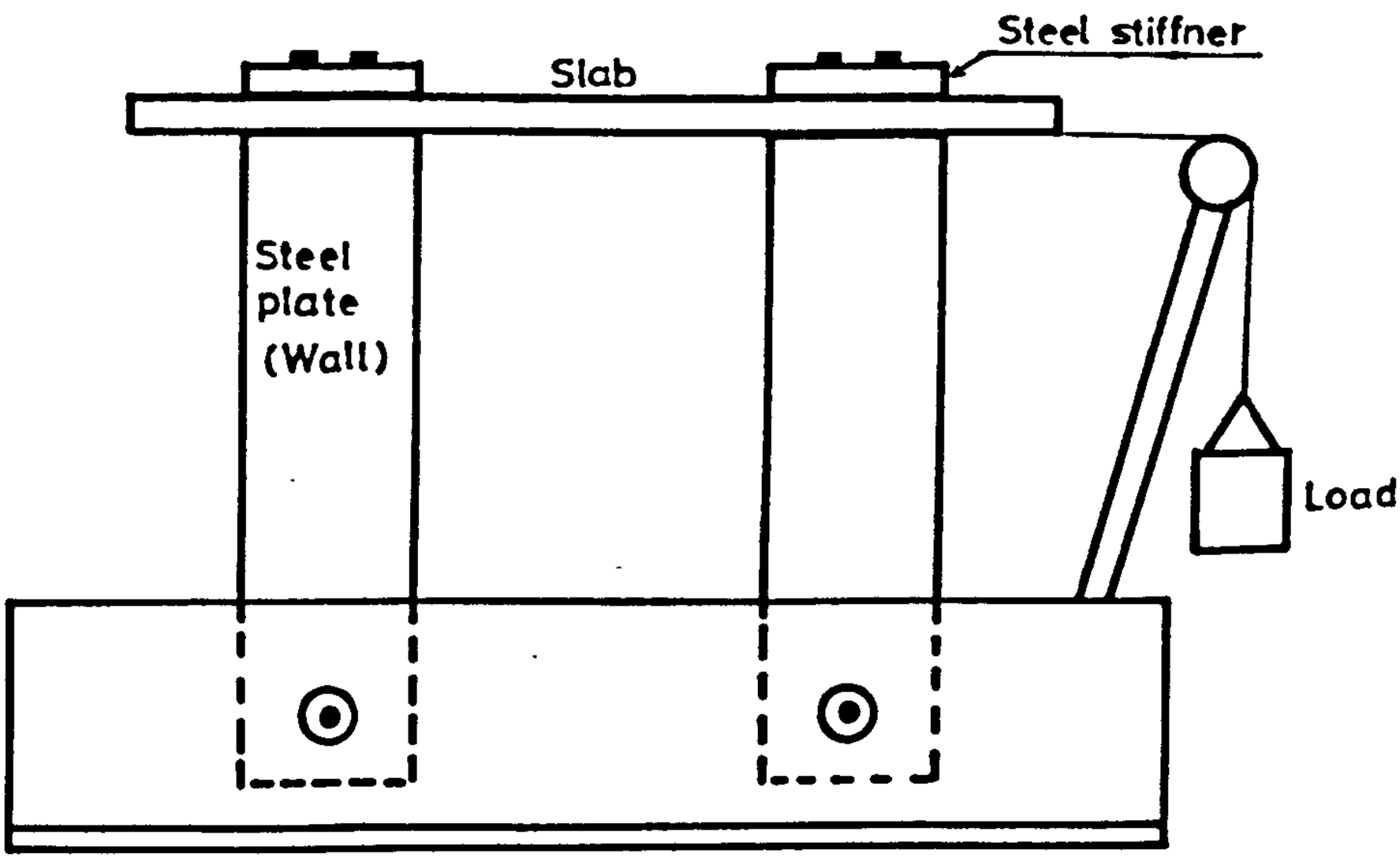

Figure (2.16) : Typical testing arrangement for experimental study of effective width problem (Elastic range).

the wall thickness. They were of the opinion that the reinforcing steel should be provided in coupling slabs to resist the lateral loading, arranged as shown in Figure (2.19).

2.4 DISTRIBUTION OF MOMENTS IN SLABS DUE TO LATERAL LOADS

Better understanding of the distribution of moments induced in the slab due to lateral loads is essential not only for the economical flexural design of the slab but also for the design of the wall-slab connection, since the strength of this connection is also affected by the distribution of the forces around the wall-slab junction.

Using finite differences method Chang (9) obtained the variation of both the longitudinal and transverse moment along certain sections for a unit vertical displacement of the line of contraflexure simulating lateral loads. A number of parameters like bay width sizes (Y_w) corridor opening widths L_w and overall width of the building X_w were considered. He plotted his results as moment factors K_1 and K_2. Then moments along these sections can be found from:

$$M_x = K_1 \left(\frac{D}{(L_w/2)^2}\right)$$

$$M_y = K_2 \left(\frac{D}{(L_w/2)^2}\right) \qquad (2.28)$$

where D is flexural rigidity.

Using the finite element method, the contours of bending moment factors $\bar{M}_x$ and $\bar{M}_y$ for slabs with ratios $\frac{L_w}{Y_w}$ ranging from 1-4-and with a wall thickness ratio t_w/L_w of 0.1 were produced by Coull & Wong (10). The contours allow a rapid evaluation of bending moments M_x and M_y at any point on the slab.

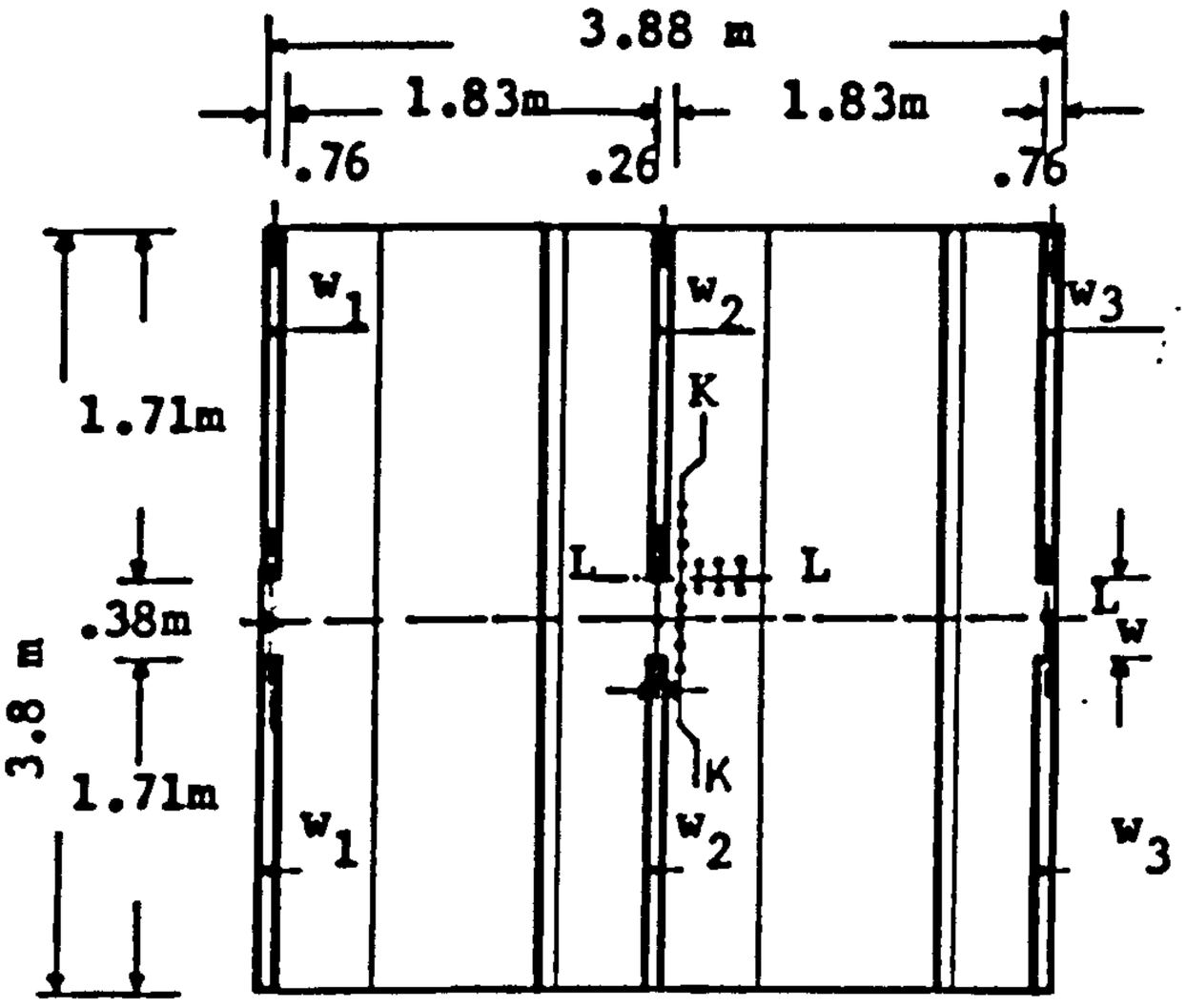

Fig. 2.17 Plan of the model tested by Schwaighofer & Collins.

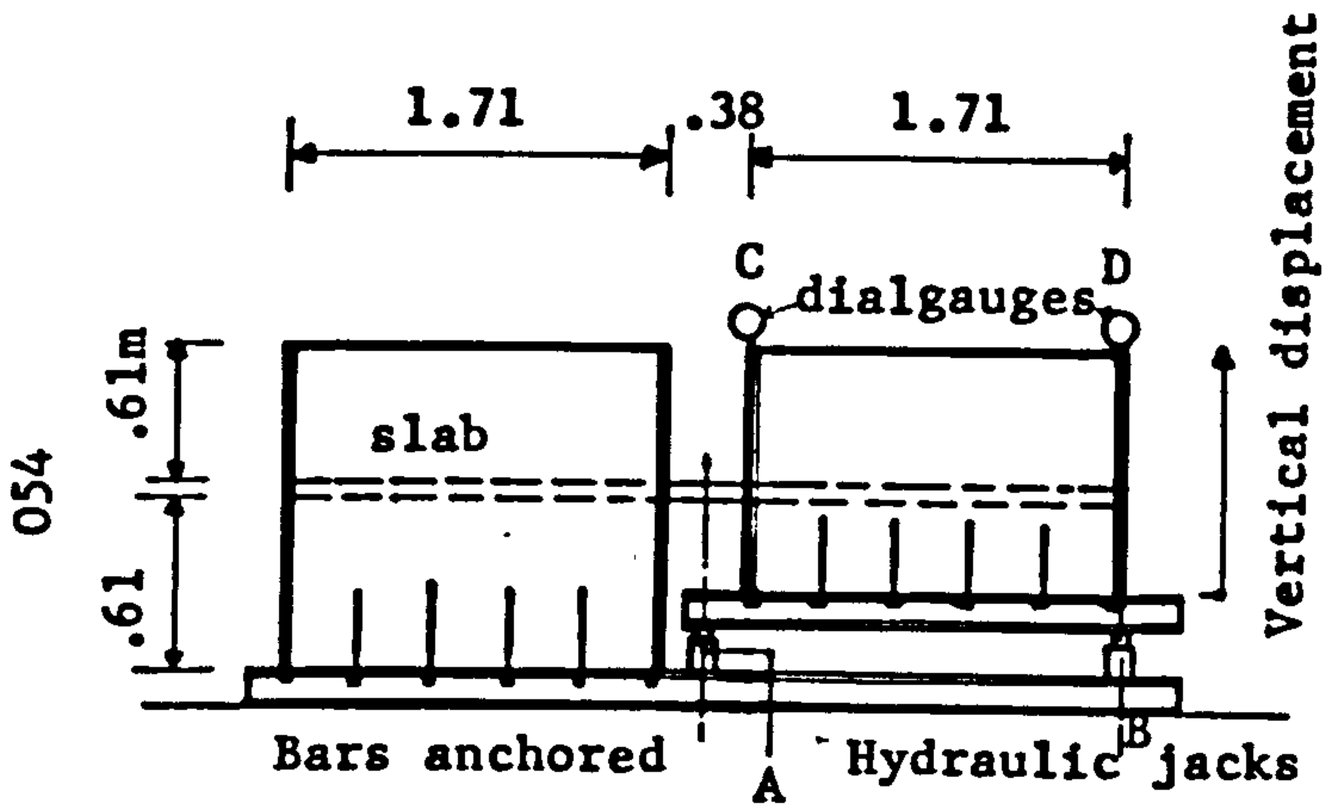

Fig. 2.18 Elevation & Testing arrangement of the model.

Fig. 2.19 Proposed arrangement of flexural steel bars in connecting slab of a shear wall structure subjected to lateral loads.

In the early stages of a design or a feasibility study of the structural system, the stresses at critical sections are of immediate interest to the designer, who is required to establish fairly quickly realistic member sizes for the structure. The maximum longitudinal bending moments due to lateral loads in the connecting slabs of a shear wall-slab structure act along a transverse section at the slab-wall junction. A knowledge of the approximate variation of this longitudinal bending moment is usually sufficient to allow the adequacy of the chosen thickness to be established. Therefore Wong & Coull (10) produced a generalized curve showing the variation of bending moment factor $\bar{M}_x$ along this section (zero wall thickness). This curve is shown in Figure (2.20). The intensity of moment M_x along this section can easily be calculated from:

$$M_x = \frac{\bar{M}_x M_a}{6(1-\gamma^2)} \qquad (2.29)$$

where M_a is the maximum average bending moment in the equivalent connecting beam and is given by: $M_a = \frac{1}{Y_e}(V_w \frac{L_w}{2})$. Here V_w is the total shear due to later load.

2.5 STRENGTH OF WALL-SLAB CONNECTION

A very large shear force is induced in the connecting slab along the line of contraflexure due to lateral loads. This shear is transferred to the wall at the wall-slab junction. Typical curves showing the distribution of shear in the slab along the transverse section BC passing through the inner edge of wall and that at a section AB along the sides of the wall, obtained by finite element analysis by Coull & Wong, are shown in Figure (2.21). It is clear that the elastic analysis predicts very high concentration of shear/

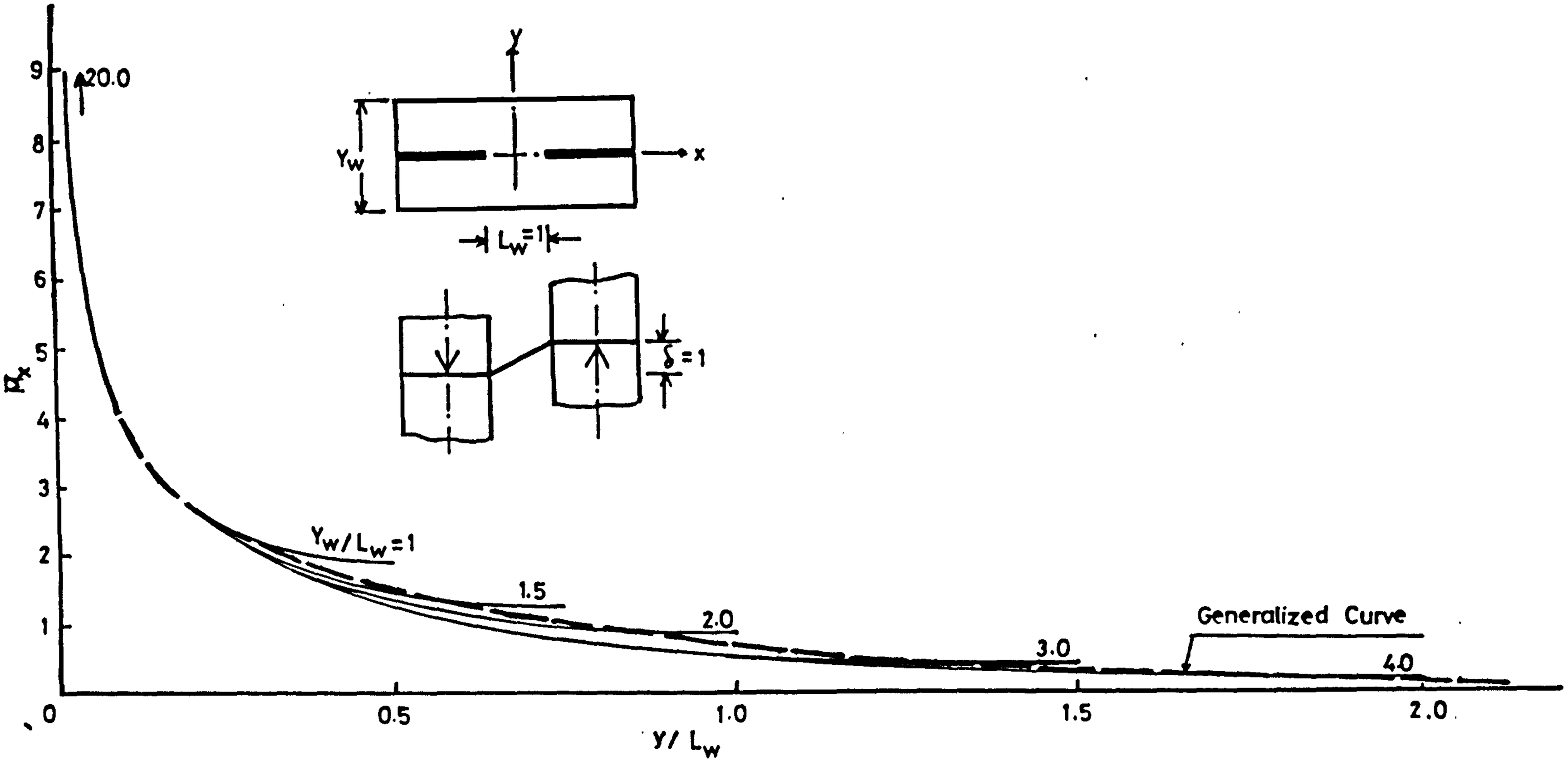

Figure (2.20) : Variation of longitudinal bending moments at critical transverse slab section for various slab widths.

force at the nose of the wall. Evidently cracking of the slab will reduce this concentration.

Recommendations by different investigators to predict the strength of wall-slab connection against the induced shear are reviewed below:

1) Based on the shape of the shear wall reaction curve, which was obtained by using finite difference method, Chang (9) suggested that for plannar walls, the critical section for shear due to lateral loads should be assumed to be located at a distance $\frac{d}{2}$ from the wall faces (where d is the effective depth of slab) and he extended to a distance equal to $L_w/4$ along the sides of the wall as shown in Figure (2.22), where L_w is the corridor opening width. Further he proposed that if M_w is the total moment induced in a connecting slab due to lateral load and V_w is the shear force, then the total positive idealized reaction, R_w, at the wall may be estimated from:

$$R_w = \frac{M_w}{.5(\frac{X_w - L_w}{2})} + V_w \qquad (2.30)$$

where X_w is the overall width of the building as shown in Figure (2.10)and L_w is the corridor opening width. The above formula has been proposed without discussing any basis for it. In fact the term $(\frac{X_w - L_w}{2})$ is the wall width W_w. It appears that the typical structure for which the wall reaction, R_w, was calculated, it was found to be equal to that obtained from the above expression.

The nominal shear stress v_i can be calculated from:

$$v_i = \frac{R_w}{(2d + t_w + \frac{L_w}{2})d} \qquad (2.31)$$

where t_w is the thickness of wall.

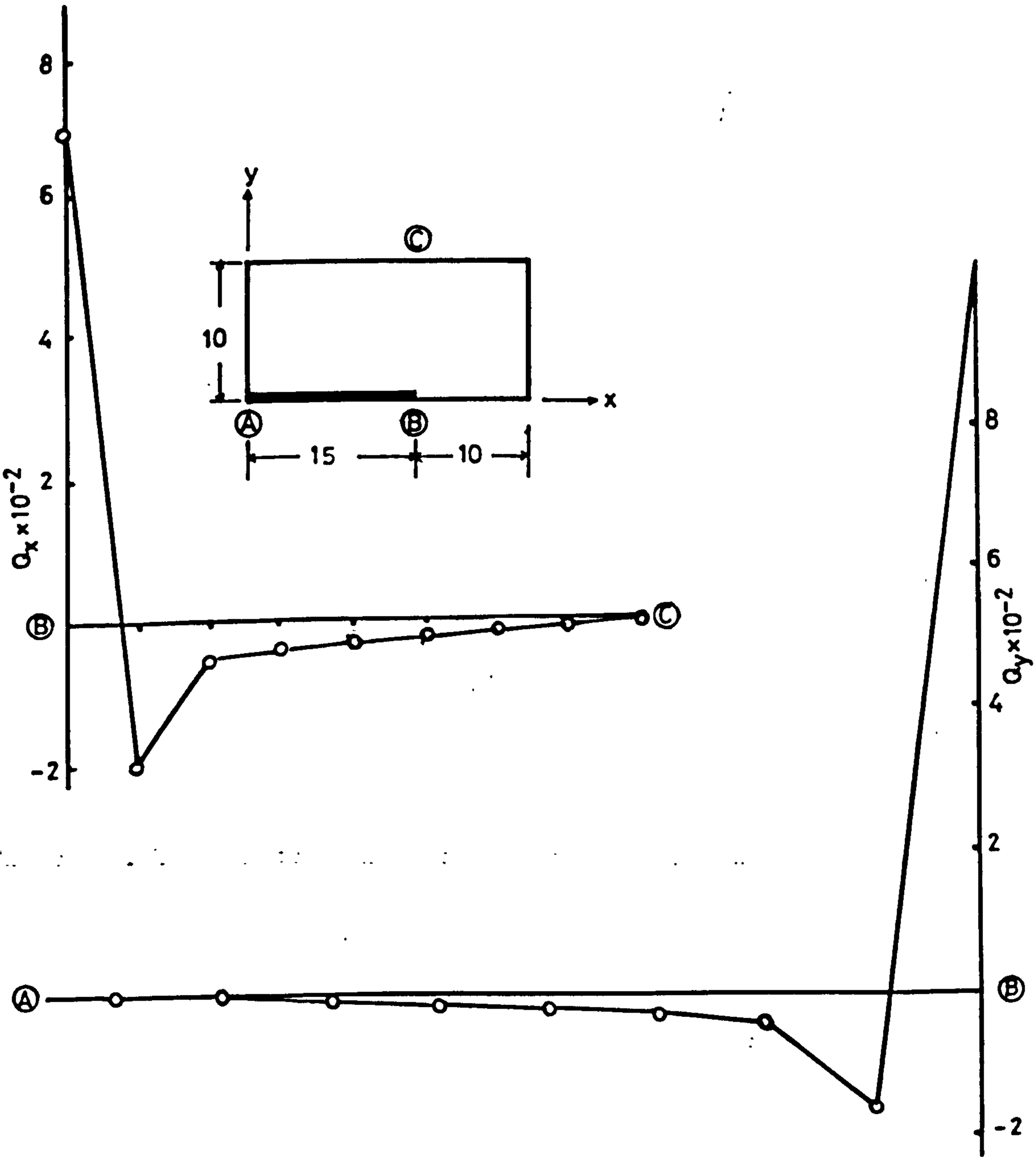

Figure (2.21) : Distribution of shear induced in slab along sections AB and BC due to lateral load.

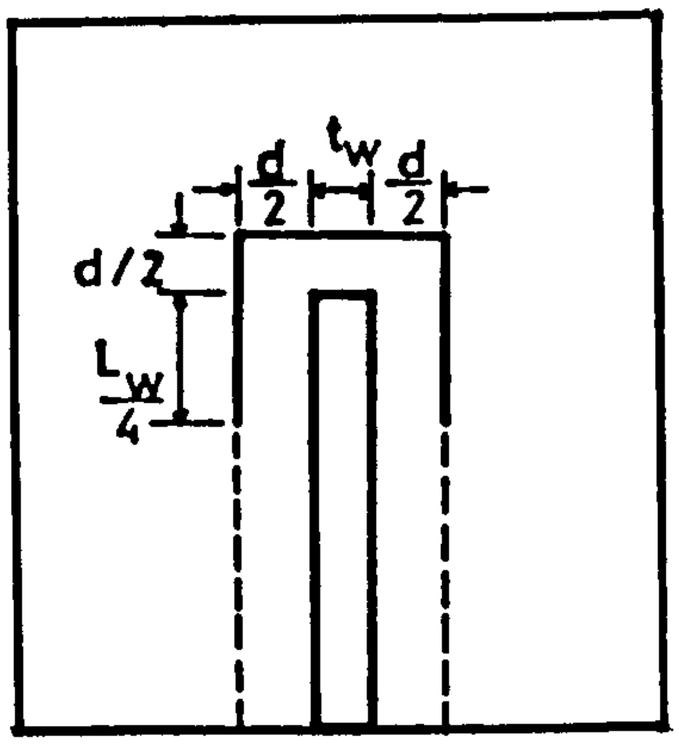

Figure (2.22) : Critical section for shears due to lateral loads, proposed by Y.C. Chang.

The shear stress calculated from the above formula may be compared with the critical value v_c given by ACI-318-71 (43).

2) Coull & Wang (10) have developed a procedure to calculate the shear stress induced along the critical section for shear. The location of the critical section depends upon the particular code of practice in use. If U is the distance of critical section from the wall periphery, then the length over which the critical section be assumed to be extended along the sides of the wall may be taken equal to 0.5U. Thus if the critical section is taken at a distance of 1.5 h as prescribed by CP 110 (44) for slab-column connections, then the total length of the critical section is equal to $t_w + (1+\pi)1.5h$ where h is the overall thickness of the slab and t_w is the thickness of wall.

Due to the transfer of moment, the total +ve shear induced at the wall-slab connection is more than that induced at the line of contraflexure (i.e. centre line of corridor opening), due to lateral load. Let V_w be the shear induced at the line of contraflexure due to lateral load and Q_w be the total +ve shear induced at the wall-slab connection, then

$$K_q = Q_w / V_w$$

The shear stress at the wall-slab connection can be calculated from:

$$= \frac{K_q V_w}{t_w + (1 + \pi)1.5h} \qquad (2.32)$$

The shear stress calculated from the above formula can be compared with the critical shear stress recommended by the codes of practice (43, 44).

Using the elastic finite element analysis, curves for values of non-dimensional structural parameteric ratios, $^{Y_w}/_{L_w}$ equal to 1,2 and 4 have been produced by Coull & Wong which can be used to estimate the value of shear modification factor, K_q, at any non-dimensional peripheral distance, $^{U}/_{L_w}$, from the wall. These curves are shown in Figure (2.23).

The work presented in this section so far is theoretical in nature and is not supported by any experimental evidence. Due to the redistribution of shears and moments at high loads, the behaviour of the connection could be different from the one predicted on the basis of elastic analysis.

3) In the light of cracking pattern of slab at different stages of loading of their model, Schwaighofer and Collins (8), have inferred that the critical section for shear lies at a distance $\frac{d}{2}$ (where d is the effective depth of slab) away from the wall along the inner edge of the wall and it extends to a distance $t_w + d$ (where t_w is the wall thickness) as shown in Figure (2.24). They have proposed that for calculating the strength of the connection a value of critical shear stress v_c, equal to $0.33\sqrt{fc'}N/mm^2$ as recommended by ACI 318 (43) be adopted.

2.6 STRENGTH OF SLAB-COLUMN CONNECTION SUBJECTED TO COMBINED LOADING.

2.6.1 General

In many respects the problem of the strength of wall-slab connection carrying lateral loads in addition to normal gravity loads is similar to the problem of flat slab-column structures/

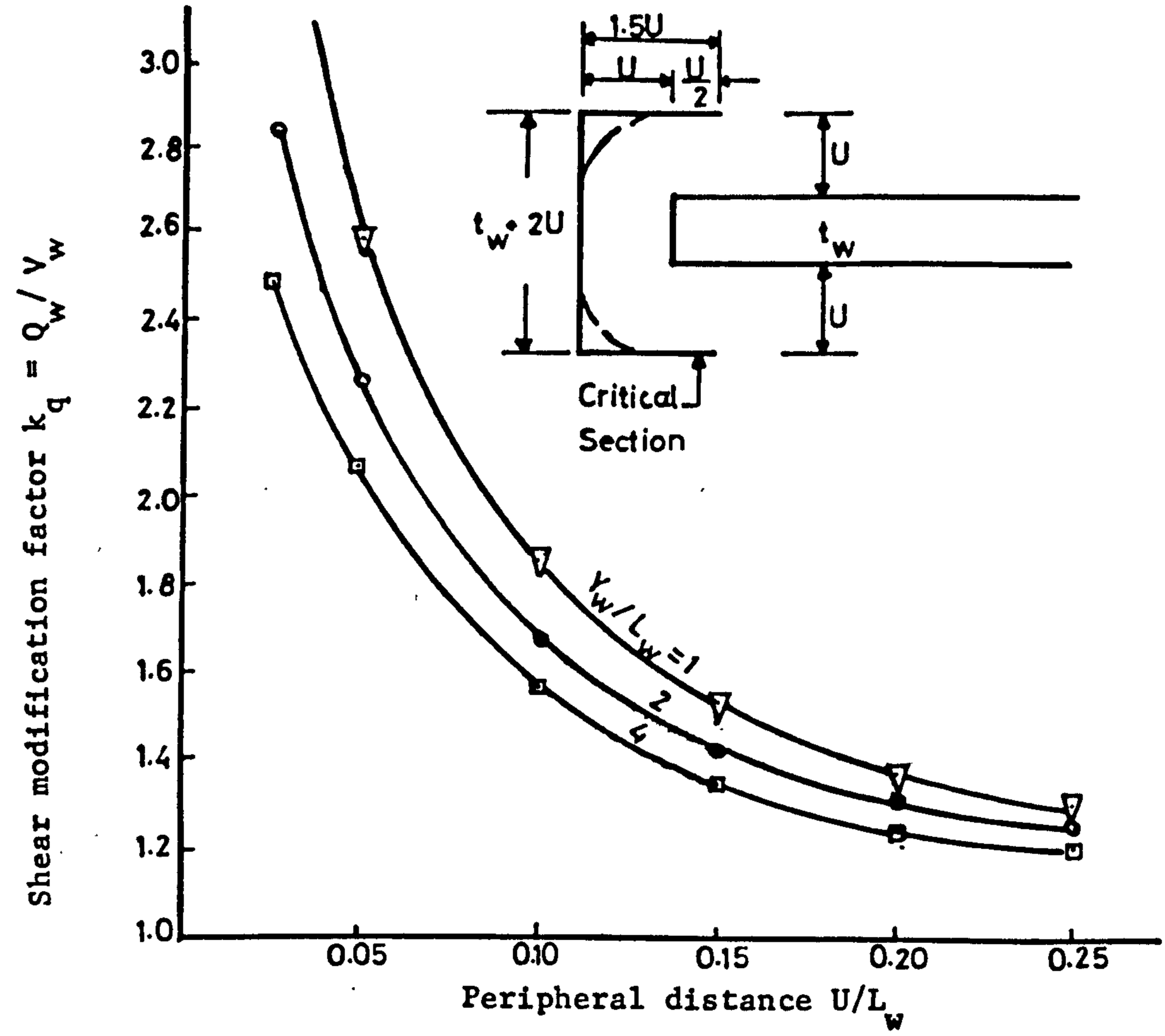

Figure (2.23) : Design curves for shear modification factor.

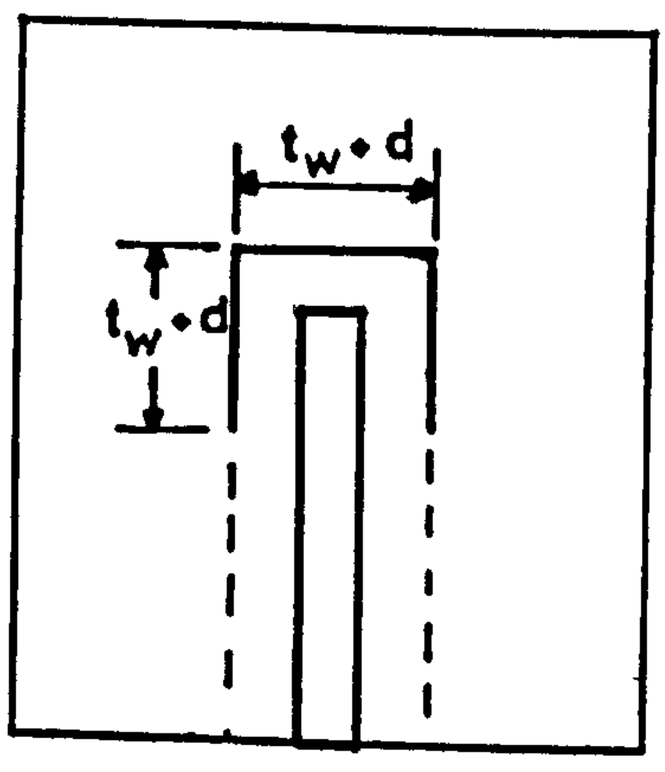

Figure (2.24) : Critical section for shear due to later load, proposed by Schwaighofer & Collins.

subjected to simultaneously applied lateral and gravity loads. The shear wall in this case may be assumed to be a wide column. Therefore a brief review of the existing knowledge in this regard is presented in the following sub-sections.

2.6.2 Recommendations by Codes

Due to the combined gravity and wind loading very large bending moments, shear forces and torsion are induced at slab-column connection and this may cause punching failure in the column head regions of flat slabs. Plan of a typical flat slab-column structure and different structural actions due to lateral loads at slab interior column connection are shown in Figure (2.25) In any design procedure it is necessary to consider the interaction of the shear, moment and torsional "stresses".

Around the column periphery at some distance from it there exists a critical section at which unbalanced moment is transferred partly directly by flexure and partly by torsion inducing vertical shear stress in addition to the shear stress due to applied shear V, thus producing uneven distribution of shear stress around the critical perimeter. Therefore $v_{max} = v_{shear} + v_{sm}$ where v_{sm} is a function of applied unbalanced moment M_w and properties of the critical section such as second moment of area, I, and distance from the centroid, Y_{max}. Thus,

$$v_{max} = \frac{V}{A_{cp}} + \text{Function of } (\frac{M}{I} , Y_{max}) \qquad (2.33)$$

where A_{cp} is the area of critical perimeter.

Different codes treat this function in different ways.

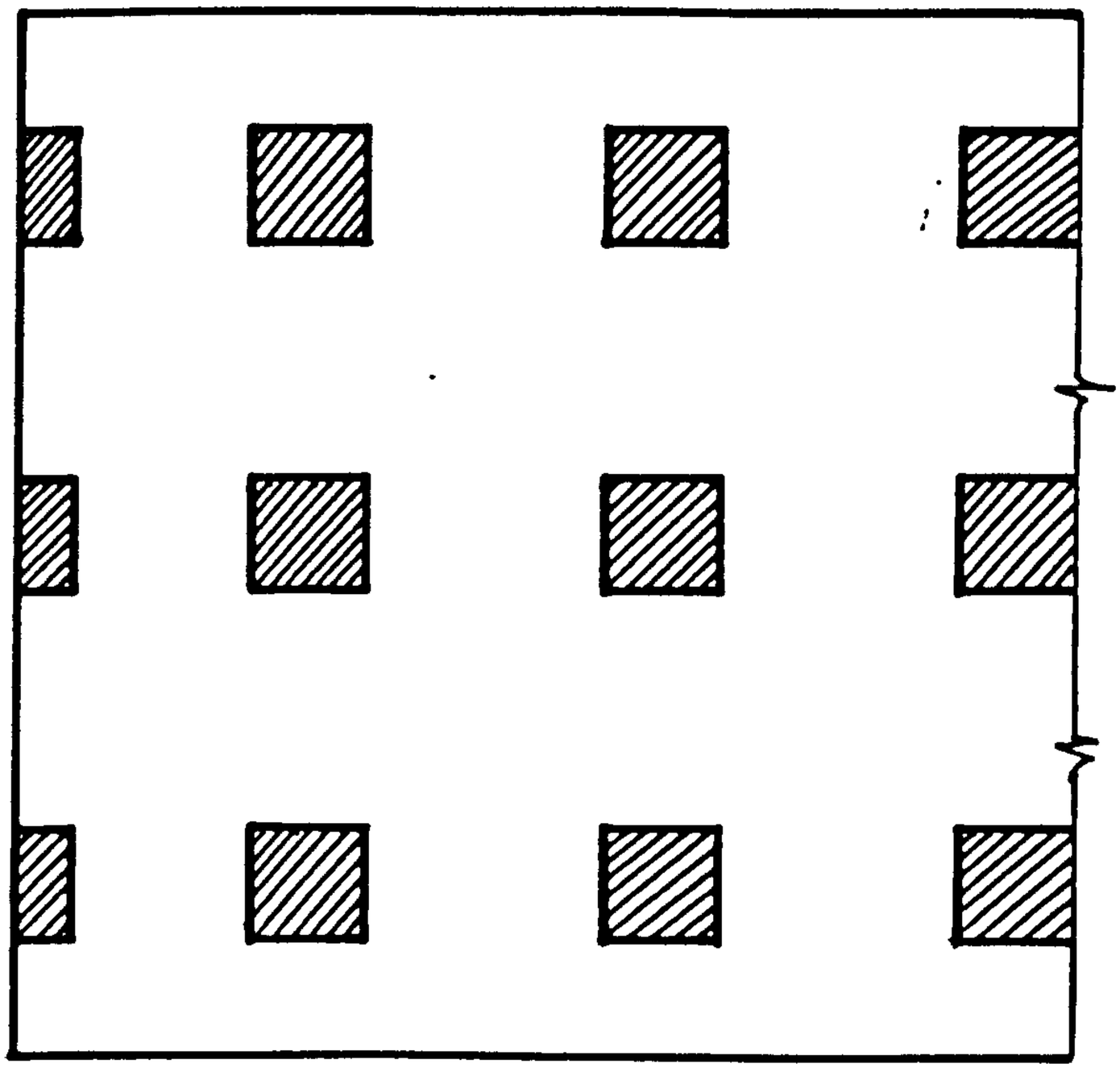

Figure (2.25a) : Plan of a typical flat slab-column structure.

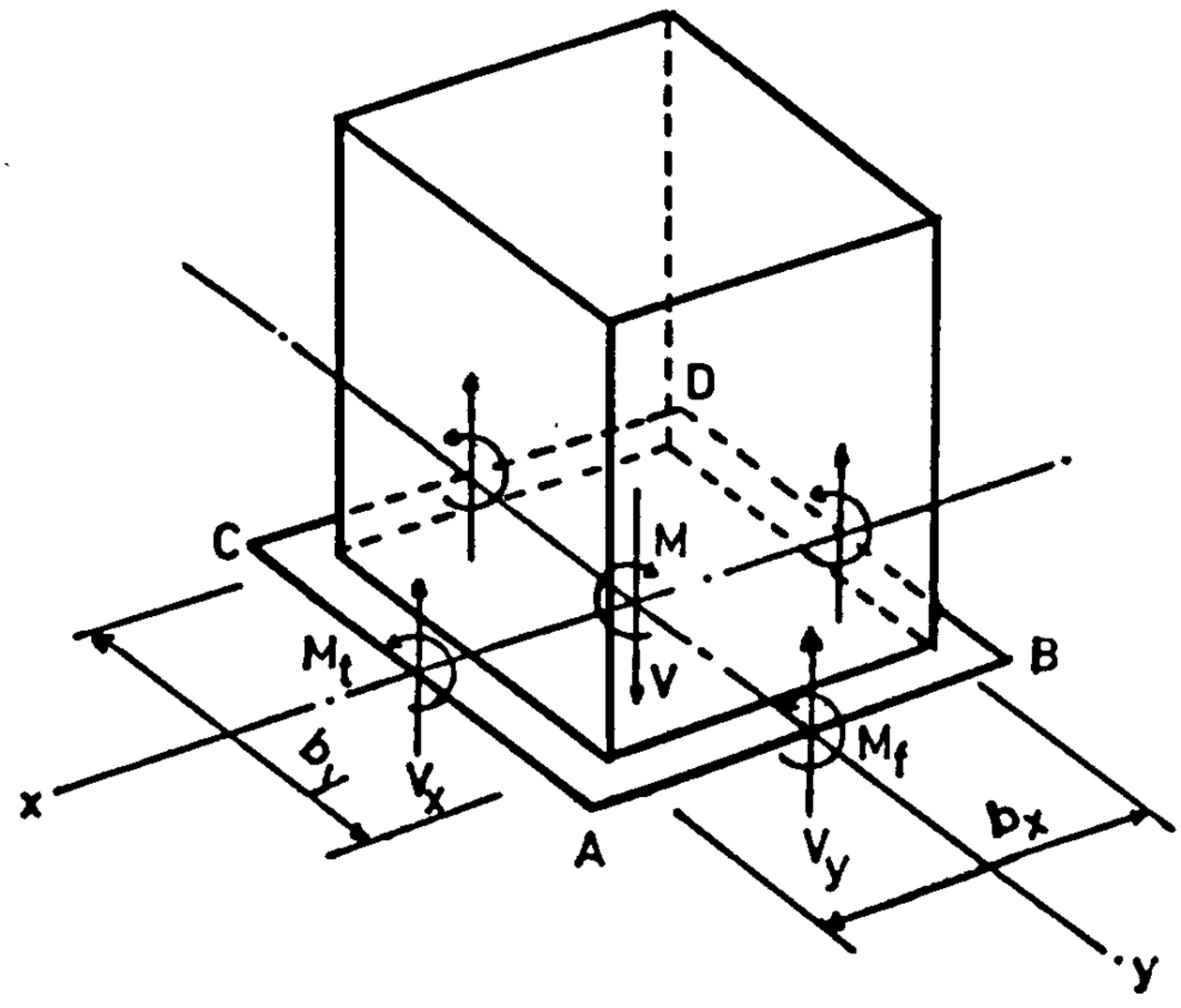

Figure (2.25b) : Different structural actions at critical section around a column.

CP110

It is assumed that there is a ring of contraflexure around the column with a radius R, equal to .2 times the longer span and the second part of the equation (2.33) is replaced by the ratio of the eccentricty of loading, e, to raidus R multiplied by a constant C and v_i. Thus,

$$v_{max} = \frac{V}{A_{cp}} + C \frac{M}{I_{polar}} Y_{max}$$

$$= \frac{V}{A_{cp}} \left(1 + \frac{Ce}{R} \right) \qquad (2.34)$$

where $e = \frac{M}{V}$

C = constant found emperically by experiments: = 2.5

R = radius of the ring of contraflexure

Substituting for C, e and R and rearranging the above equation, we get,

$$V_i = \frac{v_{max} A_{cp}}{\left(1 + 12.5 \frac{M}{VL}\right)} \qquad (2.35)$$

In the limiting case when v_{max} reaches its design ultimate value .8 ξ_s v_c, the applied shear becomes equal to $\frac{1}{\lambda_m} V_u$ where λ_m is the factor of safety. A_{cp} may be replaced by b_p d, where,

d = effective depth of slab

b_p = the length of a perimeter at a distance 1.5 h from the column faces as shown in Figure (2.26) and is given by:

$$b_p = b_o + 3\pi h \qquad (2.36)$$

here b_o = column perimeter and

h = the overall depth of the slab

Equation (2.35) can then be rewritten as:

$$\frac{1}{\lambda_m} . V_u = 0.8 \, \xi_s v_c \, b_p d / \, (1 + 12.5 \, \frac{M}{VL}) \qquad (2.37)$$

This is a well known CP 110 equation, from which factors of safety may be removed, then

$$V_u = \xi_s \, v_c \, b_p \, d \, / \, (1 + 12.5 \, \frac{M}{VL}) \qquad (2.38)$$

Here L is the longer span.

In the case of an edge column, it is very difficult to define an eccentricity in the direction perpendicular to the slab edge, as successive perimeters from b_o outwards are not concentric with one another. However where there is no moment transfer in the direction parallel to the edge, the slab behaviour is similar to that around an internal connection and equation (2.37) is applicable.

For edge column referring to Figure (2.27), b_p can be calculated from: $b_p = 2b_x + b_y + 1.5\pi h$ (2.39)

Further CP 110 specifies that:

(i) No shear reinforcement should be provided in a slab the thickness of which is less than 200 mm (Regan (11) is of the opinion that this restriction is unnecessary).

(ii) When shear reinforcement is provided, the bars must pass round main steel in both the top and bottom of the slab, though the direct contact betwen the two is not necessary.

(iii) The shear links should be uniformly distributed around the perimeter at a spacing not exceeding 0.75h.

In addition Regan (11) suggests that the diameter of the shear bar should not exceed $\frac{h}{25}$ if they are vertical or $\frac{h}{20}$ if they are inclined at 45 degrees.

Since the aim of the investigation presented in this thesis is to find a suitable method for predicting the strength of wall-slab connection without shear reinforcement, therefore formulae pertaining to slab-column connection with shear reinforcement are not given here.

ACI

The ACI approach considers that failure occurs when the (nominal) maximum shear stress on the periphery reaches a critical value. To calculate maximum shear stress it is assumed that the shear stresses on the critical perimeter vary linearly with the distance from the centroidal axis of the perimeter so that the maximum shear stress v_{max} is given by:

$$v_{max} = \frac{V}{A_{cp}} + \frac{\alpha_i M Y_{max}}{J_c} \qquad (2.40)$$

$$\text{Here } A_{cp} = 2d\,(b_y + b_x + 2d) \qquad (2.41)$$

J_c is a property of the critical perimeter analogous to the polar moment of inertia, $\alpha_i M$ is the fraction of the total moment M transferred by torsion and Y_{max} is the distance from the centre of the twist to the section where v_{max} stress acts Figure (2.28). The value of α_i is given by:

$$\alpha_i = 1 - \frac{1}{1 + \frac{2}{3}\sqrt{\frac{b_y + d}{b_x + d}}} \qquad (2.42)$$

Here b_y and b_x are respectively the column dimensions parallel and perpendicular to the eccentricity of the load, as shown in Figure (2.28).

The critical section is taken at a distance $\frac{d}{2}$ from the column (where d is the effective width of slab) and is rectangular for a rectangular column, so that for an internal column:

$$J_c = \frac{d(b_y + d)^3}{6} + \frac{(b_x + d)d^3}{6} + \frac{d(b_x + d)(b_y + d)^2}{2} \qquad (2.43)$$

A slightly modified value of J_c is used for exterior columns.

The ultimate value of shear stress, v_{max}, is taken as

$v_c = 4\sqrt{f'_c}\ p_{si}$ i.e. $.33\sqrt{f'_c}$ N/mm^2.

Here f'_c is the cylinder compressive strength of concrete.

According to the 1974 revision of ACI 318-71, sufficient reinforcement should be present in the slab between lines which are 1.5 times the slab thickness on each side of the column to resist the remainder of the unbalanced moments i.e. $(1 - \alpha_1)M$, considered to be carried by flexure.

2.6.3 Comparison and criticism of code requirements and further investigations.

Long, Cleland and Kirk (12) presented the following comparison of the recommendations of the three codes (i.e. CP 114, CP 110 and ACI):

(i) Relative to ACI and CP 114, the location of critical section 1.5 of slab depth in CP 110 increases the resisting shear by approximately 50%.

(ii) The level of moment transfer is of great importance for CP 110 (44) of moderate importance for ACI-71 (43) and of no consequence to CP 114 (45).

(iii) CP 114 is based on working stress design. The permissible stresses of CP 114 and ACI-71 are in reasonable agreement. The fact that ACI recommends the use of a permissible stress which is approximately twice as high as that of CP 110 reflects their assumption that slabs have higher shear resistance than beams (i.e. $4\sqrt{f'_c}$ psi versus $2\sqrt{f'_c}$ psi)

(iv) The specified panel loading of CP 110 is more severe than that of ACI-71.

(v) The method of computing moments of CP 110 is based on frame analysis whilst ACI adopts a modified frame analysis based on columns with greatly reduced stiffness.

The permissible ultimate shear stress of CP 110 is lower than that of CP 114 (working stresses) and substantially lower than that specified by ACI-71. However, the critical section for the former is larger which reduces this difference by about 30%.

In ACI-71 only approximately 40% of the total moment transferred is assumed to induce shear stresses at the critical section while hundred percent is used in CP 110 in calculating the magnification factor.

In order to determine whether the shear requirements of CP 110 are unnecessarily restrictive, Long, Cleland and Kirk (12) tested three models the shape of which is shown in Figure (2.29). In/

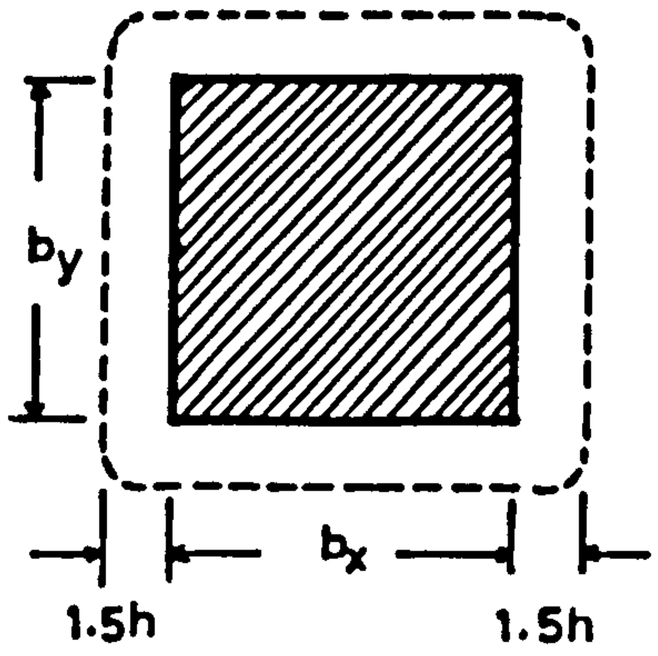

Figure (2.26) : Location of critical section for shear around an interior column (CP110)

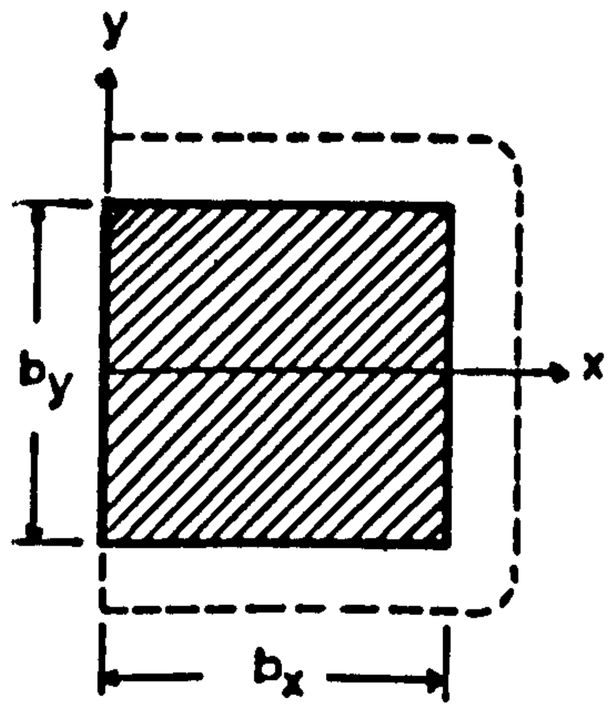

Figure (2.27) : Critical section at an edge column periphery.

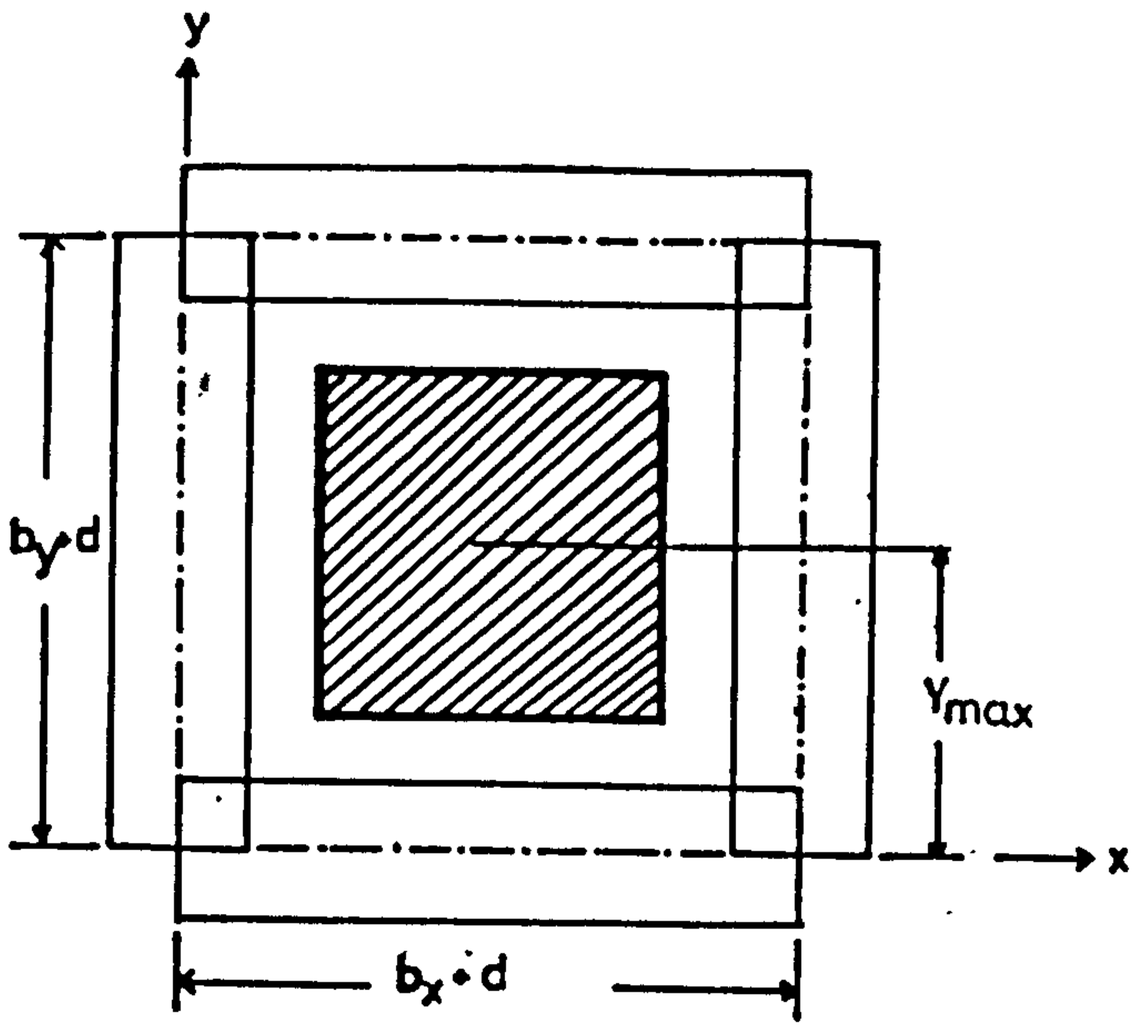

Figure (2.28) : Location of critical section for shear (ACI 318).

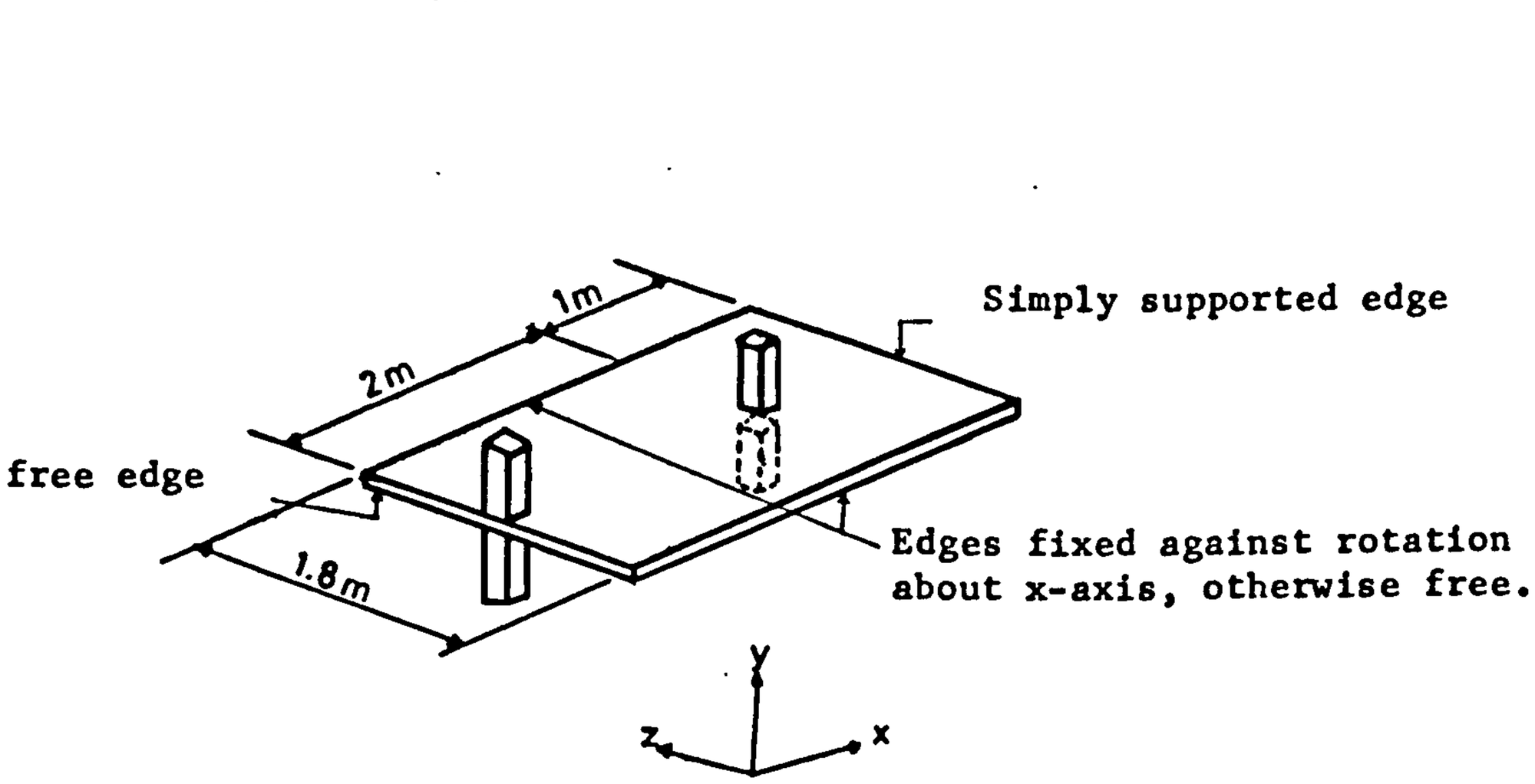

Figure (2.29) : Boundary conditions and overall dimensions of a model tested by Long et al.

order to obtain the appreciable levels of moment transfer a ratio of spans of approximately two was utilized for all three model slabs tested. The distribution of flexural reinforcement in the slabs of the prototype structure was designed in accordance with CP 110 for a characteristic live load of 2.86 kN/m^2 which could be applied over either or both the panels. A prototype slab depth of 190 mm giving a dead load of 4.3 kN/m^2 resulted. For reasons of economy one-third scale models were adopted. For each of the tests the sequence of loading was as follows:

1) Dead load on both the spans and design live load on the long span.
2) Dead load on both the spans and increasing loading on the long span until failure occurred.

Columns were pin supported at mid height between floors. Along the simply supported edge use was made of five lengths of threaded rod designed to provide adequate vertical stiffness whilst permitting lateral displacements to take place freely. The longitudinal edges were fixed against rotation about the x-axis with the help of a tie back system consisting of eight pairs of tie-pieces which were used in conjunction with eight struts.

From the comparison of the test failure loads with predictions based on the methods proposed in CP 110, CP 114 and ACI-71, they showed that CP 110 is unduly conservative even when the actual moment transferred is utilized in calculations. CP 114 surprisingly yields the best results. ACI-71 gives reasonably conservative results which would probably be more acceptable to designers.

They have summed up their conclusions as follows:

(i) The application of frame analysis to slab-column structures subjected to gravity loading results in the amount of moment being transferred from slab to column being overestimated by approximately 50%.

(ii) The use of a modified frame analysis such as that suggested in ACI-71 results in the realistic estimates of the level of moment transferred. However in some cases unsafe estimates result at interior columns whilst relatively conservative estimates are obtained at edge columns.

(iii) The adoption of the longer span, which has a sound logical basis in the CP 110 magnification factor i.e. $1 + (12.5 \frac{M}{VL})$ gives rise to safe estimates of the shear capacity.

(iv) The 20% reduction in the ultimate shear stress which is recommended in CP 110 can be neglected without giving rise to unsafe design.

They have also recommended that:

(a) Estimated levels of moment transfer from slab to column be based on 75% of those computed using frame analysis.

(b) A higher permissible ultimate shear stress should be applied to slabs subjected to concentrated loads. One possible suggestion should be to use a value of $2\ v_c$.

Ghali, Elmasri and Dilger (13) presented the results of their experimental study which was aimed at finding the strength and deformation of flat slab floors at their connection with columns/

when subjected to static or dynamic horizontal forces. Six full scale models representing the region of an intermediate flat plate of a typical multistorey structure at its junction with an interior column were tested(Figure (2.30)). The amount of flexural reinforcement was taken as variable and no shear reinforcement was provided. The columns and panels of prototype were assumed to be square. For testing the model all the four edges of the slab of the specimen were simply supported by assuming those to be the lines of contraflexure in the actual slab under the effect of uniformly distributed gravity load. A constant axial load V_g was applied on the column to simulate the effect of uniformly distributed gravity load in all the six models. The force P as shown in Figure (2.30) was applied on column to simulate the effect of lateral load which induced a moment (M = P L), which was transferred at the connection between the slab and column. The first three specimens were subjected to gradually increasing moment M up to failure while the other three were tested under the dynamically applied moment, M. In all the specimens the slab had uniformly distributed bottom and top reinforcement in the x and y direction. In the x-direction the top reinforcement ratio was 0.5, 1.0 or 1.5%.

From this study they concluded that:

(i) Within a wide range of flexural reinforcement ratio, the increase of M produces sudden punching failure following plastic rotation. The amount of rotation immediately before punching is smaller with the higher reinforcement ratios.

(ii) Increase in the percentage of flexural reinforcement ratio, up to 1% increases the ultimate moment (M_u) transferred. With/

higher flexural steel ratios, failure occurs due to shear before mobilization of the full flexural strength.

The increase in flexural reinforcement has unfavourable effect on the energy absorption capacity which is defined as the area below the moment-rotation curve. This should warn against using highly reinforced slabs when resistance to earthquake or blasts are considered.

(iii) Failure occurs at higher M_u compared to static loading when applied at a high rate, and the increase corresponds to the expected strength of the materials, concrete and steel, due to rapid straining.

The tests which followed the publication of ACI-71 showed that moment transer capacities calculated by the ACI procedures are conservative and the fraction of moment to be transferred by flexure according to ACI 318-71 method is much larger than that predicted by elastic thin plate analysis. Consequently when the applied moment is large, there is difficulty in arranging the flexural reinforcement within the width of the slab section specified by the code (Kanoh & Yoshizaki (14)).

Kanoh and Yoshizaki (14) investigated experimentally the contribution of flexure, shear and torsion at the critical section to the moment transfer capacity of slab-column connections. Torsion tests of slab-column connections were carried out in order to directly investigate the magnitude of the moment that could be transferred by torsion and a simple method was proposed for predicting the moment transfer capacity of slab-column connections failing in shear.

They tested 25 specimens under gravity load, repeated lateral load simulating earthquake or both. Major variables were:

(i) The tensile reinforcement ratio.

(ii) The arrangement of tensile steel.

(iii) Shear reinforcement.

(iv) The aspect ratio for the column.

(v) The column side length to slab depth ratio.

(vi) The magnitude of the gravity load.

Eight specimens of the type shown in Figure (2.31) were tested for pure torsional moment transfer between the slab and central column. (This is the only test series for which the test set-up has been fully described). The slab was supported at each end on rollers and the column stub fitted with steel arms pulled in opposite directions by hydraulic jacks. Thus torsion was transferred from the column stub to the slab. Measurements were taken of the angle of rotation of the column stub relative to a line connecting the two supports, the difference in the angle of rotation between the column stub and the slab and the strains in the tensile reinforcement.

Based on the test results they concluded that:

1) The fraction of the moment transferred by torsion and by eccentricity of the shear force, need not be taken as small as the value currently specified in ACI 318-71. During experimental work a value of α_1 as high as 0.9 was achieved.

2) The moment which can be transferred between the slab and the column by torsion, when converted into torsional shear stress by/

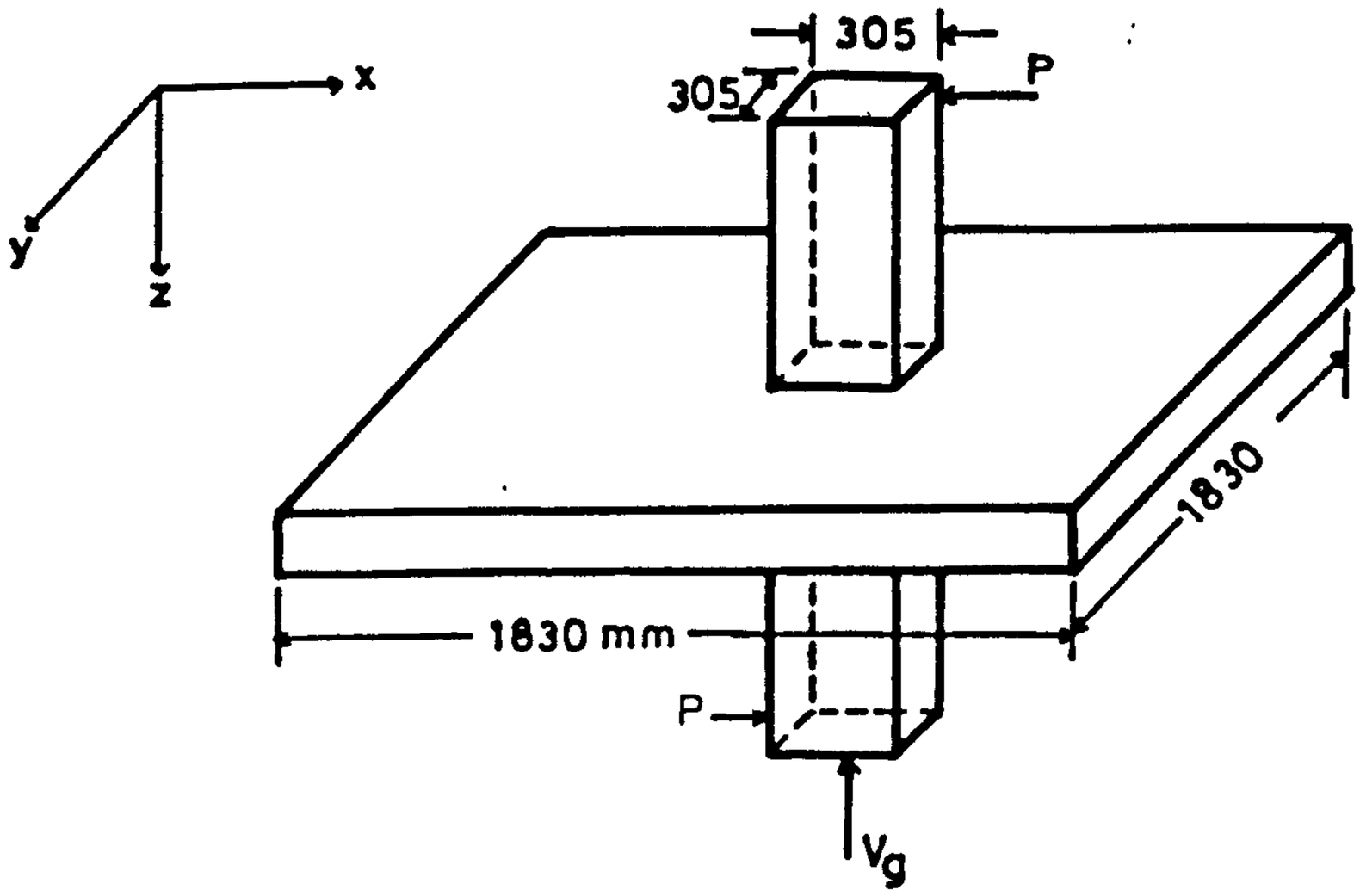

Figure (2.30) : Shape and dimensions of a typical model tested by Ghali et al.

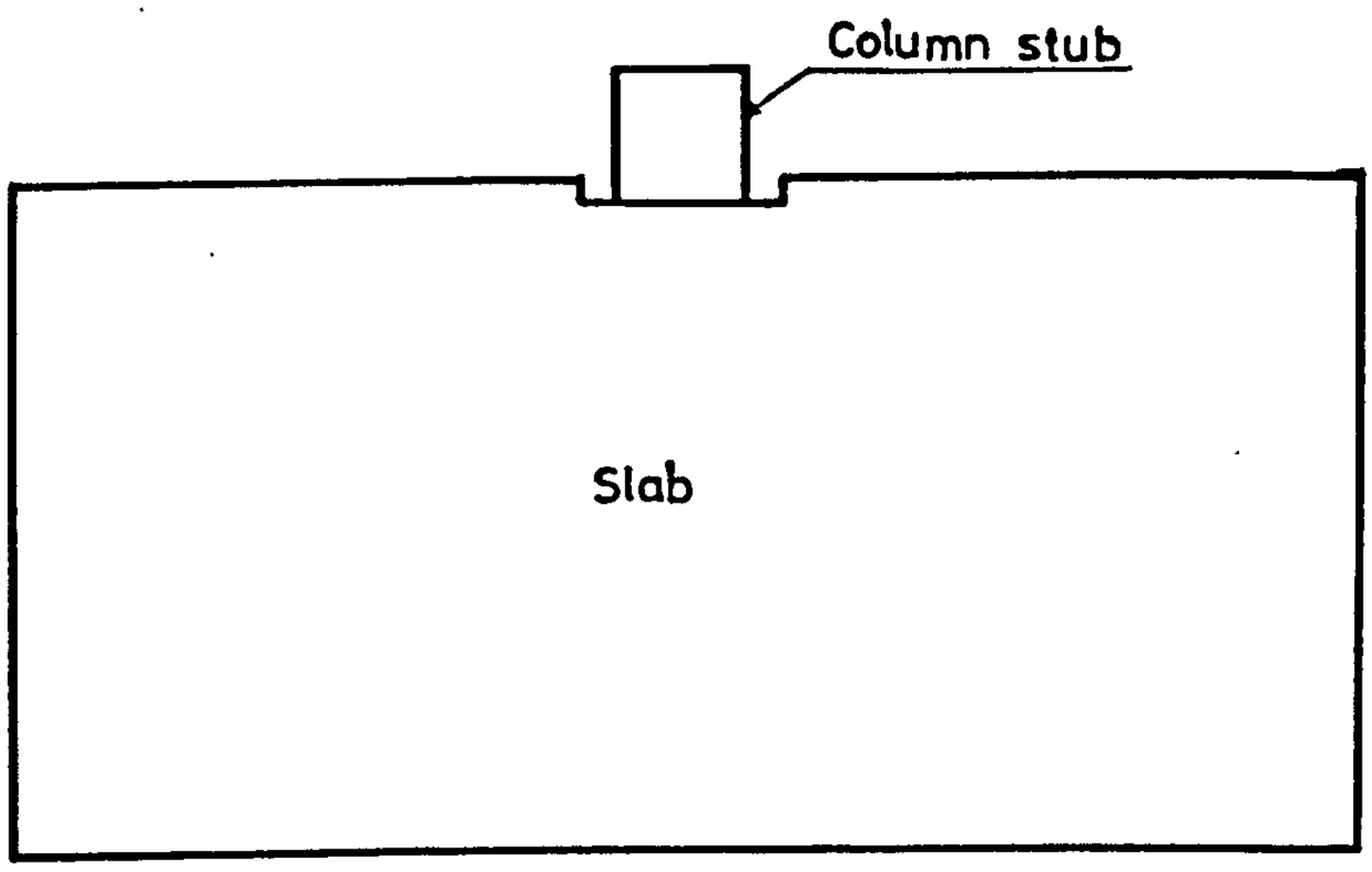

Figure (2.31) : Plan of a typical model tested by Kanoh & Yoshizaki.

the full plastic formula, equals about 9.7 N/mm^2 (1400 psi) and is far greater than the value assumed in the ACI 318-71 i.e. $.4\sqrt{f'_c}$ N/mm^2 ($4.8\sqrt{f'_c}$ psi), which for the concrete used by them with $f'_c = 26$ N/mm^2, should be equal to $2\sqrt{f'_c}$ N/mm^2

3) When an interior slab-column connection (as shown in Figure (2.25b) is subjected to moment alone, a part of this moment is transferred directly by flexure (i.e. M_f), which is equal to the sum of the flexural yield moment for the front and back column faces. Thus this part of moment can be calculated from:

$$M_f = 0.9\, A_s\, f_y\, d_t\, (b_x + d)/S_t + 0.9\, A_s\, f_y\, d_b\, (b_x + d)/S_b \qquad (2.44)$$

where A_s = the area of steel

f_y = the yield stress of steel

d_t = the effective depth to centroid of top reinforcement for negative moment.

S_t = the spacing of top reinforcement for negative moment.

d_b = the effective depth to centroid of bottom reinforcement for positive moment.

S_b = the spacing of bottom reinforcement for negative moment and b_x is as shown in Figure (2.25b).

Second part of the applied moment is transferred by eccentricity of shear and referring to Figure (2.25b), it is given by:

$M_s = V_y\, (b_y + d)$ where,

$\text{Max.}V_y = v_c\, (b_x + d)\, d$

$\therefore M_s = v_c\, (b_x + d)\, (b_y + d)d \qquad (2.45)$

Here v_c may be taken as $.33\sqrt{f'_c}$ N/mm^2 as specified by ACI 318-71.

And third part of the applied moment is transferred by torsion along the sides of the column and referring to Figure (2.25b), the following expression can be written for this part of moment:

$$M_t = v_{tu} (b_y + d - \frac{d}{3}) d^2 \qquad (2.46)$$

where v_{tu} may be taken as $2.\sqrt{f'_c}$ N/mm^2 ($24\sqrt{f'_c}$ psi) based on test results.

Then the expression for the total ultimate moment, M_o, transferred at the junction can be written as:

$$M_o = M_f + M_s + M_t \qquad (2.47)$$

4) When there is transfer of shear alone, the maximum shear capacity V_o should be calculated according to ACI 318-71 procedures, i.e.

$$V_o = v_c A_{cp} \qquad (2.48)$$

5) When the measured moment capacity M_{test} and the measured shear capacity V_{test} are divided by M_o and V_o respectively, the interaction between M_{test}/M_o and V_{test}/V_o be expressed as:

$$M_{test}/M_o + V_{test}/V_o \leqslant 1 \qquad (2.49$$

In a recent paper, Hawkins, Bao and Yamazaki (15) reported the results of 36 slab-interior column specimens for which both shear and moment were transferred between the column and the slab. There were seven test series with variables between series being slab thickness, concrete strength, concrete type, integral beam stirrup reinforcement, flexural reinforcement pattern and column/

rectangularity. The variables within series were the flexural reinforcement ratio and the ratio of the moment transferred to the column.

The test specimens modelled to about three-quarters scale conditions likely to exist for an interior column connection in a prototype flat plate structure several storeys high and with columns at 6.1 m centres. The dimensions and loading arrangements for the test specimens are shown in Figure (2.32). Slabs were 2.1 m square and supported on a central column. Most columns were 305 mm square. However for the test series where aspect ratio of the column was a parameter, the column perimeter was held constant at 1219 mm and aspect ratio (b_y/b_x) varied from 0.5 to 3.0. See Figure (2.32).

Unequal vertical forces were applied at 610 mm intervals around the perimeter of the slab and the resultant overturning moment balanced by jacking horizontally between the top of the upper column and an independent reaction frame. Horizontal forces providing that moment acted 1040 mm above and below the slab. The column was prestressed to the labortory floor with a rod extending down its centre. The prestress force was 223 kN for all except one series for which the force was 356 kN. Two loading patterns were used. For high moment loading, the $^{M}/V$ ratio was nominally 584 mm and for low moment loading, the ratio was nominally 130 mm.

Comparing the results they showed that the stiffness increased with increasing strength of concrete at a rate less than $\sqrt{f'_c}$. Aspect ratios of 0.5 and 1 showed little change in behaviour. However marked decrease in ductility was observed when it was equal to 2 and 3.

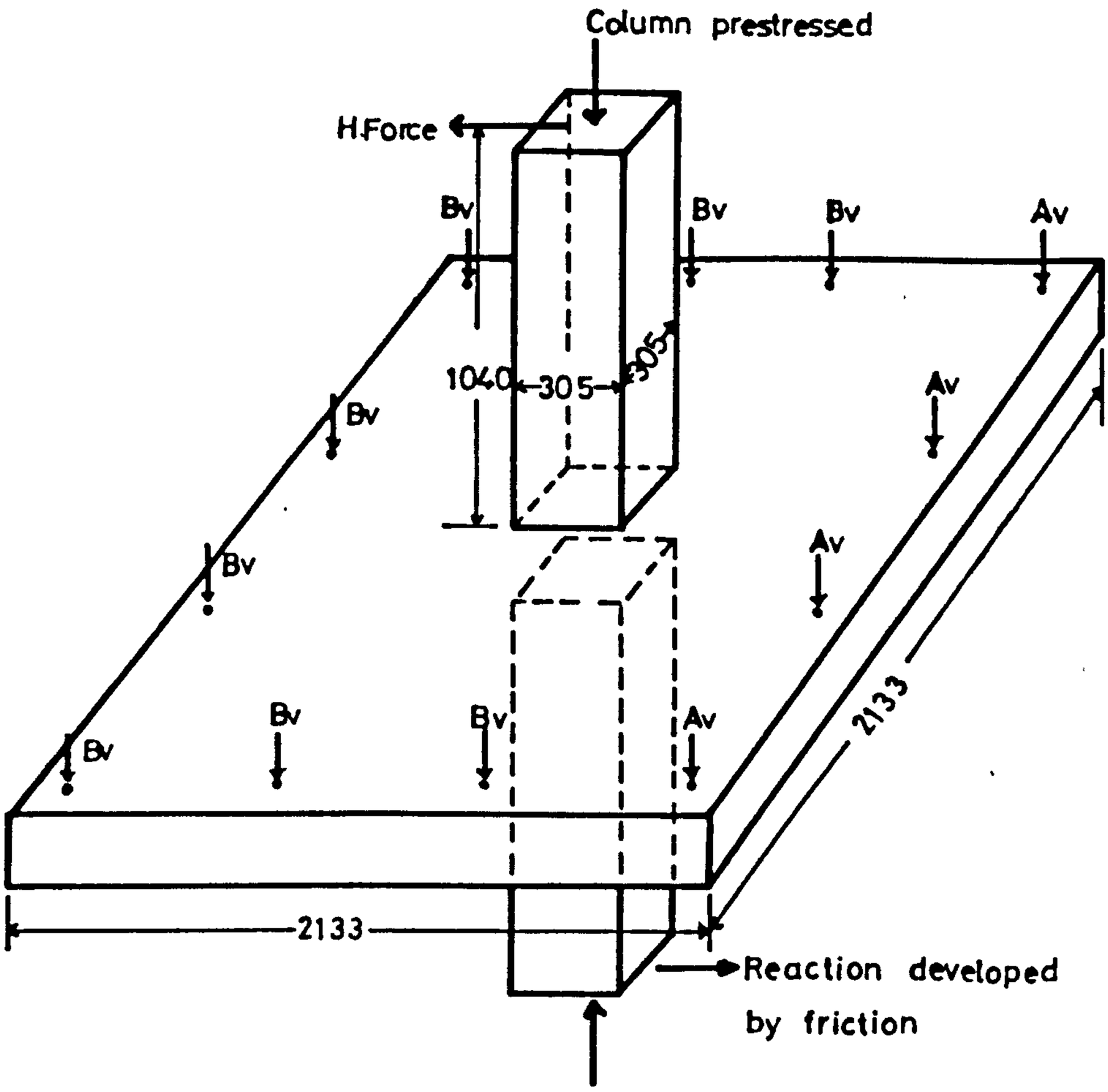

Figure (2.32) : Dimensions and loading arrangement of a typical specimen tested by Hawkins et al.

From the test results following conclusions were drawn by them.

1) ACI code 318-77 provisions for determining the strength of slab to interior column connections transferring moment are reasonable for design. They yield results which are conservative when the ratio of flexural steel in a width 1.5 times the slab thicknesses on either side of the column exceeds 0.7%. This conservatism increases as this ratio increases and the warning of impending failure decreases. ACI 318-77 provisions may be non conservative for steel ratios less than 0.7%. However the flexural capacity of the reinforcement in the column region then controls and significant deformations occur before any punching failure.

2) Dowel effects of the reinforcement passing through the column can reduce the moment transfer capacity. Such reinforcement should have clear spacings between bars not less than 3 bar diameters for 19 mm (3/4") cover in normal weight concrete, and the shear capacity for connections in light weight concrete should not be taken as greater than 85% of the same connection in normal weight concrete regardless of the tensile strength of the light weight concrete.

3) The rotational stiffnesses of the test connections decreased continuously with increasing load. For connections essentially uncracked in torsion or shear ACI 318-77 provisions predicted equivalent column stiffnesses about double those measured. For connections probably cracked in torsion or shear, stiffnesses were directly proportional to the amount of reinforcement within a width two slab thicknesses on either side of the column.

Literature review presented in this section so far pertains to the behaviour of slab-interior column subjected to unbalanced/

moments and uneven shears. Therefore a brief review of the experimental study of slab-edge column connections is described below.

Very recently tests on five half size models of edge panels of a flat plate floor, one model with and four models without spandrel beams have been carried out by Rangan and Hall (16). An overall view of their test specimens is shown in Figure (2.33). Column A was regarded as the test column, edge CAD as the edge of the building and boundary CEBFD as an interior column line. Some stiffening was provided along the artificial boundary CEBFD to simulate in part the stiffness in a real building provided by the adjacent panels.

Each model was tested by applying uniformly distributed vertical load, simulated by sixteen point loads on each panel. The loads were applied through specially designed loading pads which allowed the concrete surface to move under load. In addition to the load cells, electrical strain gauges were attached to the reinforcing bars in the test panel in each model. Measured strains were converted to unit slab moments using bilinear moment-strain curve and the unit slab shears were obtained by calculating the slope of the moment curves at the spanderal face. The procedure is fully explained in reference (17).

Defining a strip of slab of width $b_x + h$ as beam strip, the moment M_f and shear V_f directly transferred to column by this strip were calculated for each specimen as follows,

(i) $M_f/M = .04 + .65\ Z_e$ (2.50)

(ii) $\frac{V_f}{V} = .5\ Z_e$ (2.51)

where $Z_e = \frac{(b_x + h)h}{(b_x + h)\ h + 2\ b_y h}$ (2.52)

Here M = Total applied moment

V = Total applied shear

Here b_x and b_y are the column dimensions as shown in Figure (2.33) and h is the overall thickness of the slab.

Because of the range of the tests, they have suggested that the above equation be limited to the range Z_e = .15 to 0.6.

From their experimental results and making use of the space-truss theory of torsion, they have proposed the following expression to calculate the strength of the spanderal in combined torsion and shear.

$$T_u = \frac{2A_o}{(1 + \frac{A_o\ V_u}{T_u\ y_o})}\sqrt{\frac{A_w}{S}\ f_{wy}\ (A_t + .25\ \ell_n\ h\ \frac{E_c}{E_s})\ \frac{f_{ty}}{U_o}} \qquad (2.53)$$

A_o = area of the rectangle defined by the longitudinal bars in the corners of the hoops.

x_o and y_o = width and depth, respectively, of the rectangle making the area A_o.

A_w = cross-sectional area of the bar from which the hoops are made.

f_{ty}, f_{wy} = yield strengths of longitudinal steel and hoop steel, respectively.

A_t = total area of longitudinal steel.

S = spacing of hoops.

ℓ_n = smaller span

U_o = perimeter of the area A_o.

2.6.4 Beam analogies

Several beam analogies have also been put forward to provide a convenient method for determining the strength of reinforced concrete slab-column connections transferring shear and moment. In this method the slab adjacent to the column is considered to act as beams running in two directions at right angles framing into the column faces. The slab strips,making up the beams, are subjected to bending moment, torsinnal moment and shear force, and redistribution of these actions is assumed to be able to develop its ultimate bending moment, torsional moment and shear force, making due allowance for interaction effects, at the critical sections near the column faces. The strength of the connection is calculated by summing the contributions of the strengths of the beams (18). A review of various beam analogies which have been proposed is given by Hawkins (19).

2.7 FAILURE MODES FOR SLAB-COLUMN CONNECTIONS TRANSFERRING UNBALANCED MOMENTS.

At loads less than the flexural capacity two modes of failure are possible viz. (i) Moment torsion and (ii) Shear torsion.

(i) Moment torsion:- This mode involves the failure on all the four column faces Figure (2.34). This mode places a limit on the moment transferred to the column rather than limiting the shear. The torsional strength is reached on the side faces AB and CD and at the same time the flexural strength is reached in negative bending on the face BC and positive bending on the face AD. For a moment-torsion failure, significant rotations occur near the column prior to ultimate load. These rotations are/

sufficient to permit the top bars passing in the face BC to yield in negative bending and bottom bars passing into the face AD to yield in positive bending. The balance of the applied moment is taken in torsion on the side faces.

(ii) Shear-torsion failure:- This mode necessitates failure on three faces only. This mode is likely when the shear transferred is significant. For moderate values of the shear the torsional strength is reached on the side faces and the shear strength on the face BC. For high shears, the shear strength and the flexural strength are also reached on the face AD Figure (2.34).

For a shear torsion failure, the rotations will be less than those for a moment-torsion failure. The moments due to loads on the side BC cause yielding of the top steel in negative bending across the face BC while the balance of this moment will be resisted in torsion on the side faces. Similarly, the moments due to loads on the AD side of the y-y axis will be resisted initially at the face AD. The flexural strength of this face in positive or negative bending, as appropriate, must be exhausted before the balance of this moment can be distributed as a torque to the side faces.

The distribution of shears is more difficult to establish. One approach is to consider the potential yield line pattern. Lines emanating from the column divide the slab into areas which can be considered tributory to a particular face. In the first instance, the loads on the tributory areas will be resisted by shears developed at the appropriate column face. However since shears can be transferred across an yield line, it is reasonable to/

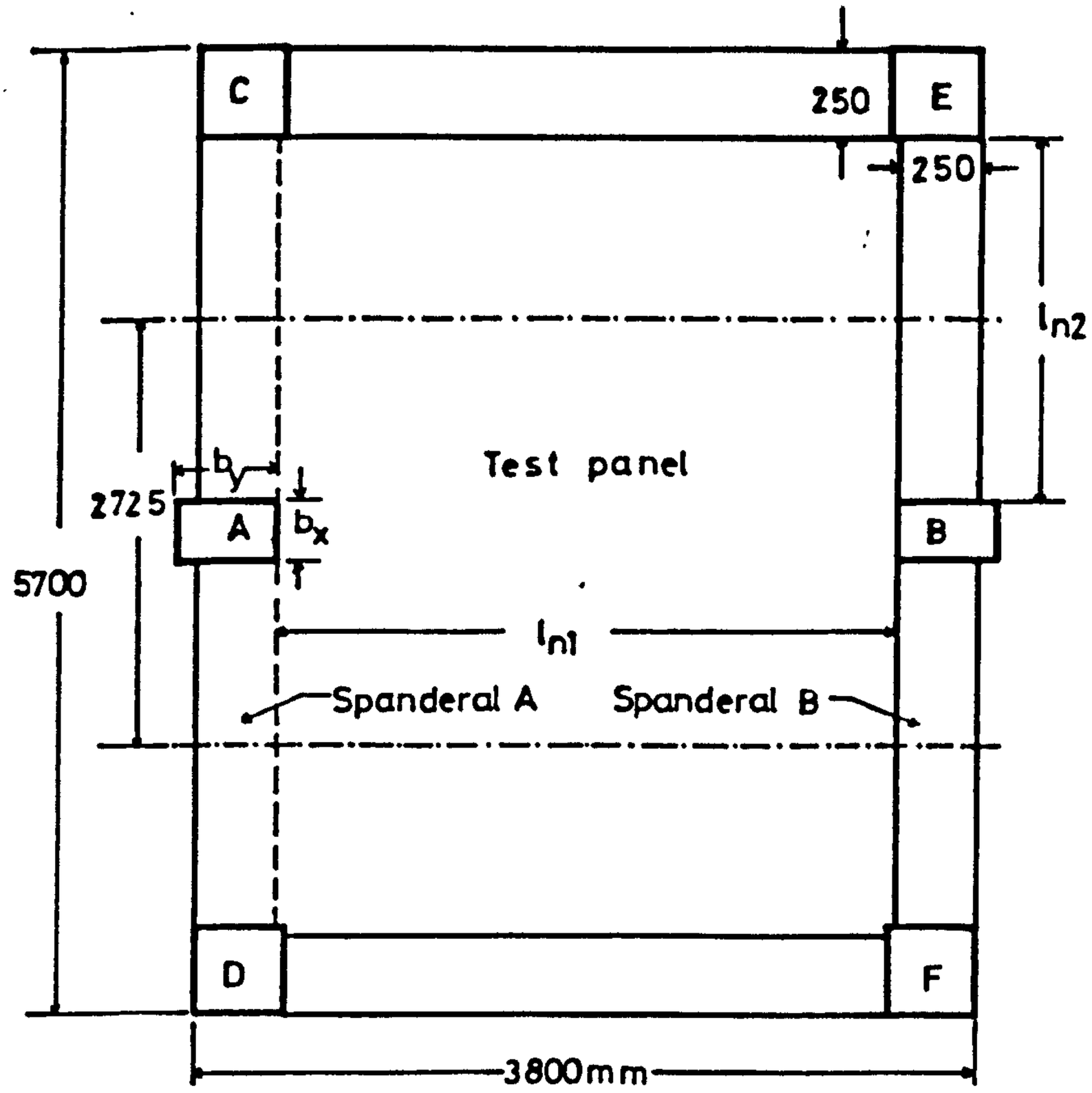

Figure (2.33) : Plan of a typical specimen tested by Rangan & Hall.

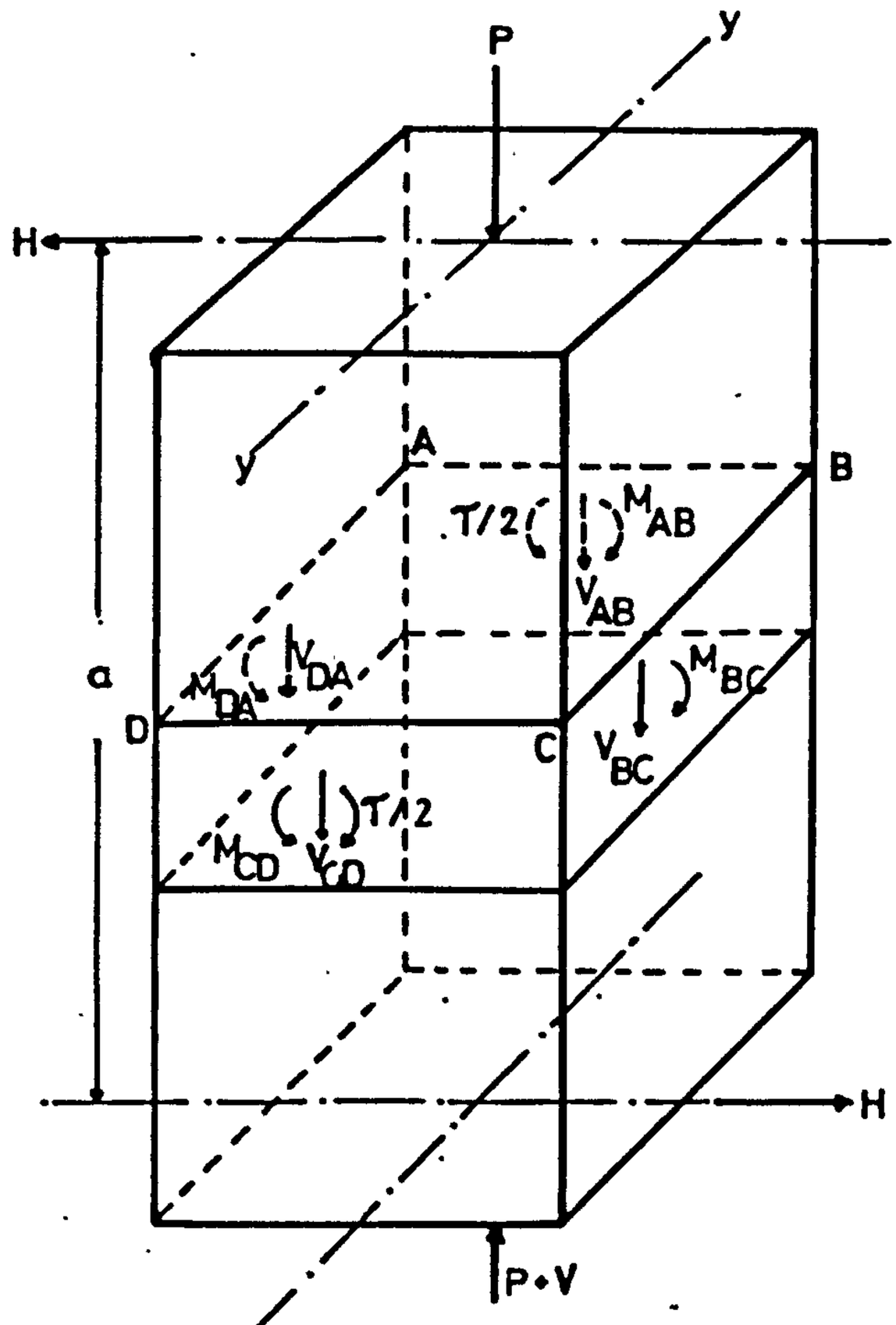

Figure (2.34) : Moments and forces induced at the faces of an interior column.

expect that once the shear on that particular column face is close to ultimate value, with or without torsion, additional shears can be transferred to the side faces until a failure condition is also reached on these faces (Hawkins and Corely (20)).

2.8 GENERAL DISCUSSION

As can be seen from previous sections, the methods proposed to calculate the strength of wall-slab connection are mainly based on theoretical investigations and are not supported by any experimental evidence. Furthermore, only elastic behaviour is taken into consideration, though it is expected that due to cracking redistribution of stresses will take place and the behaviour of the connection would deviate from that assumed by elastic theory. Method proposed by Schwaighofer and Collins (8), though based on experimental behaviour of a real reinforced concrete model, but it doesn't take any account of the effect of the transfer of unbalanced moments on the strength of connection. Apart from that all those models estimate the strength of wall-slab connection against the lateral load alone and the case of combined wind and gravity loading has not been dealt with.

The methods proposed for the prediction of slab-column connections also, might not prove satisfactory for wall-slab connection, since the length of wall is much greater than the side width of columns. Although from the elastic distribution of shear around the wall periphery it has been observed that only a very small portion of the total wall length is effective in resisting the shear due to lateral loads, cracking will undoubtedly redistribute the forces and greater amount of shear might be transferred by the torsion on the sides. It is for this reason that the present work reported in this thesis was undertaken.

CHAPTER THREE

FINITE ELEMENT METHOD

3.1 GENERAL

Finite element method of analysis is used extensively in the study presented in this thesis, both, for calculating the elastic moment fields for the design purpose as well as for the nonlinear analysis of models tested. As the standard procedure of the finite element analysis is well known, it is not described in detail here. However some specific features of the nonlinear analysis of reinforced concrete and the particular details of the programme used are presented in this chapter.

The nonlinear plate bending finite element programme used for this study was originally written by Johnnary (21) and modified by Hago (22). The programme uses a four noded rectangular layered element with five degrees of freedom at each node, i.e. u, v, w, $\frac{\partial w}{\partial y}$ and $\frac{\partial w}{\partial x}$.

Here u and v are the inplane deformations in x and y directions respectively.

w is the transverse deformation.

$-\frac{\partial w}{\partial y}$ is the rotation about x-axis i.e. θ_x.

and $\frac{\partial w}{\partial x}$ is the rotation about y-axis i.e. θ_y.

3.2 THE STIFFNESS OF LAYERED FINITE ELEMENT USED

In the nonlinear analysis of reinforced concrete,it is important/

to take into account the propagation of the crack through the depth of the slab. For this purpose the most sophisticated two dimensional approach is to use the layered approach.

In this approach, plate thickness is divided into a finite number of layers parallel to the plate middle plane as shown in Figure (3.1). Each layer is assumed to be in a state of plane stress. A layer is also assumed to be of one material whose nonhomogenious properties are represented at the Gaussian integration points.

The strain in any layer is the sum of the inplane strain at the middle plane and the strain due to bending. The layer strains are calculated using classical theory of plates, from the following equations, with the assumption that plane sections before bending remain plane after bending:

$$\varepsilon_x = \frac{\partial u}{\partial x} - z\frac{\partial^2 w}{\partial x^2}$$

$$\varepsilon_y = \frac{\partial v}{\partial y} - z\frac{\partial^2 w}{\partial y^2} \qquad (3.1)$$

$$\varepsilon_{xy} = \frac{\partial u}{\partial y} + \frac{\partial v}{\partial x} + 2z\frac{\partial^2 w}{\partial x \partial y}$$

where Z is the distance of the layer from the midplane of the plate.

The above equation can be written as:

$$\begin{vmatrix} \varepsilon_x \\ \varepsilon_y \\ \varepsilon_{xy} \end{vmatrix} = \begin{vmatrix} 1 & 0 & 0 & z & 0 & 0 \\ 0 & 1 & 0 & 0 & z & 0 \\ 0 & 0 & 1 & 0 & 0 & z \end{vmatrix} \begin{bmatrix} \partial u/\partial x \\ \partial u/\partial y \\ \frac{\partial u}{\partial y} + \frac{\partial v}{\partial x} \\ -\frac{\partial^2 w}{\partial x^2} \\ -\partial^2 w/\partial y^2 \\ 2\frac{\partial^2 w}{\partial x \partial y} \end{bmatrix} \qquad (3.2)$$

ε R ε_m

Or $\{\varepsilon\} = [R]\{\varepsilon_m\}$ (3.3)

where ε is the vector of total inplane strains in a layer at level Z, and ε_m is the element strain vector of the plate and [R]is a transformation matrix and is a function of Z.

The mid surface inplane deformations u and v are represented by the following bilinear functions:

$$u = a_1 + a_2x + a_3y + a_4xy$$

$$v = a_5 + a_{6x} + a_7y + a_8xy \qquad (3.4)$$

giving a linear variation of strain within the element. The constants a_1 to a_8 can be expressed in terms of the two degrees of freedom (u_i , v_i) at each of the four nodes.

The bending deformations are represented by

$$w = a_9 + a_{10}x + a_{11}y + a_{12}x^2 + a_{13}xy + a_{14}y^2 + a_{15}x^3 + a_{16}x^2y$$

$$+ a_{17}xy^2 + a_{18}y^3 + a_{19}x^3y + a_{20}xy^3 \qquad (3.5)$$

Here transverse deformation w is represented by a fourth order polynomial variational function with twelve unknown constants. The twelve constants a_9 to a_{20} are expressed in terms of three degrees of freedom, w_i ,$(\frac{\partial w}{\partial y})_i$ and $(\frac{\partial w}{\partial x})_i$ at each of the four nodes.

The constants of polynomials a_1 to a_{20} can be evaluated by writing down the twenty simultaneous equations linking the nodal displacements when the coordinates take up their appropriate values.

In matrix form, the nodal displacement vector of the element δ^e can be written as:

$$\{\delta\}^e = [C]\{a\} \tag{3.6}$$

where C is a 20 x 20 matrix depending on nodal coordinates, and $\{a\}$ a vector of 20 unknown constants a_1 to a_{20}. Therefore

$$\{a\} = [C]^{-1}\{\delta\}^e \tag{3.7}$$

The strain vector $\{\varepsilon_m\}$ is related to the element nodal displacement vector δ^e through the differential operators , therefore operating upon equations (3.4) and (3.5),

$$\varepsilon_m = \begin{bmatrix} a_2 & a_{4y} & & \\ a_7 & a_{8x} & & \\ a_3 & a_{4x} & a_6 & a_{8y} \\ -2a_{12} & -6a_{15}x & -2a_{16}y & -6a_{19}xy \\ -2a_{14} & -2a_{17}x & -6a_{18}y & -6a_{20}xy \\ 2a_{13} & 4a_{16}x & 4a_{17}y & 6a_{19}x^2 \quad 6a_{20}y^2 \end{bmatrix}$$

Or $\{\varepsilon_m\} = [Q]\{a\} = [Q][C]^{-1}\{\delta\}^e$

or in standard notation $\{\varepsilon_m\} = [B]\{\delta\}^e$ (3.7)

where strain matrix $[B] = [Q][C]^{-1}$ (3.8)

Here Q is a 6 x 20 matrix and can be written as:

$$Q = \begin{bmatrix} 0 & 1 & 0 & y & 0 & 0 & 0 & 0 & 0 & 0 & 0 & 0 & 0 & 0 & 0 & 0 & 0 & 0 & 0 & 0 \\ 0 & 0 & 0 & 0 & 0 & 0 & 1 & x & 0 & 0 & 0 & 0 & 0 & 0 & 0 & 0 & 0 & 0 & 0 & 0 \\ 0 & 0 & 1 & x & 0 & 1 & 0 & y & 0 & 0 & 0 & 0 & 0 & 0 & 0 & 0 & 0 & 0 & 0 & 0 \\ 0 & 0 & 0 & 0 & 0 & 0 & 0 & 0 & 0 & 0 & 0 & -2 & 0 & 0 & -6x & -2y & 0 & 0 & -6xy & 0 \\ 0 & 0 & 0 & 0 & 0 & 0 & 0 & 0 & 0 & 0 & 0 & 0 & -2 & 0 & 0 & -2x & -6y & 0 & -6xy & \\ 0 & 0 & 0 & 0 & 0 & 0 & 0 & 0 & 0 & 0 & 0 & 0 & 2 & 0 & 0 & 4x & 4y & 0 & 6x^2 & 6y^2 \end{bmatrix}$$

Using equation (3.7) in equation (3.3)

$$\{\varepsilon\} = [R]\ [B]\ [\delta]^e \qquad (3.9)$$

The stress vector in any layer is given by:

$$\{\sigma\} = [D]\{\varepsilon\} = [D][R][B]\ [\delta]^e \qquad (3.10)$$

where constitute matrix [D] for isotropic materials is given by:

$$[D] = \frac{E}{1-\nu^2}\begin{bmatrix} 1 & \nu & 0 \\ \nu & 1 & 0 \\ 0 & 0 & \frac{1-\nu}{2} \end{bmatrix} \qquad (3.11)$$

where E is the modulus of elasticity and

ν is the Poisson's ratio

The moments and inplane stress resultants are calculated from stresses using following relationships:

$$\begin{aligned} M_x &= \int_{-h/2}^{+h/2} \sigma_x z\,dz \\ M_y &= \int \sigma_y z\,dz \\ M_{xy} &= \int \tau_{xy} z\,dz \\ N_x &= \int \sigma_x dz \\ N_y &= \int \sigma_y dz \\ N_{xy} &= \int \tau_{xy} dz \end{aligned} \qquad (3.12)$$

$$N = \begin{bmatrix} N_x \\ N_y \\ N_{xy} \end{bmatrix} , \qquad M = \begin{bmatrix} M_x \\ M_y \\ M_{xy} \end{bmatrix}$$

From the standard procedures, stiffness matrix is given by:-

$$[K] = \int [B]^T \quad [D] \quad [B] \quad dvol \qquad (3.13)$$

For layered element this equation may be rewritten as:-

$$[K] = \iiint (RB)^T D \; (RB) \; dx \; dy \; dz$$

$$\therefore \quad [K] = \iiint B^T \; (R^T D R) B \; dx \; dy \; dz \qquad (3.14)$$

From which $[K] = \iint B^T \; D' B \; dx \; dy$

where $D' = \int [R]^T \; [D] \; [R] \; dz \qquad (3.15)$

Here D' is the equivalent constitutive matrix for layered element.

In equation (3.14) only the bracketted term is dependent on the Z coordinate, and the integration can be performed by using the layers contributions.

Equation (3.15) can be rewritten as:-

$$D' = \int [R]^T \; [D] \; [R] \, dz$$

$$= \sum_{i=1}^{N} \frac{E_i}{1-\nu_i^2} \left[\begin{array}{ccc|ccc} 1 & \nu_i & 0 & z_i & \nu_i z_i & 0 \\ \nu_i & 1 & 0 & \nu_i z_i & z_i & 0 \\ 0 & 0 & \frac{1-\nu_i}{2} & 0 & 0 & \frac{1-\nu_i}{2} z_i \\ \hline z_i & \nu_i z_i & 0 & z_i^2 & \nu_i z_i^2 & 0 \\ \nu_i z_i & z_i & 0 & \nu_i z_i^2 & z_i^2 & 0 \\ 0 & 0 & \frac{1-\nu_i}{2} z_i & 0 & 0 & \frac{1-\nu_i}{2} z_i^2 \end{array}\right] (dz)_i$$

$$= \sum_{i=1}^{N} \begin{bmatrix} D_i & Z_i D_i \\ Z_i D_i & Z_i^2 D_i \end{bmatrix} (dZ)_i \qquad (3.16)$$

Equation (3.16) shows the important feature of this model in treating composite materials made up as a combination of various constituents. If the element is made up of layers with symmetric properties about the middle plane of the plate, the summation terms of ZdZ in (3.16) would vanish, and the constitutive matrix exhibits uncoupling between membrane and flexural effects. For reinforced concrete, such a coupling effect is bound to occur due to unsymmetric cracking, even if the slab element was initally isotropic.

The membrane terms $D_i dZ_i$ in (3.16) can be evaluated exactly (using any number of layers across the thickness of the slab) even if the whole thickness of slab is considered as one layer. But the flexural terms $(Z_i^2\ dZ_i)$ representing the flexural rigidity of the plate, depend on the number of layers used.

3.3 PROPERTIES OF REINFORCED CONCRETE MATERIALS AND THEIR MATHEMATICAL REPRESENTATION FOR NONLINEAR FINITE ELEMENT ANALYSIS.

3.3.1 Behaviour of Concrete

(i) Uniaxial state of stress

The behaviour of concrete can be explained with the aid of the uniaxial stress-strain curve of Figure (3.2). When subjected to small compressive loads, it behaves in a quasi-elastic manner. Under increasing loads, deviation from linearity takes place. The material has got a limited ductility and under high compressive stresses, the material fails by crushing.

For mathematical representation of experimental stress-strain/

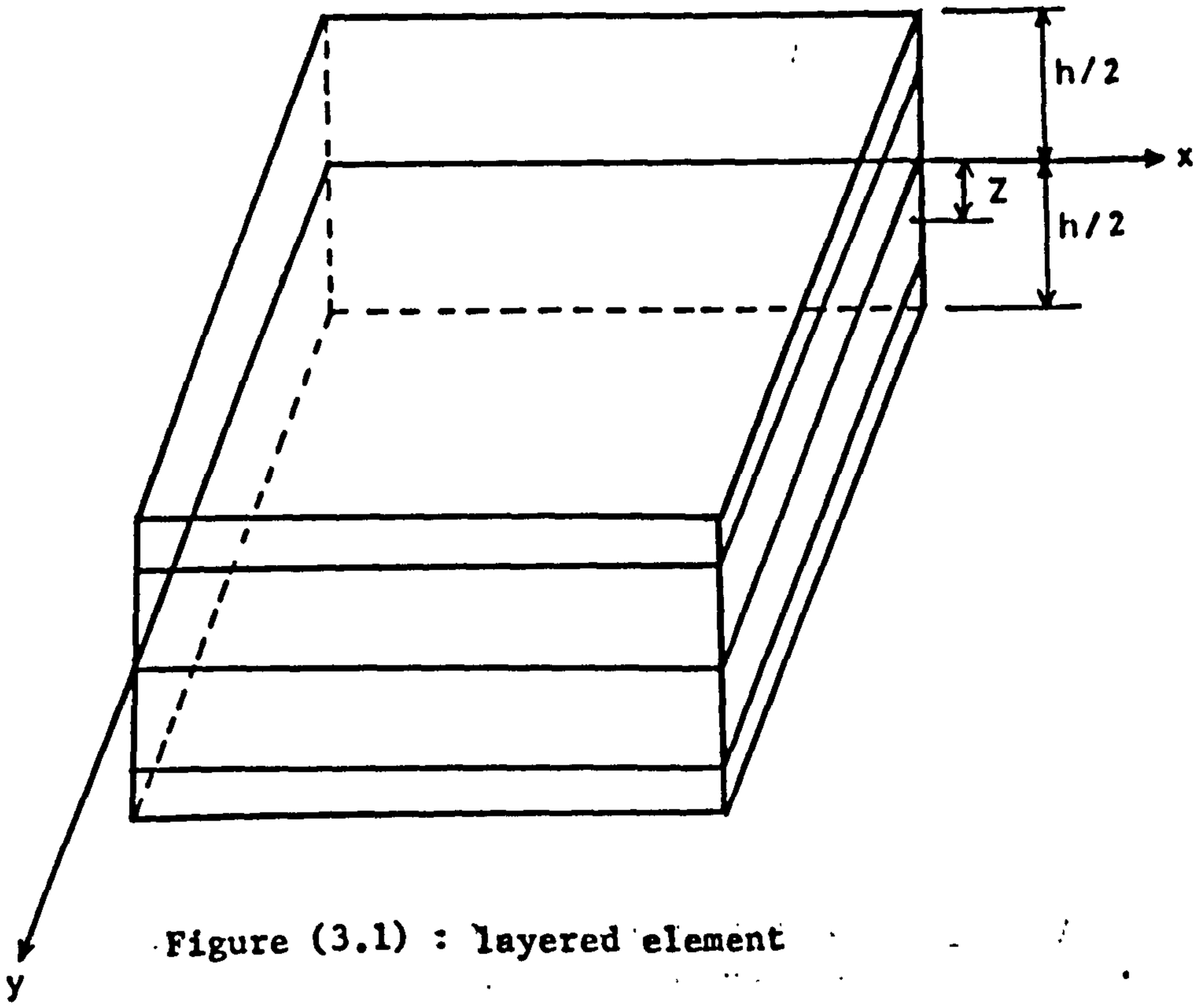

Figure (3.1) : layered element

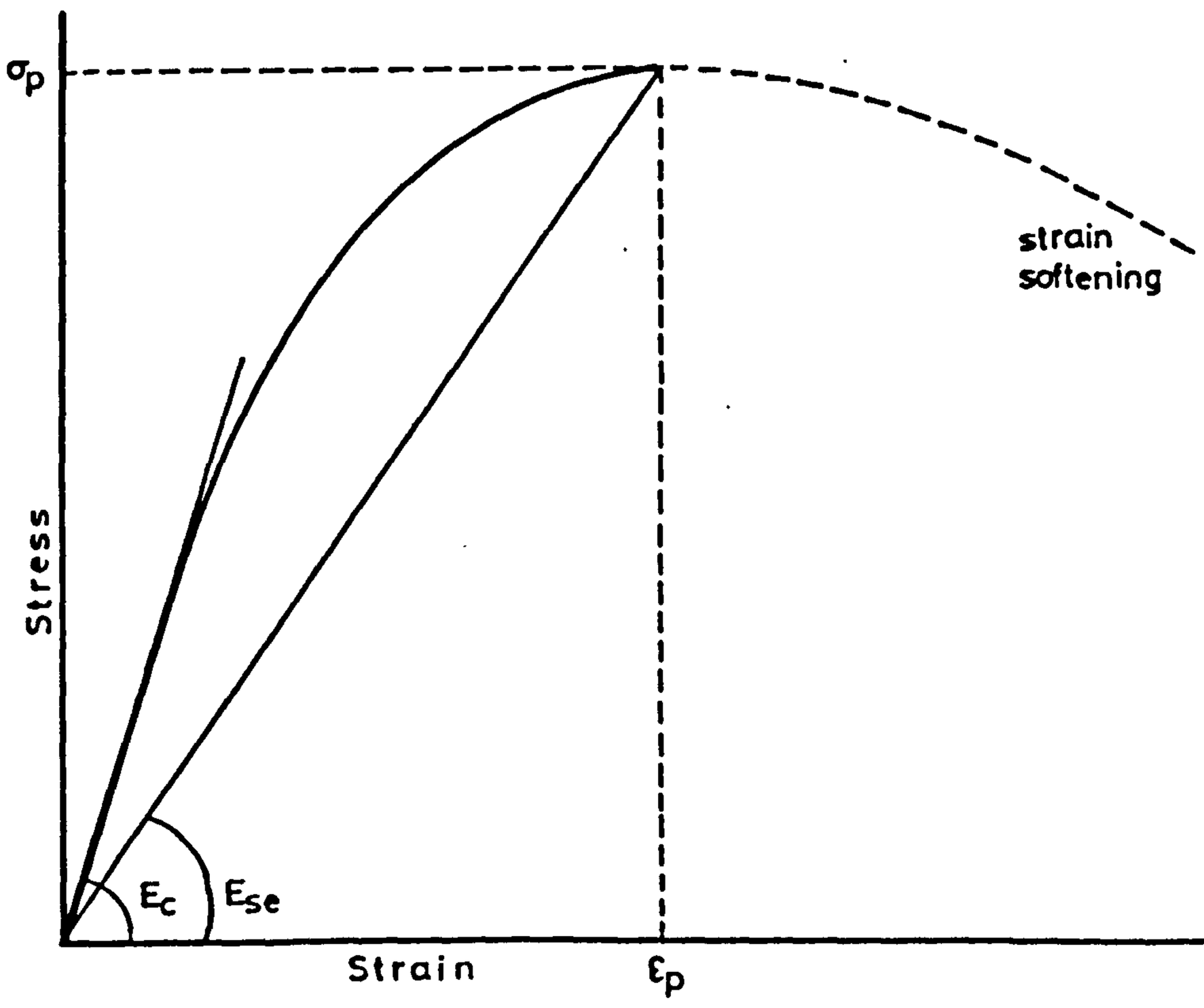

Figure (3.2) : Stress-Strain Curve for Concrete in Compression.

curves of plain concrete, several emperical equations have been proposed by different investigators, however the following equation originally proposed by Liu et al (23) representing uniaxial stress-strain curve for concrete is most commonly used for numerical analyses.

$$\sigma = \frac{E_c \varepsilon}{1 + \left[\frac{E_c \varepsilon_p}{\sigma_p} - 2\right] \times \left[\frac{\varepsilon}{\varepsilon_p}\right] + \left[\frac{\varepsilon}{\varepsilon_p}\right]^2} \qquad (3.17)$$

where σ is the level of stress reached, in the material, corresponding to a state of strain equal to ε .

σ_p = f_{cu} for uniaxial compression where

f_{cu} = ultimate compressive stress of concrete,

ε_p may be taken equal to .0025.

(ii) Multiaxial state of stress

The ultimate compressive strength of concrete increases when subjected to multiaxial state of compressive stress.

From the experimental results of Kupfer et al (24), it can be observed that the increase in ultimate strength due to biaxial stressing depends upon the ratio of the two principal stresses. A maximum increase in compressive strength of 25% is achieved at a stress ratio of lateral/axial stress of .5, whereas the minimum increase of 16% corresponds to equal biaxial compressive stresses.

When subjected to biaxial tension-compression, the compressive strength of concrete decreases approximately linearly with the increase in the tension.

Concrete is very weak in tension and its tensile strength is approximately only 10% of that in compression.

For finite element applications the yield surface produced by (24)
Kufer et al(Figure (3.3))can be used for simplicity. A multilinear fit of this surface can be obtained in terms of the octahedral shear stress of the form (25):

$$\tau_{oct} - a - b\,\sigma_o = 0 \qquad (3.18)$$

$$\text{where} \quad \tau_{oct} = \frac{\sqrt{2}}{3}\sqrt{\sigma_x^2 + \sigma_y^2 - \sigma_x\,\sigma_y + 3\,\tau_{xy}^2} \qquad (3.19)$$

Here σ_o is the mean normal stress, a and b are constants.

Taking f_c as the uniaxial compressive strength of concrete and f_d as the equivalent compressive strength under biaxial compression and expressing the ratios : $m = \frac{f_t}{f_c}$ and $n = \frac{f_d}{f_c}$ (3.20)

Then for uniaxial compression, $\tau_{oct} = \frac{\sqrt{2}}{3} \times f_c$ and

mean stress = $\sigma_o = -\frac{f_c}{3}$

Therefore from (3.18)

$$\frac{\sqrt{2}}{3}\,f_c = -b\,f_{c/3} + a \qquad (3.21)$$

For biaxial compression $\tau_{oct} = \frac{\sqrt{2}}{3}\,f_d$ and

mean stress = $\sigma_o = -\,2\,f_d/3$, then

$$\frac{\sqrt{2}}{3}\,f_d = -\frac{2}{3}\,b\,f_d + a \qquad (3.22)$$

Solving (3.21) and (3.22) and substituting (3.20),

$$\tau_{oct} + \sqrt{2}\ \frac{(n-1)}{(2n-1)}\ \sigma_o\ - \frac{\sqrt{2}}{3}\ \frac{n}{(2n-1)}\ f_c\ = 0 \qquad (3.23)$$

Taking n = 1.16 from Figure (3.3).

$$\tau_{oct}/f_c\ + (0.1714\ \sigma_o/f_c) - 0.4143\ =\ 0 \qquad (3.24)$$

For tension - compression,

$$\tau_{oct}/f_c + \sqrt{2}\ \frac{(1-m)}{(1+m)}\ \frac{\sigma_o}{f_c}\ -\ \frac{2\sqrt{2}}{3}\ (\frac{m}{1+m}) \ =\ 0 \qquad (3.25)$$

and for <u>tension-tension</u>

$$(\frac{\sigma_1}{f_t})^2\ +\ (\frac{\sigma_2}{f_t})^2\ - 1\ =\ 0 \qquad (3.26)$$

(iii) <u>Subsequent yield surface:-</u>

Equations (3.24) to (3.26) define the final yield surface but unlike elastic perfectly plastic materials such as steel, plasticity in concrete starts before the maximum stress is reached (or yielding has taken place in conventional sense). In order to incorporate this phenomena in the analysis the following approach is adopted.

In uniaxial terms it amounts to saying that

Uniaxial compressive stress $\sigma \leq 0.5\ f_{cu}$, elastic

$\sigma = f_{cu}$, final yielding

If $0.5\ f_{cu} < \sigma < f_{cu}$, then an intermediate yield stress f_{cc} is used to define yielding.

where $f_{cc} = f_c + f_t \left(\frac{E_c}{E_i} - 1\right)$ (3.27)

E_c = the initial modulus of elasticity

E_i = the instantaneous modulus

The above equation was proposed by Johnnary (21).

For the numerical procedure adopted in the programme used for the study presented in this thesis, equation (3.17) is incrementally linearized. This is done by using intermediate loading surfaces(26) as shown in Figure (3.4). The first loading surface corresponds to the initial discontinuity in the stress-strain diagram. Subsequent loading surfaces are assumed to have the shape of the limiting yield surface. Accordingly, the intermediate surfaces are represented by equation (3.24) but with an intermediate strength f_{cc} replacing the ultimate strength f_c.

The process of treating the behaviour of the concrete, in the programme proceeds as follows, and is repeated for all sampling points in each layer of each element.

1) Solve elastic problem first and calculate strains and stresses.

2) Calculate the principal strains and stresses and find the maximm strain.

3) Check the state of stress whether it is (i) Compression - Compression, (ii) Compression-tension or (iii) Tension-tension.

If it is compression-compression, then

4) Calculate f_{cc}, from equation (3.27), using $f_c = 0.5\ f_{cu}$ and $E_i = E_c$ for the first time.

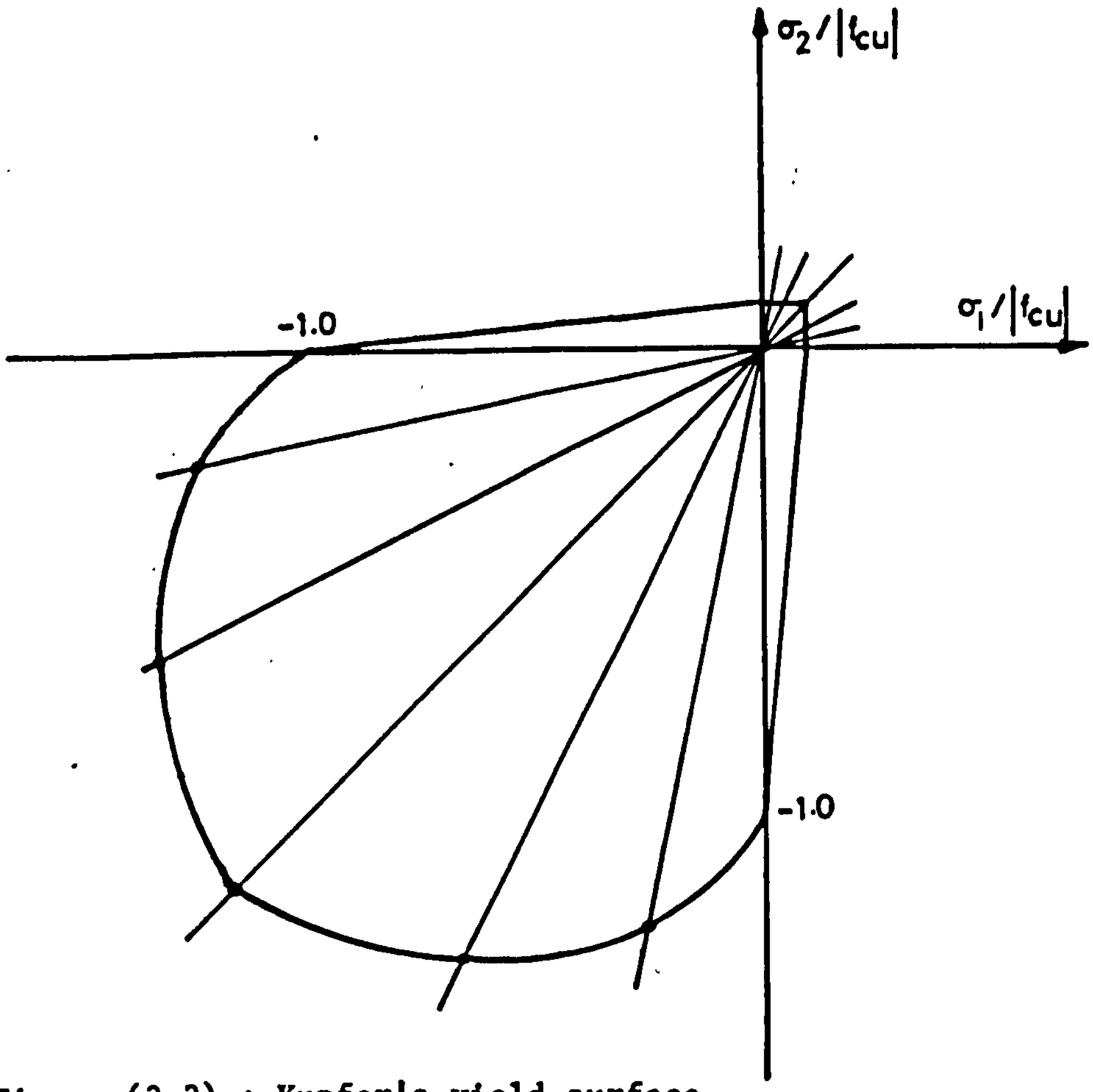

Figure (3.3) : Kupfer's yield surface.

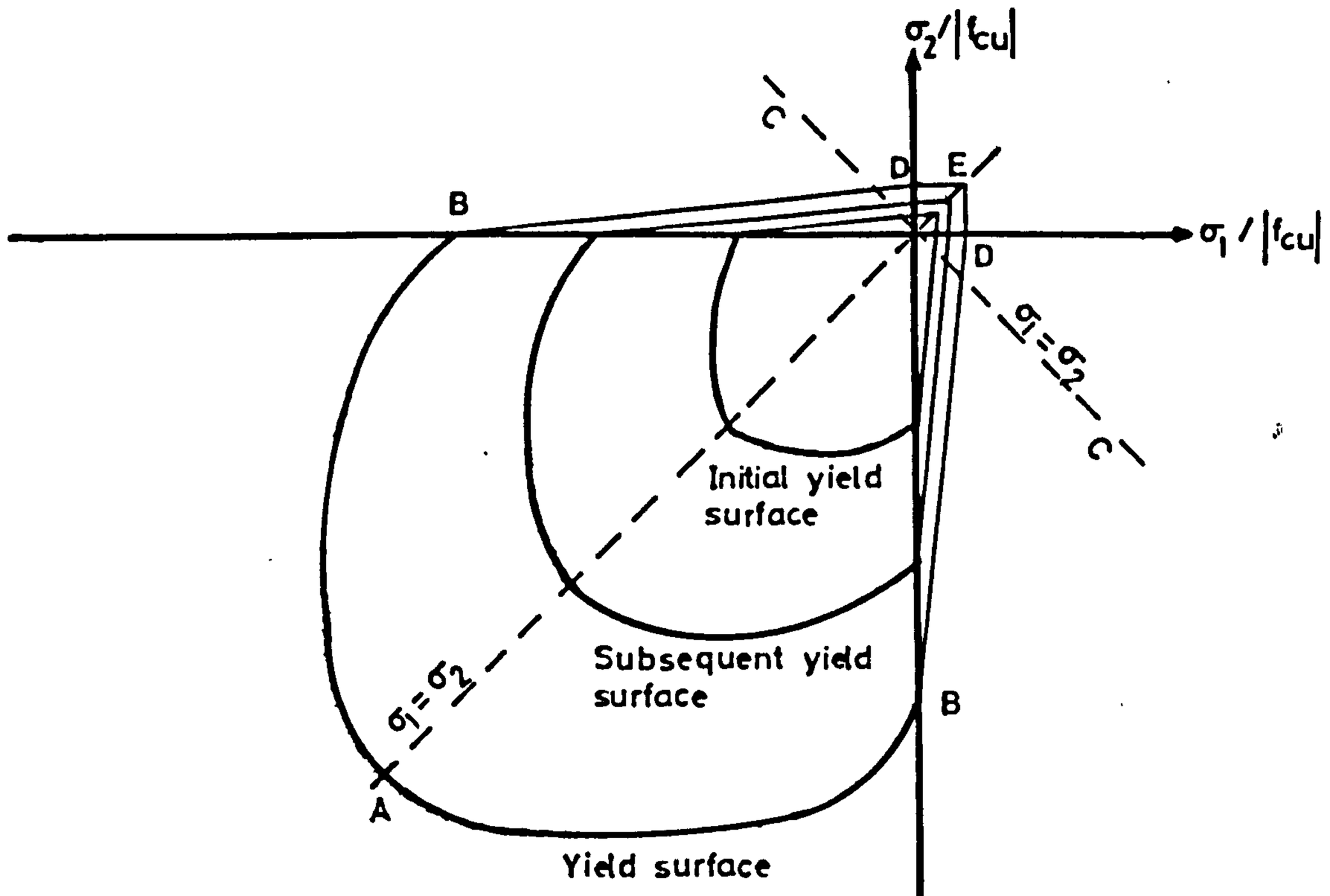

Figure (3.4) : "Zoning" the yield surface-initial and subsequent loading surfaces.

5) Using value f_{cc} calculated above, check against yield criteria from equation (3.24)

where $\sigma_o = \frac{\sigma_x + \sigma_y}{3}$

6) If the value calculated from the above is less than or equal to zero, that means yield criteria is not violated. In that case calculate the point contribution of the stresses towards the elemental forces N and M.

7) If the condition is violated, check the state of strain. If maximum strain ε_{max}, is less than .0025, then $E_i = \frac{\sigma}{\varepsilon_{max}}$ where σ is calculated from equation (3.17).

8) Find the factor $\frac{E_c - E_i}{E}$ and multiply all the three components of stress at the given point with this factor and subtract these values from the corresponding stresses to bring the state of stress in the material back on the yield surface Figure (3.2). Calculate the point contribution of stresses towards the total elemental forces N and M.

9) If maximum principal strain, ε_{max}, is greater than .0025, calculate E_i, from:

$E_i = \frac{f_{cu}}{\varepsilon_{max}}$ and repeat step 8.

10) If ε_{max} is greater than or equal to .0035, concrete is crushing and all the stress is removed.

11) If the state of stress in concrete is <u>Comp:-Tension</u>,

Working on the same lines, check against yield criteria using equation (3.25) with f_c equal to f_{cu} this time.

If the yield criterion is violated, the layer at that particular point is assumed to have cracked.

12) Case of tension-tension is treated in the same way, except that equation (3.26) is used to check the yield criteria. The direction of principal stress causing cracking is calculated from:

$$\text{Tan } 2\theta = \frac{2\sigma_{xy}}{\sigma_x - \sigma_y} \qquad (3.28)$$

The angle θ given by the above equation lies between 0^o and 45^o, therefore the actual crack direction θ_{cr} is determined from a Mohr's circle.

Before cracking concrete is assumed to be a linear, elastic, isotropic material having the constitutive matrix of (3.11). Upon cracking the stiffness of concrete normal to the crack is reduced to zero. Therefore x-coordinate axis is then placed parallel to the crack(Figure (3.5))and the material stiffness matrix is modified, so that

$$D^* = \begin{bmatrix} E_c & 0 & 0 \\ 0 & 0 & 0 \\ 0 & 0 & \beta G \end{bmatrix} \qquad (3.29)$$

After cracking, due to the aggregate interlocking concrete is still capable of transferring some shear through the cracked zones. Shear strength along the crack is a function of crack width. As the applied load increases, the cracks become wider and thus the shear transfer capacity of cracked concrete is reduced. However it is a common practice to adopt a constant reduction factor $\beta \leq 1.0$, called 'shear retention factor', by which the shear modulus G, of the cracked concrete must be multiplied while calculating the shear/

stresses. The value of β lies between unity for uncracked sections and zero for extensively cracked sections. As reported by Hand et al (27) especially for sections subjected to torsion, mathematical instability is created if a value of β equal to zero is adopted. For $\beta > 0$, any variation in its numerical value does have very little effect on the computed response of reinforced concrete. To study the effect of β on the theoretically predicted behaviour of particular type of slabs connecting shear walls, author tried values of β= 0.0, 0.2, 0.4 and 0.6 and the details of that study are presented later in this chapter.

Since constitutive matrix D* is defined in the crack directions, therefore it is transformed to global directions,

$$\text{Thus } D' = T^T D \; T \tag{3.30}$$

$$\text{where } T = \begin{bmatrix} C^2 & S^2 & CS \\ S^2 & C^2 & -CS \\ -2CS & 2CS & C^2-S^2 \end{bmatrix} \tag{3.31}$$

Here $C = \text{Cos } \theta_{cr}$ and $S = \text{Sin } \theta_{cr}$.

3.3.2 Reinforcing steel

In the present layered approach, steel bars are represented by an equivalent smeared layer, which can carry stresses only in the direction of the original bars. The equivalent thickness of the steel layer in any direction is determined in such a way that the corresponding ratio of steel in that particular direction in the element remains unchanged. The stress-strain curve for the bars may be assumed to have a definite yield point f_y. The idealized/

stress-strain curve is shown in Figure(3.6). For high yield steel, proof stress corresponding to .2% strain may be taken as f_y.

Before yielding, stresses are computed using the initial modulus. After yielding, a secant modulus is calculated and used in the subsequent load increment, as

$$E_i = f_y / \varepsilon_i \tag{3.32}$$

3.4 CALCULATIONS FOR SHEAR

3.4.1 Elastic range

For problems of pure bending of slabs, the shear force per unit length Q_x and Q_y can be calculated from the derivatives of the moments as

$$Q_x = \left(\frac{\partial M_{yx}}{\partial y} + \frac{\partial M_x}{\partial x}\right) \tag{3.33}$$

$$Q_y = \left(\frac{\partial M_y}{\partial y} - \frac{\partial M_{xy}}{\partial x}\right) \tag{3.34}$$

and for isotropic material in the elastic range shear in any layer at a distance Z from the middle surface is given by:

$$\tau_{xz} = \frac{3}{2h} Q_x \left(1 - \frac{4z^2}{h^2}\right) \tag{3.35}$$

$$\text{and } \tau_{yz} = \frac{3}{2h} Q_y \left(1 - \frac{4z^2}{h^2}\right) \tag{3.36}$$

3.4.2 Nonlinear range

To allow for cracking, during the present study the vertical shear/

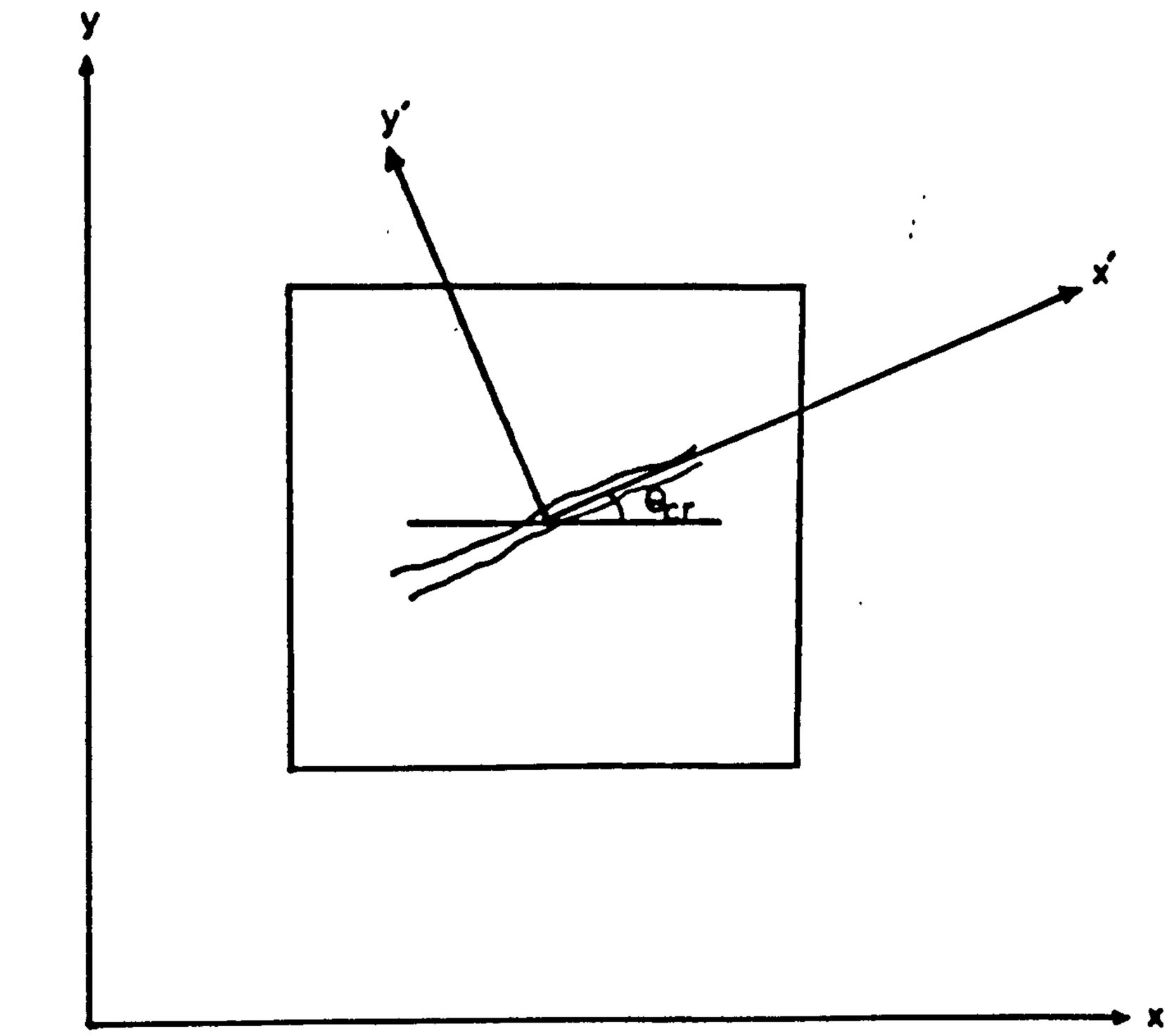

Figure (3.5) : Transformation of cracked stiffness to global directions.

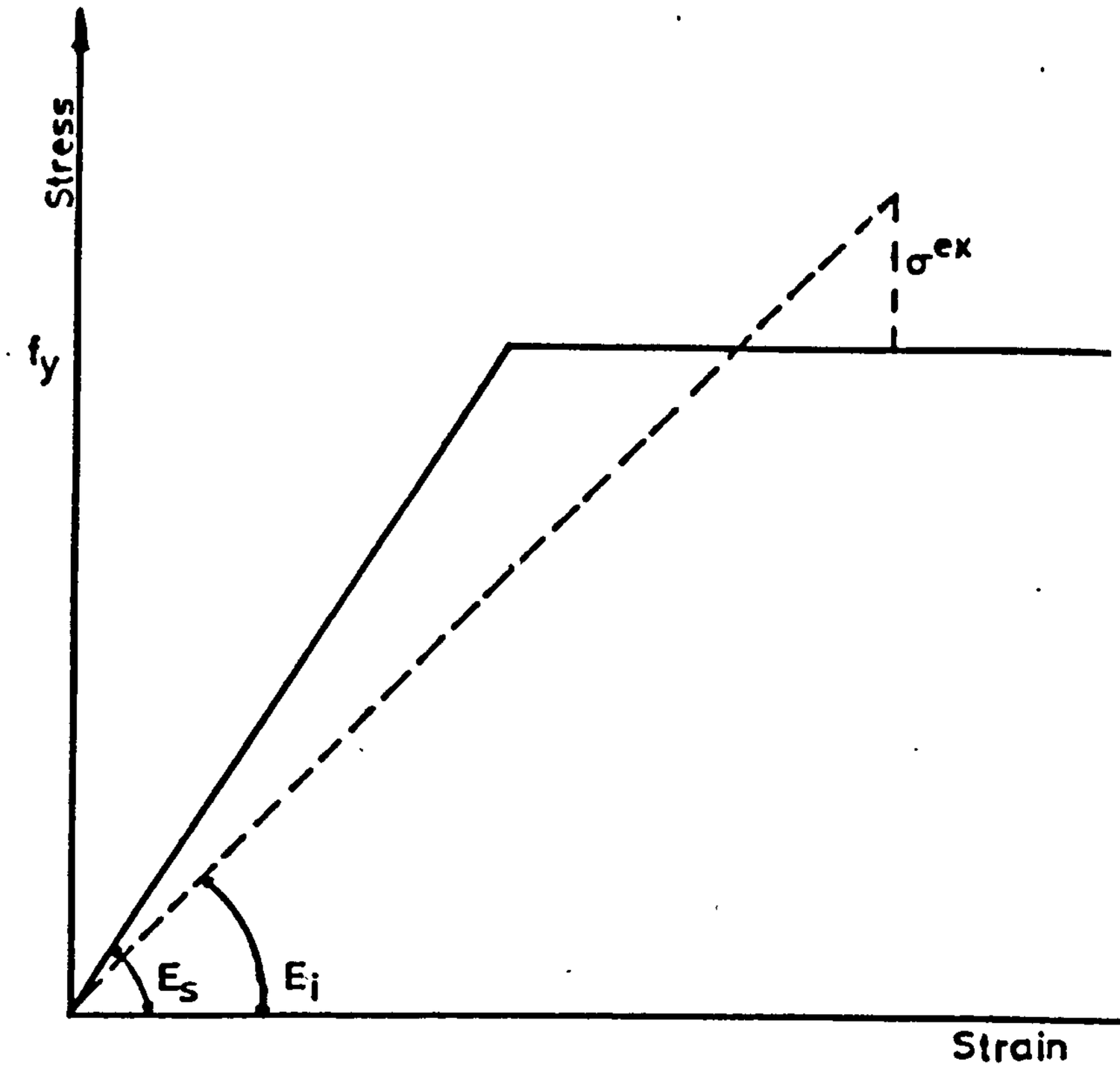

Figure (3.6) : The Idealized stress-strain curve for steel.

stresses τ_{xy} and τ_{yz} were calculated from the rate of change of horizontal stresses σ_x, σ_y and τ_{xy} *(Figure (3.7))* using the following equilibrium equations:

$$\frac{\delta\sigma_x}{\delta x} + \frac{\delta\tau_{xy}}{\delta y} + \frac{\delta\tau_{xz}}{\delta z} = 0 \qquad (3.37)$$

Therefore $$\frac{\delta\tau_{xz}}{\delta z} = -\frac{\delta\sigma_x}{\delta x} - \frac{\delta\tau_{xy}}{\delta y}$$

Therefore $$\tau_{xz} = -\int_z^{h/2} \left(\frac{\delta\sigma_x}{\delta x} + \frac{\delta\tau_{xz}}{\delta z}\right) dz \qquad (3.38)$$

Similarly $$\frac{\delta\sigma_y}{\delta y} + \frac{\delta\tau_{xy}}{\delta x} + \frac{\delta\tau_{yz}}{\delta z} = 0 \qquad (3.39)$$

from which

$$\tau_{yz} = -\int_z^{h/2} \left(\frac{\delta\sigma_y}{\delta y} + \frac{\delta\tau_{xy}}{\delta x}\right) dz \qquad (3.40)$$

Here dx was taken as the distance between the two consecutive Gaussian sampling points within the same element in x-direction, while dy the distance between two consecutive sampling points in y-direction and dz the thickness of the particular layer under consideration. In order to adopt it for the numerical calculation, the integration was replaced by summation (Ref. Figure (3.8)) and the contribution of each layer towards τ_{xz} and τ_{yz} was calculated from the rate of change of horizontal stresses i.e.

$$\frac{\delta\sigma_x}{\delta x}, \quad \frac{\delta\sigma_y}{\delta y}, \quad \frac{\delta\tau_{xy}}{\delta x} \text{ and } \frac{\delta\tau_{xy}}{\delta y}$$

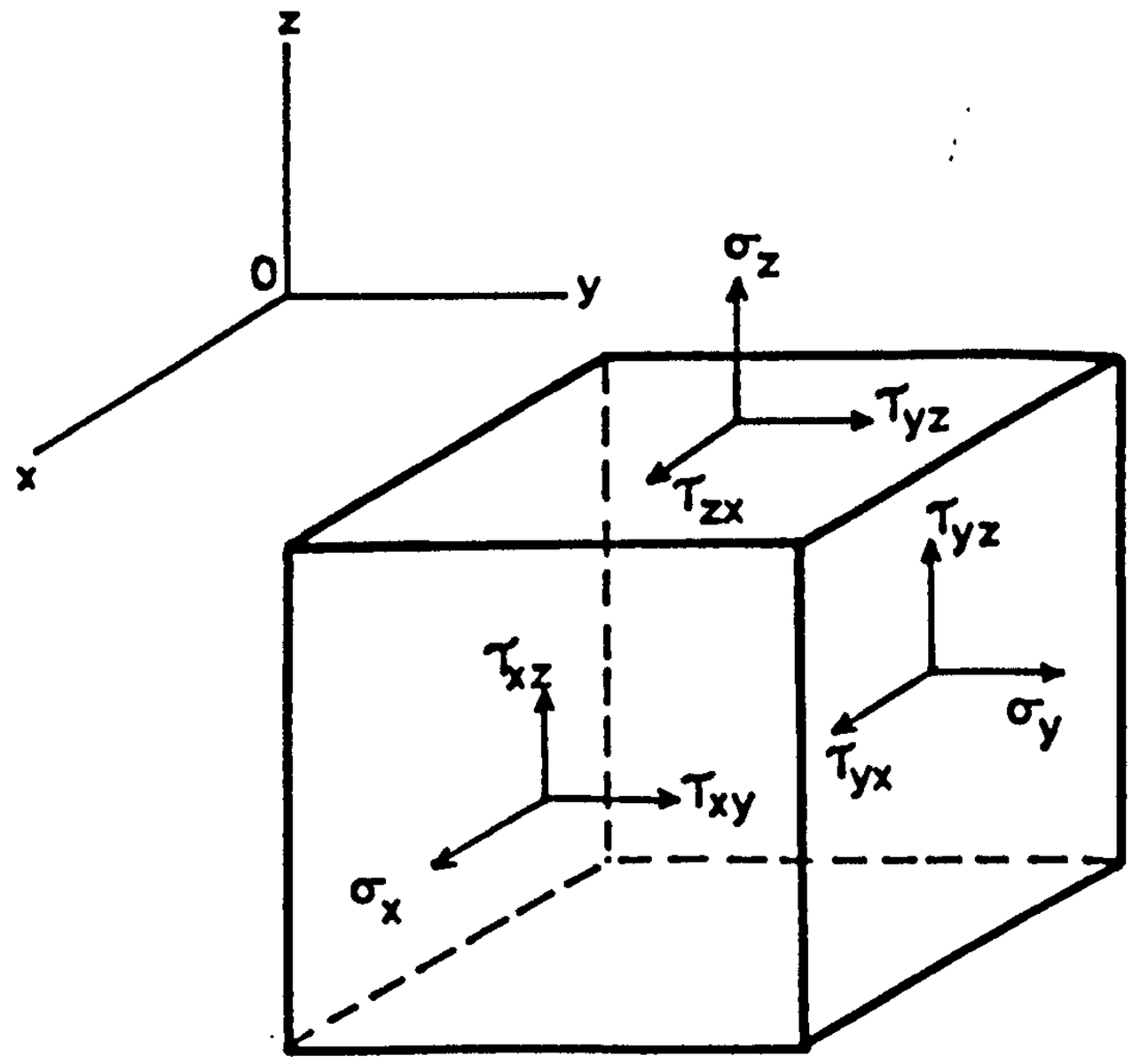

Figure (3.7) : Stresses acting on different faces of a cubic element.

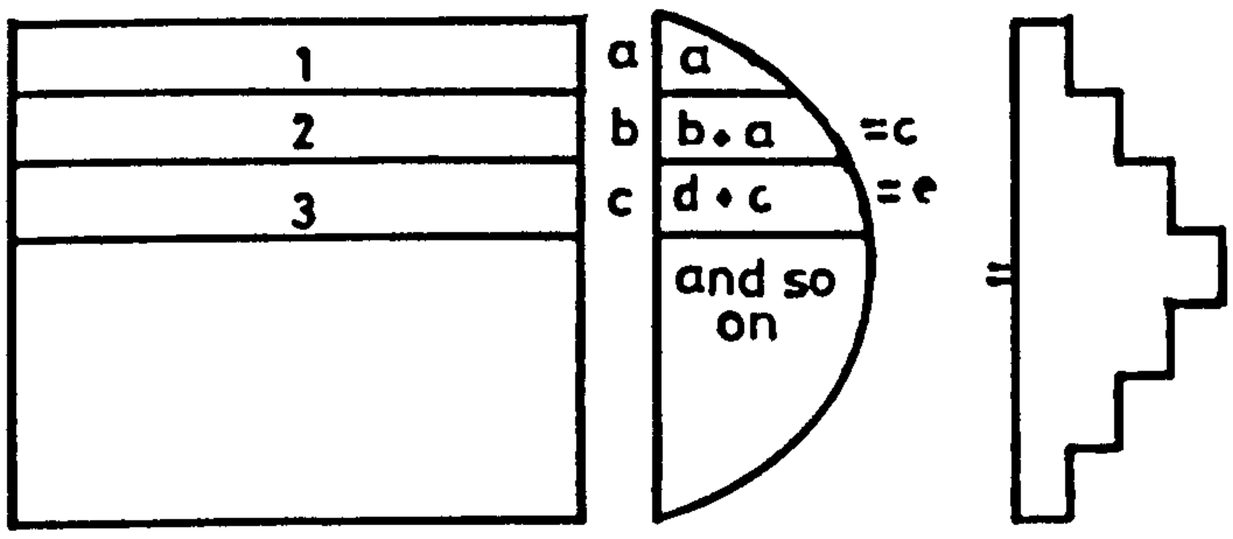

Figure (3.8) : Intensity of shear stress in different layers.

The intensity of vertical shear stresses τ_{xz} and τ_{yz} at the top and bottom should practically be zero but since these stresses are calculated at the central plane of the thickness of every layer, they have some finite value in the top and bottom layers as well. Nevertheless after cracking, shear transfer capacity of concrete layer covering the steel is assumed to be zero.

3.4.3 Yield criterion for shear

The main draw back of two dimensional nonlinear finite element models is that there is no yield criterion at present which could be adopted for the prediction of shear failures. The reason for this is that unlike tensile or compressive failure, shear carrying capacity is much more complex. Tensile or compressive failure is a function of the state of stress in concrete only but shear strength is governed not only by the strength of concrete but also by aggregate interlock etc. The different actions and the mechanism involved in resisting the applied shear at any section are discussed here with particular reference to a beam.

After cracking the total external vertical shear V (Figure 3.9), acting on any section is resisted by the combination of

1) A shear force across the compression zone, V_c.

2) A shear force transmitted across the crack by the flexural reinforcement by dowel action, V_{dowel}.

3) The vertical components of inclined shearing stresses transmitted across the inclined crack by means of interlocking of the aggregate/

particles, $V_{aggregate}$.

Thus $V = V_c + V_{dowel} + V_{aggregate}$ (3.41)

The following is a brief description of the contribution of each of the components.

(i) V_c:

From the well known equilibrium relationship between shear force and the rate of change of moment M along a reinforced concrete member, the following modes of internal shear resistance result:

$$V = \frac{dM}{dx} = \frac{d}{dx}(T_b \ell a) = \ell a \frac{dT_b}{dx} + T_b \frac{d(\ell a)}{dx} \quad (3.42)$$

where T_b = the tensile force in steel

ℓ_a = the lever arm.

The term $\ell a(\frac{dT_b}{dx})$ expresses the behaviour of a true prismatic flexural member in which the internal tensile force T_b acting at a constant lever arm ℓa changes from point to point along the reinforced concrete member to balance exactly the external moment intensity. The term $\frac{dT_b}{dx}$, the rate of change of the internal tensile force, is termed the bond force q', applied to the flexural reinforcement per unit length. Should the internal lever arm remain constant so that $\frac{d(\ell a)}{dx} = 0$, the equation of perfect 'beam action' is obtained thus,

$$V = \ell a \frac{dT_b}{dx} = q' \ell a \quad (3.43)$$

When for any reason the bond between steel and concrete is destroyed over the entire length of the shear span, the tensile/

force T_b can not change, hence $\frac{dT_b}{dx} = 0$. Under such circumstances the external shear can be resisted only by inclined internal compression. This extreme case is termed 'arch action'. Shear resistance due to arch action is expressed by the second term on the right hand side of equation (3.42).

$$V = T_b \frac{d(la)}{dx} = C_b \frac{d(la)}{dx} \qquad (3.44)$$

Here the internal tension T_b is replaced by the internal compression force C_b, which balances the external shear force.

Normally the two mechanisms offer combined resistance to shear force. The extent to which each mechanism contributes to shear resistance at various levels of external load intensity will depend on the compatibility of deformations associated with these actions (28).

In fact a greater part of the applied shear is transferred through the compression zone. The maximum vertical shear which concrete in compression zone can resist, not only depends upon the strength of concrete but also on the state of compression as well. It is expected that the capacity of concrete to transfer the vertical shear is improved with the increase in the applied compression, provided the compressive force can be resisted by the section.

(ii) V_{dowel}:

When shear displacement along an inclined crack occurs, a certain amount of shear will be transferred by means of the dowel action of the flexural reinforcement. Where the bars bear against the cover concrete, the dowel capacity will be limited by the tensile strength/

of the concrete. Once a splitting crack occurs, the stiffness, hence the effectiveness, of the dowel action is greatly reduced. The splitting strength of the concrete in turn will depend on the effective concrete area between bars of a layer across which the tension is to be resisted.

(iii) $V_{aggregate}$:

When the two faces of a flexural crack of moderate width are given a shear displacement relative to each other, a number of coarse aggregate particles projecting across such a crack will enable small shear forces to be transmitted. Clearly among many variables, the width and coarseness of the crack, the shear displacement and the shear strength of the interface, are likely to be the most important. Surprisingly a very considerable force can be transmitted this way. However since the cracks become wider as the load increases, it is presumed that at a very high load the capacity of cracked concrete to resist shear stress would be reduced.

Reliable predictions of shear failure could be made with the aid of two dimensional nonlinear finite element programmes if the variation of shear transfer capacity of the concrete in compression zone with the change in the state of compression and that of tension zone (due to aggregate interlock etc) as function of level of strain in steel is known.

Extensive experimental studies had been carried out to investigate quantitatively the effect of different parameters such as strength of

concrete, crack opening width and level of strain in steel on the shear transfer capacity of cracked concrete by aggregate interlock and dowel action of flexural reinforcement. Full account of those investigations is given in reference (29). A simple form of relationship between the shear stress which can be transferred through the cracked concrete, v_{crs}, and the shear displacement based on experimental data, given by Houde and Mirza (30), is as follows:

$$v_{crs} = 11.3 \left(\frac{1}{C_{cr}}\right)^{3/2} \Delta \qquad (3.45)$$

where C_{cr} = Initial crack width, mm

Δ = Shear displacement, mm

From the experimental results of Pauley & Loeber(31)(Figure(3.10)) performed on precracked concrete block specimen it appears that for an initial crack opening width of .5mm (.02 inch), the shear stress transmitted levels off at a value of Δ= .76 mm (3. x 10^{-3}) inch.

3.5 DETAILS OF NUMERICAL PROCEDURE

An incremental, total strain, iterative procedure using the initial stiffness matrix is used. The load is applied in small increments. Within each increment an elastic solution is first tried, followed by a succession of linearized iterations until the equilibrium is maintained. At any stage of loading, the equilibrium equation to be satisfied is given by

$$F^{ex} = P - \int B^T \cdot \sigma \, d(vol) \qquad (3.46)$$

Here σ is the actual current state of stress reached in the material and F^{ex} which is the difference between the applied load P and the/

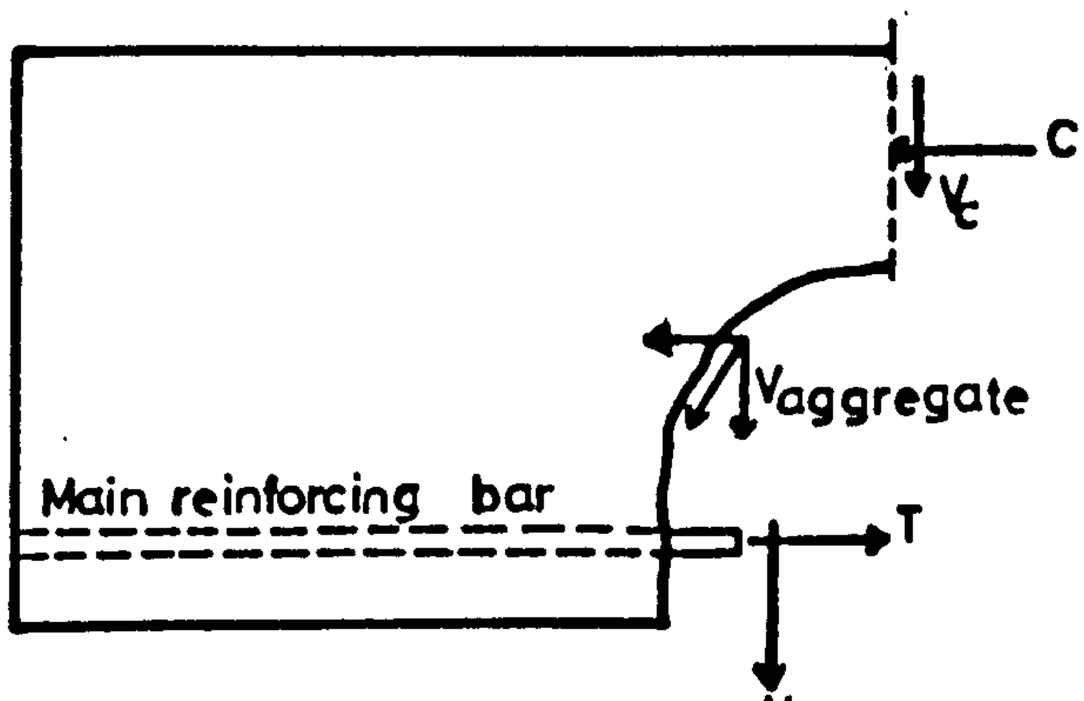

Figure (3.9) : Shear transfer mechanism.

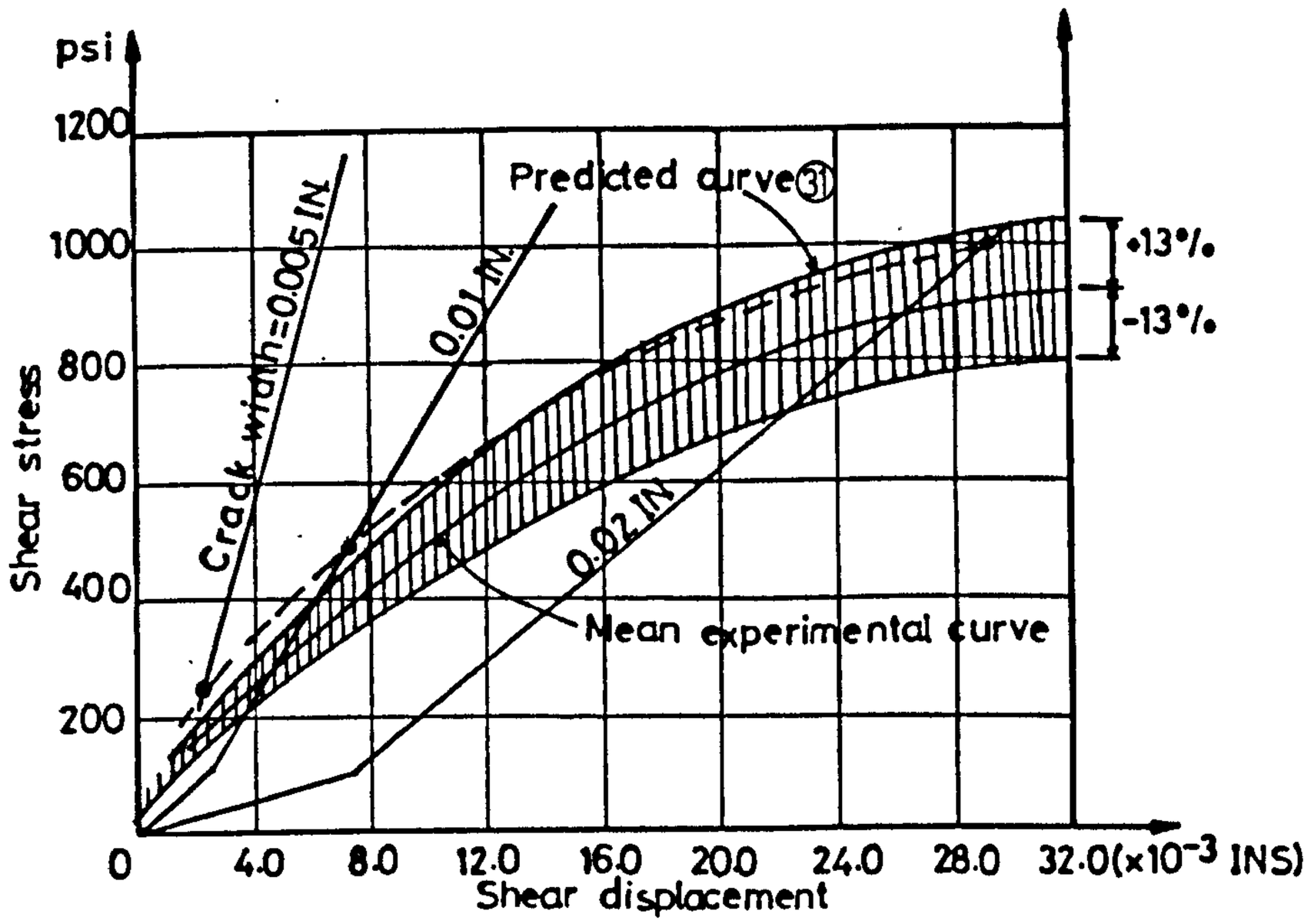

Figure (3.10) : Mean Regression Curve for Shear Stress-Shear Displacement
Relationship With Constant Shear Stress to Crack Width Ratio.

total elemental force, is termed as pseudo or out-of-balance force.

Due to cracking and crushing of concrete, yielding of steel and other material nonlinearities, the loss of stress takes place, since the excessive stress is removed and the stress vector is kept on the material yield surface. Thus lack of equilibrium between the applied load P and the total element force F (calculated from the point contribution of stresses towards the elemental forces N and M) results whenever stresses beyond the yield surfaces are removed and the stress state is brought back on the yield surface. The excessive force, F^{ex}, representing the lack of equilibrium at any stage is recycled until equilibrium is achieved. At the end of a cycle of iterations these excess forces are added to the load vector at the start of the next load increment. Accordingly, the elastic solution at the beginning of a load increment is obtained using a fictitious load vector that contains all applied loads in addition to the accumulated nonlinear effects resulting from previous load increments.

The solution proceeds as follows:

1) Elements stiffness matrices are formed from the layers stiffness, using Gaussian quadrature.

2) The global stiffness matrix is formed from the elements matrices, using standard procedures. The matrix is then decomposed using the Gaussian elimination procedure.

3) A small load increment is applied, and the structure is solved for nodal displacements. From nodal displacements, middle plane strains and curvatures are found at the Gaussian points from/

equation: $\varepsilon_m = B\delta^e$ (see equation (3.7)).

4) For each sampling point in a layer, the total strains are found from: $\varepsilon = R\,\varepsilon_m$ (see equation (3.2)).

Using the current constitutive matrix D for the point, stresses and principal stresses are found.

5) The stress state at the point is checked against the relevant transition criteria. If none are violated, steps 4 and 5 are repeated for all sampling points in all layers in all elements.

6) If any of the criteria are violated, the constitutive matrix D at the sampling point is changed. The change in the stiffness matrix D is used to compute the excess stress, and the stresses are then brought back on to the yield surface. The point contribution to the stress resultant vectors N, M are calculated from equation (3.12).

7) Previous steps are repeated for all sampling points in all layers and in all elements.

8) For each element, numerical integration is used to evaluate the nodal forces resulting from the stress resultants N and M, thus

$$F = \int B^T \begin{Bmatrix} N \\ M \end{Bmatrix} dA \qquad (3.47)$$

The global force vector is assembled from elements contributions at the nodes and equilibrium is then examined, using

$$[F^{ex}] = [P] - [F] \qquad (3.48)$$

9) The excess force vector F^{ex} is added to the load vector and the structure is analysed and steps 4 to 8 are repeated and convergence/

is checked, using the displacement norm:

$$\text{Norm} = \left([\delta d]^T \{\delta d\} / [d]^T \{d\} \right)^{\frac{1}{2}} \qquad (3.49)$$

Iterations are assumed to converge when the iterate norm $\leq 10^{-4}$.

(10)If convergence is achieved, or a predefined limit on the iterations is exhausted a new load increment is added to the load vector and steps 3 to 9 repeated.

3.6 STUDY OF CONVERGENCE OF FINITE ELEMENT RESULTS

3.6.1 General

Hago (22) checked the accuracy of this programme and used it for the prediction of ultimate flexural loads and distribution of stresses, strains, moments and inplane forces in slabs with different boundary conditions. In this work convergence study was carried out by analysing one of the models of preliminary test series, conducted by the author (full descriptions of that experimental work are given in chapter six),using different mesh sizes and load increment sizes.

Hago (22) showed that using a total number of eight layers produced an error in predicted flexural rigidities of 1.56% while that with ten layers was of the order of 1%. This point was not therefore investigated further and for the analysis presented in this thesis, the thickness of slab was divided into eight layers (two for steel and six for concrete) except for one model with doubly reinforced slab (MT9), for which a total number of ten layers was used, four for steel (two at top and two at the bottom) and six for concrete.

3.6.2 Effect of mesh size for elastic analysis

Taking advantage of symmetry, only one half of the model was analysed, using mesh sizes 8 x 9, 5 x 9, 5 x 6, 4 x 6 and 4 x 4. A typical mesh with dimensions, boundary conditions and coordinate axes is shown in Figure (3.11).

A uniform edge displacement of .2mm, simulating the effect of wind loading, was imposed along the line of contraflexure (line KL in Figure (3.11)) and the distribution of stresses, strains and moments was obtained. The wall thickness was assumed to be zero for this analysis, though the effect of finite wall thickness upon the theoretically predicted behaviour was also investigated, This is described in chapter seven. For comparison, the distribution of moment M_y along section BC Figure (3.11)obtained by using different mesh sizes is shown in Figure (3.12). As can be observed from this figure, the distribution of moment M_y for different mesh sizes closely follow each other except in the region of stress concentration near the nose of the wall. Table (3.1) shows the percentage difference in computed equivalent forces required to displace the line of contraflexure by .2 mm and the total moment acting along BC, obtained by using different mesh sizes. It can be seen from this table that this difference is also very small. It was therefore concluded that even a rough mesh of 4 x 4 should produce acceptable results.

3.6.3 Effect of mesh size in nonlinear range.

Effect of only three mesh sizes viz. 5 x 6, 4 x 6 and 4 x 4 was investigated by performing full nonlinear analysis of model PT2 /

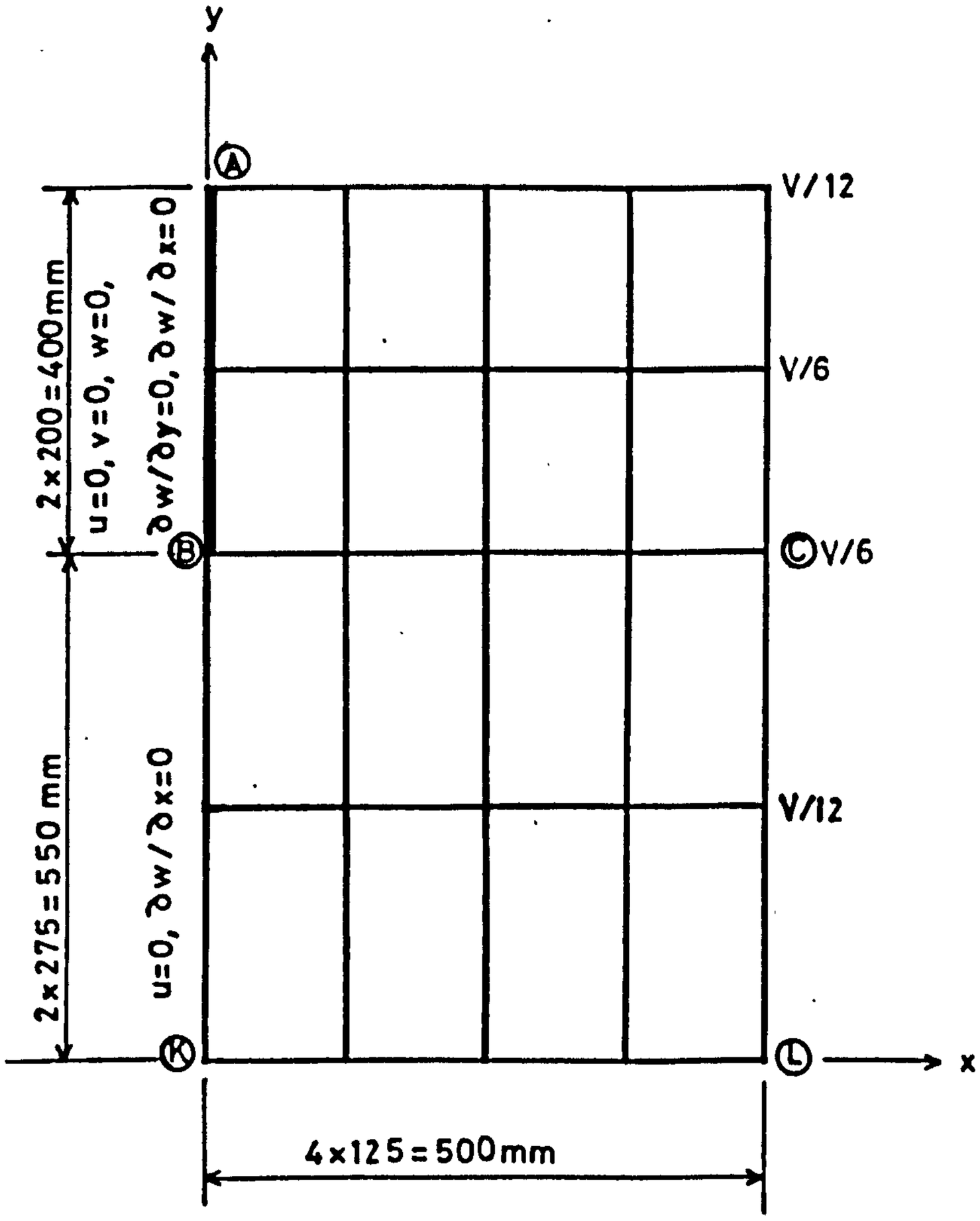

Figure (3.11) : Typical mesh with dimensions and boundary conditions used for the analysis of model PT2.

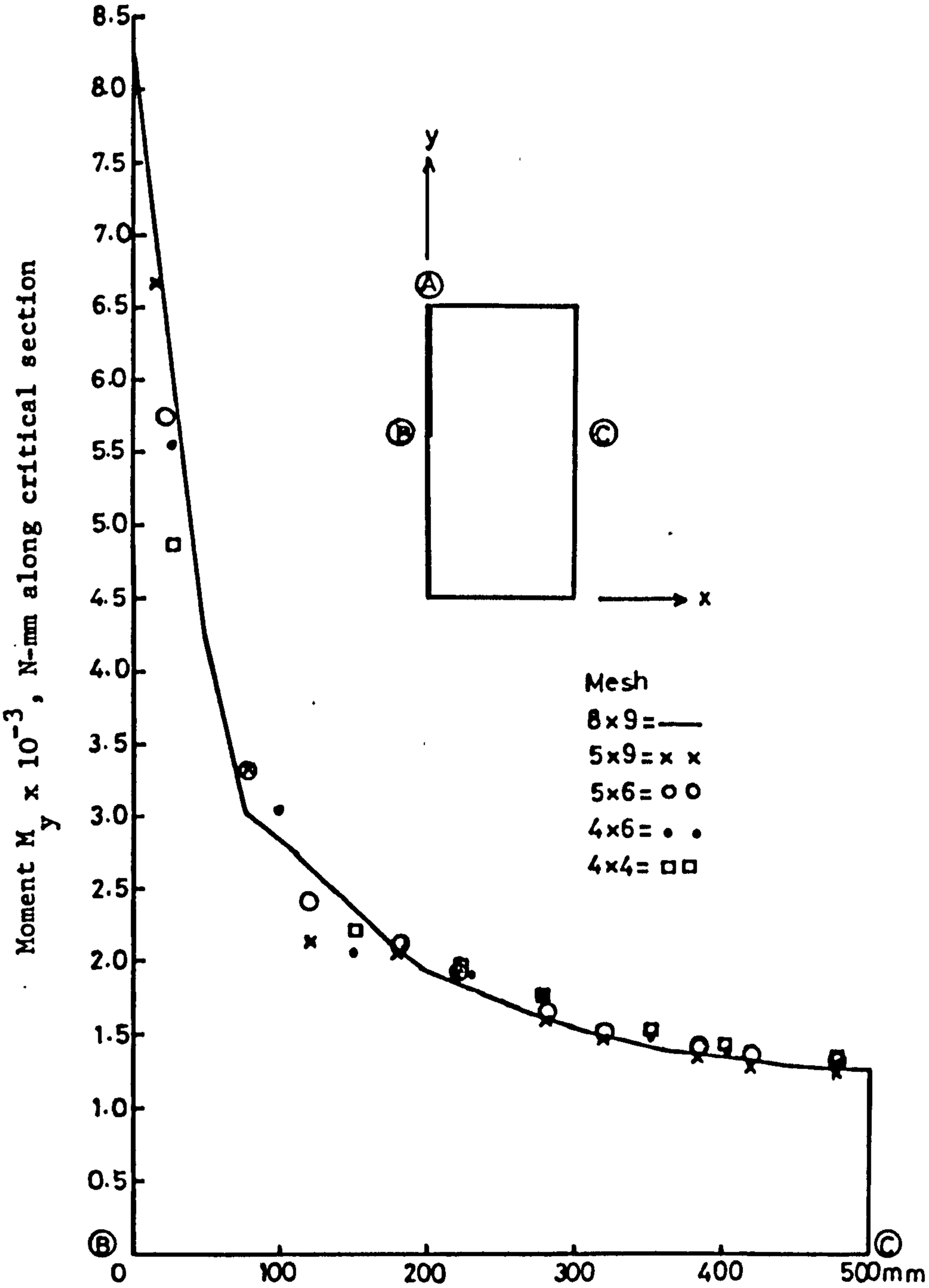

Figure (3.12) : Elastic distribution of moment M_y along transverse critical section BC obtained by using different mesh sizes.

Table 3.1. Effect of size of mesh (Elastic range).

Mesh	Displ. mm.	Equivalent load kN	% Difference of	Moment M_y kN-M	% Difference of moments
8 x 9	.2	4.23	00	2.3	00
5 x 9	.2	4.27	+.95%	2.32	+.87%
5 x 6	.2	4.24	+.24%	2.29	-.43%
4 x 6	.2	4.22	-.24%	2.3	00%
4 x 4	.2	4.17	-1.4%	2.26	-1.6%

of preliminary test series. Figure (3.13) shows the comparison of the theoretical wind load-displacement curves. From this figure it can be observed that at early stages of loading all the curves closely follow each other. However lower ultimate loads are predicted by analysis if the mesh is finer. This is basically due to the fact that higher intensities of strains, stresses and moments etc. (called singularity of stresses) are predicted in the slab at its junction with the wall if finer mesh is used, thus causing an early yielding of constitutive materials and hence early failure of that region of the slab. This singularity of stresses is discussed in chapter seven. The ultimate load predicted by nonlinear analysis was only 65% of the design ultimate load of the slab when mesh of (5 x 6) elements was used, while it was 85% of the ultimate design load when mesh of (4 x 4) elements was used. It was therefore deemed sufficient to use a mesh of (4 x 4) elements for the analysis.

3.6.4 Effect of size of load increment

For full nonlinear analysis of reinforced concrete member using this programme, initially a very small load is applied and elastic solution is sought. The load is then increased to the cracking load P_{cr}, and afterwards it is incremented by a fixed percentage of cracking load. Hago (22) has recommended the use of a load increment size of .15 P_{cr}. However since for this particular type of slabs due to higher concentration of stresses near the edge of wall, the cracking load is relatively low, the load increments of .2 P_{cr} and .25 P_{cr} were tried and load-displacement curves were obtained which are shown in Figure (3.14). It can be observed from this figure that the effect of increase in the size of load increment

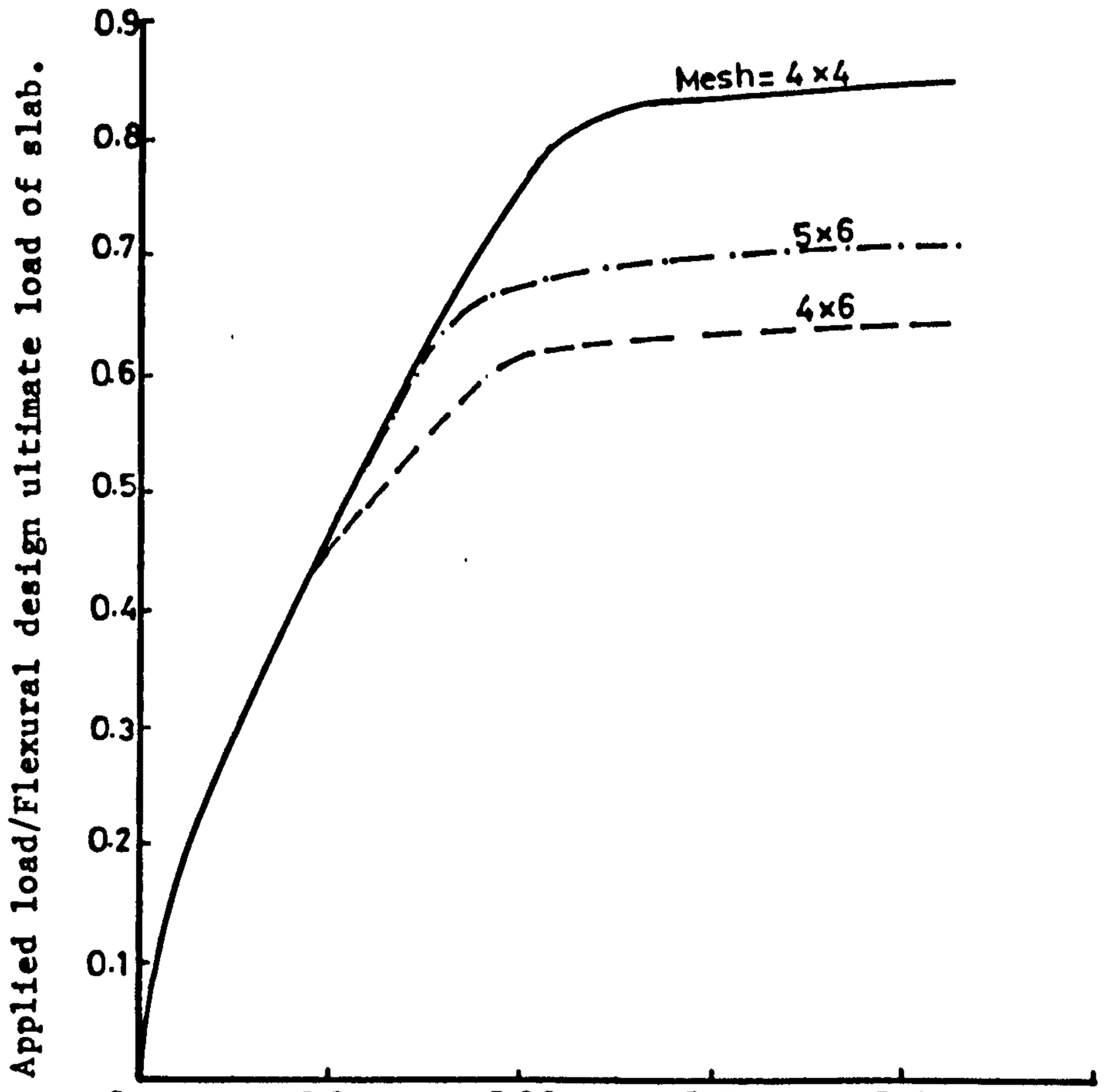

Figure (3.13) : Comparison of theoretical load-displacement relationship for model PT2 obtained by using different mesh sizes.

up to .25 P_{cr} is negligible. Therefore .25 P_{cr} was adopted.

The effect of the size of the load increment was further investigated by reducing it to half its original size after yielding of steel took place for the first time in the most highly stressed element. The load-displacement curve thus obtained, (Figure (3.15)) is compared with that obtained without reducing the size of load increment. Since local yielding of steel in slab near the inner edge of wall took place when the load was in the region of approximately 65% of the ultimate load, this caused considerable increase in the time of computation. However as is obvious from Figure (3.15), the effect of this strategy was also negligible. Therefore the idea of reducing the load increment after the steel has yielded, was abandoned.

3.6.5 Maximum number of iterations.

It has already been discussed that after application of each load increment the unbalanced forces are recycled during iterations. Hago (22) showed that for each load increment 10 to 15 iterations were enough for sufficiently accurate results. Therefore a maximum limit of 15 had been imposed upon the no. of iterations which were performed and for every iteration displacement norm was checked. A limit of 1×10^{-4} was placed upon this norm as well. It was observed that at very early stages of loading this limit of norm was achieved well before the maximum no. of iterations was reached. However at very late stages of loading the above value of displacement norm (i.e. 1×10^{-4}) could not be achieved, though in each case a considerable reduction in its value took place. Thus when the load was in the region of approximately 90% of the load at failure, the/

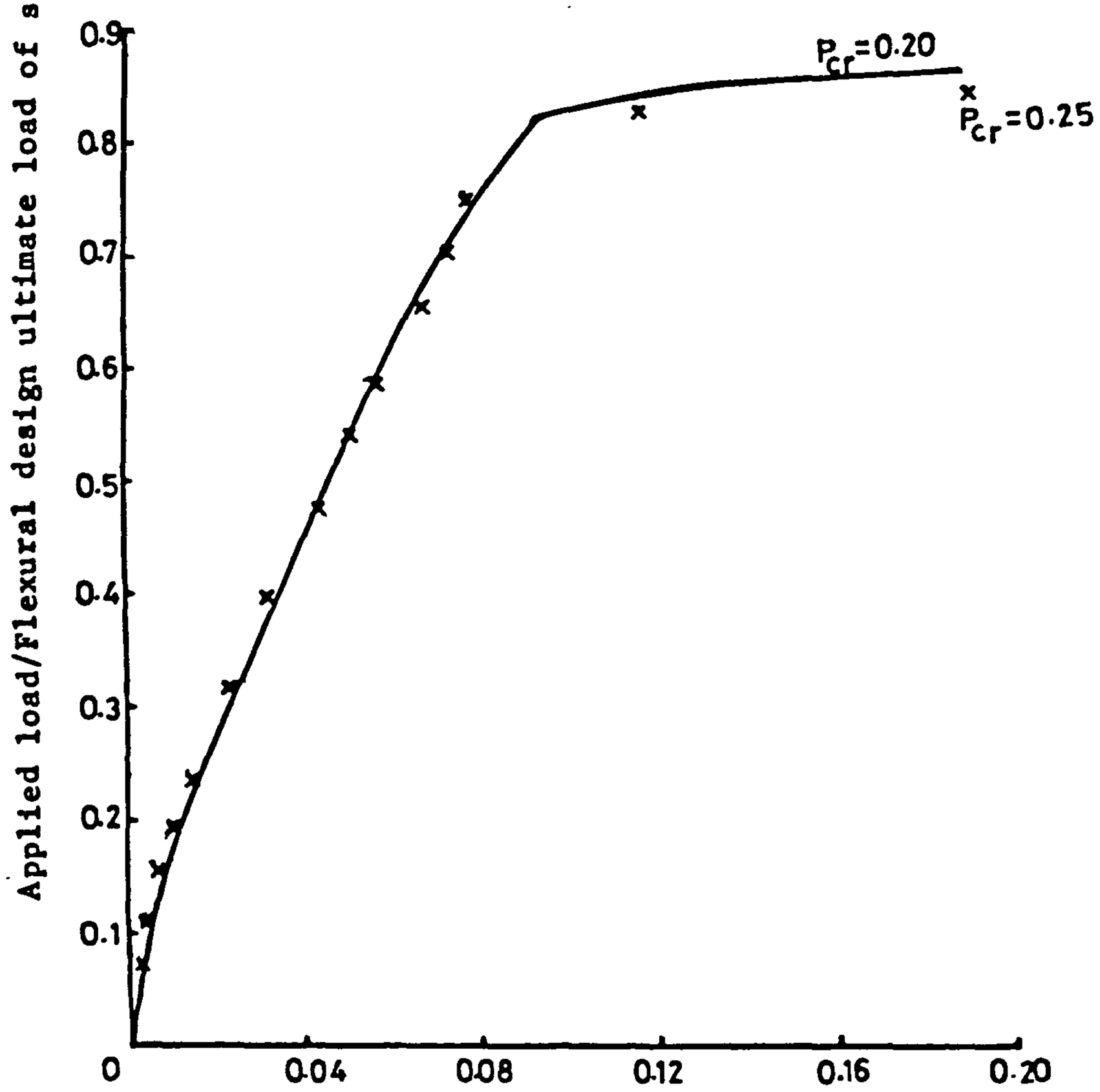

Figure (3.14) : Effect of the size of load increment on the Load-displ. behaviour.

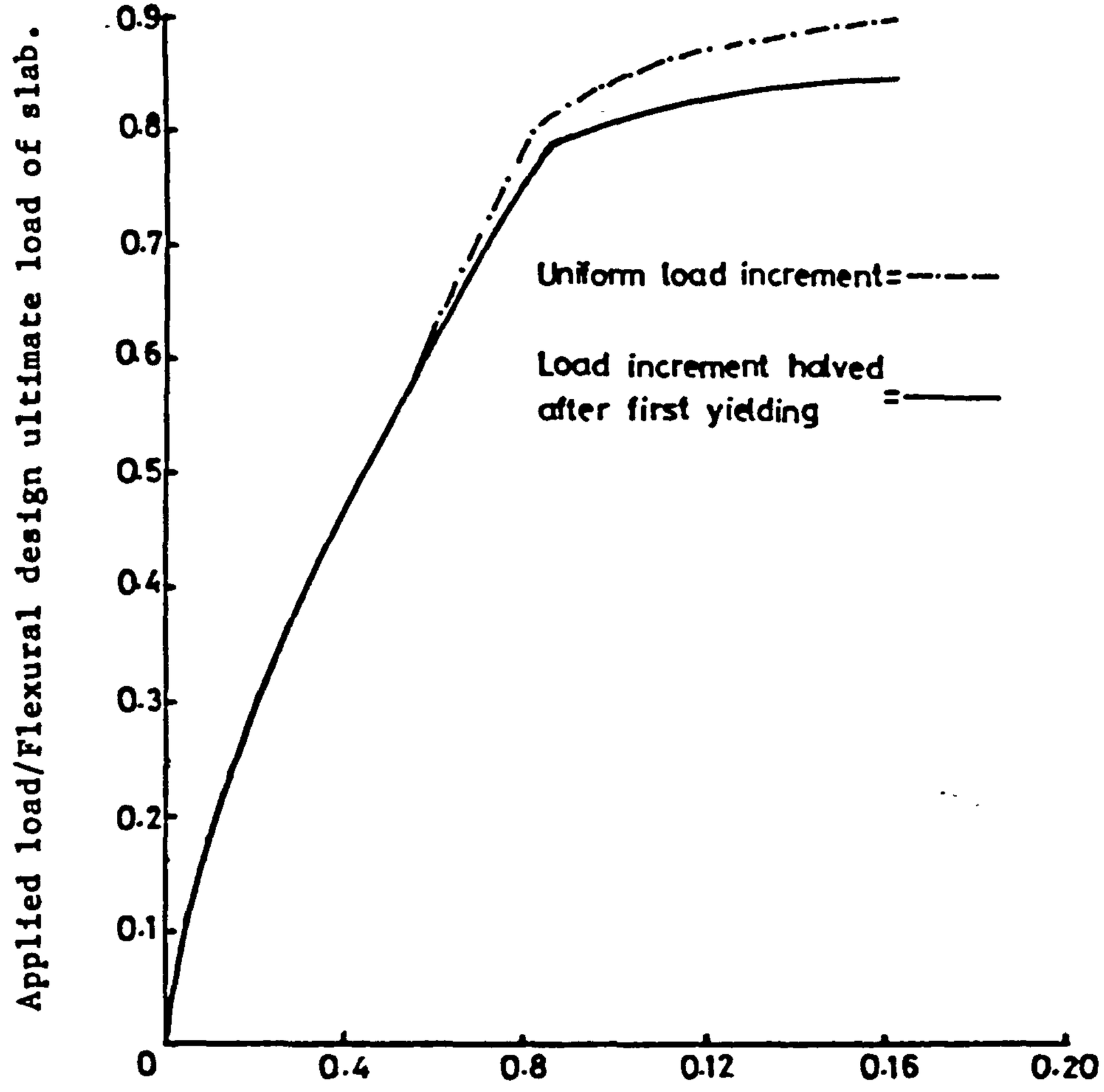

Figure (3.15) : Effect of reducing the size of load increment on Load-displ. behaviour.

displacement norm at the 15th iteration was found to be only 4.6% of that at first iteration and its value was 1.6×10^{-4}.

3.7 FLEXURAL FAILURE OF SLABS

As a matter of principle, the analysis should be continued until the determinant of the stiffness matrix becomes zero, indicating the formation of a mechanism. This can be done only if the equations of equilibrium remain well conditioned, but in practice this is hardly possible. As constant stiffness matrix approach was used, another alternative is to put a maximum limit upon the deflection in terms of a certain ratio of slab thickness. As quoted by Johnnary (25), different investigators have achieved a maximum deflection which ranges between .15h to .45h for slabs with different boundary conditions. However he was of the opinion that analysing a concrete slab up to beyond a maximum deflection of .25h might be rather too ambitious because for cases where this had been done, large differences between experimental and theoretical results had been noticed after the stage corresponding to the yielding of steel. He suggested that the maximum deflection should not be related to the thickness of slab alone but to the span/depth ratio of the structure and proposed that a limit for deflection of $\frac{\text{displ.}}{L} = \frac{1}{200}\left(\frac{L}{10h}\right)$ be adopted. Here L is the span and h the overall thickness of slab.

For the models tested and analysed by the author, the span of slab was relatively very small and consequently the span/depth ratio was also very low, and in all the cases it was found to be in the region of 3.2 to 7.5. Therefore the above criterion resulted in very small displacements which could not be adopted as limiting values to discontinue analyses.

The classical theory of plasticity assumes that at failure sufficient number of elements would have attained their limit strength to create a mechanism. In our particular case the plastic action is concentrated in only a few elements along the transverse critical section for moments, BC Figure (3.11). For such cases Johnnary (25) writes, "Experience indicates that if a single element near the point of maximum displacement yields completely with the steel in the element also reaching a strain of more than .005, the ultimate state is reached". This was adopted as failure criteria. However the analysis was in some cases continued for a few more load increments and displacement as high as .19h was achieved.

3.8 SHEARS

3.8.1 Test for shears

Case 1: Since this programme had not been used before, for the calculation of shears, it was tested for shears first by analysing simple case of a cantilever shown in Figure (3.16), using a very rough mesh of 2 x 2 elements. A total load of 2 kN was applied along the free edge. From the vertical shear stresses τ_{xz}, elastic distribution of shear Q_x along CD was obtained. The total shear force transferred along section CD was found to be 1.973 kN which is only 1.35% less than the applied load. The load was then incremented till the yielding of steel started and the rate of change of horizontal stresses in steel was reduced to zero. It was observed that at any stage of loading the total shear induced along section CD was in good agreement with applied load.

Case 2: The convergence for shears was checked by analysing a more complex case of connecting slab of a shear wall structure.

A portion of the shearwall -slab structure as shown in Figure (3.17) was analysed using a mesh of 4 x 4 elements and distribution of shear Q_y and Q_x along BC and AB respectively was obtained. The distribution is shown in Figures(3.18) and (3.19). The total shear induced is equal to the area under the curve. The total shear transferred along BC in this case was found to be 2.108 kN which is approximately 5% more than the applied load. The same structure was reanalysed by using a mesh of 10 x 10 elements. For comparison, graphs showing the distributinn of shears Q_y and Q_x obtained from this run are also presented in Figure (3.18) and (3.19). The total shear transferred along BC was found to be equal to 2.04 kN in this case which is 2% more than the applied load.

Case 3: Model PT2 of preliminary test series which was tested for wind load alone, was analysed by applying the point loads at the nodes along the line of contraflexure, so that this edge was displaced uniformly by .05 mm. A mesh of 4 x 4 was used for this purpose. A total load of .521 kN was applied and distribution of shears Q_y and Q_x along sections BC and AB Figure (3.11)respectively was obtained. The total shear transferred along BC was found to be .541 kN which is 3.9% more than the applied load. From the full nonlinear analysis of this model it was observed that at any stage of loading the total shear Q_y induced along BC was in good agreement with the applied load.

3.8.2 Distribution of shears and mesh size

The distribution of shears for simple cases of cantilevers etc. doesnot require any special attention, therefore here it is discussed/

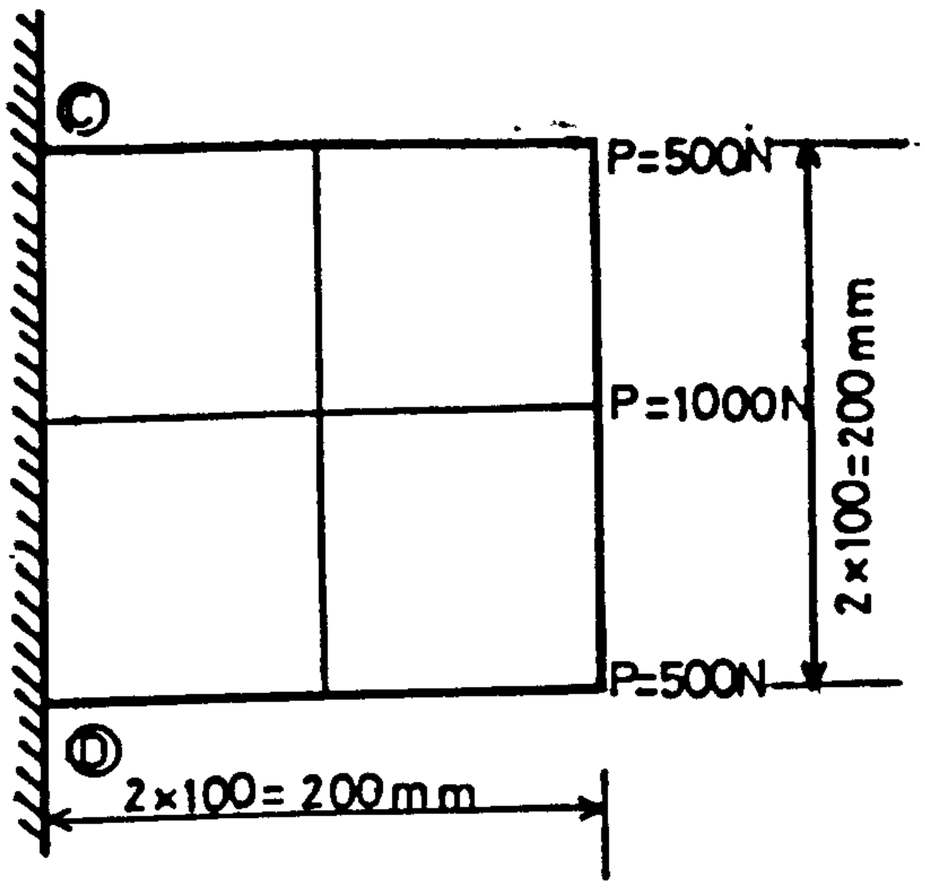

Figure (3.16) : Cantilever slab with mesh and loading.

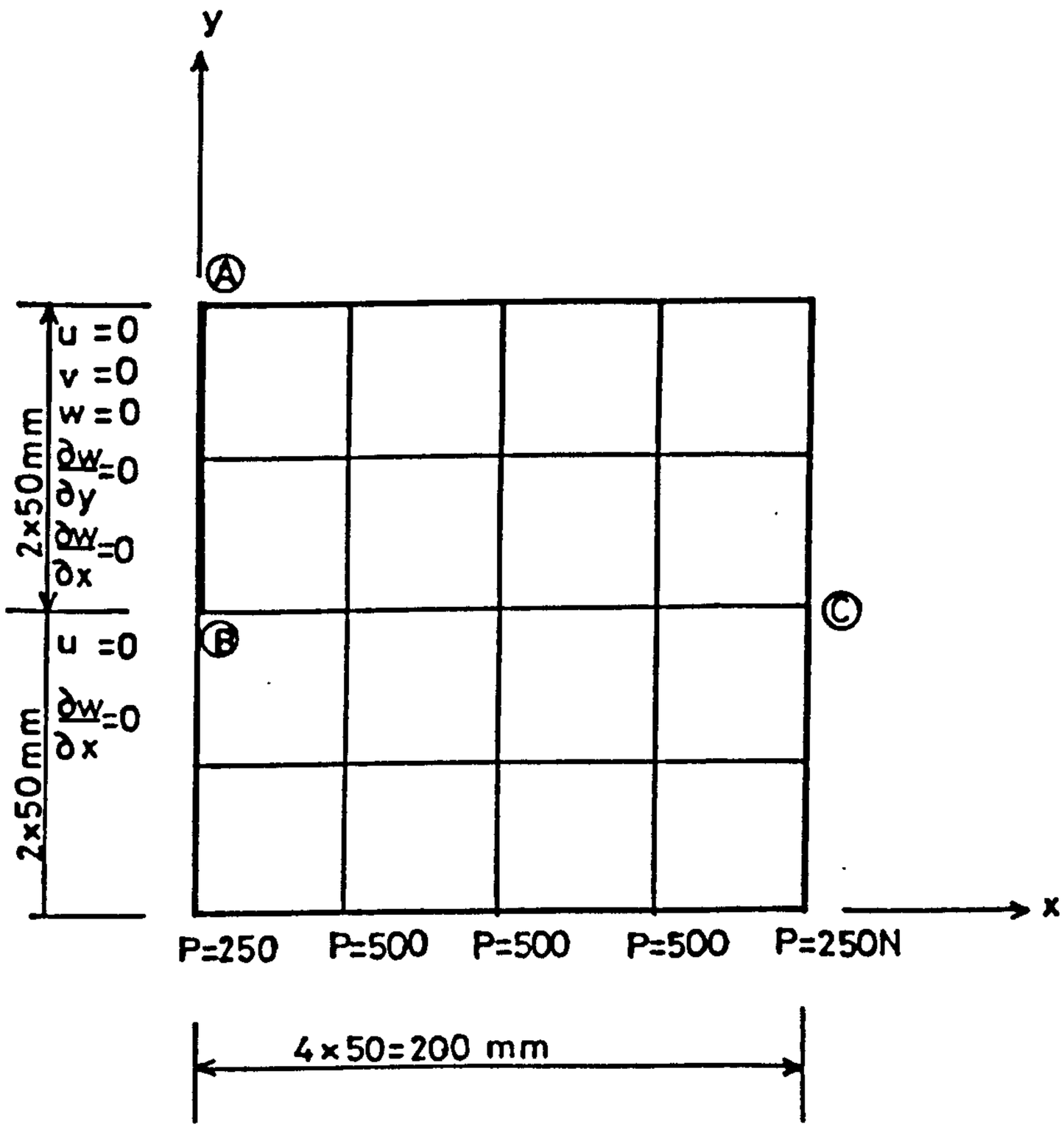

Figure (3.17) : Connecting slab of a shear wall structure with mesh, boundary conditions and loading.

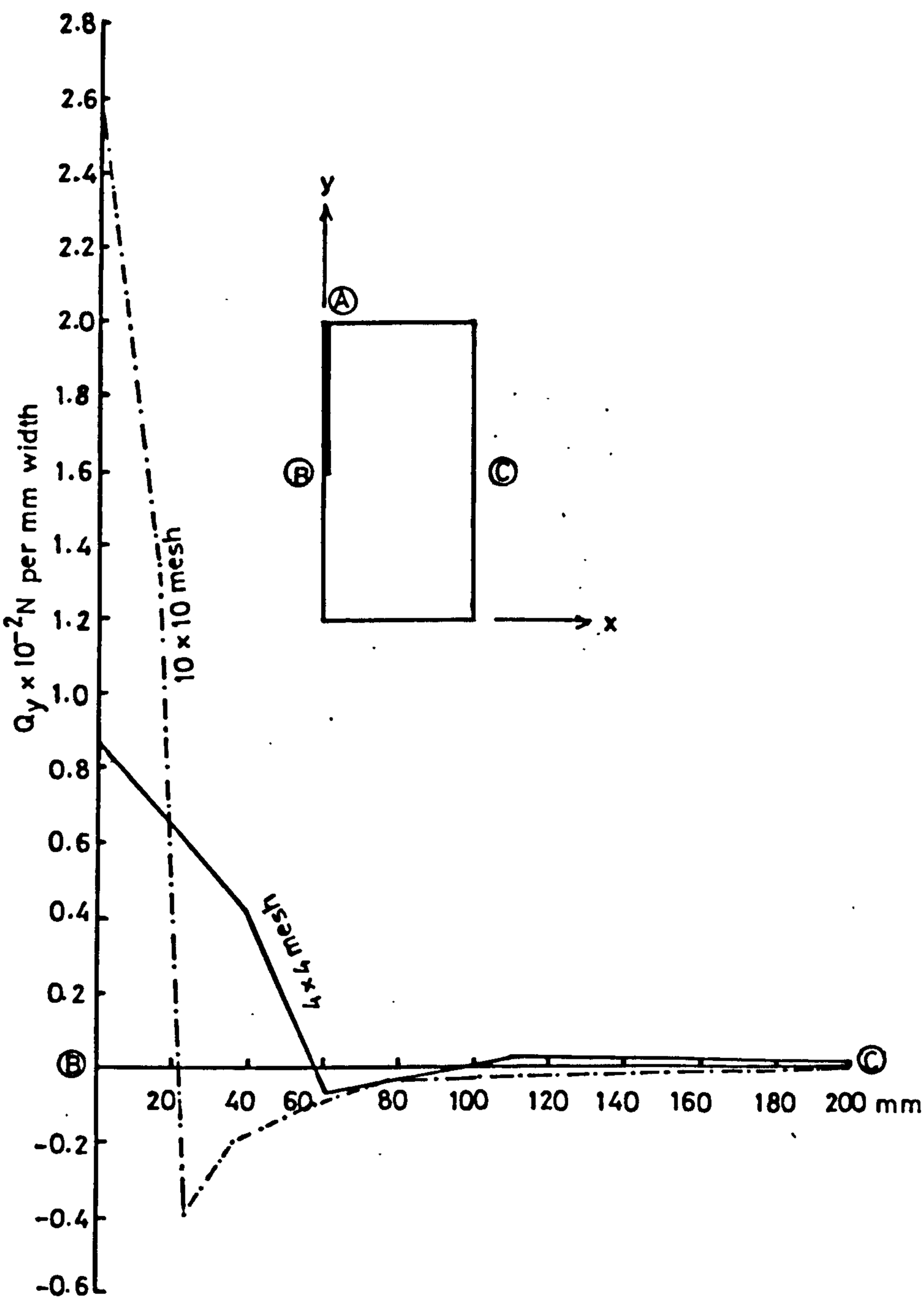

Figure (3.18) : Distribution of shear Q_y along transverse section BC.

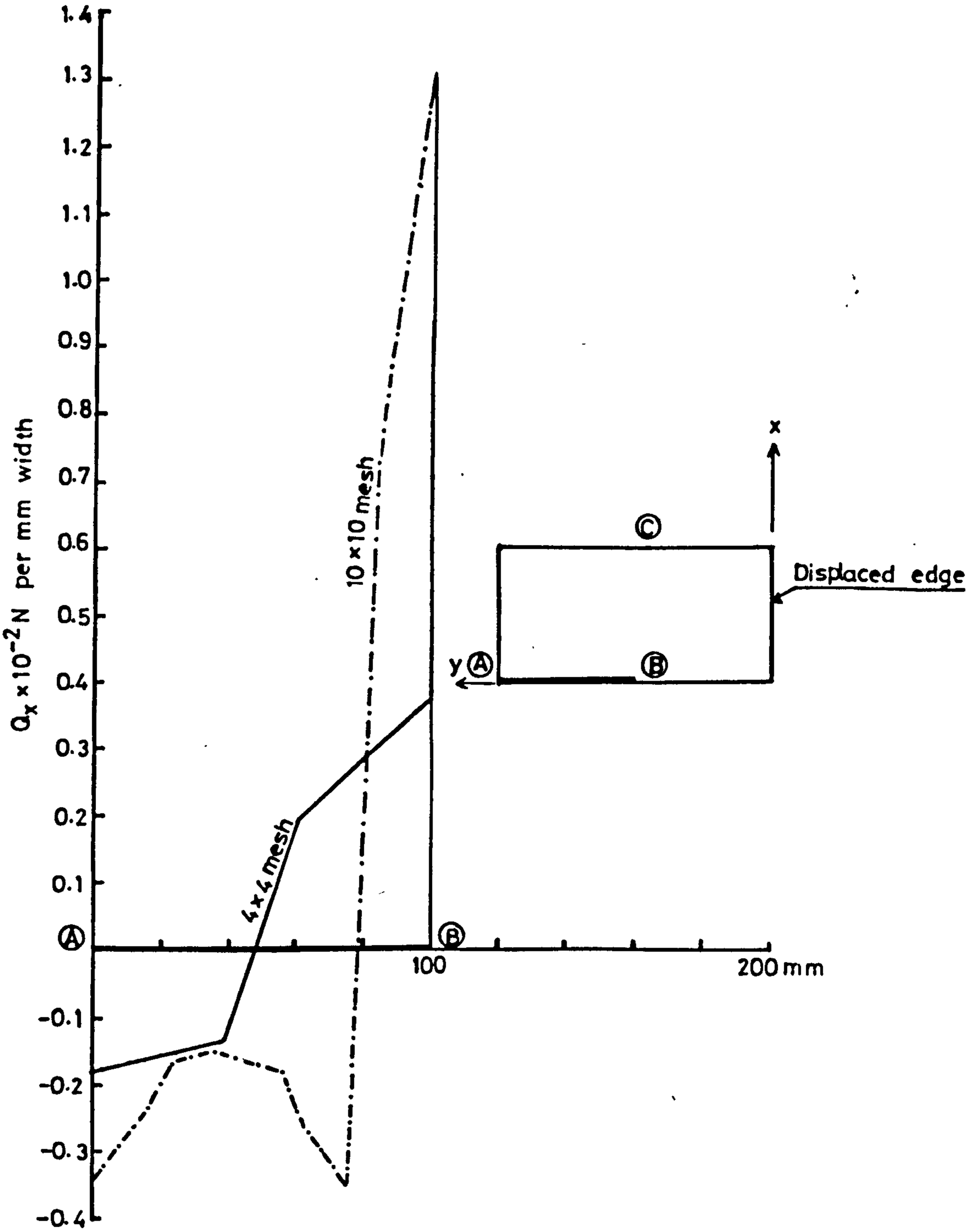

Figure (3.19) : Distribution of the shear, Q_x, along section AB.

with particular reference to the slab of a shear wall structure.

The curve showing the distribution of shear along transverse critical section BC, produced by Coull & Wong is shown in Figure (2.21) of chapter two. Comparing that with Figure (3.18) it can be observed that the curve produced by using fine mesh of (10 x 10) elements is similar to this one in many respects. The small differences are due to different boundary conditions, different loads, different mesh sizes and different nondimensional structural parameteric ratios. From this it can be concluded that the distribution of shear obtained from this programme is valid.

From Figure (3.18) it can be observed that the intensity of shears predicted by finite element in the slab at the tip of the wall is very high if 10 x 10 mesh is used. Since this very high intensity of shears is due to 'singularity of stresses', which in real structures does not exist, it was concluded that, when using this programme, use of mesh 4 x 4 should produce acceptable results regarding shears as well and therefore all the analysis presented in this thesis was performed by using this mesh size.

3.9 EFFECT OF SHEAR RETENTION FACTOR

In the beginning all the convergence study was carried out using a value of shear retention factor $\beta = 0.0$. However the effect of β was studied by analysing one of the models of main test series (MT7) using $\beta = 0.2, 0.4$ and 0.6. The model was analysed for combined loading and the boundary conditions used for this purpose are as shown in Figure (3.11). The gravity load was simulated by point loads, along the sides of slab (Figure (3.11))

and was applied during first five load increments. Wind load was simulated by the uniform displacement of centre line of corridor opening (line of contraflexure). For this purpose the elastic distribution producing a uniform edge displacement of .2mm was first obtained and then applied and incremented till failure. The behaviour of the model was studied in terms of wind load-displacement relationship and ultimate wind loads. Curves showing this relationship are presented in Figure (3.20). From this figure it can be observed that the curves obtained using β = .2, .4 and.6 are all coincident. However curve obtained using β = 0.0 showed slightly lower stiffness when the applied wind load was approaching the ultimate value. The effect on the ultimate load is not very much pronounced either. Thus it can be concluded that the effect of this factor for the case of combined loading of a slab connecting shear walls is negligible.

The effect of β on theoretically predicted load-displacement relationship and the ultimate load for the case of wind load alone, was investigated by analysing model (PT2) of preliminary test series, using β = .2 and .6. The load-displacement curves thus obtained are presented in Figure (3.21). It is apparent from this figure that the effect of using a finite value of β has some effect on theoretically predicted behaviour and the ultimate loads. It is interesting to note that the slab exhibited a slightly higher stiffness when β = .2 was used than that with β = .6. The maximum increase in the theoretically predicted ultimate load when β was changed from 0 to 0.2, was of the order of 10%.

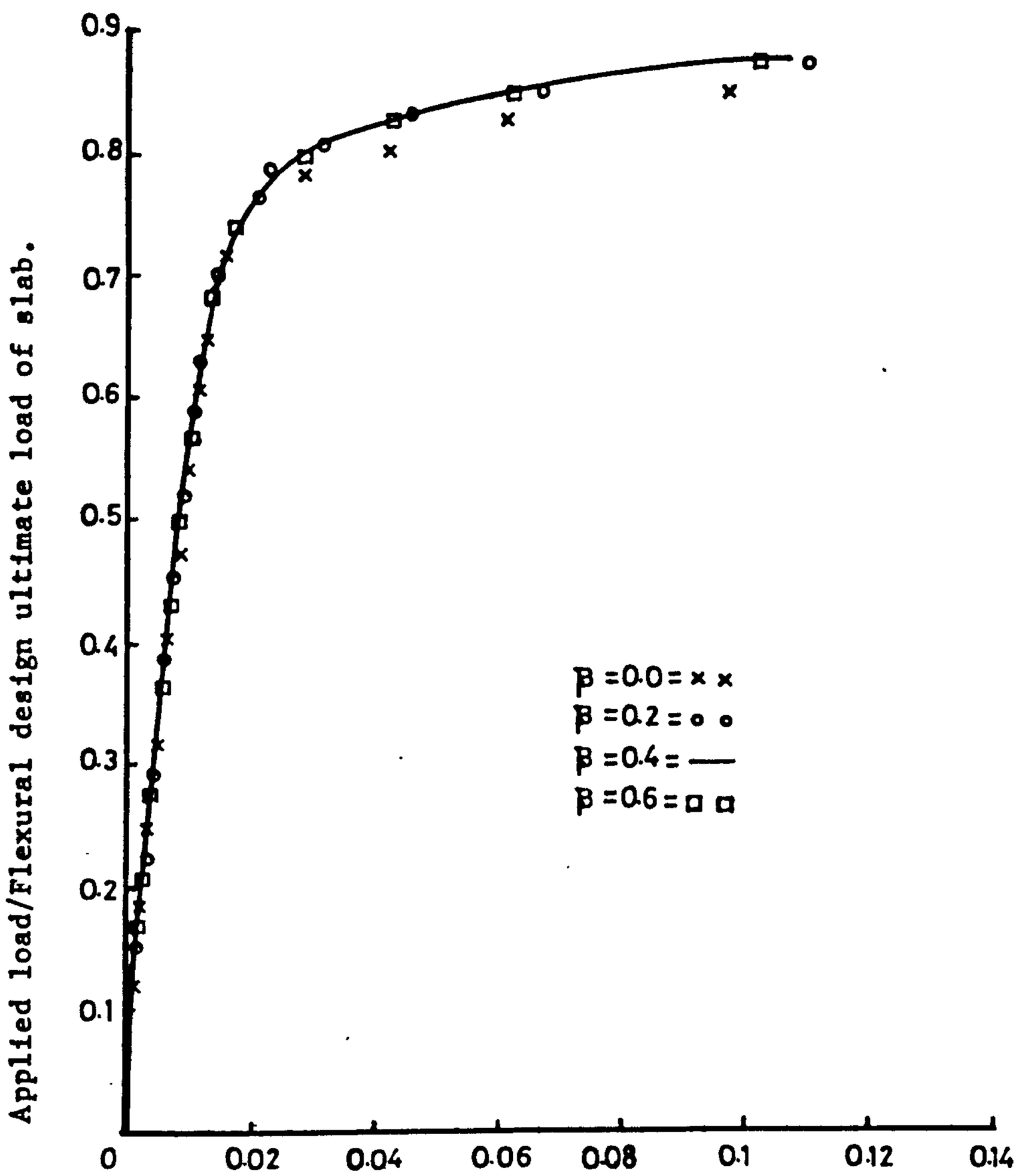

Figure (3.20) : Effect of shear retention factor on w.load-displacement behaviour (Model MT7)

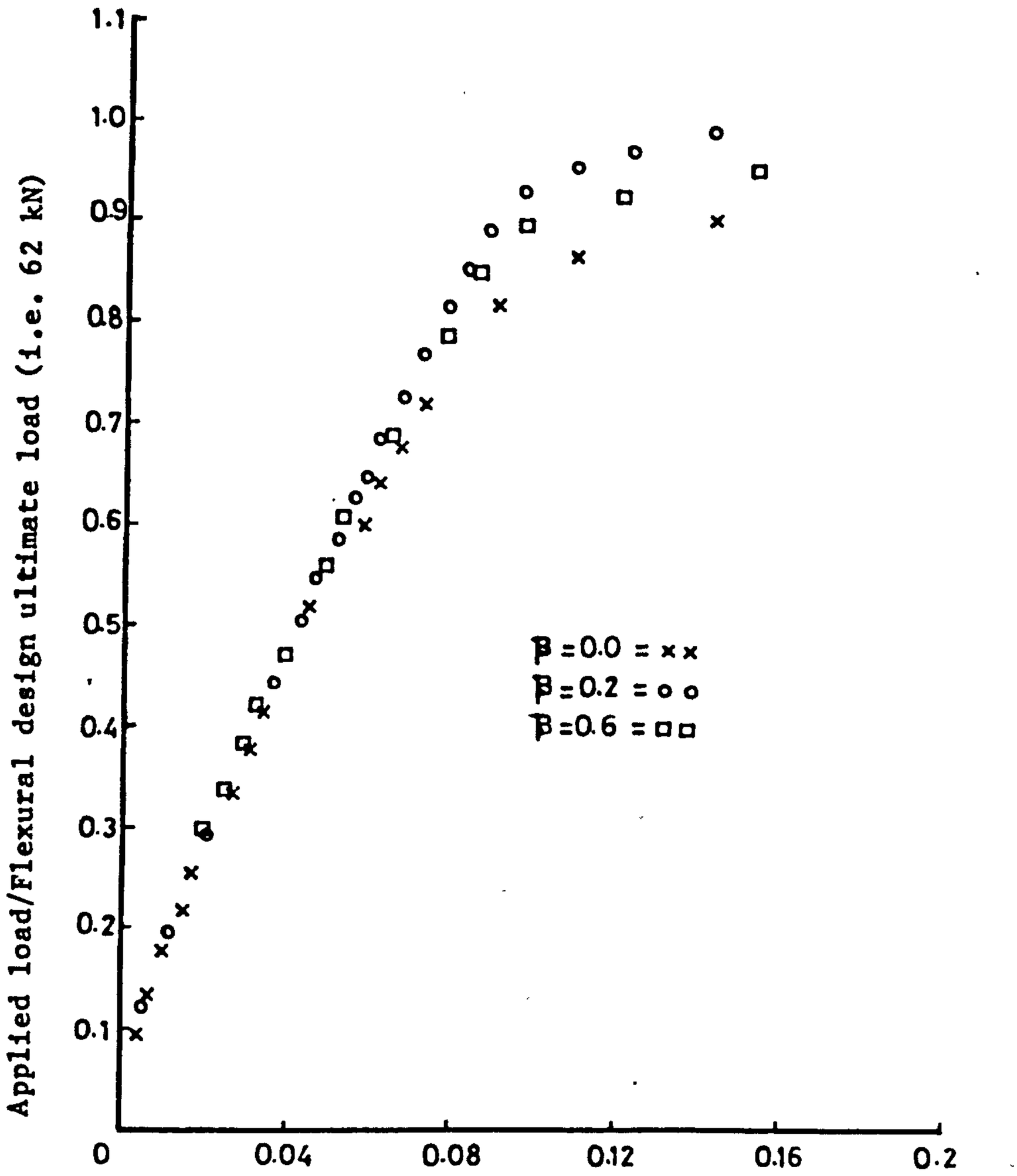

Figure (3.21) : Effect of shear retention factor on the w.load-displacement relationship (Model PT2).

CHAPTER FOUR

DESIGN OF SLABS

4.1 GENERAL

In order to obtain some idea of the range of percentage of flexural steel in the connecting slab of a shear wall structure, it was deemed best to analyse typical shear wall structures. The continuous connection method (Rosman method (1)) was chosen as being simple and accurate for the type of structures being analysed. A number of typical slabs connecting shear wall structures with dimensions shown in table (4.1) were analysed to find the forces (shears, moments) etc. induced in slab due to wind loading. The static equivalent wind loads used in the analysis correspond to the recommendations of CP3 (32). The flexural steel for these slabs was then designed for combined wind and gravity loading using 'Direct design method' (see section 4.4). The continuous connection method (1) of calculating the moments and shears due to wind loading in a connecting beam was described in chapter two. In the following sections the direct design method will be described first and then the design of the typical structures will be described.

4.2 DESIGN OF SLABS CONNECTING SHEAR WALLS

4.2.1 Introduction

The design of reinforced concrete slabs involves two operations viz. finding the distribution of stresses under the applied load and calculation of steel areas. The distribution of stresses depends upon several factors such as the shape of the slab, boundary conditions, the state of stress in the material and the constitutive material properties.

As discussed earlier in chapter two, the concept of effective width enables shear wall structure to be analysed as a two dimensional frame. However when it comes to the design of the slab, one needs detailed information on the distribution of moments (M_x, M_y, M_{xy}) throughout the slab. As an example Figure (4.1) shows the distribution of M_y at a typical section in a typical floor slab in a shear wall structure. These moments were caused by wind loading and their distribution was obtained by linear elastic finite element analysis. As can be seen from the figure, the intensity of moments varies continuously and this requires the rapid variation of steel ratio, which is impractical. It is more practicable to divide the slab into a number of strips and use average ratio of steel in each strip so that the ratio is constant within a strip but varies from strip to strip. Since in the design procedure followed in this thesis, elastic stress analysis is used exclusively, this is discussed in the following sub section.

4.2.2 Elastic analysis of plates

This approach is based on the following assumption:

(i) The material of the plate is homogeneous and linearly elastic.

(ii) The deflections are small compared to the thickness of the slab.

(iii) The thickness of plate is small in comparison with other dimensions.

(iv) The plane sections remain plane before and after bending.

(v) Shear deformations are negligible.

Classical plate theory is used to obtain the stress distribution. Usually the first order theory of bending is adopted. The method is derived from the considerations of equilibrium of forces and compatibility of deformations.

By considering the equilibrium of forces acting on the slab element in Figure (4.2), with sides dx and dy, the following equations can be obtained.

$$\frac{\partial Q_x}{\partial x} + \frac{\partial Q_y}{\partial y} + q = 0$$

$$\frac{\partial M_x}{\partial x} + \frac{\partial M_{yx}}{\partial y} - Q_x = 0 \qquad (4.1)$$

$$-\frac{\partial M_y}{\partial y} + \frac{\partial M_{xy}}{\partial x} + Q_y = 0$$

where Q_x and Q_y are shearing forces parallel to z-axis per unit length of sections of a plate perpendicular to x and y axis respectively.

q is the intensity of distributed load

M_x and M_y are the bending moments per unit length of sections of a plate perpendicular to x and y axis respectively.

M_{xy} is the twisting moment per unit length of section of a plate perpendicular to x-axis.

Eliminating Q_x and Q_y between the three equations, they can be combined in one equation of the form:

$$\frac{\partial^2 M_x}{\partial x^2} - 2\frac{\partial^2 M_{xy}}{\partial x dy} + \frac{\partial^2 M_y}{\partial y 2} = -q \qquad (4.2)$$

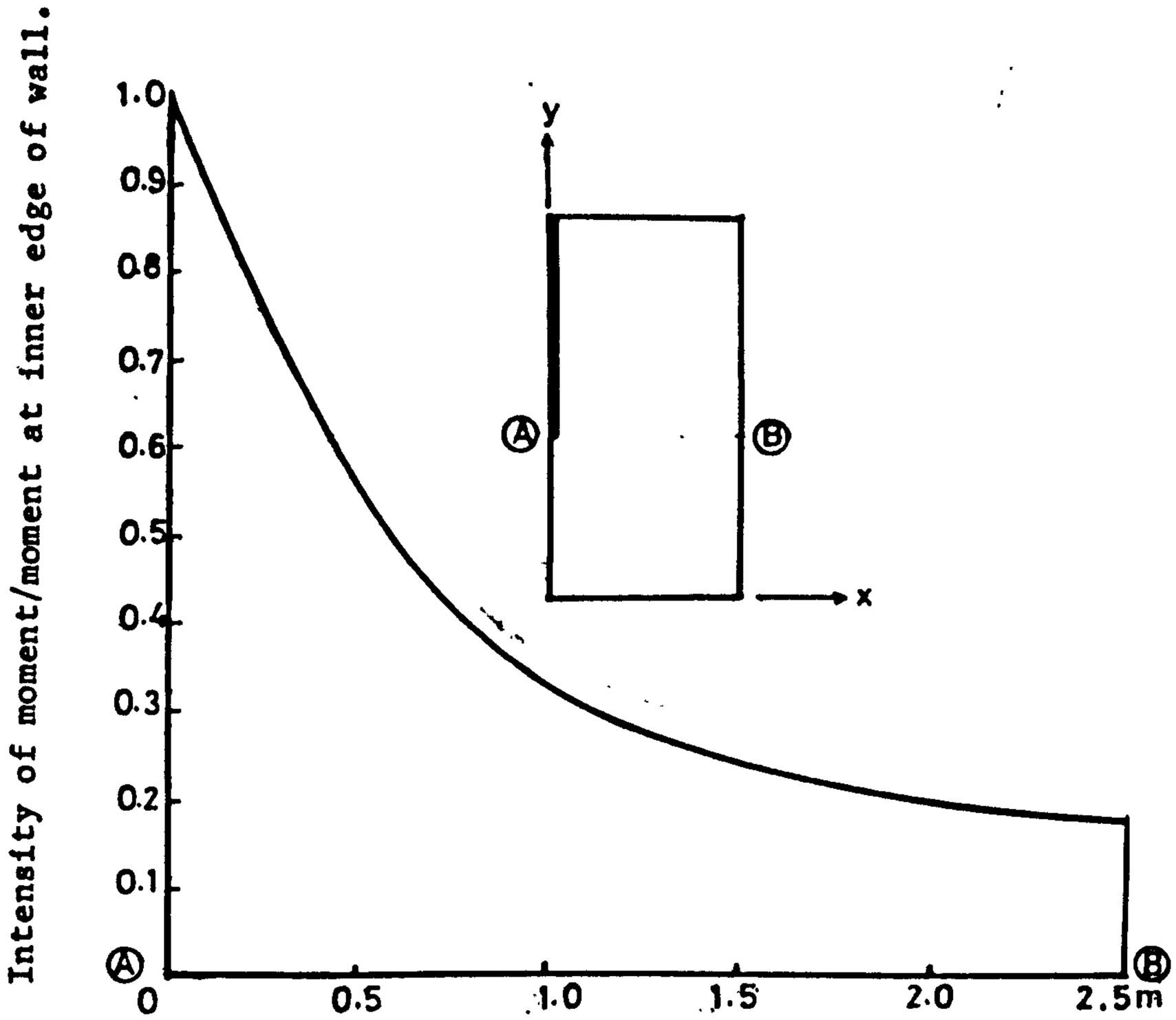

Figure (4.1) : Variation of elastic moment along transverse section AB corresponding to unit displacement (Typical structure 3).

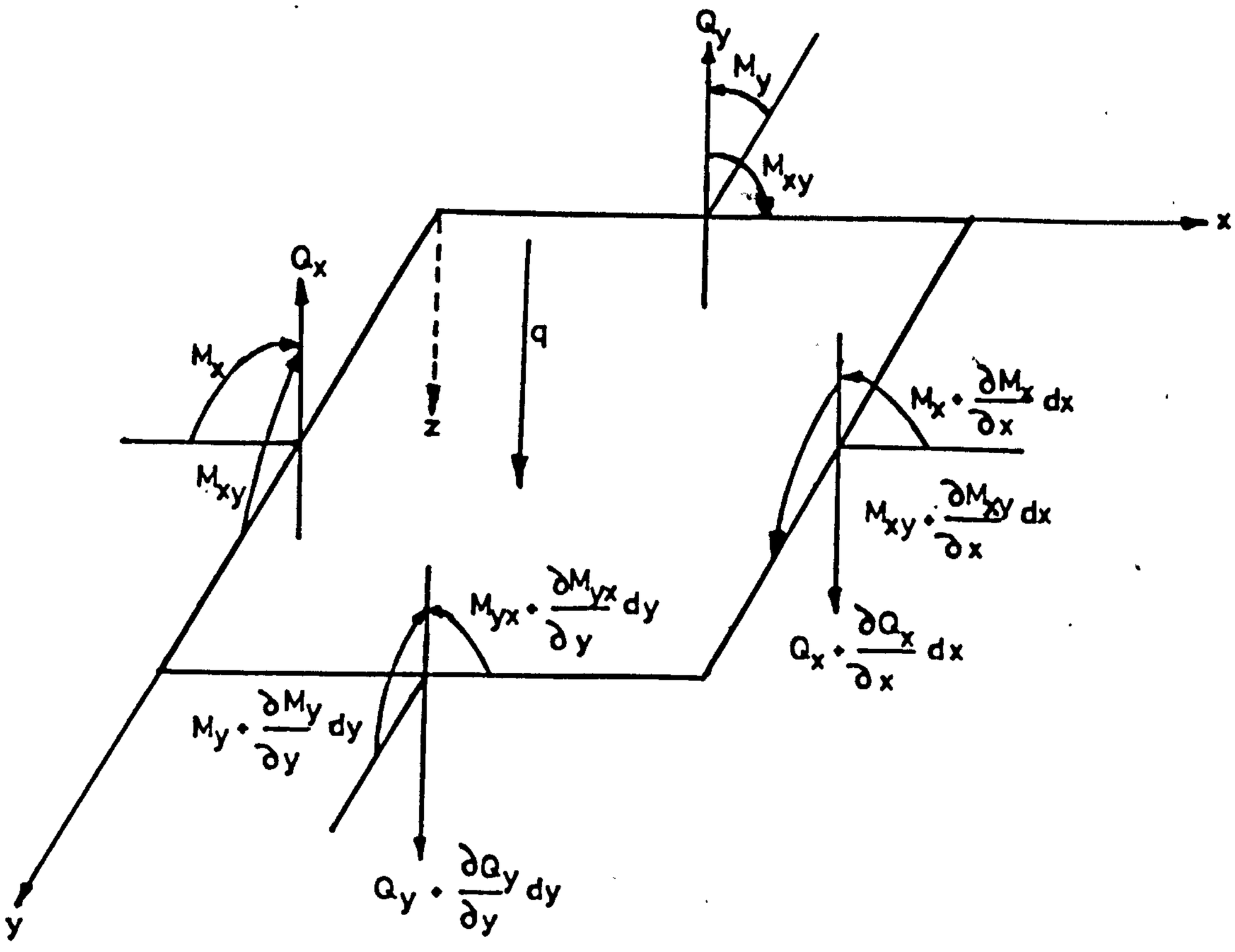

Figure (4.2) : Equilibrium of a slab element.

This equation is called plate equilibrium equation. This equation can be transformed to one in terms of lateral displacements, w, by relating the moments to the curvatures as:

$$M_x = -D\left(\frac{\partial^2 w}{\partial x^2} + \frac{\partial^2 w}{\partial y^2}\right)$$

$$M_y = -D\left(\frac{\partial^2 w}{\partial y^2} + \frac{\partial^2 w}{\partial x^2}\right) \qquad (4.3)$$

$$M_{xy} = D(1-\nu)\frac{\partial^2 w}{\partial x \partial y}$$

where $D = \frac{Eh^3}{12(1-\nu^2)}$

Here E = modulus of elasticity

h = overall thickness of slab

ν = Poisson's ratio

Using equation (4.3), equation (4.2) is transformed to

$$\frac{\partial^4 w}{\partial x^4} + 2\frac{\partial^4 w}{\partial x^2 \partial y^2} + \frac{\partial^4 w}{\partial y^4} = \frac{q}{D} \qquad (4.4)$$

The above equation is solved for given boundary conditions using the finite element method. The output from the analysis yields elastic "stresses" M_x, M_y and M_{xy} at any point in the structure.

4.2.3 "Requirements to be satisfied by the solution to the ultimate load" according to plasticity theory.

The classical theory of plasticity demands that at ultimate load the following requirements should be satisfied:

(i) The equilibrium condition :- The internal stresses must be in equilibrium with the externally applied loads.

(ii) The yield condition:- The internal stresses must not violate the yield criteria. It is generally believed that the normal moment along any line, Figure (4.3), should not exceed the corresponding moment of resistance.

(iii) The mechanism condition:- Under ultimate load sufficient plastic regions must exist to transform the structure into a mechanism.

If conditions (i) and (ii) are satisfied we get the lower bound solution. On the other hand if from an assumed collapse mechanism we calculate the collapse load using the principle of virtual work we get the upperbound solution.

4.3. THE YIELD CRITERIA

Consider the slab element in Figure (4.4) under the moment field M_x, M_y and M_{xy} with anisotropic properties. The sign convention adopted here is such that all moments acting on the element are positive. In order to derive the yield criterion in terms of three moment components, following simplifying assumptions can be made:

(i) The concrete is assumed to have zero tensile strength.

(ii) Bar diameters are small in comparison with the slab depth and they can carry stresses only in the original direction. Accordingly, kinking of bars across a yield line is not considered.

(iii) The slab element is lightly reinforced so that only ductile failures are allowed. This is necessary for moment redistribution, so that the slab moments can reach their ultimate strength at a/

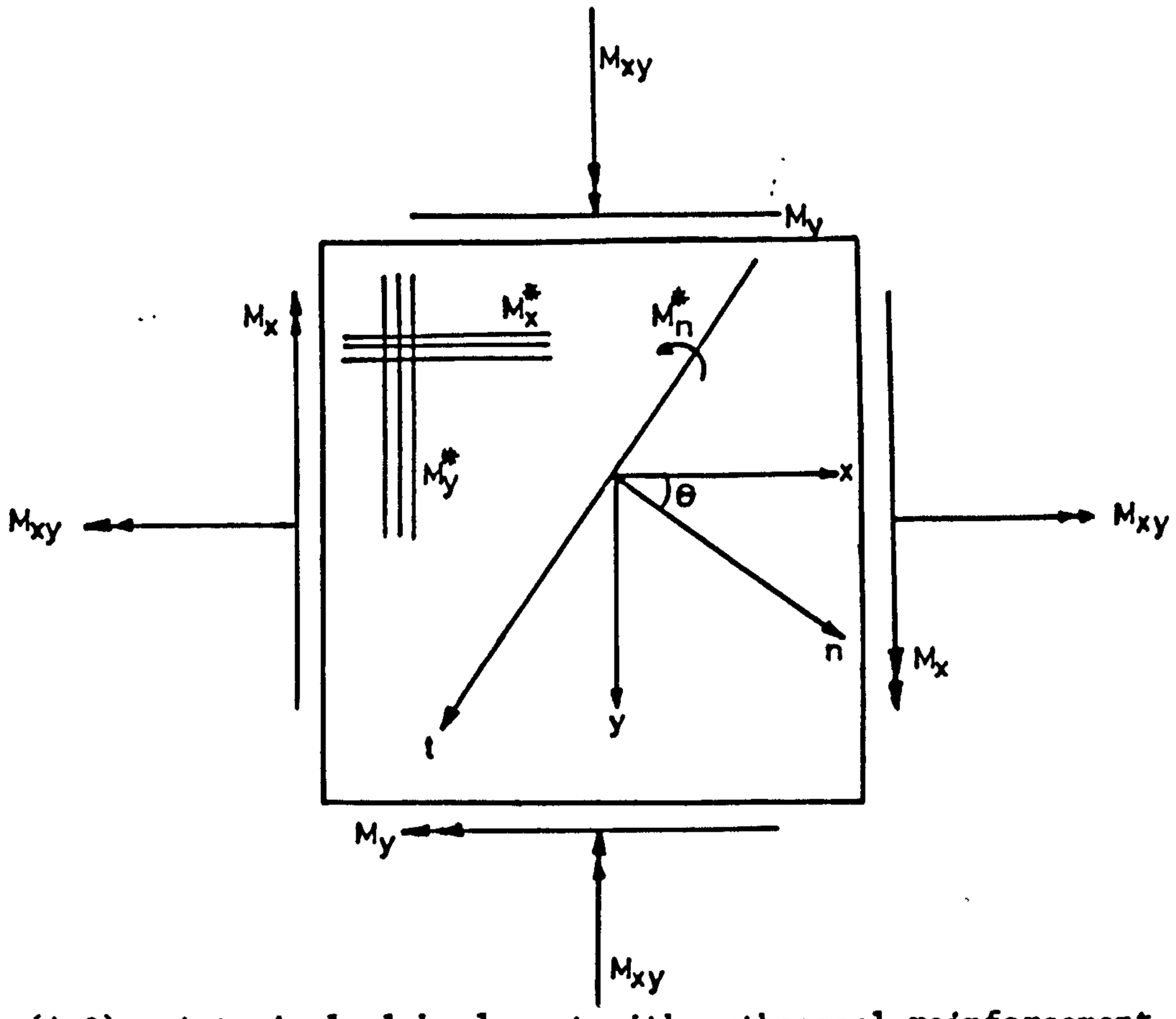

Figure (4.3) : A typical slab element with orthogonal reinforcement.

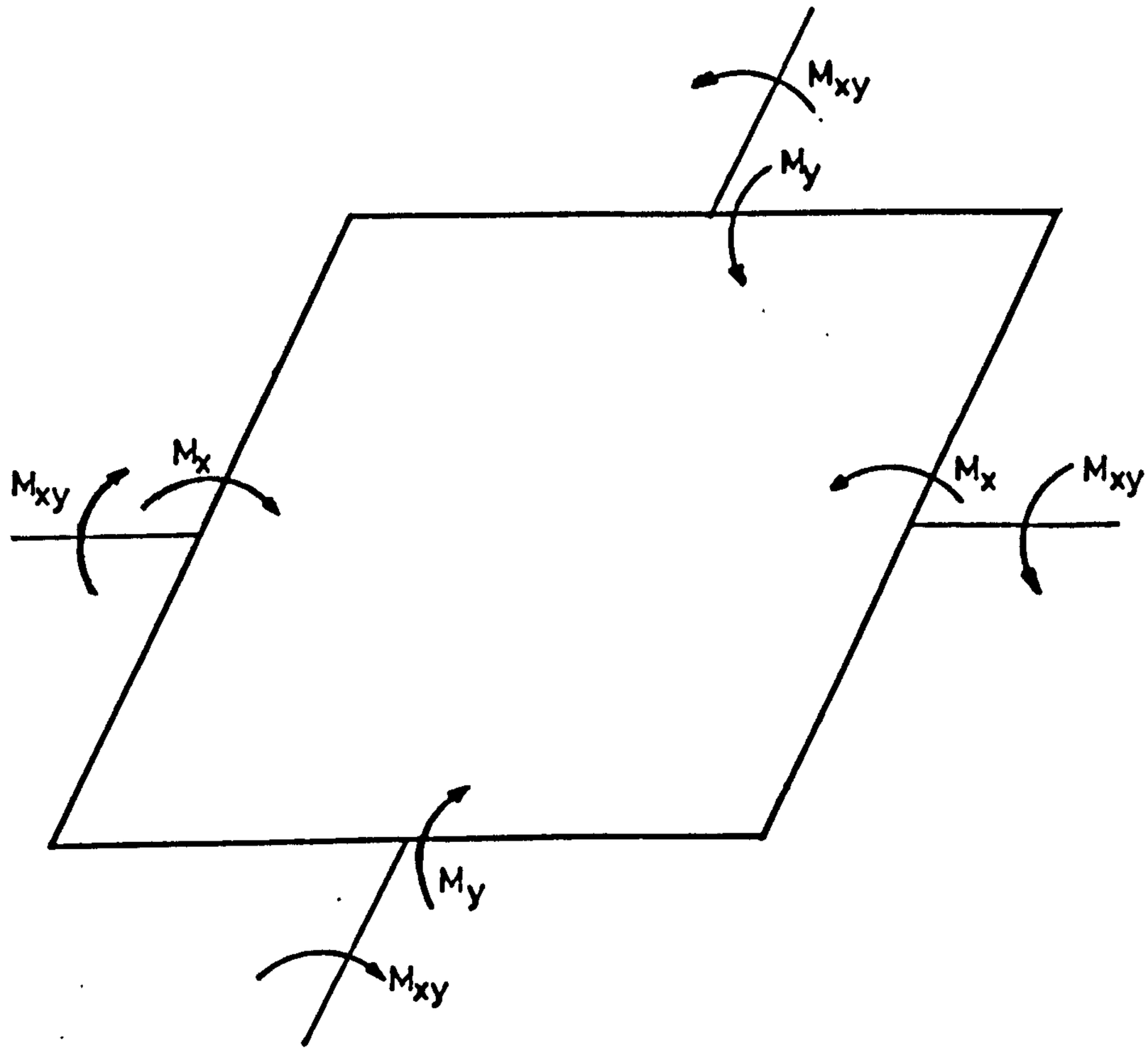

Figure (4.4) : A typical slab under moment field.

sufficient number of sections, to convert the slab into a mechanism.

(iv) Membrane forces do not exist. It is acknowledged that the co-existence of such forces with flexural moment fields on the slab elements, will considerably enhance or reduce the resisting moment of the slab element, depending on whether they are compressive or tensile, respectively.

For simplicity, the reinforcement in the element will be assumed to lie parallel to the element sides (Figure (4.3)). The element may be reinforced on the top and bottom faces.

If at any point in the slab element (Figure (4.3)), a line with a normal n and direction t is examined, then the normal moment M_n must not exceed the moment of resistance which the reinforcement in the slab could develop in direction n. This is therefore a normal moment criterion.

Taking the normal to the yield line at an angle θ to the x-axis and considering the equilibrium of the element shown in Figure (4.5), we have:

$$M_n = M_x \cos^2\theta + M_y \sin^2\theta - M_{xy} \sin 2\theta \qquad (4.5)$$

$$M_t = M_x \sin^2\theta + M_y \cos^2\theta + M_{xy} \sin 2\theta \qquad (4.6)$$

$$M_{nt} = (M_x - M_y)\frac{1}{2} \sin 2\theta + M_{xy} \cos 2\theta \qquad (4.7)$$

The normal moment M_n should be compared with the resisting moment M_n^*. In calculating M_n^* Johanson (33) assumed that:

(i) The yield line is divided into small steps parallel to, and at right angles to, the reinforcement as shown in Figure (4.6).

(ii) All the reinforcement crossing the yield line yield.

(iii) The normal moment of resistance is obtained by the addition of the individual effects when considering each band of reinforcement in turn.

(iv) When each band of reinforcement is considered on its own, on the small steps at right angles to the reinforcement there is only a normal moment per unit length.

(v) The yield line orientation does not generally coincide with the principal directions of either the applied or the resisting moments, except for isotropic reinforcement. Consequently, twisting moments do exist at the yield lines, but their existence do not reduce the flexural yield capacity due to interaction between flexural and torsional moments.

Thus referring to Figure (4.5), equation for resisting normal moments can be written as:

$$M_n^* = M_x^* \cos^2\theta + M_y \sin^2\theta \qquad (4.8)$$

where M_x^* = Moment of resistance in x-direction

M_y^* = Moment of resistance in y-direction

Equating it to the applied moments,

$$M_x^* \cos^2\theta + M_y^* \sin^2\theta = M_x \cos^2\theta + M_y \sin^2\theta + 2 M_{xy} \sin\theta \cos\theta \qquad (4.9)$$

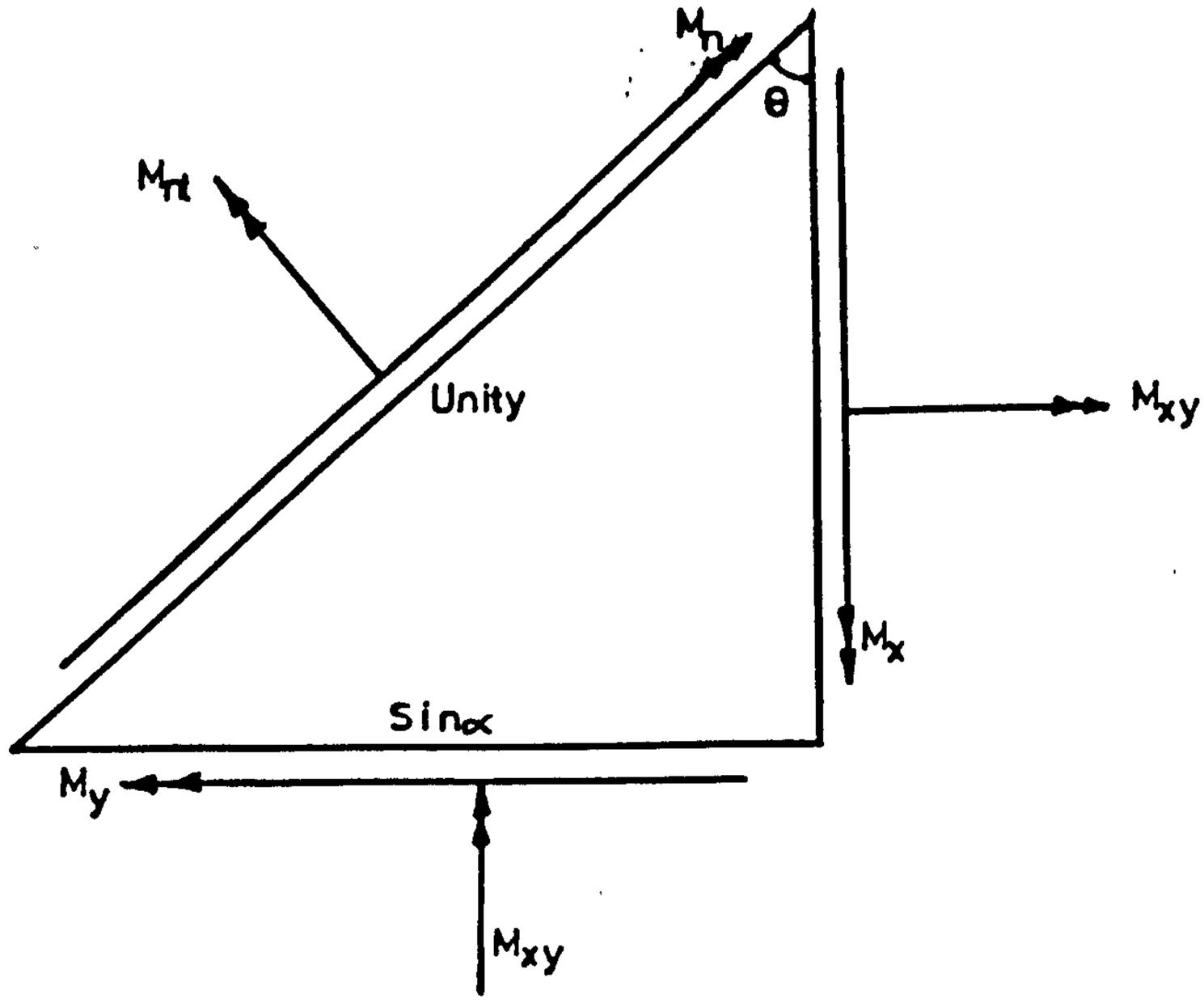

Figure (4.5) : Equilibrium of slab element under applied moment.

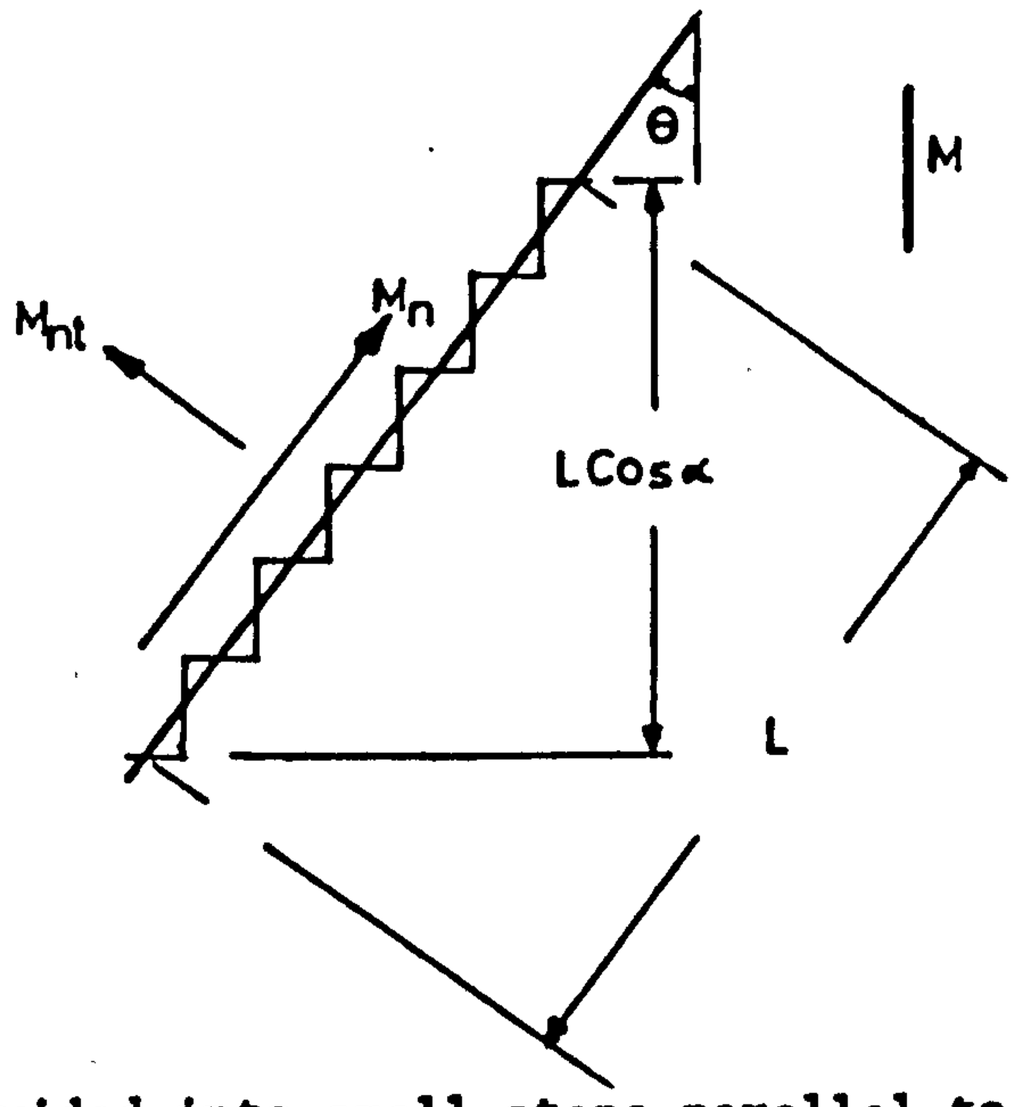

Figure (4.6) : Yield line divided into small steps parallel to and at right angles to, the reinforcement.

If $M_x^* = M_x + M_{xy} \tan \theta$ (4.10)

and $M_y^* = M_y + M_{xy} \cot \theta$ (4.11)

Then equation (4.9) takes the form:

$$(M_x^* - M_x)(M_y^* - M_y) = M^2_{xy} \quad (4.12)$$

This equation is the yield criterion for orthotropically reinforced concrete slabs.

4.4 DIRECT DESIGN METHOD

Unlike a steel structure, the strength of a concrete structure can be tailored to match the required resistance at each point (ideally) by providing just the necessary amount of steel reinforcement. This suggests a way of ultimate strength design of the reinforced concrete using elastic stress fields. This method is called 'direct design method'.

According to this method the elastic distribution of moments at ultimate load is determined usually by the finite element method. Using the moment triad (M_x, M_y, M_{xy}) thus obtained, the design moments are calculated so as to satisfy the yield criteria of equation (4.12), and then steel area is calculated to resist the corresponding ultimate design moments M_x^* and M_y^*.

The method satisfies the three conditions of plasticity i.e. equilibrium, yield criteria and mechanism conditions as follows:

(i) Equilibrium condition: Since the distribution of stresses is found using finite element method which is derived from equilibrium equations, this condition is automatically satisfied.

(ii) Yield condition: Having obtained M_x, M_y and M_{xy}, we have to derive M_x^* and M_y^* such that,

$(M_x^* - M_x)(M_y^* - M_y) - M_{xy}^2 = 0$, is satisfied.

This is easily done as follows:

If $M_x^* = 0$ (i.e. there is no steel in x-direction),

$$M_y^* = M_y + \left|\frac{M_{xy}^2}{M_x}\right| \tag{4.13}$$

If $M_y^* = 0$ (i.e. there is no steel in y-direction),

$$M_x^* = M_x + \left|\frac{M_{xy}^2}{M_y}\right| \tag{4.14}$$

If $M_x^* \neq 0$ and $M_y^* \neq 0$, then from equation 4.10 and 4.11

$$M_x^* + M_y^* = (M_x + M_y) + M_{xy}(\tan\theta + \operatorname{Cot}\theta) \tag{4.15}$$

where $\tan\theta$ is an undetermined parameter, the value of which from the consideration of minimum total amount of reinforcement is found to be 1.

Then $$M_x^* = M_x + |M_{xy}| \tag{4.16}$$

$$M_y^* = M_y + |M_{xy}| \tag{4.17}$$

(iii) The mechanism condition: Since the necessary resistance is made equal to the calculated stress at every point in the slab, it is anticipated that all slab parts will attain their ultimate strength under the design load. Accordingly, with minimum amount of redistribution, every point will yield at the design load, thus converting the slab into mechanism.

4.5 RULES FOR PLACING ORTHOGONAL REINFORCEMENT

Equations 4.13 to 4.17 can be expressed as "design rules" as follows:

(i) Bottom steel

(a) Compute the normal moments from:

$$M_x^* = M_x + |M_{xy}| \qquad (4.16)$$

$$\& \quad M_y^* = M_y + |M_{xy}| \qquad (4.17)$$

If $M_x^* < 0$, then

$$M_y^* = M_y + \left|\frac{M_x^2 y}{M_x}\right| \text{, with } M_x^* = 0 \qquad (4.13)$$

If $M_y^* < 0$, then

$$M_x^* = M_x + \left|\frac{M_x^2 y}{M_x}\right| \text{, with } M_y^* = 0 \qquad (4.14)$$

(b) If both equations (4.16) and (4.17) yield -ve sign no reinforcement is required.

(ii) Top steel

(a) Compute the normal moments from:

$$M_x^{*\prime} = M_x - |M_{xy}|$$

$$M_y^{*\prime} = M_y - |M_{xy}| \qquad (4.18)$$

If $M_x^{*\prime} > 0$, then

$$M_y^{*\prime} = M_y - \left|\frac{M_x^2 y}{M_x}\right| \text{, with } M_x^{*\prime} = 0 \qquad (4.19)$$

If $M_y^* > 0$, then

$$M_x^{*\prime} = M_x - \left|\frac{M_{xy}^2}{M_y}\right| \text{, with } M_y^{*\prime} = 0 \qquad (4.20)$$

(b) If equations (4.19) and (4.20) yield a positive sign no reinforcement is required.

Figures (4.7) to (4.9) give a detailed picture of these rules. For general use, the variables are sketched in a nondimensional form. After establishing a point ($\frac{M_x}{|M_{xy}|}$, $\frac{M_y}{|M_{xy}|}$) on the diagram, we can easily know which equation to use to get the required design normal moments. Bottom steel equations are given in Figure (4.7), while those for top steel in Figure (4.8).

Figure (4.9) shows the diagrams 4.7 to 4.8 superimposed and indicates the directions of the steel to be provided at any point. Primed moments refer to top steel.

The quations in this section were derived by Wood (34) and on a similar basis were extended by Armer (35) to cover skew direction of steel.

4.6 DESIGN OF TYPICAL SHEAR WALL STRUCTURES

4.6.1 General

As had already been said, some typical shear wall - slab structures were designed to find the practical range of:

(i) The forces acting on such structures.

(ii) Magnitude and distribution of stresses induced in the most highly stressed slabs due to combined action of wind and gravity loads and,

(iii) The percentage of flexrual reinforcement.

In all eight structures were designed as described below.

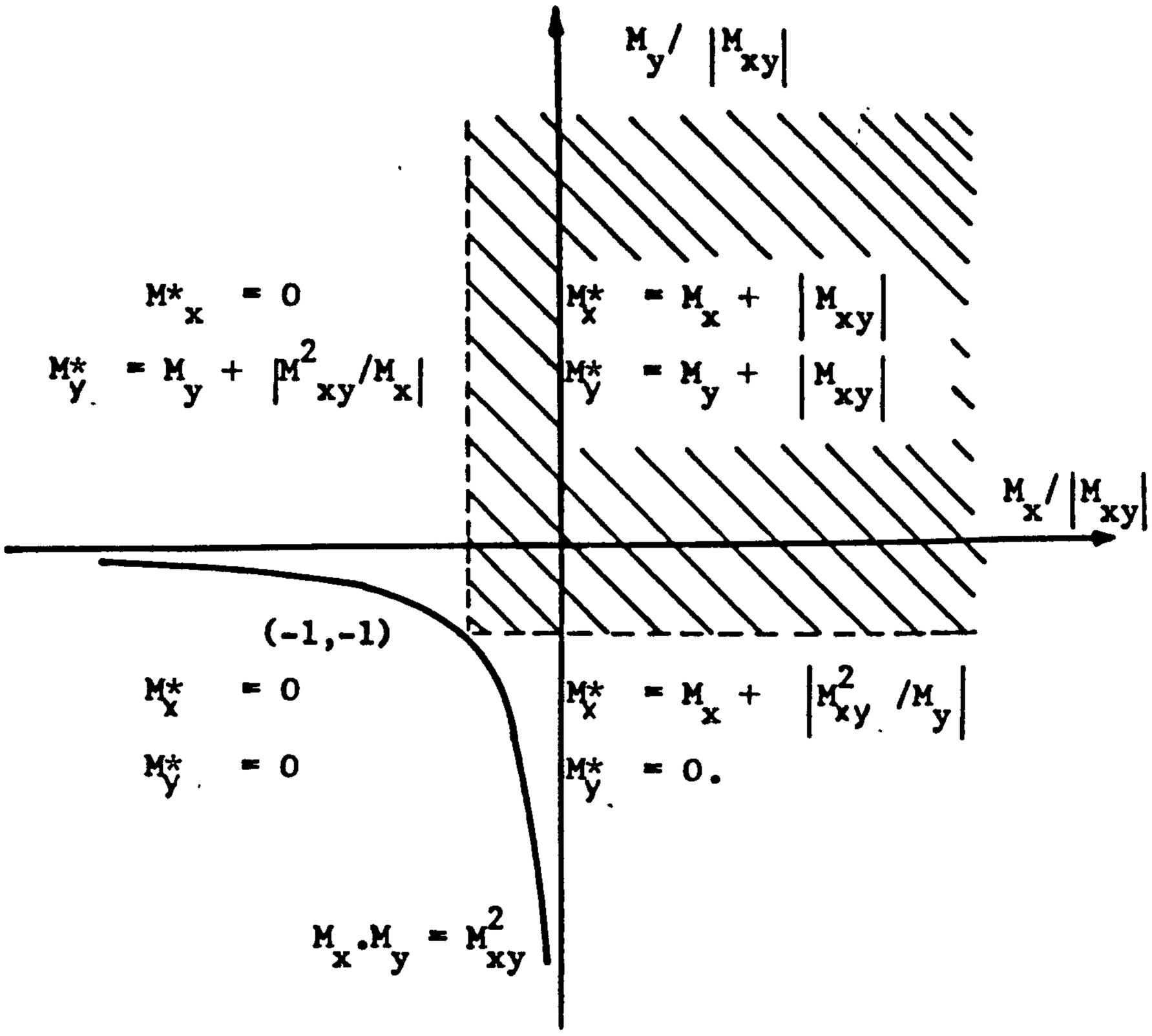

Figure (4.7) : Design Equations for Bottom Steel.

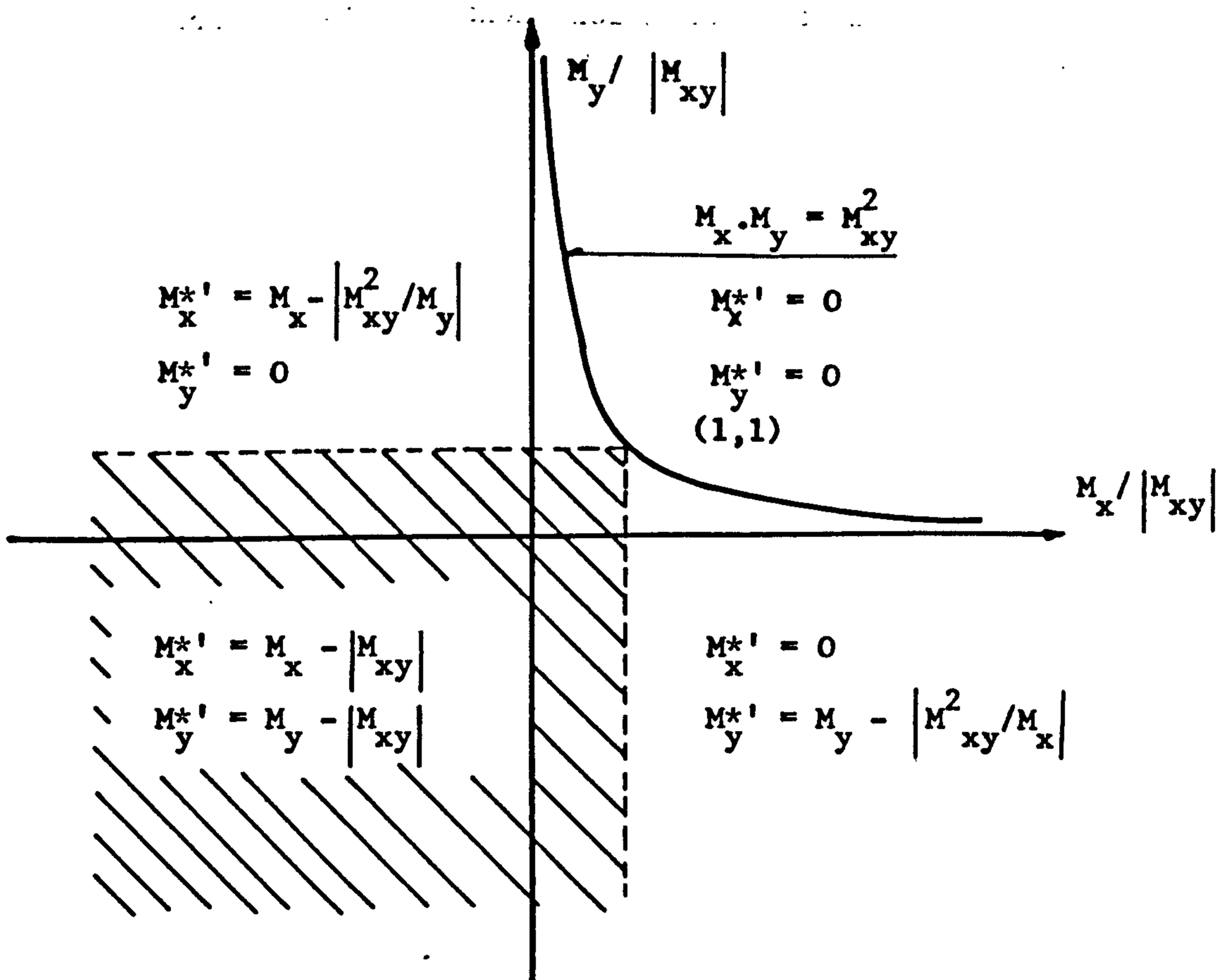

Figure (4.8): Design Equations for top Steel

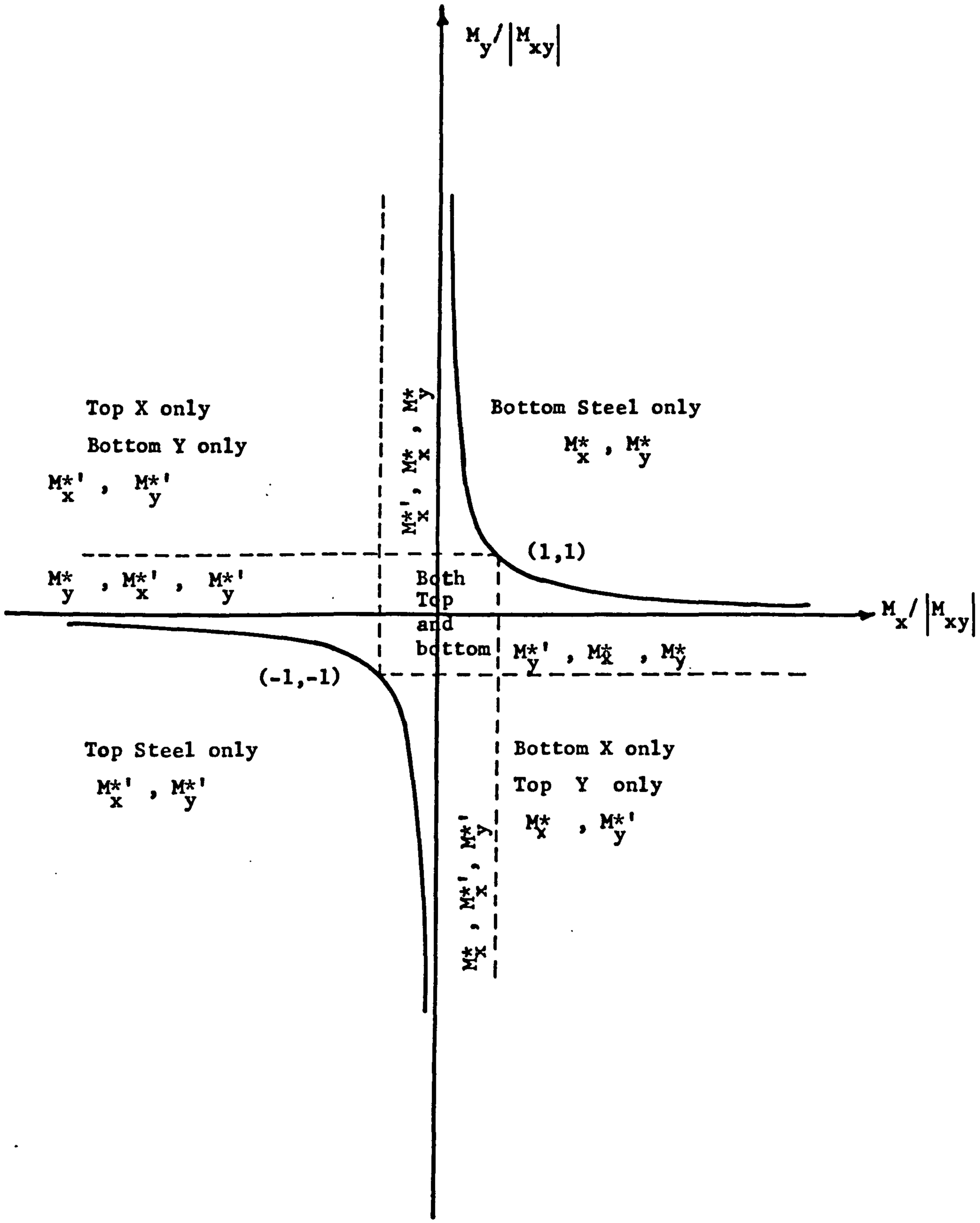

Figure(4.9): Reinforcement required for a given Moment Triad

4.6.2 Dimensions of typical structures

The shear wall-slab structure system is particularly efficient in resisting horizontal forces when the height of the building is more than 15-20 storeys. Therefore all the typical structures were analysed as 25 storeys high buildings except one which was only 15 storeys high.

Commonly encountered architectural layouts of apartment buildings lead to bay sizes of 6-10 metres and widths of buildings between 9 to 24 m. Floor to floor heights seldomnexceed 3m. Therefore the dimensions of the sample structures were so chosen as to cover this practical range. The plan of these structures is shown in Figure (4.10) while the dimensions are given in table (4.1). A slab thickness of 230 mm and a floor to floor height of 3 m was adopted for all the buildings.

4.6.3 Material properties for typical structures

The material properties were assumed as follows:-

Concrete

Compressive strength = 30 N/mm^2

Modulus of elasticity,E = 21 kN/mm^2

Poisson's ratio, ν = 0.15

Steel

Yield stress , f_y = 460 N/mm^2

Modulus of elasticity,E = 210 kN/mm2

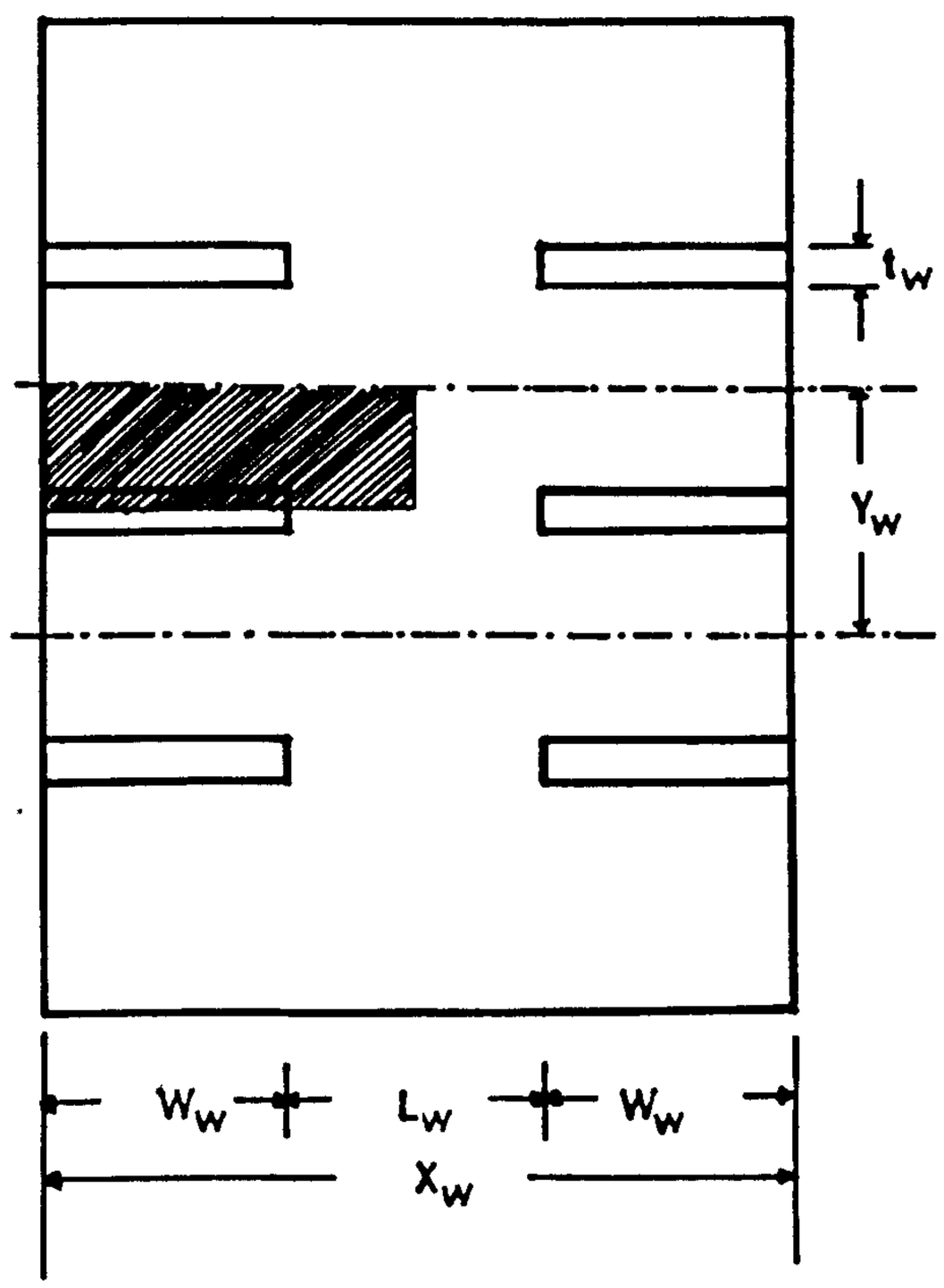

Figure (4.10) : Plan of a typical structure.

Table 4.1 : Dimensions of typical structures.

Structure No.	Corridor opening width L_w m	Bay width Y_w m	Wall width W_w m	Wall thickness t_w m	Overall width of Building X_w m	Height H m	αH
Structure 1	2	6	4	.3	10	75	8.534
Structure 2	3	6	5	.3	13	75	5.102
Structure 3	3	5	4	.3	11	75	5.947
Structure 4	3	3	4	.3	11	75	5.947
Structure 5	3	4	4	.3	11	45	3.285
Structure 6	3	8	5	.3	13	75	5.05
Structure 7	3	10	5	.3	13	75	4.85
Structure 8	3	12	5	.3	13	75	5.095

4.6.4 Loading

It was assumed that the buildings were to be erected in Glasgow area with maximum basic wind speed of 51 m/seconds. As regards gravity loading, all the slabs were designed for a characteristic live load of 1.5 kN/m^2 in addition to self weight, in accordance with the recommendations of CP3 (36) assuming that the buildings were to be used for residential purposes. As recommended by CP 110(44) the following combination of loads was adopted as design loading, for which the slabs were to be designed.

Design load = (1.2 x wind load + 1.2 live load + 1.2 x Dead load).

4.6.5 Procedure adopted for analysis and design of typical structures

From the basic wind speed, the equivalent static wind loading as recommended by CP3 (32) is calculated. Assuming the wind pressure to be constant with height, the maximum shear V_w and moment M_w induced in most highly stressed slab along critical section were calculated. The effective width, as obtained from the curves Figure (2.13) produced by Coull & Wong (5) was used in the calculations. The value of effective width for these structures ranged between .53 to.25 Y_w. In order to find the moment distribution due to wind loading in the slabs of different structures within elastic range, a portion of slab shown shaded in Figure (4.10) was analysed for each structure, using a finite element programme for theelastic analysis of plates. A typical mesh with boundary conditions used for this analysis is shown in Figure (4.11). The wind loading was simulated by the uniform displacement of the line of contraflexure (central line of corridor opening), A uniform displacement of unity was imposed and the total M_y induced along the critical section (Section AB, /

Figure (4.11)) obtained. The total moment acting along this section due to wind loading, M_w was then divided by 2 M_y to find the factor by which all the moments in different regions of the slab were multiplied to find the actual distribution of moments due to applied wind loading. The slabs were reanalysed for gravity loading with a different set of boundary conditions as shown in Figure (4.11). Stresses were calculated at the centre of each element and they were taken as representative values for the element as a whole.

Since wind may blow from any direction, for each region of a slab the moment triad (M_x, M_y and M_{xy}) for combined wind and gravity loading was obtained from $M_{gravity} \pm M_{wind}$, for top and bottom of the slab, with appropriate sign for each region, and then the design moments were found from the moment triads using Wood & Armer method (section 4.5). Flexural steel required to resist these design moments at ultimate conditions were calculated in the following manner:

Referring to Figure (4.12), for equilibrium.

$$C_b = T_b$$

$$\therefore \frac{2}{3} f_{cu} \cdot d_n \cdot b = A_s \cdot f_y$$

$$\therefore d_n = \frac{3}{2} \frac{f_y}{f_{cu}} \frac{A_s}{bd} d$$

$$= \frac{3}{2} \frac{f_y}{f_{cu}} d \phi$$

where $\phi = A_s/bd$

$$\therefore M_r = A_s \cdot f_y \cdot la = A_s \cdot f_y \left(d - \frac{d_n}{2}\right)$$

$$\therefore M_r = \phi b d f_y \left(d - \frac{3}{4} \frac{f_y}{f_{cu}} d \phi\right)$$

$$= \phi b d^2 f_y \left(1 - .75 \frac{f_y}{f_{cu}} \phi\right)$$

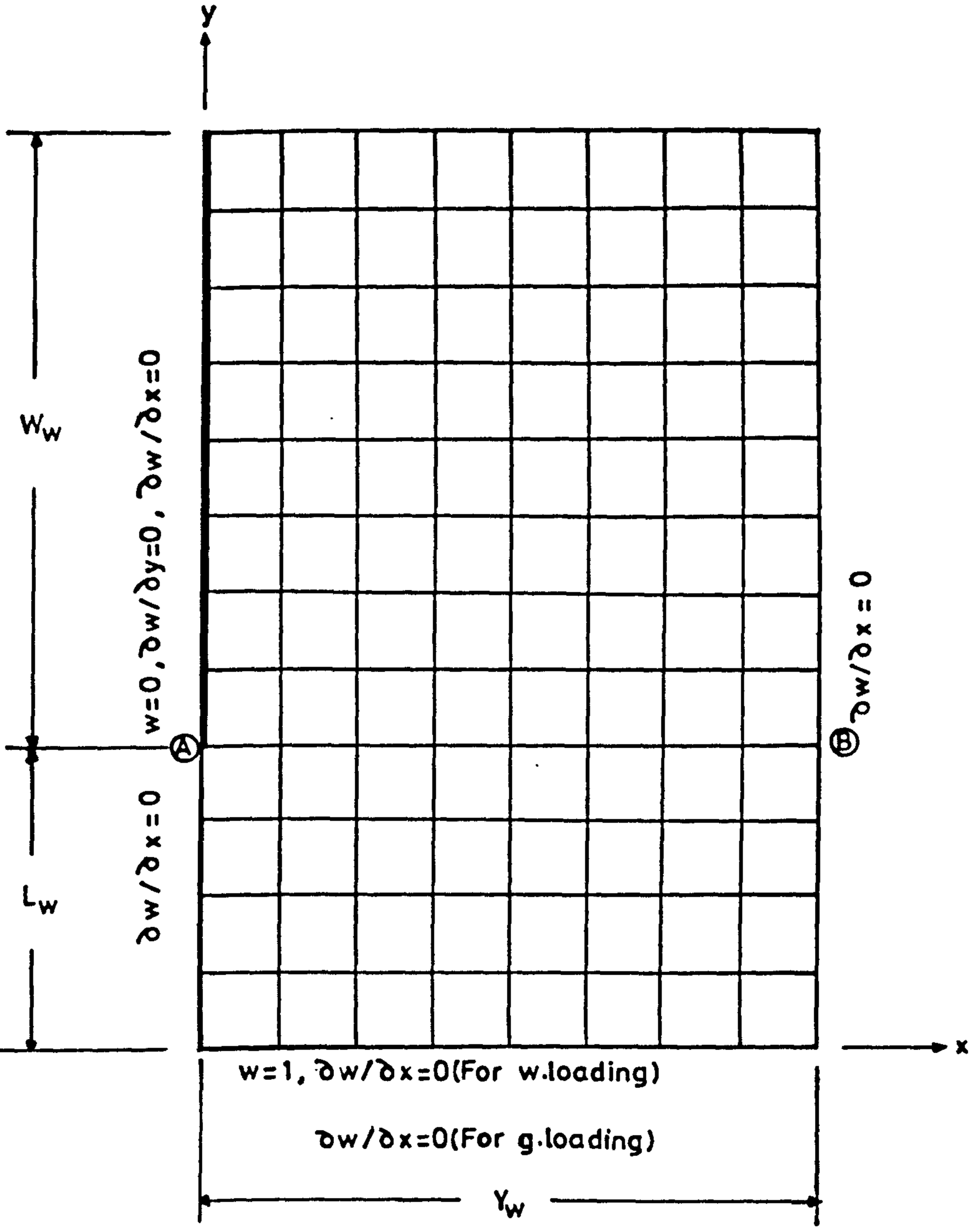

Figure (4.11) : Typical mesh with boundary conditions, used for the analysis of typical structures.

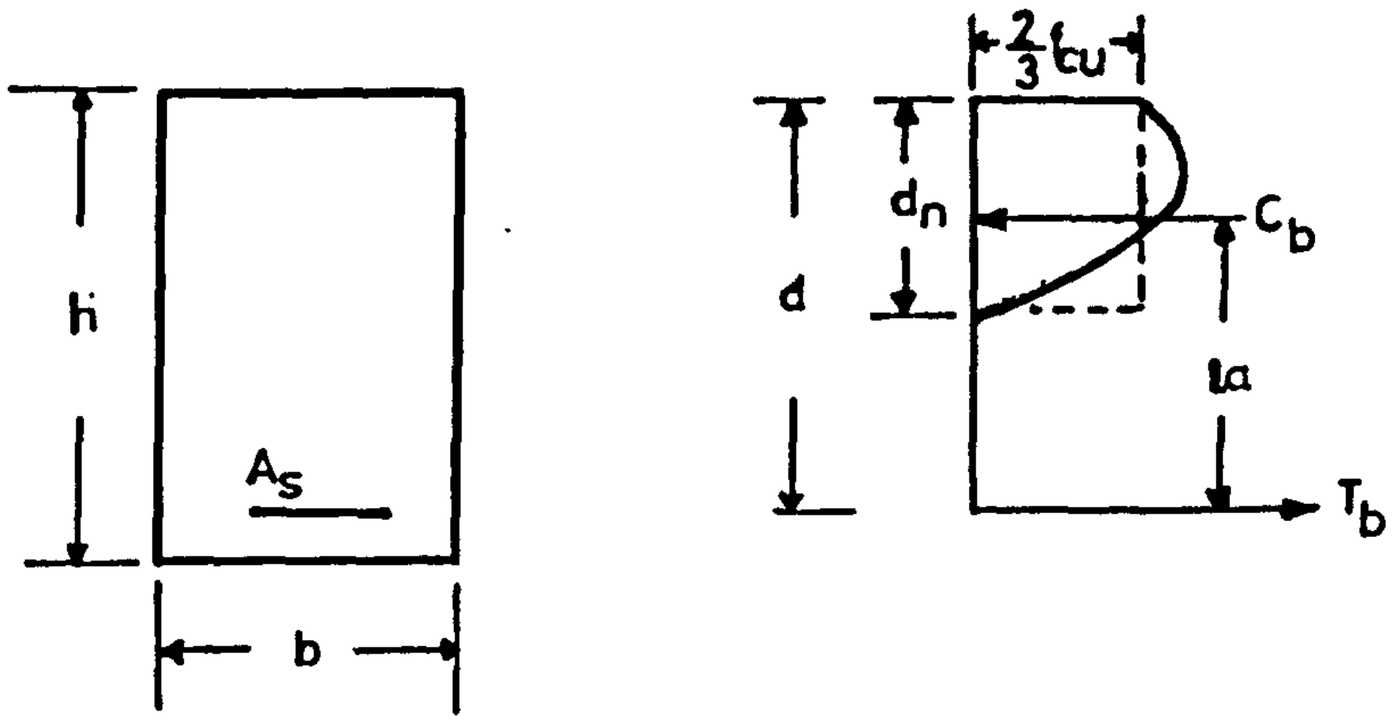

Figure (4.12) : Singly reinforced concrete section when flexural strength is reached.

Rearranging,

$$\therefore \left(.75 \frac{f_y}{f_{cu}}\right) \phi^2 - \phi + \left(\frac{M_r}{bd^2 f_y}\right) = 0$$

$$\therefore \phi = \left(1 - \sqrt{1 - \frac{3M_r}{bd^2 f_{cu}}}\right) / 1.5 \frac{f_y}{f_{cu}}$$

$$\therefore A_s = \phi\, bd = \frac{f_{cu}\, b\, d}{1.5\, f_y} \left[1 - \sqrt{\left(1 - \frac{3M_r}{bd^2 f_{cu}}\right)}\right] \qquad (4.24)$$

The variation of the final ratio of the steel in y-direction at the top of the most highly stressed slab, along critical section AB is shown in Figure (4.13) and that in x-direction along AC in Figure (4.14). Table (4.2) shows the forces obtained and the corresponding maximum value of steel percentage for the structures analysed. From this table it can be observed that a flexural steel ratio as high as 1.76% may be required in the main direction.

In order to get some idea about the resistance of the wall-slab junctions against the induced moment and shear due to wind loads, the strength of connection in each case was calculated using

(i) CP 110 and ACI formulae for the design of slab-column connections (ii) Chang recommendations(9) (iii) Schwaighofer & Collins (8) recommendations and (iv) Coull & Wong (10) recommendations. The strengths of connection thus obtained are shown in table (4.3). Referring to this table it can be observed that the methods predict wide variation in the strength of the connection for the same structure. This clearly shows that a systematic study of the problem is necessary to find the most suitable method for the prediction of the strength of the wall-slab connection of a shear wall structure subjected to wind loading in addition to gravity loading.

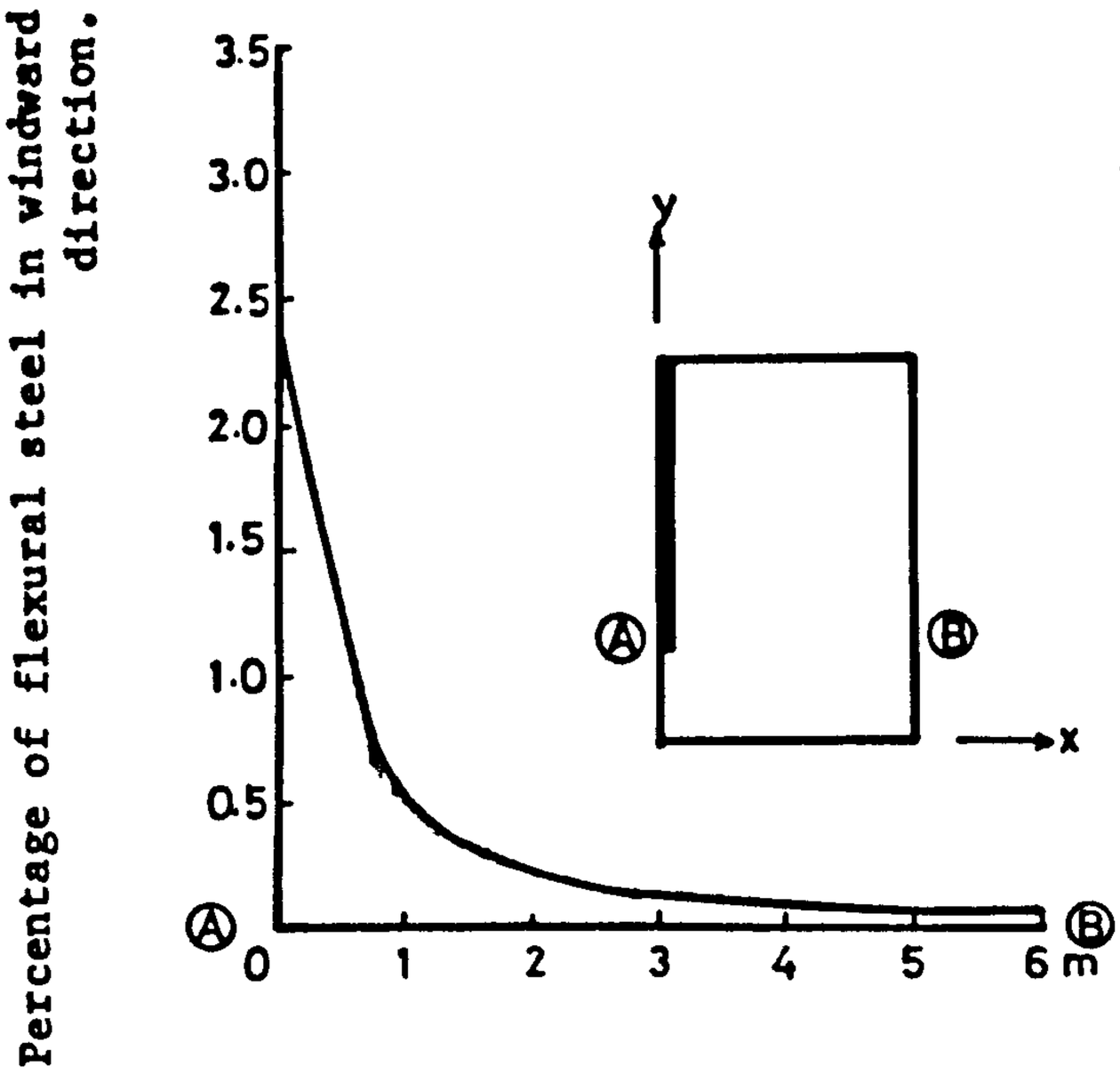

Figure (4.13) : Variation of flexural steel in windward direction along critical section AB, in the slab of a typical structure.

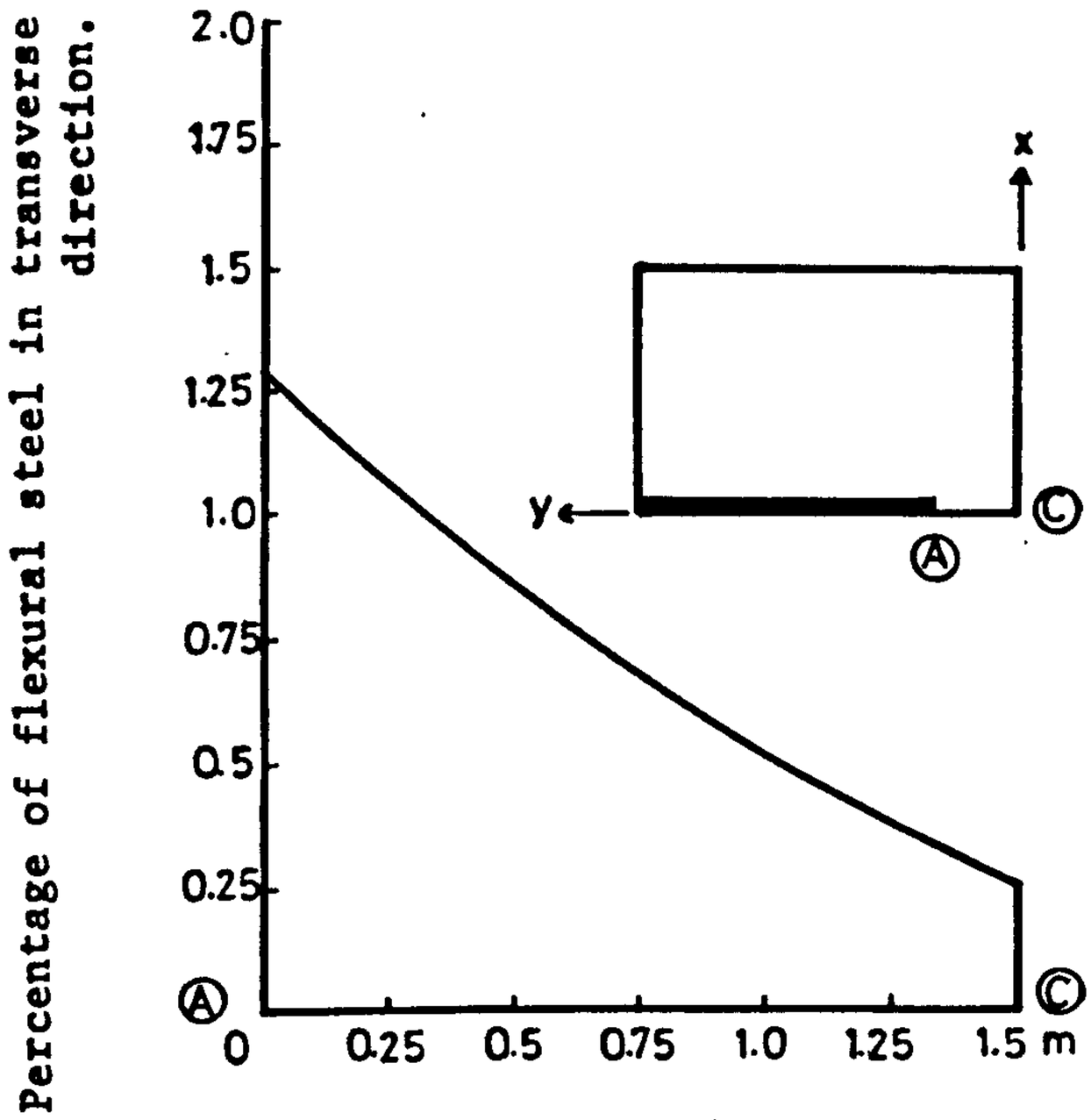

Figure (4.14) : Variation of flexural steel in transverse direction along section AC.

Table 4.2 Maximum ratio of flexural steel required in the slabs of typical structures.

Structure No.	Wind Shear kN	Moment due to wind kN-M	Maximum Ratio of steel in y-direction %	Maximum Ratio of steel in x-direction %
Str. 1	260.4	260.4	.97	.58
Str. 2	152.5	228.8	.78	.48
Str. 3	162.0	243.0	.84	.46
Str. 4	123.8	185.7	.73	.41
Str. 5	52.8	79.0	.33	.21
Str. 6	201.3	302.0	1.04	.69
Str. 7	243.8	365.7	1.29	.94
Str. 8	303.4	455.1	1.76	1.25

Table 4.3 : Strength of wall-slab connections of typical structures calculated using different methods.

Structure No.	Calculated strength of the connection					
	CP110 without transfer of moment kN	CP110 with transfer of moment kN	ACI method kN	Chang method kN	Schwaighofer & Collin's method kN	Coull & Wong method kN
Structure 1	976.5	316.7	1725.8	401.7	538	148
Structure 2	1184.6	462.3	2599.6	485.4	538	126
Structure 3	976.5	350.5	1725.8	485.4	538	126
Structure 4	976.5	350.5	1725.8	443.8	538	114.85
Structure 5	976.5	350.6	1725.8	443.8	538	114.85
Structure 6	1184	462.3	2249.3	443.8	538	126.2
S tructure 7	1184.6	462.3	2666	485.4	538	204.4
Structure 8	1184.6	462.3	2509.6	485.4	538	164

4.7 DETERMINATION OF DESIGN MOMENTS IN A CONNECTING SLAB

It has already been mentioned that though the finite element method is not an integral part of the 'direct ultimate load design method' but it is probably the most suitable method for finding the elastic distribution of moments especially in the connecting slabs of a shear wall structure subjected to lateral loads. However in most cases, to assist the designer, design charts can be easily prepared for the rapid determination of the design moments M_x^* and M_y^* due to lateral load, in the connecting slabs. For this purpose, depending upon the intensity of M_x^*, the slab is divided in four different regions R_{xc}, R_{x1}, R_{x2} and R_{x3} as shown in Figure (4.15). Similarly depending upon the intensity of M_y^*, again the slab has been divided in four regions i.e. R_{yc}, R_{y1}, R_{y2} and R_{y3} as shown in Figure (4.16). Corresponding to each region there are graphs presented in Figures (4.17) to (4.22). showing the design moments K^*_{yc}, K^*_{y1}, K^*_{y2}, K^*_{y3}, K^*_{xc}, K^*_{x1}, K^*_{x2}, K^*_{x3}, induced in that particular region as percentage of the total moment M_w due to lateral load, acting along the transverse critical section passing through the inner edge of wall, for different non-dimensional structural parameteric ratios. From the analysis it was observed that the distribution of moment in the corridor opening portion of slab was unaffected by the structural parameteric ratio W_w/L_w. Therefore curves for this region are produced only for different values of L_{w/Y_w} (i.e. L_{w/Y_w} = 1. , .75, .5 and .25). However due to the rapid variation of moments in the corridor opening portion, there is separate curve showing design moments M_y^* in each strip of width 0.1 Y_w in the region R_{yc}(Figures (4.17) and (4.18)). Similarly there is a separate curve showing design/

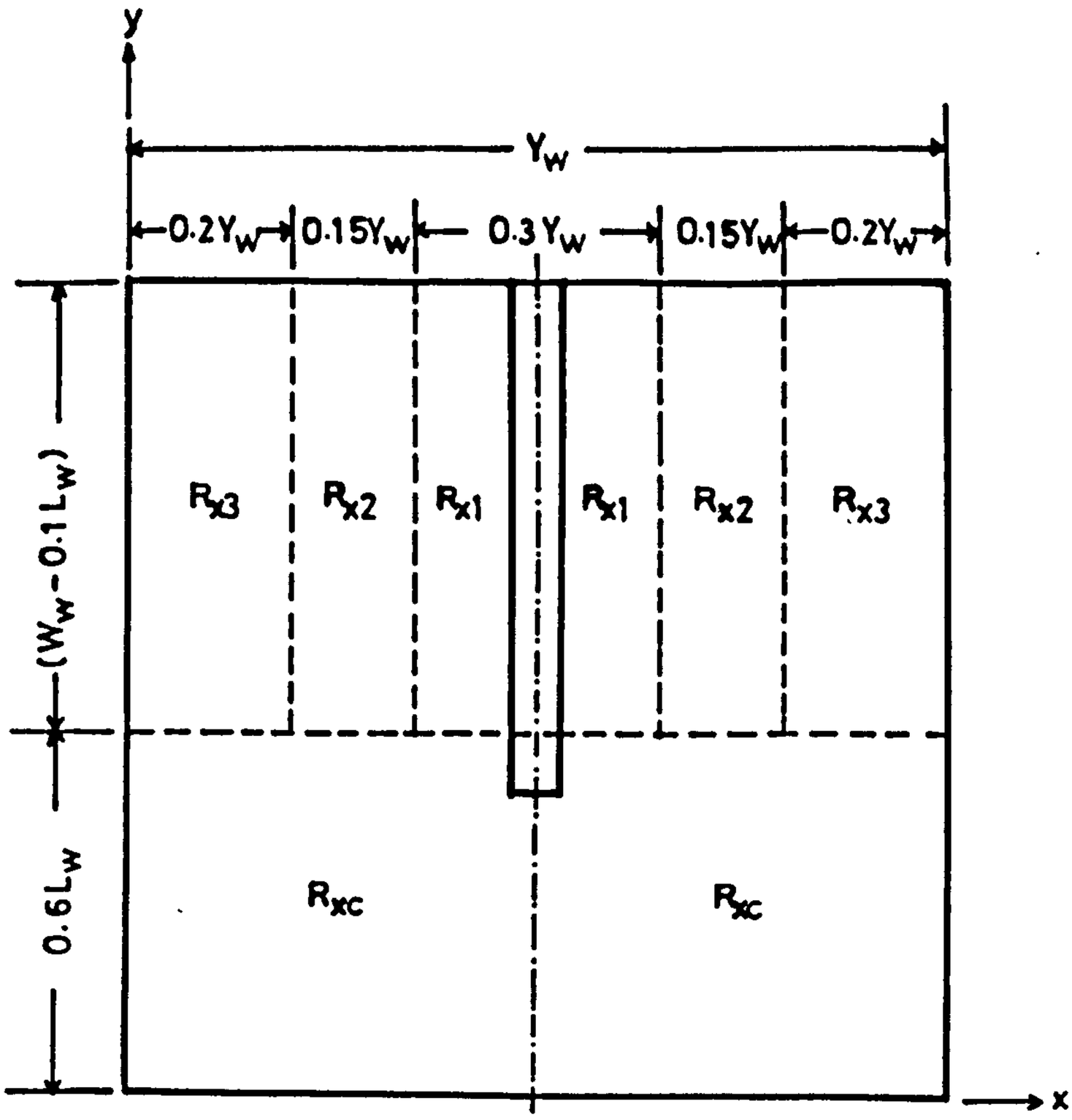

Figure (4.15) : Connecting slab of a shear wall structure divided into strips depending upon the intensity of moment M_x^* (due to lateral load).

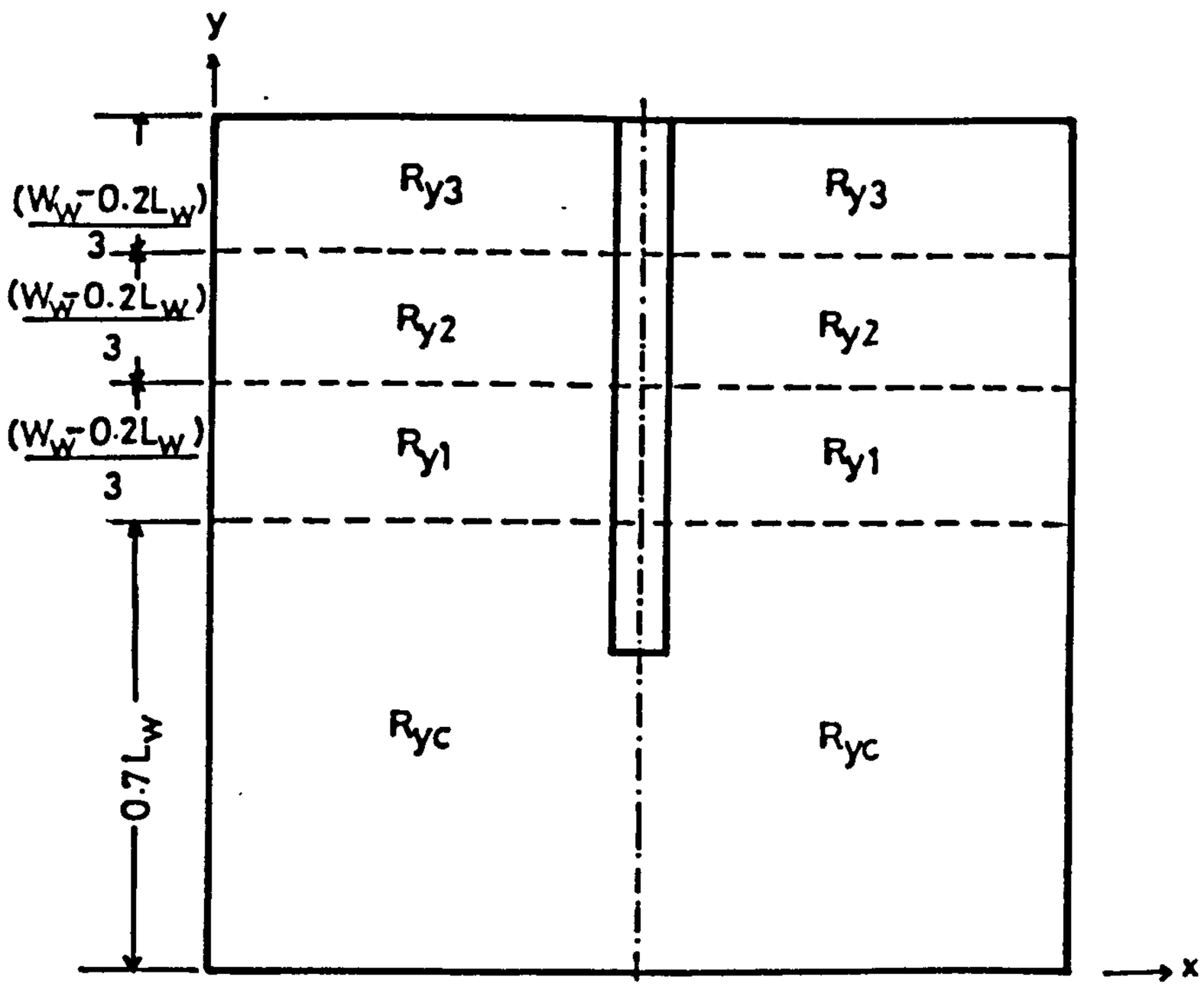

Figure (4.16) : Connecting slab of a shear wall structure divided into strips depending upon the intensity of moment M_y^* (due to lateral load).

moment M_x^* in each strip of width 0.1 L_w in the region R_{xc} (Figures (4.20) and (4.21)). Since the distribution of moments in the regions R_{y1}, R_{y2}, R_{y3}, R_{x1}, R_{x2} and R_{x3} is affected by the structural parameteric ratio W_{w/L_w} as well there are separate curves for values of $\frac{W_w}{L_w}$ = 0.8, 1.2, 1.6 and 2.0 for these regions (Figures (4.19) and (4.22)).

From the analysis it was also observed that torsional moment M_{xy} affected considerably the design moments M_x^* and M_y^* in some regions. Since wind may blow from any direction it is recommended that steel for moments be provided both, at top and bottom of the slab.

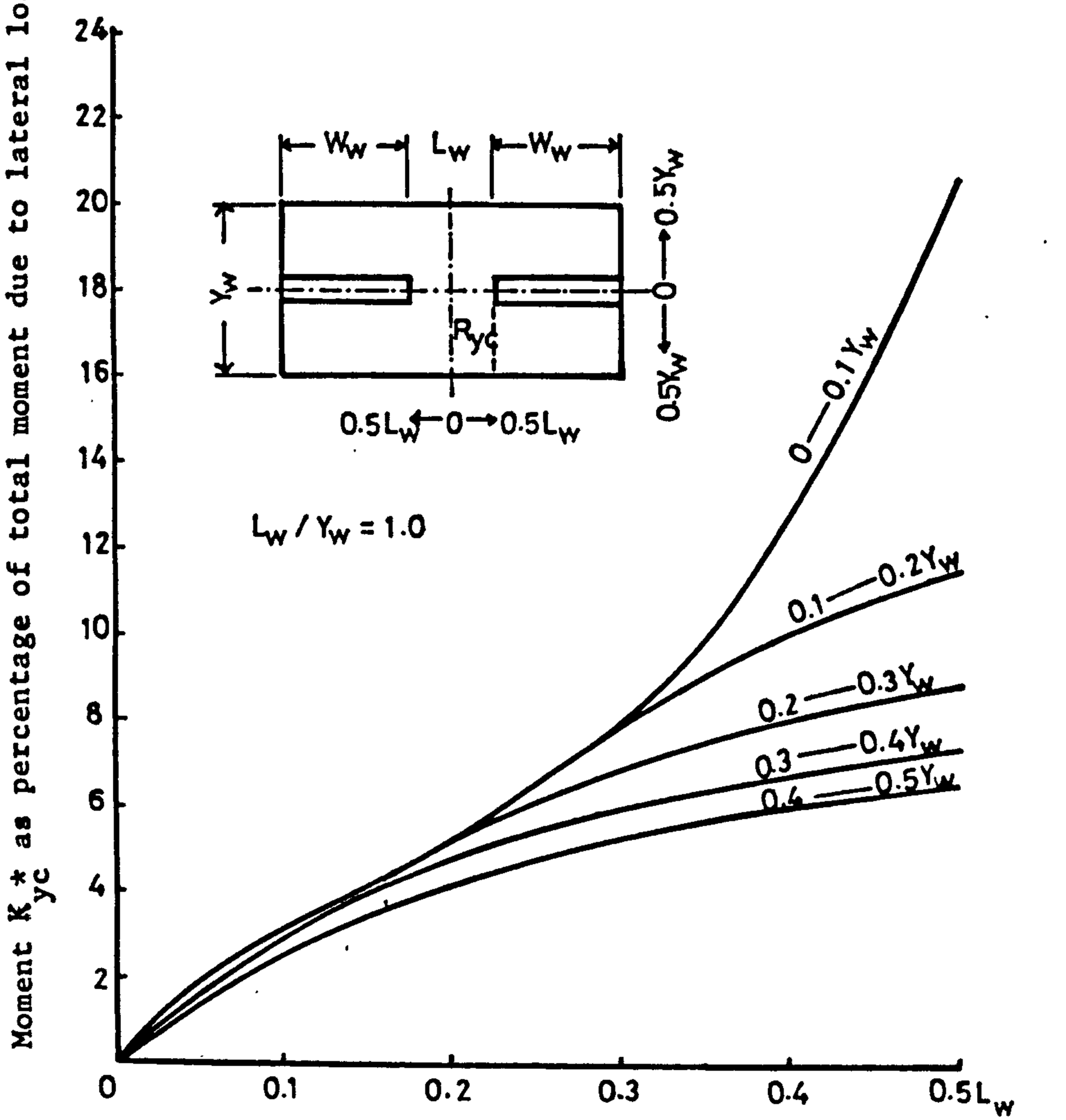

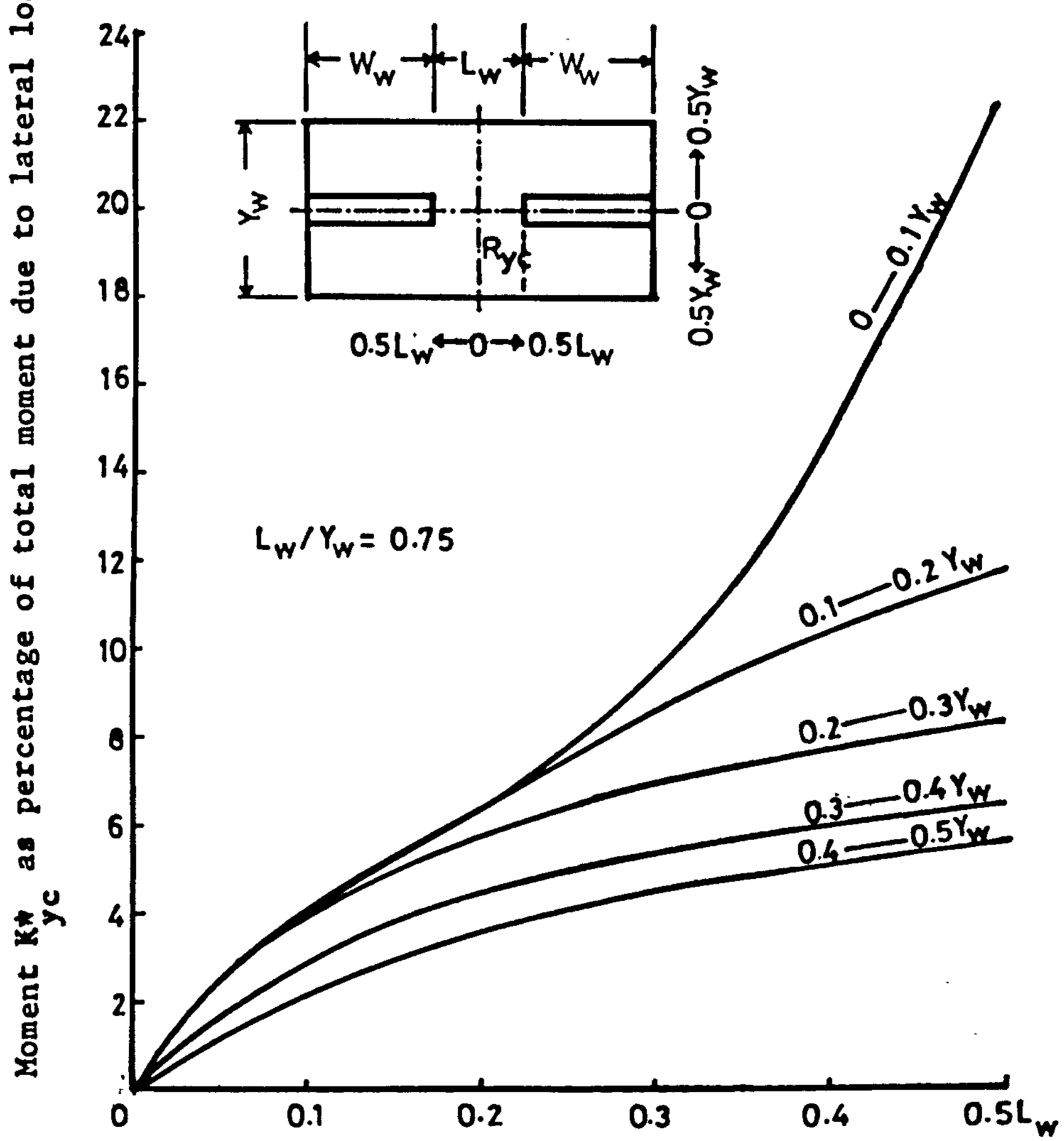

Figure (4.17) : Charts for determination of moment K^*_{yc} in the region R_{yc}.

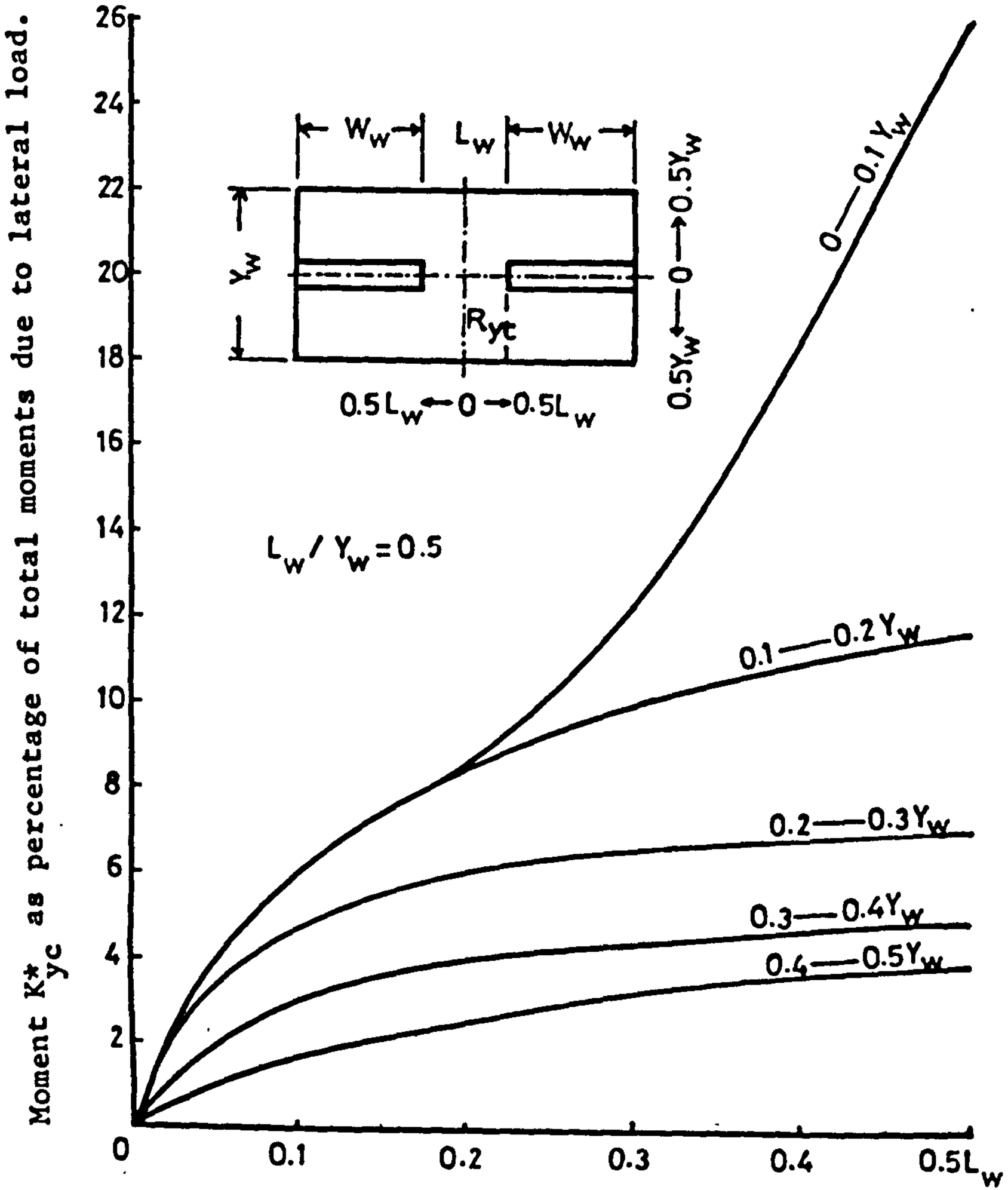

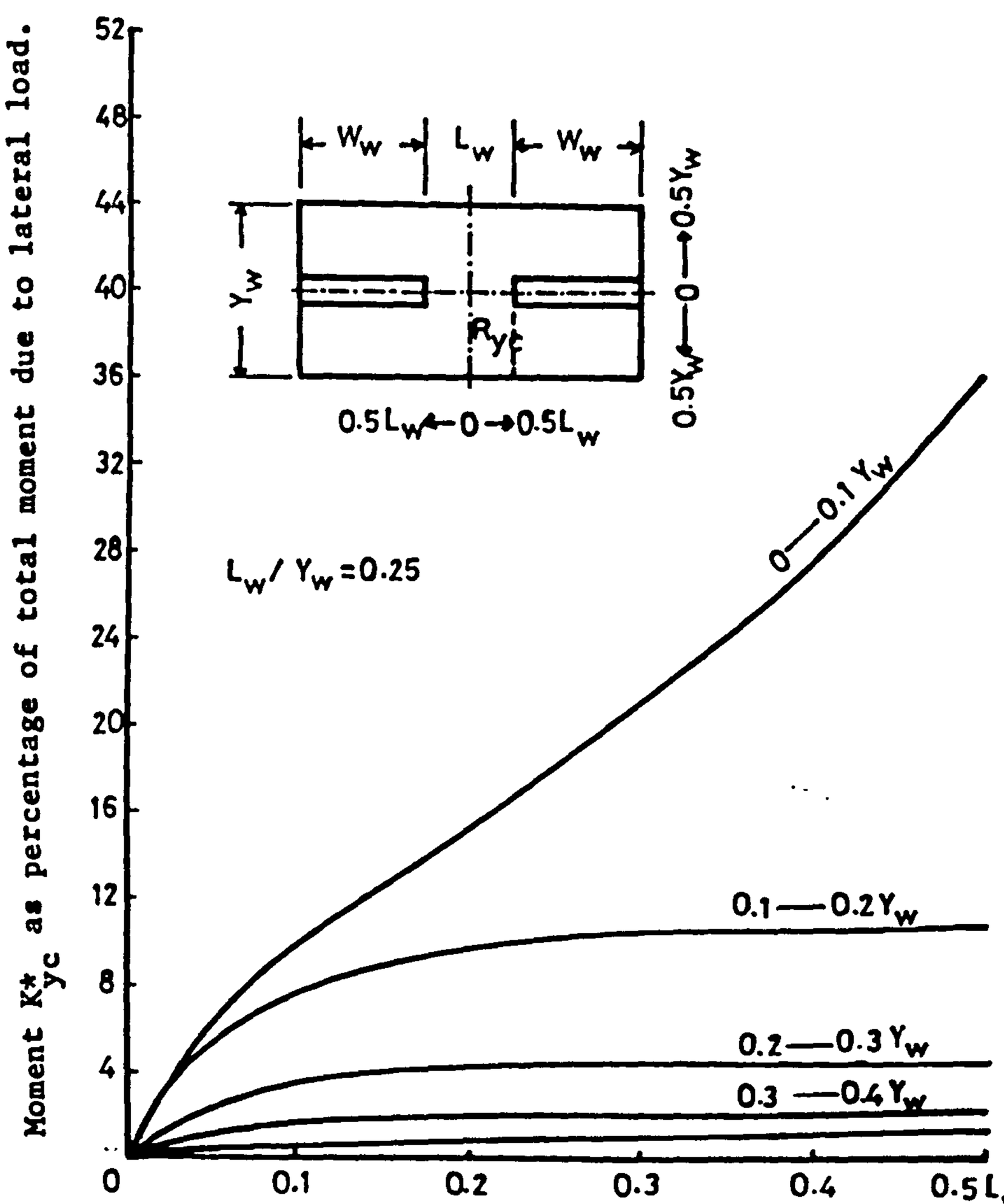

Figure (4.18) : Charts for determination of moment K^*_{yc} in the region R_{yc}.

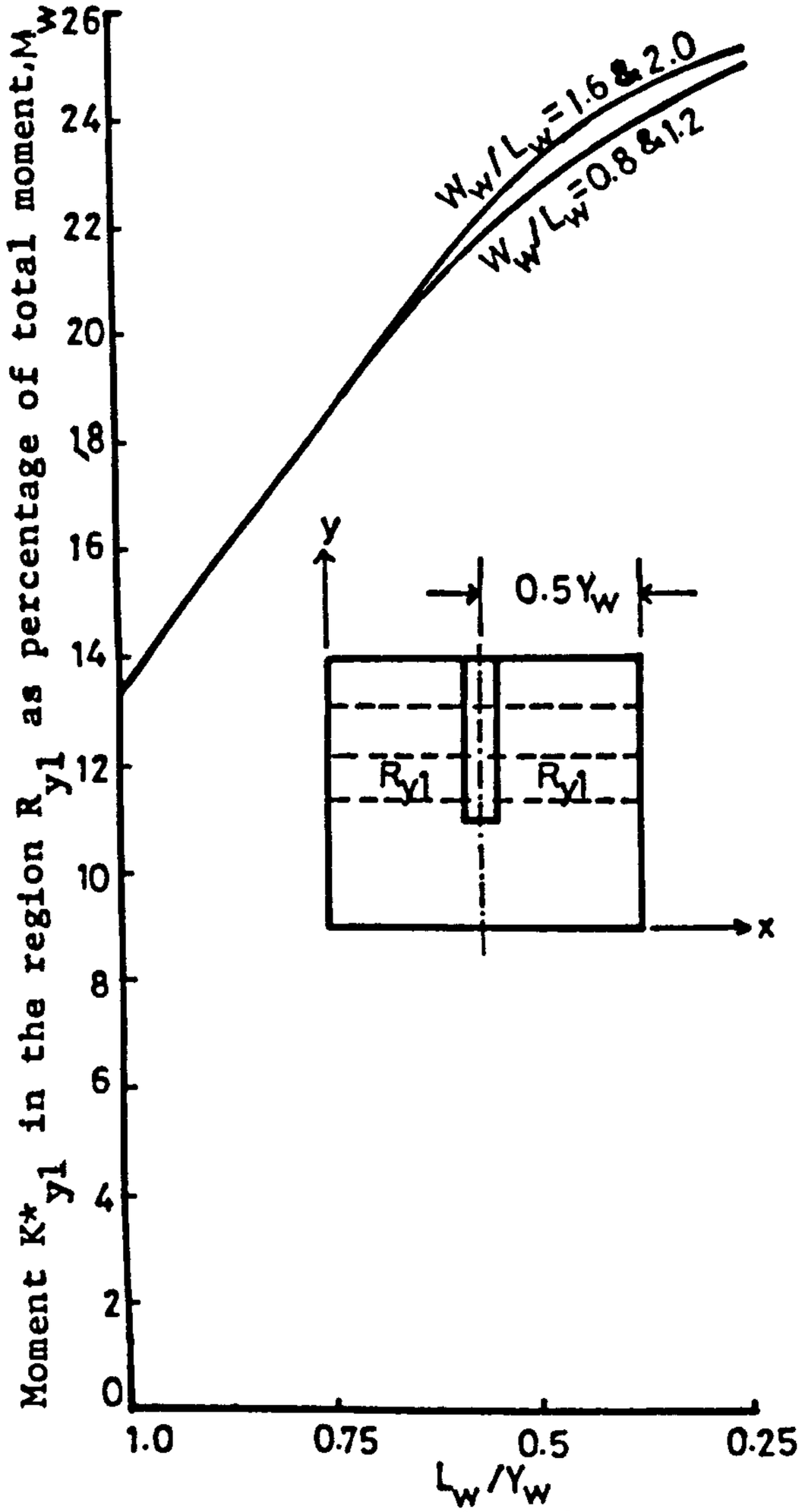

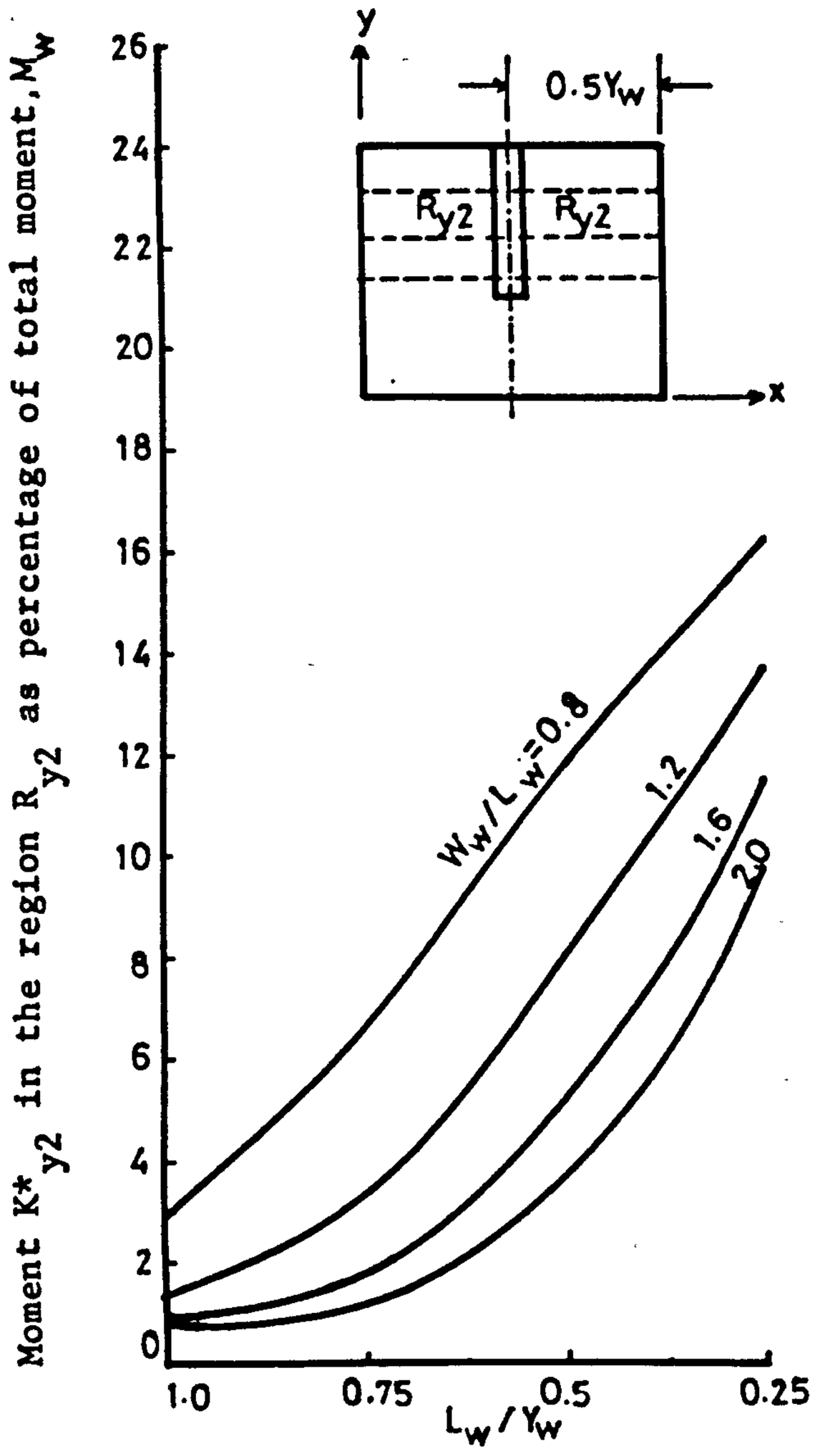

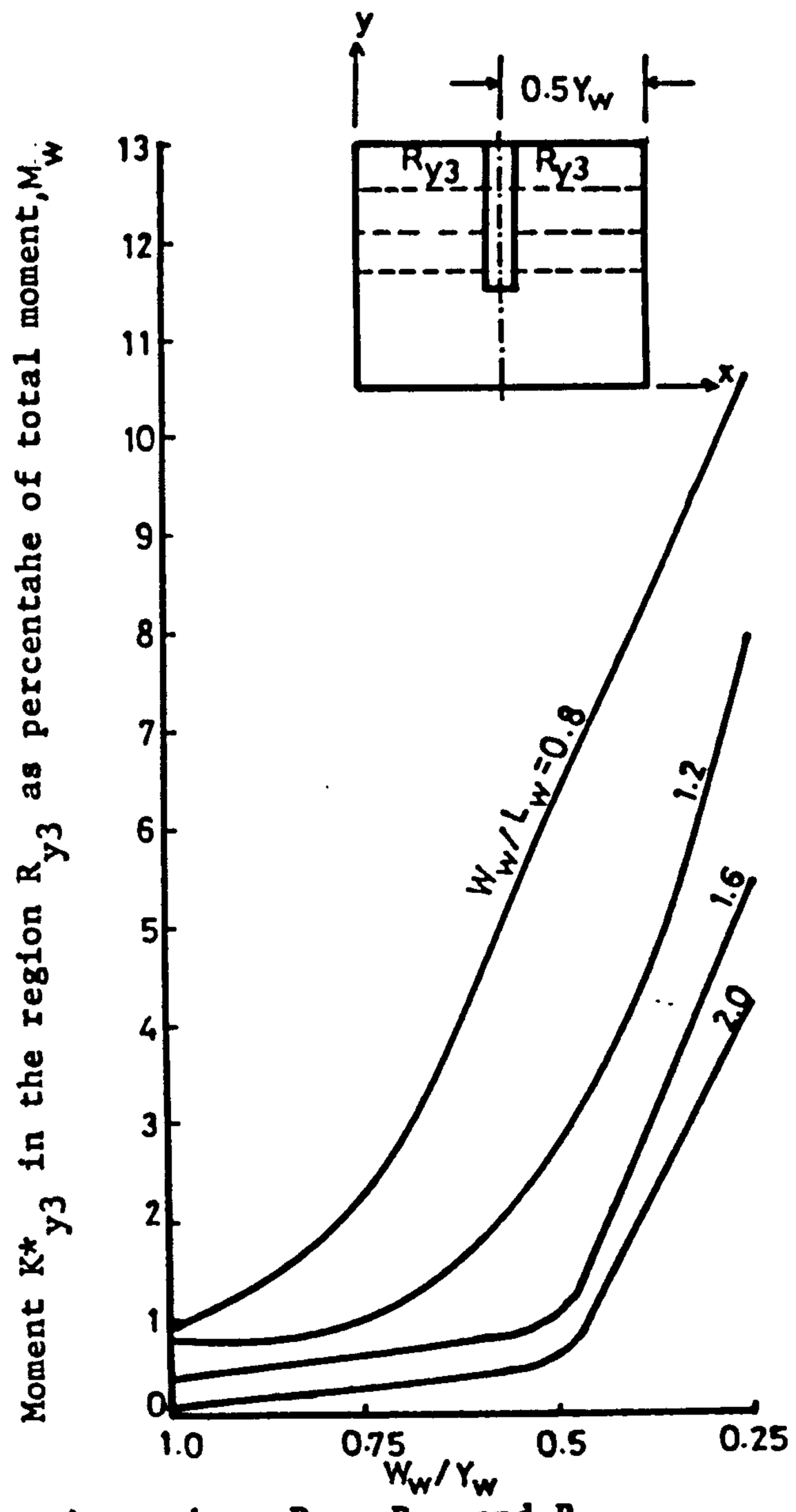

Figure (4.19) : Charts for determination of moments K^*_{y1}, K^*_{y2} and K^*_{y3} in regions R_{y1}, R_{y2} and R_{y3}.

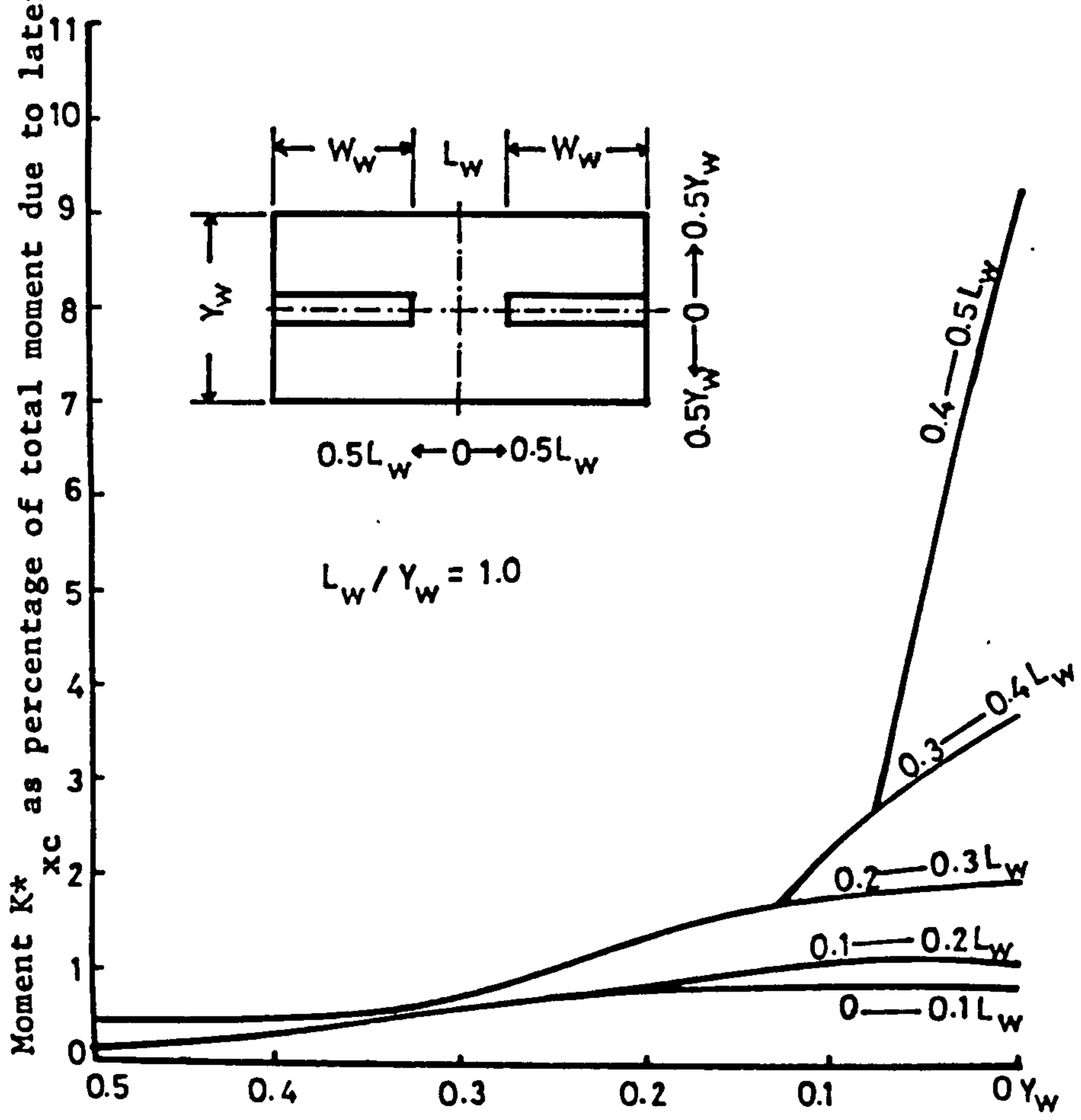

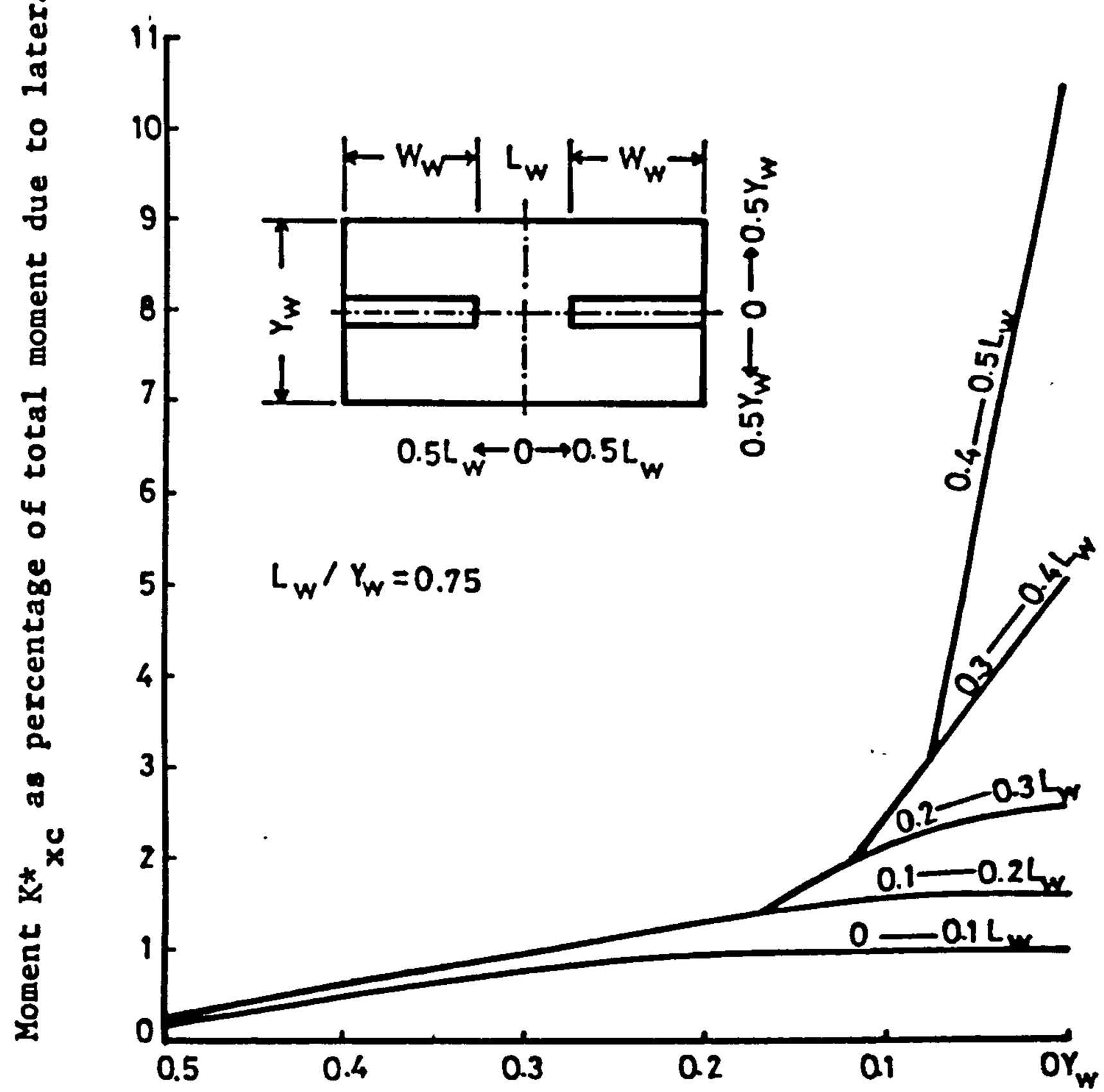

Figure (4.20) : Charts for determination of moment K^*_{xc} in the region R_{xc}.

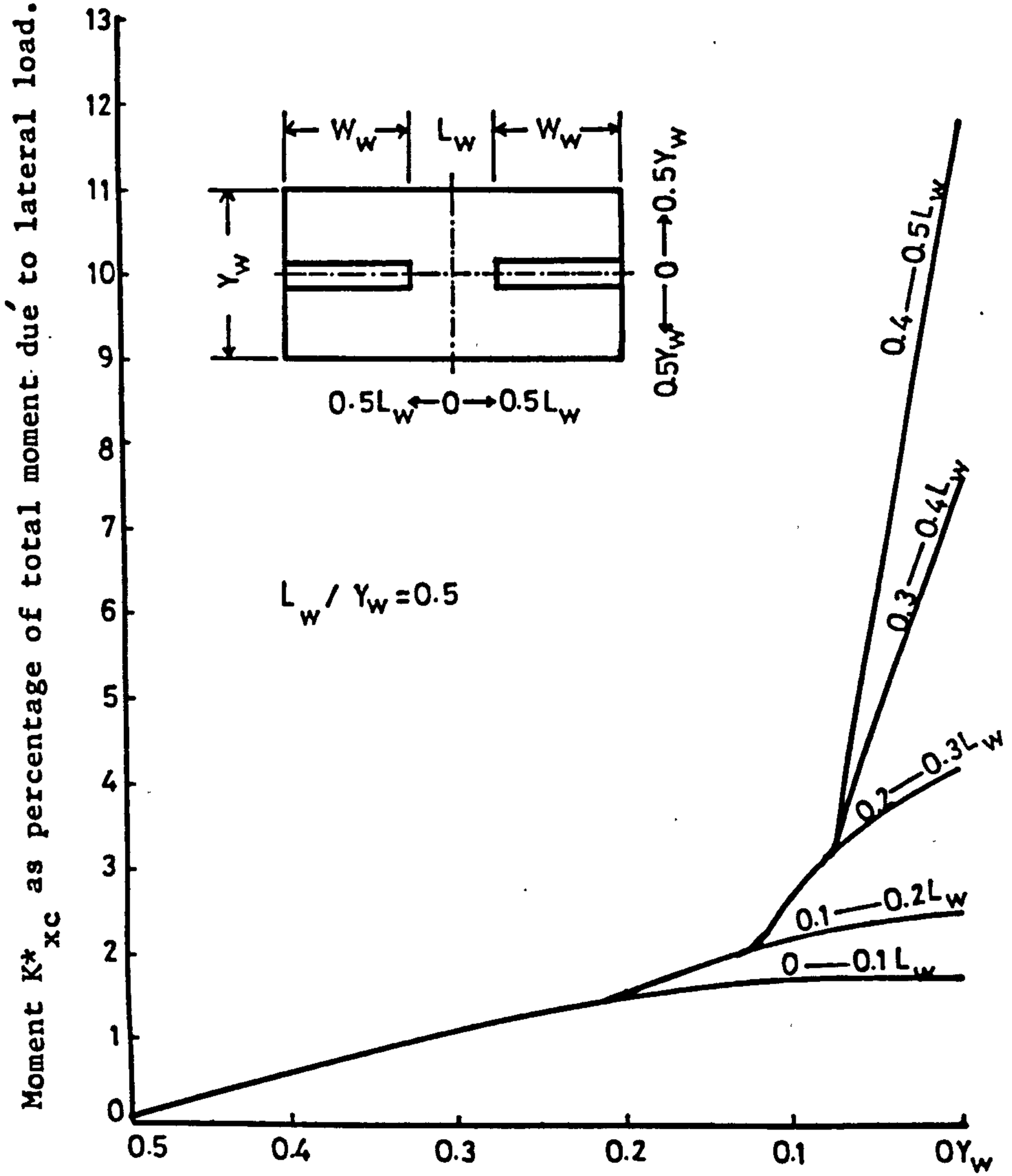

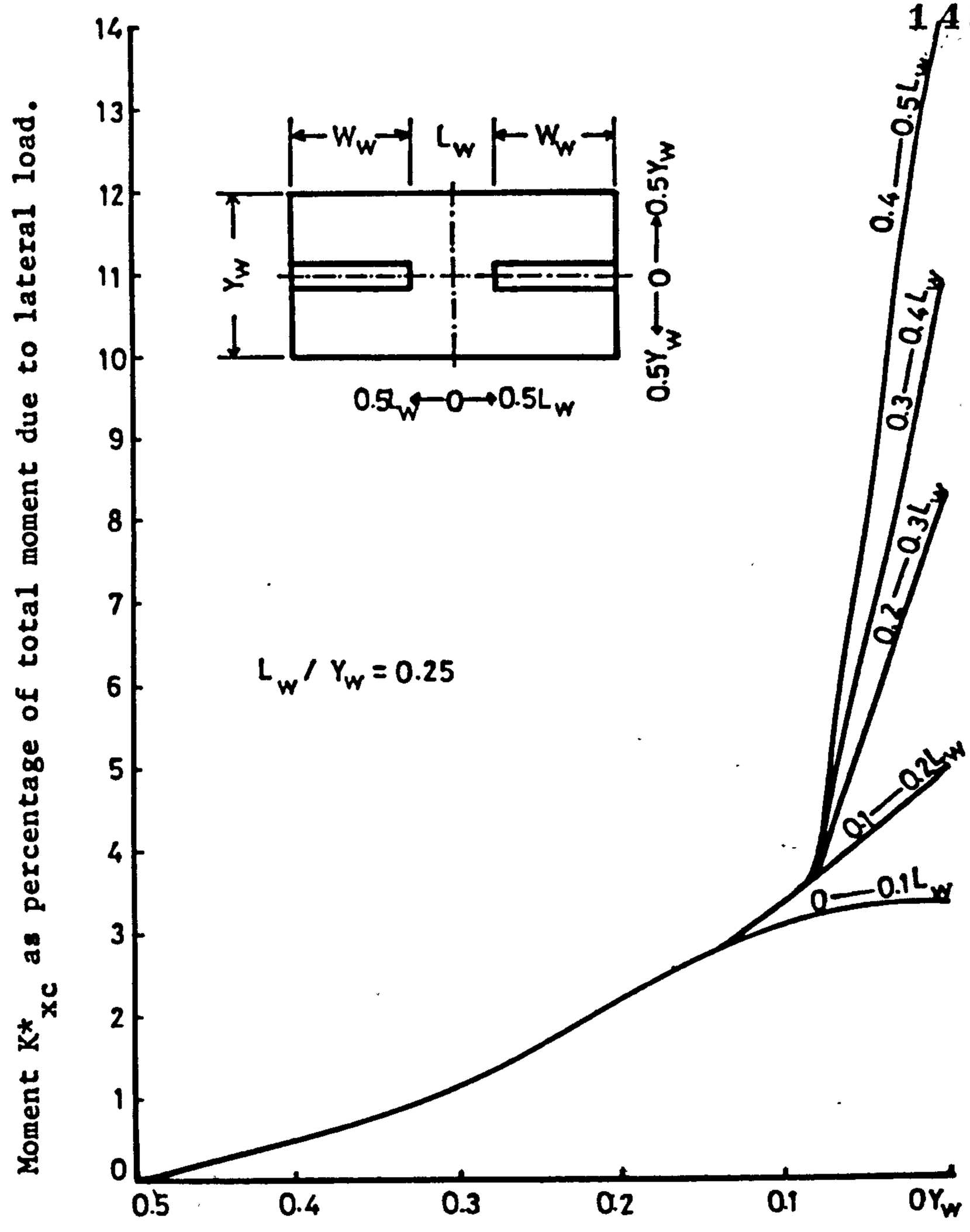

Figure (4.21) : Charts for determination of moment K^*_{xc} in the region R_{xc}.

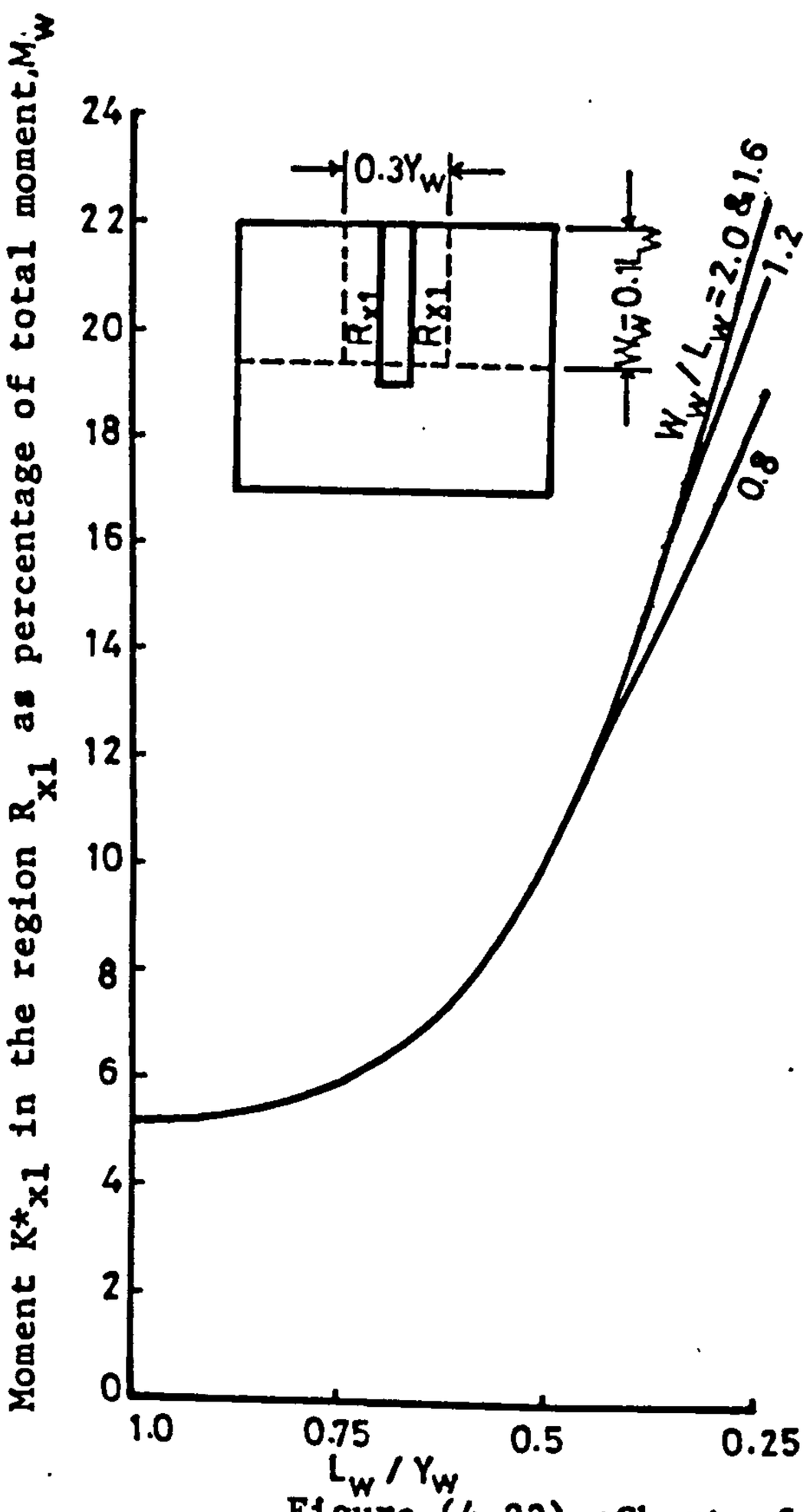

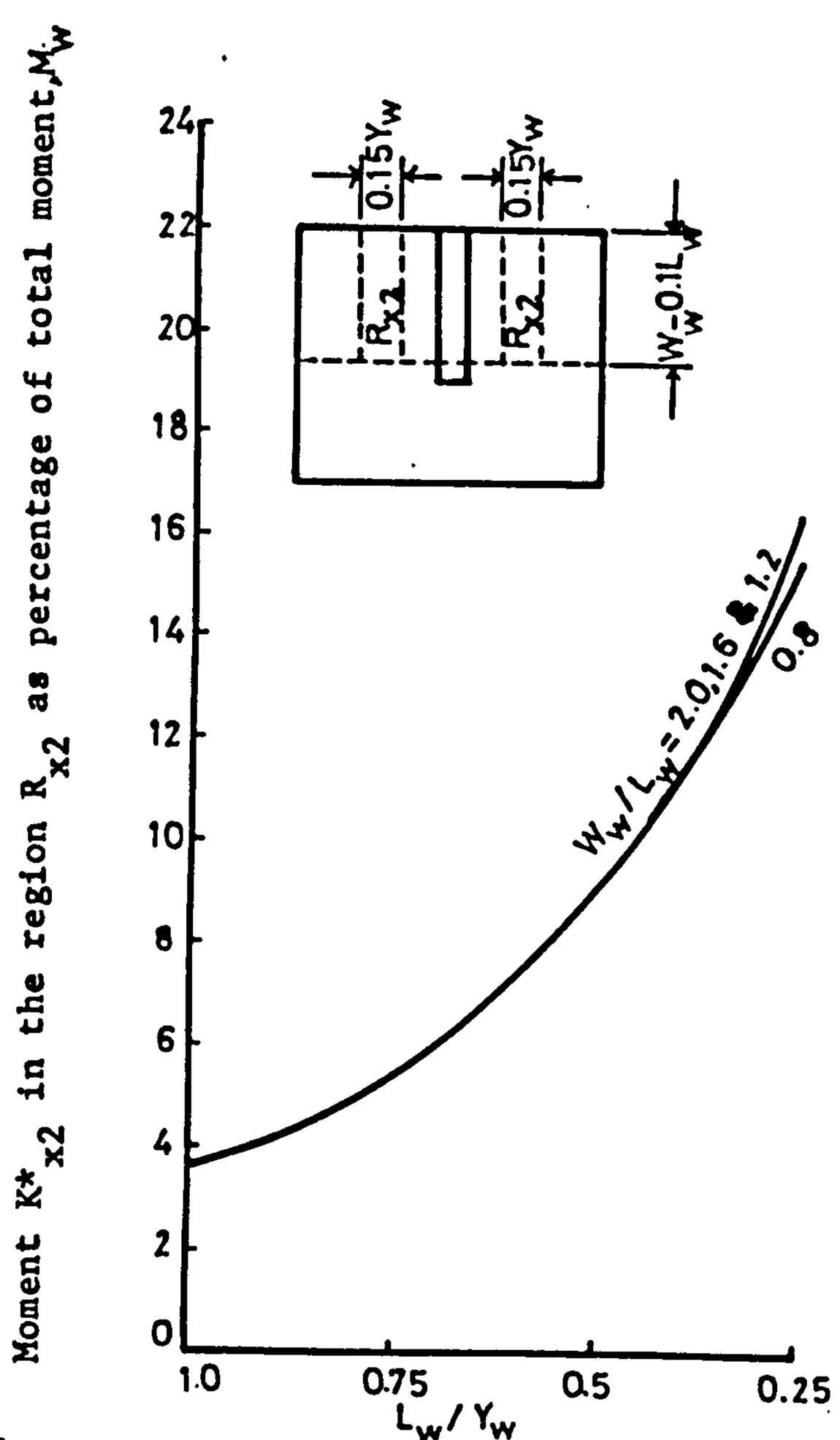

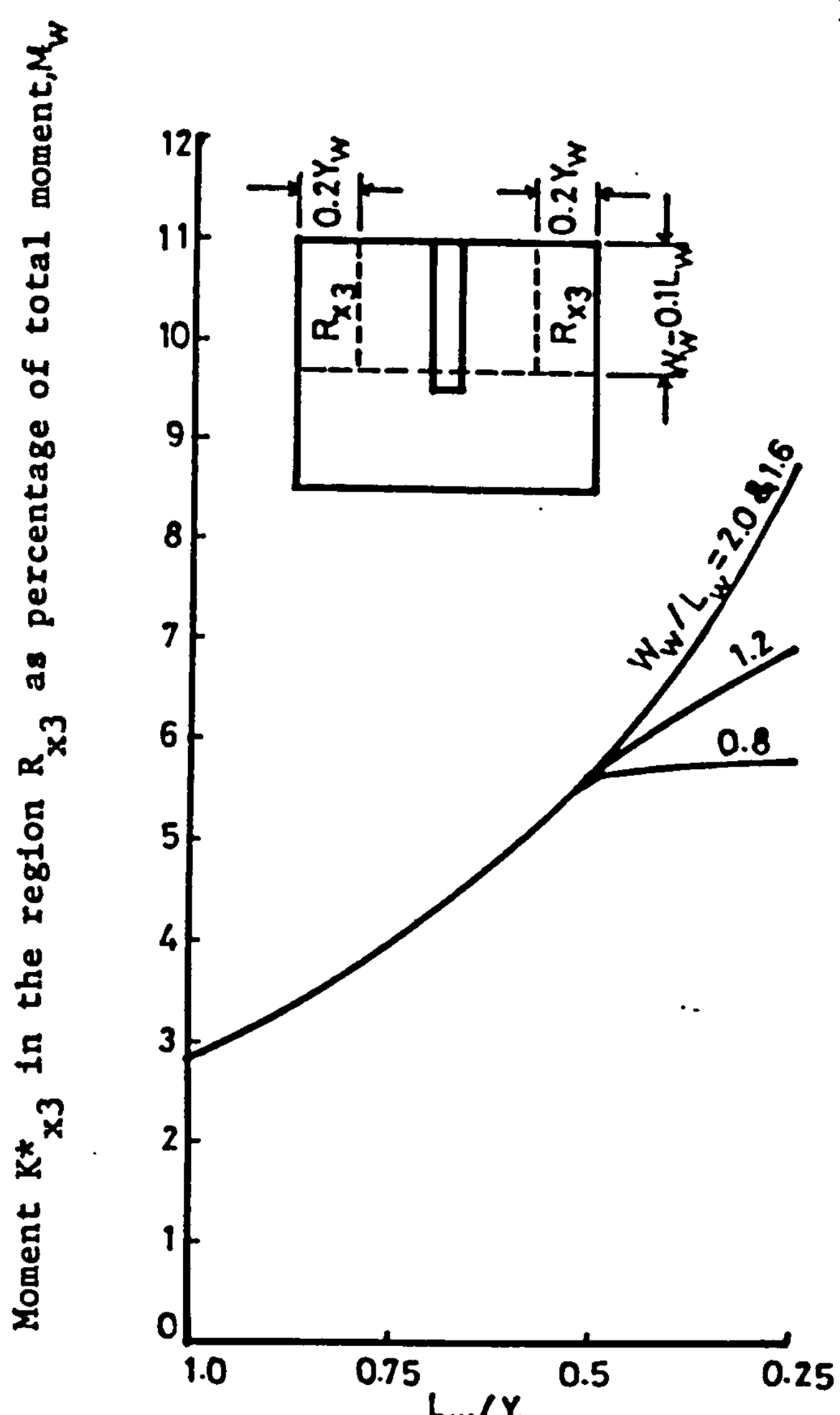

Figure (4.22) :Charts for determination of moments K^*_{x1}, K^*_{x2} and K^*_{x3} in the regions R_{x1}, R_{x2} and R_{x3}.

C H A P T E R F I V E

MATERIALS - APPARATUS AND EXPERIMENTAL SETUP

5.1 GENERAL

The experimental work can be divided into two test series, viz. (a) Preliminary test series, which consisted of three models (PT1 to PT3) and (b) main test series which consisted of eleven models (MT1 to MT11). The full description of these models and their behaviour during experimentation is given in chapter six. In this chapter the materials used for the construction of the models and their properties are described first. Then the procedure adopted for the manufacture of the models is briefly explained. The instrumentation used for the measurement of strain, displacements and load are also discussed. In the end the testing arrangements which were tried and the procedure adopted for testing of the models are discussed.

5.2 MATERIALS

5.2.1 Concrete

Concrete grade 30 with target mean compressive strength of 43 N/mm^2 on 28th day was used to cast all the models except model MT2. Because of the large quantity which was needed for every model, concrete was prepared in batches. Ordinary portland cement with hyndford sand and 10 mm uncrushed gravel (max. size) were used for all concrete mixes. The grading of sand was in zone 2 (37). For each batch 13 kg of cement, 20.3 kg of sand and 41 kg of 10 mm aggregate (giving a mix ratio of 1:1.56:3.15) were mixed dry thoroughly for about two/

minutes in a .085 cubic metre pan mixer and then water (6.1 kg) was added, giving a water to cement ratio of .47 and it was allowed to mix for five more minutes to prepare the concrete of required consistency. For determination of strength properties of hardened concrete, six 100 mm cubes and four 150 x 300 mm cylinders were cast and cured with each model. All the cubes and cylinders were removed from their moulds one day after the casting.

The compressive strength of concrete was taken as an average of three - 100 mm cubes, while the cylinder splitting tensile strength was taken as an average value of two - 150 x 300 mm cylinders. Two cylinders were used to determine the modulus of elasticity and cylinder compressive strength.

5.2.2 Determination of modulus of elasticity of concrete

The following procedure was adopted to find the modulus of elasticity: Immediately before the modulus of elasticity test, three cubes were tested to determine the cube crushing strength of concrete. Then the value of "C_m" which is equal to one third of the average compressive strength was calculated to the nearest 1 N/mm^2. Demec pads were stuck with the help of Araldite on the opposite sides of the specimen and parallel to its axis, in such a way that the gauge points were symmetrical about the middle of the specimen. The load was applied gradually and increased continuously at a rate of approximately 15 N/mm^2 per minute until an average stress of (C_m + 2) N/mm^2 was reached. The load was maintained at this figure for one minute and was then reduced gradually to an average stress of 1 N/mm^2 and demec gauage (extensometer) reading was taken. The load was then/

reapplied at the same rate until an average stress of $(C_m + 1)$ N/mm^2 was reached. It was then reduced gradually to an stress of 1 N/mm^2 and readings were taken once again.

The load was then applied a third time at the same rate and demec gauge readings taken at approximately ten equal increments of stress up to an average of $(C_m + 1)$ N/mm^2. The typical stress-strain curves obtained from two cylinders of the same batch of concrete are shown in Figure (5.1). From this figure, it can be observed that the modulus of elasticity determined from the test data of two cylinders differs by approximately 3.3%. An average of the two values was adopted as the modulus of elasticity of that batch of concrete. Figure (5.2) shows the stress-strain relationship up to crushing of a typical concrete cylinder.

The procedure mentioned in this subsection is in accordance with the reference (38).

5.2.3 Reinforcement

Ribbed torsteel bars made by British Steel Corporation were used in all models. These were the cold drawn bars complying with the requirements of CP 110 for the type of deformed bars. Four different bar sizes i.e. 6 mm, 8 mm, 10 mm and 12 mm diameter were used for reinforcing the models and the ultimate tensile strength was obtained experimentally by testing three specimens of each bar size and taking an average of three values.

The Olsen testing machine was used for the determination of the tensile strength of steel bars. In each case the ends of the bar/

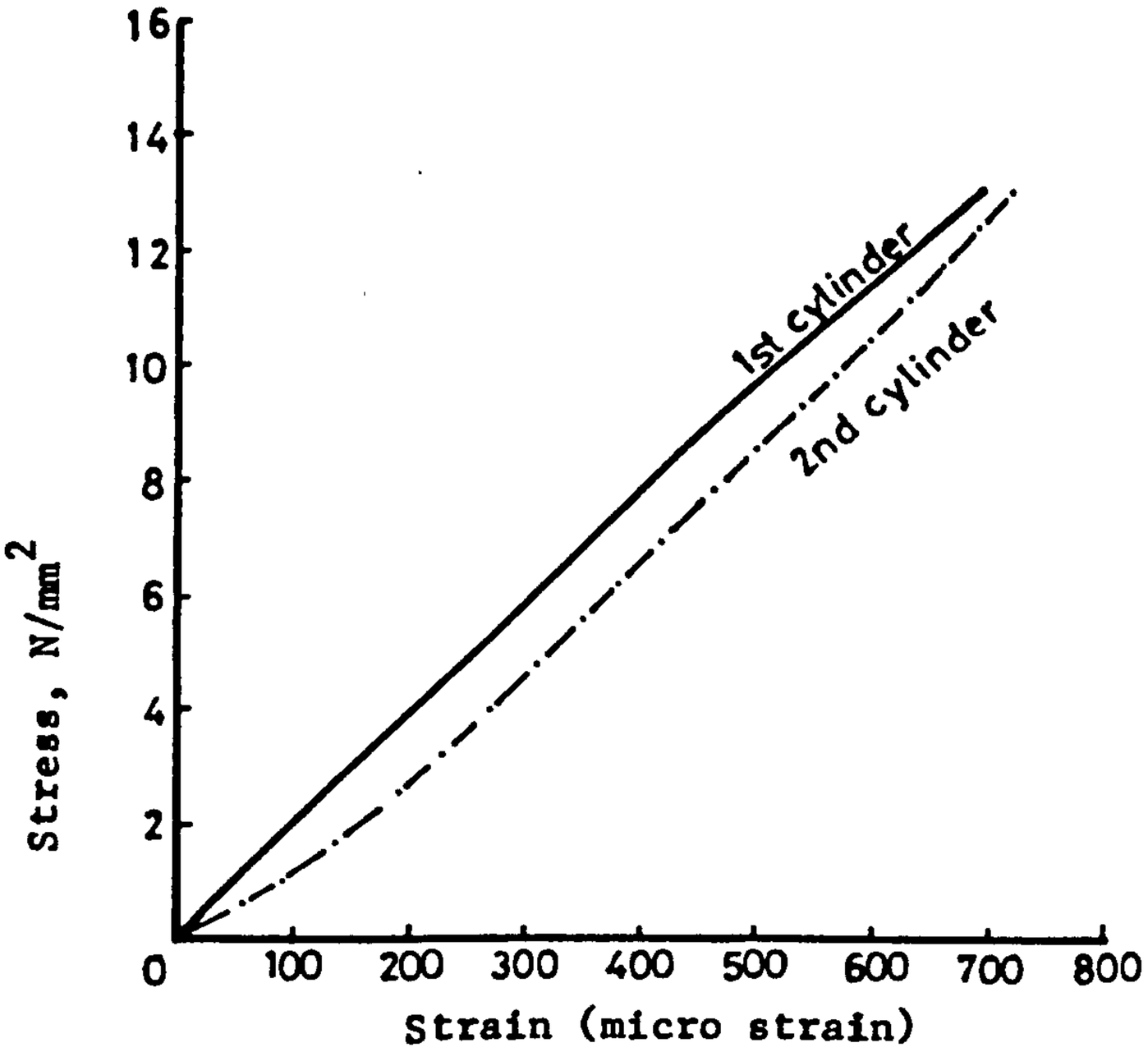

Figure (5.1) : Stress-strain relationship for two different cylinders from the same batch of concrete obtained during modulus of elasticity test.

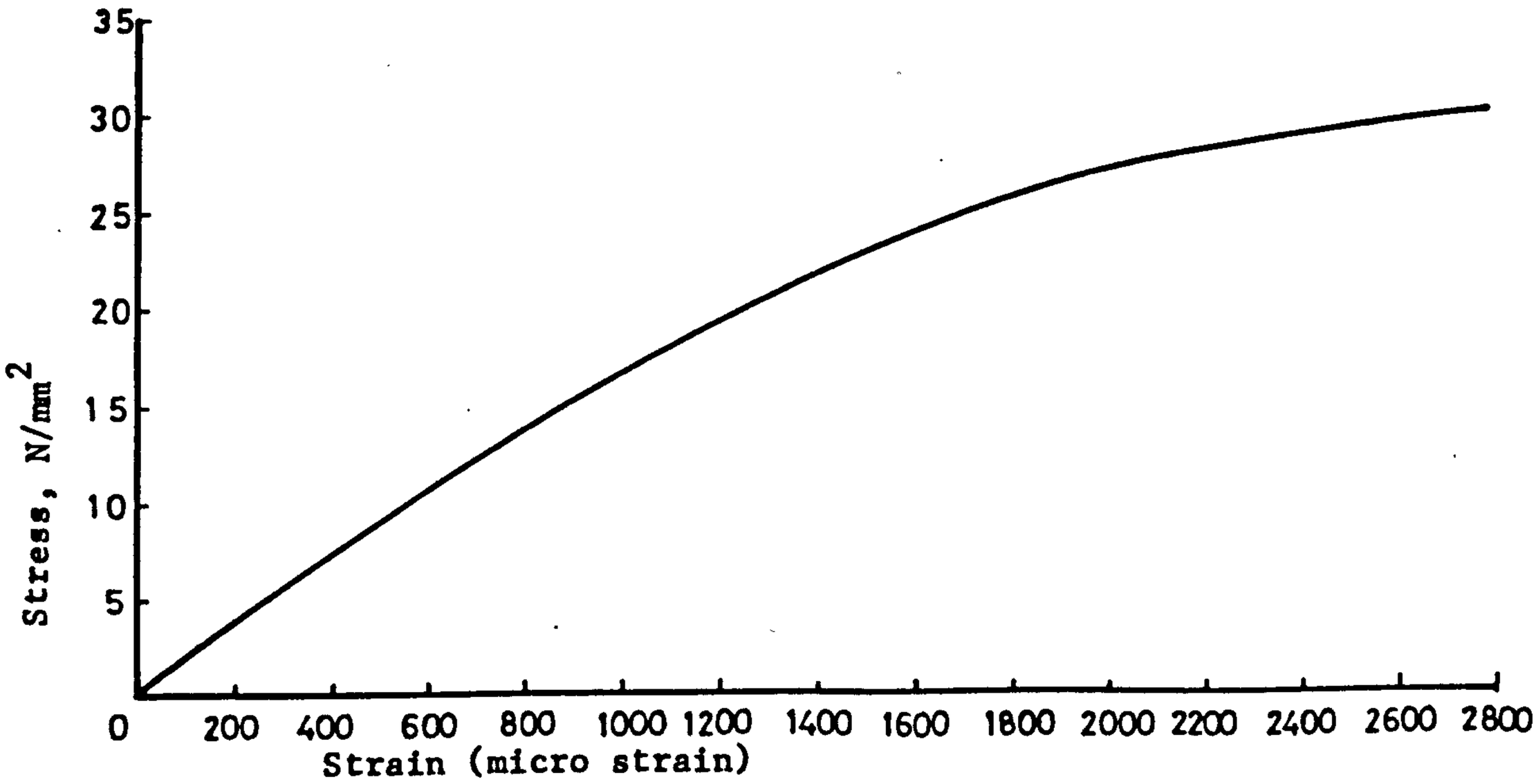

Figure (5.2) : Uniaxial stress-strain curve for plain concrete.

were firmly held in the grips of the machine and S-type Olsen extensometer was attached to the bar near its centre. Olsen extensometer is an electronic strain instrument designed to operate in conjunction with the Olsen Model 51 Electronic Recorder. The standard instrument operates on a 50.8 mm (2 inches) averaging gauge length and a magnification factor of 250 was adopted for our purpose. Tests were carried out in accordance with the recommendations of the "Panel for standard practices in Testing", DOE - TRRL (39) working group on long term research into steel box girder bridges.

The stress-strain curve was obtained directly on a graph paper from the recorder. The units of extension (strain) mm per mm as recommended by operating manual of the Olsen machine, were marked off on the abscissa of the curve and the load divided by the area of cross-section of bar (i.e. stress) was marked off as ordinate of the graph. For the determination of yield stress a straight line through the straight portion of the curve, starting from the origin was drawn and an other straight line parallel to this line was drawn starting from the .2% proof strain. The value of stress at intersection of this line and the actual curve was taken as yield stress. Modulus of elasticity was calculated by dividing this stress by the corresponding strain.

The typical stress-strain curves obtained for different reinforcing bars are shown in Figure (5.3). The properties such as modulus of elasticity, yield stress, ultimate stress and strain at 0.2% proof stress etc. of different bars are shown in table (5.1).

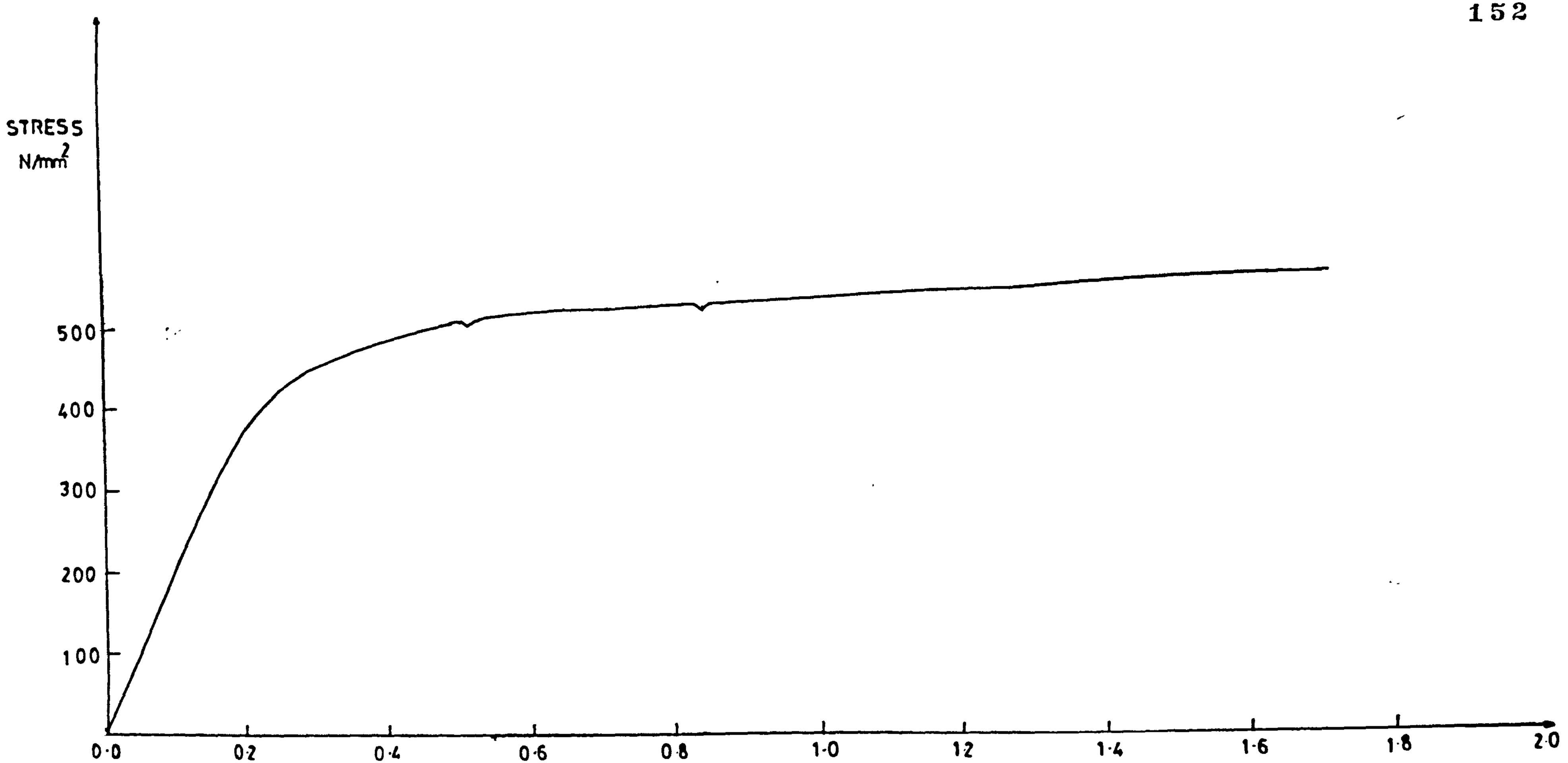

Figure (5.3a) : Typical Stress-Strain Relationship For Various Sizes of Bars (D = 6 mm).

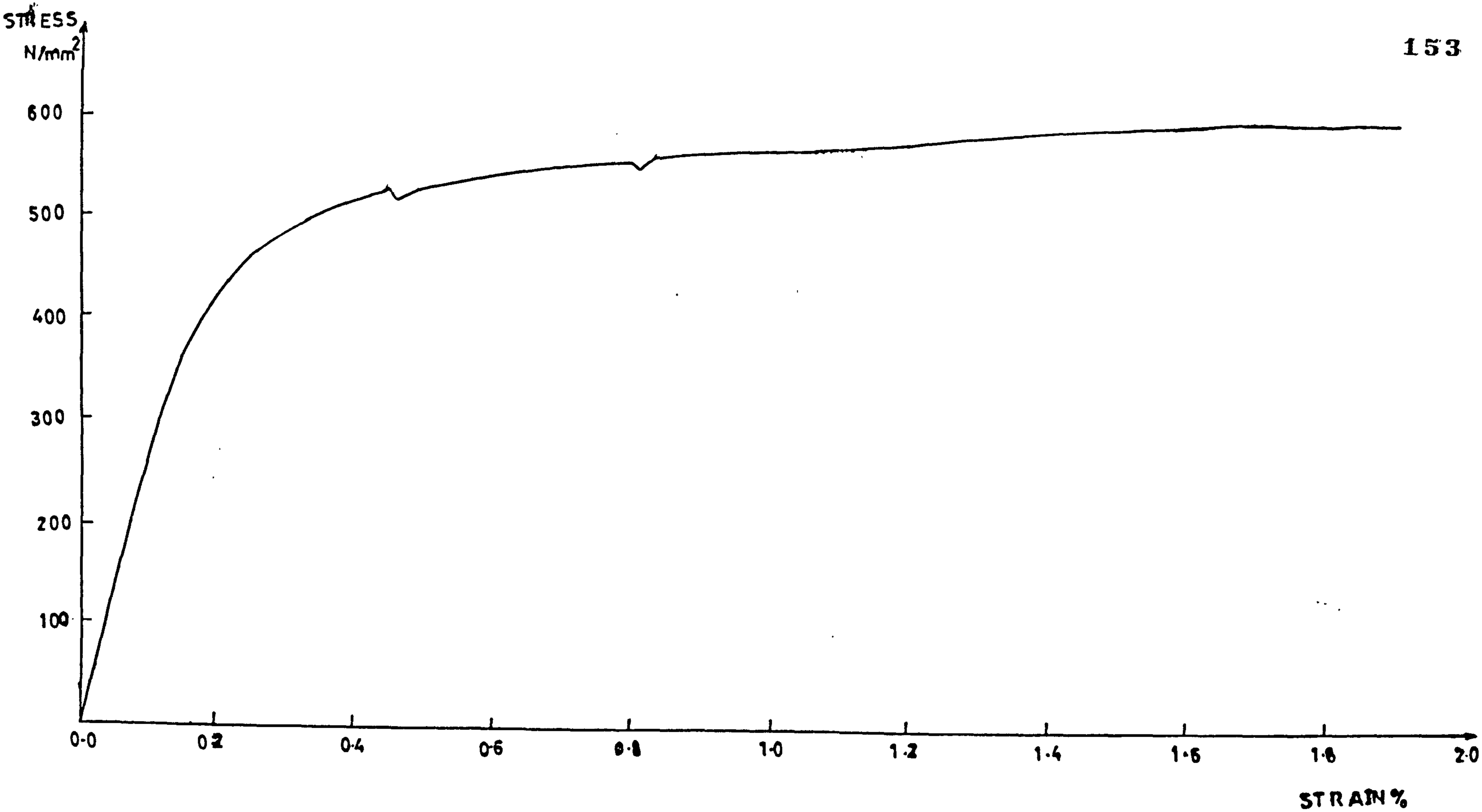

Figure (5.3b) : - Continued - (D = 8 mm).

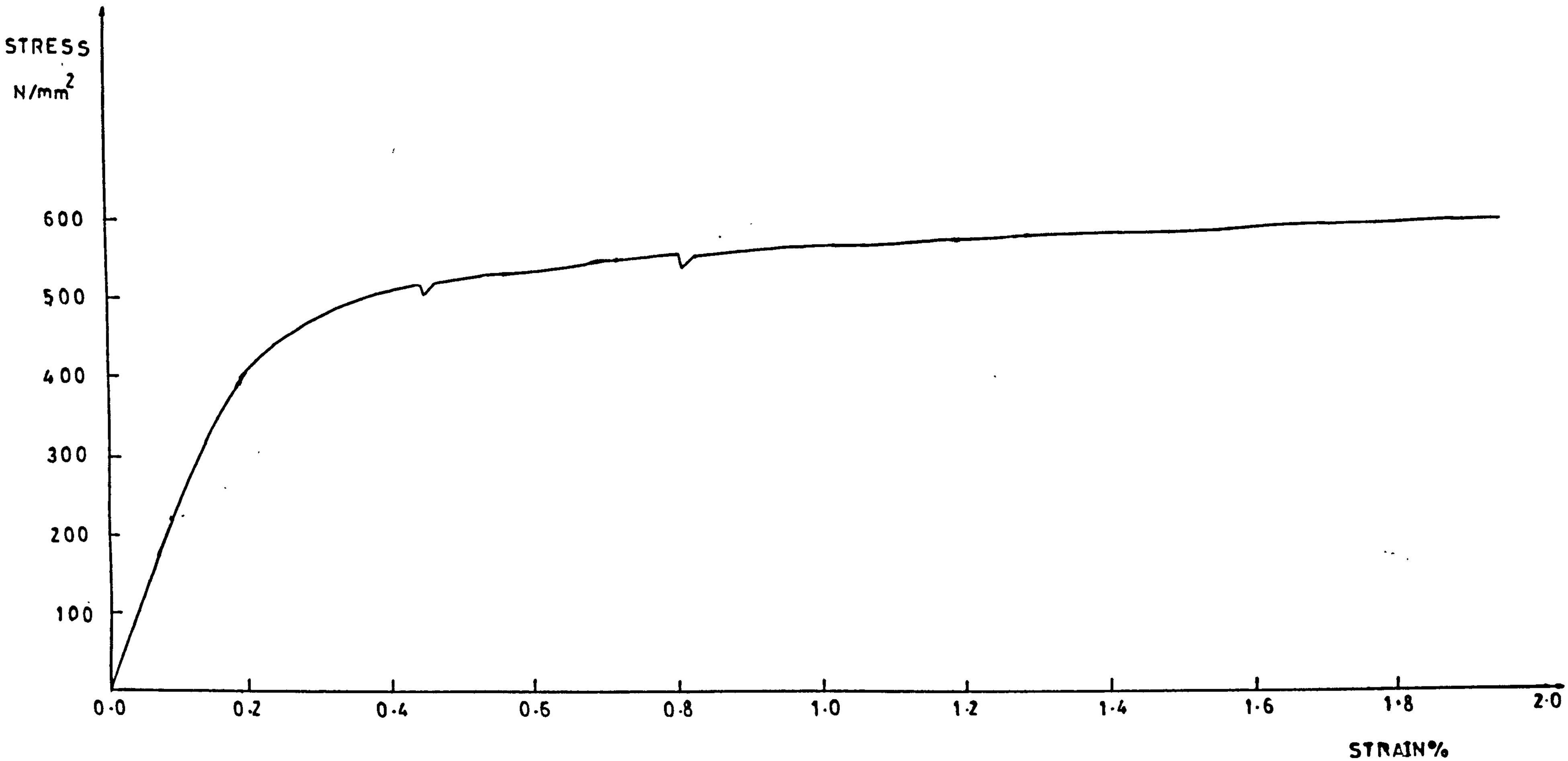

FIGURE (5.3c) : - Continued - (D = 10 mm)

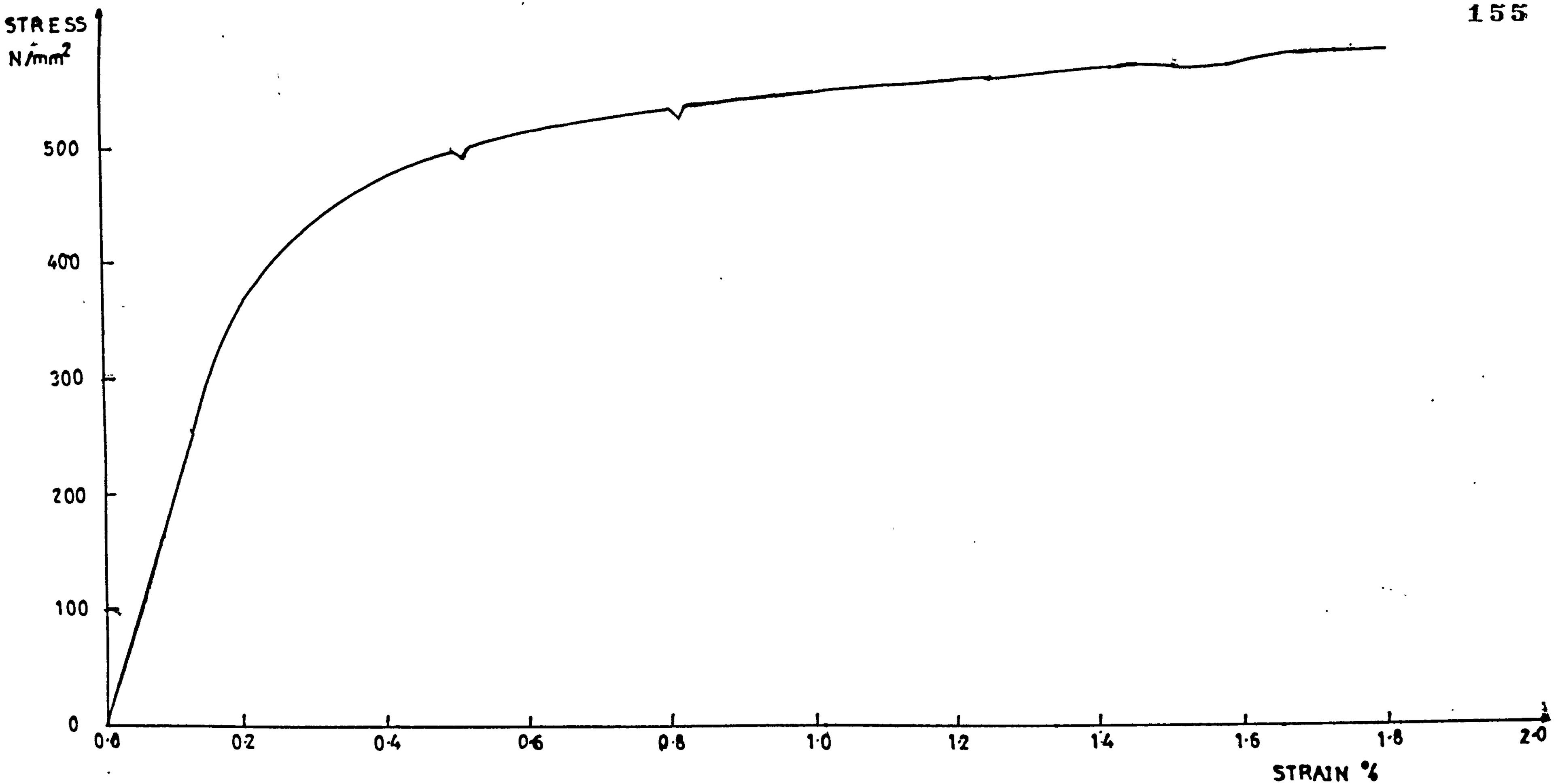

FIGURE (5.3d) : - Continued - (D = 12 mm)

Table 5.1. Properties of Reinforcement

Nominal bar diameter mm	Young's modulus kN/m^2	0.2% proof stress, f_y N/mm^2	Strain at .2% proof stress y	Ultimate stress N/mm^2
6	210.0	503.0	.24	566.0
8	267.5	514.0	.192	542.0
10	237.0	507.0	.22	586.0
12	214.0	519.0	.24	573.0

5.3 CASTING AND CURING

The formwork (shuttering) needed for fabrication was manufactured from 18 mm thick plywood sheet.

The overall shape of a typical model is shown in Figure (5.4). The formwork and reinforcement cage are shown in Figure (5.5). All the formwork was oiled to facilitate easy removal.

Reinforcement cage was properly positioned in the formwork. Thin soft iron wire was used for tying the reinforcing bars to make the cage. Spacers were used for obtaining the required cover. Hooks were provided at the top of the wall in suitable positions for lifting the model. The concrete was placed in the formwork and was compacted with vibrating pokers. In order to prevent the downward drift of fresh concrete in the upper portion of the wall towards the slab, the slab and the lower portion of wall were cast first and after a break of about three hours, the upper portion of the wall was cast. The cubes and cylinders were compacted by means of a vibrating table. The concrete was cured for seven days under wet sacks and polythene sheeting. The sides of formwork were removed after two days of curing.

5.4 INSTRUMENTATION

5.4.1 Strain Measurement

Electrical resistance strain gauges were used to measure the tensile strain in steel and compressive strain on the concrete surface of the bottom of the slab along a section passing through the slab near the inner edge of wall. Strains in wall at certain/

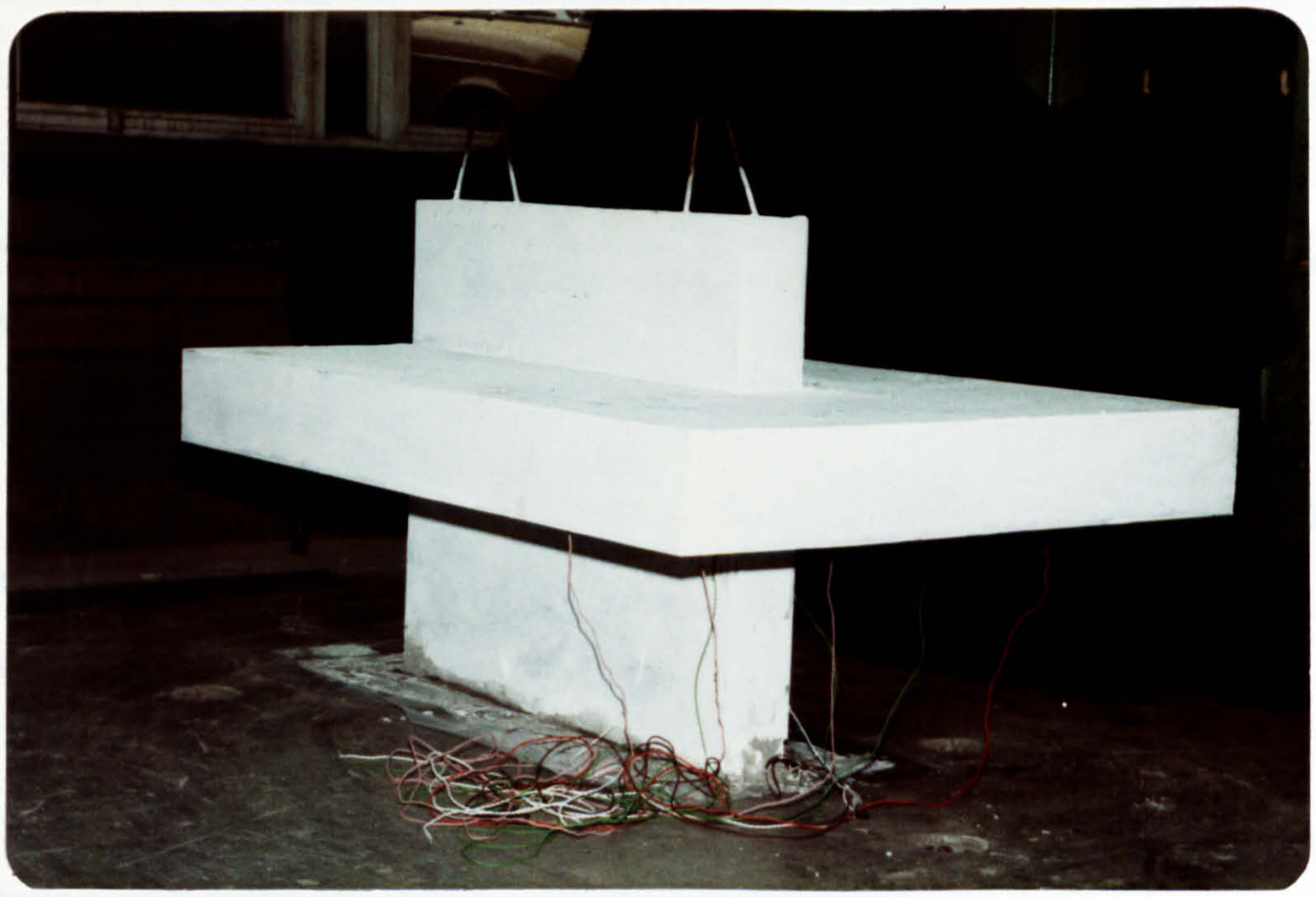

Figure (5.4) : Overall shape of a typical model.

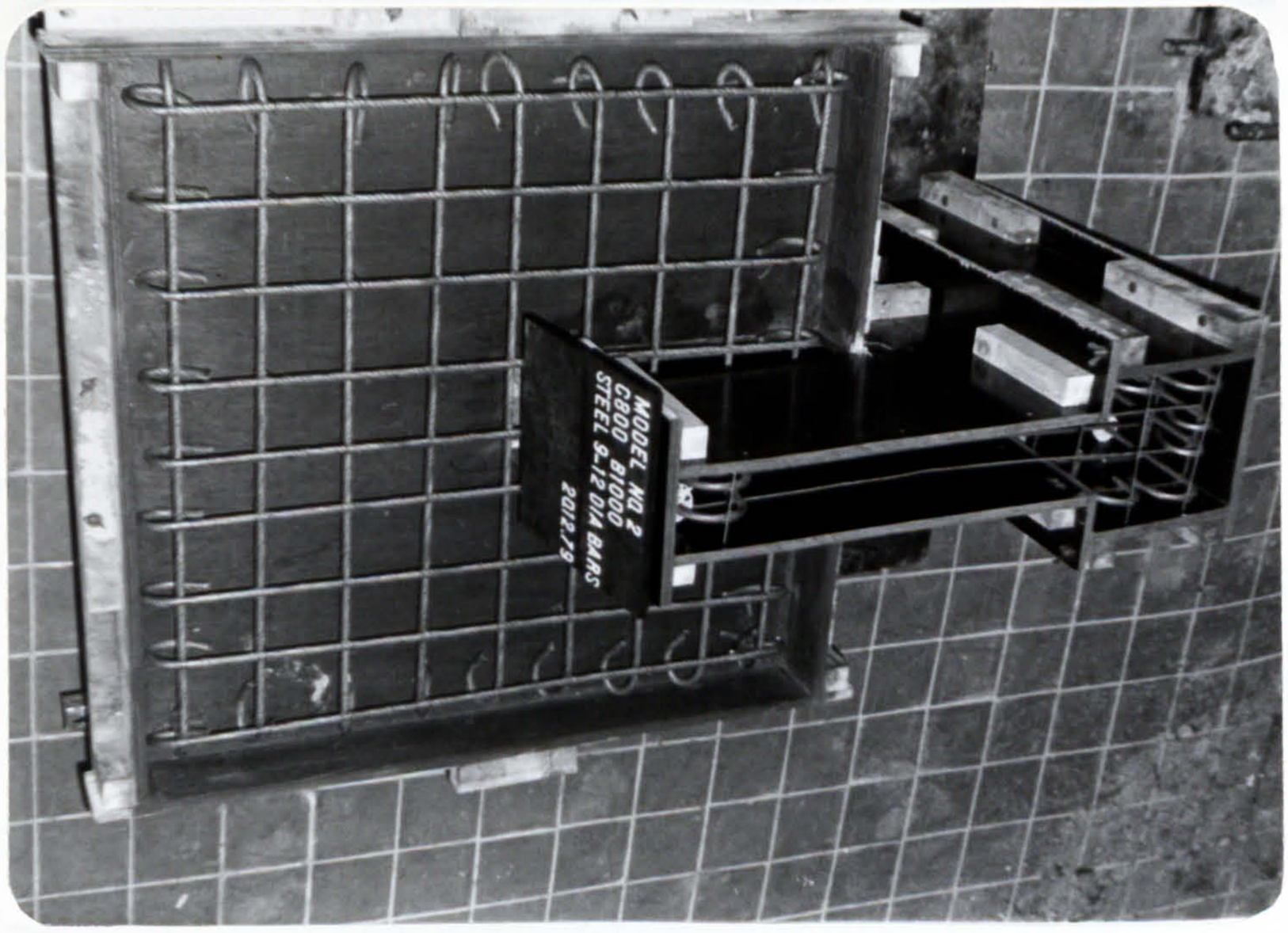

Figure (5.5) : The formwork with reinforcement cage for a typical model.

sections were also measured. The location of these points in the slab and the wall of a typical model is shown in Figure (5.6). The strain gauges used for concrete were 10 mm long with the elongation capacity of $\pm$ 6% and a gauge factor of 2.06 at a temperature of $75^{o}F$. Their internal resistance was 120 $\pm$ .3% Ohms. Depending on the availability, two different types of strain gauges were used on the steel bars. They were 6 mm long with an elongation capacity of 3-5% at a temperature of $75^{o}F$ and an internal resistance equal to 120 $\pm$ .3%. The only difference between the gauges was the gauge factor, which was either 2.03 or 2.105.

For fixing the strain gauges, the concrete surface was firstly cleaned and made smooth by grinding, using a grinding stone and then by a fine sand paper. Carbon tetrachloride was used to remove the dirt and grease. A thin coating of Adhesive (Drug A) and Hardener (Drug B) mixture was applied to the cleaned surface and the strain gauge was stuck on it, by firmly pressing with the thumb for about two minutes. After 24 hours of curing the lead wires were connected to the gauges by soldering. Protective coating (white M-Coat D) was then applied to the strain gauges.

For fixing the strain gauges on steel, the ribs were first removed by filing and then smoothened with the help of 'smooth file single cut'. The surface was further smoothened with emery paper. It was then cleaned with conditioner (water based acidic surface cleaner) and afterwards with neutralizer (water based alkaline surface cleaner). The Adhesive (M-Bond-200) specially supplied for this purpose was smeared to the back of the strain gauge and it was then stuck to the steel at required point by pressing it/

firmly for about two minutes and then was covered with adhesive tape. After 24 hours the tape was removed, lead wires were connected and M-white coat was applied. To prevent the strain gauges from the damaging effects of concrete they were covered with a coat of Araldite.

For all the models except MT2, the strain gauges were connected to the laboratory Datalogger (PDP8), which directly recorded the strains at each point for each load increment. For model MT2, a dummy or balancing gauge was fixed on the concrete cube. The strain gauge and the dummy gauge were connected to the balancing arms of the strain indicator. A multichannel strain indicator measuring down to one microstrain was used for measuring the strain.

5.4.2 Displacement measurement

Eight RR102 displacement transducers were used to measure the displacement of the model at different points. The RR102 transducer is the classical instrumentation potentiometer with a precision wound resistance element along which the D.C. output voltage is accurately defined. All the transducers used had a stroke length of 50.8 mm (2 inches). In order to instal these transducers at proper positions, a supporting frame of handy angles was made and the transducers were fixed to it at the required points by using clamp brackets. The location of the transducers is shown in Figure (5.7). The transducers were connected to the data logger (PDP8) which recorded directly the displacement in mm to accuracy of .01 mm.

In addition four dial gauges reading to .01 mm, three in the/

front and one at the back were also installed to cross check the accuracy of the transducers measurements.

5.4.3 Load measurement

Models PT1, PT2 and PT3 were tested for wind load alone. A compression load cell of 100 kN capacity and a load cell Amplifier (LCA) model 91A were used to measure the intensity of the applied load. This LCA displays the figures in volts. . The conversion factor from DVM units to load in kN was obtained by calibrating the load cell in the Olsen testing machine.

For models MT1 and MT2 a compression load cell of 500 kN capacity was used to measure the intensity of imposed wind load. Four small load cells of 50 kN capacity each were used to measure the intensity of the gravity load. Their location is shown in Figure (5.8). All these load cells were connected to the same LCA by means of a channel selector. The sixth channel of the selector was connected to a dummy gauge to measure the temperature drift of LCA with time, which was later applied as a correction to the readings of all the five load cells.

For models MT3 through MT11 the LCA was not used but the same load cells were connected to data logger. Since the data logger also records the readings in volts, the load cells were recalibrated in conjunction with it.

5.5 SUPPORTING ARRANGEMENT FOR MODELS

Different arrangements such as base slab, extended wall and steel stand, were tried before arriving at a final arrangement to/

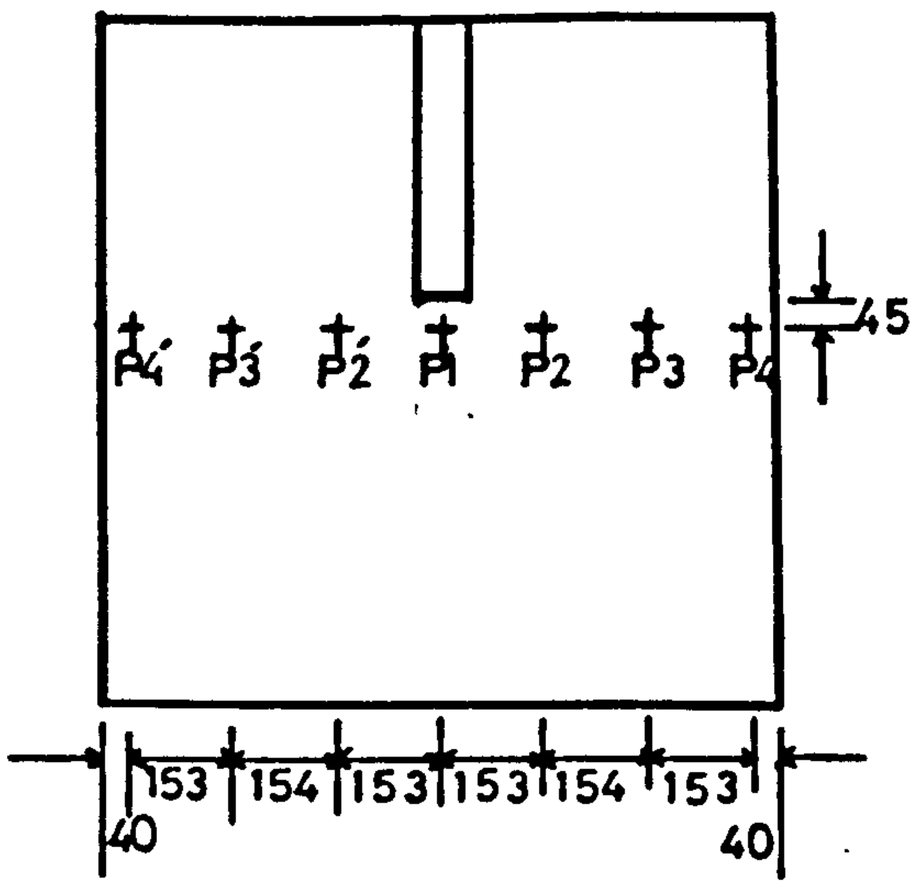

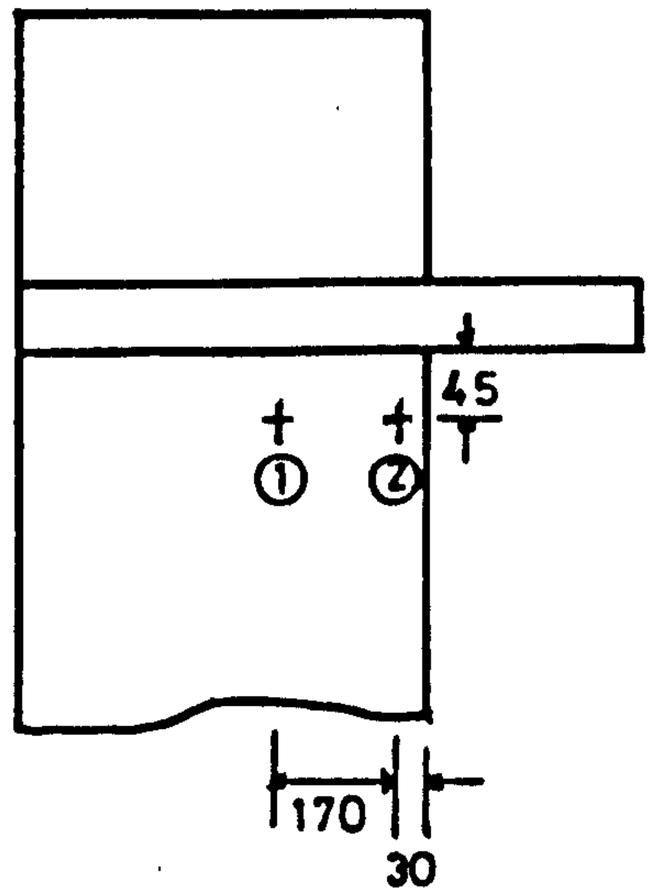

Figure (5.6) : Location of strain gauges in the slab and wall of a typical model.

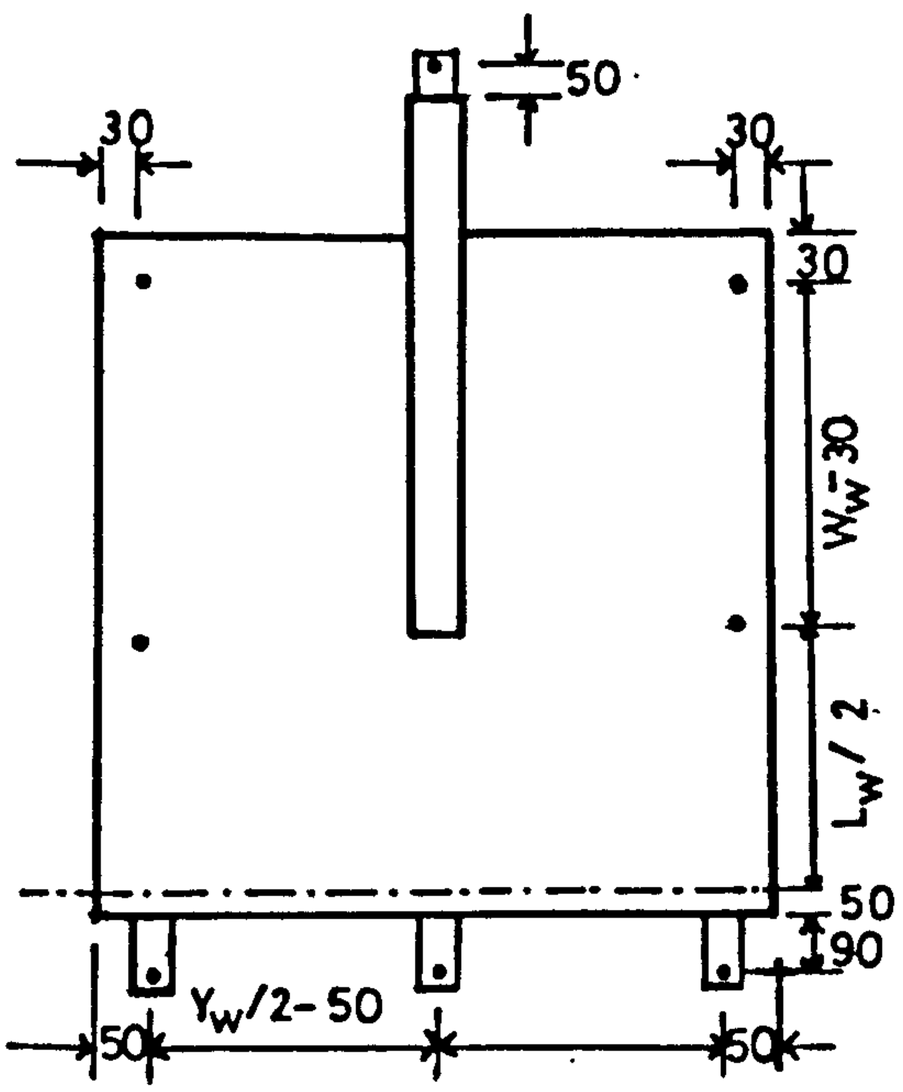

Figure (5.7) : Location of transducers.

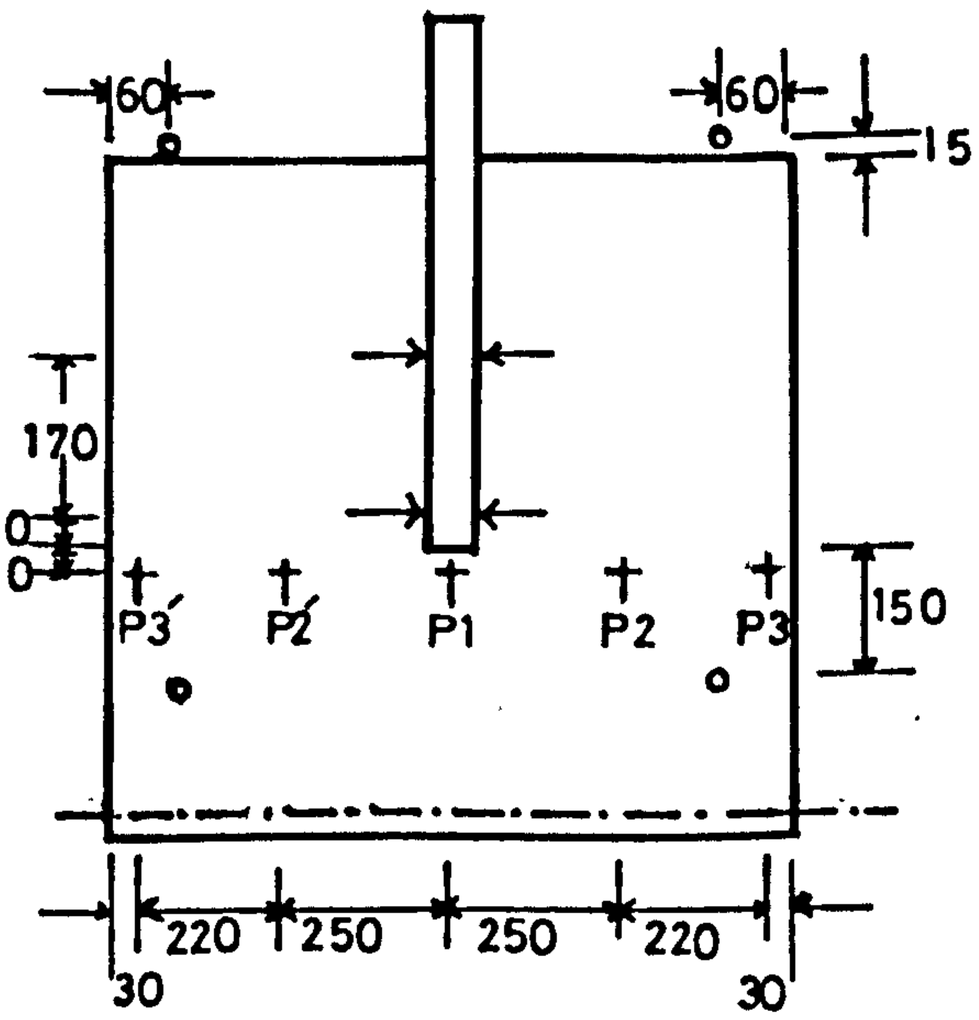

Figure (5.8) : Location of small load cells and strain gauges in models of MT series.

support the models while testing. Model PT1 was provided with a reinforced concrete base which was fixed to the floor of the laboratory by means of two hollow rectangular steel sections and four - 20 mm diameter steel rods and nuts. This arrangement is shown in Figure (5.9). To reduce the total quantity of materials and labour required for each model and consequently the overall cost of the model, slightly different arrangement was used for models PT2 and PT3. Instead of a base slab, the wall of these models was made larger and at its end it was provided with a vertical rectangular concrete box with a central hole in it. The model was fixed to the floor of the laboratory by passing a 40 mm diameter mild steel rod through the hole in the model and in the floor. This arrangement is shown in Figure (5.10). All the other models had a vertical hole in the wall and were positioned by using the steel stand and a prestressing strand as shown in Figure (5.11). A small prestressing force of 2 kN was applied to the strand.

5.6 LOADING ARRANGEMENT

It has already been mentioned in the previous chapters that the wind load was simulated by the uniform displacement of the edge of the slab representing the centre line of corridor opening (line of contraflexure). This was achieved by means of a loading frame which consisted of two rectangular hollow sections. The upper beam rested on the edge of the slab while the lower beam was supported from upper beam by means of the two threaded steel rods of 25 mm diameter mild steel, one on each side of the beams. The Frame was pulled down by a manually operated hydraulic jack with the help of a steel rod, the upper end of which was fixed to the lower/

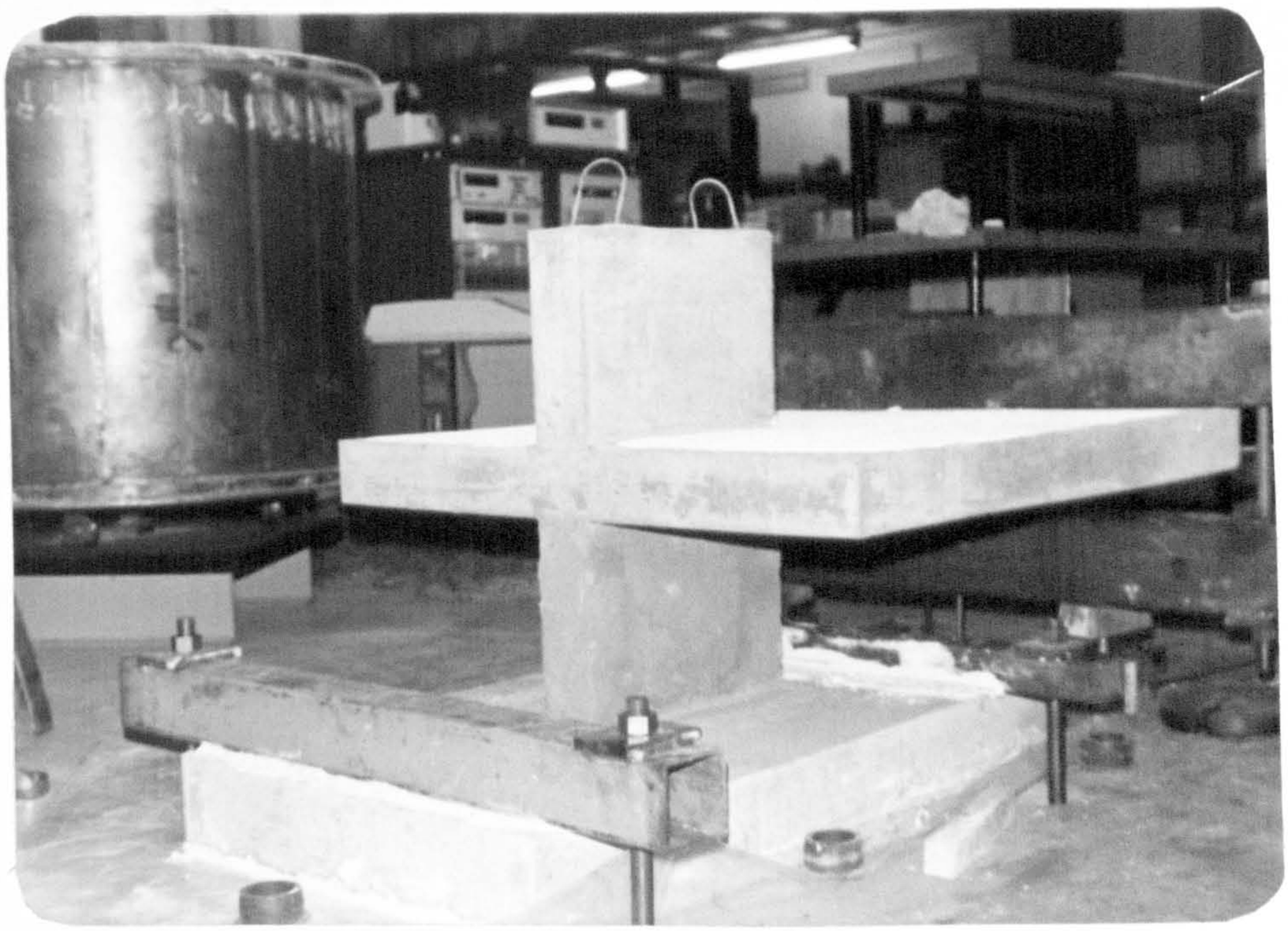

Figure (5.9) : Arrangement to support model PT1 during test.

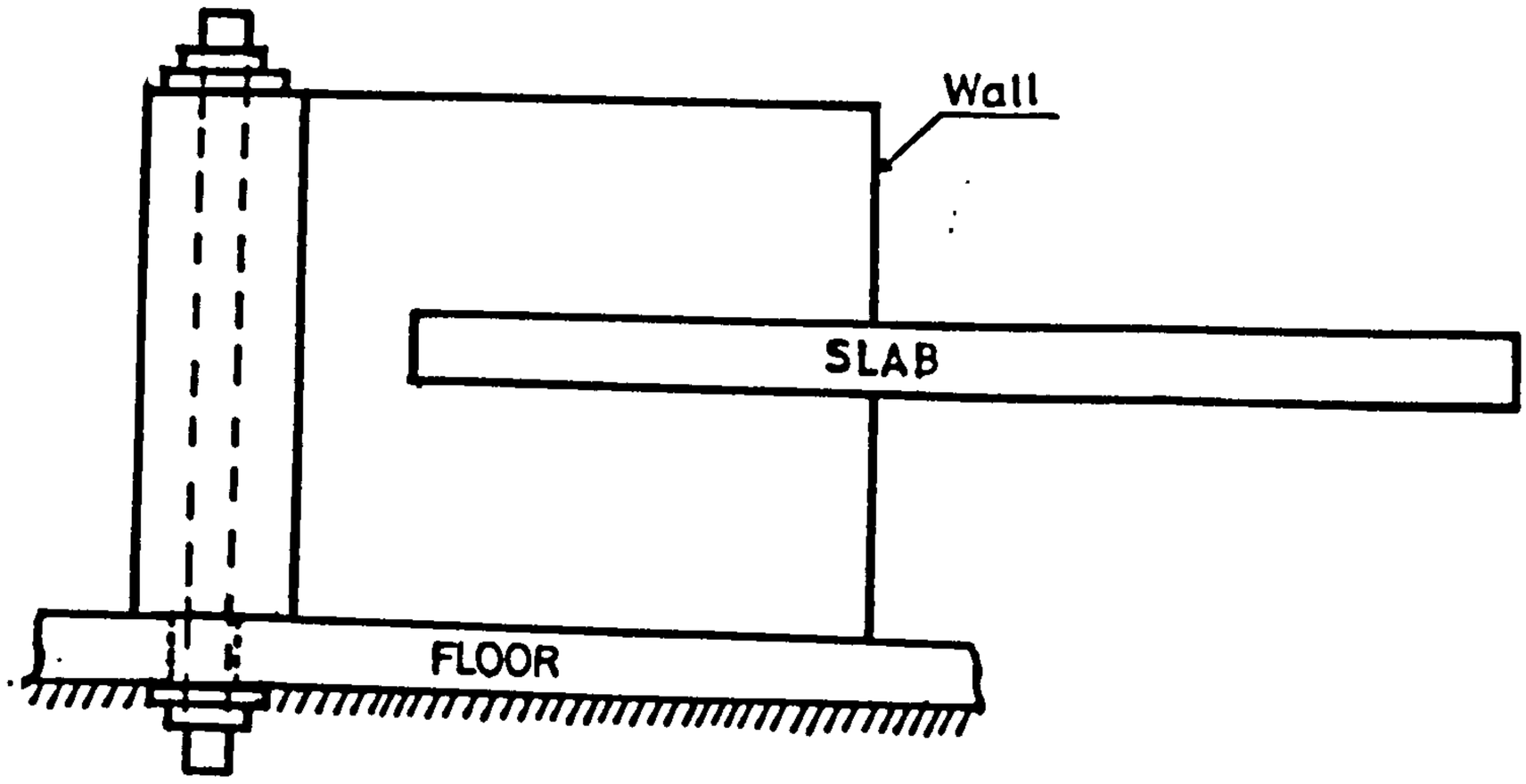

Figure (5.10) : Supporting arrangement for models PT2 and PT3.

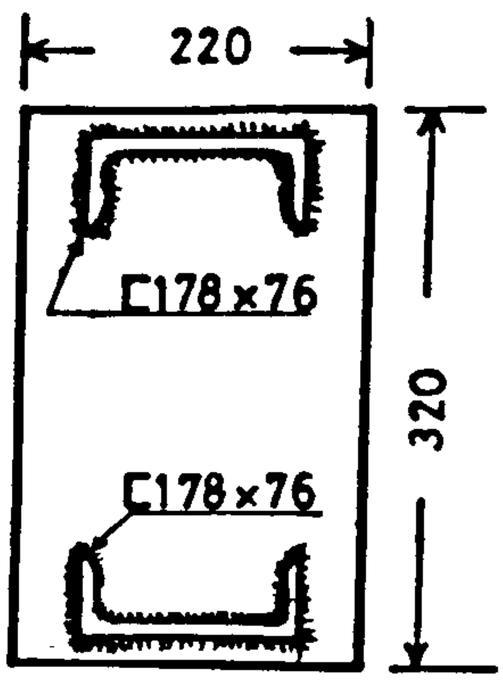

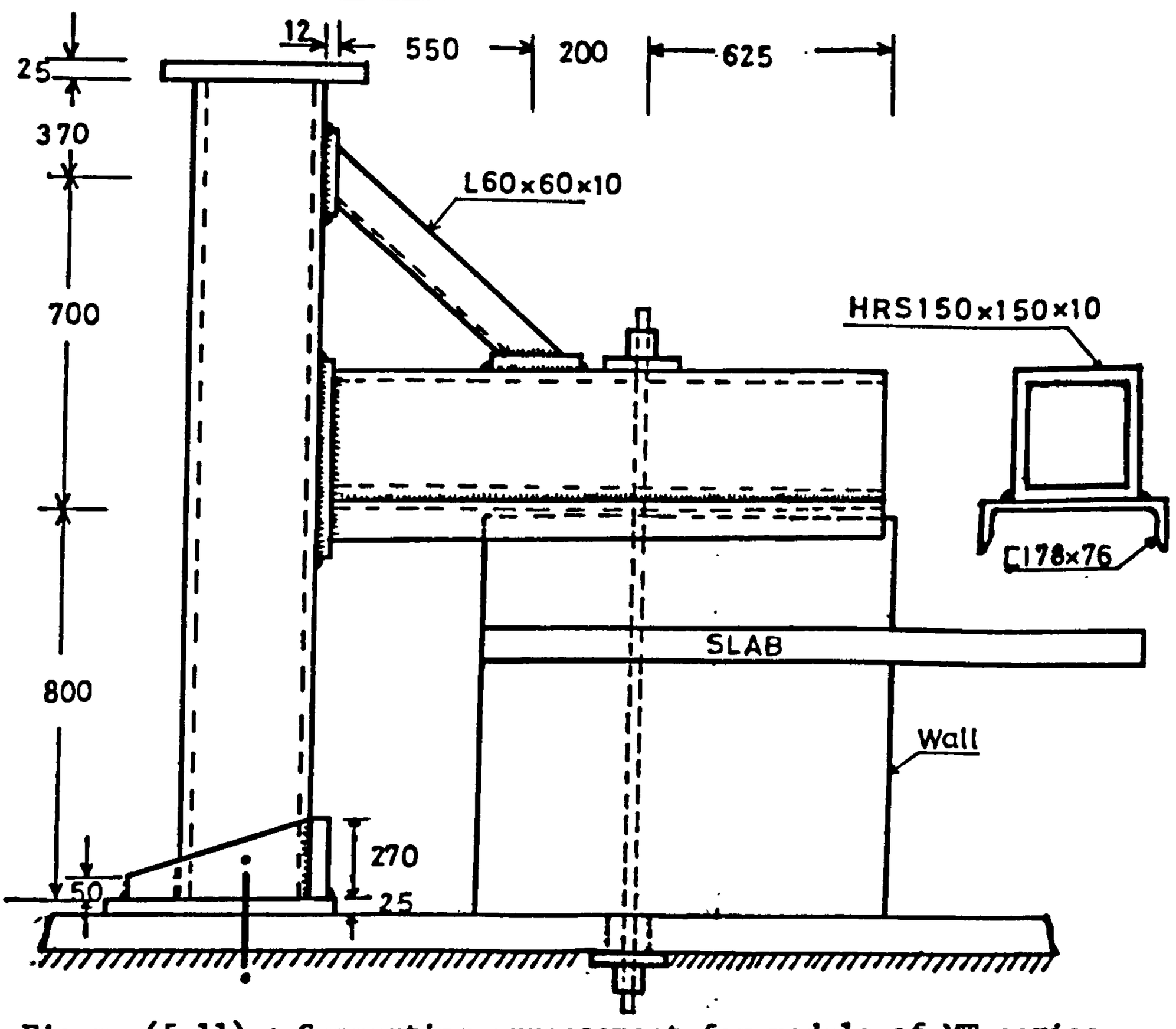

Figure (5.11) : Supporting arrangement for models of MT series.

beam at its centre. This arrangement is shown in Figure (5.12). For the models which were tested for combined loading, the additional gravity load was applied with the help of two additional side beams (Rectangular hollow steel sections) by tightening the nuts of four 12 mm diameter steel rods which were passed through the holes in the beams, slab of the model and the bottom beams (which were fixed to the floor of the laboratory), provided for this purpose. The loading arrangement for applying the gravity load is shown in Figure (5.13). Photographs showing loading arrangement are shown in Figure (5.14).

5.7. TEST PROCEDURE

Initial no load readings were taken of all the dial gauges, transducers, load cells and strain gauges for each of the models before starting the test. Care was taken to see that the applied load was not causing any eccentricity and consequent twisting of the model. To allow for the overall deformation, creep etc., the readings were taken five minutes after application of each load increment and the possibility of crack formation if any, was observed. If there were any cracks formed, they were marked on the model and the number of that loading stage was written at the tip of the crack by drawing a short cross line. The total time for each test was in the range of four to six hours.

The strength properties of the concrete were obtained by testing the cubes & cylinders on the day of testing each model.

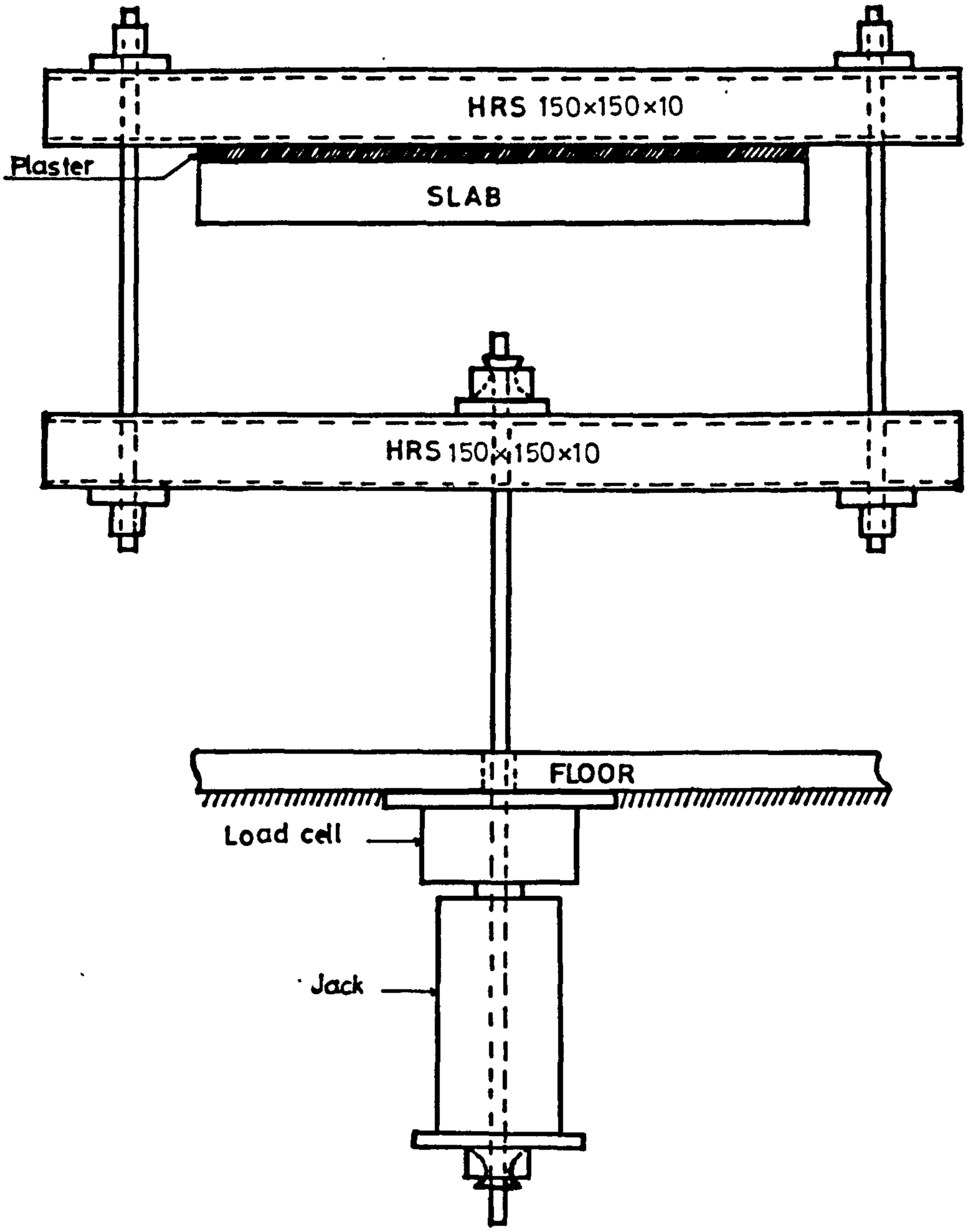

Figure (5.12) : Loading arrangement for models (gravity load omitted).

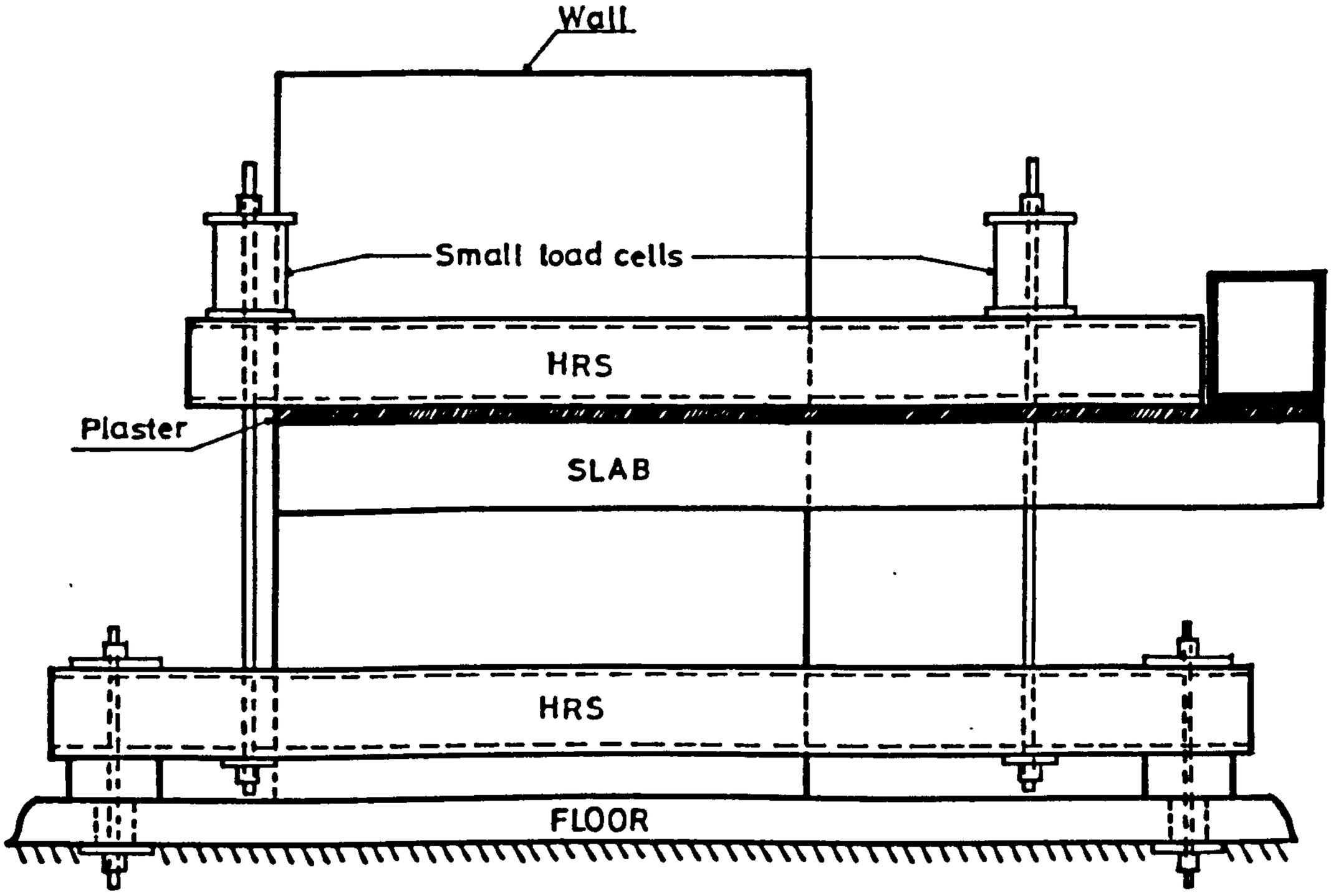

Figure (5.13) : Loading arrangement for models (gravity load alone).

Figure (5.14) : Loading arrangement of a typical model.

C H A P T E R S I X

EXPERIMENTAL STUDY

6.1 GENERAL

It was stated in chapter two that due to the effect of lateral loads very large moments and shears are induced in the connecting slabs of a shear wall structure. The strength of a shear wall-slab connection is greatly reduced due to the transfer of these moments. The situation is further aggravated by the presence of gravity loads. Methods have been proposed by different investigators to estimate the strength of wall-slab connections subjected to lateral loads alone. But all the work is mainly theoretical in nature and is based on elastic analysis. Therefore the object of the experimental study presented in this chapter was to obtain a better understanding of the strength and stiffness of cast insitu concrete shear wall and slab junctions subjected to different combinations of lateral (wind) and vertical (gravity) loads. A typical wall-slab junction acted upon by shear and moment due to wind and gravity loads is shown in Figure (6.1).

It was intended to study the behaviour of the specimens in terms of

(a) Load-deflection relationship (i.e. bending stiffness of the connecting slabs).

(b) Strain distribution in steel and concrete at critical section.

(c) Crack pattern and crack propagation.

(d) Modes of failure and failure characteristics and

(e) Ultimate load.

The shear force due to wind load acts along the line of contraflexure (approximately the centre line of the corridor opening), while the critical section for moment passes through the slab at the inner edge of the wall as shown in Figure (6.1). Since the distribution of shear due to wind loads is not uniform, this shear will hereafter be referred to as uneven shear and the moments due to wind load will be called unbalanced moments. Usually the term unbalanced moments is used for the moments acting on a slab only on one side of the column in a slab-column structure. Unbalanced moment results from uneven loading of adjacent bays, unequal consecutive slab spans, edge columns and in the case of slab-column structures due to lateral load where the columns are required to act with the slabs as a frame resisting lateral forces.

6.1.1 Parameters of Study

The effect of the following parameters on the strength of the connection was studied.

1. Wall width.
2. Ratio of total gravity load to wind load. (V_g/V_w).
3. Ratio of unbalanced moment (i.e. maximum moment due to wind load) to uneven shear (i.e. maximum shear due to wind), (M_w/V_w)
4. Ratio of moment due to gravity load to shear due to gravity load (M_g/V_g).
5. Ratio of flexural reinforcement in the slab.

The range of parameters are so chosen that the nondimensional structural parameteric ratios would cover the practical range of tall buildings.

6.1.2 Boundary Conditions

The boundary conditions in the original structure require that the slab of the specimens should be continuous along its sides and the central line of the corridor opening (representing the line of contraflexure) be displaced uniformly to simulate the effect of wind loading. But due to practical difficulties it was not possible to simulate the continuity of the slab along its sides during experimental work. Therefore only a portion of shear wall structure shown double shaded in Figure(6.2), with all the edges of slab free, was chosen for this study. This might have affected the overall behaviour of the models to some extent but as appears from literature review for column-slab connections this effect is not significant.

6.1.3 Overall dimensions of models

In scaling down the prototype dimensions, uniform scaling down of all the dimensions could not be adopted, since it would have resulted in too thin walls and slabs. However it was possibly not necessary because the investigation was concerned with the local effect near the wall-slab junctions. Therefore the overall dimensions were fixed based on the factors such as required non-dimensional structural parameteric ratios, $\frac{V_w}{V_g}$ (where V_w stands for uneven shear due to wind load and V_g for shear due to gravity load), $\frac{M_w}{V_w}$ ratios (Here M_w is for unbalanced moments due to wind loads along critical section for flexure) and other factors such as the location of the holes in the floor of the laboratory (which are staggered at a spacing of $440\sqrt{2}$ mm), which dictated the loading and support positions to a certain extent. The loading and supporting arrangements have already been described in chapter five.

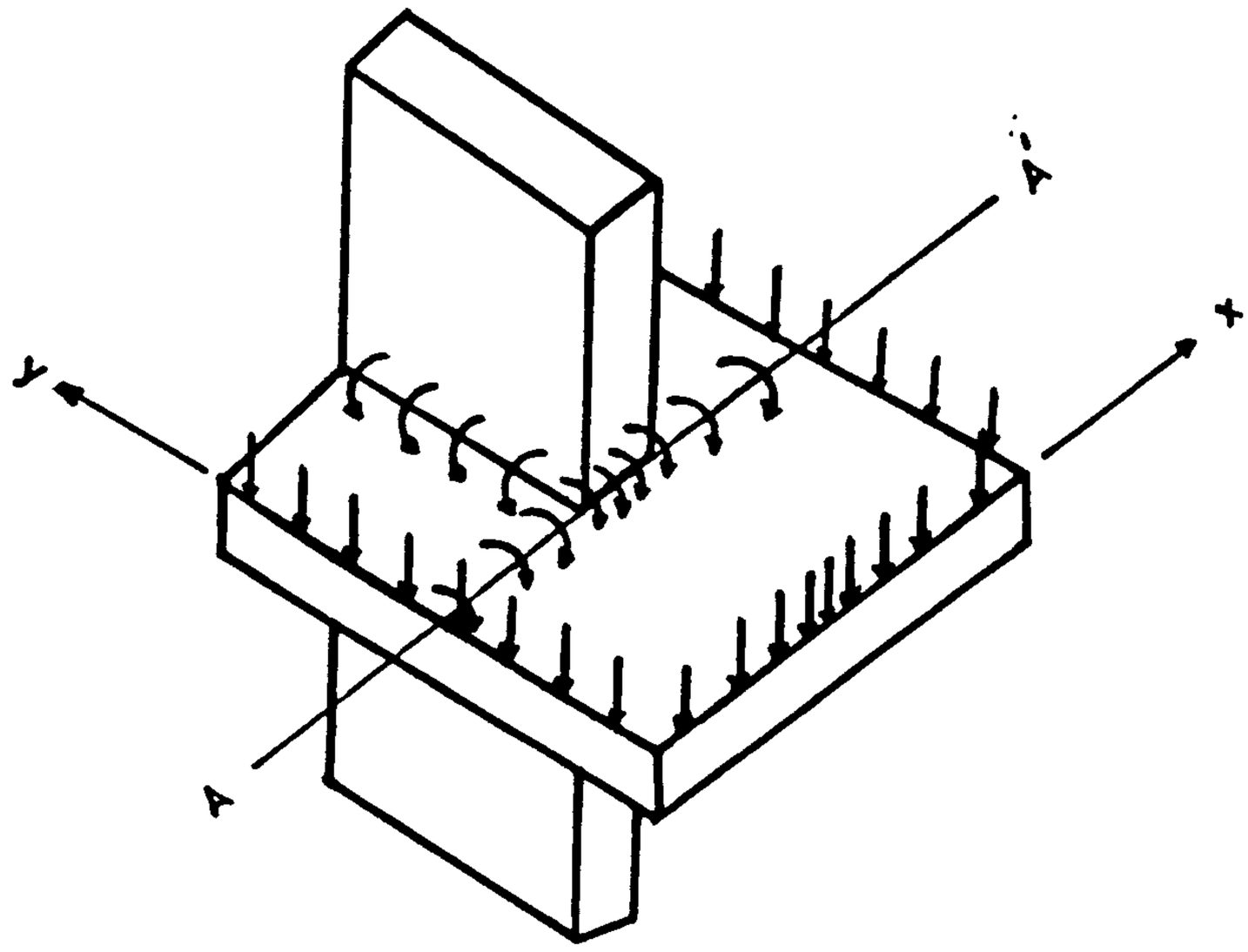

Figure (6.1) : A typical wall-slab connection showing moments and shear due to lateral and gravity loads.

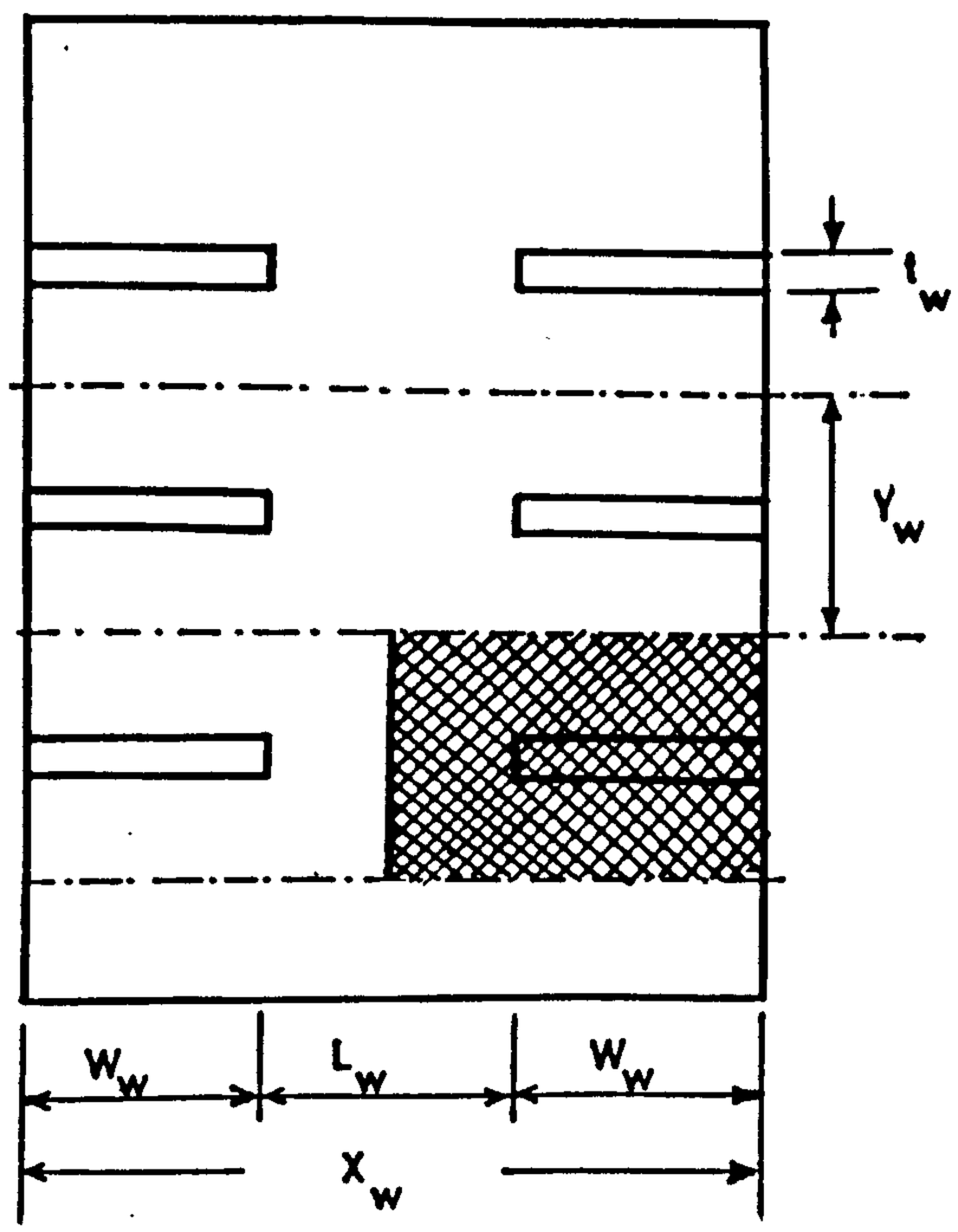

Figure (6.2) : Plan of a typical shear wall-slab building.

6.2 TEST PROGRAMME

The test programme may be divided into two parts:

(i) PT series (Preliminary Tests)

In all three models were tested

(a) PT1 ; with base clamp

(b) PT2 ; with enlarged column clamp

(c) PT3 ; with slot to prevent direct moment transfer from the slab to the wall.

Preliminary tests were conducted on those models to study their behaviour and experimental setup before actually proceeding with the test programme. These models were tested for wind load alone which was applied by means of rigid beam along the centre line of corridor opening, displacing it uniformly.

(ii) MT Series (Main Tests)

This series of tests contains eleven tests, which depending upon the parameters involved can be subdivided into different groups as shown in table (6.1). These models were tested for combined wind and gravity loading.

From the various experimental data using dial gauges, displacement transducers and strain gauges, desired values of deflections and strains were evaluated. Photographs showing different views of crack pattern were prepared.

All the measured displacements were corrected for rigid body rotations of the model about the bottom inner edge of wall as shown in Figure (6.3) and for this purpose the upward movement of the model/

Table 6.1

Group No.	Main parameter	Tests in group
I	Wall width	MT1, MT2 & MT3
II	$\frac{\text{Gravity load}}{\text{Wind load}}$ ratio	MT2, MT4 & MT5
III	$\frac{M_w}{V_w}$ ratio	MT6, MT3 & MT7
IV	$\frac{M_g}{V_g}$ ratio	MT3 & MT8
V	Flexural steel	MT3 & MT9
VI	Flexural steel	MT10, MT7 & MT11

Subscripts: g = gravity, w = wind

M = moment) at wall-slab junction

V = shear force)

Note: Certain tests are common to more than one groups.

MT2 is common to groups I & II.

MT3 is common to groups I, III, IV & V.

MT7 is common to groups III & VI.

at its back was measured by a dial gauge.

In addition to the corrections due to rigid body rotations the measured displacements were corrected against wall deformation as well, using the following procedure.

It is assumed that along a vertical line the strains are constant in the wall. In other words any horizontal section of the wall will have the same strain. Therefore

$$\delta = H.\varepsilon$$

Therefore referring to Figure (6.4)

$$\delta_1 = H.\varepsilon_1 \text{ and } \delta_2 = H.\varepsilon_2$$

$$\text{Then } \theta = \frac{\delta_1 - \delta_2}{B}$$

where ε_1 and ε_2 are the measured strains in the walls at points (1) and (2)

δ_1 and δ_2 are the wall deformations at sections (1) and (2) and H and B are as shown in Figure(6.4).

$$\text{Then correction} = \theta.L_c \qquad (6.1)$$

where L_c is as shown in Figure (6.4)

The various experimental data on the behaviour of the models and the results are presented for each model in the following order.

(i) Sketches showing shape and dimensions of the model.

(ii) Reinforcing details of the model.

(iii) Load-deflection curve for the model.

(iv) Distribution of strains.

(v) Crack pattern of the model.

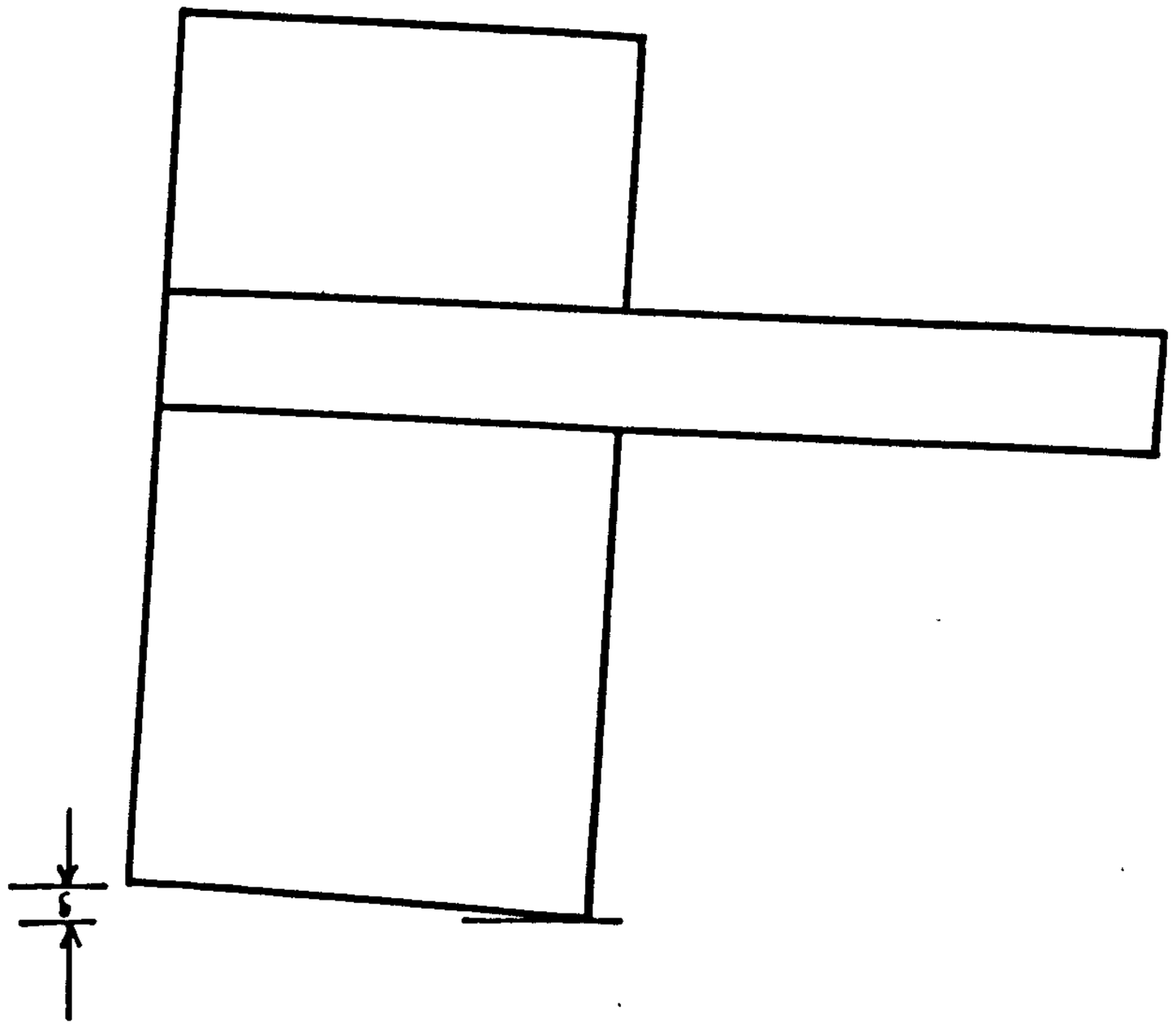

Figure (6.3) : Rigid body rotation of a model due to wind load.

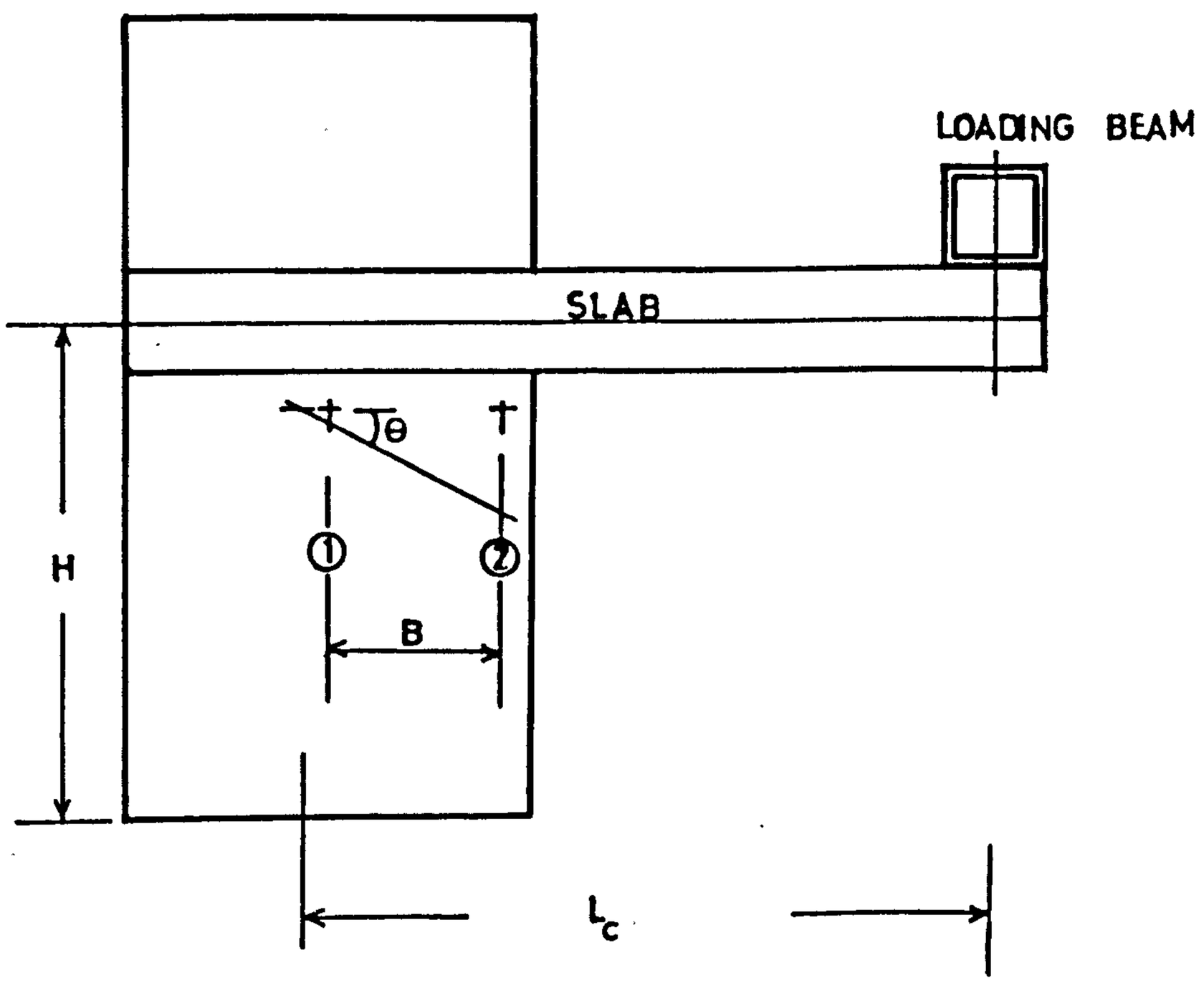

Figure (6.4) : Correction of displacement due to wind loading against wall deformation.

The tensile and compressive strength of concrete and modulus of elasticity on the day each model was tested are given in Table (6.2).

6.3 PRELIMINARY TESTS - PT series

6.3.1 Design of models

The slabs of the models of preliminary test series were provided with a uniform ratio of flexural steel 1.03% both ways at the top only. The flexural ultimate moment of resistance along the critical section was calculated from:

$$M_r = A_s f_y Z \quad \text{where } Z = \left(1 - \frac{f_y A_s}{1.33 f_{cu} bd}\right)d \qquad (6.2)$$

Here f_y is the yield stress of steel

A_s is the area of the steel

f_{cu} is the cube crushing strength of the concrete

b is the width of the slab and

d is the effective depth of the slab

This is similar to CP 110 stress block approach except that material factors of safety have been eliminated and measured values of f_{cu} for concrete and f_y for steel were used in the calculations.

For models PT1 and PT2 the equivalent maximum design wind load to be applied along the line of contraflexure was calculated from M_r which was found to be equal to 51 kN and 62 kN respectively. The reason for the change is the effective depth of slab which was/

Table 6.2. Properties of the concrete at the time of testing of each model.

Model No.	No of days	f_{cu} N/mm^2	f N/mm^2	E N/mm^2
PT1	28	40.0	2.79	19,581
PT2	28	40.6		
PT3	28	40.3		
MT1	28	37.0	2.95	18,500
MT2	28	50.2	3.6	20,830
MT3	22	42.8	3.0	
MT4	23	33.1	3.1	
MT5	14	33.2	3.15	
MT6	15	32.2	2.6	
MT7	21	41.8	3.2	
MT8	30	32.0	2.86	
MT9	18	33.77	2.62	20,069
MT10	19	34.85	3.2	
MT11	15	32.8	3.05	

70 mm for PT1 and 80 mm for PT2. The wall was designed for relatively higher load of 80 kN, using CP 110 recommendations for eccentrically loaded columns.

6.3.2 Model PT1

Having decided to test a portion of structure shown double shaded in Figure (6.2) the next question was how to support the model and that is how models of preliminary test series were tested.

As an initiation of experimental work a model, the shape and dimensioned sketch of which is shown in Figure (6.5), representing a portion of shear wall - slab structure, with half corridor opening and one plannar wall and nondimensional structural parameteric ratios, $\frac{L_w}{X_w} = 0.58$, $\frac{Y_w}{X_w} = 0.53$, $\frac{Z_w}{W_w} = 0.25$ & $\frac{Z_w}{Y_w} = 0.1$ was tested. The effective width of slab of this model (as found from the curves prepared by Coull & Wong (5)) was 0.63 Y_w, where Y_w is the bay width. The slab was reinforced only at the top, with nine - 12 mm diameter steel bars in each direction (i.e. 1.03%). The bars were uniformly spaced and the clear concrete cover was 24 mm. The wall was reinforced with six - 12 mm diameter bars, the clear distance of bars from edges being 20 mm. Links of 6 mm diameter mild steel bars were used in the wall at a spacing of 85 mm c/c in vertical direction. The arrangement of steel is shown in Figure (6.6). The model was tested for wind load alone, which was applied in equal increments of about .89 kN and the readings of dial gauges and strain gauges were noted for each load increment. When the load reached at 43.9 kN (approximately 90% of the load at/

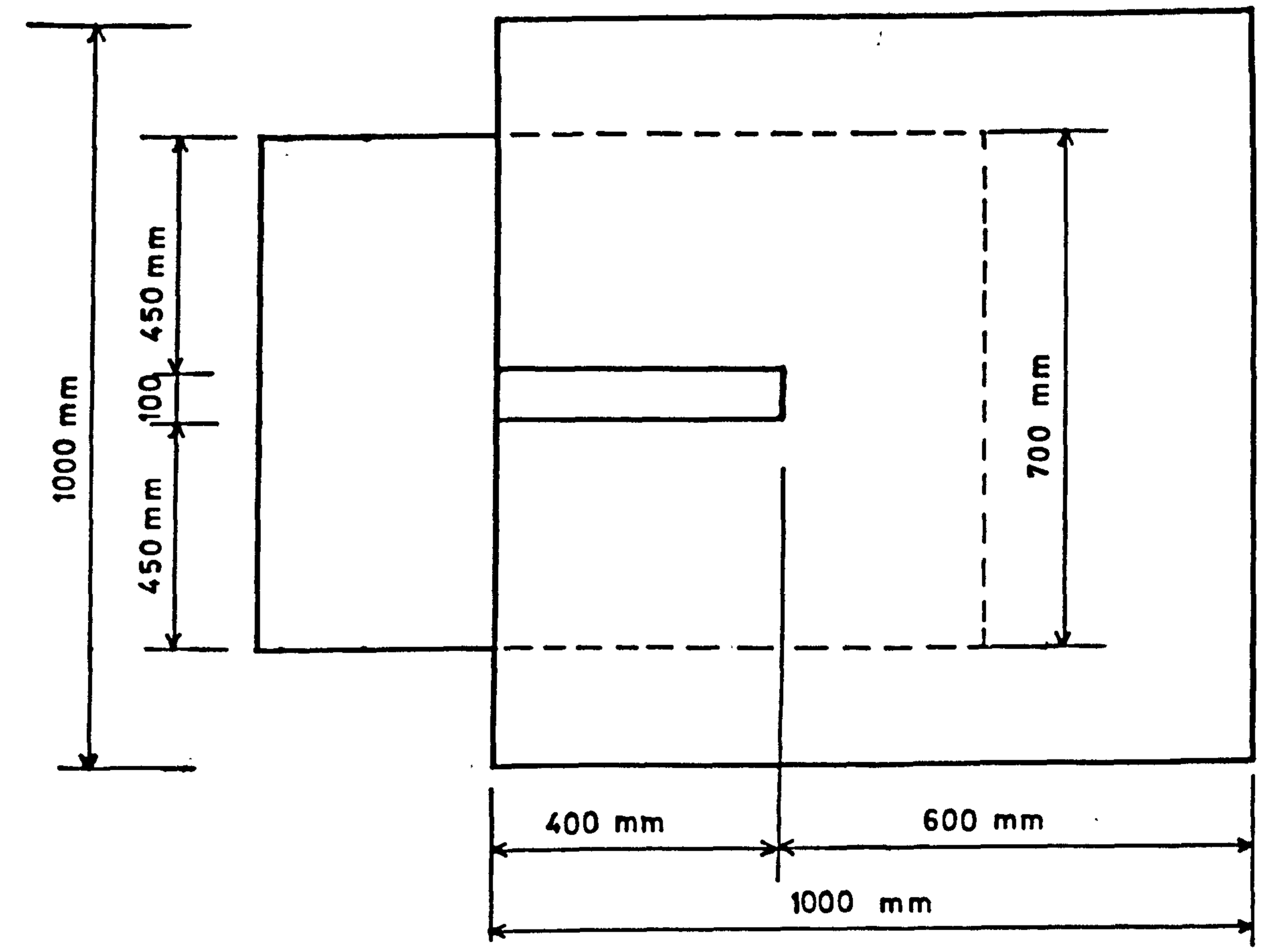

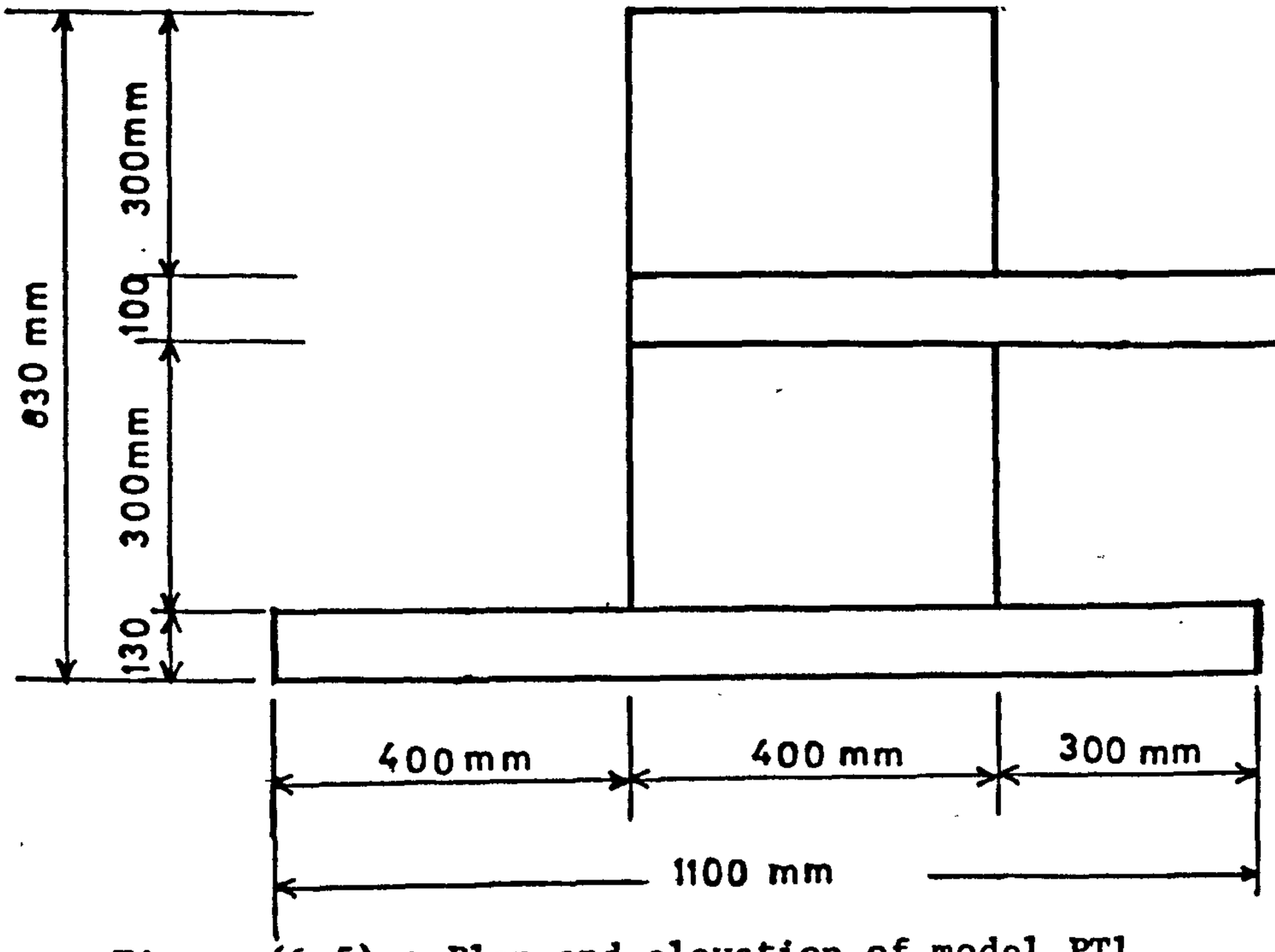

Figure (6.5) : Plan and elevation of model PT1.

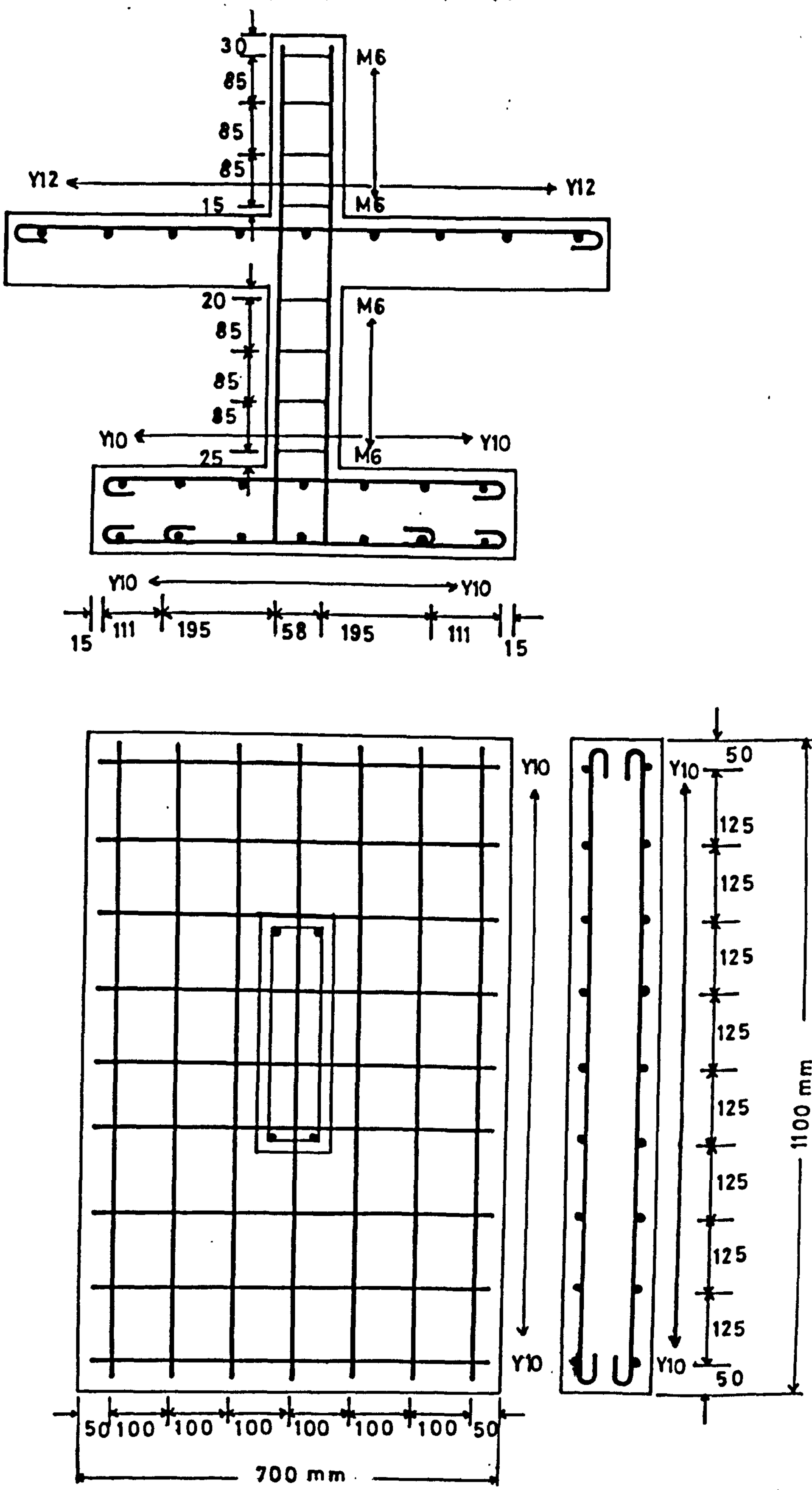

Figure (6.6) : Arrangement of reinforcing bars in model PT1.

failure), the main central bar of the testing arrangement yielded, therefore the model was unloaded. The zero load readings were taken. After replacing the main central bar by a prestressing strand, the model was reloaded with a load increment of 4.45 kN till it reached the previous load limit (43.8 kN) and then the load increment was reduced to 0.89 kN. After nondimensionalizing the applied loads. V_{app}, by dividing them by the flexural design ultimate load (V_{design} = 51 kN) of the slab and the strain in the concrete at the bottom of the slab by nominal ultimate strain in concrete (ε_{max} = .0035), graphs showing V_{app}/V_{design} versus $\frac{\text{strain}}{.0035}$ at different points along the transverse critical section for both loading cycles are plotted and shown in Figure (6.7). During second cycle of loading the strain gauge at point P_3 stopped working. Therefore V_{app}/V_{design} versus $\frac{\text{strain}}{.0035}$ for second cycle are plotted for points P_1, P_2 and P_4 only. The variation of strain in concrete at the bottom of the slab along transverse critical section at different stages of loading is shown in Figure (6.8). The curves showing V_{app}/V_{design} versus $\varepsilon_{max} = .0035$ for wall at different points is shown in Figure (6.9). Strain in wall was taken as an average value of the corresponding points on the two sides of the wall.

From Figure (6.8) it can be observed that the concentration of strains near the inner edge of wall was a maximum till the load reached 75% of the ultimate load and then the rate of increase of strain at central point P_1 started decreasing so that when the load reached 89% of its ultimate value, the strain at this point was slightly lower than at the neighbouring point P_2.

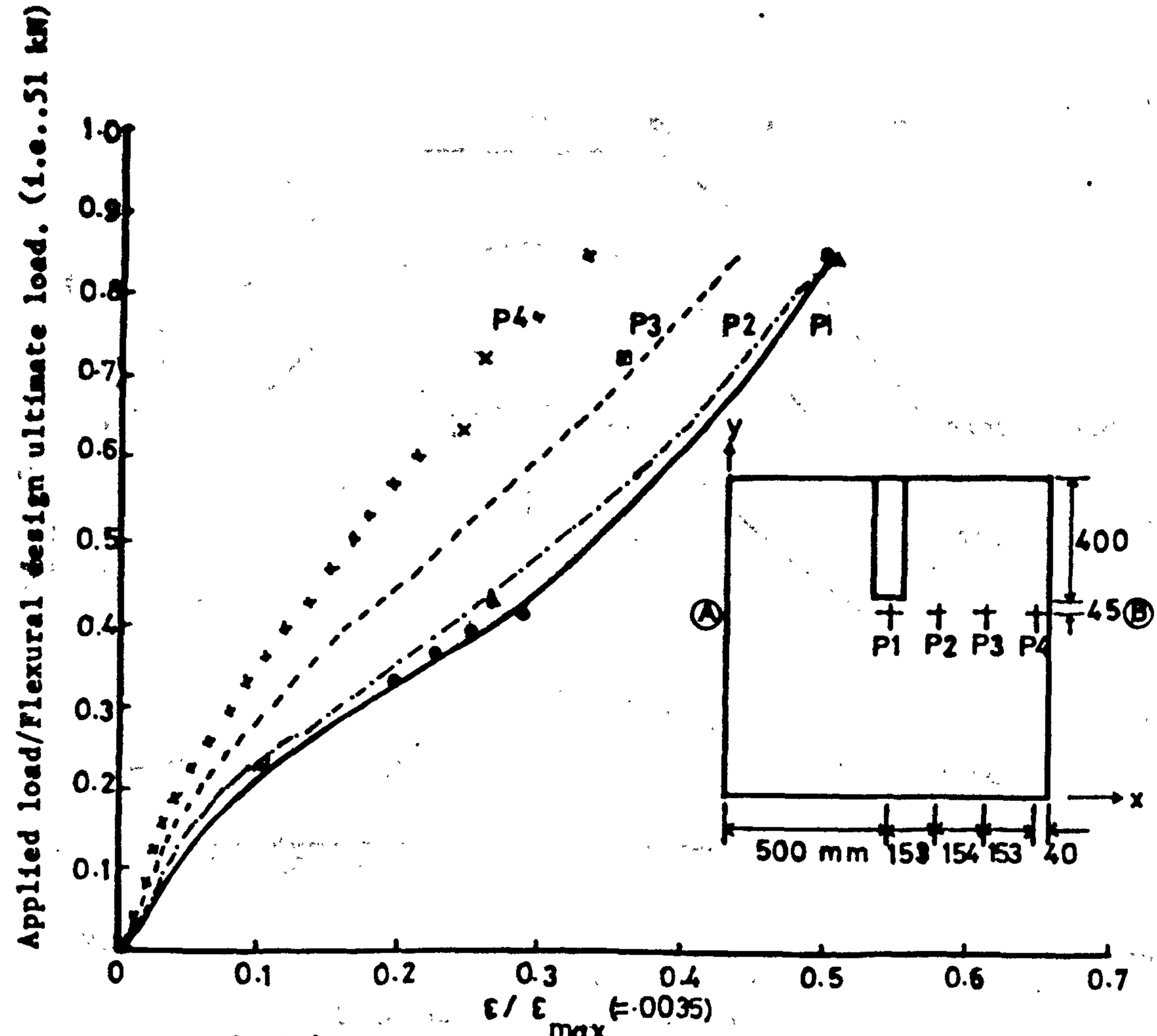

Figure (6.7a) : Comp. strain in concrete in windward direction at different points along transverse section AB in the slab of model PT1 during 1st loading cycle.

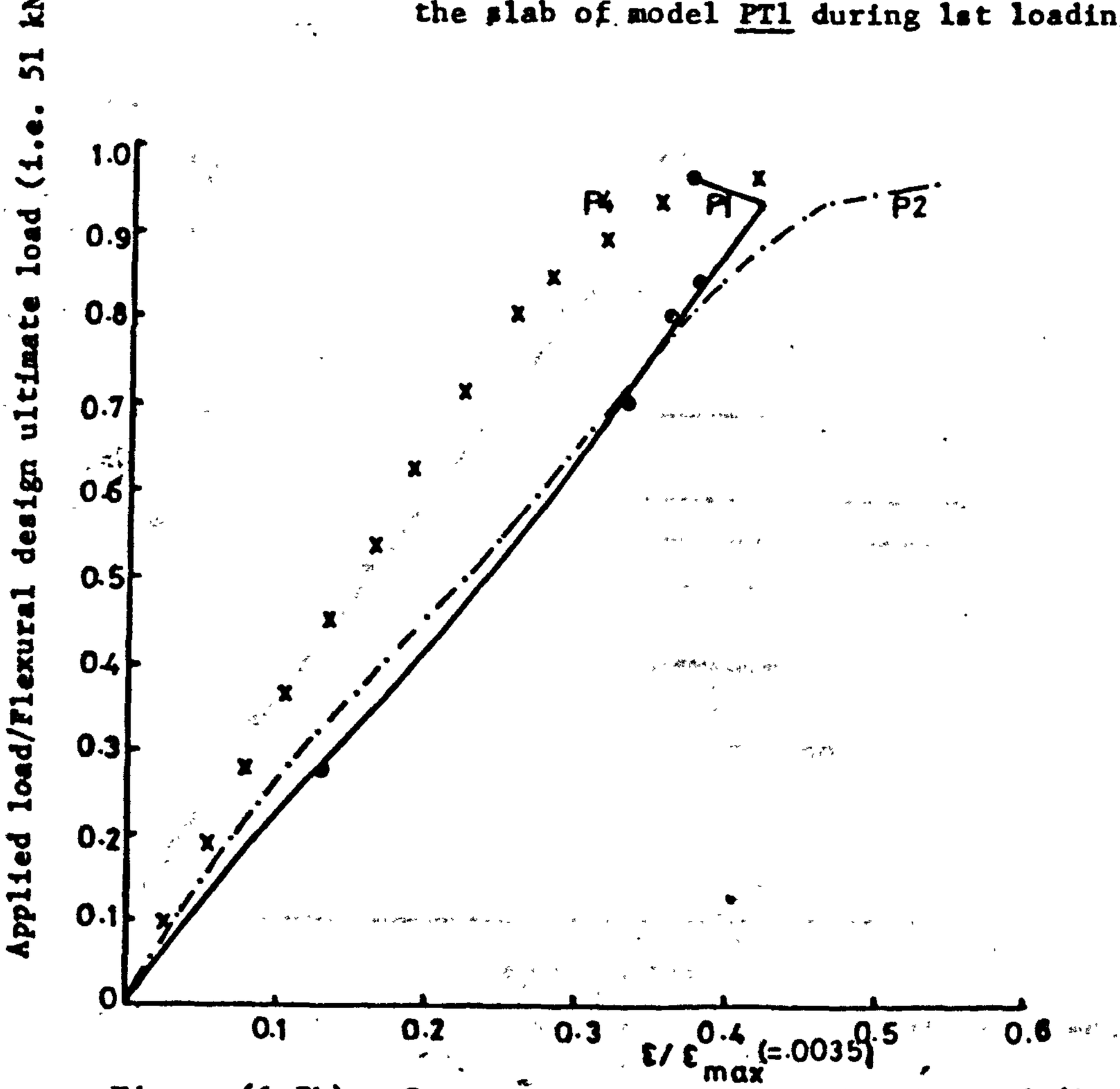

Figure (6.7b) : Comp.strain in concrete in windward direction at different points along transverse critical section AB, in the slab of PT1, during IInd cycle.

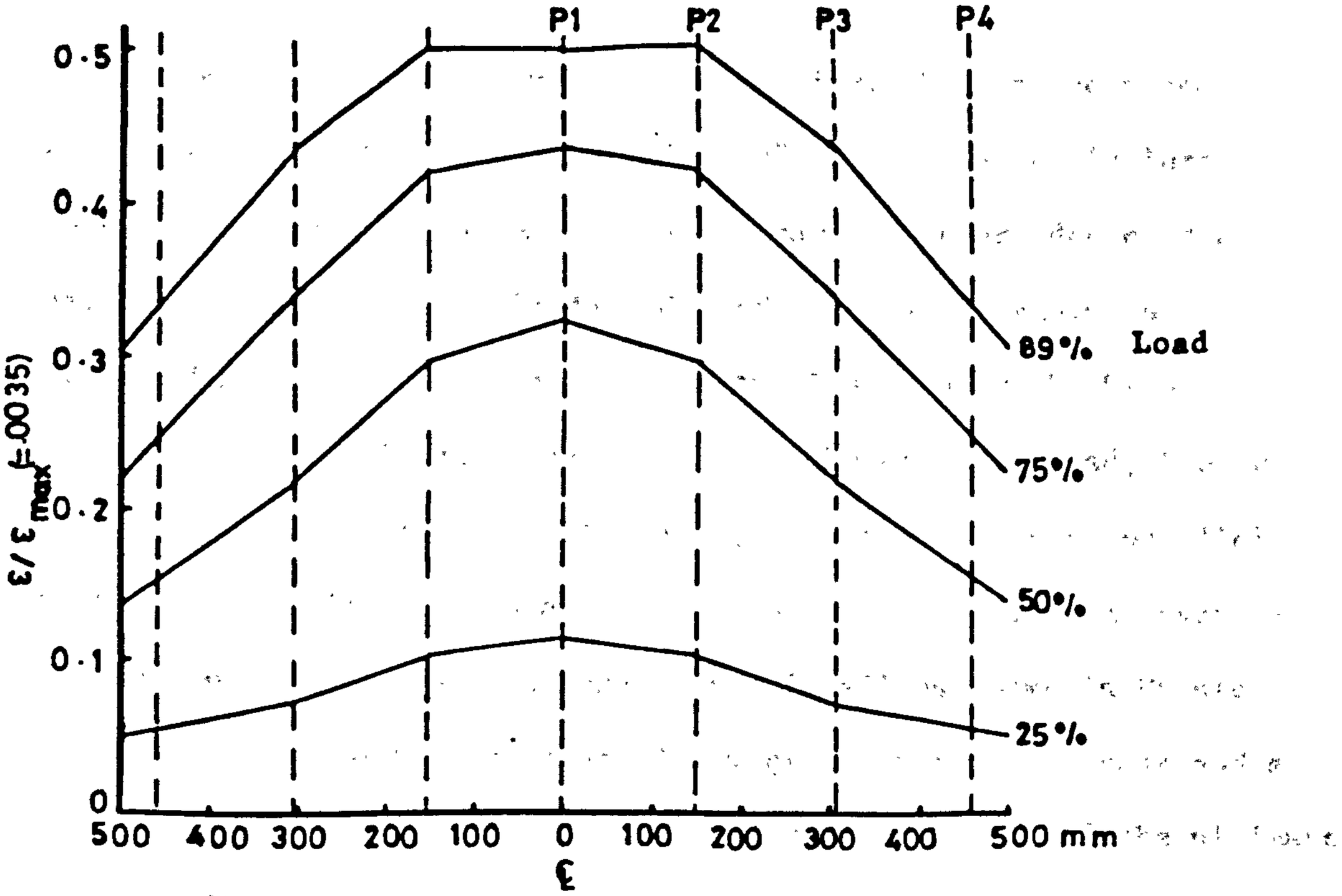

Figure (6.8) : Variation of compressive strain in concrete along transverse critical section at different stages of loading in the slab of PT1.

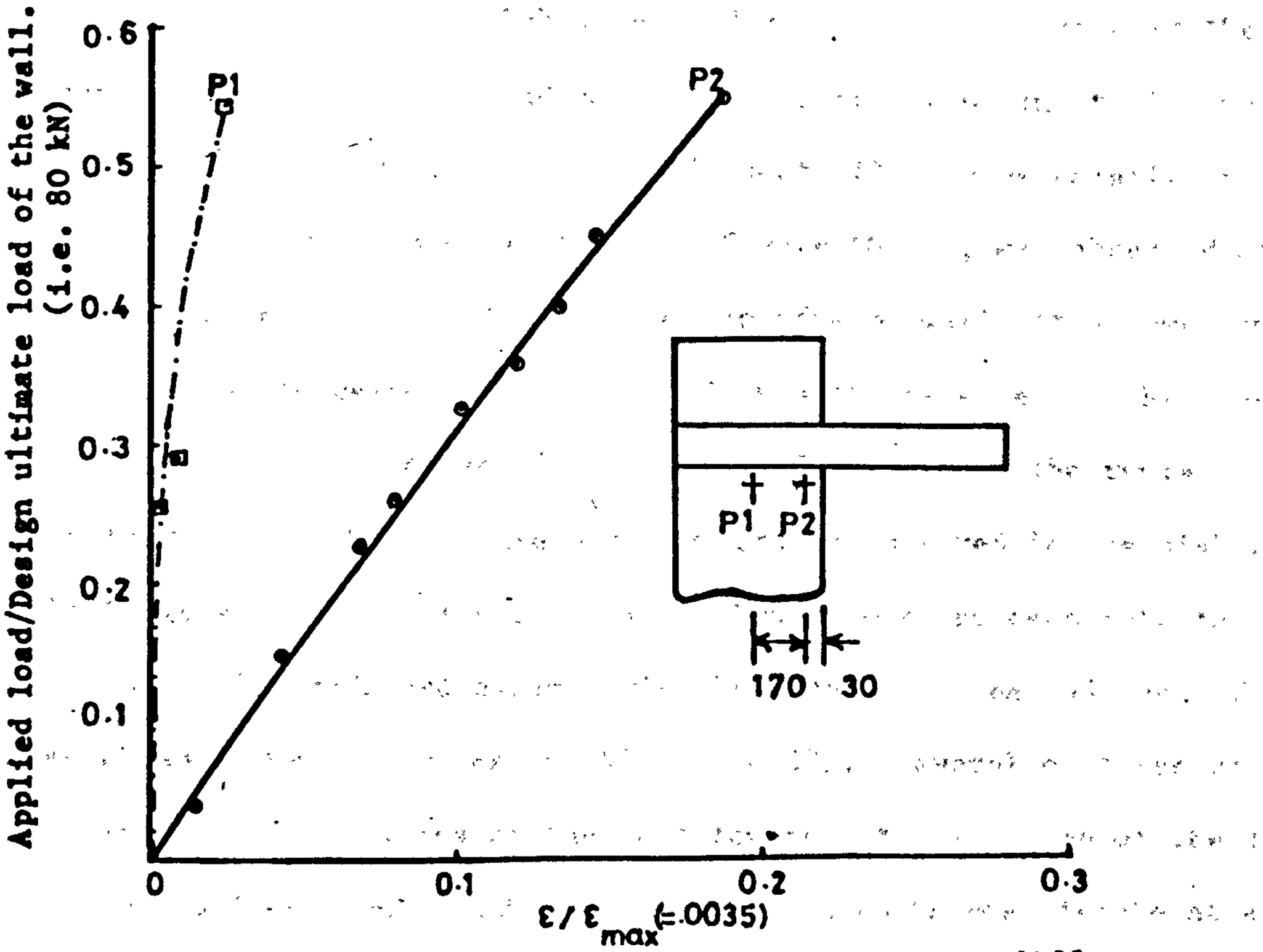

Figure (6.9) : Compressive strain in concrete at different points in the wall of PT1.

Behaviour of the model: Very fine cracks invisible to the naked eye appeared in the slab at a load of 9% of the load at failure. These cracks were approximately 75 mm from the inner edge of the wall and parallel to the loaded edge of the slab as shown in Figure (6.10). With the increase in the load the cracks became clearly visible till at a load of 13% of the ultimate load, the two joined together as shown in Figure (6.11). Another crack parallel to the loaded edge of slab occurred at a load of 24%, at an average distance of 175 mm from the inner edge of wall as shown in Figure (6.12). As the loading progressed new cracks began to appear and a vertical crack shown in Figure (6.13) developed at 35% of the ultimate load. A crack shown in Figure (6.14) at wall-slab junction had already been noted at a load of 27%, which then became more pronounced at a load of 37%, accompanied by an increase in length towards the free edge of the slab. The vertical crack travelled further towards the loaded edge of the slab at a load of 47% and reached near the centre of loading at a load of 88% and no extension in its length was found thereafter. At a load of about 51% a crack parallel to the loaded edge of slab as shown in Figure (6.15), was observed at an average distance of 275 mm from the edge of wall. It became longer as the load increased till it joined on both its sides to the cracks which were already detected when the load was within the range of 30 to 33%. In the meantime many new cracks appeared in the slab on both sides of the wall and a few of them penetrated deep into the depth of slab and were clearly visible from the sides and back of the model as shown in Figures (6.16) and (6.17). Several of these cracks radiated from the sides of the wall towards the back edge of the slab. In the wall only one crack in the tensile zone became visible at a/

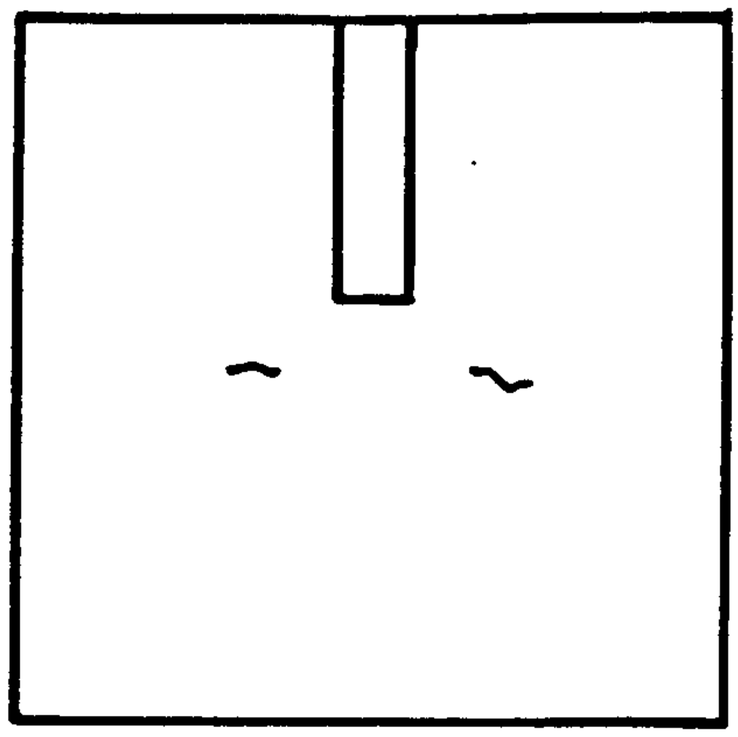

Fig. (6.10)

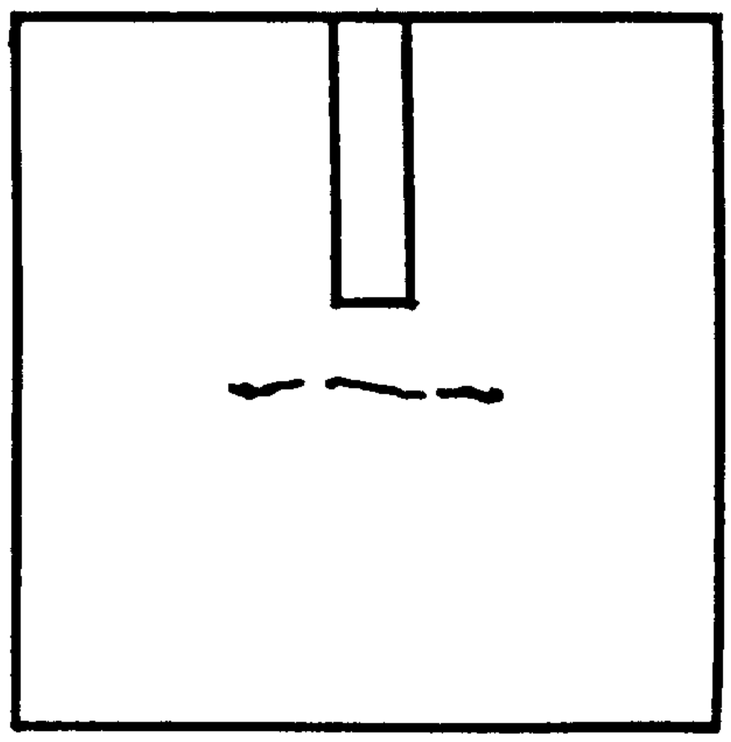

Fig. (6.11)

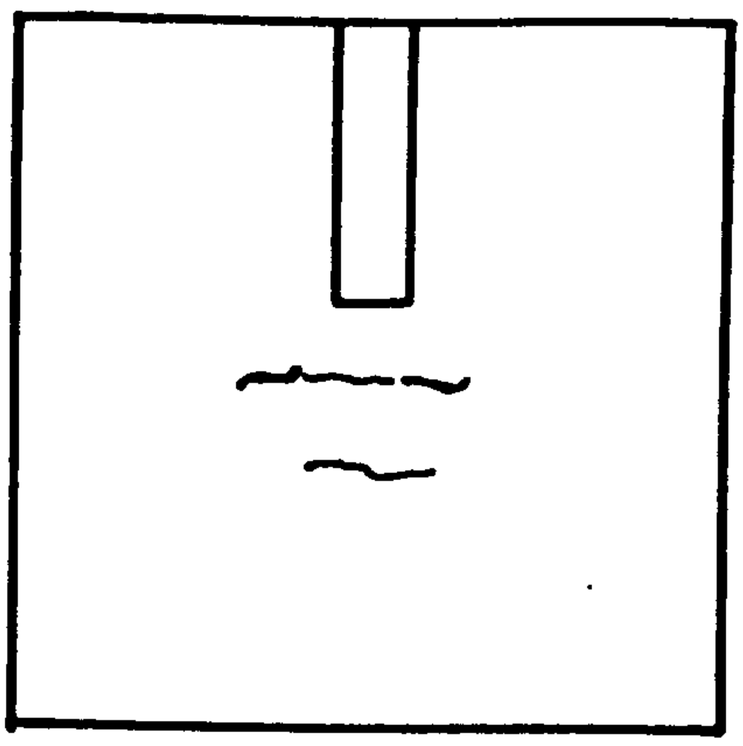

Fig. (6.12)

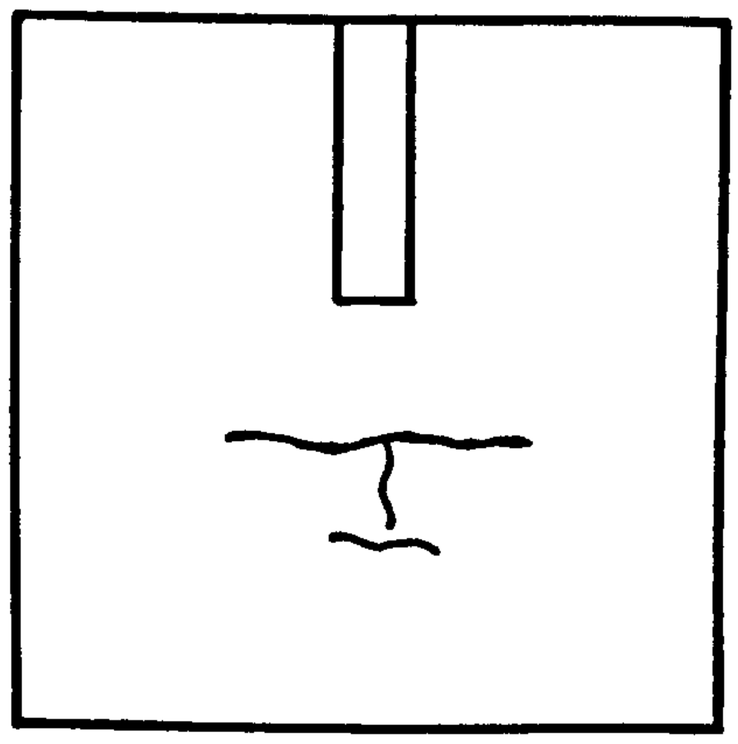

Fig. (6.13)

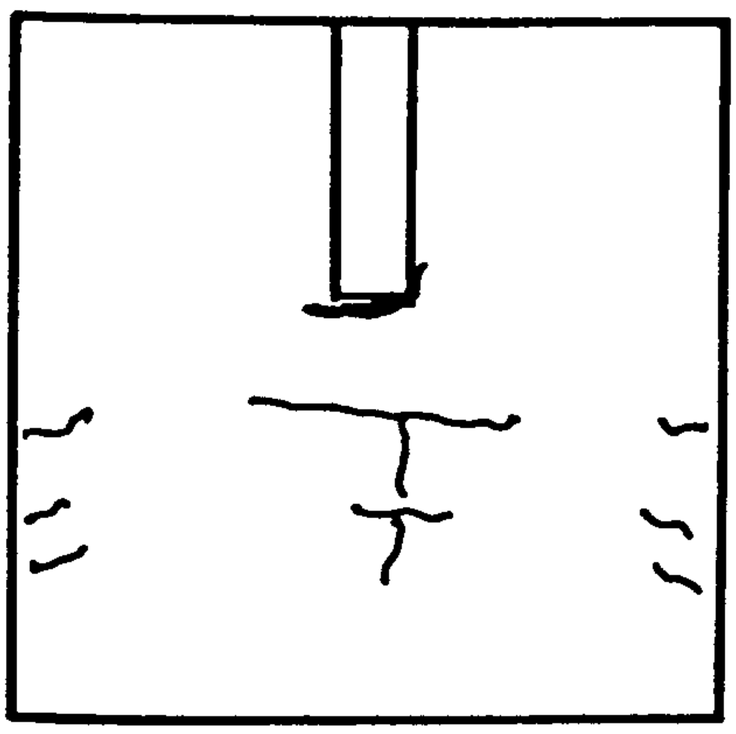

Fig. (6.14)

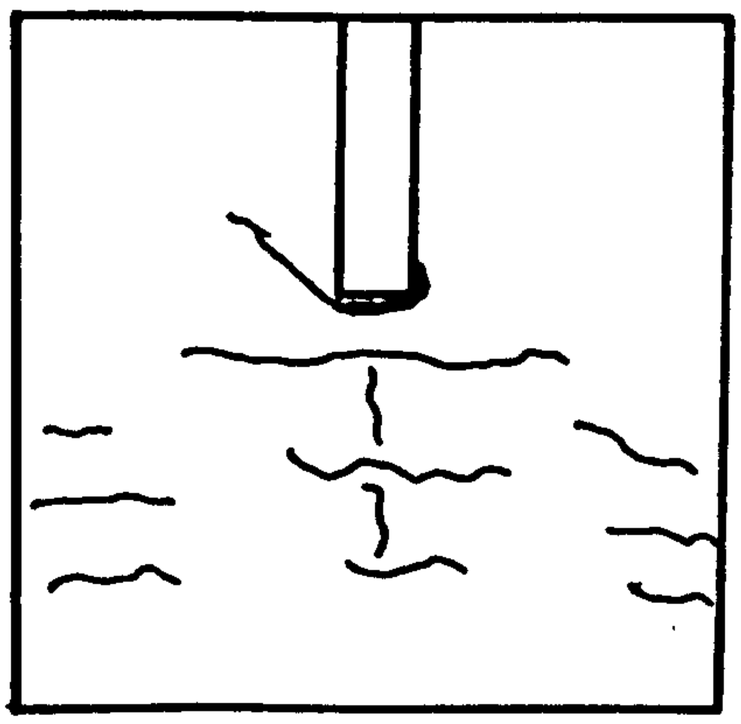

Fig. (6.15)

Figures (6.10) to (6.15), showing initiation and step by step cracking of slab of model PT1 as the loading progressed.

load of 53% and it widened when the load was about 70% of the ultimate load. Inclined shear cracks as shown in Figure (6.17) visible at the back of the model appeared in the slab when the load was only 45% of the load at failure. Several other cracks also appeared in their vicinity as the loading progressed. The crack pattern of the slab just before (at a load of 98%) and after the failure is shown in Figures (6.18) and (6.19) and the photographs are presented in Figures (6.20) and (6.21). The load at failure was 48.97 kN.

From the measured strains in concrete at the bottom of the slab along transverse critical section for flexure it was observed that the concrete had not reached its ultimate strength. Therefore it was not a failure of slab itself due to crushing of concrete. Though the strain in steel was not measured but working back from the measured compressive strain in concrete at the bottom of the slab, the strains in steel were calculated using the following approach.

Referring to Figure (6.22),

$$\frac{\varepsilon_s}{d - d_n} = \frac{\varepsilon_c}{d_n}$$

$$\text{Therefore} \quad \varepsilon_s = \frac{d - d_n}{d_n} \varepsilon_c \qquad (6.3)$$

where ε_s is the strain in steel

ε_c is the strain in concrete

d is the effective depth

d_n is the depth to the neutral axis

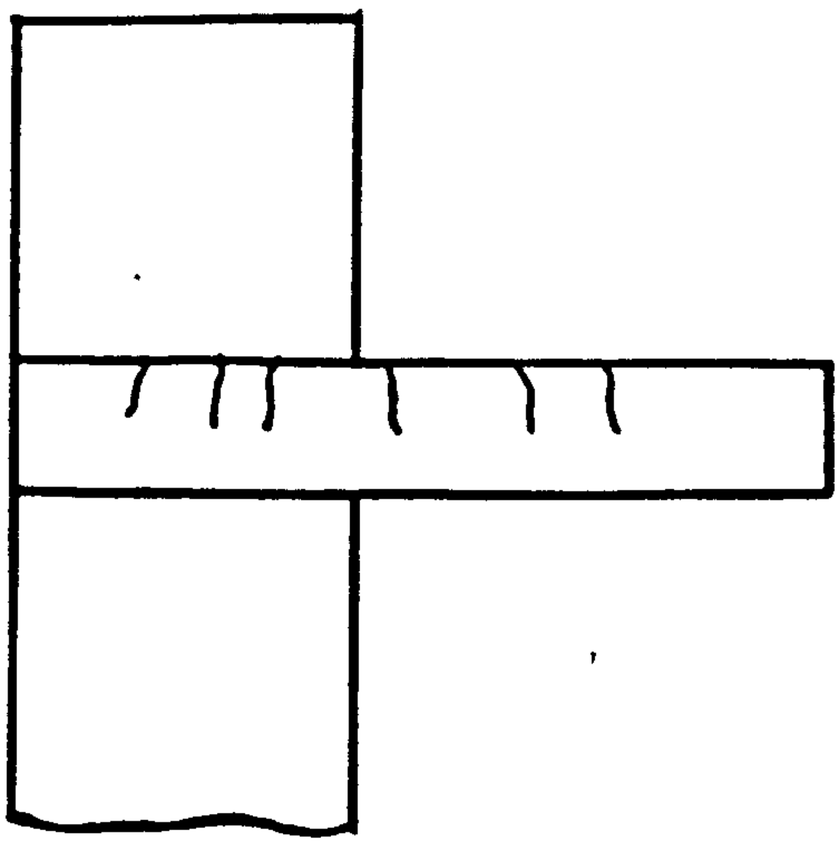

Figure (6.16) : Cracking of slab along its sides.

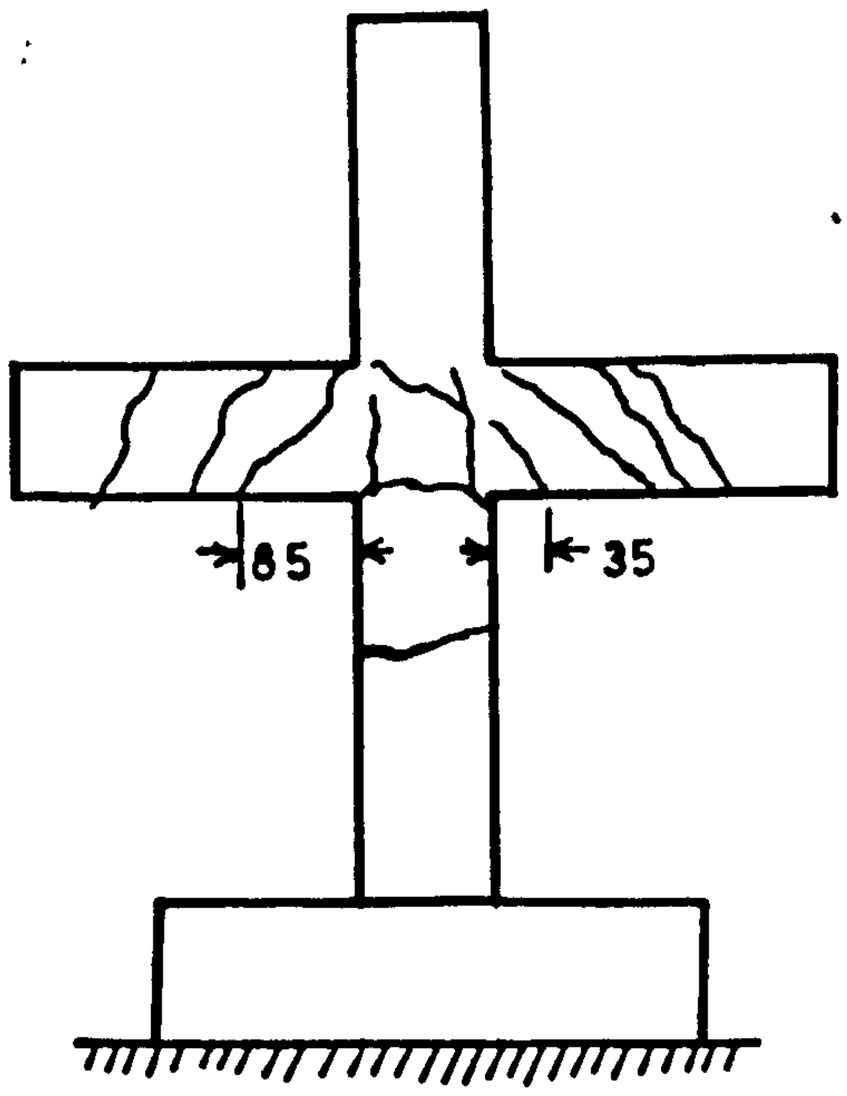

Figure (6.17) : Crack pattern after failure at the back of model PT1.

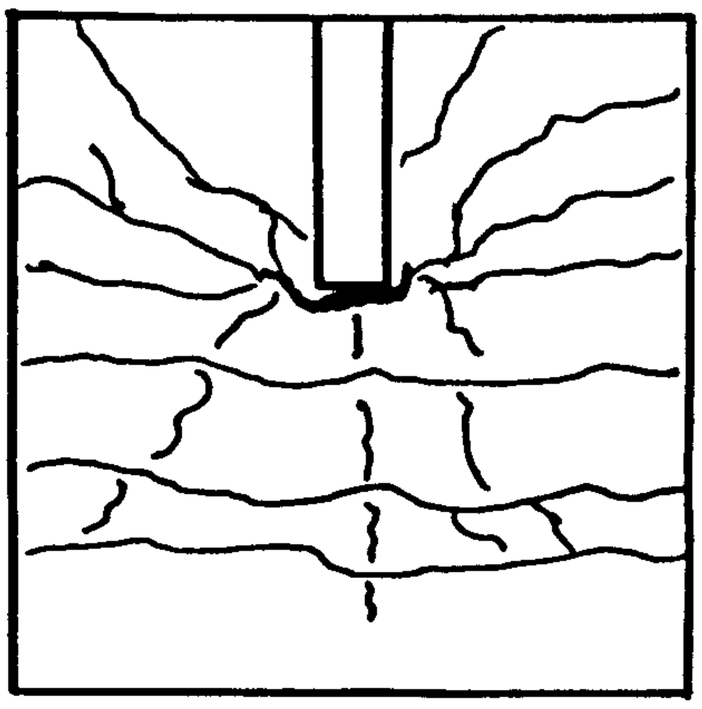

Figure (6.18) : Crack pattern of slab of PT1 just before failure.

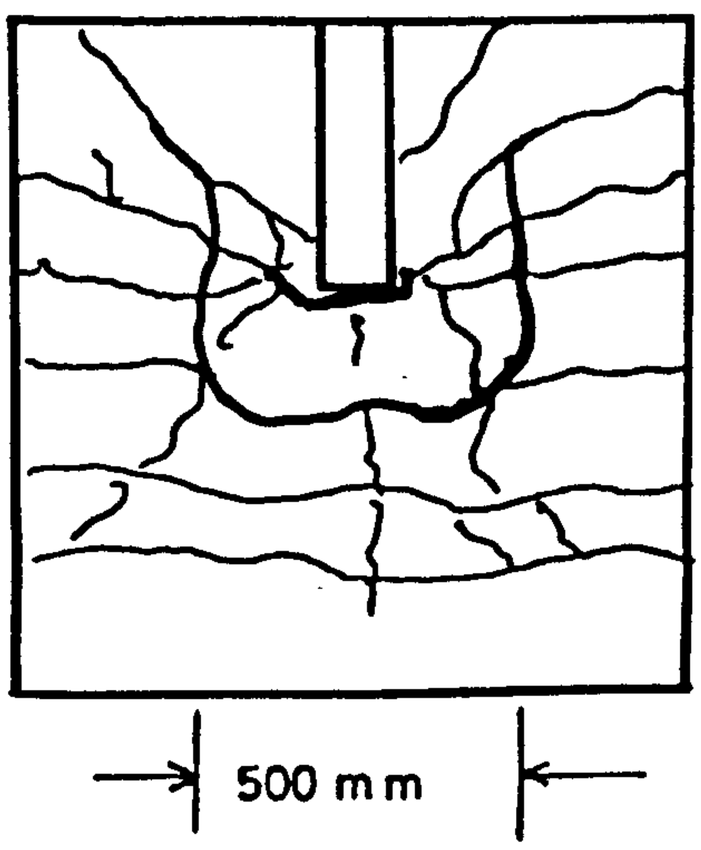

Figure (6.19) : Crack pattern of slab of model PT1 after failure.

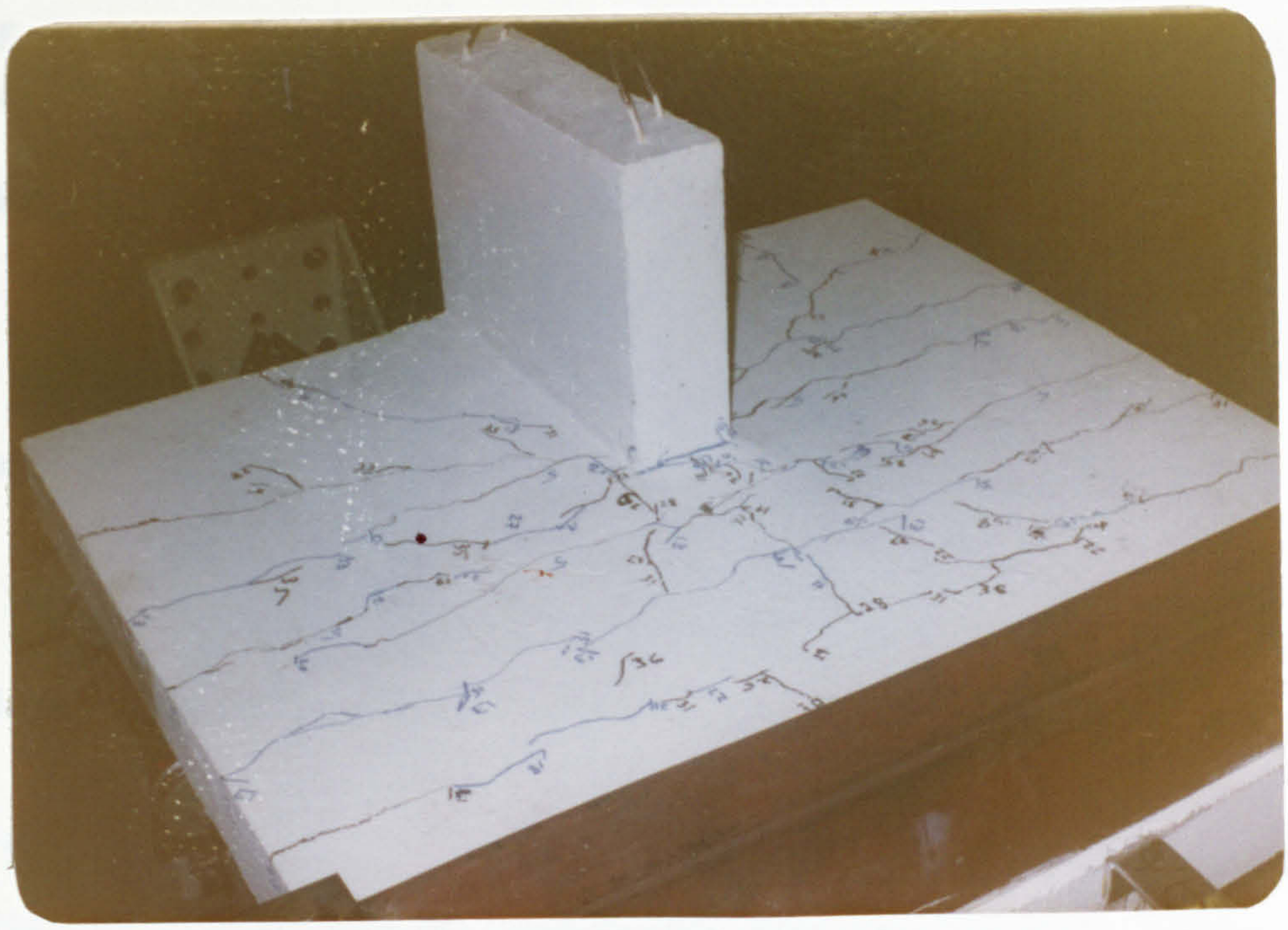

Figure (6.20) : Photograph showing the crack pattern of model PT1 after failure.

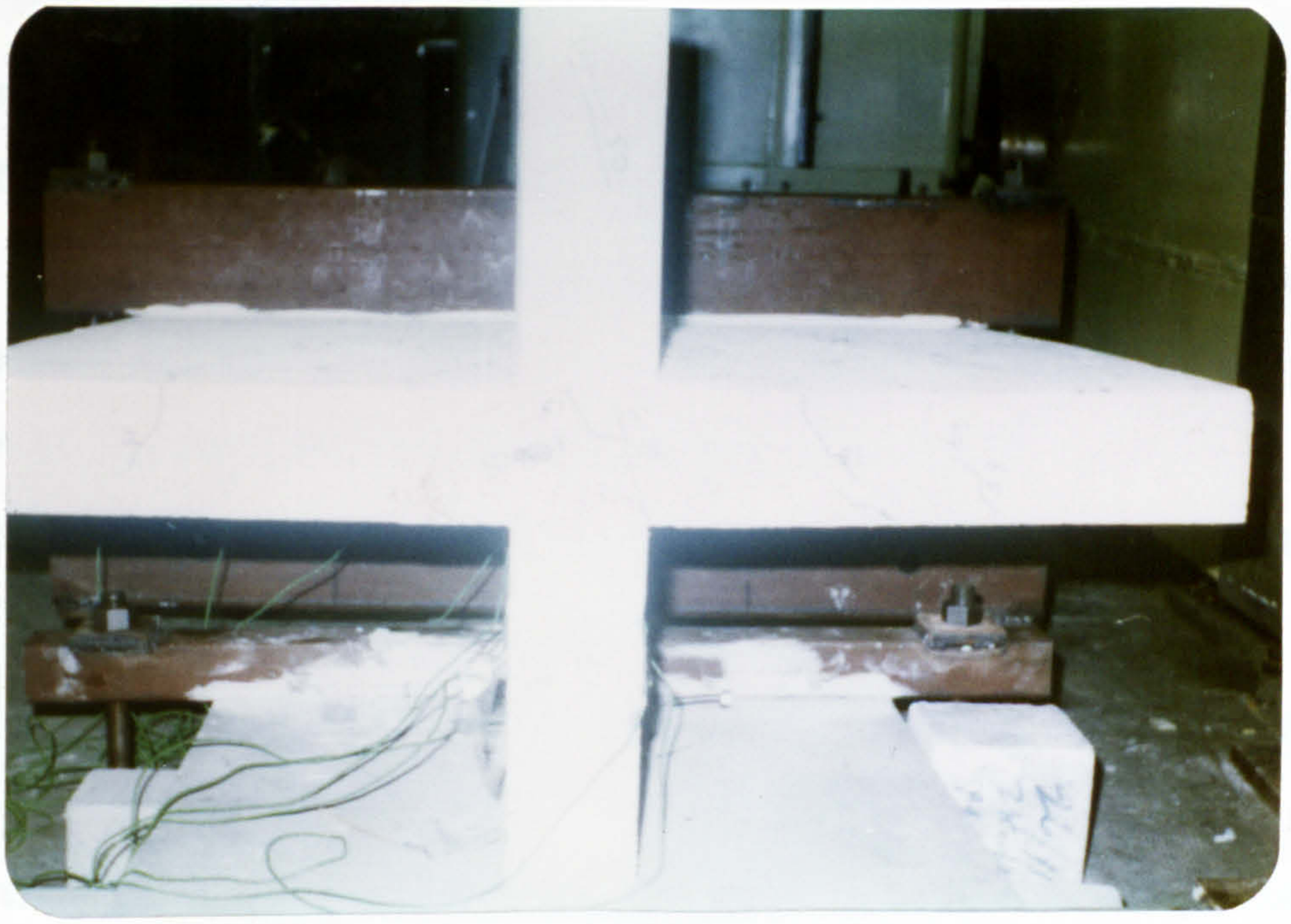

Figure (6.21) : Photograph showing the crack pattern of model PT1 at its back, after failure.

Here the depth of the neutral axis can be found from

$$\frac{E_s}{E_c} A_s (d - d_n) = \frac{1}{2} b' d_n^2 \qquad (6.4)$$

where E_s is the modulus of elasticity of steel

E_c is the modulus of elasticity of concrete

A_s is the area of steel

and b' is the breadth of the section

From these calculations it was concluded that this was not a failure of slab itself due to yielding of steel.

The shear strength of slab itself along transverse critical section passing through the inner edge of wall was also calculated and was found to be 131 kN which is much greater than the load at failure i.e. 48.97 kN. This was therefore a case of "Junction failure".

From Figure (6.19) and (6.20) which show the crack pattern after failure it can be observed that the failure took place aroumd the wall periphery in such a way that it appeared as if the wall punched through the slab. It has already been discussed in chapter two of this thesis, that two modes of failures have been identified for slab-column connection subjected to the unbalanced moments in addition to shears, viz: moment-torsion and shear-torsion. First kind of failures require that the ultimate strength of slab in flexure be achieved at the inner face, which did not happen in this case. Therefore it was not a moment-torsion failure/

The failure of this model was sudden and brittle. Therefore failure type of this model was shear-torsion. The distance of the plane of failure at the top of the slab was about 70-75 mm far from the inner edge of wall, while at the bottom slab was separated from inner edge of the wall just at the connection. Lower ends of the diagonal cracks in the slab at the back of the model were at a distance of 85 mm and 35 mm from the wall on left and right sides respectively as shown in Figure (6.17).

6.3.3 Model PT2

For the sake of convenience in the casting and in order to reduce the cost of the model, it was necessary to change the supporting arrangement of the model. Therefore unlike model PT1 in which a base slab was provided, in this model the wall was projected outside at the back of the model and a hole was provided in the extended portion of the wall. The model was clamped to the floor of the laboratory by means of a steel rod passing through the hole. The dimensioned sketch of this model is shown in Figure (6.23). All the other features were identical to those of model PT1.

Like model PT1, the load was applied in equal increments of .89 kN in this case also. However this time the model was tested in only one loading cycle. Experimental data are shown in Figures (6.24) and (6.25). The graphs in Figure (6.24) which show $\frac{V_{app}}{V_{design}}$ versus $\frac{\text{Comp. strain}}{(\varepsilon_{max} = .0035)}$ at different points in the slab of this model, were prepared after taking an average of the corresponding values of strains measured on both sides of the central point P1/

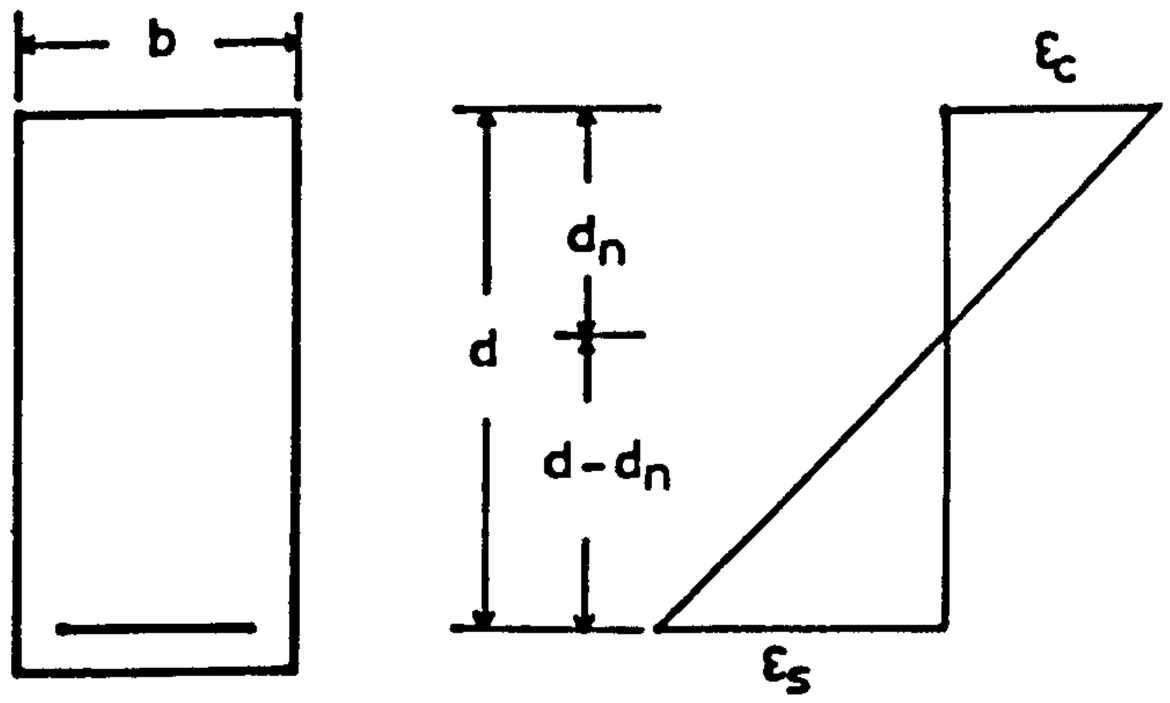

Figure (6.22) : Strain diagram for a singly reinforced concrete section.

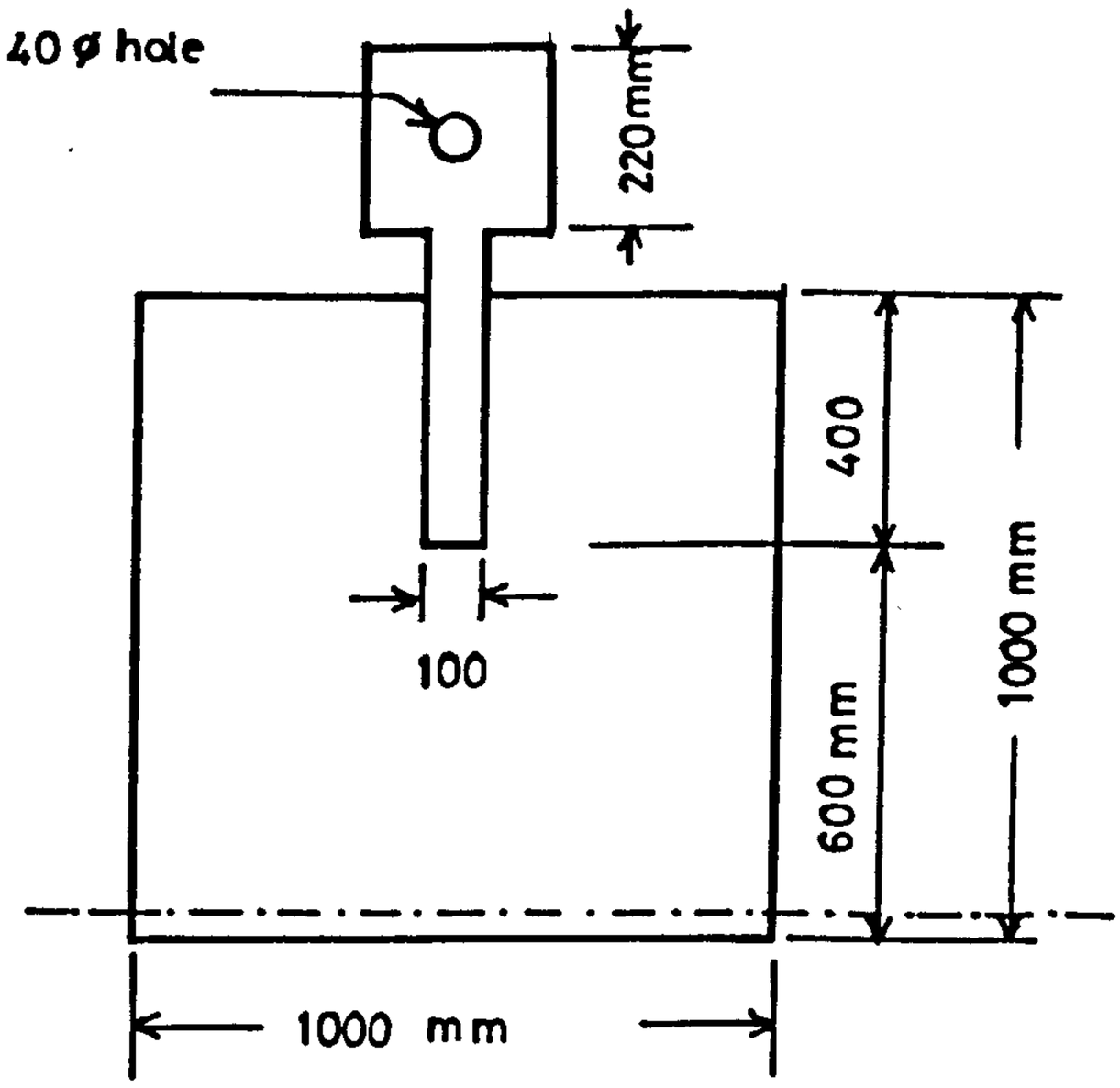

Figure (6.23) : Dimensioned sketch of model PT2.

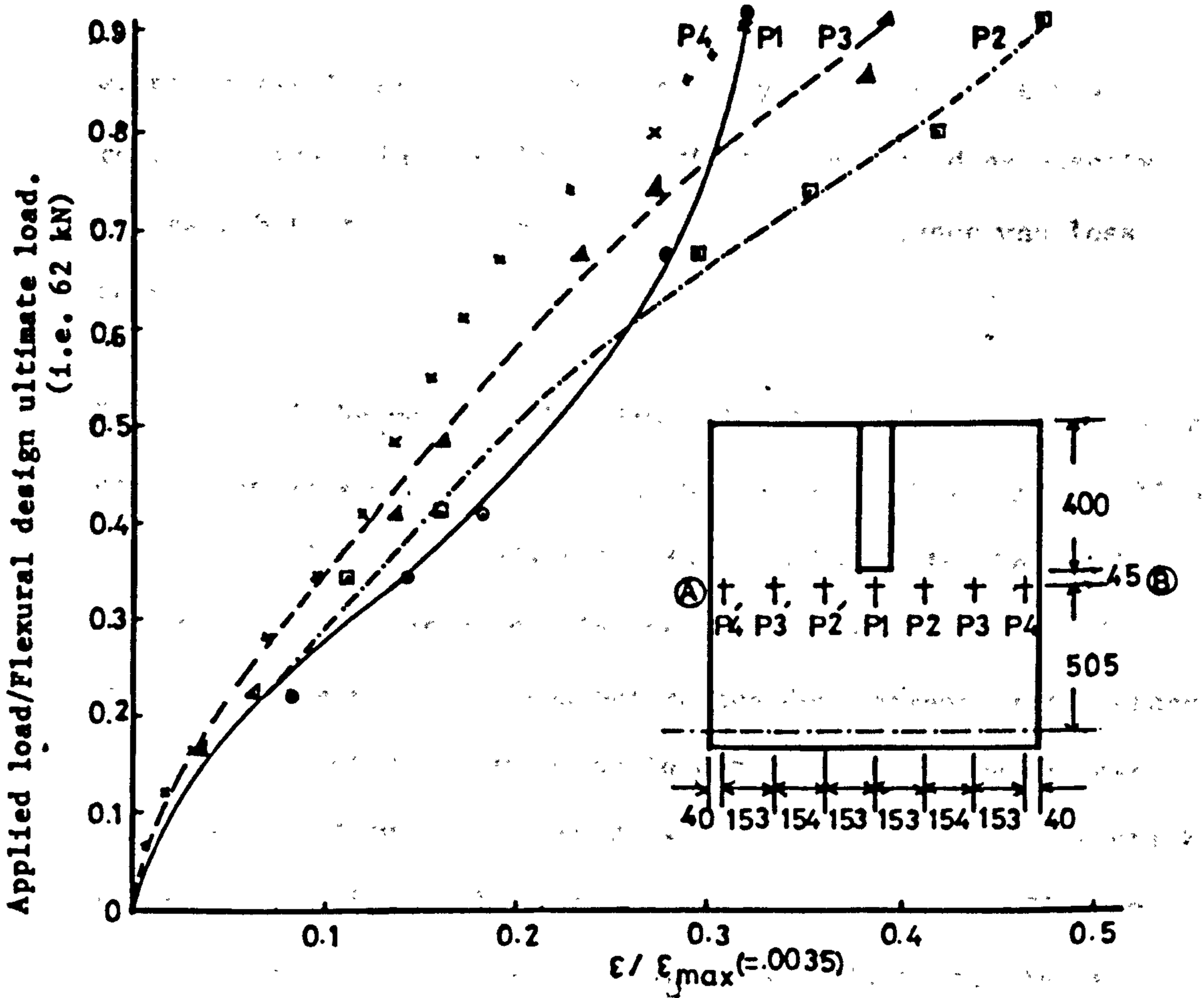

Figure (6.24) : Compressive strain in concrete in windward direction at different points along transverse section AB, in the slab of PT2.

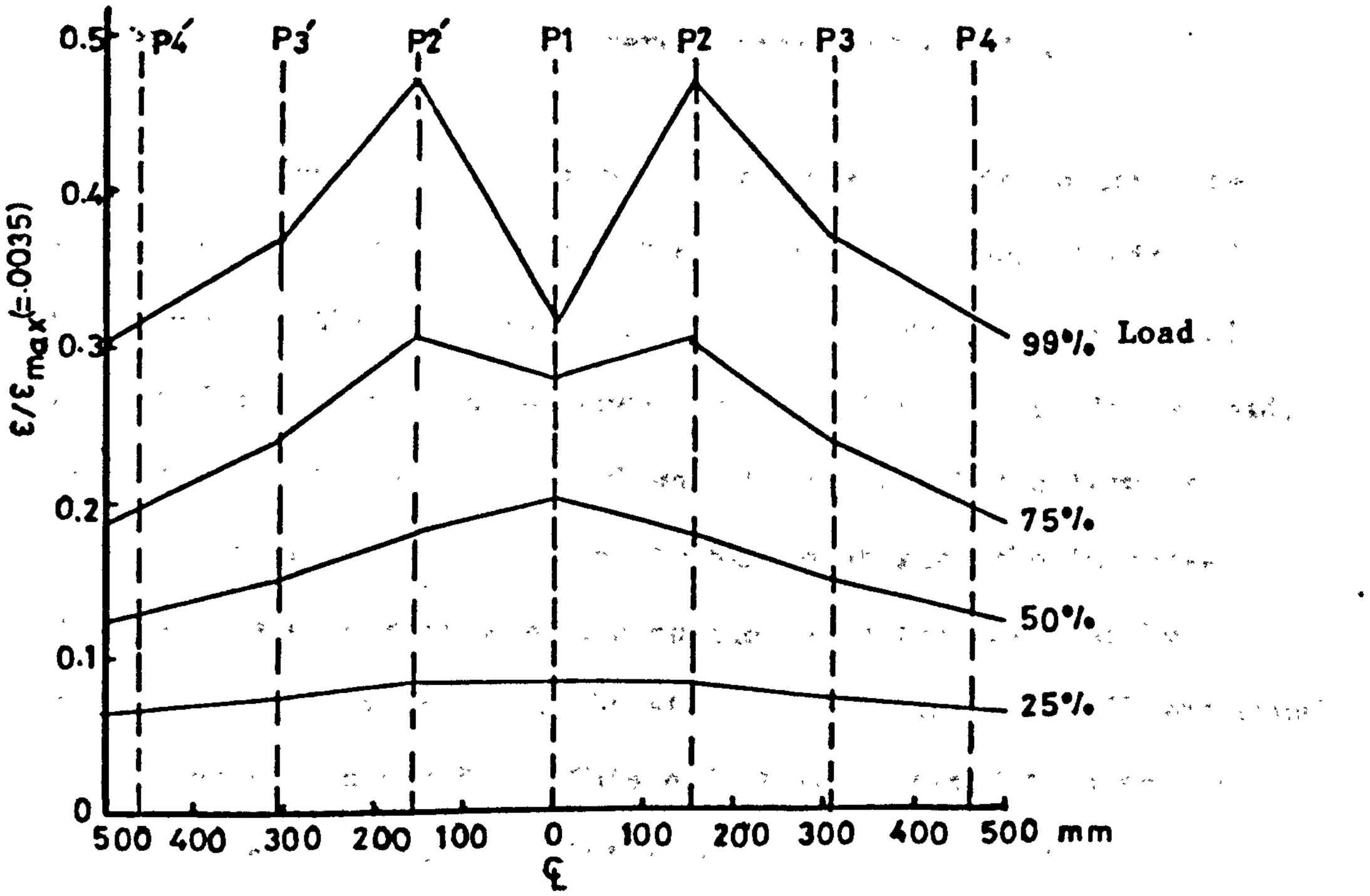

Figure (6.25) : Variation of compressive strain in concrete along transverse critical section at different stages of loading in the slab of PT2.

along critical section. Theoretically the strains at the corresponding points on left and right side should be exactly the same but it was not so, although the difference was less than 10%.

Behaviour of the model: The first visible crack at the wall-slab connection as shown in Figure (6.26) appeared at a load of 21% of the load at failure. This point is marked as A in the graph showing the load versus displacement presented in Figure (6.31). It can be observed that even before the development of the crack the stiffness of the slab began to deteriorate. More or less same crack pattern was observed as that of model PT1. The crack pattern at 98% load and after the failure is shown in Figures (6.27) to (6.29). The load at failure was 54.74 kN. As is apparent from these figures, this was also shear failure of the connection itself, as desired. Generally the behaviour of this model was not appreciably different from that of PT1.

An unexpected behaviour of the measured strain in concrete at the bottom of the slab near the inner edge of wall (Point P1 in Figure (6.24)) was observed. Along the transverse critical section for flexure, up to approximately 50% of the ultimate load, the measured strain at point P1 was the highest but afterwards the rate of increase of strain at this point with the increase of load decreased so that when the applied wind load was nearly equal to the ultimate load, the strain at central point P1 was equal to that at edge point P4. This effect was noticed to a certain extent in model PT1 as well but it was not so pronounced.

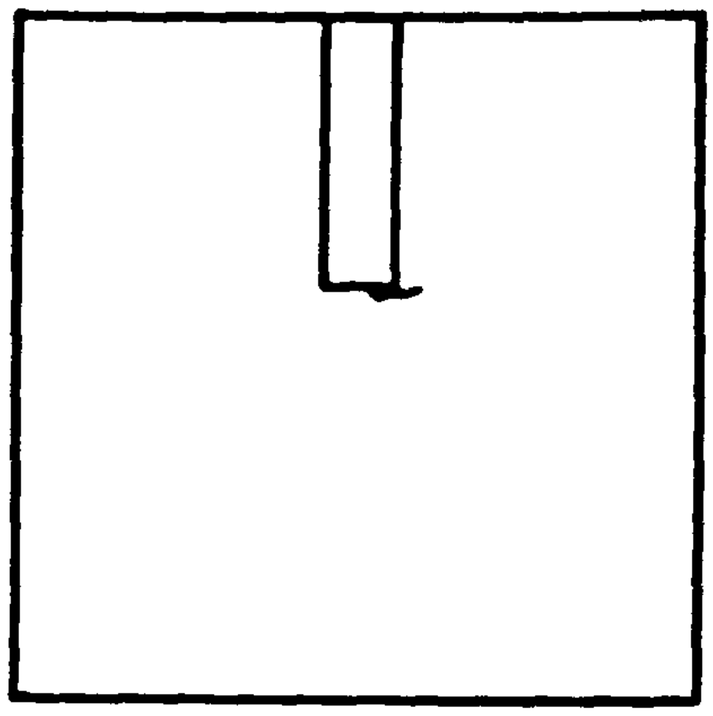

Figure (6.26) : Initiation of cracks in the slab of PT2.

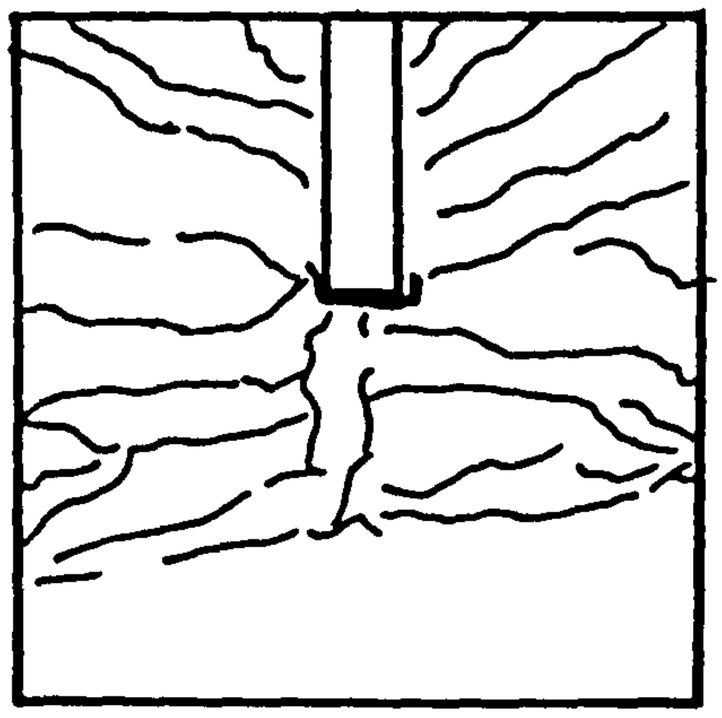

Figure (6.27) : Crack pattern of the slab of PT2 just before failure.

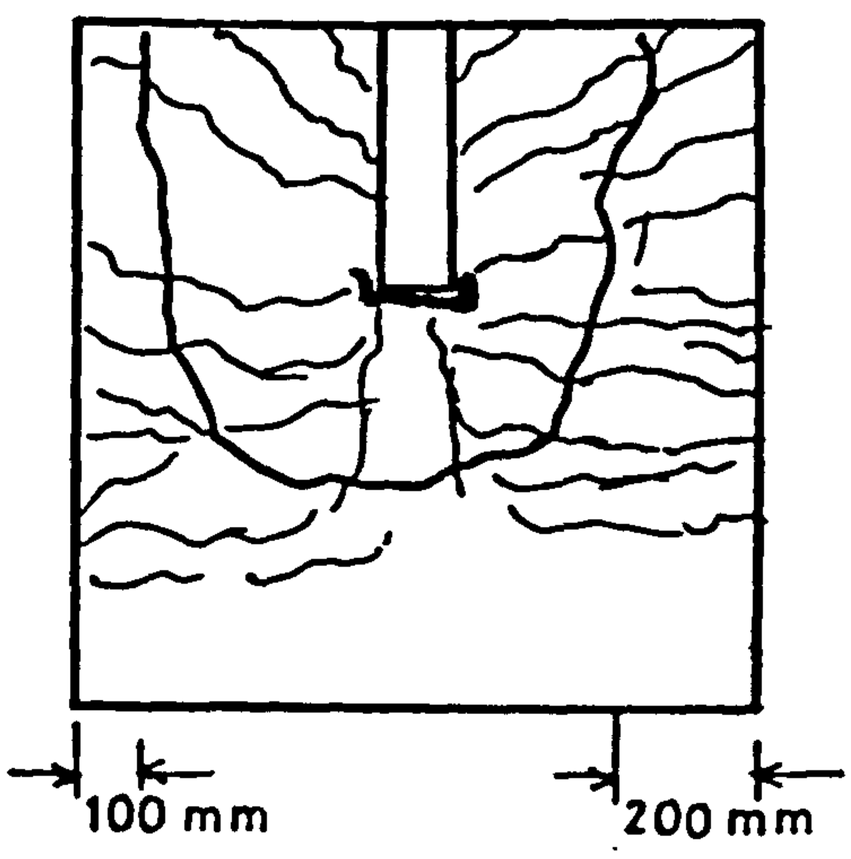

Figure (6.28) : Crack pattern of the slab of PT2, after failure.

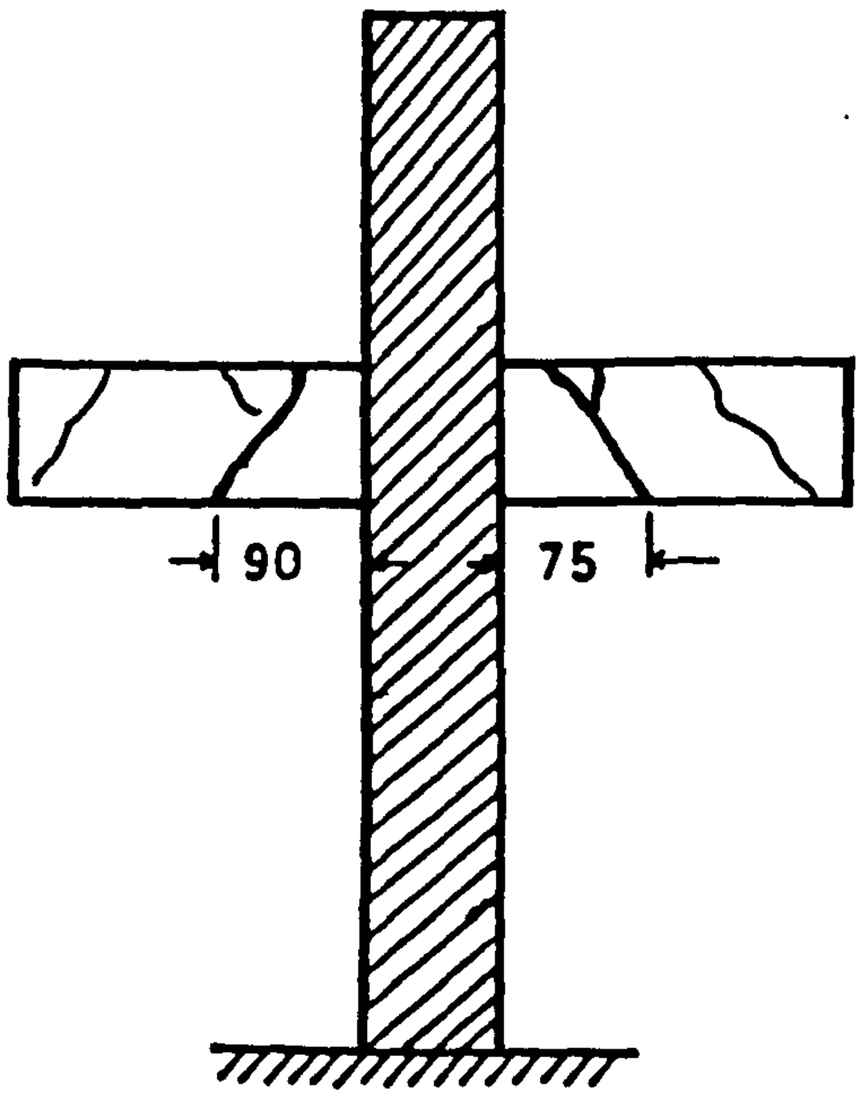

Figure (6.29) : Crack pattern after failure at the back of PT2.

6.3.4 Model PT3

Since the unbalanced moments due to wind loads are transferred from the slab to the wall partly directly at the inner edge of wall and partly by torsion through the sides of the wall, this model was tested to see the level of transfer of unbalanced moments by torsion through the sides of the wall. All the other features of this model were same as those of model PT2 except that a rectangular slot was provided in the slab at the inner face of wall, thus preventing the direct transfer of bending moment and the shear between the slab and wall. This model is shown in Figure (6.30). For comparison, the load-displacement curve for this model and models PT1 and PT2 are presented in Figure (6.31). From this curve it can be observed that, as expected, the stiffness of slab in this case was less than that of model PT2. The compressive strain in concrete at the bottom of the slab along transverse critical section is shown in Figure (6.32).

Behaviour of model: For the first time two cracks appeared as shown in Figure (6.33) at a load of 27% of the load at failure. At a load of 74% the width of these cracks was found to be nearly 2 mm. In the meantime many new cracks had developed at different stages of loading. As expected, due to the concentration of the stresses caused by the slot in the slab near the inner edge of wall, at early stages of loading the cracks were developing in the slab on both sides of the wall, starting at the connection with wall and were extended up to the edges of the slab, and some penetrated through the thickness and were clearly visible from the sides of slab. The failure was sudden and brittle. The load at failure was 40.62 kN.

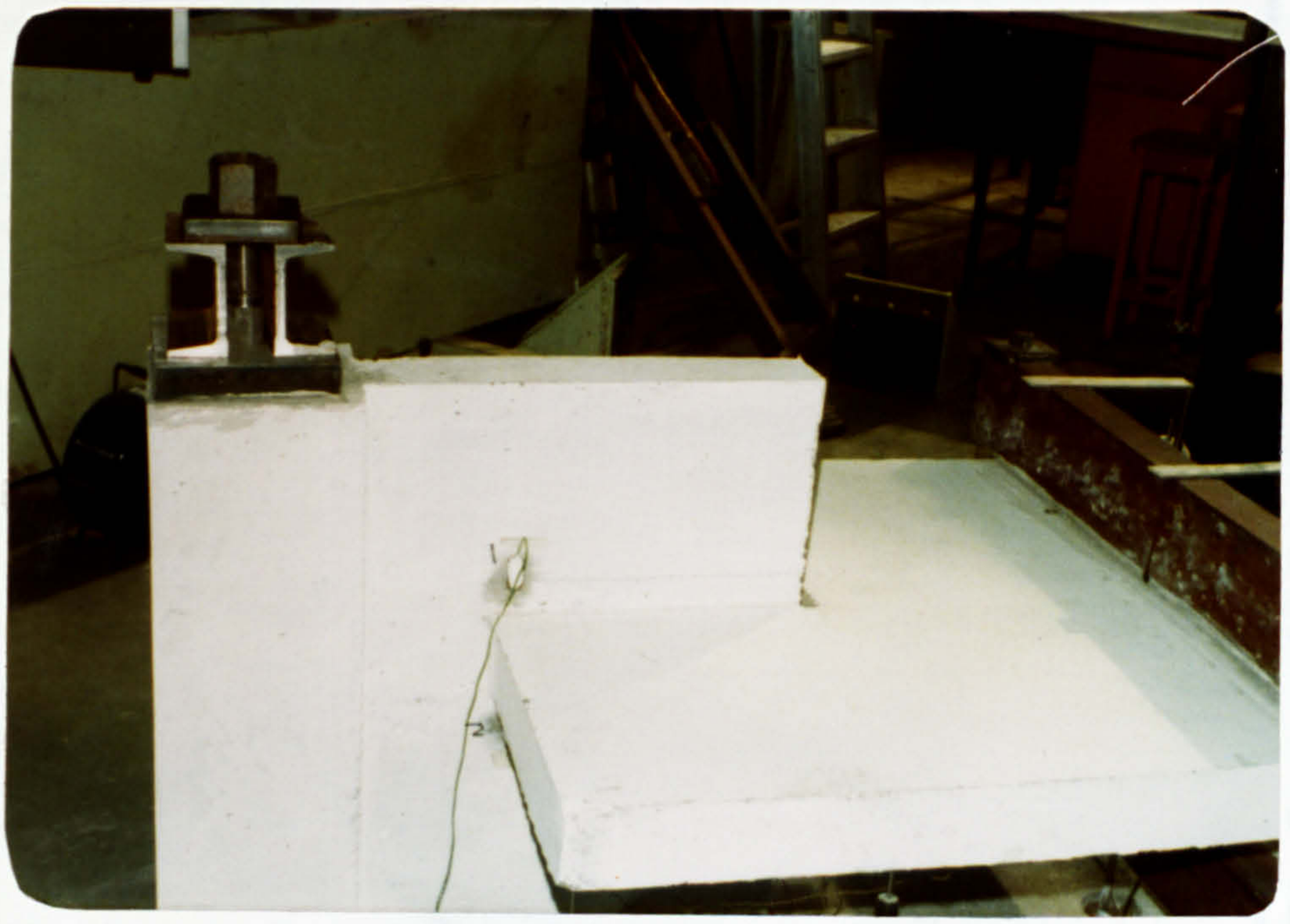

Figure (6.30) : Photograph showing model PT3 before test.

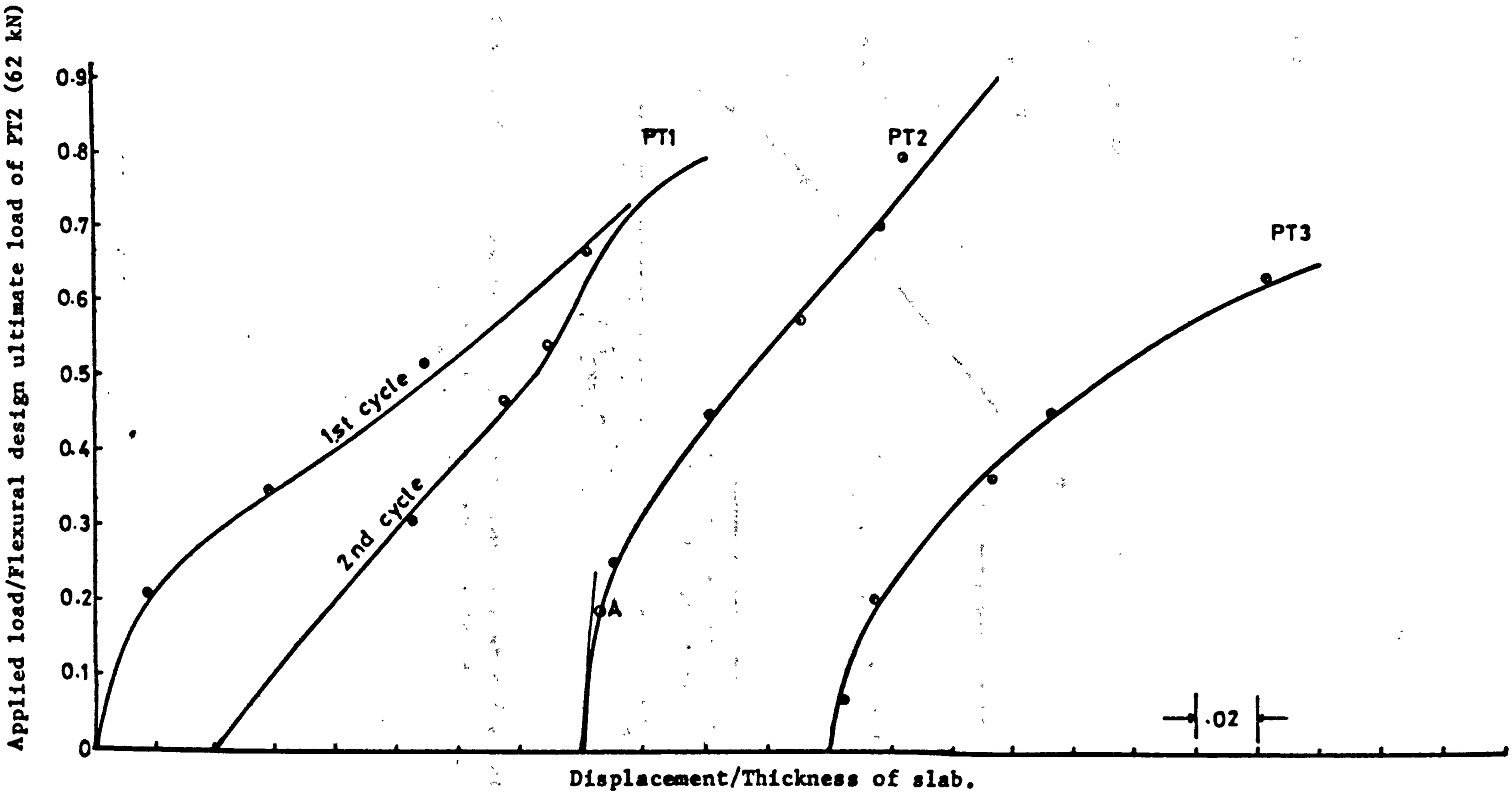

Figure (6.31) : Wind load-displacement relationship for models of preliminary test series.

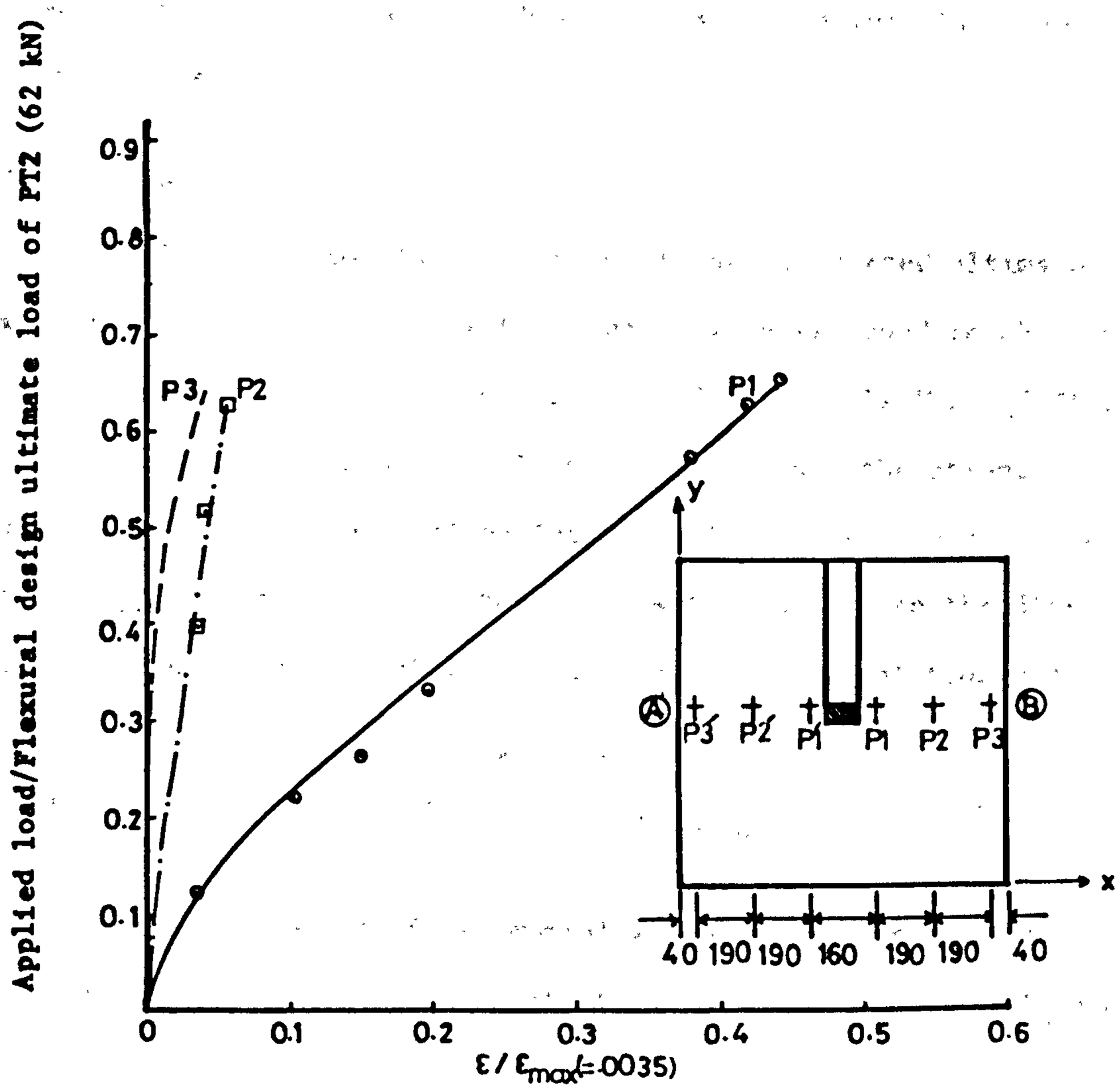

Figure (6.32) : Compressive strain in concrete at different points along transverse critical section AB, in the slab of PT3.

Due to concentration of stresses near the slot concrete spalled in the regions near it at the time of failure of the model. The crack pattern of this model after failure is shown in Figure (6.34).

6.3.5 Comparison

Table 6.3 shows the comparison of the calculated ultimate wind load using different methods (which were reviewed in chapter two), with the experimental ultimate load for models PT1 and PT2. For model PT3, the only possible way to calculate the strength was the ACI318 recommendations for situations where the sections are subjected to torsional shear stress in addition to the direct shear. Thus it was calculated using the following relationship:

$$\tau = \frac{2}{3} h^2 W_w (.4\sqrt{f'_c}) \sqrt{1 - (v_u / .33\sqrt{f'_c})^2} \qquad (6.5)$$

Here τ is the torsional moment which can be transferred through the sides of the wall with the side length equal to W_w, and

v_u is the shear stress induced along the sides of the wall due to direct shear and can be calculated from:

$$v_u = \frac{V_u}{2d\ W_w}$$

where d is the effective depth of the slab

$.4\sqrt{f'_c}$ and $.33\sqrt{f'_c}$ are respectively the critical values for torsional and direct shear stresses as proposed by ACI318.

The figures in the brackets in table 6.3 show the ratio $\frac{V_{exp}}{V_{cal}}$ (i.e. Experimental ultimate load/calculated ultimate load).

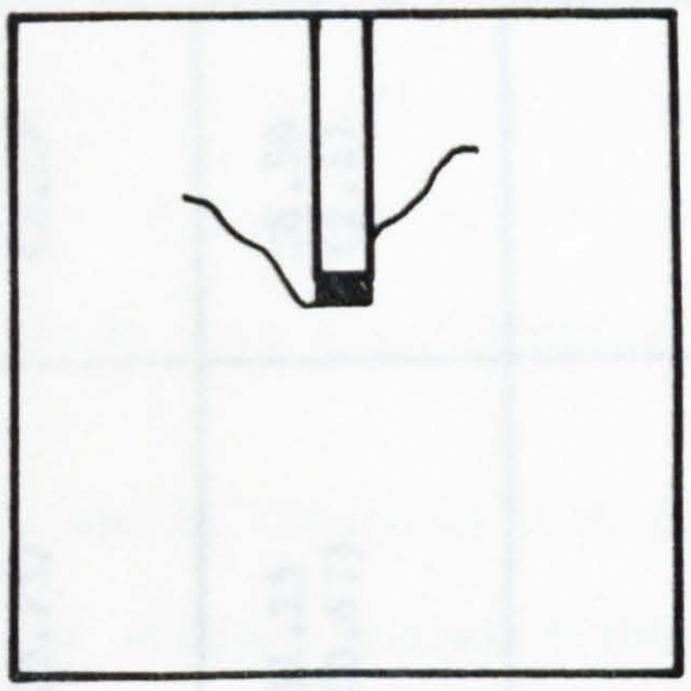

Figure (6.33) : Initiation of cracks in the slab of model PT3.

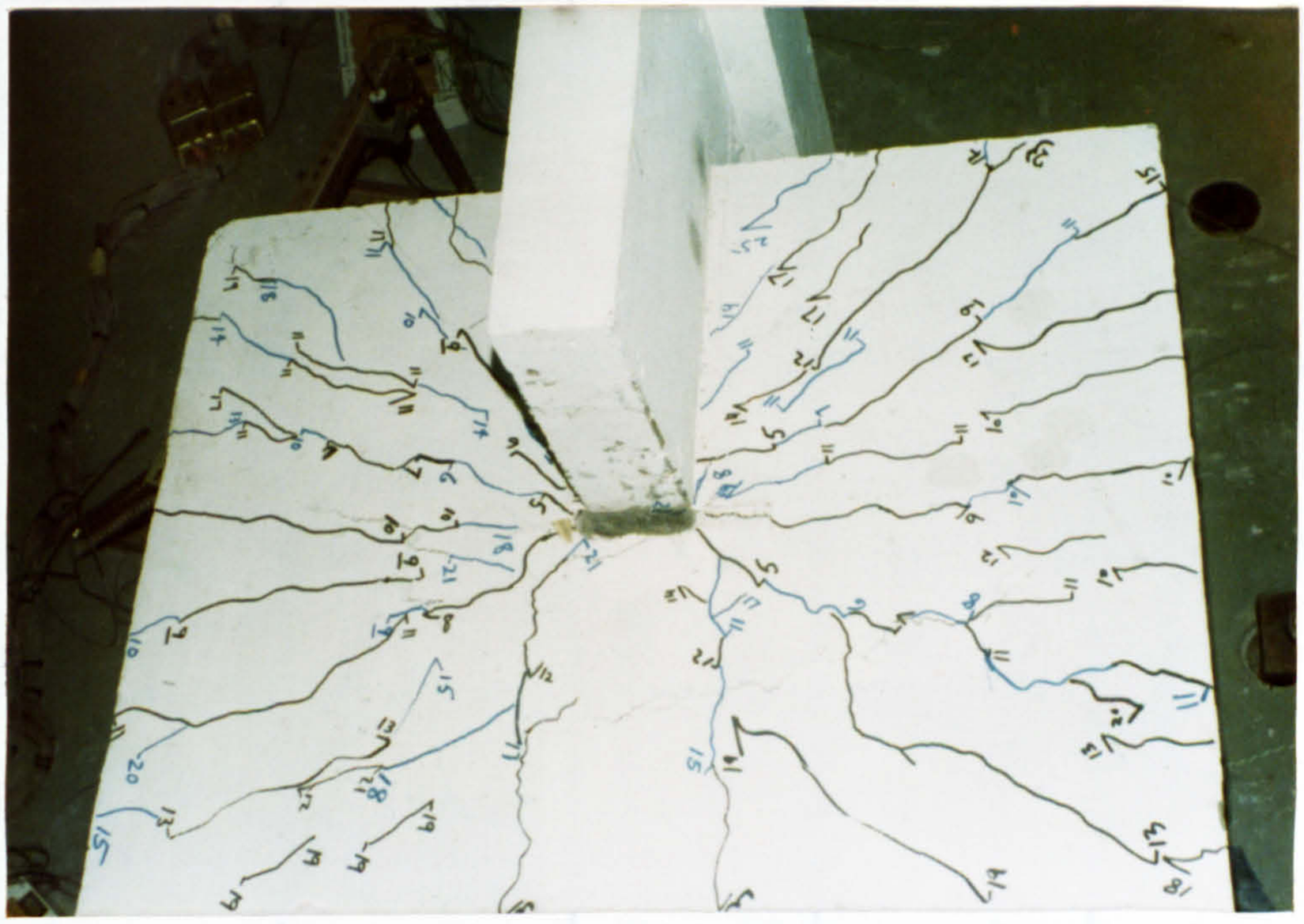

Figure (6.34) : Crack pattern of the slab of PT3 after failure.

Table 6.3. Comparison of calculated and experimental ultimate loads for models of preliminary test series

Model No.	f_{cu} N/mm^2	Experimental load at failure $V_{exp.}$ kN	CP110 without transfer of moment $V_{cal\ 1}$ kN	CP110 with transfer of moment $V_{cal\ 2}$ kN	ACI method $V_{cal\ 3}$ kN	Chang method $V_{cal\ 4}$ kN	Schwaighofer & Collins $V_{cal\ 5}$ kN	Coull & Wong $V_{cal\ 6}$ kN
PT1	40.0	48.97	69.14 (0.71)	13.62 (3.6)	37.1 (1.32)	27.58 (1.78	66.76 (0.73)	23.23 (2.1)
PT2	40.6	54.74	82.26 (0.67)	17.29 (3.17)	44.64 (1.16)	32.5 (1.68)	81.25 (0.67)	26.55 (2.1)
PT3	40.3	41.06			8.05 (5.1)			

Note: The figures in brackets show the ratio $\frac{V_{exp}}{V_{cal.}}$

Since the same mix of concrete was used for all the models of PT series and all the models were tested on 28th day, the variation of the compressive strength of concrete was very slight and therefore ultimate experimental loads were not corrected for it.

From table 6.3 it can be observed that for both the models (i.e. PT1 and PT2) CP 110 without moment transfer and Schwaighofer & Collins (8) overestimated while all the other methods underestimated the strength of connection with relatively better predictions by ACI318.

The calculated strength of the model PT3 is only one fifth of the actual one. However working back with v_{ct} (torsional critical shear stress) as unknown, and V_u equal to the experimental load at failure the same formula (equation (6.5)) gives a value of v_{ct} = 10.71 N/mm^2. This value though seems very high but compares very well with the value of v_{ct} obtained by Kanoh & Yoshizaki (14) (i.e. 11.26 N/mm^2) from the results of their tests. A brief review of their work was presented in chapter two.

Assuming the location of critical section at $\frac{d}{2}$ from the wall periphery, the strength of inner face of critical section alone, in model PT2 = 1.5 $v_c(t_w + d)d$ = 40.32 kN (where $v_c = .33\sqrt{f_c'}$ N/mm^2).

Then in model PT2 load transferred through the sides =

54.74 - 40.32 = 14.42 kN

But the maximum shear which could be transferred through the sides of PT2 must at least be equal to the ultimate load of PT3.

Therefore it may be concluded that full strength of the critical section along the sides of the walls of PT2 was not reached when the failure took place. The failure must have been governed by the strength of inner face of critical section and after failure all the load (i.e. 54.74 kN) must have been transferred to its sides which could carry only 41.6 kN hence failure took place along the sides as well.

It may therefore be concluded that considerably large amount of moment and shear can be transferred by torsion than that calculated on the basis of critical value v_{ct} (viz; $0.4\sqrt{f'_c}$ N/mm^2) as recommended by ACI318 when the connection is purely of the torsional type. However for the slab-column or shear wall-slab connections subjected to unbalanced moments, where the failure is governed by the strength of the inner face of critical section for shears, it is unsafe to use[a] higher value of v_{ct} than that recommended by ACI318.

6.4 MAIN TESTS (MT SERIES)

6.4.1 Description of models

1. Main test series; group I

   Models: MT1, MT2 and MT3.

   Main parameter, width of wall.

The following table shows the width of wall for different models of this group.

Table 6.4

Model No.	Wall width
MT1	900mm
MT2	600 mm
MT3	400 mm

Shear failure is brittle. This is why the whole perimeter along the sides of wall can never be fully effective, because as soon as a maximum value is reached that section fails and the crack propagates fairly rapidly. However it was expected that the effective length of the critical section for shears would be greatly affected by the wall width. Therefore the models of this group were tested by applying a combination of gravity and wind loads. The dimensioned sketch of these models is shown in Figure (6.35).

2. Main test series; group II.

Models:MT2, MT4 and MT5.

Main parameter: Gravity load/wind load (V_g/V_w).

The following table shows the intensity of gravity load applied to each of these models.

Table 6.5

Model No.	Gravity load
MT2	24 kN
MT4	48 kN
MT5	72 kN

The wall-slab connections are required to transfer the shear due to wind (V_w) in addition to that due to gravity load (V_g). Presence of V_g reduces the capacity of connection to transfer V_w. Since shear stress due to V_g is evenly distributed along the critical section while that due to V_w is uneven with a greater concentration near the tip of wall, the relationship between the two quantities is not linear. Therefore the models of this group were tested to study the effect of the change in the intensity of gravity load on the strength of wall-slab connection against the wind loads.

3. Main test Series; group III.

Models: MT6, MT3 and MT7.

Main parameter: $\frac{\text{unbalanced moment}}{\text{uneven shear}}$ ratio (M_w/V_w)

From the results of the tests on the slab-column connections by different investigators and reported in the second chapter of this thesis it is apparent that the magnitude of the unbalanced moments has a very pronounced effect on the overall strength of connection. Therefore these models were tested to investigate the effect of the variation in the ratio of M_w/V_w (ratio of unbalanced moment due to wind load to uneven shear due to wind load), which can be changed by changing the width of corridor opening. Therefore talking in terms of nondimensional structural parameters, the effect of change of the ratio $\frac{L_w}{X_w}$, on the strength of connection (where L_w is corridor opening and X_w is the overall width of building), was studied by testing these models. For each model of this group half corridor opening width ($\frac{L_w}{2}$) is shown in table 6.6. The dimensioned sketch of these models is shown in Figure (6.36).

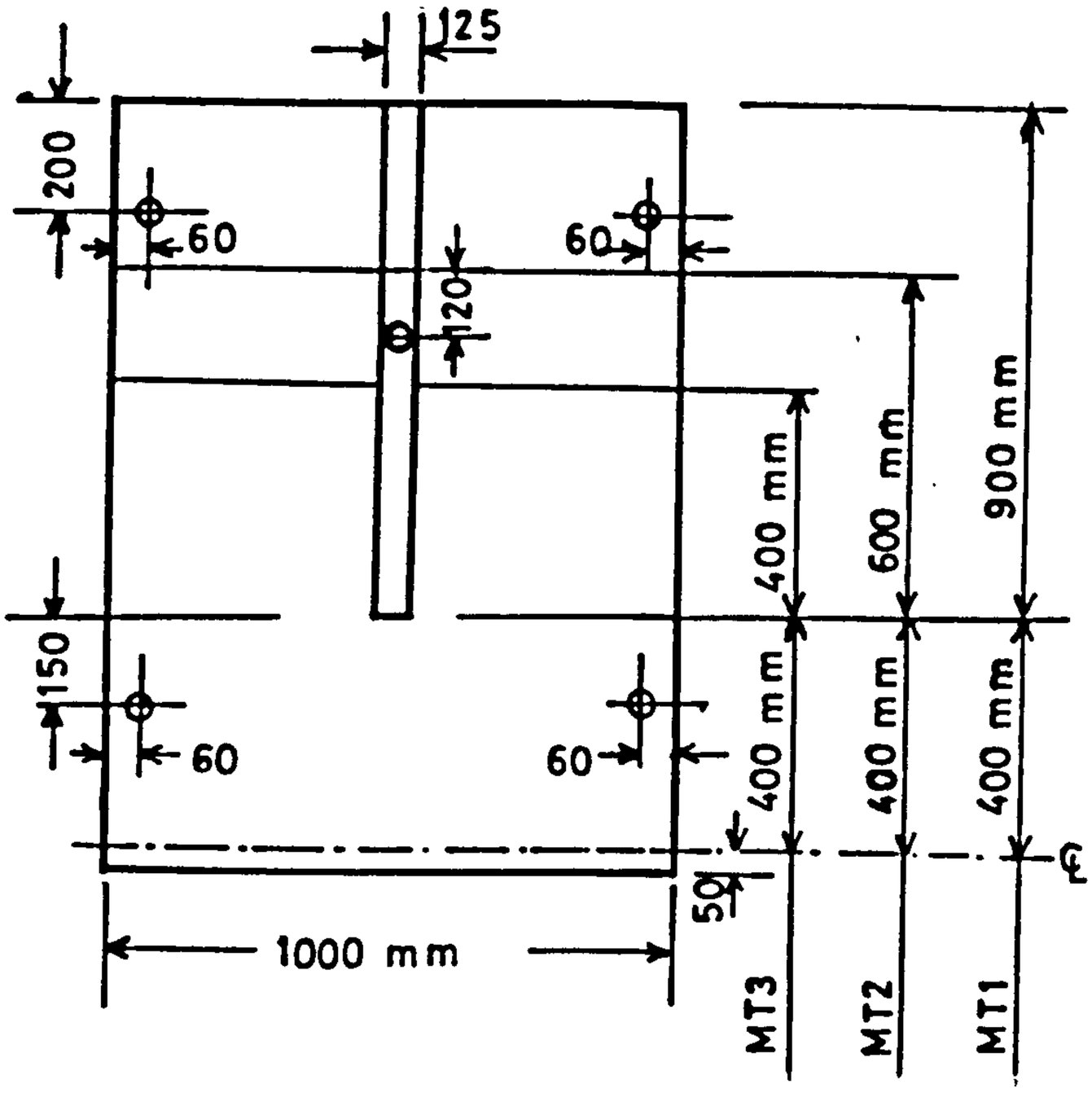

Figure (6.35) : Dimensioned sketch of models of Ist group of MT series.

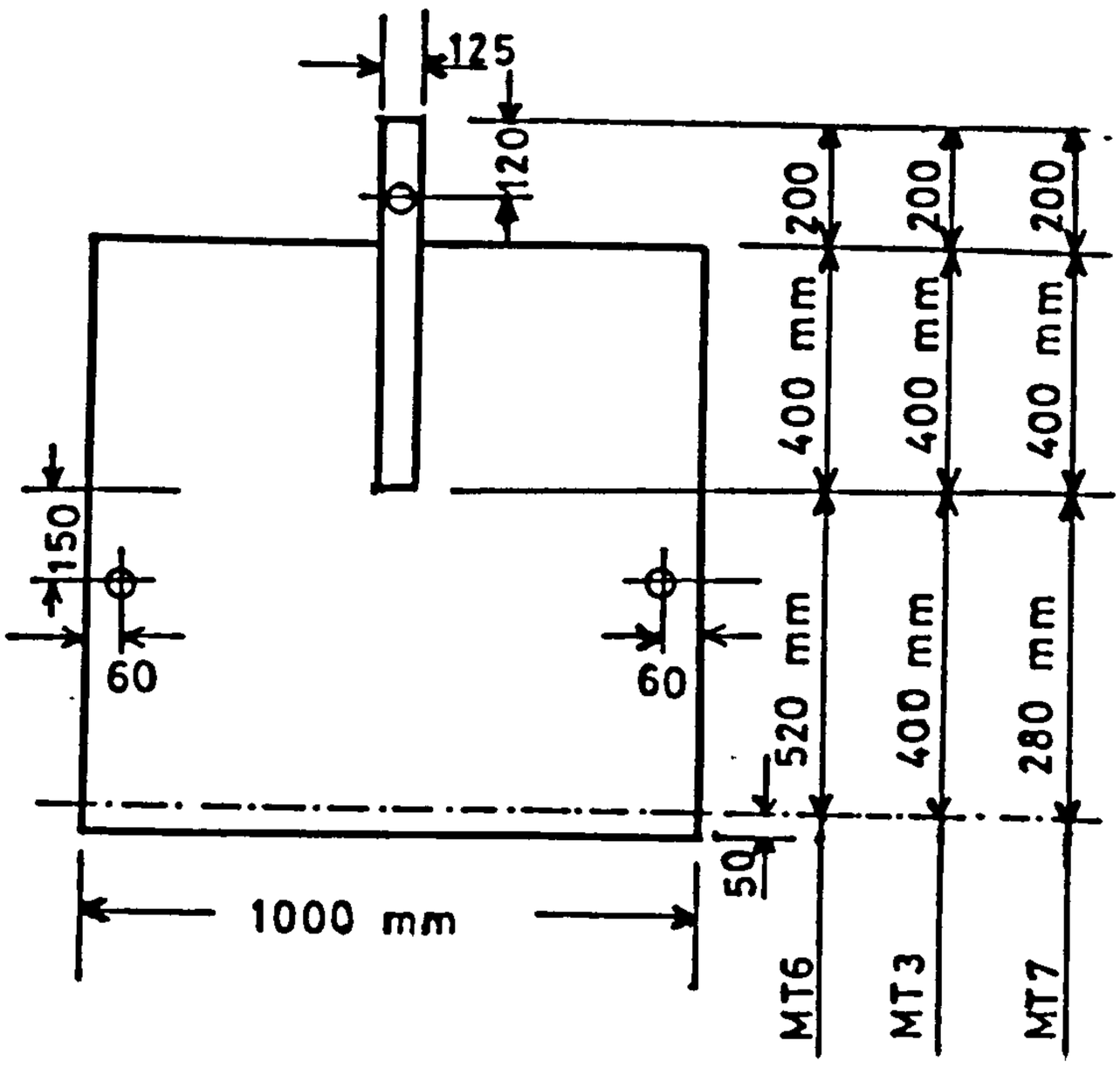

Figure (6.36) : Dimensioned sketch of models of IIIrd group of MT series.

Table 6.6

Model No.	$L_{w/2}$ mm
MT6	520 mm
MT3	400 mm
MT7	280 mm

4. Main test series; group IV.

Models: MT3 and MT8.

Main parameter: $\frac{\text{Moment due to gravity load}}{\text{shear due to gravity load}}$ ratio (M_g/V_g)

These models were tested to study the effect of change in the bay width of slab for a constant corridor opending width on the strength of connection. Table 6.7 shows the bay width for each of these models. The change in the bay width of slab causes a change in the structural parameteric ratio L_w/Y_w (where Y_w is the bay width of the slab and L_w is the corridor opening) and change in the ratio M_g/V_g.

Table 6.7

Model No.	Bay width (Y_w) mm
MT3	1000 mm
MT8	1440 mm

5. Main test series; group V.

Models: MT3 and MT9.

Main parameter: Presence of steel in top and bottom.

All the models except MT9 contained flexural steel only at the top. The wind may blow from any direction and therefore in real structures, for wind loading, the slabs are reinforced on both the faces (i.e. top and bottom). It was expected that due to grid action of the double flexural reinforcement the strength of connection would increase. Therefore model MT9 was tested in continuation with model MT3 to study this effect. All the other specifications of MT9 were same as those of MT3 except that the bottom of the slab was reinforced with steel required for wind load alone, in addition to the top reinforcement which was provided to resist combined action of wind and gravity loads.

6. Main test series; group VI.

Models: MT10, MT7 and MT11.

Main parameter: Ratio of flexural steel.

Since the shear strength of a reinforced concrete member is affected by the ratio of flexural steel (since the shear is partly transferred by the dowel action of flexural steel bars), these models were tested to find the extent to which this parameter affects the overall strength of the connection within the practical range of steel ratios.

6.4.2 Design of models of MT series

Since this investigation was aimed at studying the behaviour of the wall-slab connection, the flexural or shear failure of the slab itself was very much undesirable and therefore to ensure that it would not occur, the slabs of the models of main test series were designed for relatively higher ultimate loads than the strength/

of the connection itself. Therefore after fixing all the dimensions of the models including the thickness of wall (which was taken as 125 mm for all the models) and overall thickness of slab (which was taken as 150 mm for all the models), as a rough idea the strength of connection was calculated using different existing methods (reviewed in chapter two). From the experience of the models of PT test series (Preliminary tests), which gave a rough idea about the extent to which a particular formula may overestimate or underestimate the strength of connection, it was deemed sufficient to design the slabs of all the models of MT series except MT9, MT10 and MT11 (which were to be tested with steel ratio as main parameter), for an ultimate unbalanced moment of 85 kN-M along the critical section for flexure. In addition to this moment due to wind load, the slabs of the models were designed for the moment induced along the sides of the wall due to gravity load (shown in Figure (6.37)). The intensity of this design gravity load was such that in each case it would induce a shear stress of .42 N/mm^2 along the sides of the wall. The procedure adopted for the design was as follows:

In the first instance a uniform displacement of .2 mm was imposed upon the line of contraflexure (line KL in Figure (6.37)) and elastic distribution of moments was obtained using the finite element method. Then the total sum of the moment M_y acting along the transverse critical section (section BC in Figure (6.37)) was calculated. The required moment of resistance, viz. 85 kN.M was then divided by $2\sum M_y$ to find the factor by which all the three components of moment (i.e. M_x, M_y and M_{xy}) in each element/

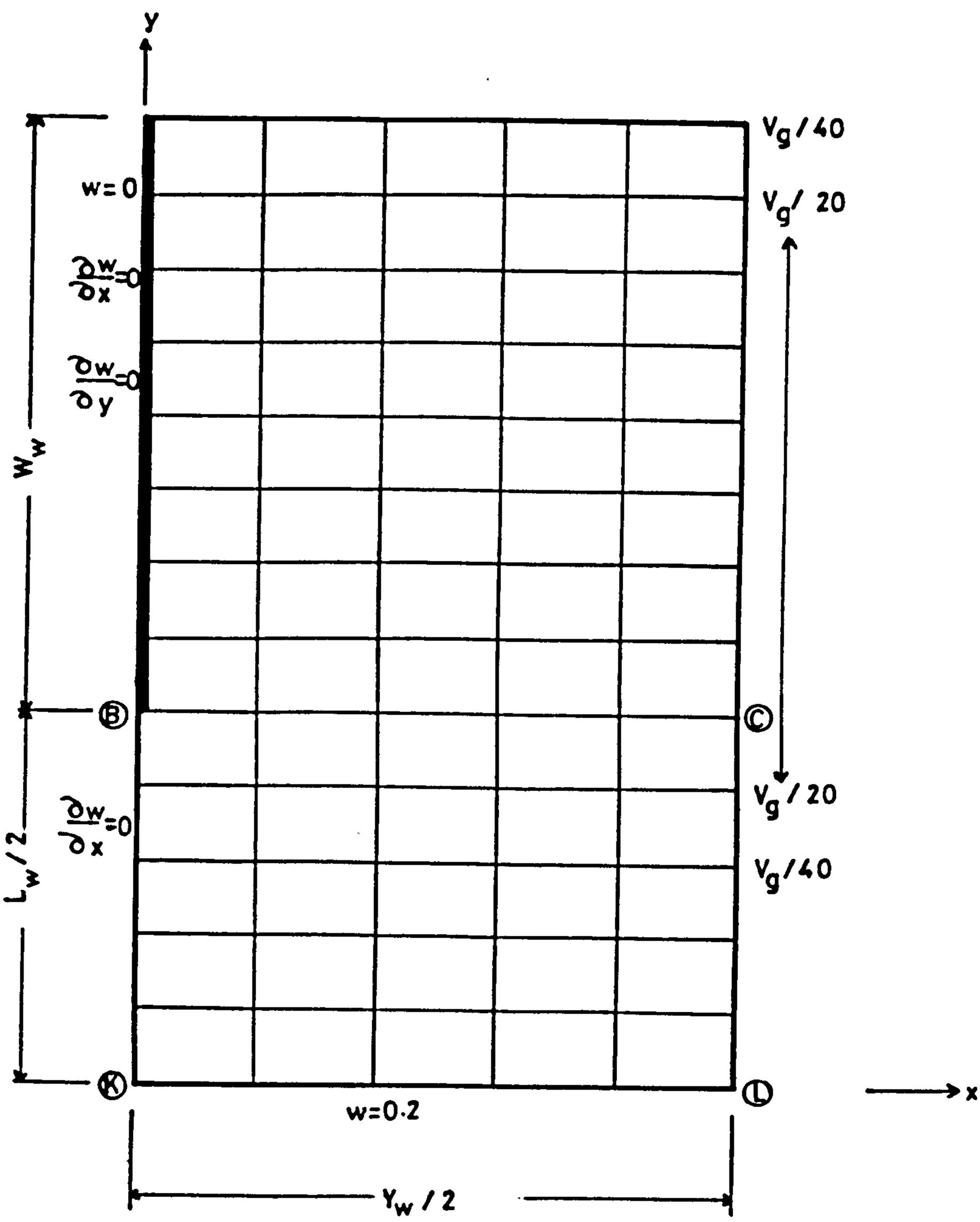

Figure (6.37) : Theoretical application of design ultimate wind load and gravity load for finding the elastic distribution of moments.

were multiplied. The elastic distribution of moments due to gravity load was obtained separately and the two moment triads (i.e. due to wind and gravity load) were combined together and the design moments were calculated using Wood & Armer method (34). The slab was divided in to strips and average ratios of steel in x and y-direction for each strip were calculated using standard procedure described in chapter four. The final ratios of steel are shown in Figures (6.38) and (6.39).

6.4.3 Models of group I (i.e. MT1, MT2 and MT3) (Effect of wall width)

6.4.3.1 General

As said earlier, all the models of main test series were tested by applying gravity load in addition to wind load. Since the intensity of vertical load was to be far less than the wind load, the vertical load was applied first, in five increments and then it was kept constant and the wind load was applied in equal increments of 8.9 kN. However the increments of wind load were halved at later stages of loading. The wind load was incremented till the failure occurred. The application of the wind load disturbs the magnitude and the distribution of the gravity load due to the fact that the deflection of the slab near the windward edge is more than that at the free edge at the back of the model as shown in Figure (6.40). Therefore the gravity load had to be readjusted after the application of each increment of wind load, to maintain the original level of gravity load. All the models of MT series except models MT4 and MT5 were tested by applying a gravity load which would induce a shear stress of .14 N/mm^2 at/

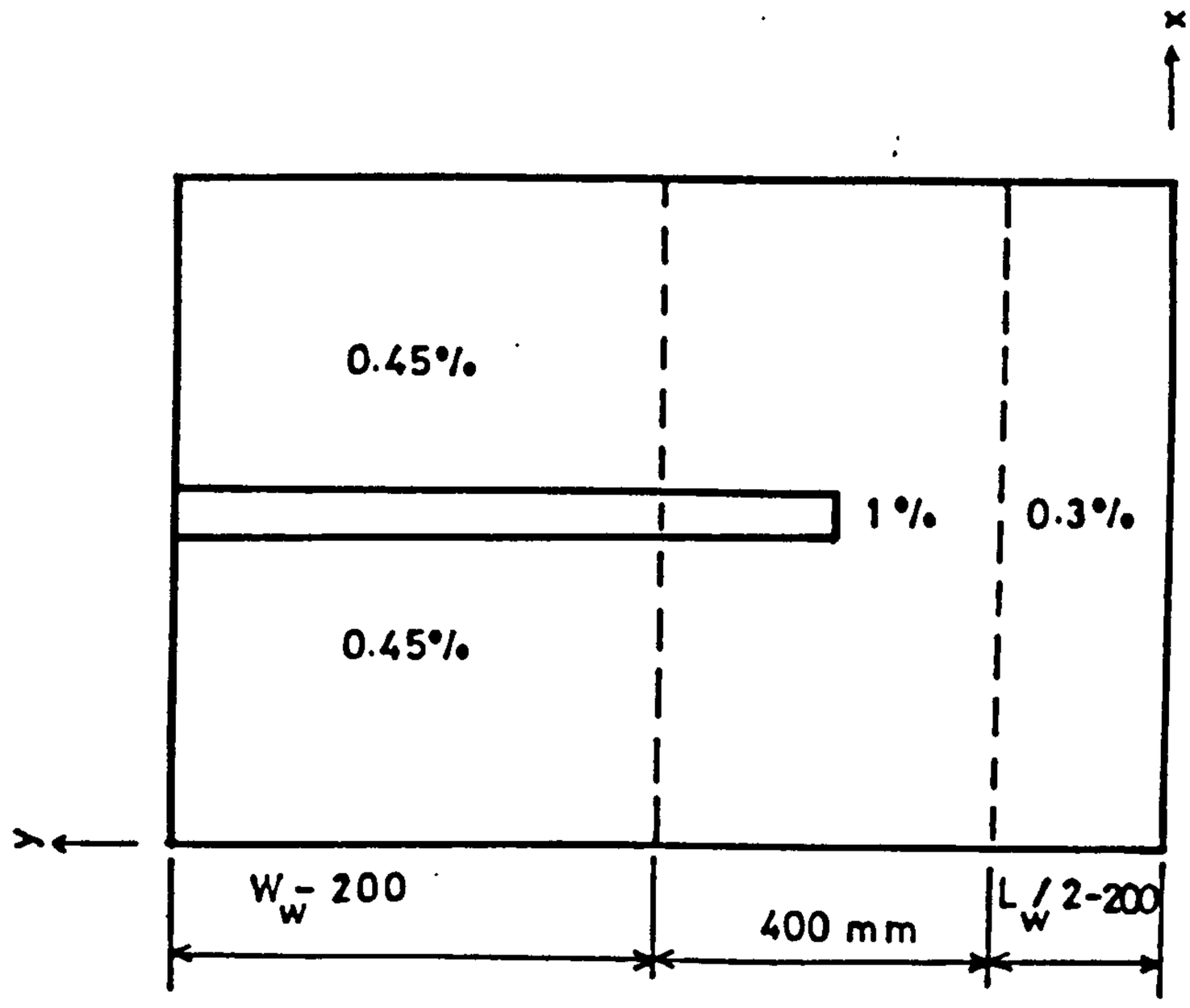

Figure (6.38a) : Ratio of flexural steel in x-direction in the slabs of all the models of MT series except MT10 and MT11.

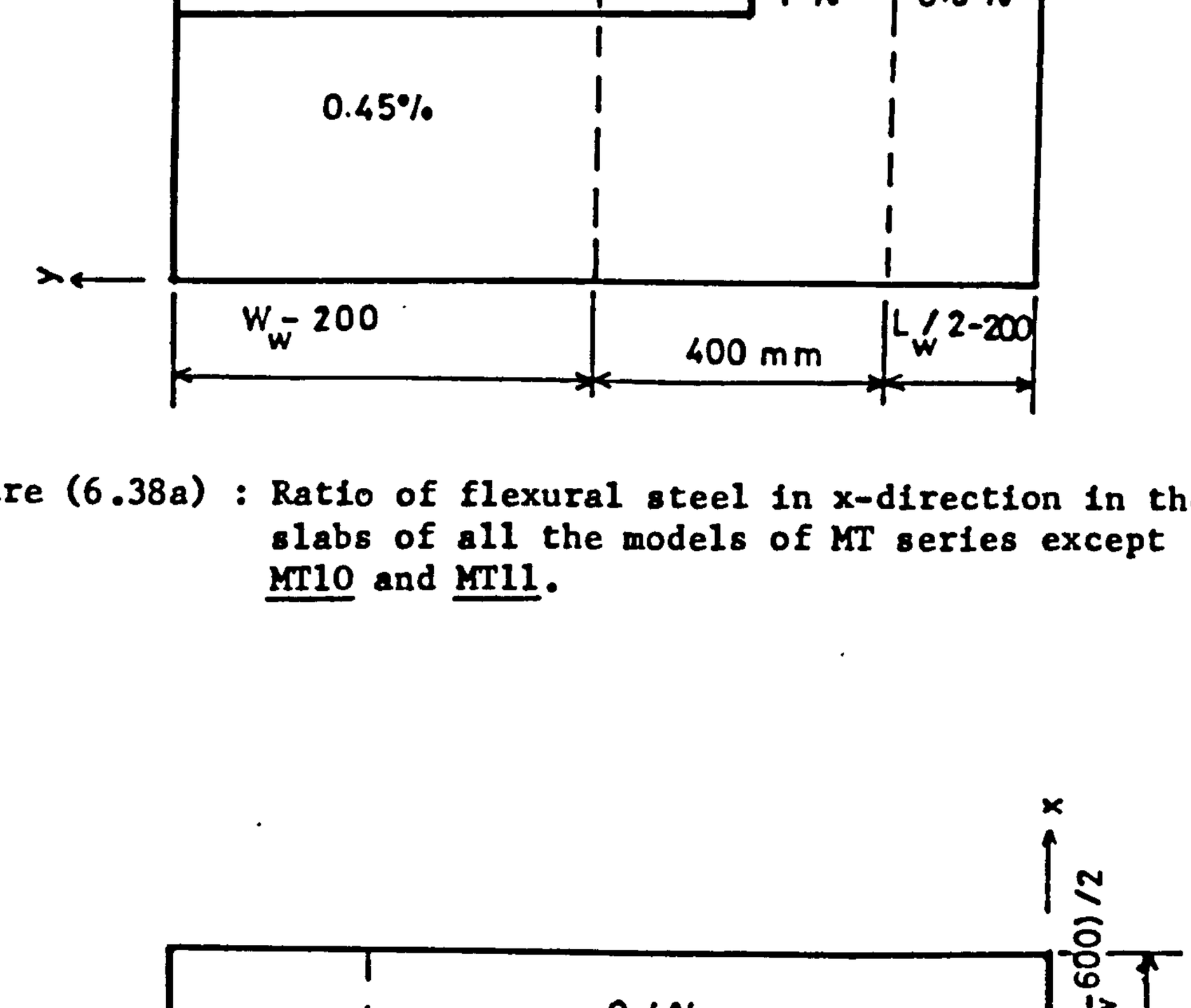

Figure (6.38b) : Ratio of flexural steel in y-direction in the slabs of all the models of MT series except models MT10 & MT11.

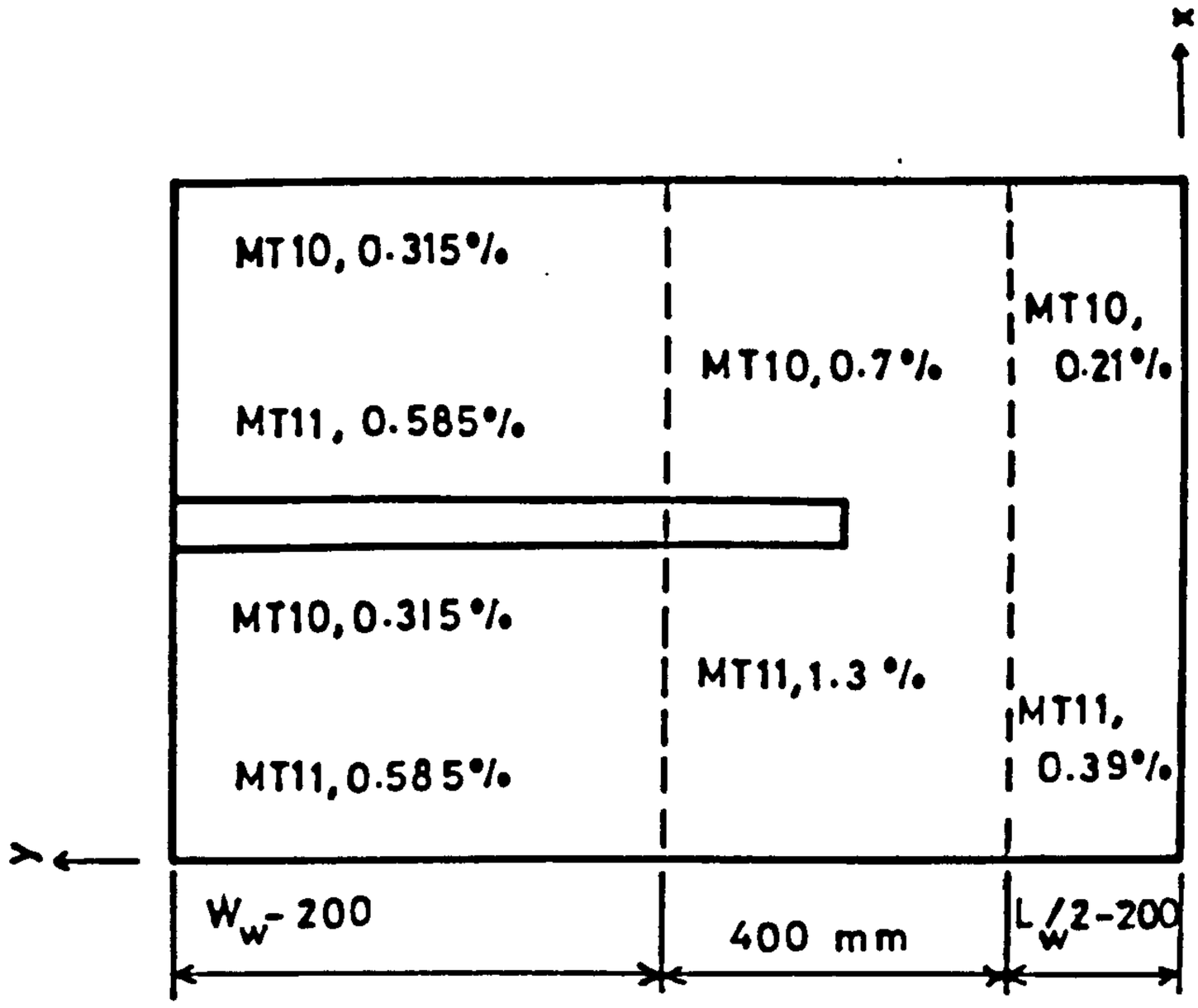

Figure (6.39a) : Ratio of flexural steel in x-direction in the slabs of model MT10 and MT11.

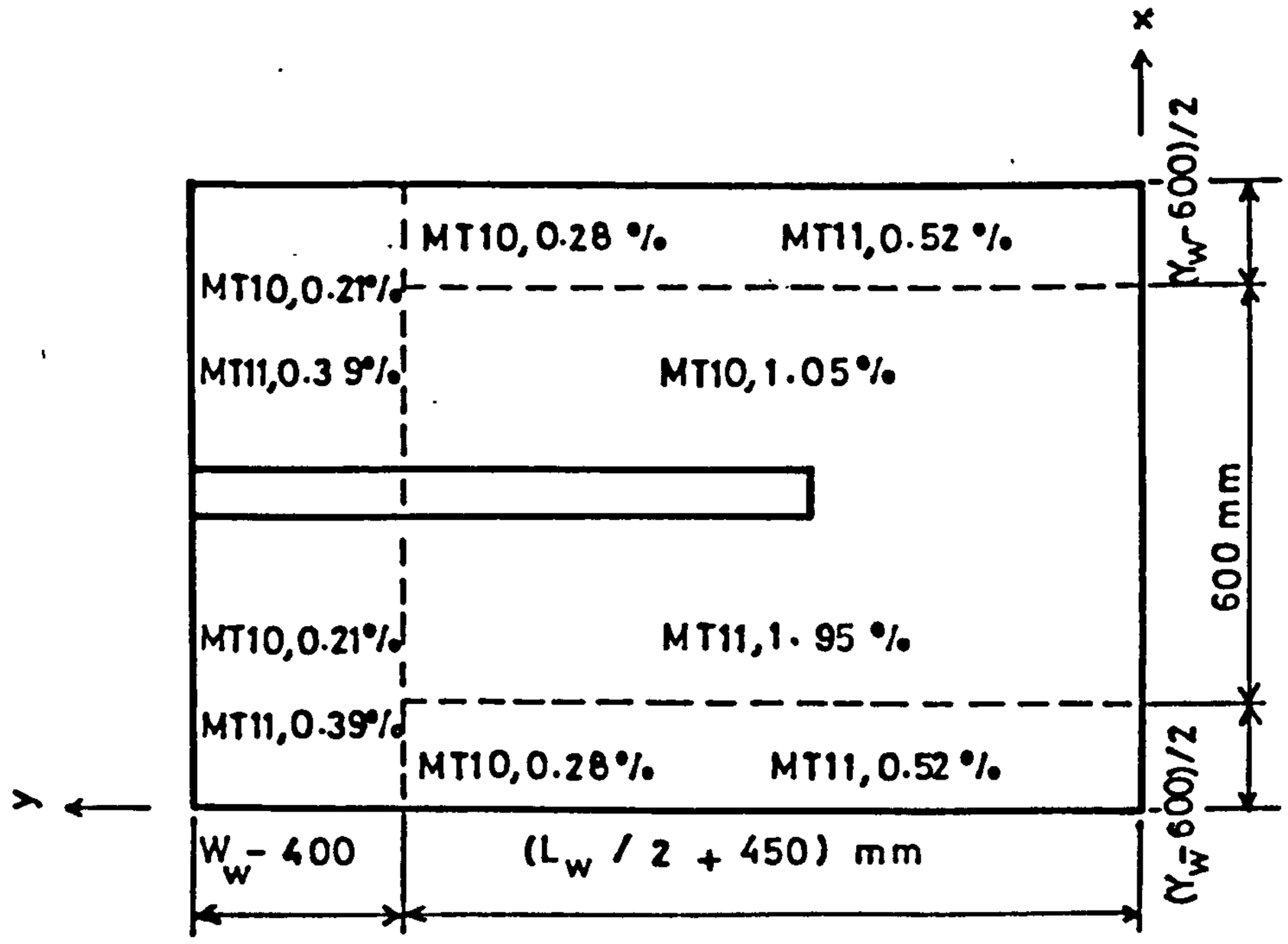

Figure (6.39b) : Ratio of flexural steel in y-direction in the slabs of models MT10 and MT11.

critical section along the sides of wall. This is equal to the stress induced in a real structure with a 230 mm thick slab and 7 m bay width by a combination of gravity load of: 1.2 (dead load + live load) = 8.4 kN/m^2. However since the main parameter of study for models MT4 and MT5 was the intensity of gravity load, they were tested by applying a gravity load which would induce a shear stress of .28 N/mm^2 and .42 N/mm^2 at critical section along the sides of the wall respectively.

The first parameter the effect of which on the strength of the connection was investigated, was the width of wall W_w and models of Ist group were tested for this purpose.

6.4.3.2 Model MT1

The arrangement of reinforcement in this model is shown in Figures (6.41) and (6.42). In the main direction (windward direction), the central strip of the slab which was 600 mm, was reinforced by twelve - 12 mm diameter steel bars. Some of the bars were curtailed at a distance of 470 mm from the back of the model while the rest were cut and welded to 8 mm diameter bar lengths, so as to maintain the required ratios of steel in each strip of the slab according to design. Similarly side strips, each 200 mm wide were reinforced in the windward direction with two - 10 mm diameter bars. In the transverse direction the slab was divided into three strips. The first strip was reinforced with one-6 mm diameter bar and two - 8 mm diameter bars, the second with eight - 10 mm diameter bars and the third strip was reinforced with six - 10 mm diameter bars. The wall was reinforced with eight - 12 mm diameter vertical bars.

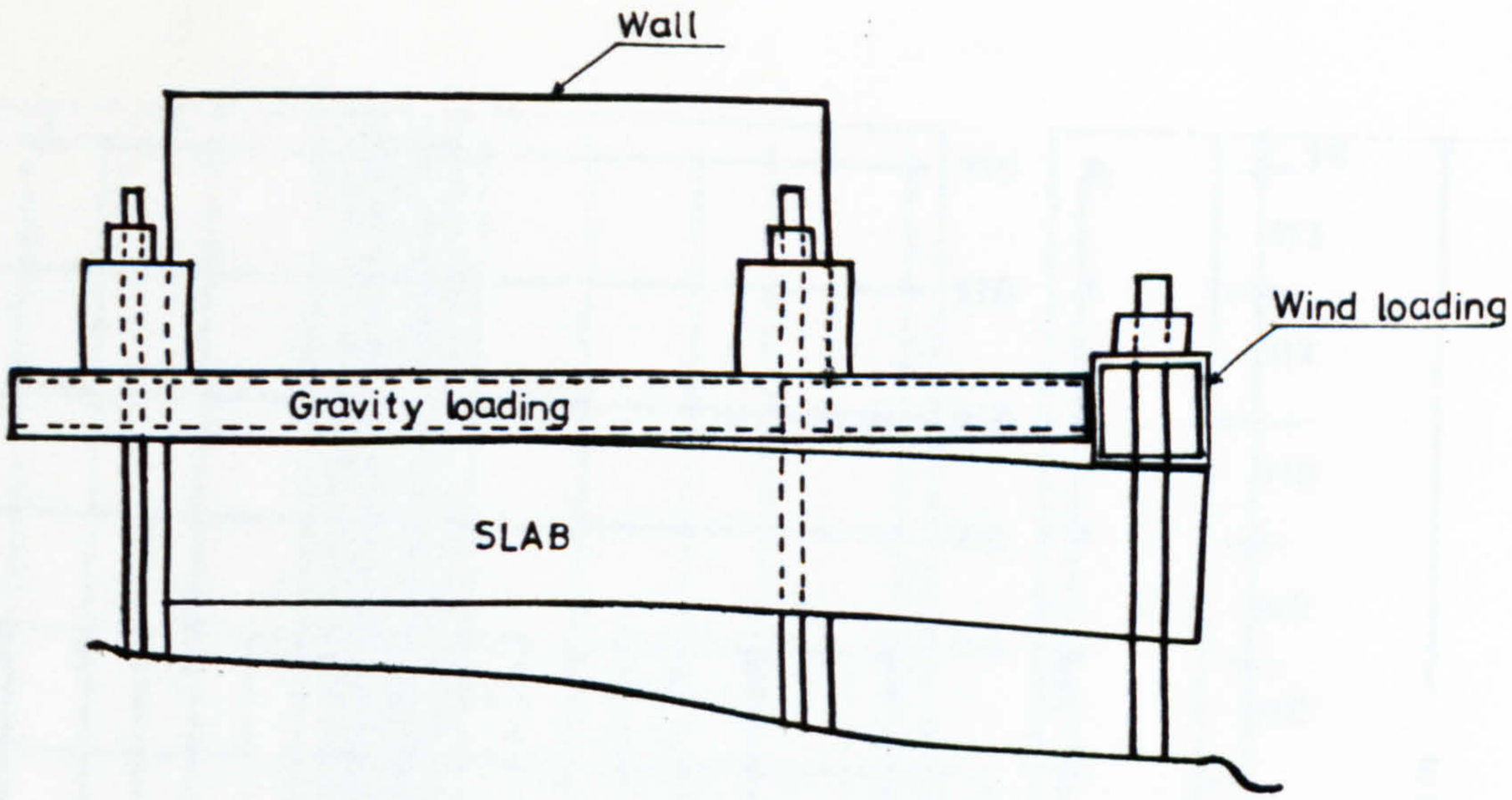

Figure (6.40) : Bending of slab of a model due to wind load alone.

Figure (6.41) : Photograph showing the arrangement of steel in model MT1.

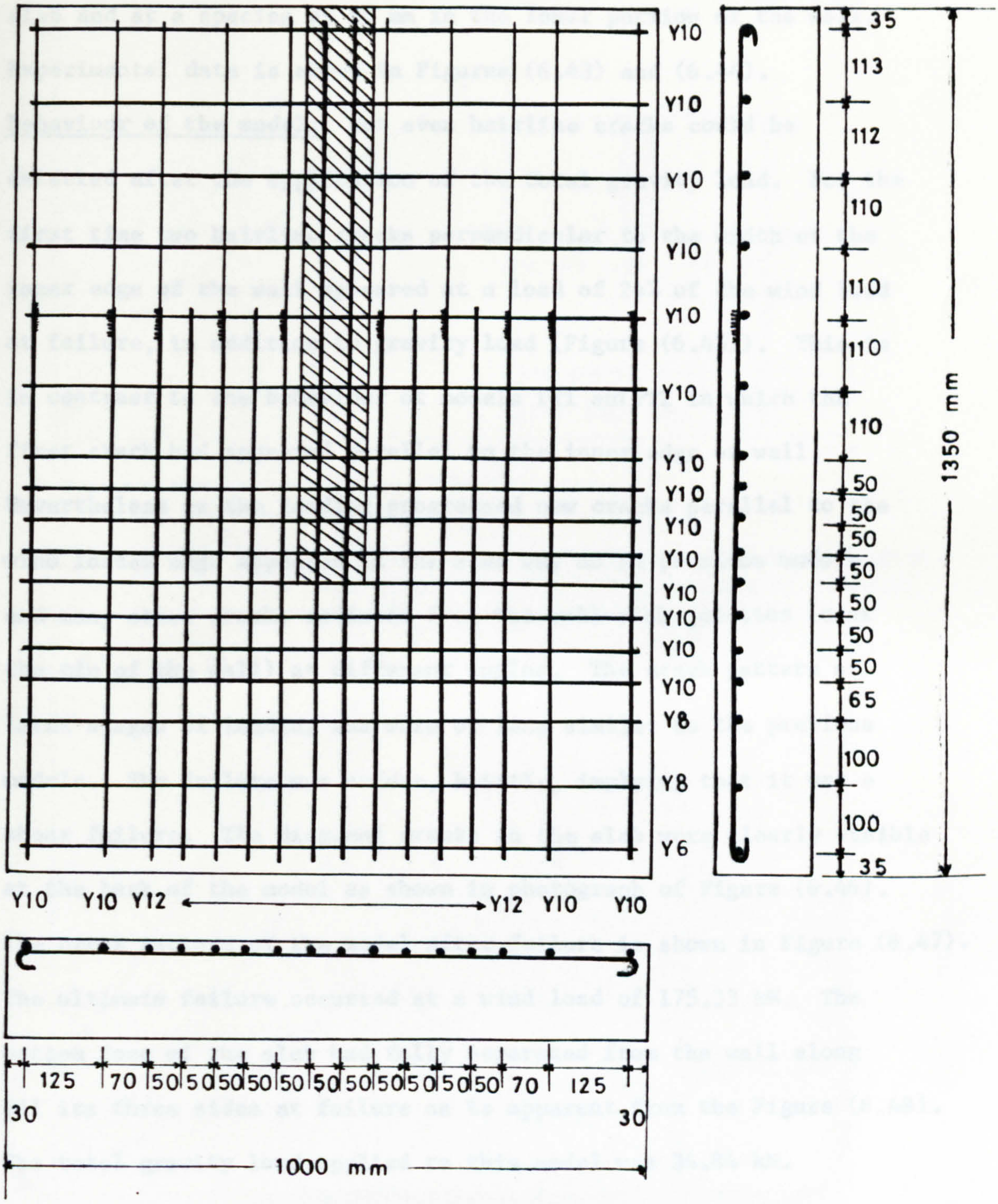

Figure (6.42) : Arrangement of reinforcing bars in the slab of model MT1.

In the wall nine links of 6 mm diameter mild steel bars were provided at a spacing of 70 mm in the portion of wall above the slab and at a spacing of 95 mm in the lower portion of the wall. Experimental data is shown in Figures (6.43) and (6.44).

Behaviour of the model: Not even hairline cracks could be detected after the application of the total gravity load. For the first time two hairline cracks perpendicular to the width of the inner edge of the wall appeared at a load of 24% of the wind load at failure, in addition to gravity load (Figure (6.45)). This is in contrast to the behaviour of models PT1 and PT2 in which the first crack had appeared parallel to the inner edge of wall. Nevertheless as the loading progressed new cracks parallel to the wind loaded edge appeared in the same way as in previous models and many other cracks radiated from the wall-slab junction (near the tip of the wall) at different angles. The crack pattern at later stages of loading was more or less similar to the previous models. The failure was sudden, brittle, implying that it was a shear failure. The diagonal cracks in the slab were clearly visible at the back of the model as shown in photograph of Figure (6.46). The crack pattern of the model after failure is shown in Figure (6.47). The ultimate failure occurred at a wind load of 175.33 kN. The bottom face of the slab had fully separated from the wall along all its three sides at failure as is apparent from the Figure (6.48). The total gravity load applied to this model was 34.84 kN.

6.4.3.3 Model MT2

All the features of this model were same as those of model MT1 except the wall width which was 900 mm for MT1 and 600 mm for MT2.

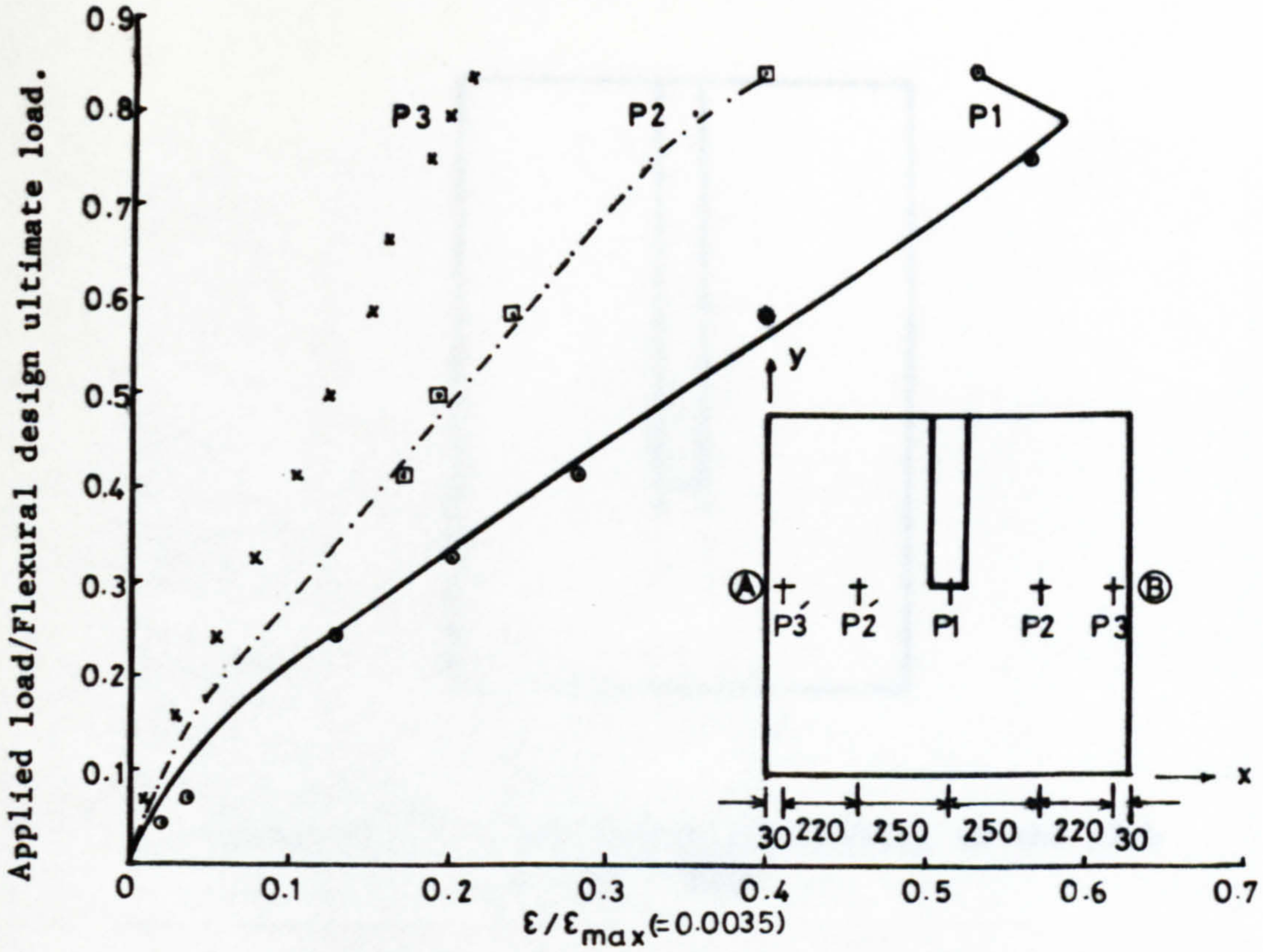

Figure (6.43) : Compressive strain in concrete at different points in wind ward direction along transverse critical section AB, in the slab of MT1.

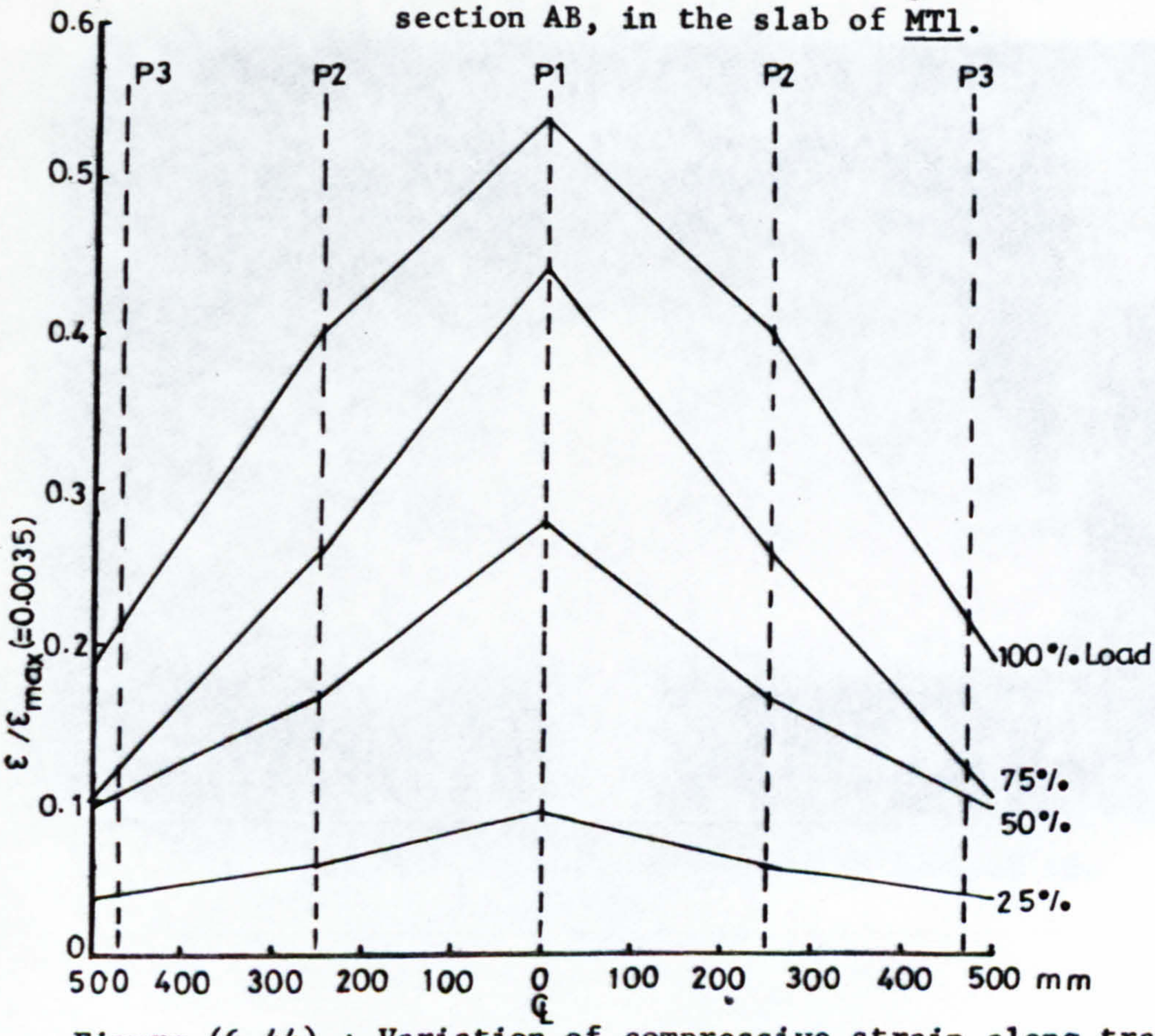

Figure (6.44) : Variation of compressive strain along transverse critical section at different loading stages in the slab of MT1.

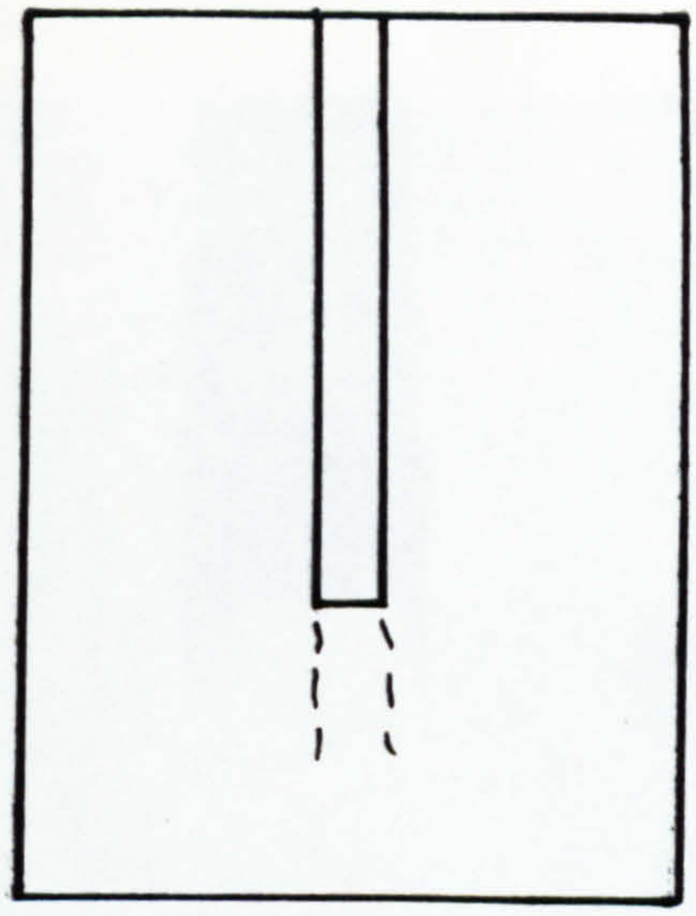

Figure (6.45) : Initiation of cracking in the slab of model MT1.

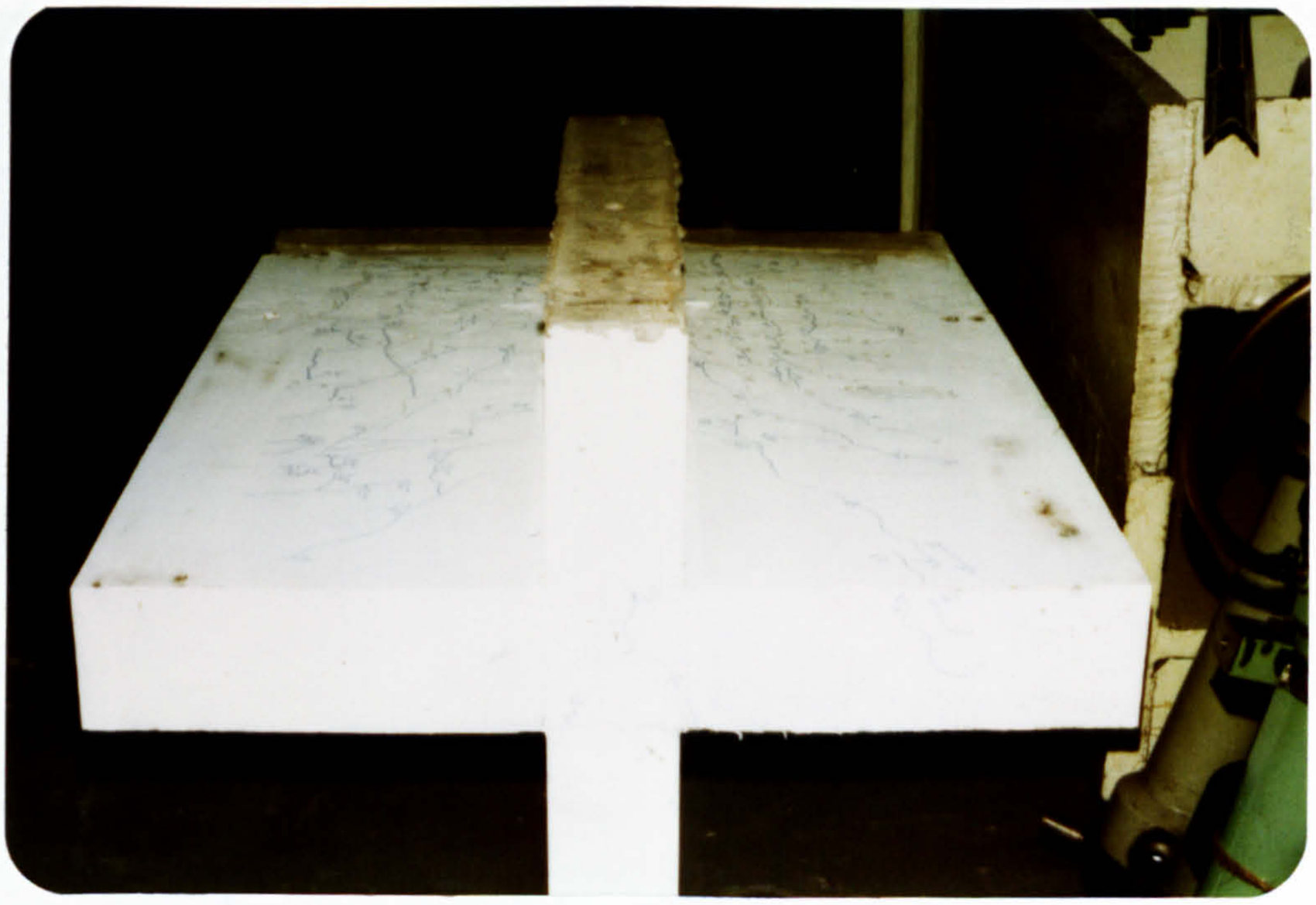

Figure (6.46) : Showing cracks at the back of the model MT1.

Figure (6.47) : showing crack pattern of model MT1 after failure.

Figure (6.48) : showing the separation of slab from the wall at its bottom in model MT1.

The arrangement of reinforcement in the slab of this model is shown in Figure (6.49). The same loading arrangement was used as in previous tests. However the intensity of the forces in the four bars used for applying the gravity load was decreased this time in order to maintain the same level of shear stress due to gravity load at the critical section as that in model MT1, which was .14 N/mm^2 (total gravity load = 24.kN).

This model was also loaded in the same way as model MT1 but with a wind load increment of 4.45 kN. However due to yielding of the thread of the central bar of loading arrangement at a load of 71% of the load at failure, the load dropped so that the model was unloaded. The model was reloaded after replacing the bar but with a load increment of 11.57 kN till it reached its previous level. Then the load increment was reduced to 4.45 kN once again. Experimental data is shown in Figures (6.50) and (6.51).

Behaviour of the model: Like model MT1, not even a single hairline crack appeared after the application of total gravity load. For the first time two cracks parallel to the inner edge of the wall appeared at a load of 28.5% of the wind load at failure in addition to the gravity load. As the loading progressed a few parallel cracks appeared in the same way as in model MT1 and many other cracks radiated from the wall-slab junction at different angles at different loading stages. The shear cracks in the slab at the back of the model which appeared at the time of failure of the model MT1, were detected at a load of 72.4% of the wind load at failure of this model. The ultimate failure occurred at a load of 192.9 kN. Photographs showing crack pattern of this model/

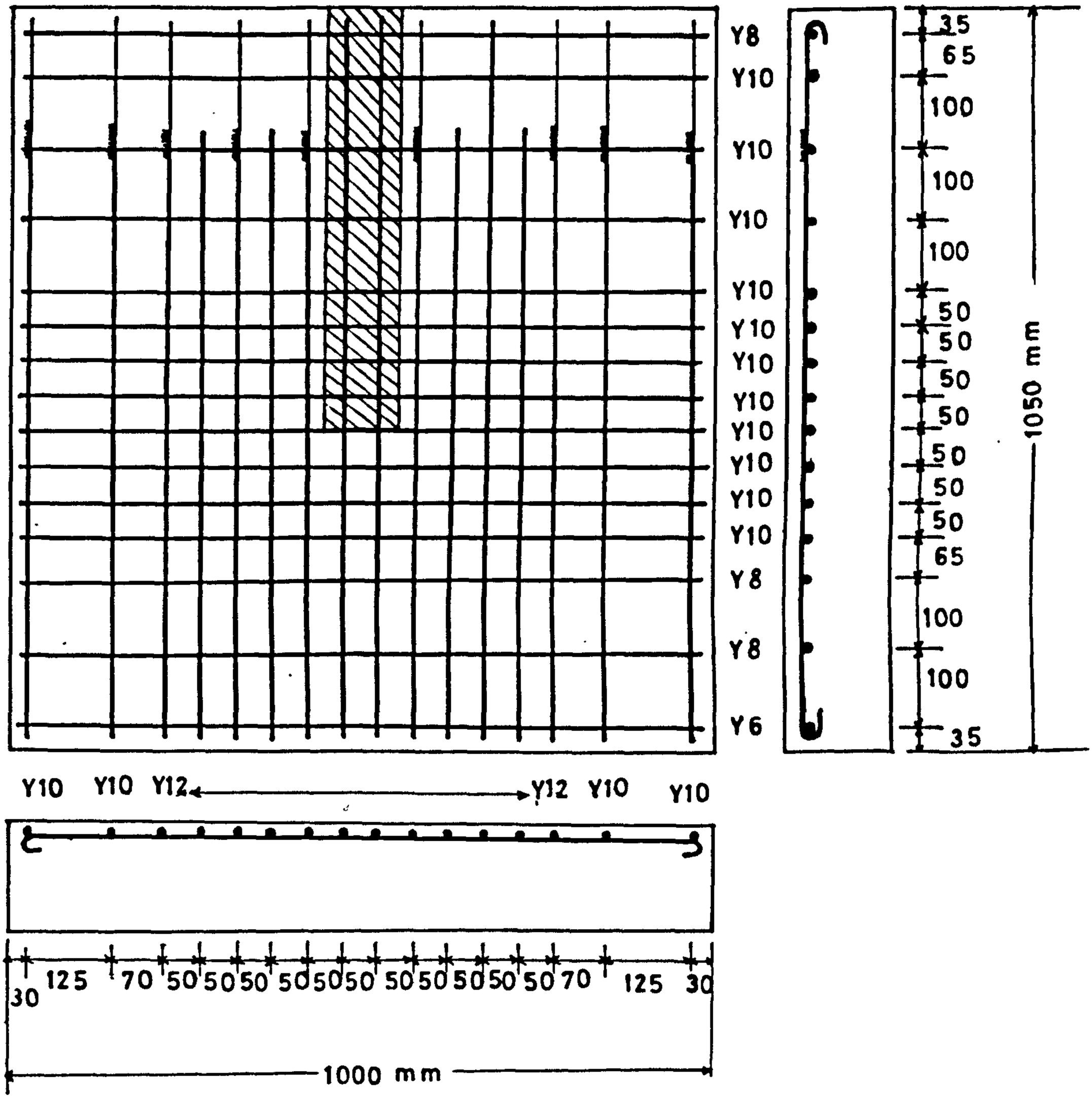

Figure (6.49) : Arrangement of reinforcing bars in the slabs of models MT2, MT4 & MT5.

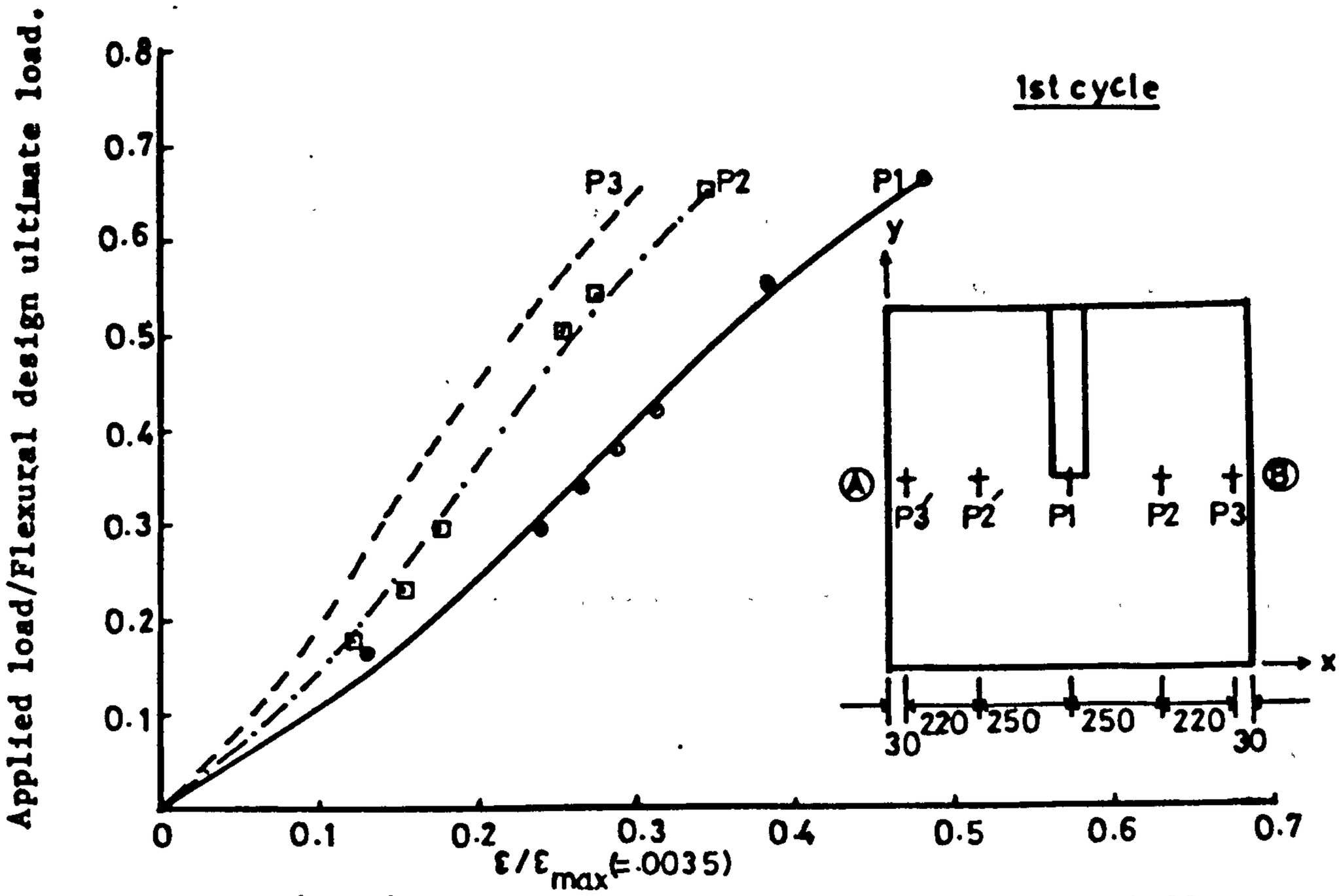

Figure (6.50) : Compressive strain in concrete at different points along transverse critical section AB, in the slab of MT2.

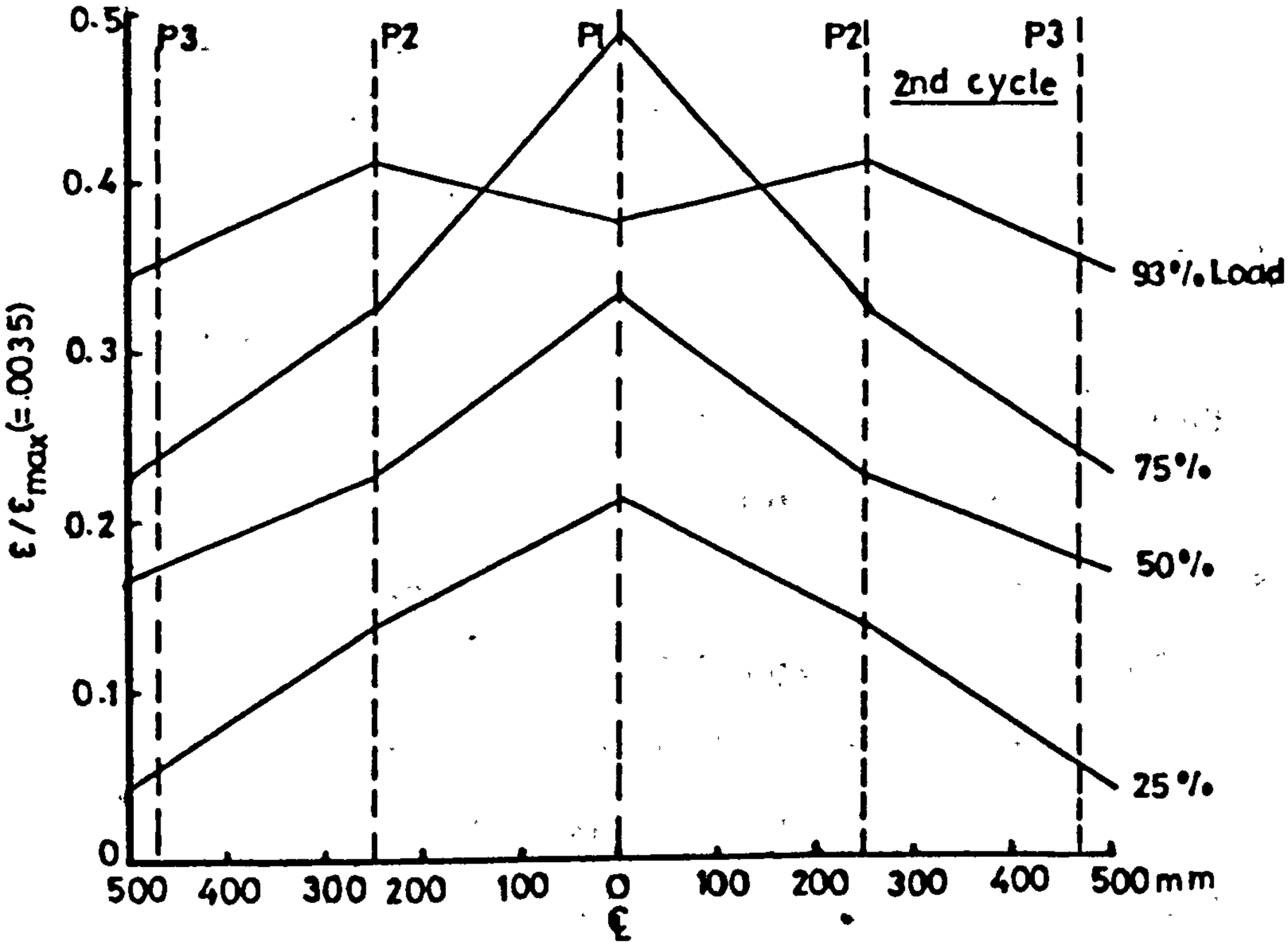

Figure (6.51) : Variation of strain in concrete along critical section in model MT2 at different stages of loading.

after failure are presented in Figures (6.52) to (6.54) and a sketch of the cracking at the free edge of the slab is shown in Figure (6.55).

6.4.3.4 Model MT3

All the specific features of this model were the same as those of model MT2 except that the length of slab was decreased by 200 mm so that the wall width along its sides in connection with the slab was only 400 mm. The length of wall could not be decreased because of the requirements of the supporting and testing arrangement of the models. The arrangement of reinforcing bars in the slab of this model is shown in Figure (6.56). For comparison the wind load-displacement curves of all the models of Ist group are shown in Figures (6.57). Different experimental data are shown in Figures (6.58) and (6.59). The total gravity load applied to this model was 18 kN.

Behaviour of the model: For the first time two cracks appeared at a load of approximately 31% of the load at failure for this model but their location was different from the previous models as can be seen in Figure (6.60). These cracks were perpendicular to the sides of the wall, though later the crack pattern became the same as for other models of this group. The shear cracks in the slab at the back of the model appeared at a load of 51% of the load at failure. These cracks after failure are shown in Figure (6.61). The failure occurred at a load of 154.2 kN. The photographs showing the crack pattern of the model after failure are presented in Figures (6.62) to (6.64).

Figure (6.52) : Crack pattern of the slab of MT2 after failure.

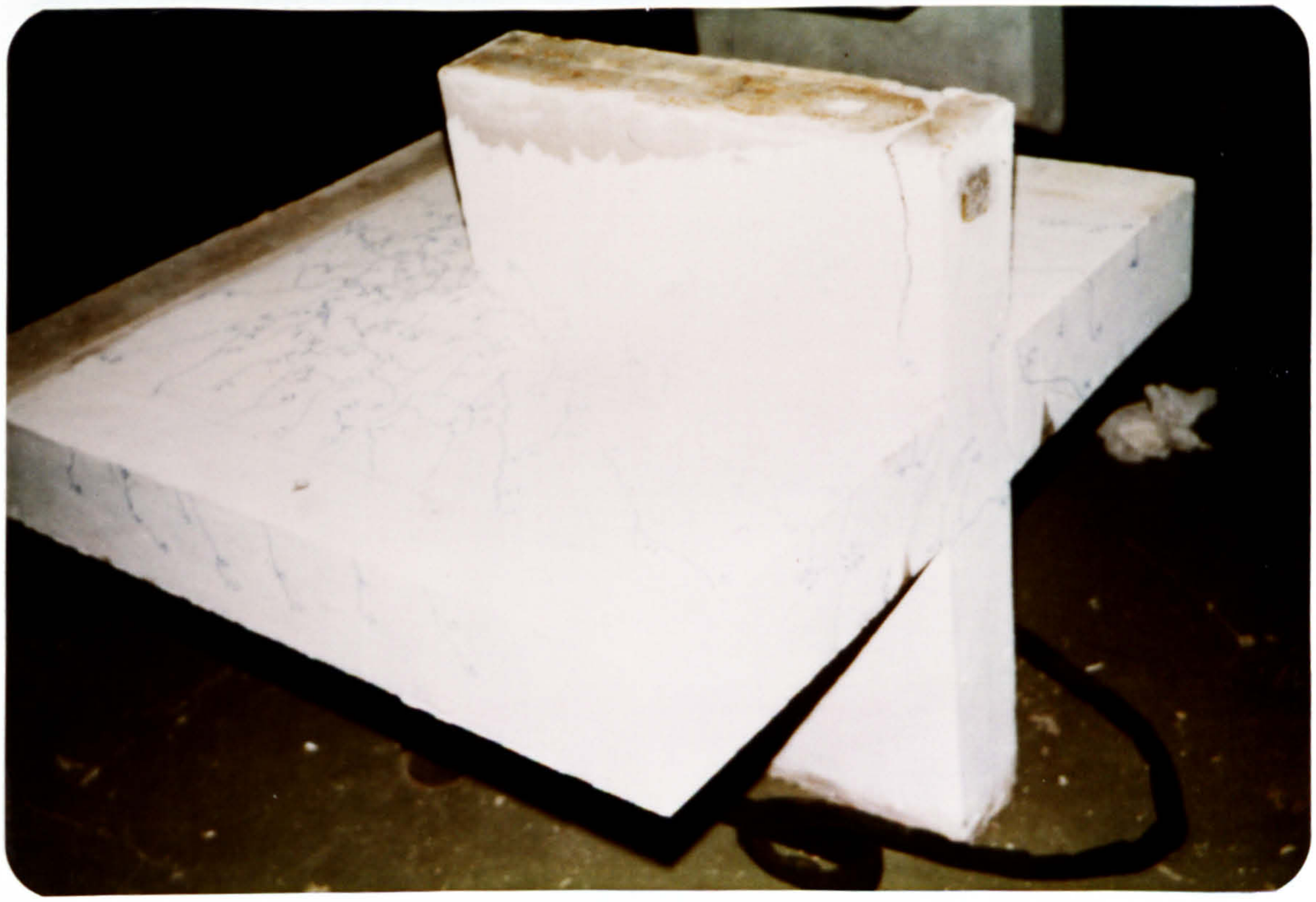

Figure (6.53) : Shear crack in the slab at the back of model MT2 after its failure.

Figure (6.54) : Photograph showing the cracking of the slab at its bottom after failure of model MT2.

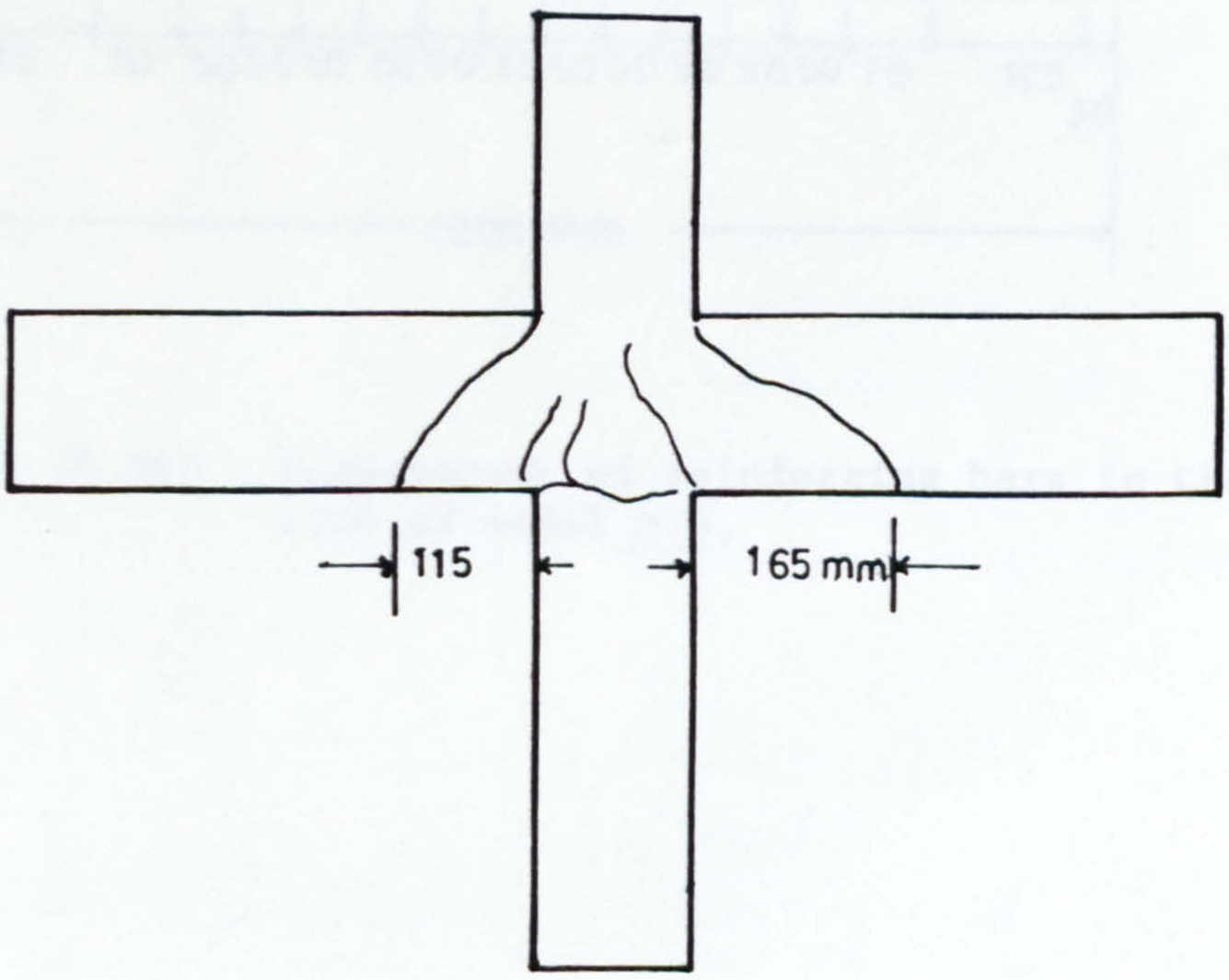

Figure (6.55) : Shear cracks after failure in the slab at the back of model MT2.

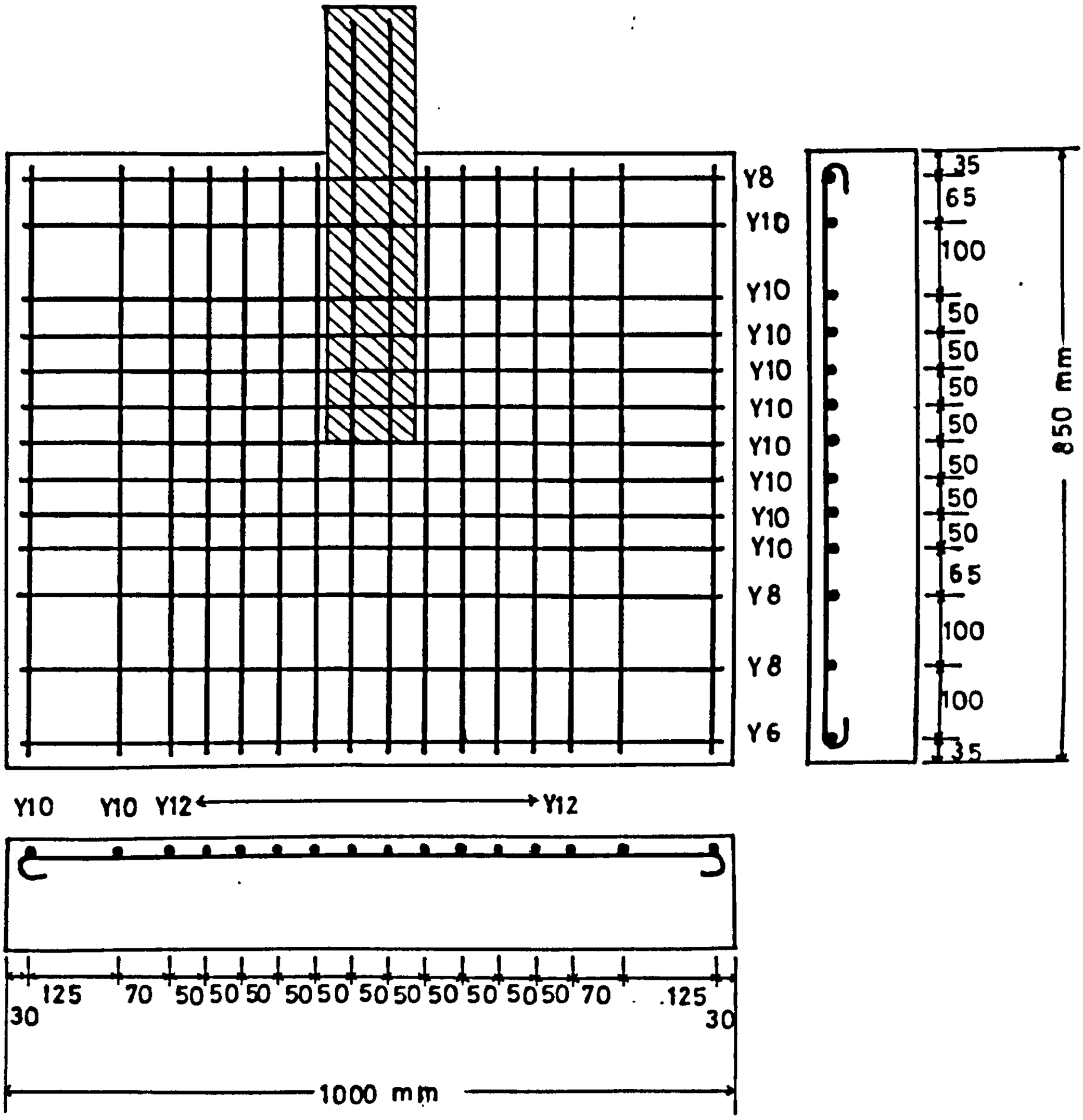

Figure (6.56) : Arrangement of reinforcing bars in the slab of model MT3.

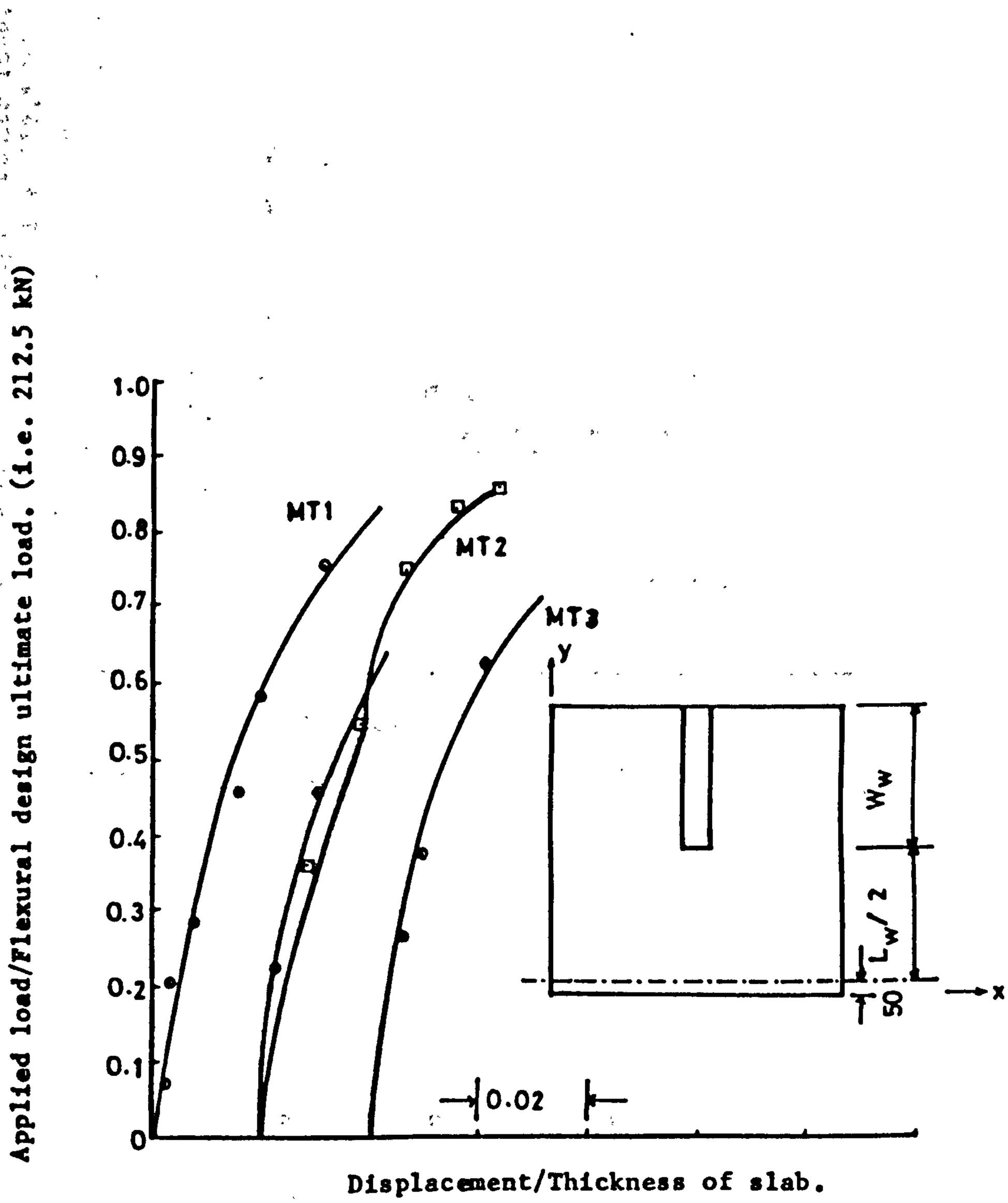

Figure (6.57) : Wind load-displacement relationship for models of Ist group of MT series.

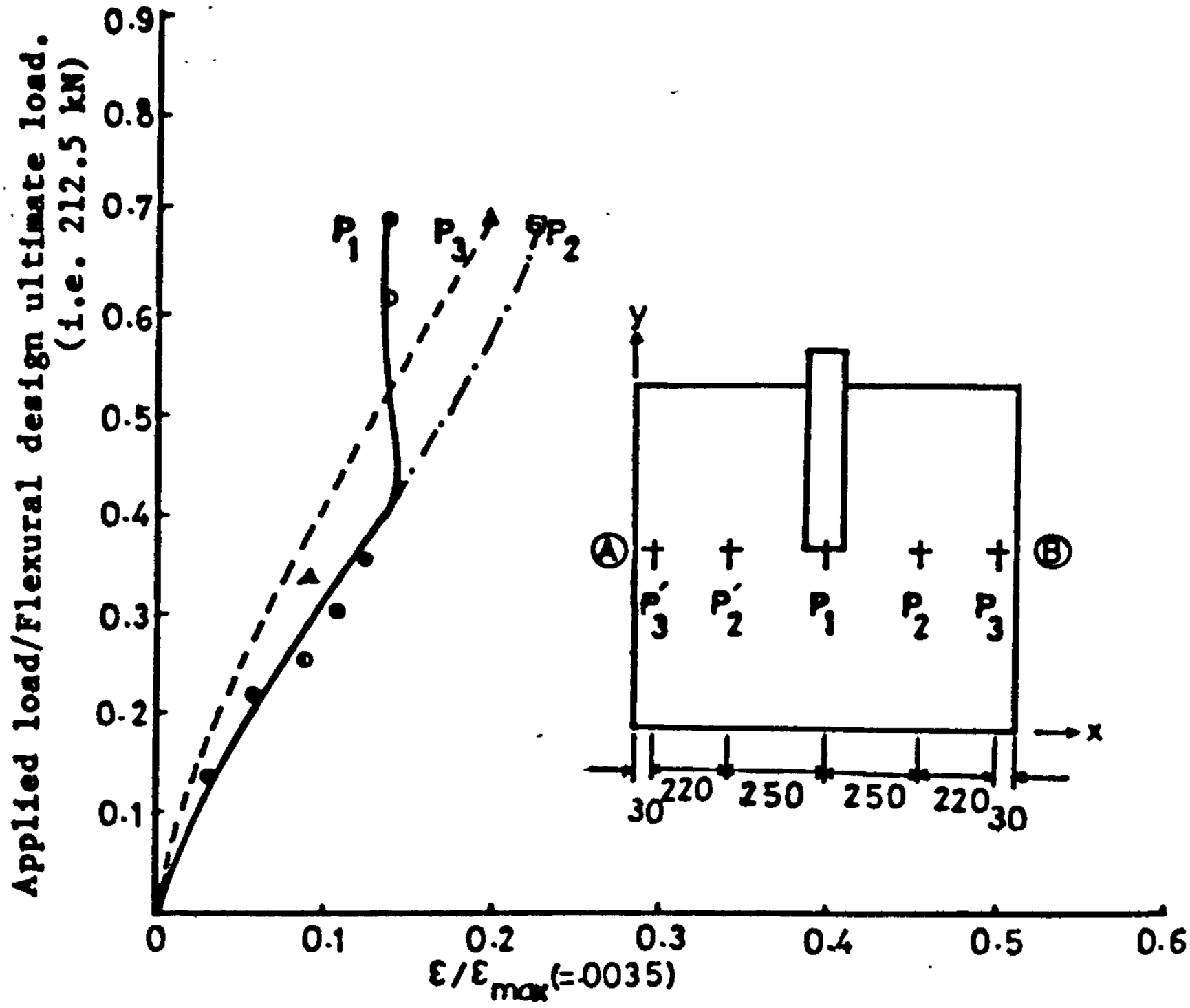

Figure (6.58) : Compressive strain at different points along transverse section AB in the slab of model MT3.

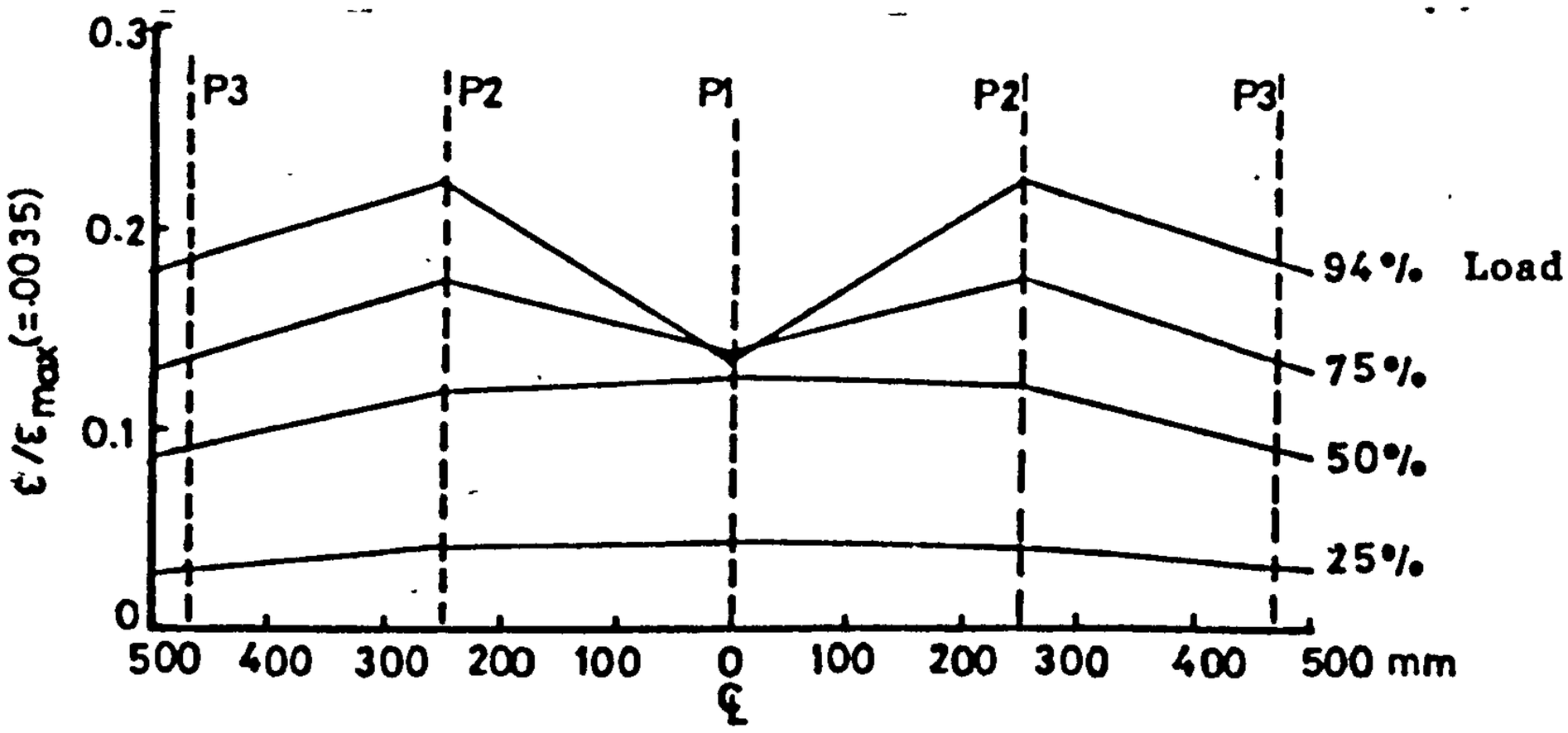

Figure (6.59) : Variation of compressive strain along transverse critical section, at the bottom of slab of model MT3.

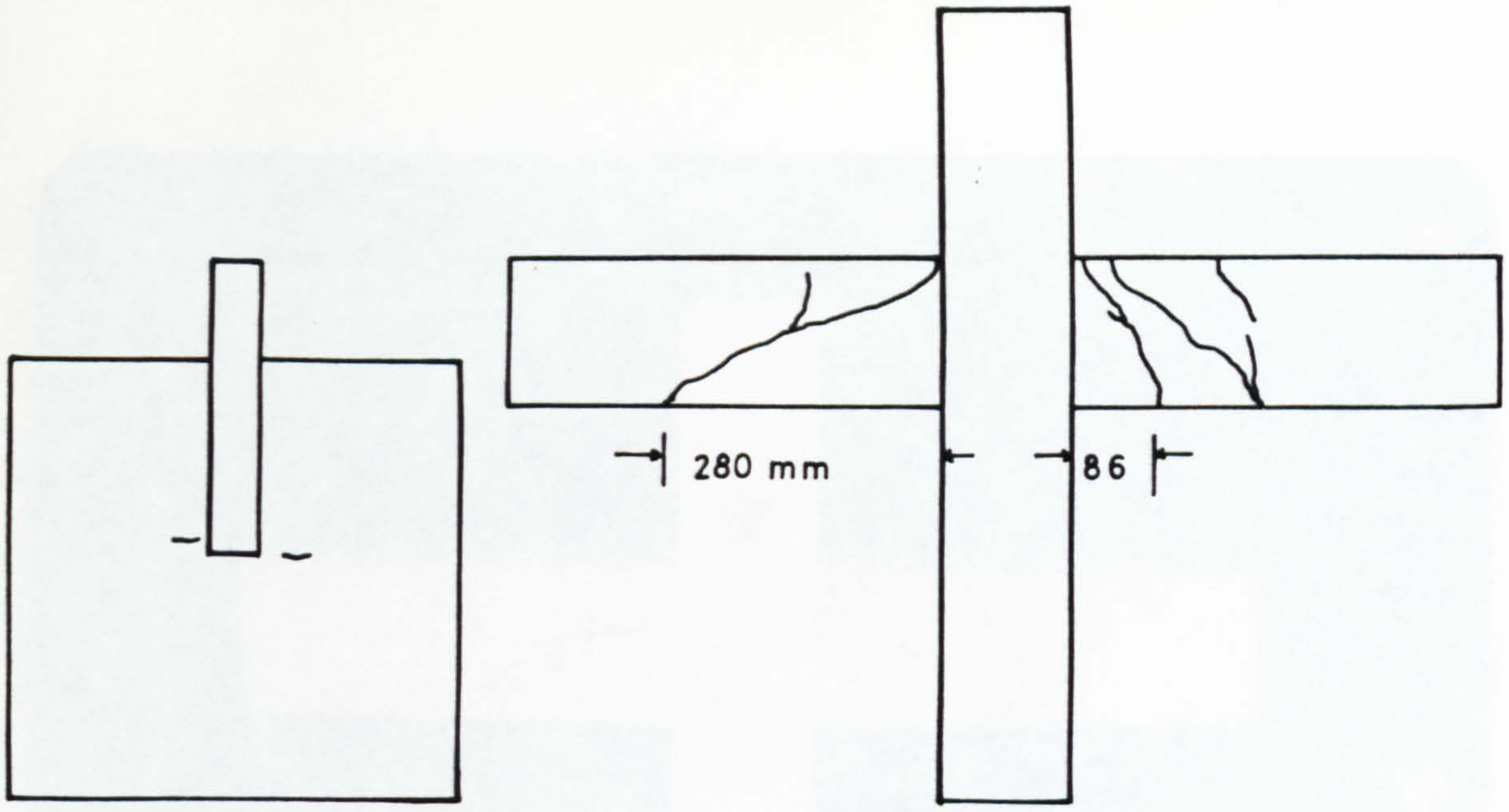

Figure (6.60) : Initiation of cracks in the slab of MT3.

Figure (6.61) : Shear cracks in the slab at the back of model MT3.

Figure (6.62) : Crack pattern of MT3 after failure.

Figure (6.63) : Crack pattern of slab after failure at the back of MT3.

Figure (6.64) : Photograph showing the bottom of the slab of MT3 after failure.

6.4.3.5 Comparison and discussion

From Figure (6.57) which compares the wind load-displacement curves for all the three models of the Ist group, it can be observed that these curves closely follow each other, though model MT2 shows slightly higher stiffness. This may be due to the fact that the compressive strength of the concrete of model MT2 on the day it was tested, was somewhat higher. Thus it may be concluded that the wall width did not affect the wind load-displacement behaviour of the connecting slab of a shear wall structure.

As can be seen from the Figure (6.44) the curve showing the variation of compressive strain in concrete at the bottom of the slab, along the transverse critical section in model MT1, became steeper with the increase in the load till the load reached 75% of its ultimate value. The rate of increase of strain at central point P1 remained fairly constant afterwards. The strain at this point showed slight decrease when final load increment was applied. Same behaviour of the measured strain at point P1 as that of model PT2 was observed in model MT2 as well. As is apparent from Figure (6.51), up to 75% of the ultimate load it was a maximum and then its rate of increase started decreasing so that at failure it was considerably lower than that at the consecutive point P2. The drop of the strain at point P1 near the inner face of wall in model MT3 took place even before the load reached 75% of its ultimate load and at failure it was the lowest along the critical section (Figure (6.59)). The strain in steel was not measured in the models of this group.

Table 6.8 compares the experimental ultimate loads with those calculated using different methods, for the models of Ist group. The effect of the presence of the gravity load was taken into account by assuming a reduced value of v_c (43) (critical shear stress) for the lengths of critical perimeter along the sides of the walls. The code value of v_c include the factor of safety. In the absence of the information regarding the accurate value of this factor, it may be assumed that the calculated ultimate strength of a connection from a certain formula is reasonable if the ratio experimental ultimate load to calculated ultimate load falls in the range of 1.25 to 1.5.

It can be observed from table 6.8 that CP 110 without transfer of moment overestimates the strength of connection and the degree of overestimation increases with the increase in the length of wall. All the other methods except ACI318 and Schwaighofer & Collins (8) greatly underestimate the strength of connection. ACI 318 (4) overestimates the strength of connection of model MT1 and the degree of overestimation decreases with the decrease in the length of wall. This may very well be because of the fact that this method is basically proposed for estimating the strength of slab-column connection. The method could probably give reasonable estimation of the wall-slab connection as well, if only a certain portion of wall width is assumed to be effective in resisting the uneven shear. Schwaighofer & Collins method (8) overestimates the strength of connection of MT3 and degree of overestimation decreases with the increase in the length of wall (opposite to the ACI318 formula).

Table 6.8. Comparison of calculated and experimental ultimate loads for models of 1st group of MT series.

Model No.	f_{cu} N/mm^2	Experimental load at failure V_{exp} kN	CP110 without transfer of moment $V_{cal\ 1}$ kN	CP110 with transfer of moment $V_{cal.2}$ kN	ACI method $V_{cal.3}$ kN	Chang method $V_{cal.4}$ kN	Schwaighofer & Collins $V_{cal\ 5}$ kN	Coull & Wong $V_{cal\ 6}$ kN
MT1	37.0	175.33	238.9 (.73)	66.69 (2.63)	234.2 (.75)	93.58 (1.87)	167.31 (1.05)	83.1 (2.11)
MT2	50.2	192.9	192.42 (1.0)	46.3 (4.17)	184.07 (1.05)	86.43 (2.23)	196.39 (0.98)	85.93 (2.24)
MT3	42.8	154.2	155.78 (0.99)	33.17 (4.65)	119.21 (1.29)	61.83 (2.49)	180.64 (0.85)	85.93 (1.79

Note: Figures in brackets show the ratio $\frac{V_{exp}}{V_{cal}}$

6.4.4 Models of group II (models MT2, MT4 and MT5) (Effect of gravity load).

The effect of the presence of evenly distributed shear stress due to gravity load on the strength of the wall-slab connection against applied wind load was studied by testing these models. The only variable among these models was the intensity of gravity load. Apart from the strain in concrete, strain in steel was also measured in the models MT4 and MT5. Since the model MT2 was common to both, group I and group II, only models MT4 and MT5 are described here.

6.4.4.1 Model MT4

This model was similar to MT2 except the intensity of gravity load which was twice that for MT2. Like the previous tests the total gravity load of 48 kN (inducing a shear stress of .28 N/mm^2 along the sides of the wall) was applied in first five increments of 9.6 kN and the wind load was applied in equal increments of 8.89 kN till it was equal to 86% of the load at failure. The load increment was then reduced to 4.45 kN till failure was reached. Experimental data are shown in Figures (6.65) to (6.69).

Behaviour of the model: Though the intensity of gravity load was twice that of the model MT2, no cracks occurred even after the full application of gravity load. Two cracks appeared at a wind load of 26% of the load at failure, in addition to gravity load. The location of these cracks is shown in Figure (6.70). Shear cracks in the slab at the back of the model developed at a load of only 40% of the load at failure. These cracks after failure are shown in Figure (6.71). As the loading progressed many other/

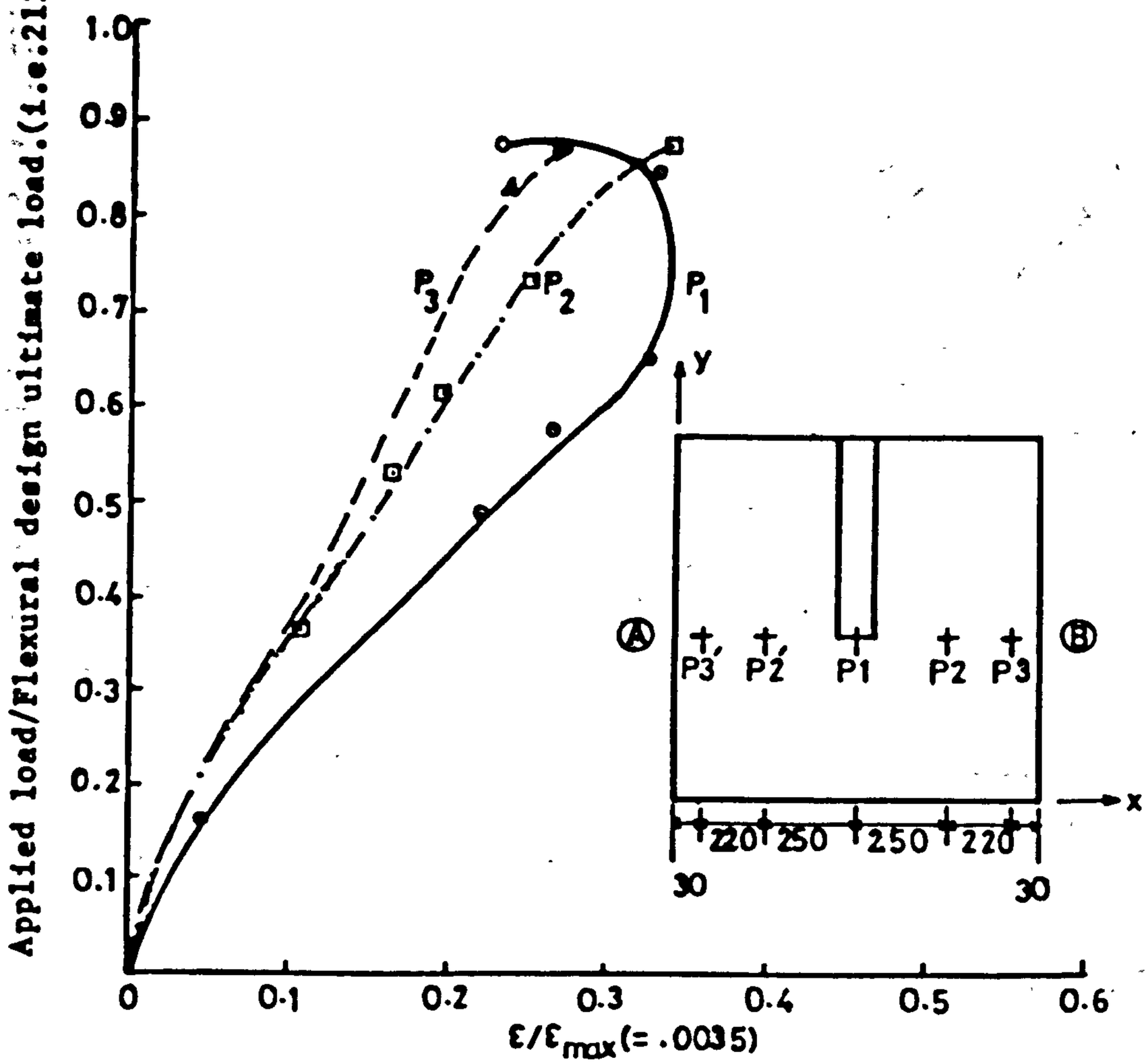

Figure (6.65): Compressive strain at different points along transverse section AB in model MT4.

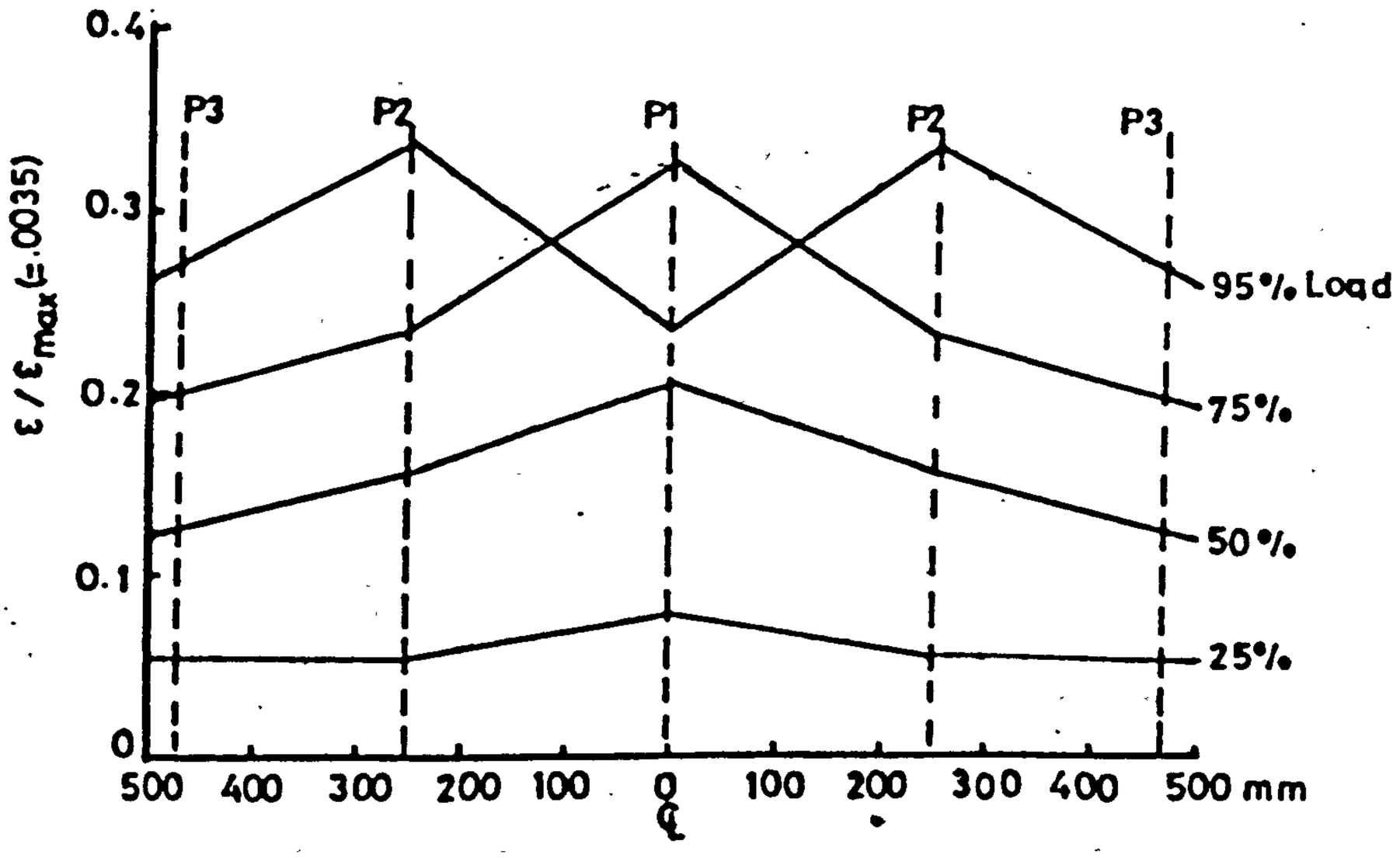

Figure (6.66) : Variation of compressive strain along transverse section at different loading stages in model MT4.

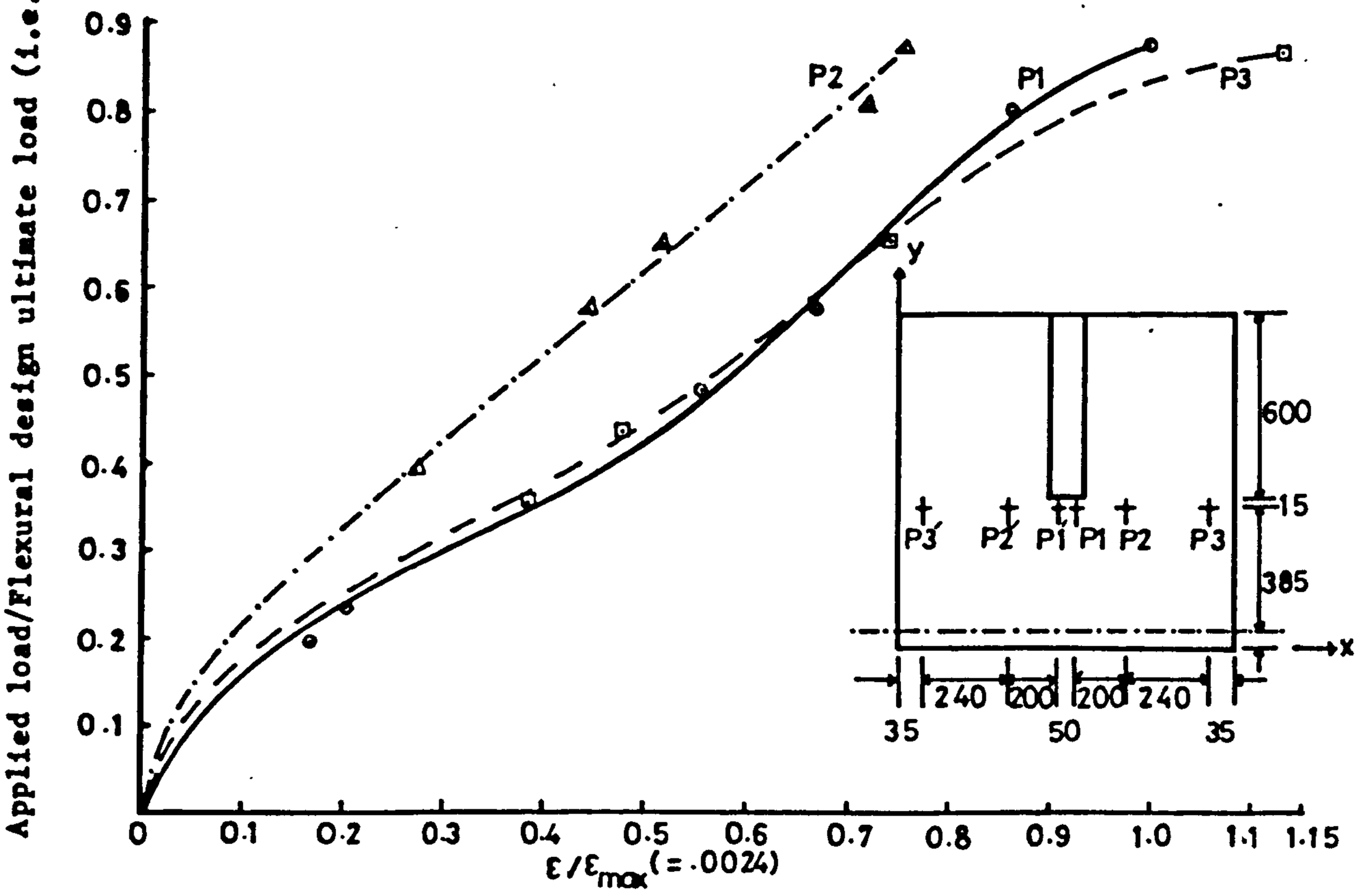

Figure (6.67) : Strain in steel in windward direction in the slab of model MT4.

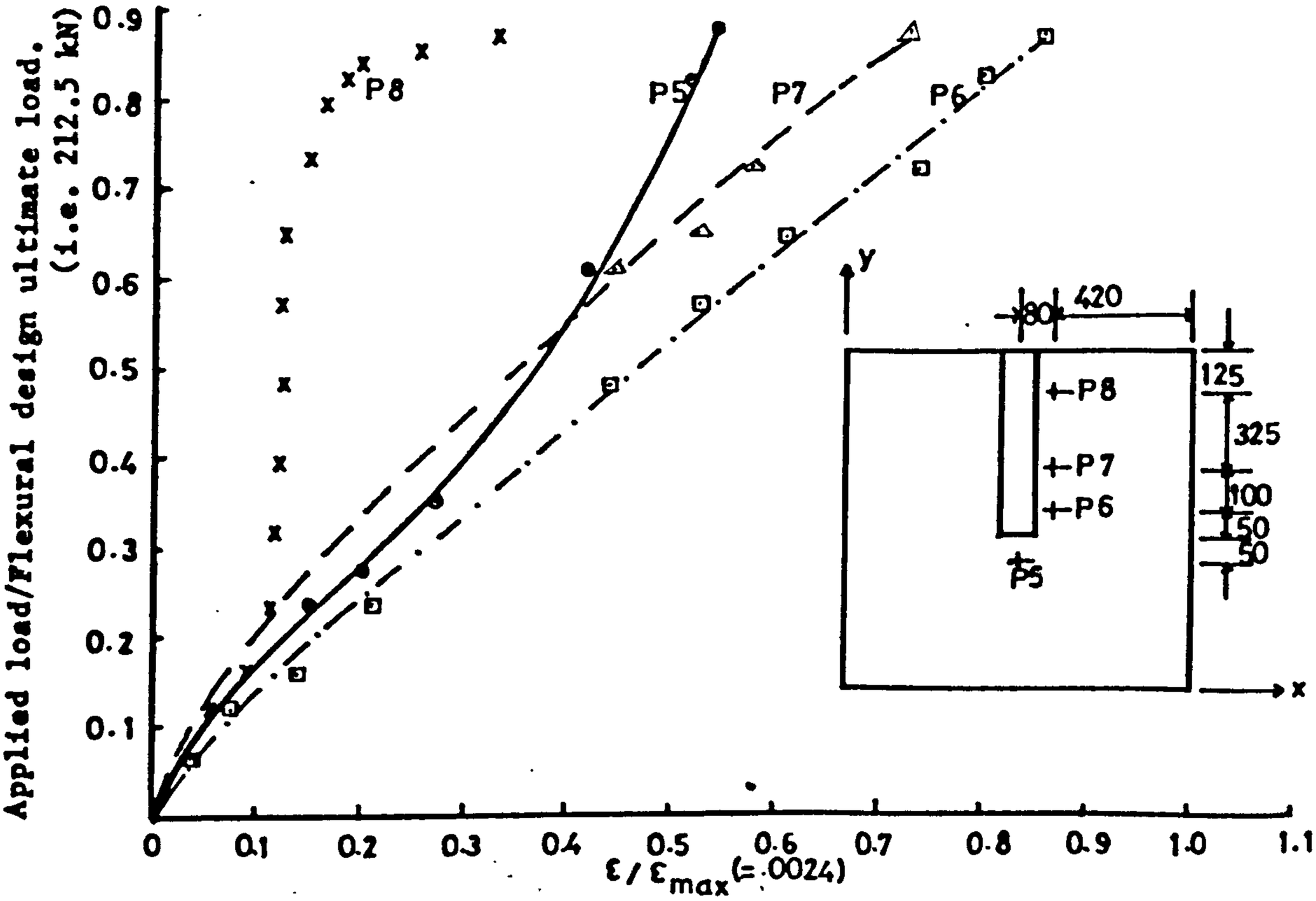

Figure (6.68) : Strain in steel in transverse direction in the slab of MT4.

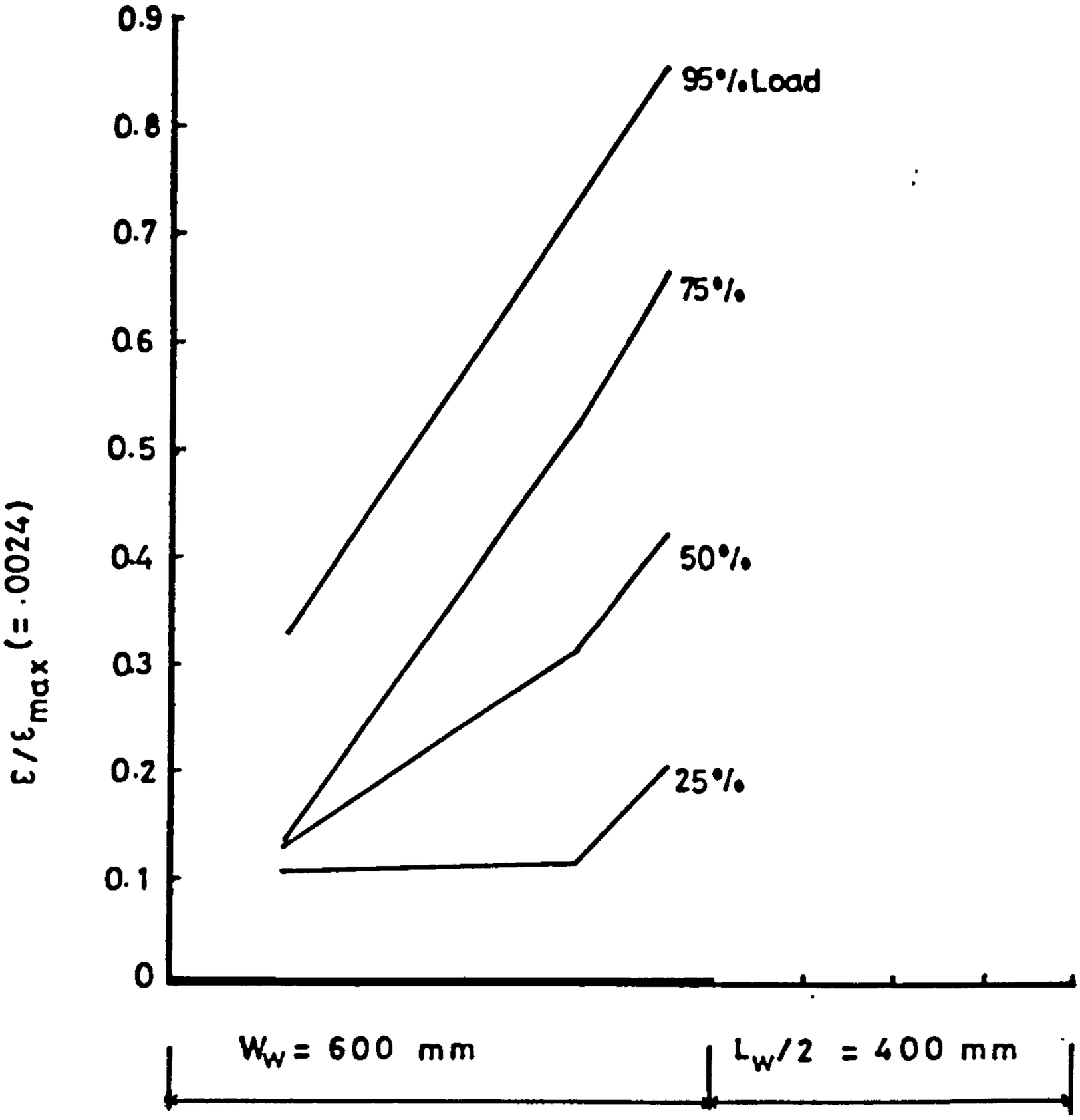

Figure (6.69) : Variation of strain in steel in transverse direction along the side of wall of model MT4.

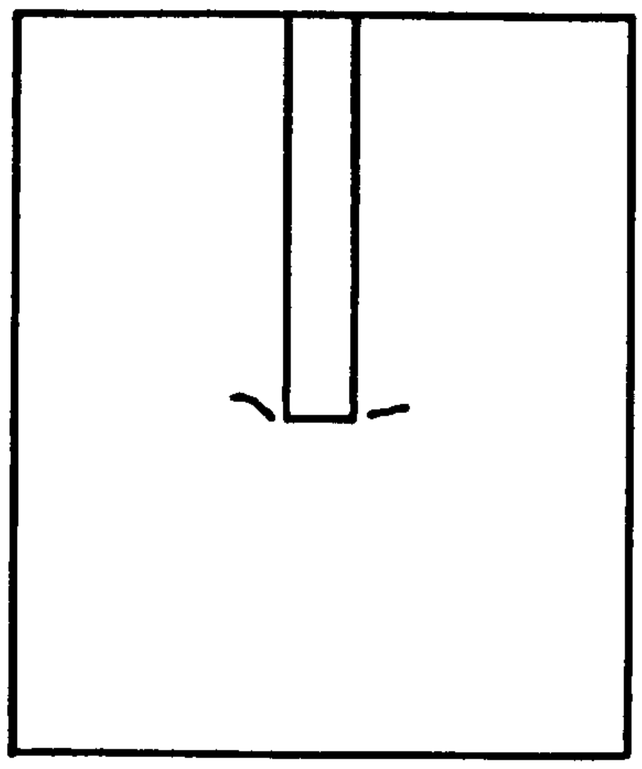

Figure (6.70) : Initiation of cracking in model MT4.

cracks appeared in the slab at its back, sides and the top. The crack pattern of this model after failure is shown in Figures (6.72) to (6.74). This is not much different from that of model MT2. The failure occurred at a wind load of 192.76 kN.

6.4.4.2 Model MT5

This model was similar to MT2 except that the gravity load was thrice that of MT2. Like other models all the gravity load of 72 kN (inducing a shear stress of .42 N/mm^2 along the sides of the wall) was applied first and then the wind load was applied in equal increments of 8.89 kN till the failure occurred. For comparison wind load-displacement curves of models MT2, MT4 and MT5 are shown in Figure (6.75). Other experimental data are shown in Figures (6.76) to (6.80).

Behaviour of the model: In spite of the fact that the gravity load applied to this model was three times as much as that of model MT2, no cracks developed after its full application in this case either. Nevertheless unlike previous models, fine flexural cracks parallel to the sides of the wall appeared in the slab on both sides of the wall of this model when the load reached a level of 28% of the load at failure. This is understandable, since the wind load is transferred partly directly to the wall at its inner edge and partly through the sides inducing negative moment M_x in the slab in transverse direction. This moment together with the moment M_g already acting on the slab along the sides of wall induced by the gravity load of higher intensity in the case of this model, caused this type of cracking. The location of these cracks is shown in /

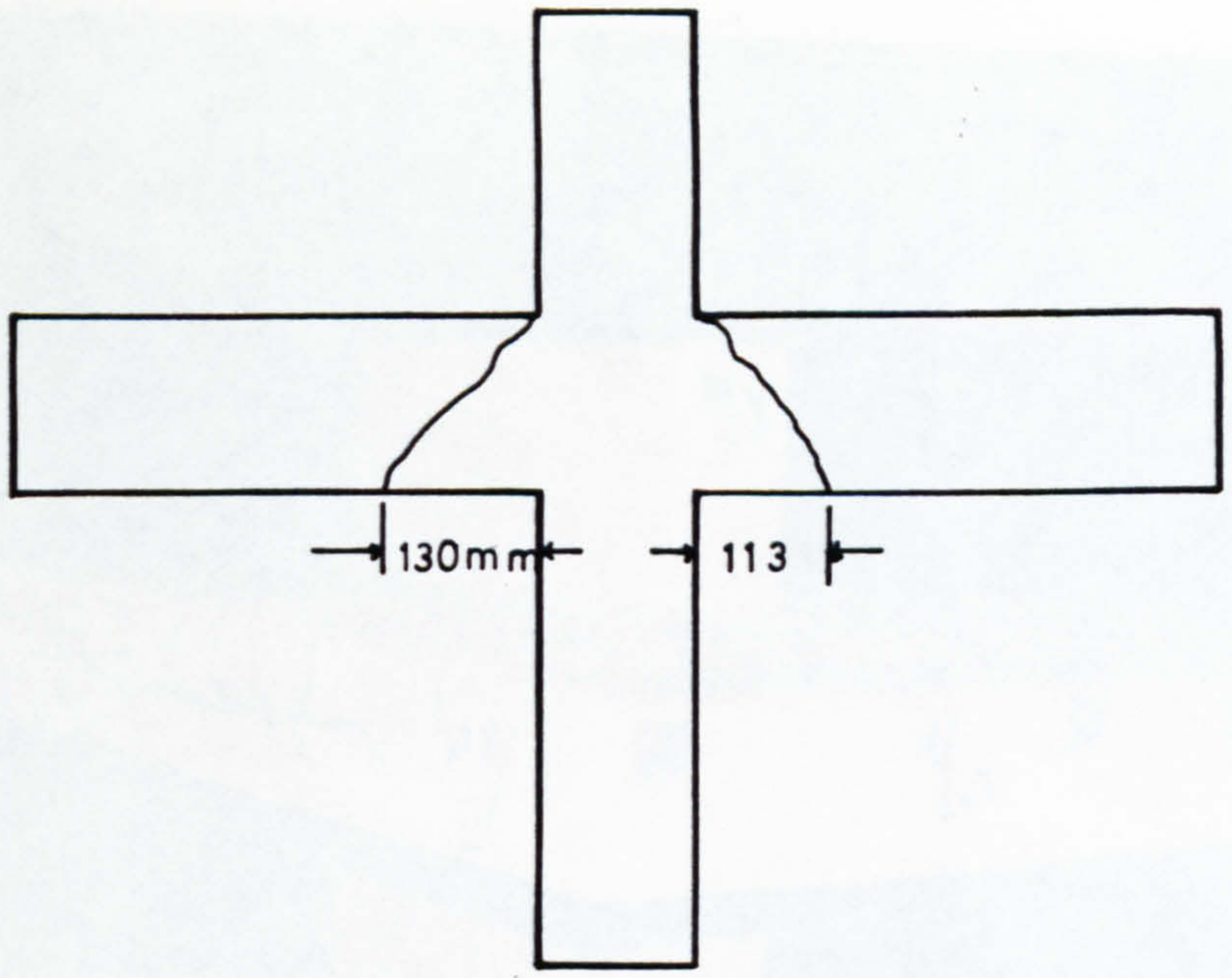

Figure (6.71) : Shear cracks in the slab at the back of model MT4 after failure.

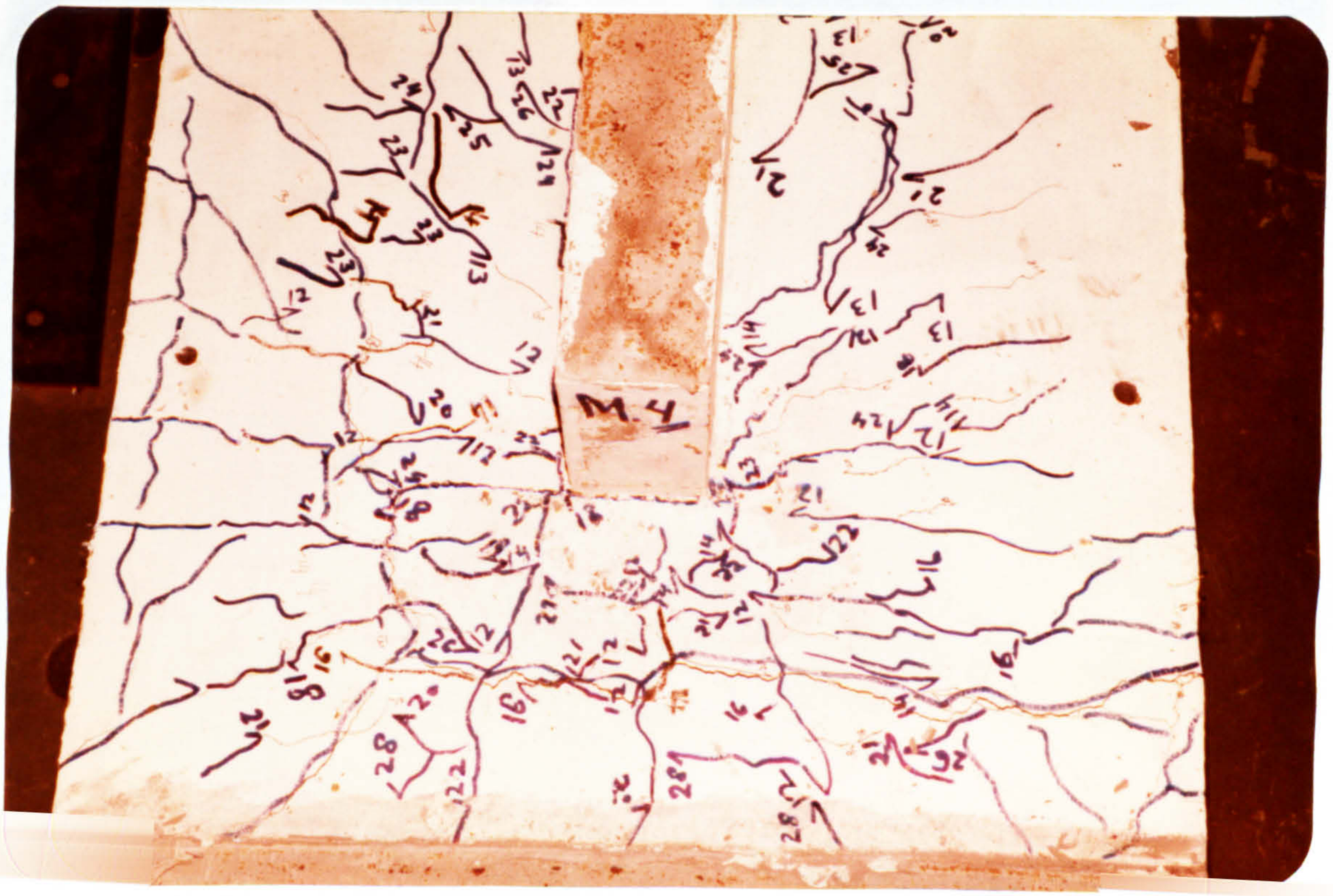

ıilure (6.72) : Crack pattern of the slab of model M after failure.

Figure (6.73) : Photograph showing the cracks in the sides of the slab of model MT4 after failure.

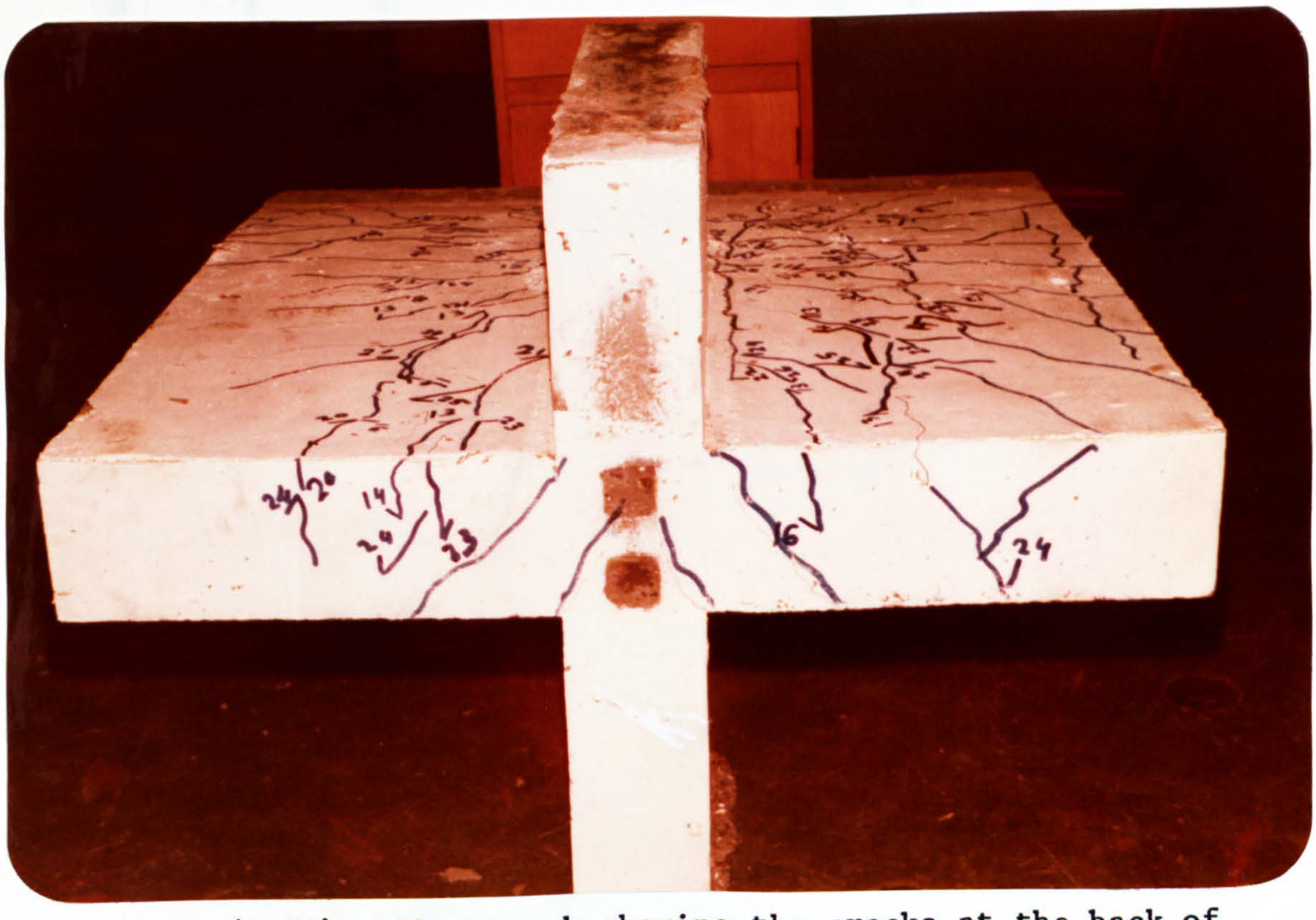

Figure (6.74) : Photograph showing the cracks at the back of the model MT4.

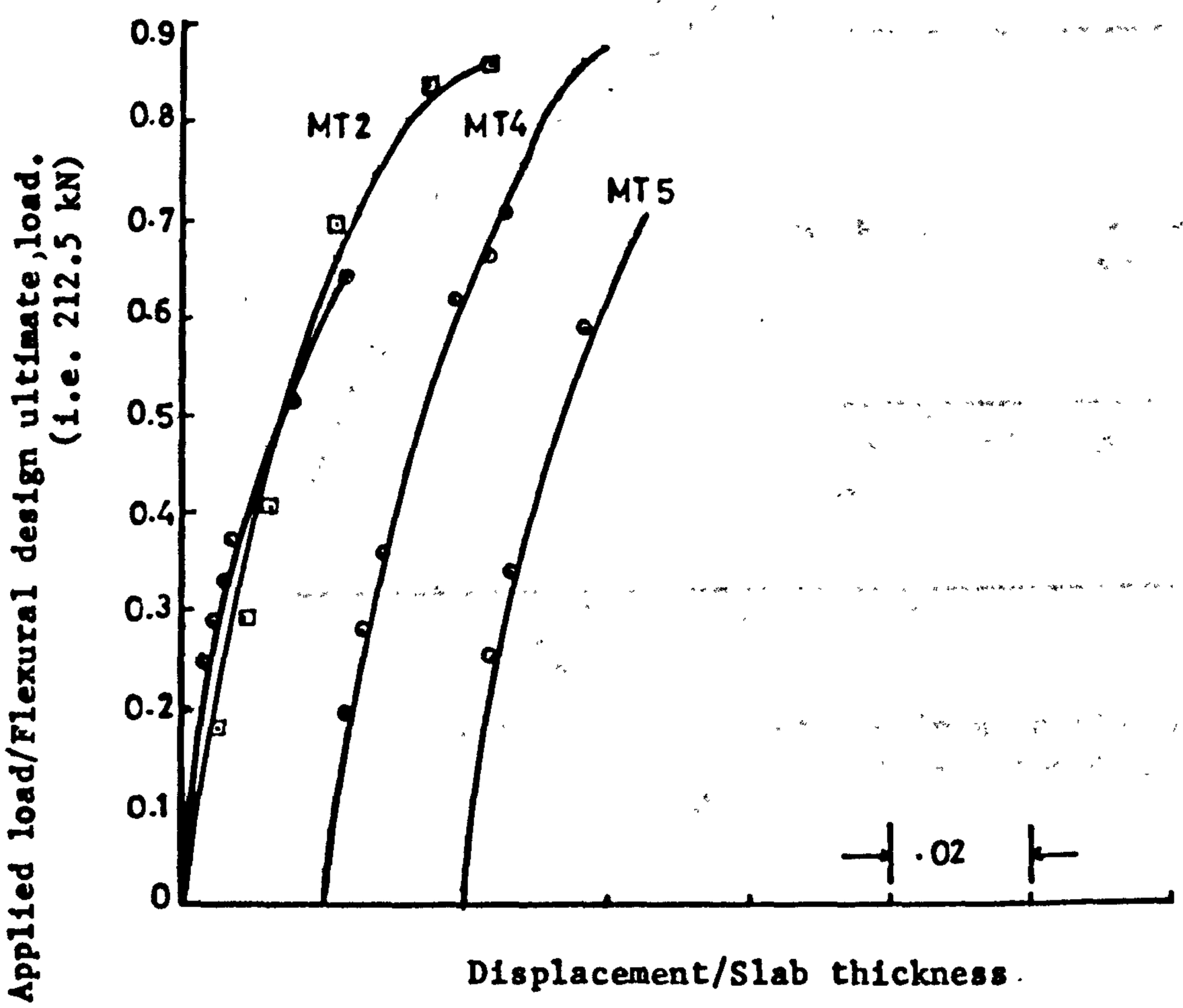

Figure (6.75) : Wind load-displacement relationship for models of IInd group.

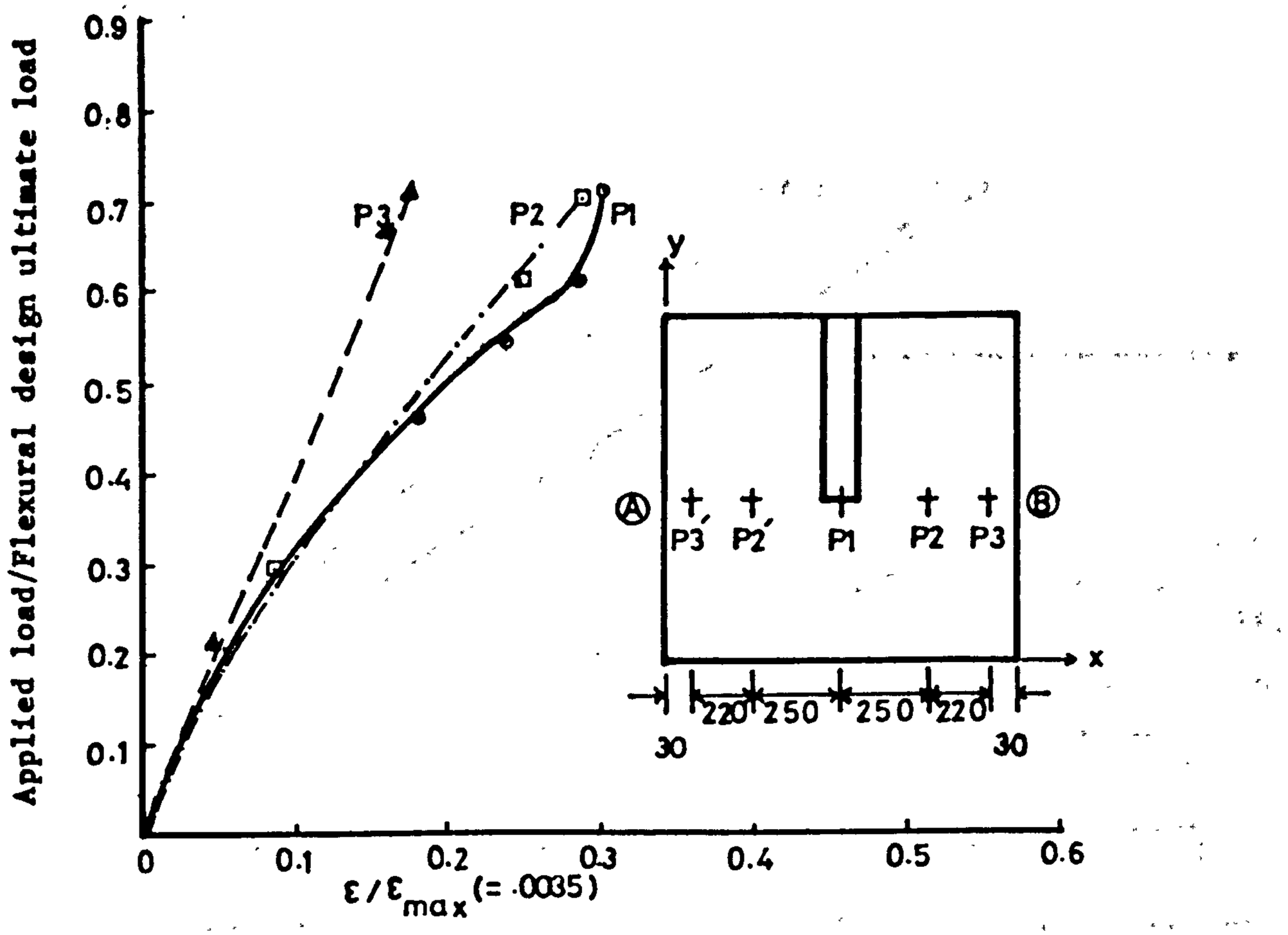

Figure (6.76) : Compressive strain at different points along transverse section AB in the slab of model MT5.

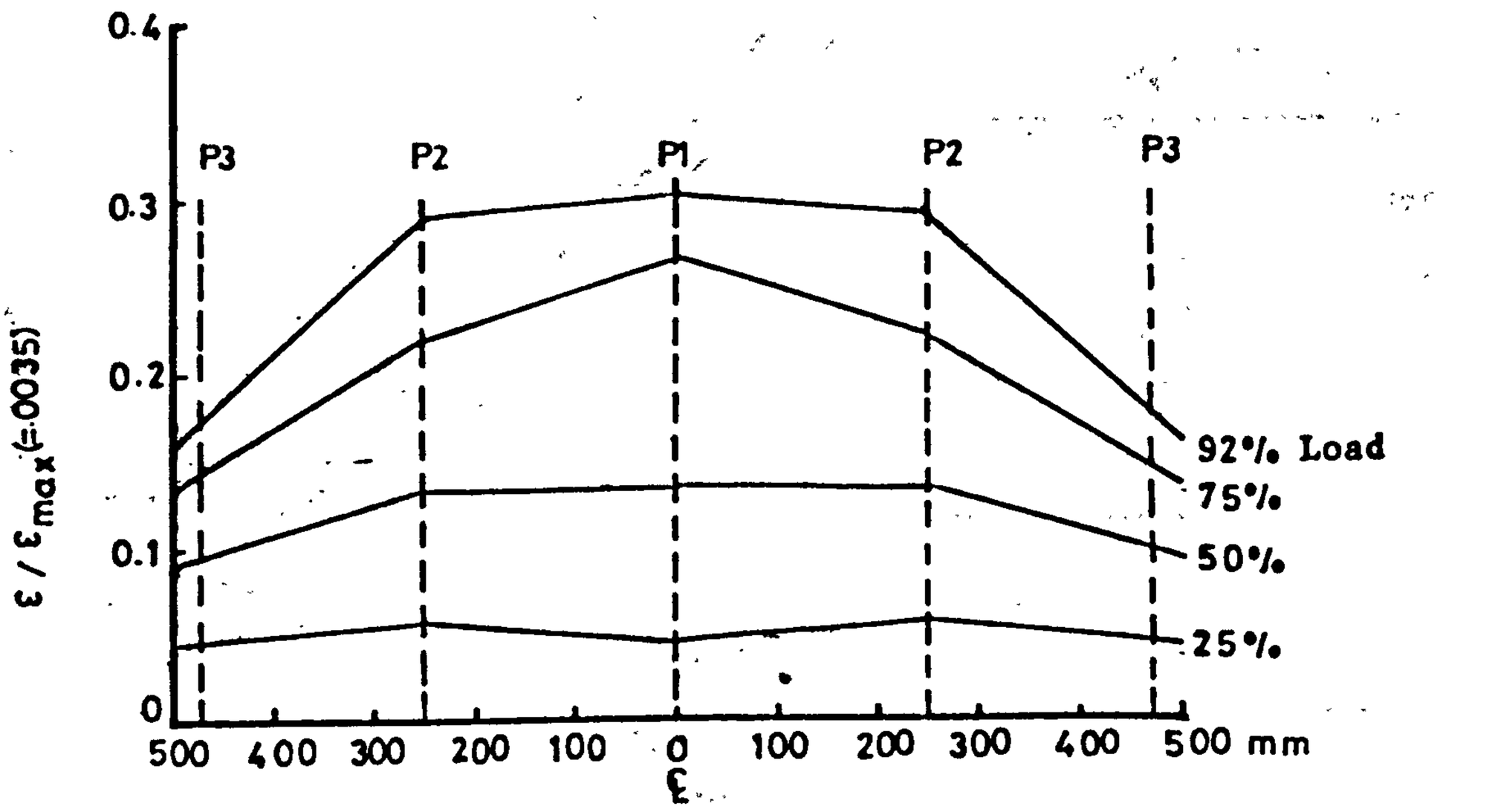

Figure (6.77) : Variation of comp. strain along transverse section at different stages of loading in the slab of model MT5.

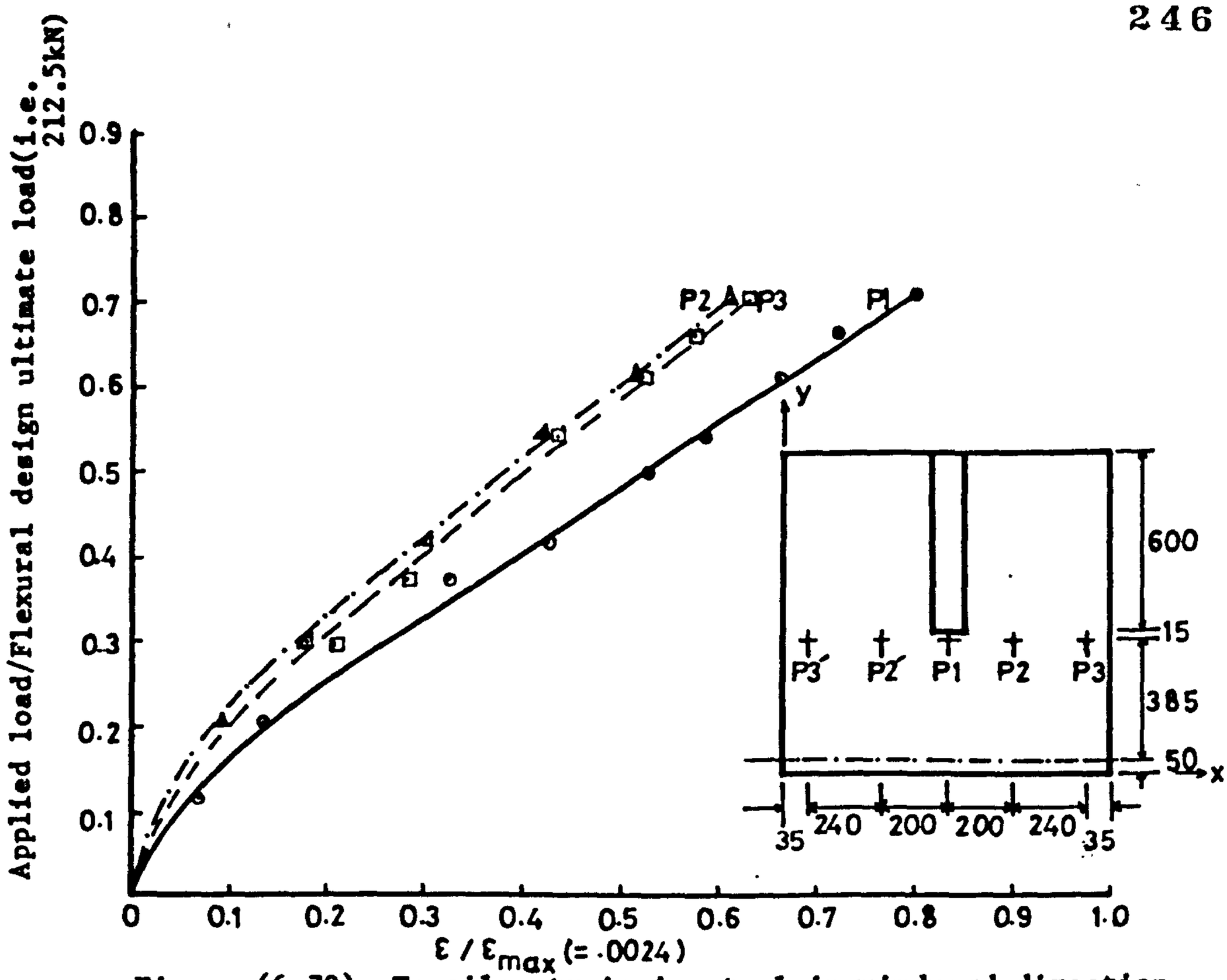

Figure (6.78): Tensile strain in steel in windward direction in slab of model MT5.

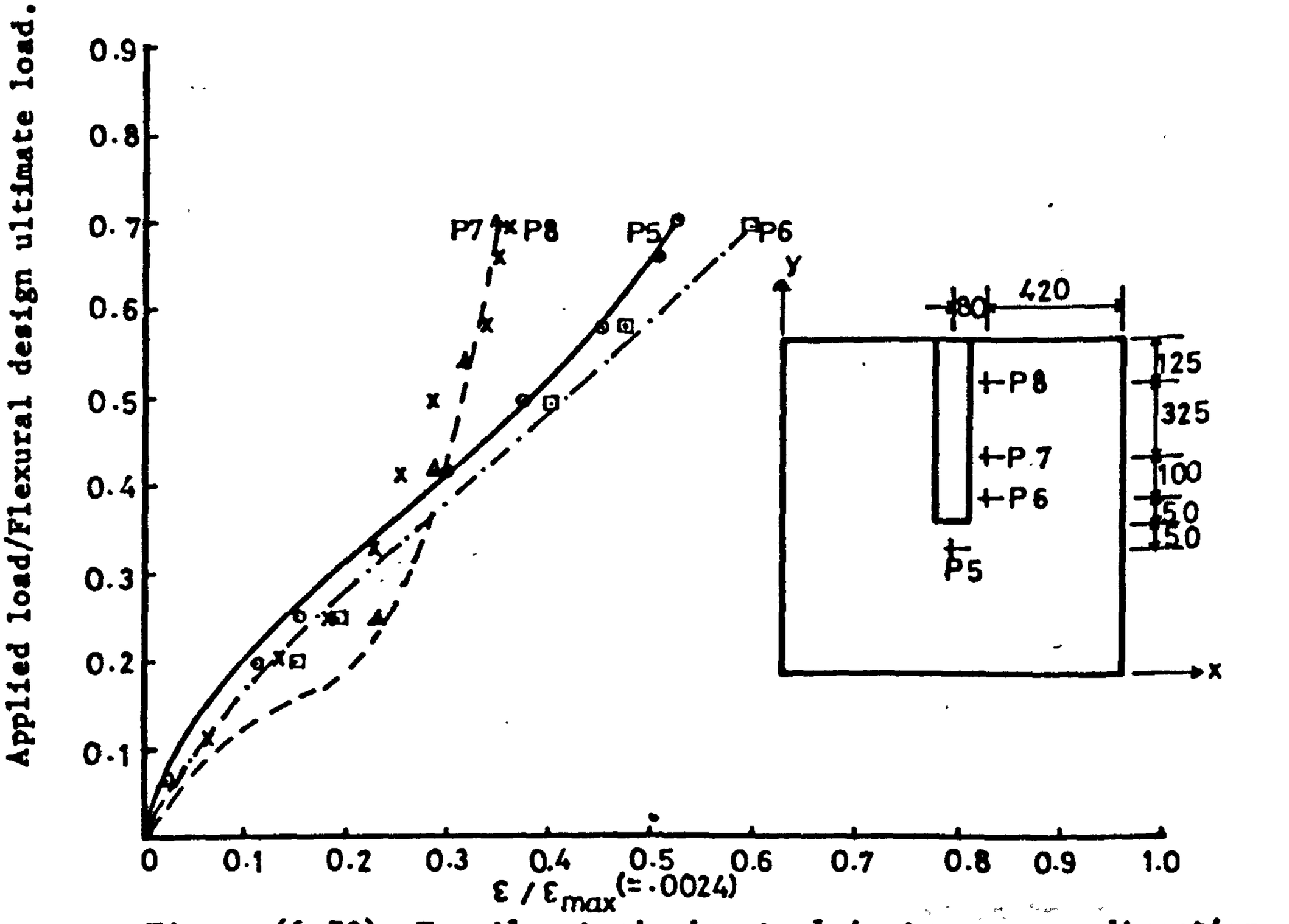

Figure (6.79): Tensile strain in steel in transverse direction in slab of model MT5.

Figure (6.81). Some more cracks parallel to the sides of wall also appeared in the slab as the loading progressed. The ultimate failure of this model is shown in Figures (6.82) to (6.85). The load at failure was 160.87 kN.

6.4.4.3 Comparison and discussion

Looking back to the Figure (6.75) which shows the wind load-displacement relationship for models MT2, MT4 and MT5, it can be seen that all the three curves follow each other very closely. It may therefore be concluded that at the level of gravity load tested, the increase in the intensity of gravity load has no pronounced effect on the wind load-displacement behaviour.

The variation of compressive strain in concrete showed the same behaviour as that in previous models (i.e. unloading at the inner edge of wall at later stages of loading). Strain in steel was also measured at different points in the slabs of models MT4 and MT5. Unlike compressive strain in concrete, strain in steel in windward direction at the tip of the wall (Figures (6.67) and (6.78) increased with the increase in the load up to the failure. However strain in MT4 at this point at failure was slightly less than the consecutive point P2. The variation of strain in steel in transverse direction at the top of the slab along the sides of the wall for models MT4 and MT5 are shown in Figures (6.69) and (6.80) respectively. It is interesting to note that up to approximately 25% of the wind load at failure, the strain in model MT4 is nearly the same everywhere except in the region of slab near the inner edge of wall. However the curve becomes steeper with the increase in the load and the variation becomes/

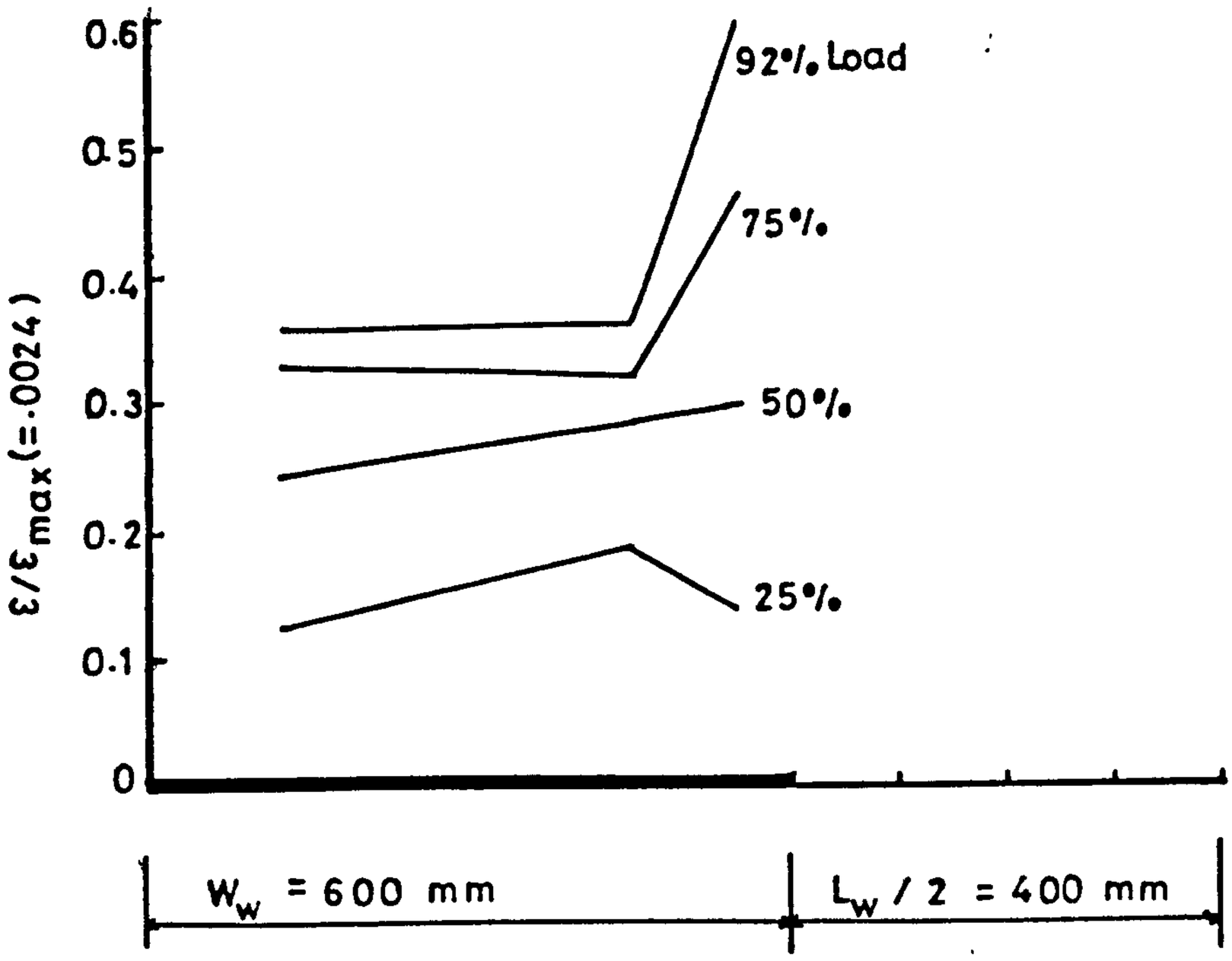

Figure (6.80): Variation of strain in steel in transverse direction along the side of wall, in the slab of model MT5.

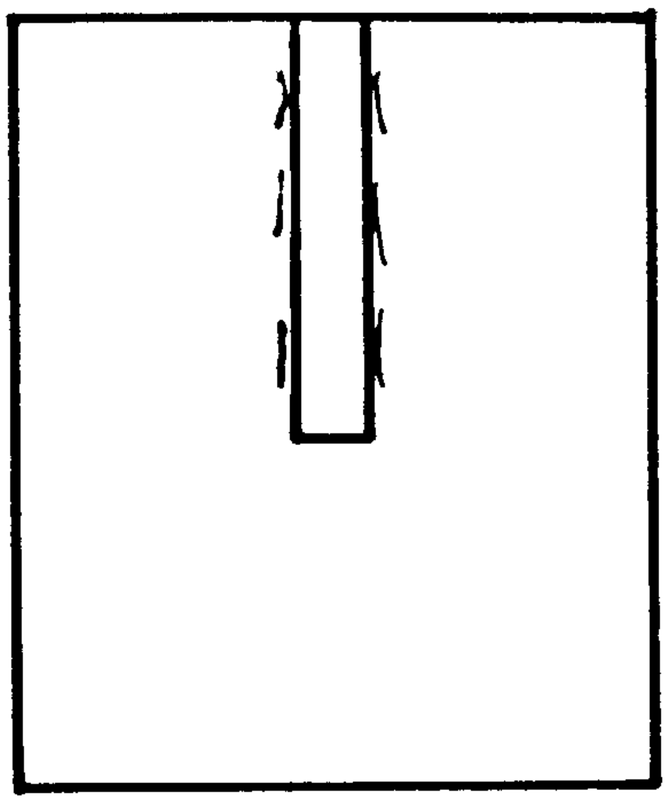

Figure (6.81): Initiation of cracks in model MT5.

Figure (6.82) : Crack pattern of the slab of MT5 after failure.

Figure (6.83) : Photograph showing failure of the connection at the bottom of the slab of model MT5.

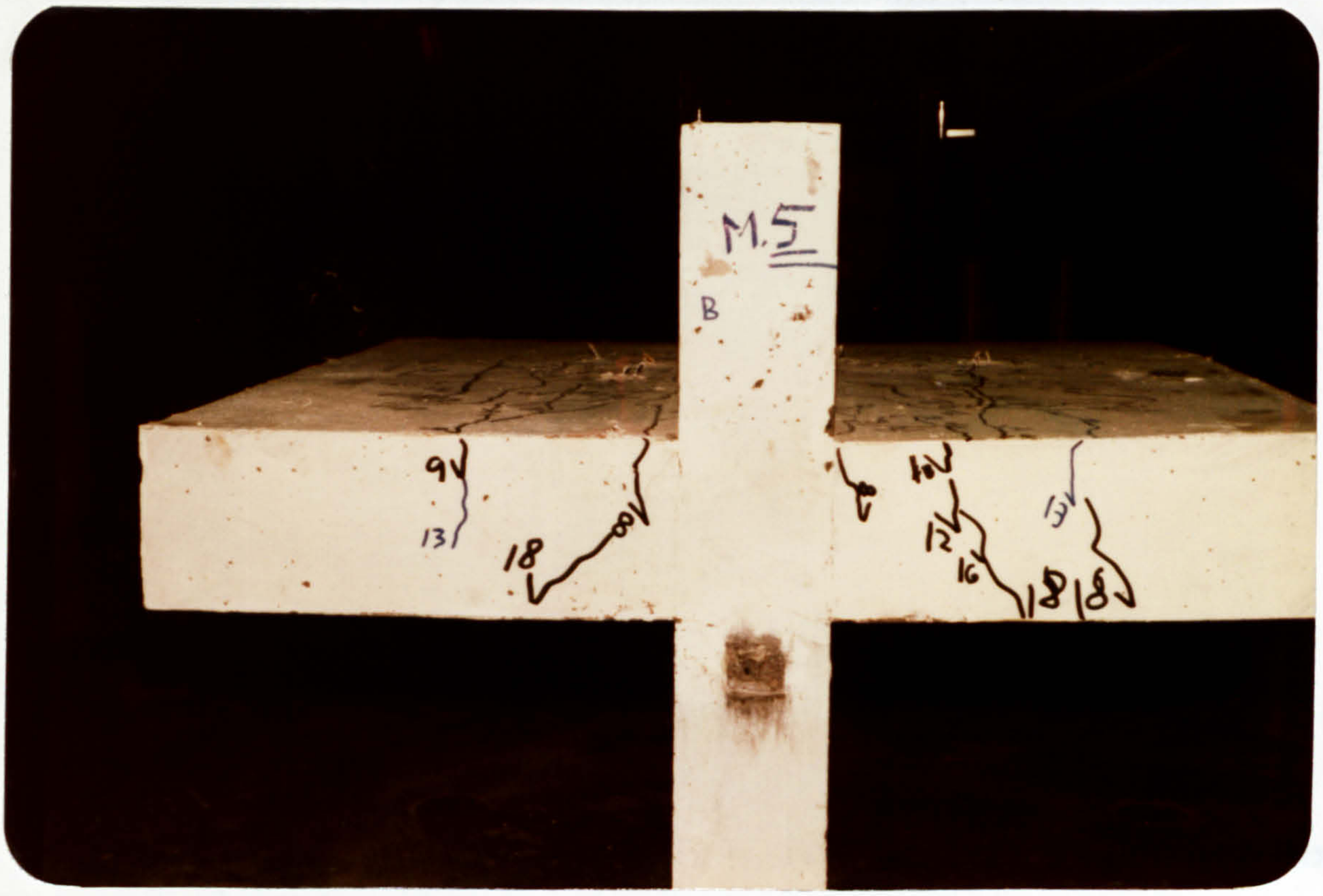

Figure (6.84) : Photograph showing shear cracks in the slab at the back of MT5 after failure.

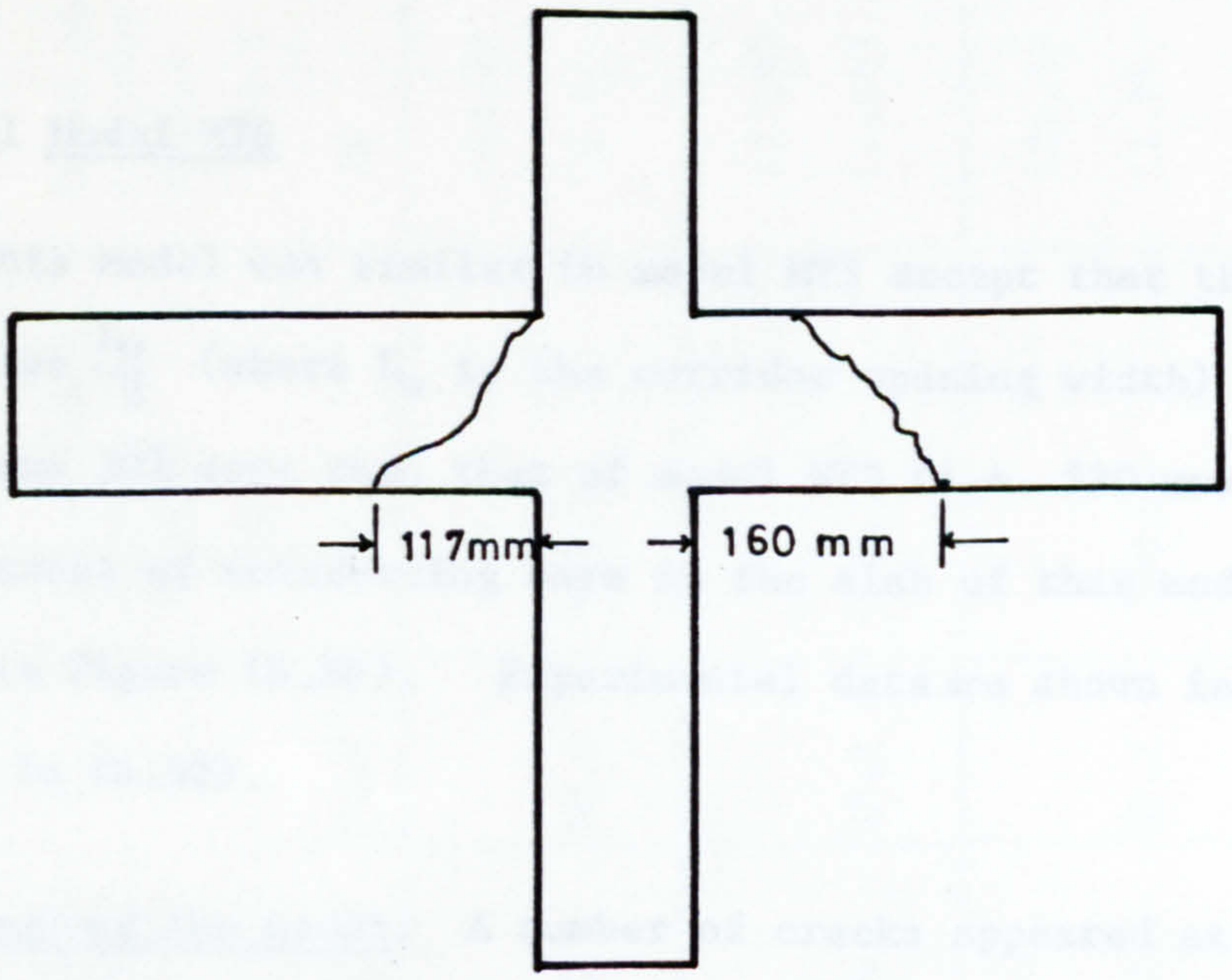

Figure (6.85) : Sketch showing the location of shear cracks at the back of MT5.

almost linear when the load reaches 75% of its ultimate value. From Figure (6.80) it appears that there is concentration of strain in a region approximately .25 times the width of wall.

Table 6.9 shows the comparison of the experimental ultimate loads to those calculated using different methods. From this table it can be observed that all the methods except CP 110 without the transfer of moment, ACI318 and Schwaighofer & Collins (8) greatly underestimate the strength of connection.

6.4.5 Models of group III (MT6, MT3 & MT7). (Effect of $\frac{\text{Unbalanced moment}}{\text{Uneven shear}}$ ratio)

The overall shear transfer capacity of a wall-slab connection is greatly reduced when an unbalanced moment due to wind load is transferred. Since the quantitative effect of this moment transfer was not known, these models were tested. Since model MT3 which is common to both, group I and group III has already been described the behaviour of the models MT6 and MT7 only, is discussed.

6.4.5.1 Model MT6

This model was similar to model MT3 except that the structural parameter $\frac{L_w}{2}$ (where L_w is the corridor opening width) of this model was 30% more than that of model MT3 (i.e. 520 mm). The arrangement of reinforcing bars in the slab of this model is shown in Figure (6.86). Experimental data are shown in Figures (6.87) to (6.92).

Behaviour of the model: A number of cracks appeared at the same time as shown in Figure (6.93), when the wind shear was equal to/

Table 6.9. Comparison of calculated and experimental ultimate loads for models of the IInd group in the MT series.

Model No.	f_{cu} N/mm^2	Experimental load at failure V_{exp} kN	CP110 without transfer of moment $V_{cal\ 1}$ kN	CP110 with transfer of moment $V_{cal.2}$ kN	ACI method $V_{cal.3}$ kN	Chang method $V_{cal.4}$ kN	Schwaighofer & Collins $V_{cal\ 5}$ kN	Coull & Wong $V_{cal.6}$ kN
MT2	50.2	192.9	192.42 (1.0)	46.3 (4.17)	184.07 (1.05)	86.43 (2.23)	196.39 (0.98)	85.93 (2.24)
MT4	33.1	192.76	155.49 (1.24)	37.4 (5.15)	136.65 (1.41)	65.4 (2.95)	148.76 (1.3)	72.45 (2.66)
MT5	33.2	160.87	125.12 (1.29)	30.36 (5.3)	125.65 (1.28)	54.23 (2.97)	139.58 (1.15)	61.82 (2.6)

Note: The figures in the brackets show the ratio $\frac{V_{exp}}{V_{cal}}$

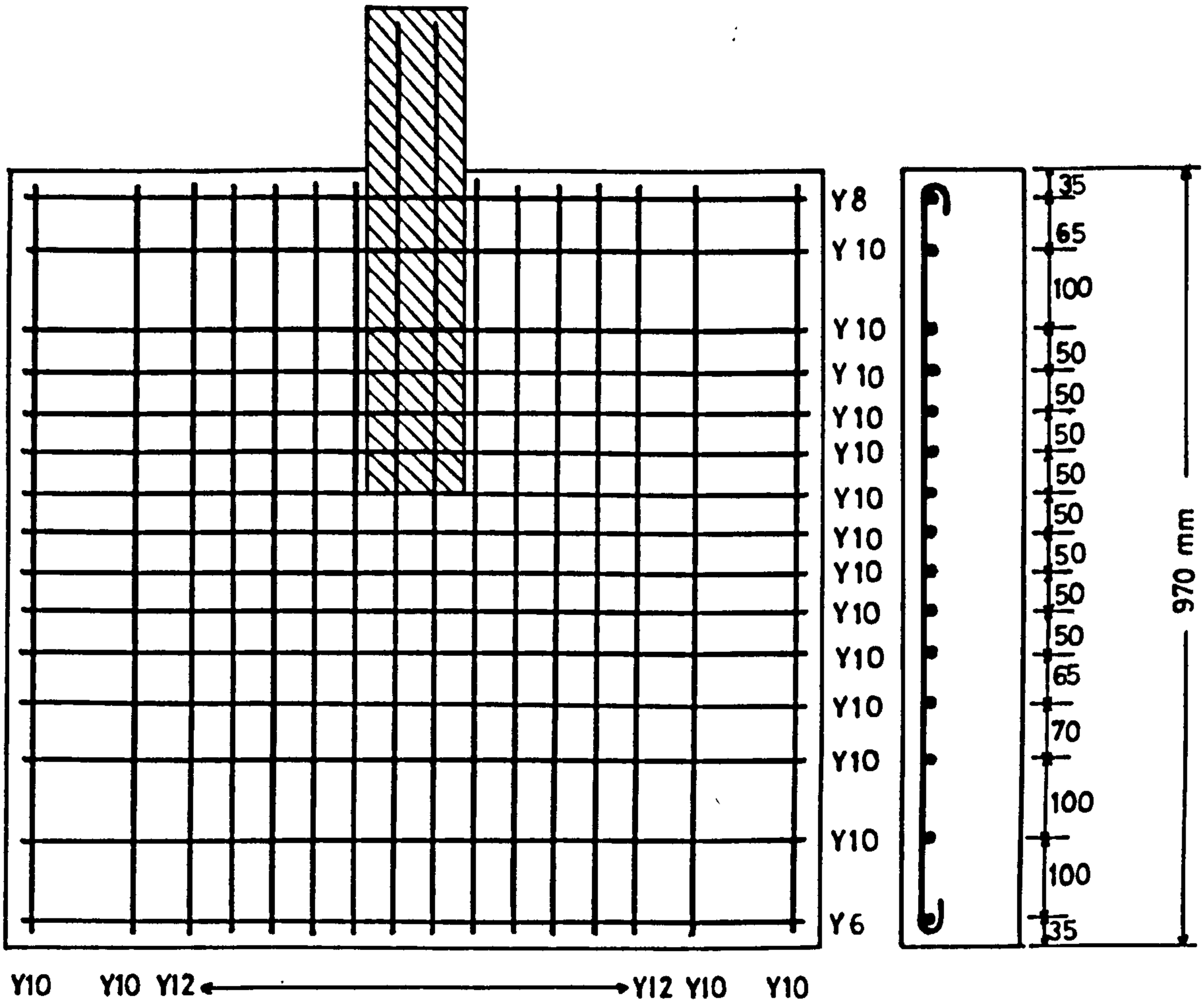

Figure (6.86) : Arrangement of reinforcing bars in the slab of the model MT6.

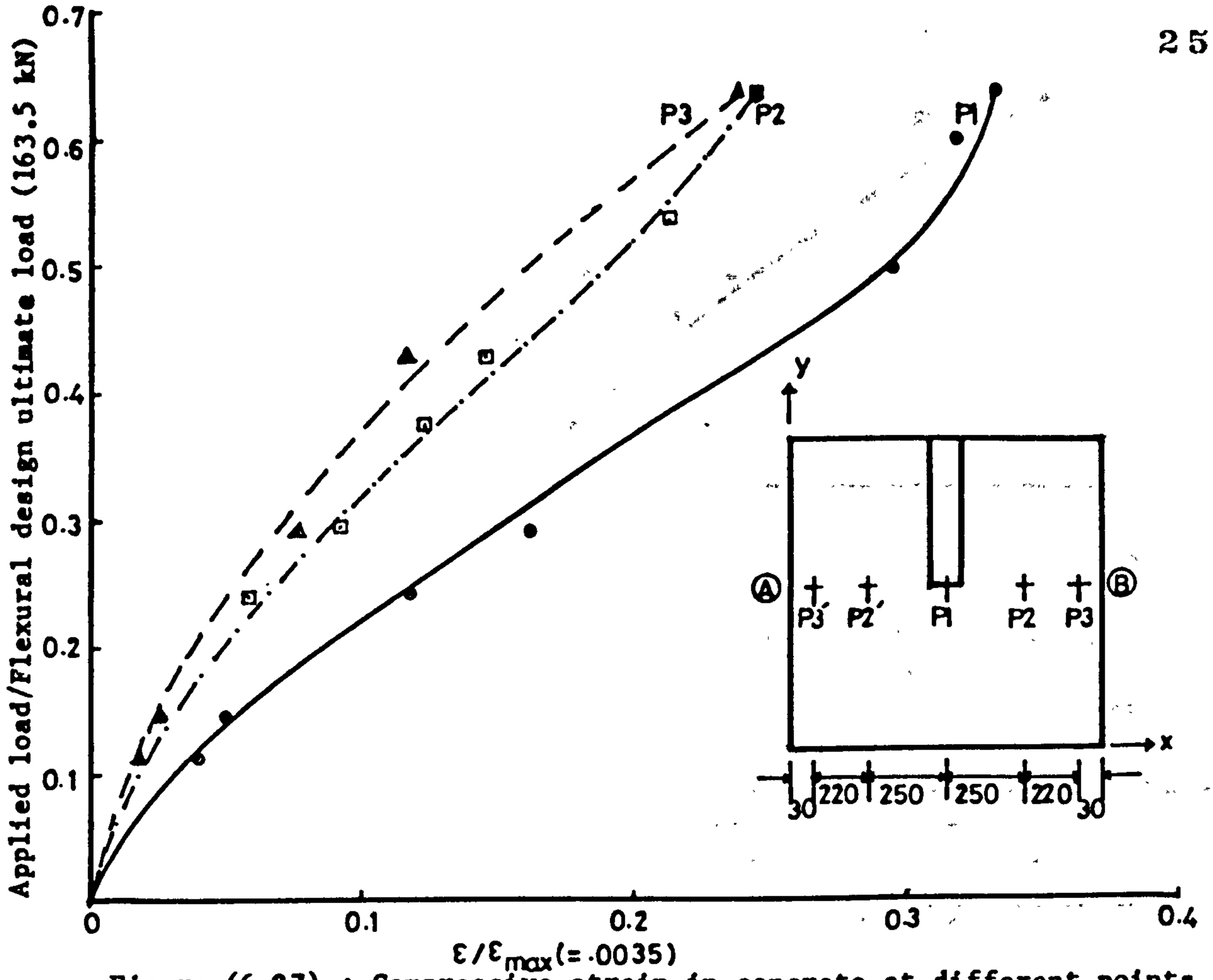

Figure (6.87) : Compressive strain in concrete at different points along section AB in the slab of model MT6.

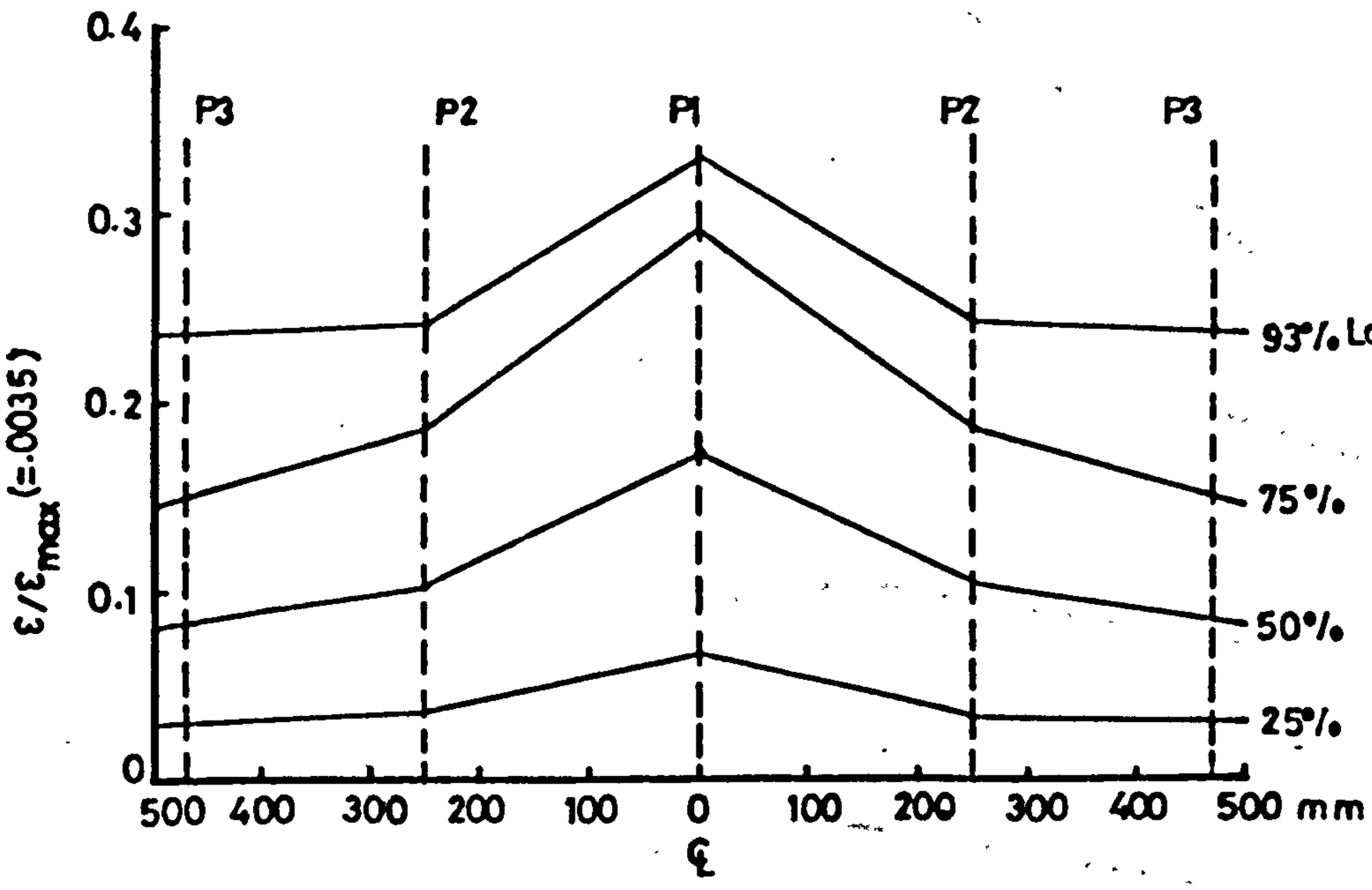

Figure (6.88) : Variation of comp. strain along transverse critical section at different stages of loading, in the slab of model MT6.

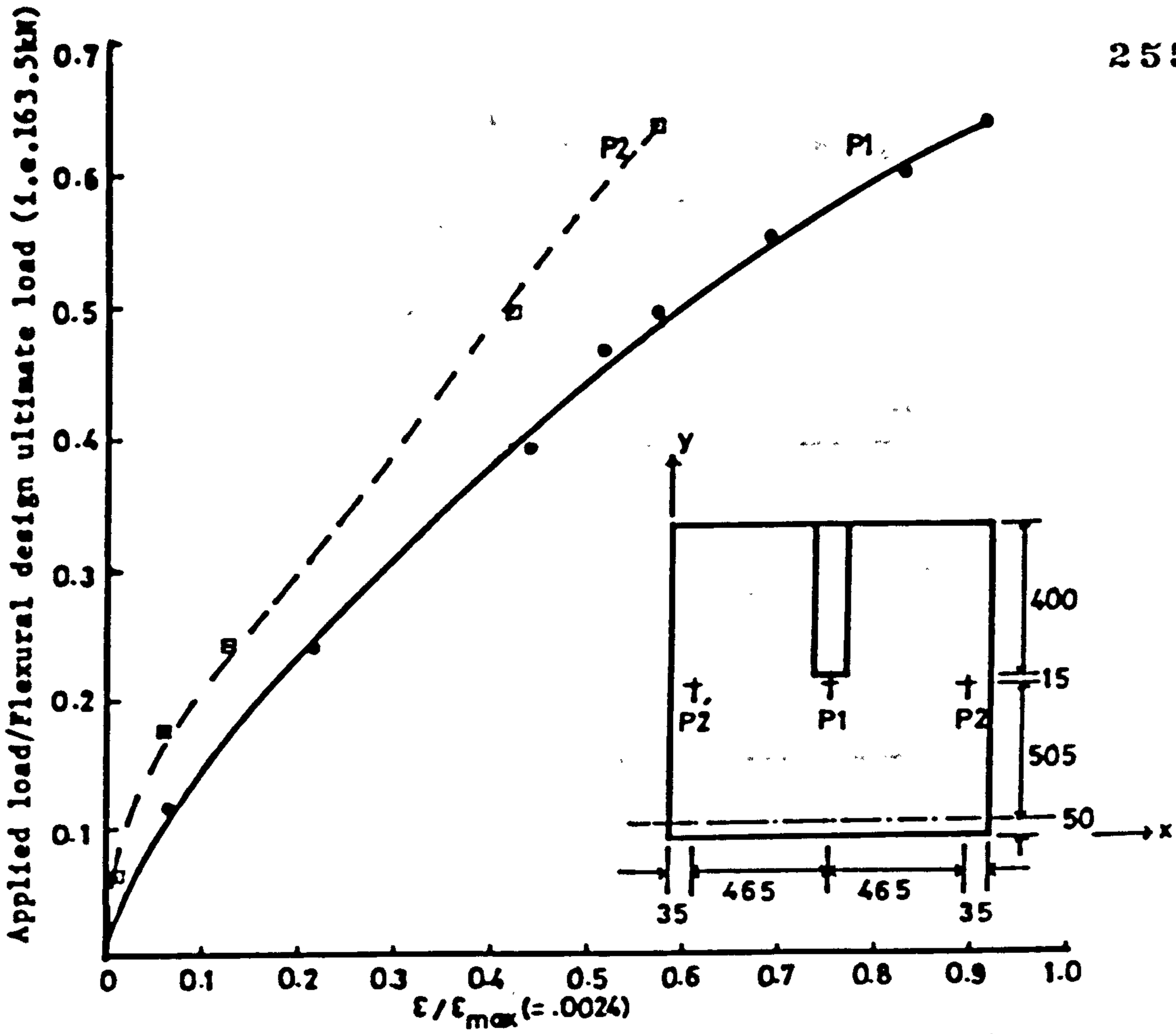

Figure (6.89) : Strain in steel in windward direction at different points in the slab of model MT6.

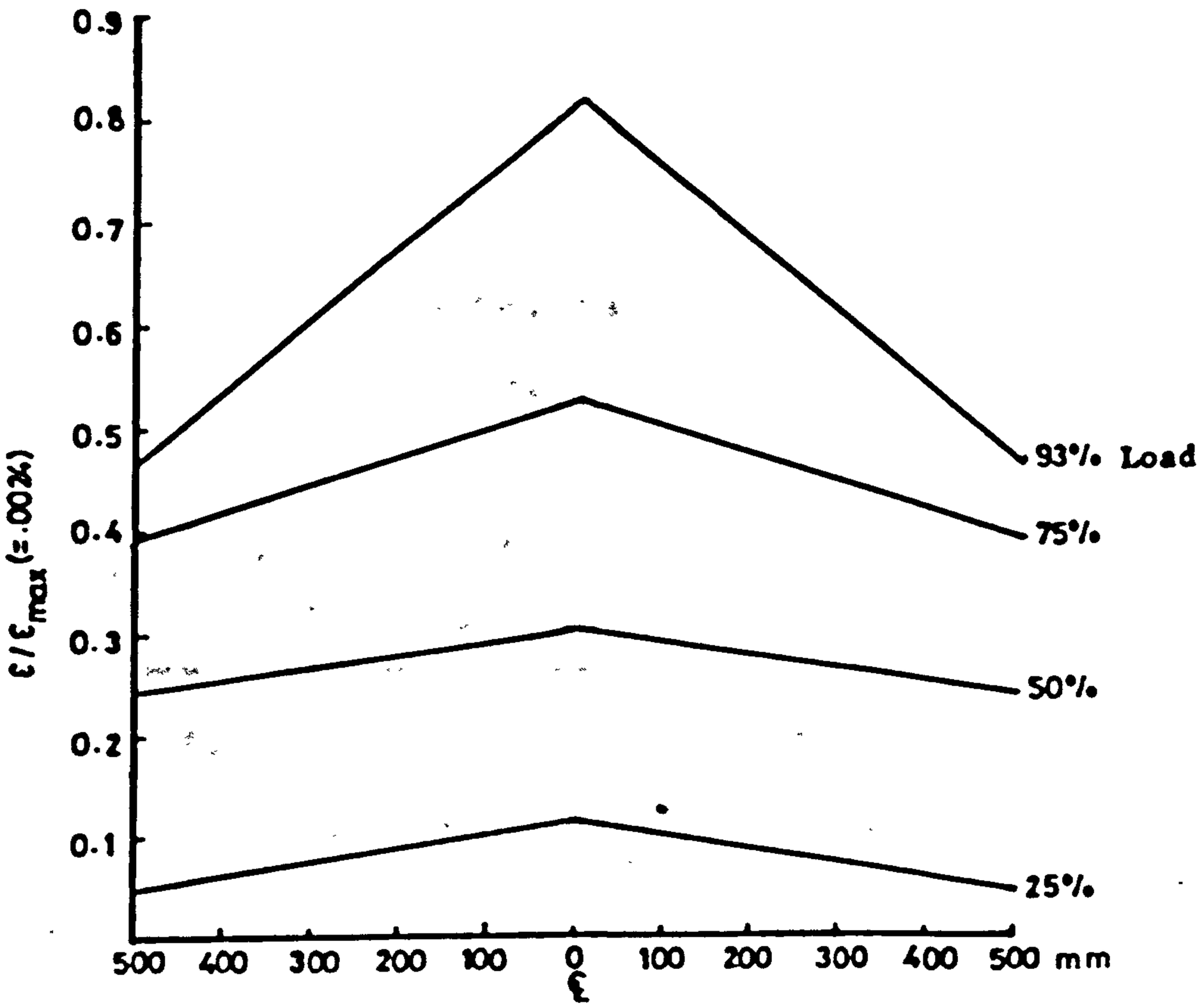

Figure (6.90) : Variation of strain in steel in windward direction along transverse critical section at different stages of loading in the slab of MT6.

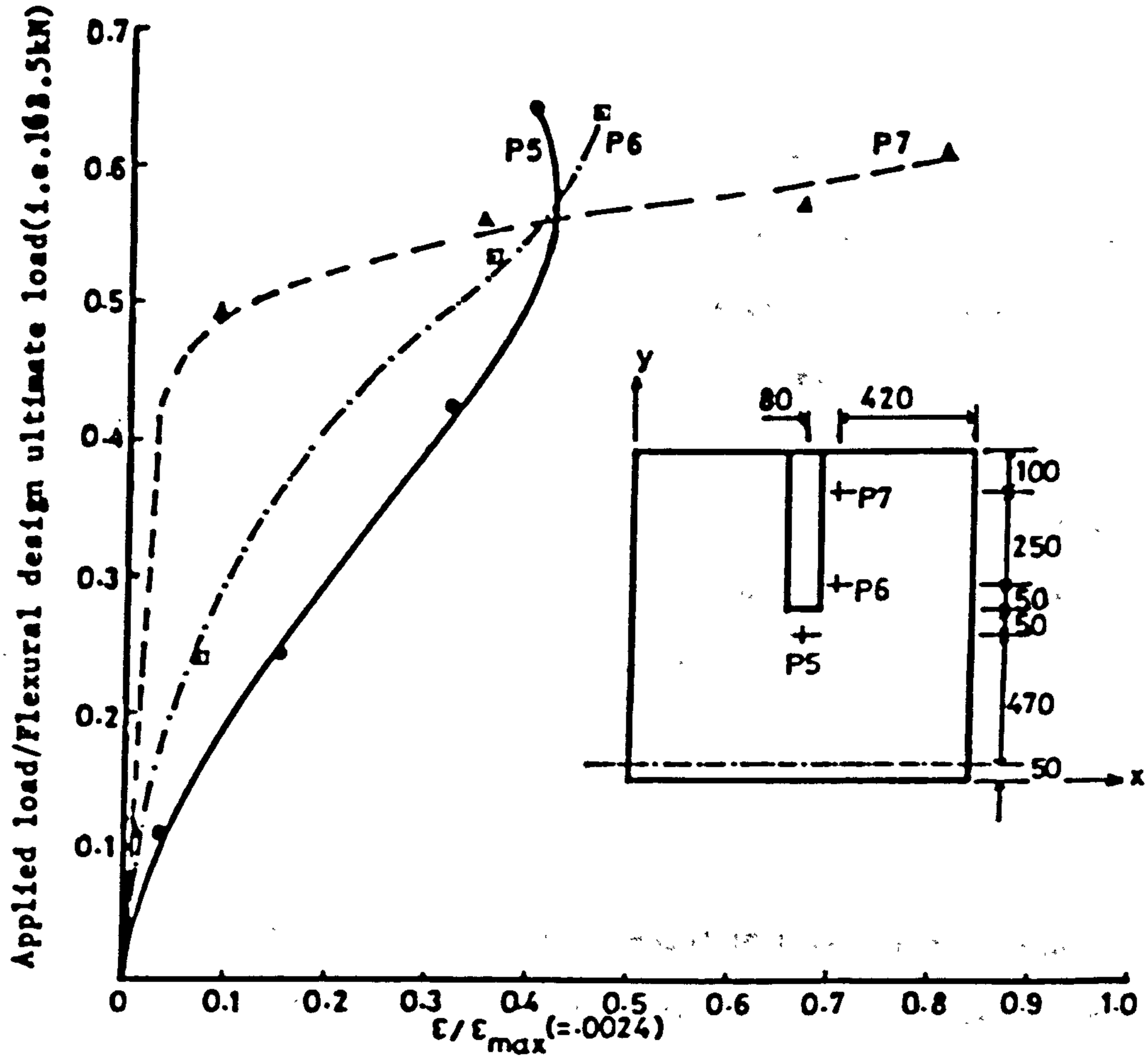

Figure (6.91) : Strain in steel in transverse direction at different points along the side of the wall in the slab of model MT6.

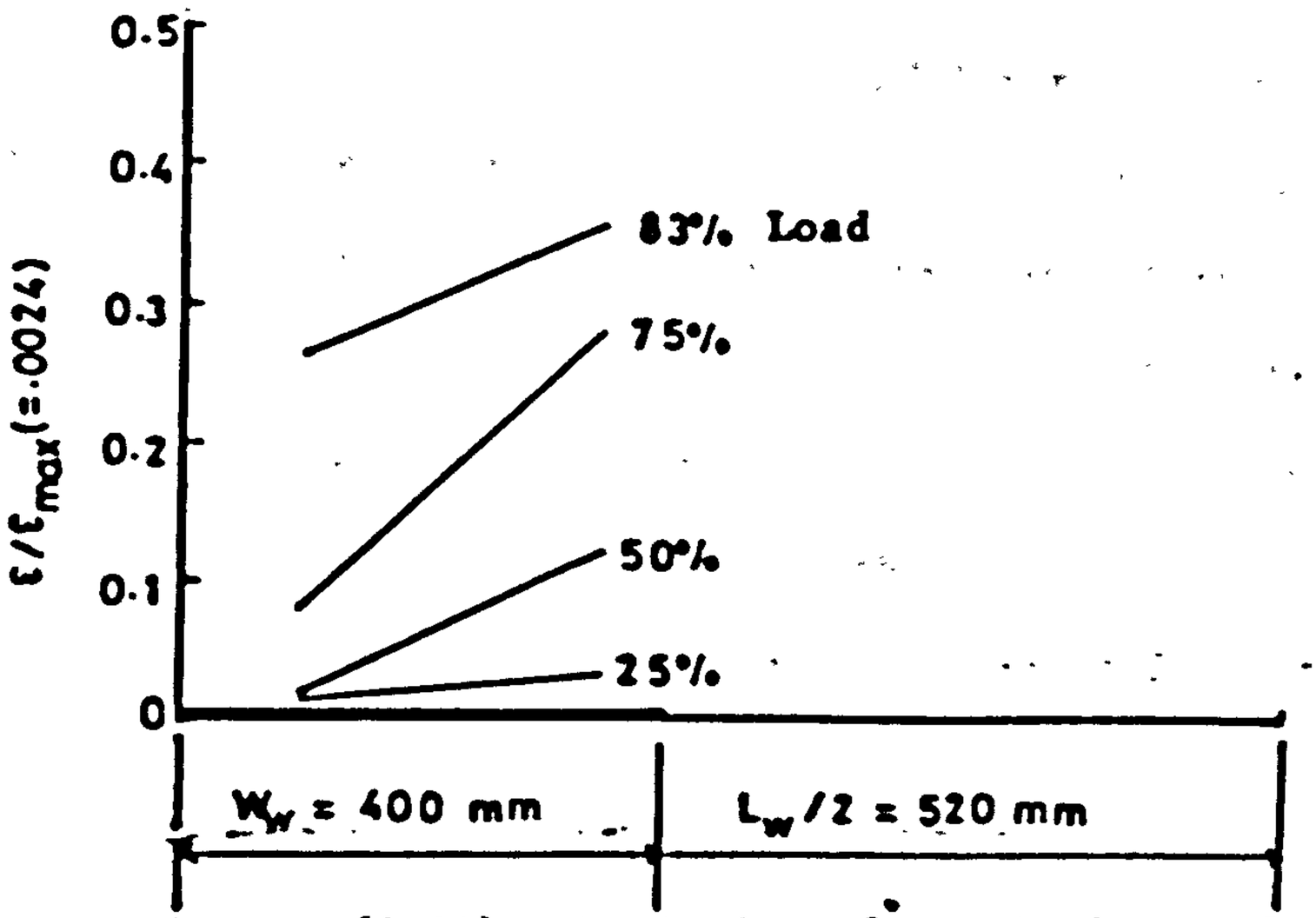

Figure (6.92) : Variation of strain in steel in transverse direction at the top of the slab, along the sides of wall of model MT6.

approximately 38% of the load at failure. The shear cracks in the slab at the back of the model appeared at a load of 56% of the load at failure. A sketch showing the distance of their tails from the wall after failure is presented in Figures (6.94). The ultimate crack pattern of this model was very similar to that of model MT3. The load at failure for this model was only 105.8 kN. Photographs showing the crack pattern of this model after failure are presented in Figures (6.95) and (6.96).

6.4.5.2 Model MT7

This model was also similar to model MT3 except that the corridor opening width was 30% less than that of MT3 (i.e. $\frac{L_w}{2}$ = 280 mm). The arrangement of reinforcing bars in the slab of this model is shown in Figure (6.97). The wind load-displacement curves of models MT6, MT3 and MT7 are shown in Figure (6.98). Experimental data for this model are presented in Figures (6.99) to (6.104).

Behaviour of the model: In this model for the first time the cracking started at a load of 30% of the ultimate load at failure and the shear cracks in the slab at the back of the model appeared at a load of only 35% of the load at failure. The ultimate cracking pattern of this model was similar to that of model MT3. The wind load at failure was 177.76 kN. The photographs showing the crack pattern of this model after failure are presented in Figures (6.105) and (6.106).

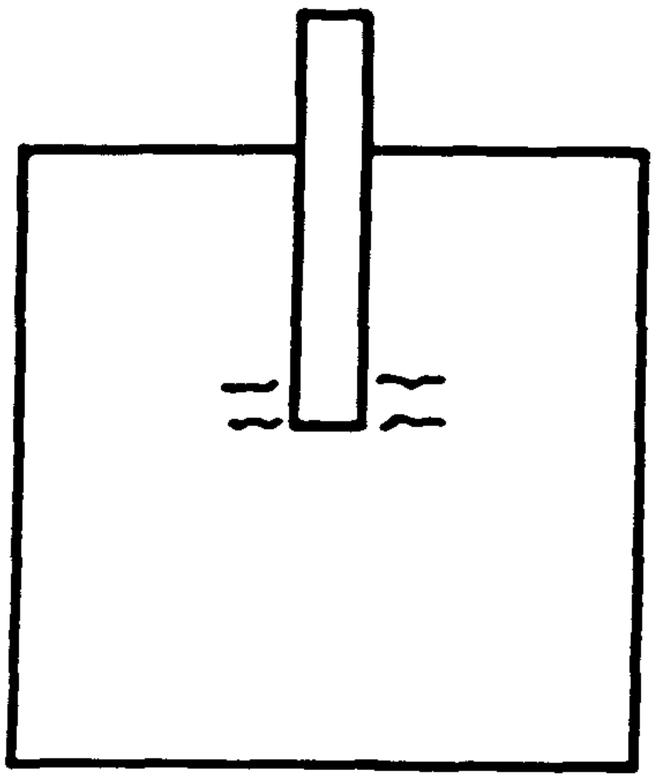

Figure (6.93) : Initiation of cracks in the slab of model MT6.

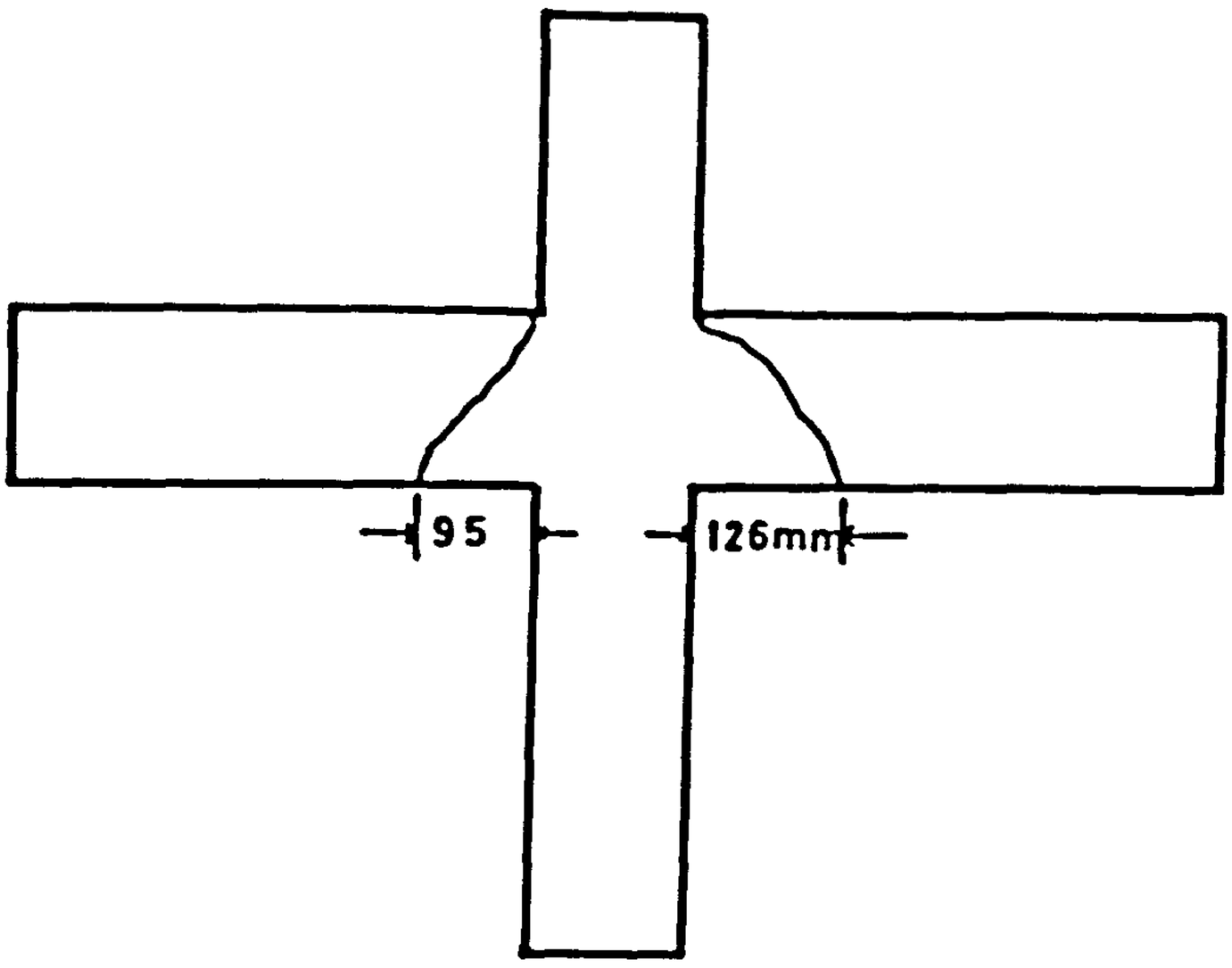

Figure (6.94) : Shear cracks at the back of the model MT6.

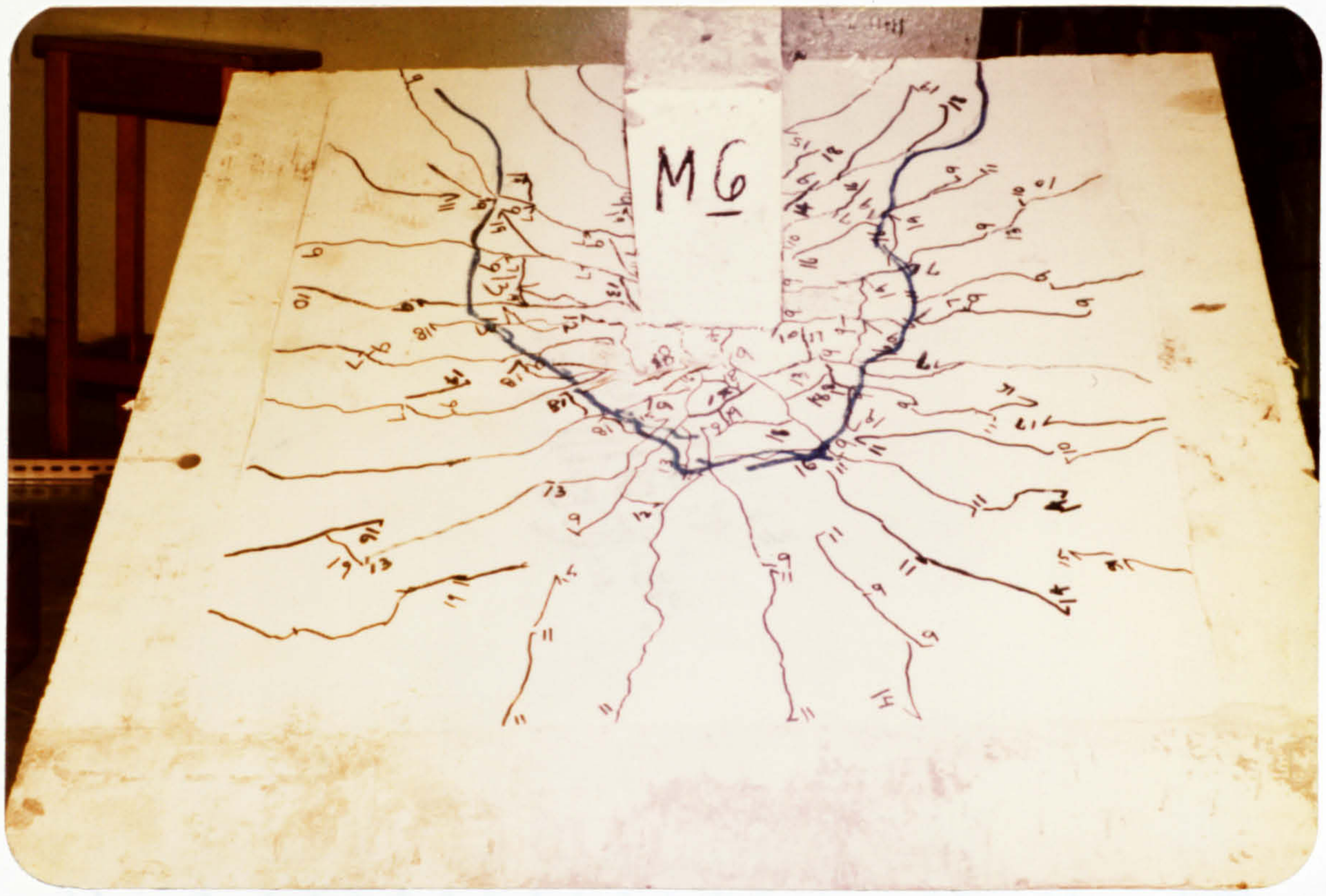

Figure (6.95) : Crack pattern of the slab of MT6 after failure.

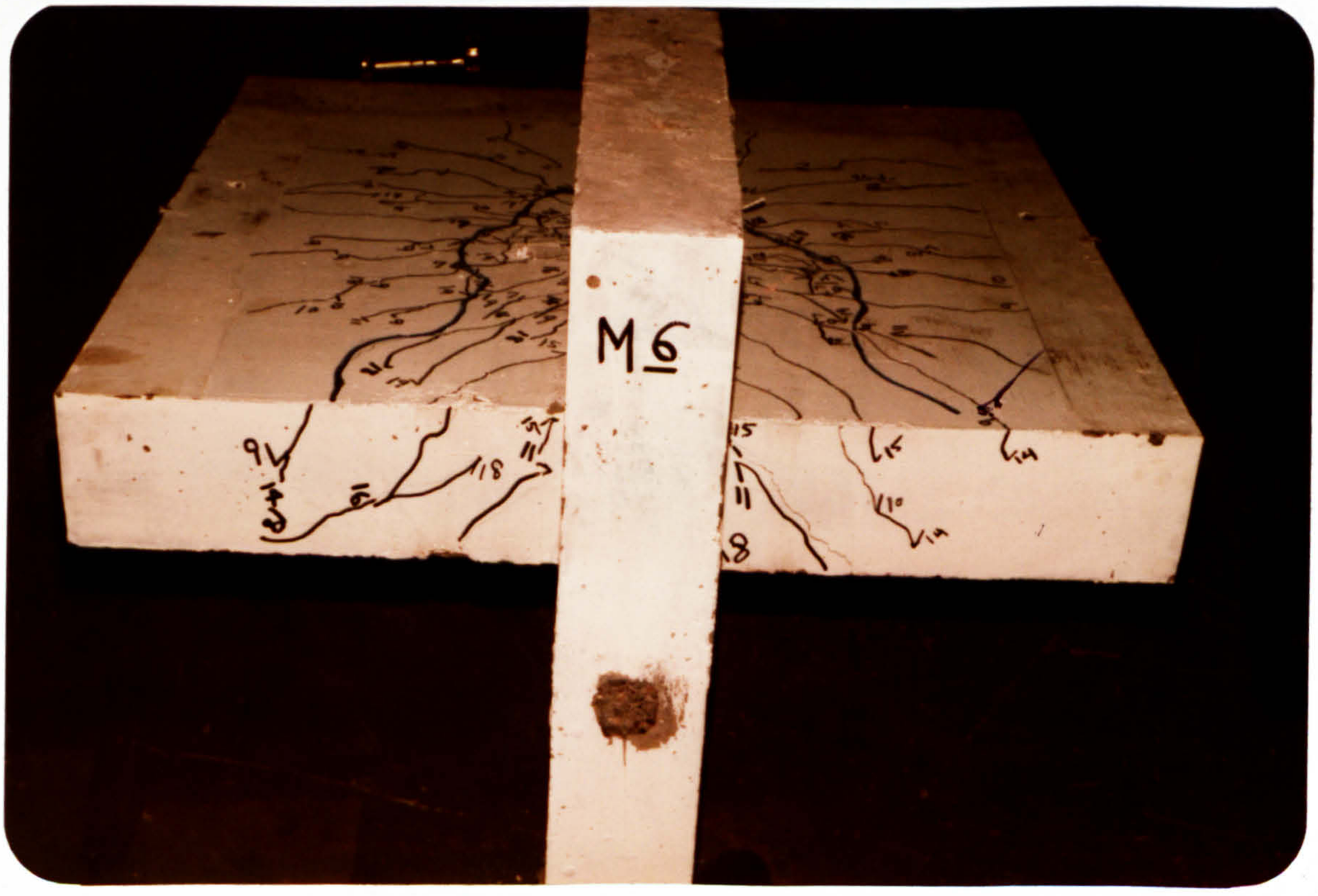

Figure (6.96) : Shear cracks in the slab at the back of MT6.

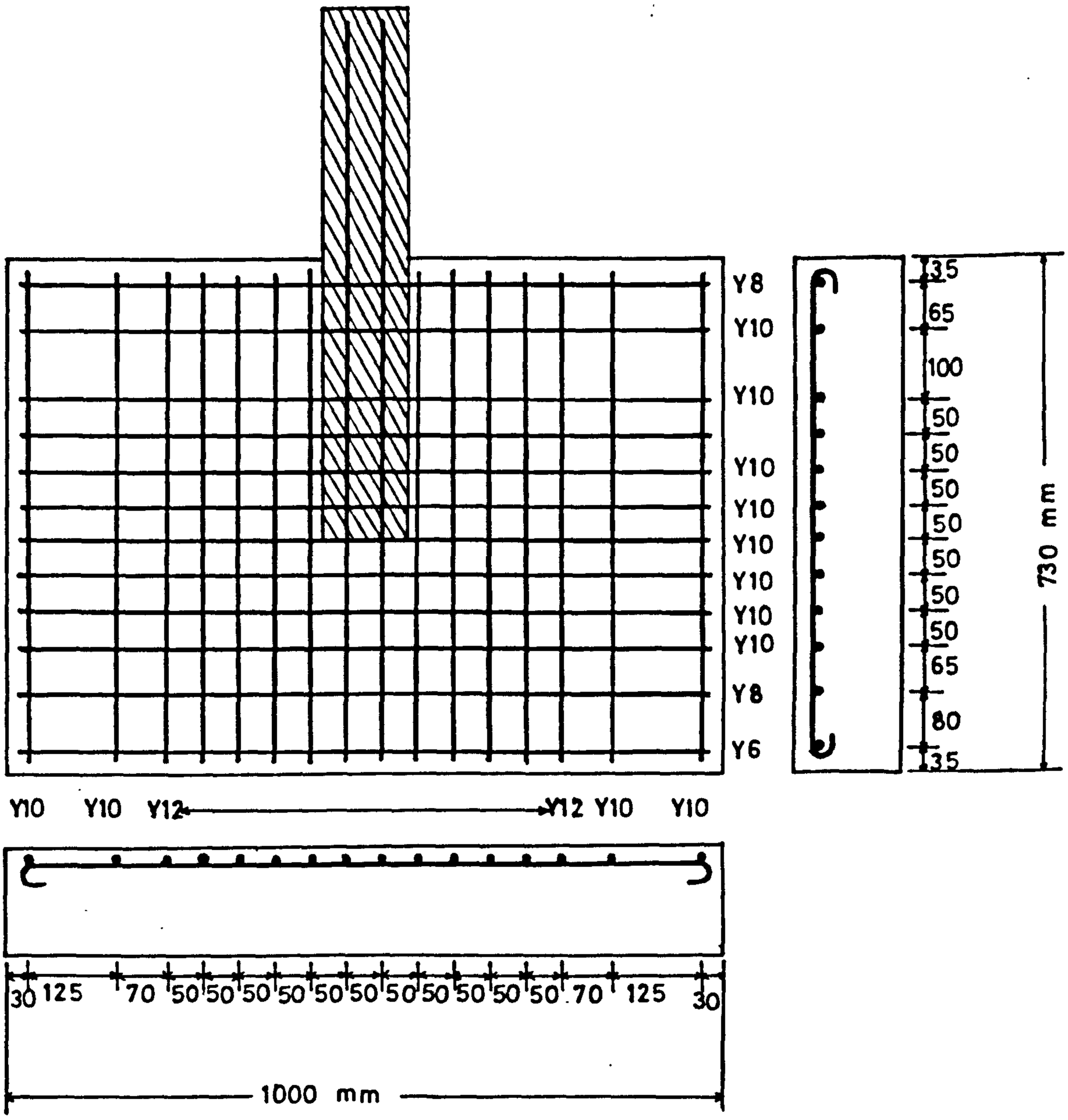

Figure (6.97) : Arrangement of reinforcing bars in the slab of model MT7.

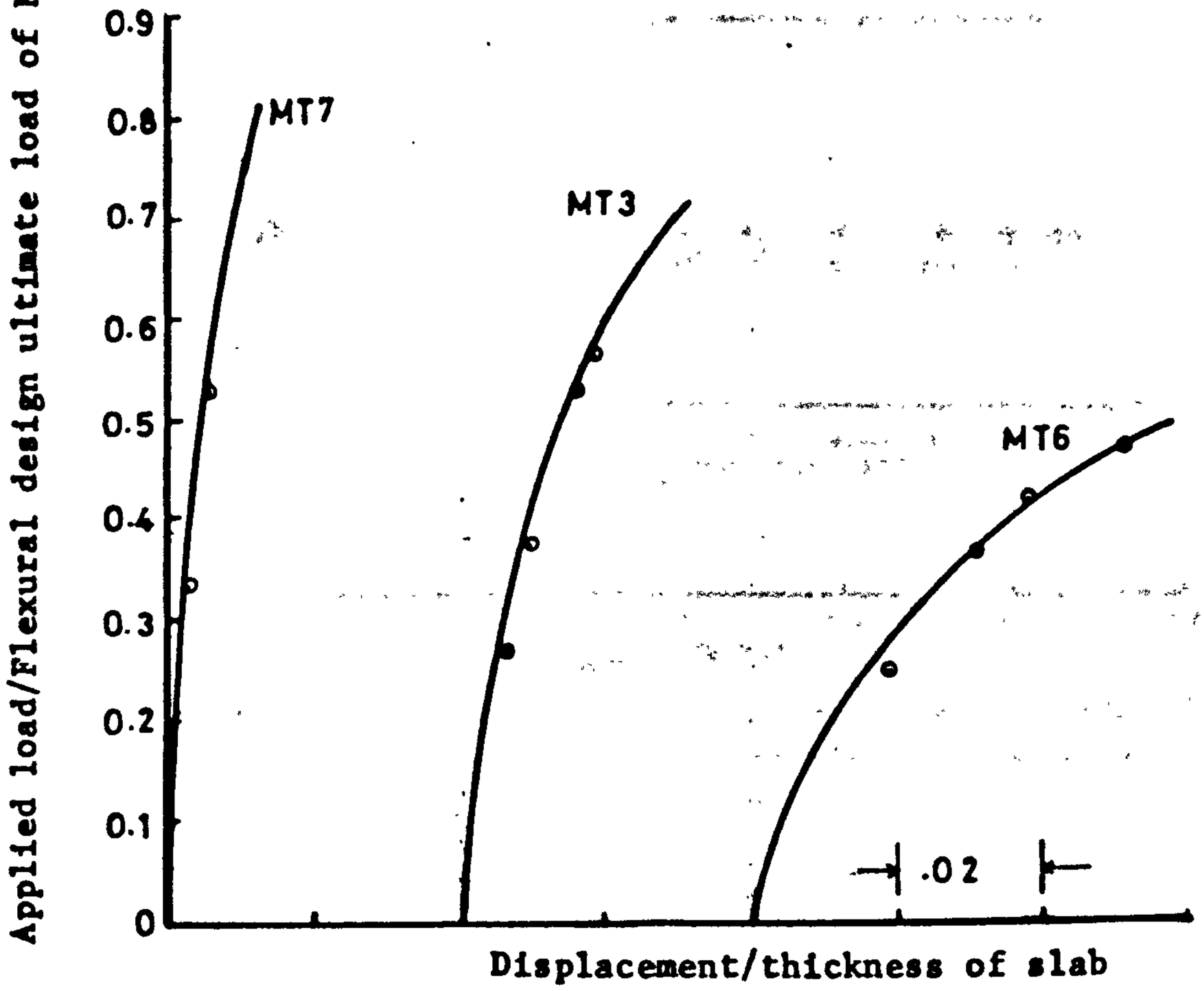

Figure (6.98) : Wind-load-displacement relationship for models of third group.

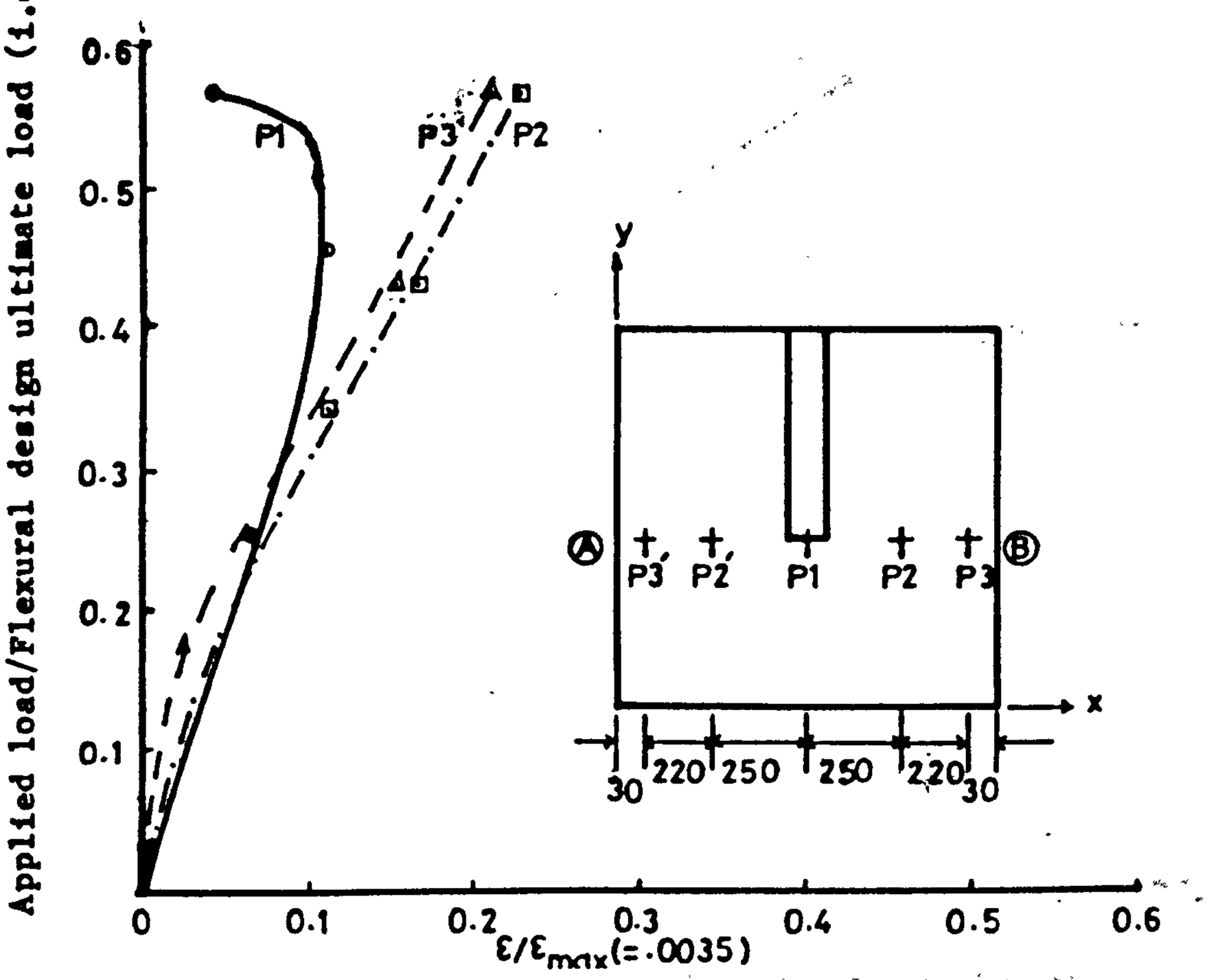

Figure (6.99) : Comp. strain in concrete in windward direction at different points along transverse critical section AB, in the slab of MT7.

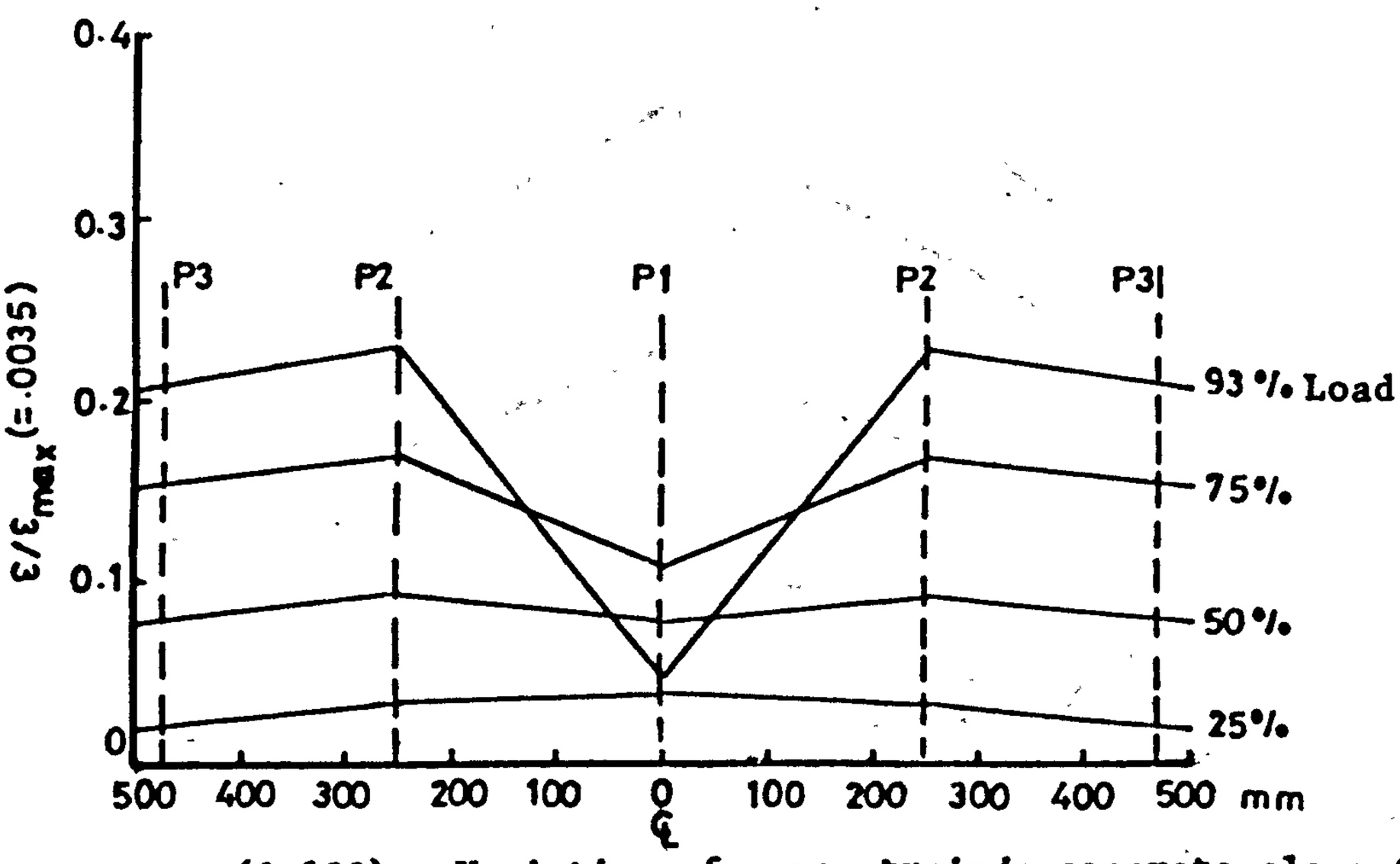

Figure (6.100) : Variation of comp.strain in concrete along transverse critical section at different loading stages in the slab of MT7.

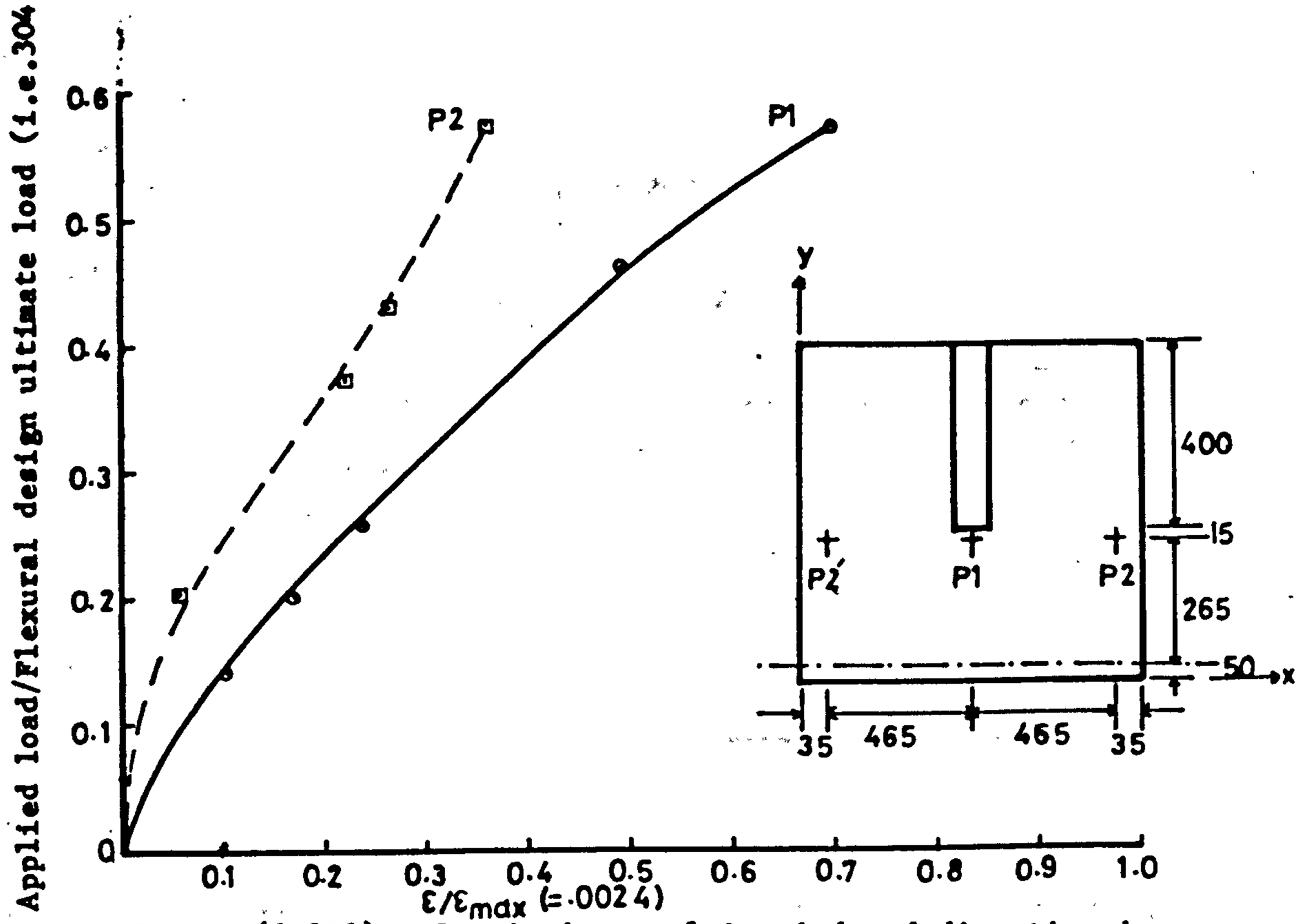

Figure (6.101) : Strain in steel in windward direction in the slab of MT7.

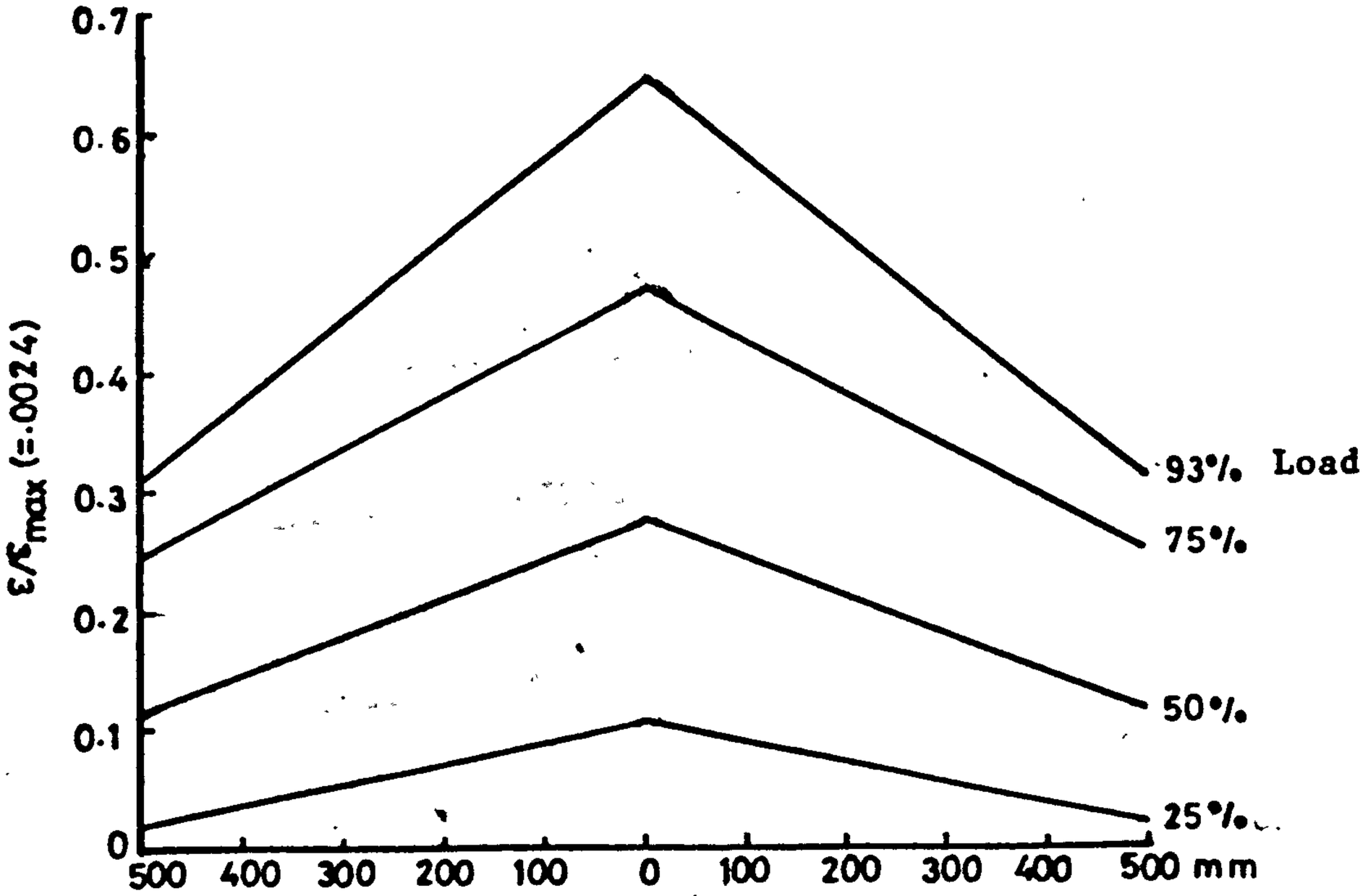

Figure (6.102) : Variation of strain in steel in windward direction along transverse critical section at different stages of loading in the slab of MT7.

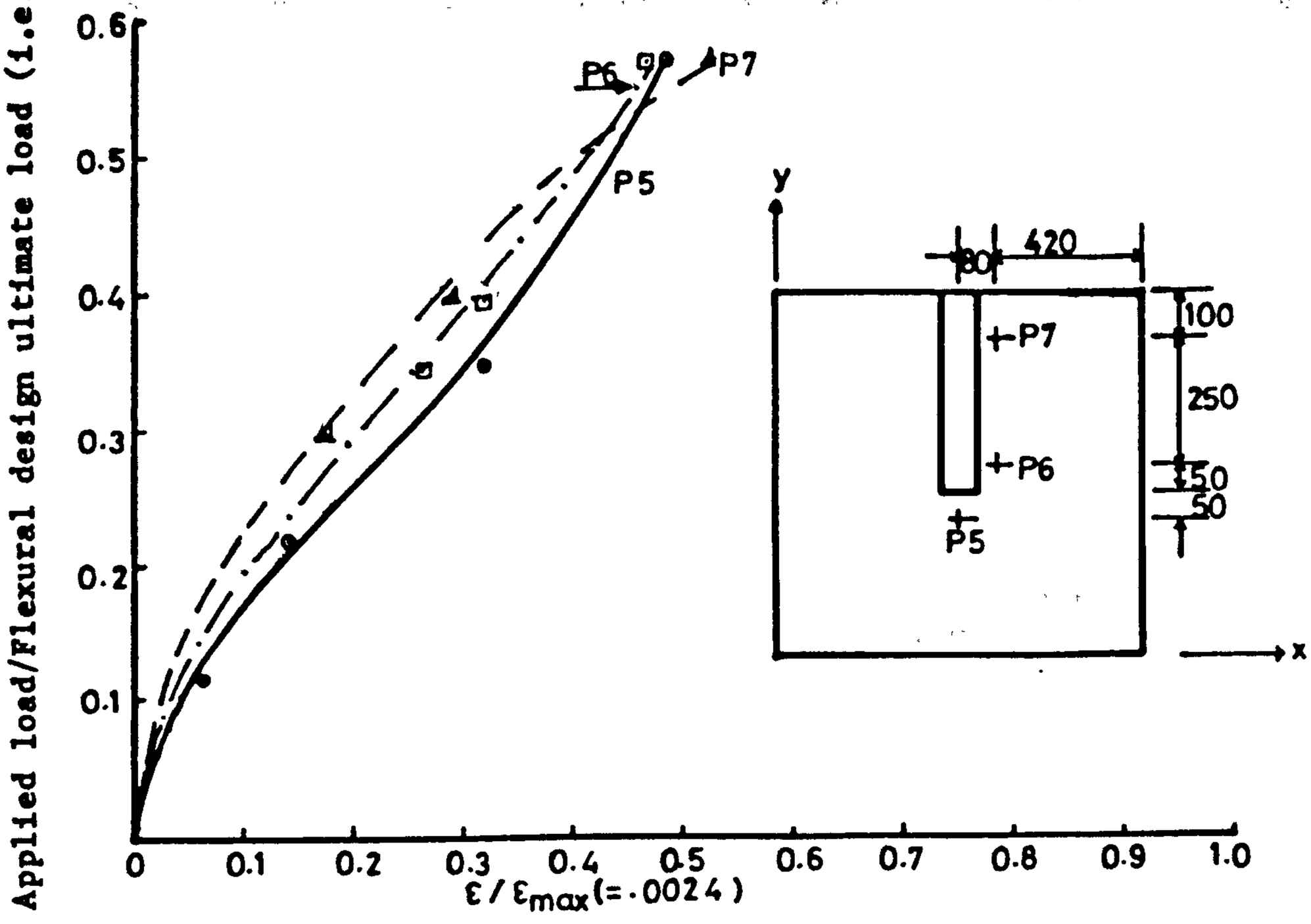

Figure (6.103) : Strain in steel in transverse direction at different points along the sides of wall in the slab of MT7.

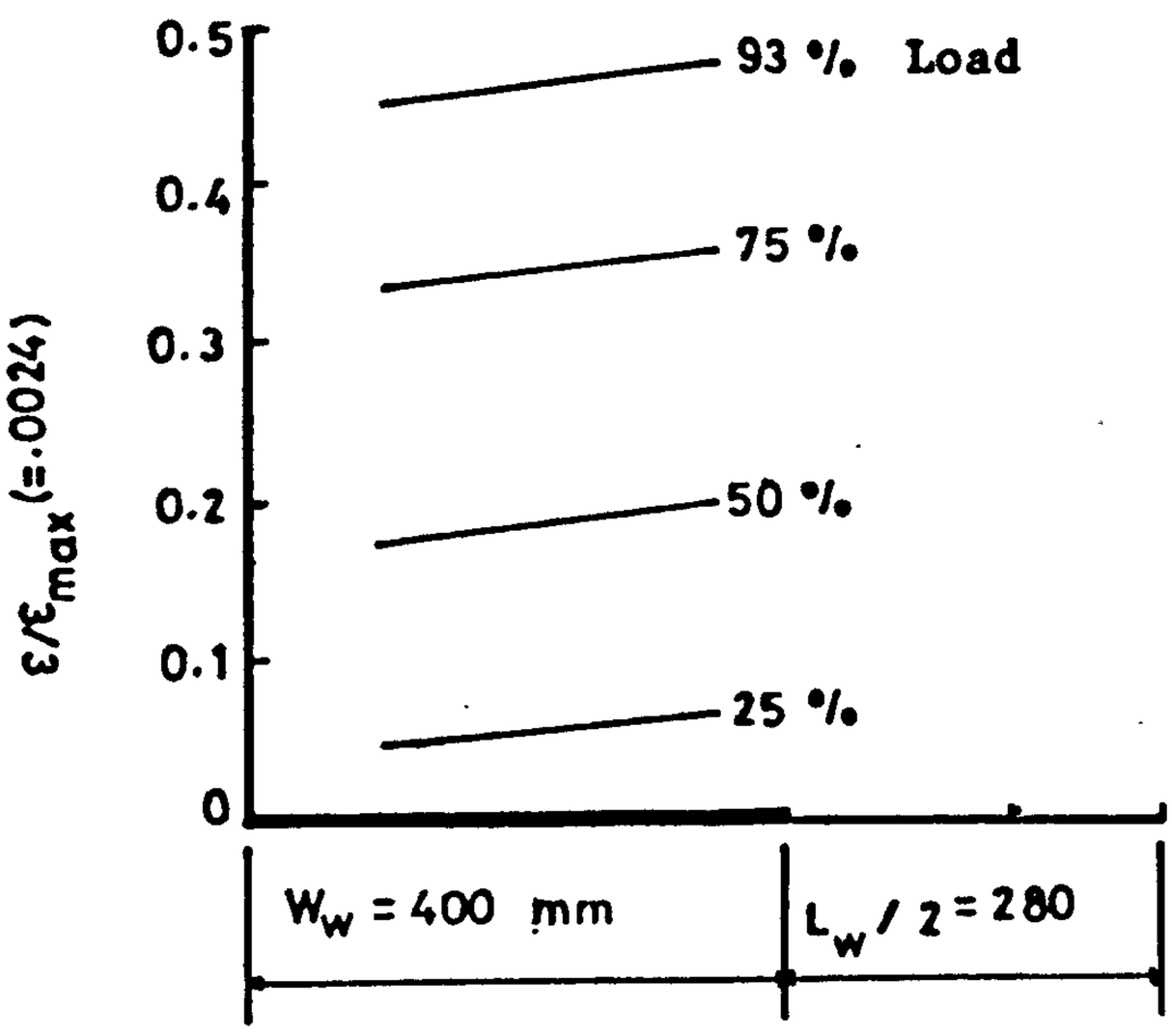

Figure (6.104) : Variation of strain in steel in transverse direction at the top of the slab along the sides of wall of MT7.

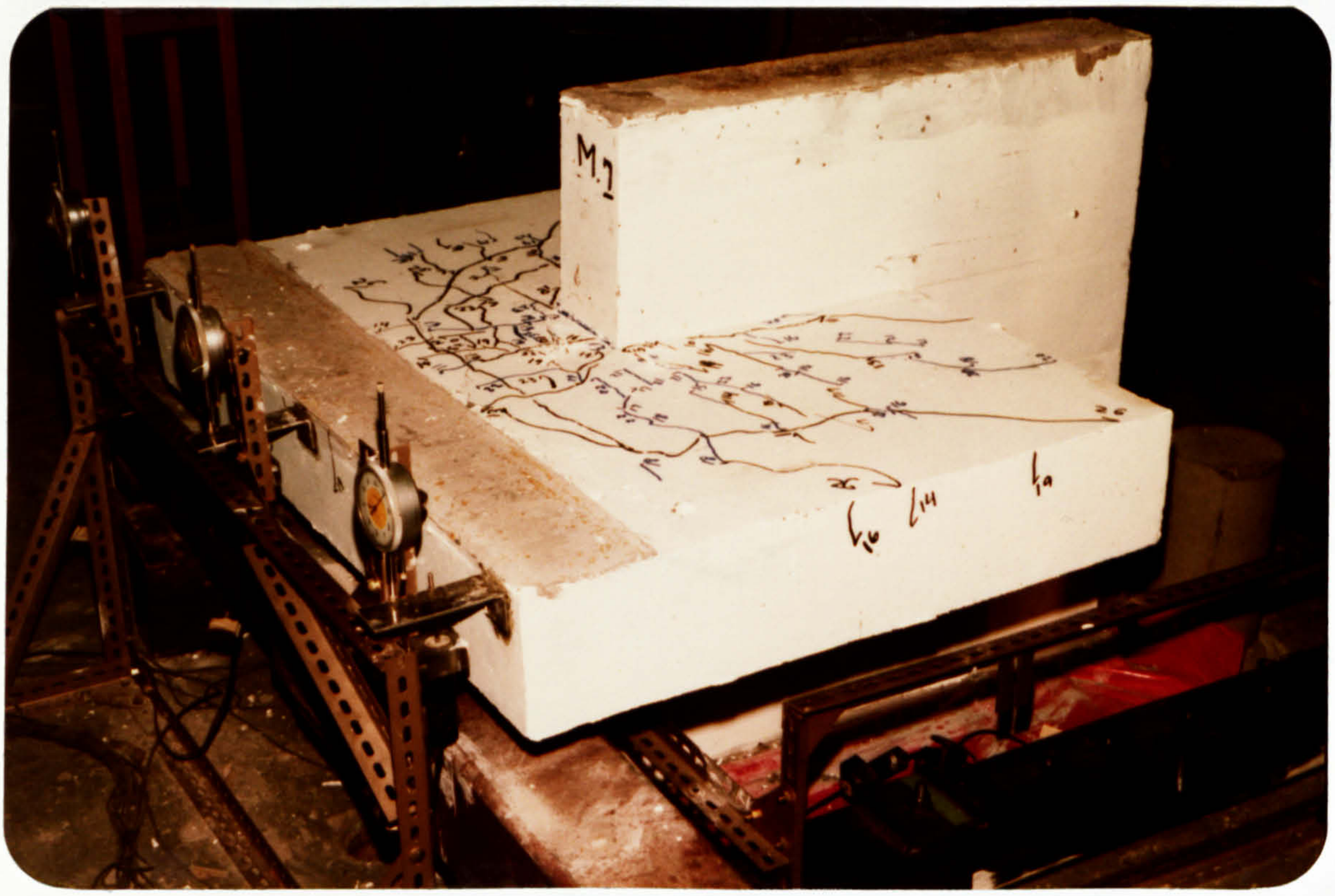

Figure (6.105) : Cracking pattern of model MT7 after failure.

Figure (6.106) : Shear cracks in the slab at the back of the model MT7 after failure.

6.4.5.3 Comparison and discussion

For both the models i.e. MT6 and MT7, the compressive strain in concrete and its variation in the slab along the transverse critical section passing through the inner edge of wall, showed the same behaviour as that of previous models. The variation of strain in steel at the top of the slabs of models MT6 and MT7 in the windward direction (y-direction) along the same section is shown in Figures (6.90) and (6.102). Comparing the two figures it may be observed that the concentration of the strains and consequently stresses in slab at the inner edge of the wall increases as the corridor opening width decreases and therefore while dividing the slab into strips, when using the direct design method, the width of the central strip should be made a function of the corridor opening width. The amount of unbalanced moment transferred seems to have more profound effect on the distribution of strains in steel in transverse direction along the sides of the wall (Figures (6.92) and (6.104)). The slope of the curves showing this distribution in the slab of model MT7 at different stages of loading is far flatter than that of model MT6, and are nearly parallel to each other. However as can be seen from Figure (6.92) there was a great deal of redistribution of forces at different stages of loading.

Figures (6.107) and (6.108) compare the strain in steel in transverse direction at points P6 and P7 respectively for models MT6 and MT7. It is interesting to note that the strains in the slab near the inner edge of wall (Point P6) in both the models was approximately same when the applied wind load approached the corresponding ultimate load.

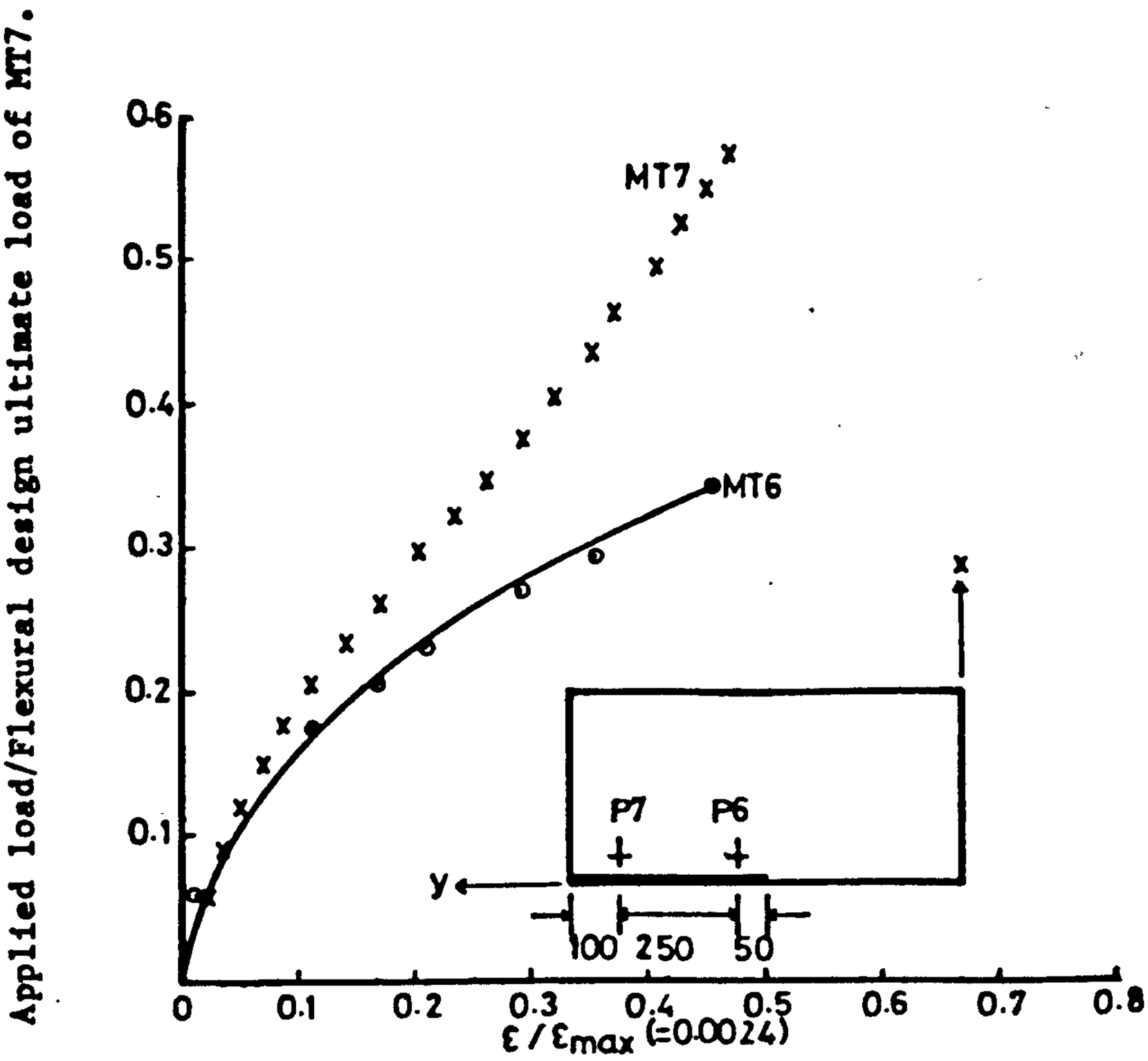

Figure (6.107) : Strain in steel in transverse direction at point P6 in the slab of models MT6 and MT7.

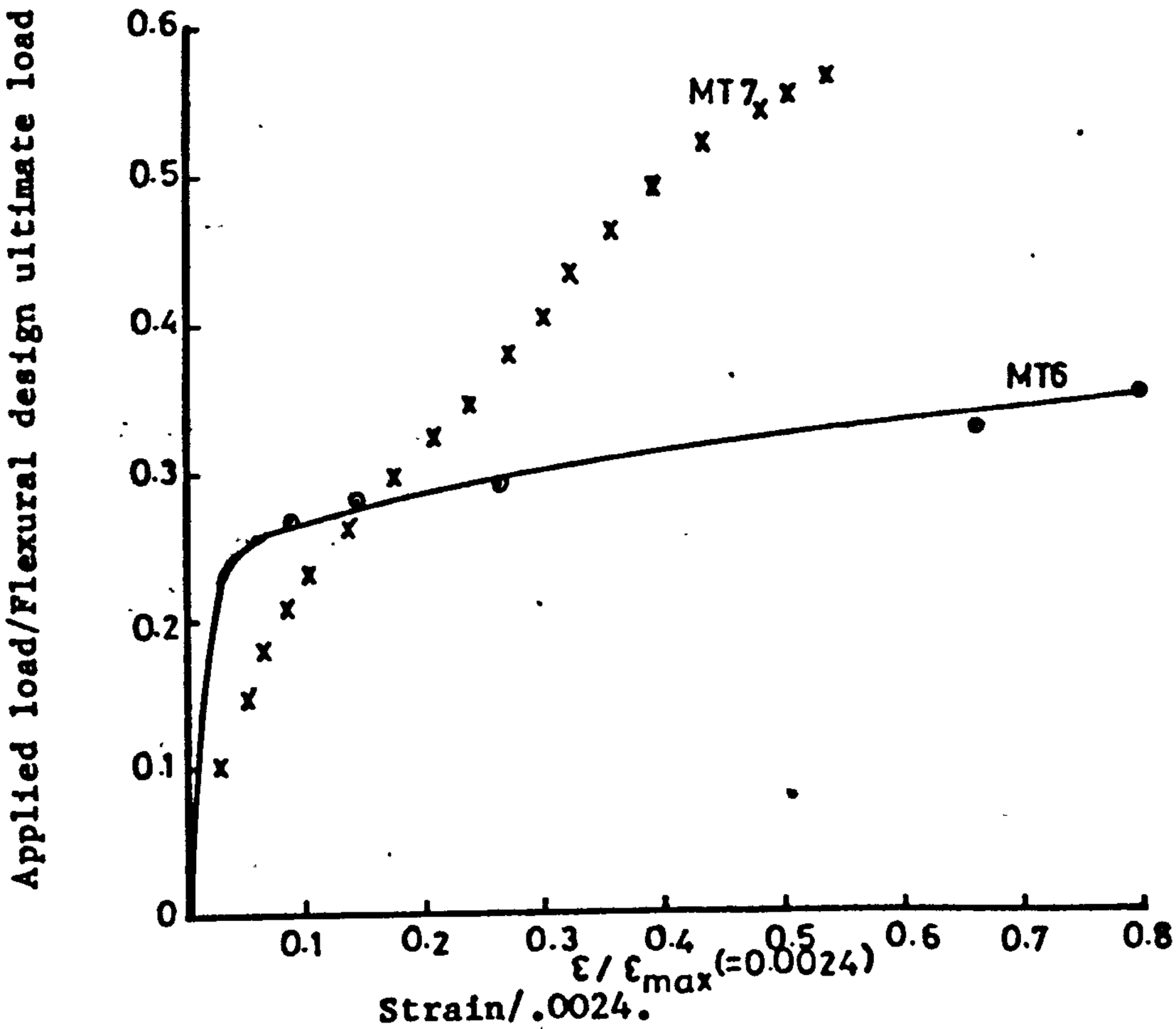

Strain/.0024.

Figure (6.108) : Strain in steel in transverse direction at point P7 in the slab of models MT6 & MT7.

Table 6.10 compares the experimental and calculated ultimate loads for models MT6, MT3 and MT7. From this table it can be observed that CP 110 without transfer of moment largely overestimates the strength of connection of MT6 (with largest ratio of M_w/V_w). Schwaighofer and Collins method (8) too, greatly overestimates the strength of connection of this model since it also does not take account of the reduction in strength due to transfer of unbalanced moment. The predictions of ACI318 are generally reasonable for all the three models. As in the other cases all the other methods greatly underestimate the strength of connection.

6.4.6 Models of Group IV (i.e. MT3 & MT8) (Effect of $\frac{M_g}{V_g}$ ratio)

6.4.6.1 MT8

The effect of change of intensity of gravity load on the strength of connection was investigated by testing the models of group II (i.e. MT2, MT4 and MT5). However the change of gravity load is always accompanied by the change in moment M_g due to gravity load. Therefore in order to investigate the effect of change of M_g alone, model MT8 was tested. The results could be compared with model MT3. The change in the ratio $\frac{M_g}{V_g}$ was achieved by increasing the bay width, Y_w. It was 1440 mm for this model as compared to 1000mm for MT3. The change in bay width of the model might affect the distribution of stresses due to wind load as well but it was unavoidable. Except the bay width other features of model MT8 were same as those of MT3. The arrangement of reinforcement in the slab of this model is shown in Figure (6.109).

Table 6.10. Comparison of the calculated and experimental ultimate loads for models of IIIrd group of MT series.

Model No.	f_{cu} N/mm^2	Experimental loads at failure V_{exp} kN	CP110 without transfer of moment $V_{cal.1}$ kN	CP110 with transfer of moment $V_{cal.2}$ kN	ACI method $V_{cal.3}$ kN	Chang method $V_{cal.4}$ kN	Schwaifhofer & Collins $V_{cal.5}$ kN	Coull & Wong $V_{cal.6}$ kN
MT6	32.2	105.8	145.26 (0.73)	28.98 (3.65)	87.7 (1.21)	51.1 (2.1)	155.97 (0.68)	59.57 (1.78)
MT3	42.8	154.2	155.78 (0.99)	33.17 (4.65)	119.21 (1.29)	61.83 (2.49)	180.64 (0.85)	85.93 (1.79)
MT7	41.8	177.56	155.78 (1.14)	36.89 (4.81)	142.02 (1.25)	64.93 (2.73)	178.41 (1.0)	74.51 (2.38)

Note. The figures in brackets show the ratio $\frac{V_{exp}}{V_{cal}}$

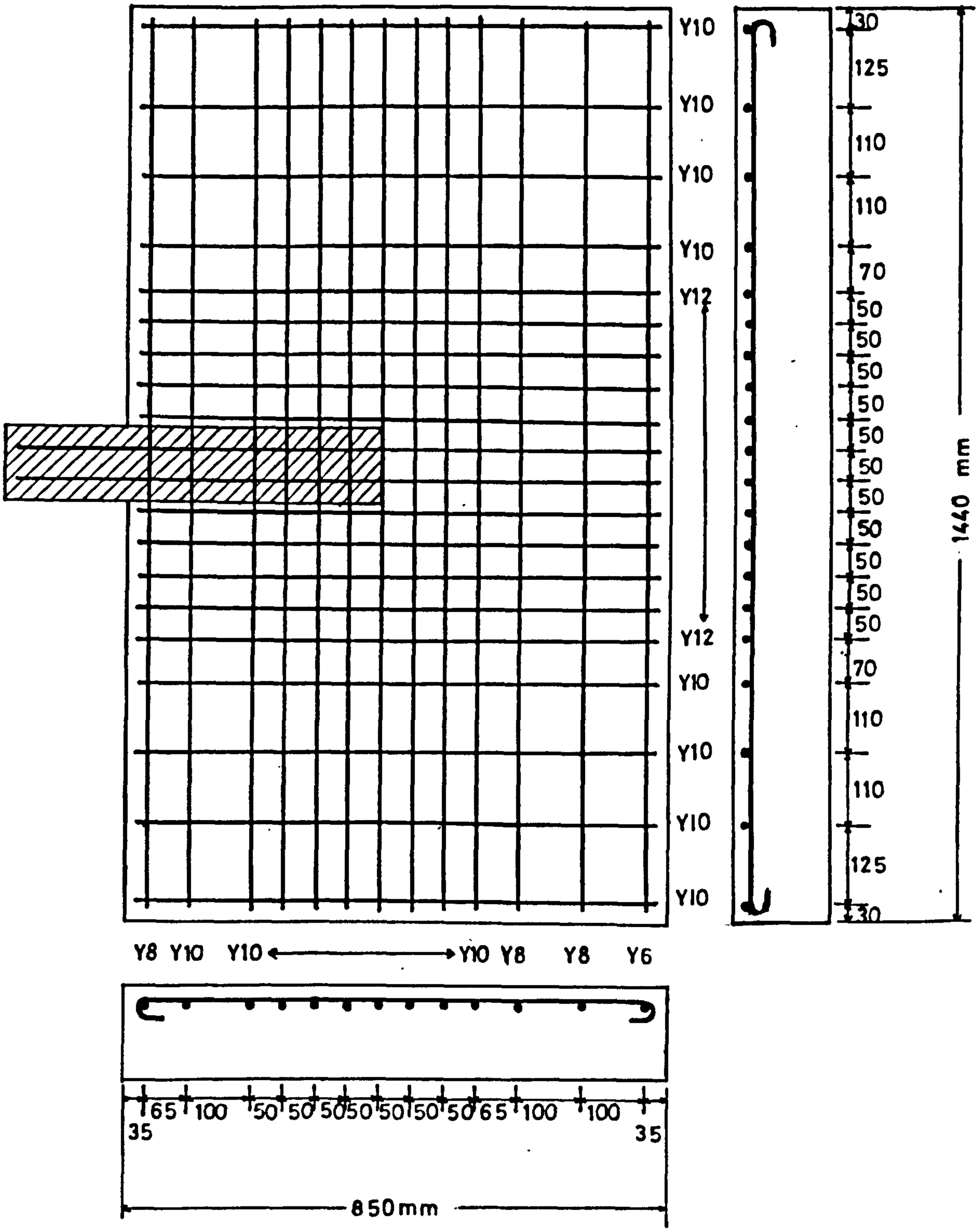

Figure (6.109) : Arrangement of reinforcing bars in the slab of the model MT8.

The wind load-displacement curves for this model and MT3 are shown in Figure (6.110). The other experimental data are shown in Figures (6.111) to (6.116). The total gravity load applied to this model was also same as that of MT3 (i.e. 18 kN).

Behaviour of the model: The first cracks, as shown in Figure (6.117) appeared at a load of 20% of the wind load at failure in addition to gravity load. Two hairline cracks appeared in the slab at the back of the model at the same load level. The overall crack pattern was similar to that of MT3. Sketch showing the location of the shear cracks at the back of the model after failure is shown in Figure (6.118). Photographs showing ultimate crack pattern of this model are presented in Figures (6.119) and (6.120). The ultimate wind load for this model was 163.65 kN.

6.4.6.2 Comparison and discussion

As can be observed from Figure (6.110) that in the beginning model MT8 showed somewhat lower stiffness than that of MT3. However at higher stages of loading the stiffness of MT3 deteriorated before that of MT8. The behaviour of the measured compressive strain in concrete and tensile strain in steel in the slab of model MT8 was not very much different from the previous models. From table 6.11 it can be observed that the trend of calculated strength of connection from different methods is also similar to the previous models.

6.4.7 Models of Group V (i.e. MT3 and MT9) (Steel at both faces of slab)

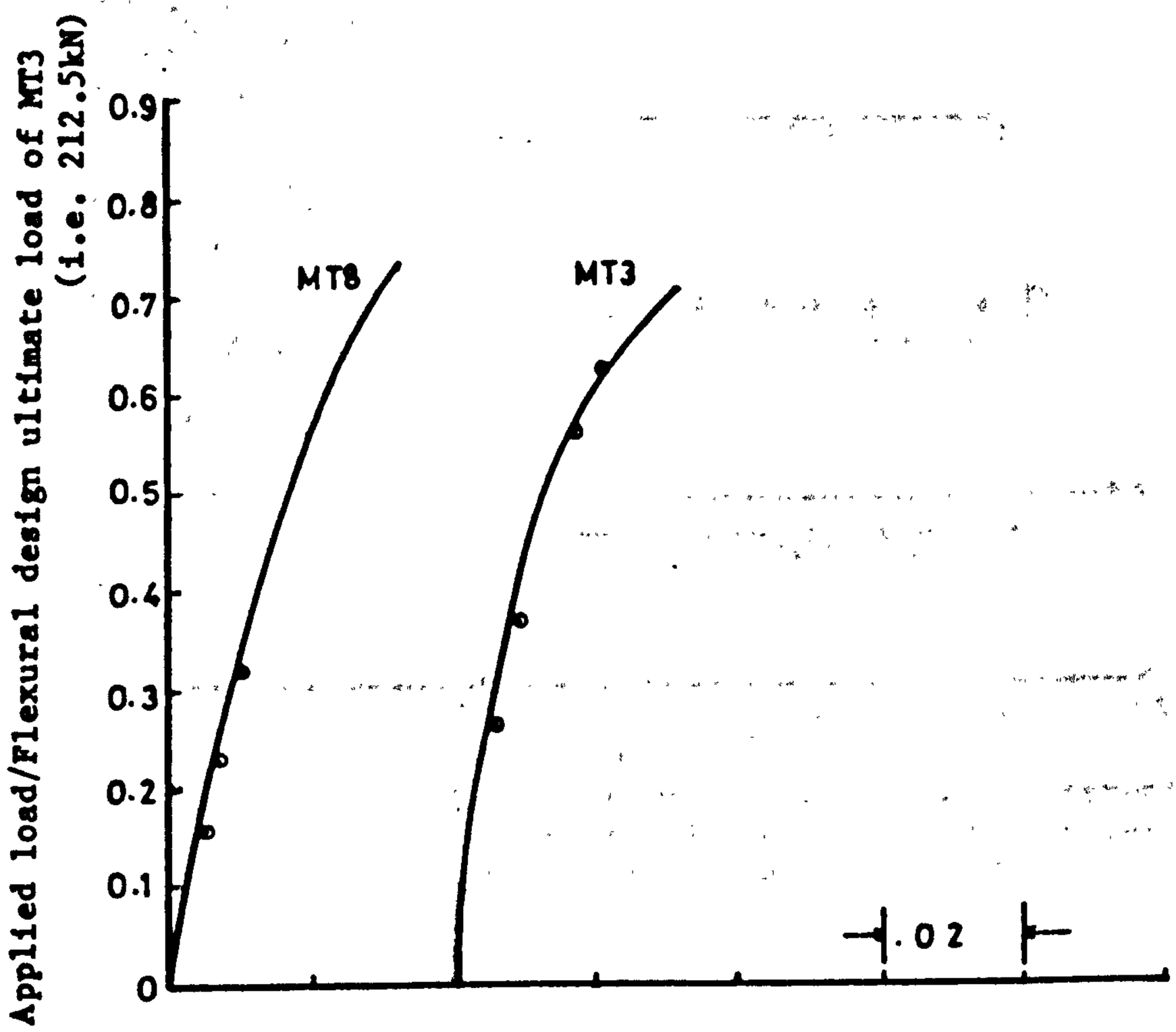

Figure (6.110) : Wind load-displacement relationship for models of IVth group of MT series.

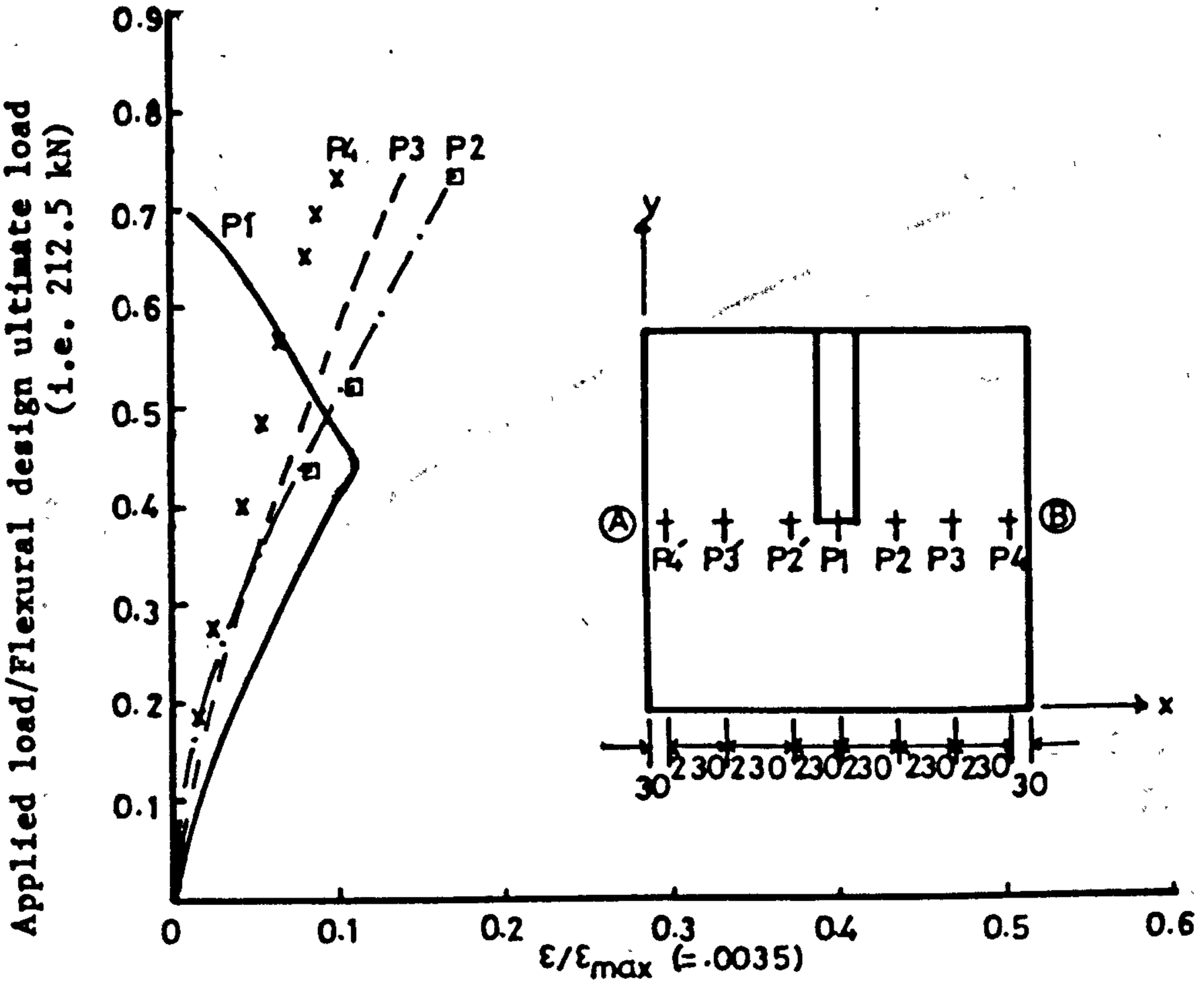

Figure (6.111) : Comp. strain in concrete at different points in windward direction along transverse critical section AB in the slab of MT8.

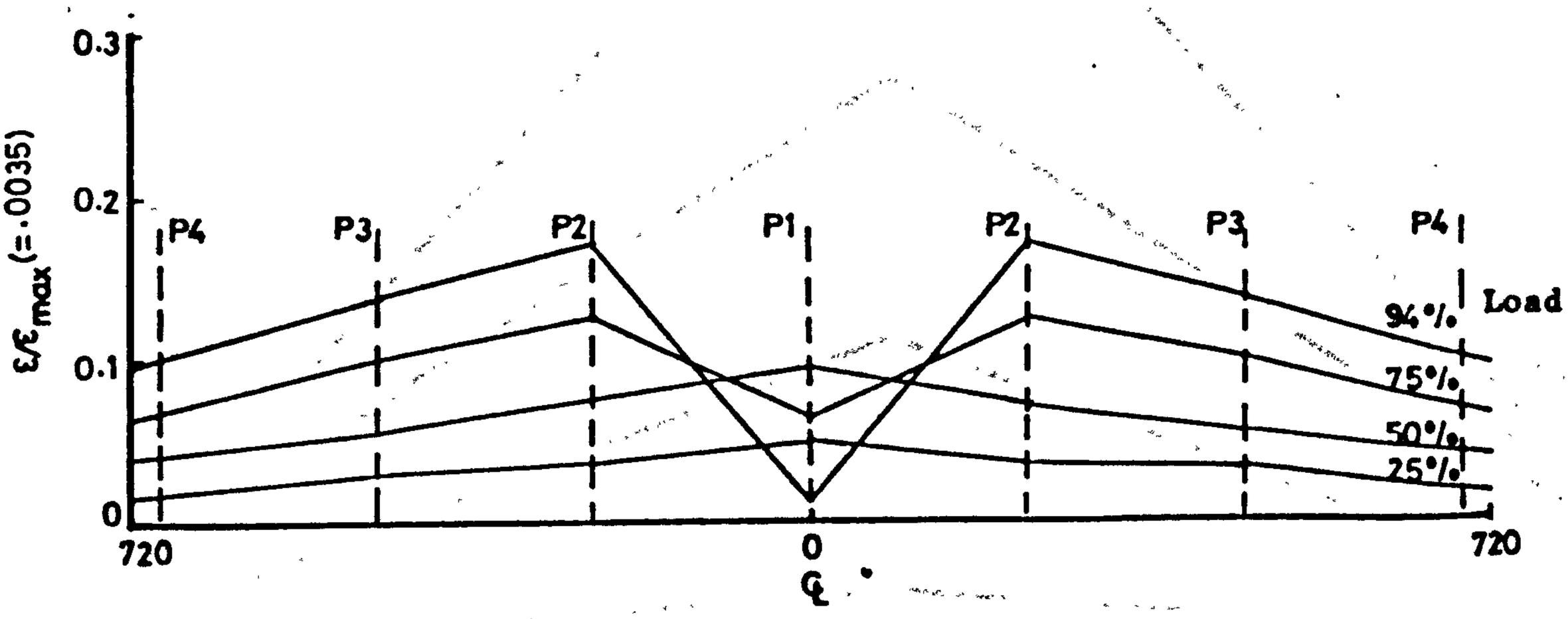

Figure (6.112) : Variation of comp. strain in concrete along transverse critical section at different loading stages in the slab of MT8.

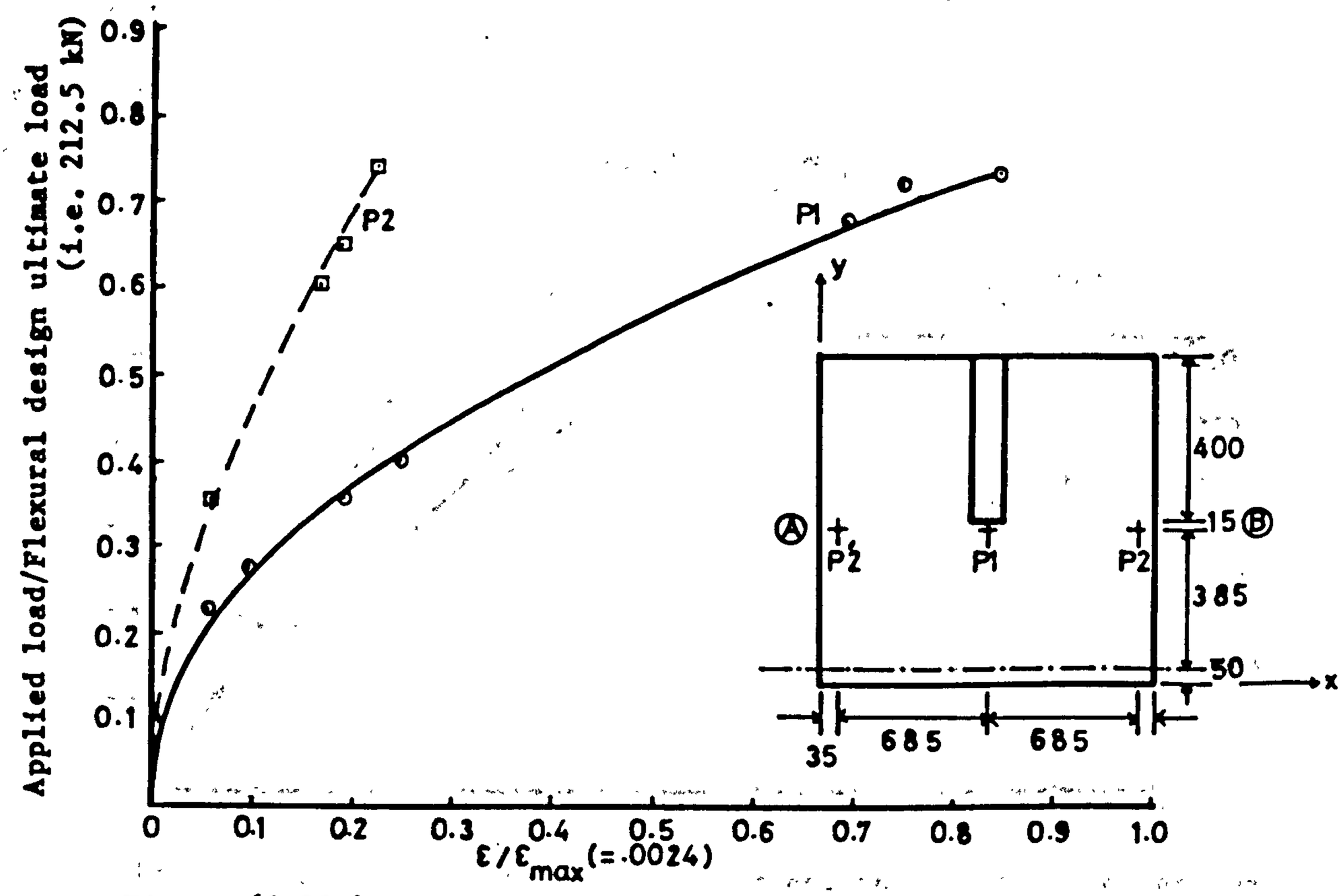

Figure (6.113) : Tensile strain in steel in windward direction at different points along section AB in the slab of MT8.

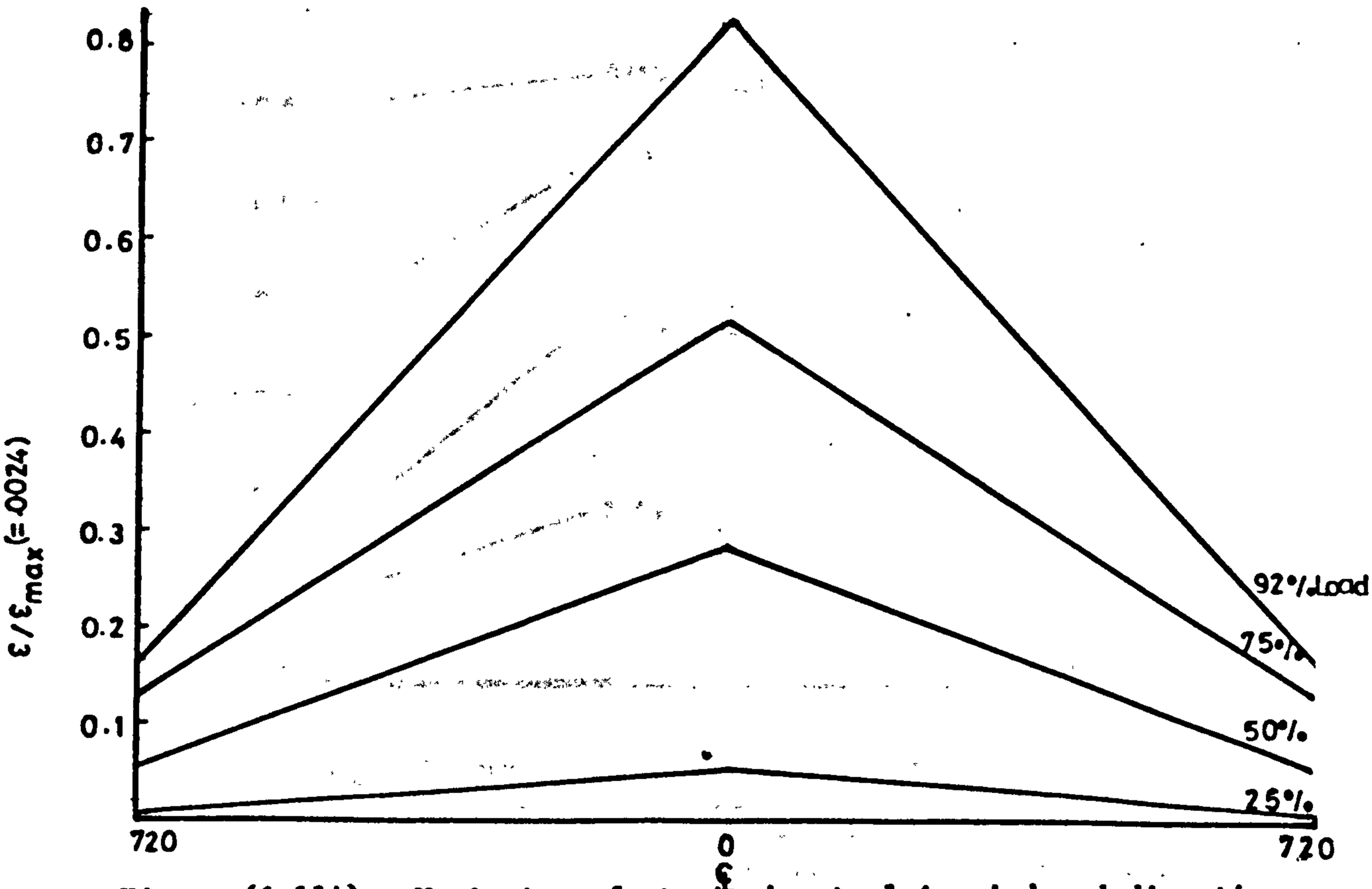

Figure (6.114) : Variation of strain in steel in windward direction along transverse critical section of the slab of MT8.

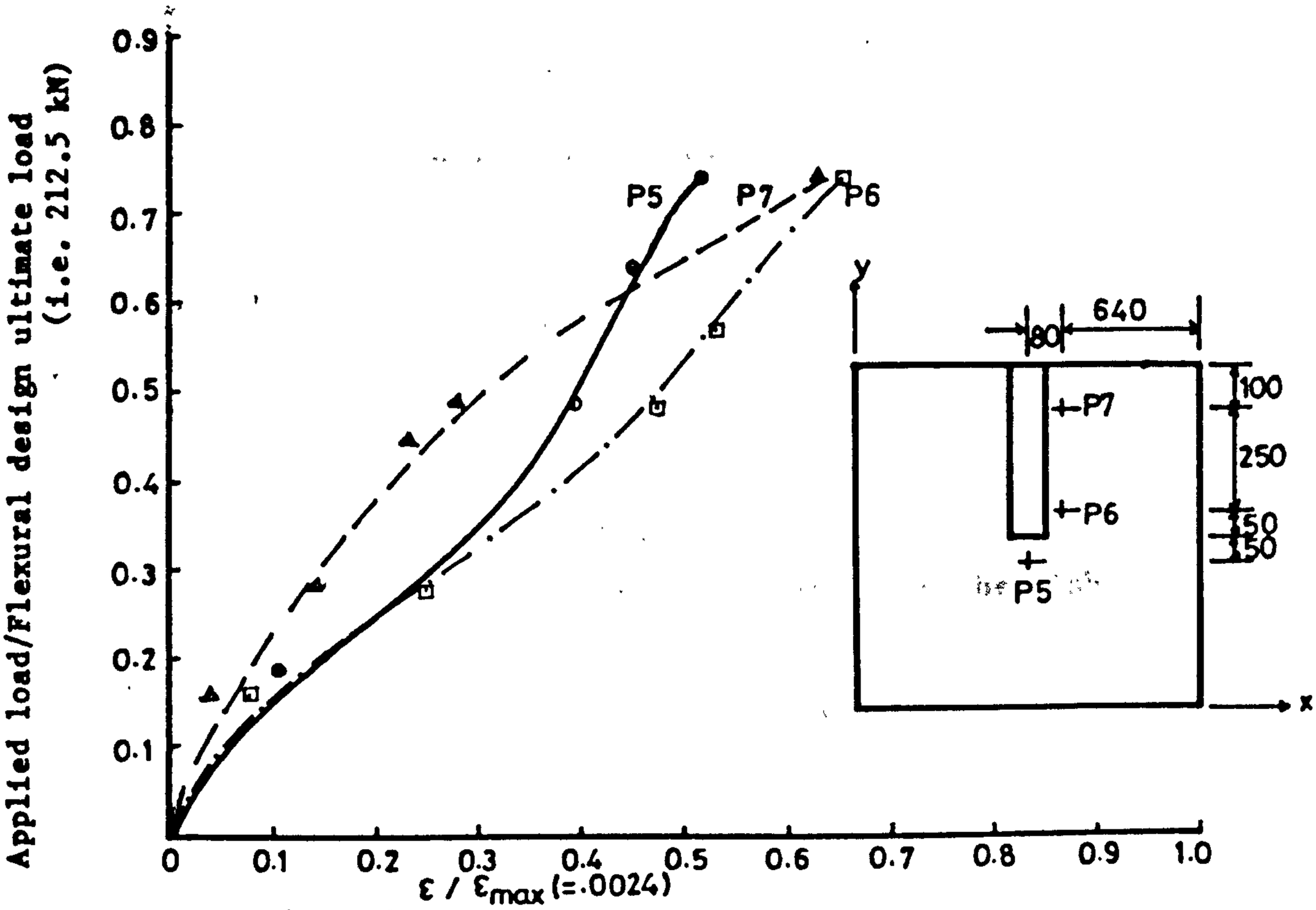

Figure (6.115) : Tensile strain in steel in transverse direction along the side of wall in the slab of model MT8.

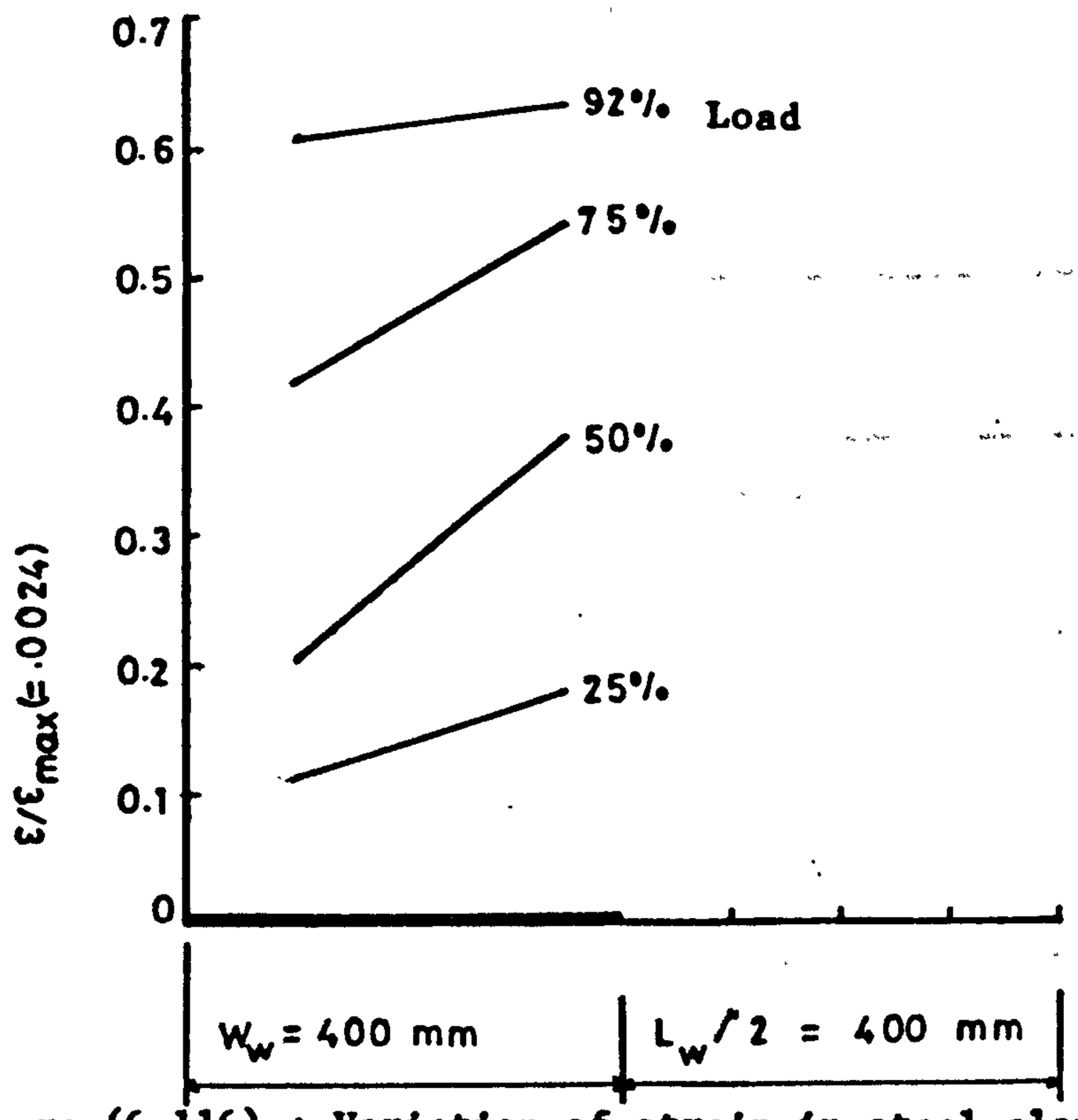

Figure (6.116) : Variation of strain in steel along the side of the wall at different stages of loading in the slab of MT8.

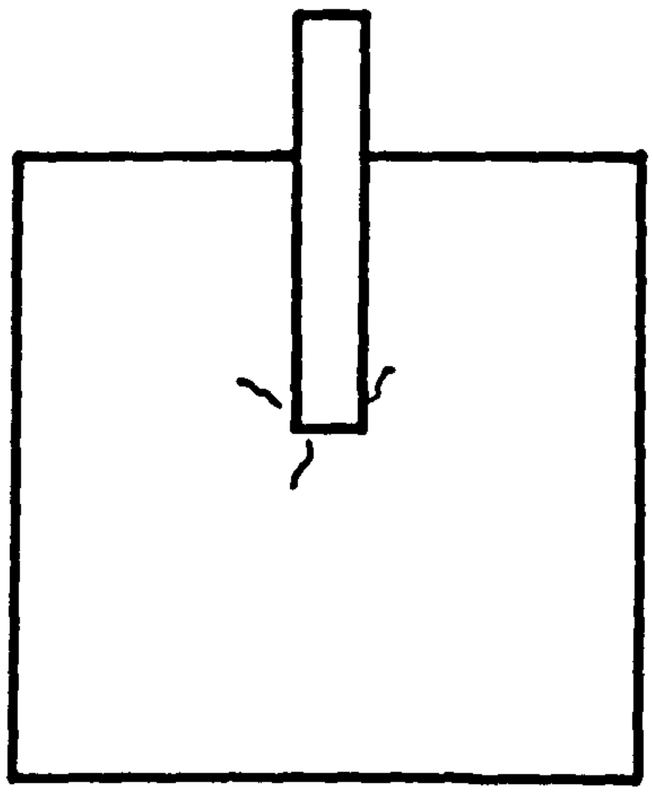

Figure (6.117) : Initiation of cracks in the slab of MT8.

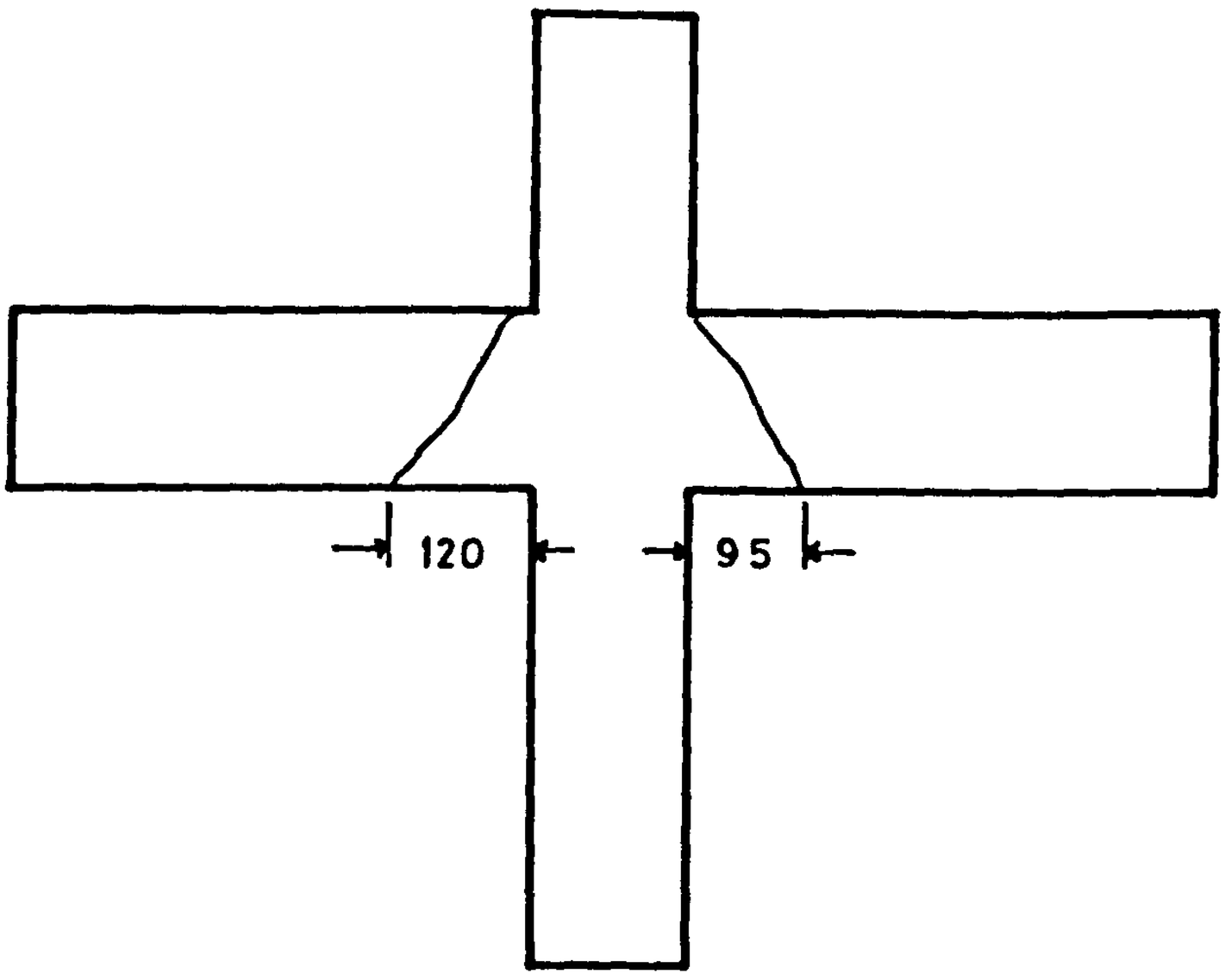

Figure (6.118) : Shear cracks in the slab at the back of model MT8.

Figure (6.119) : Crack pattern of the slab of MT8 after failure.

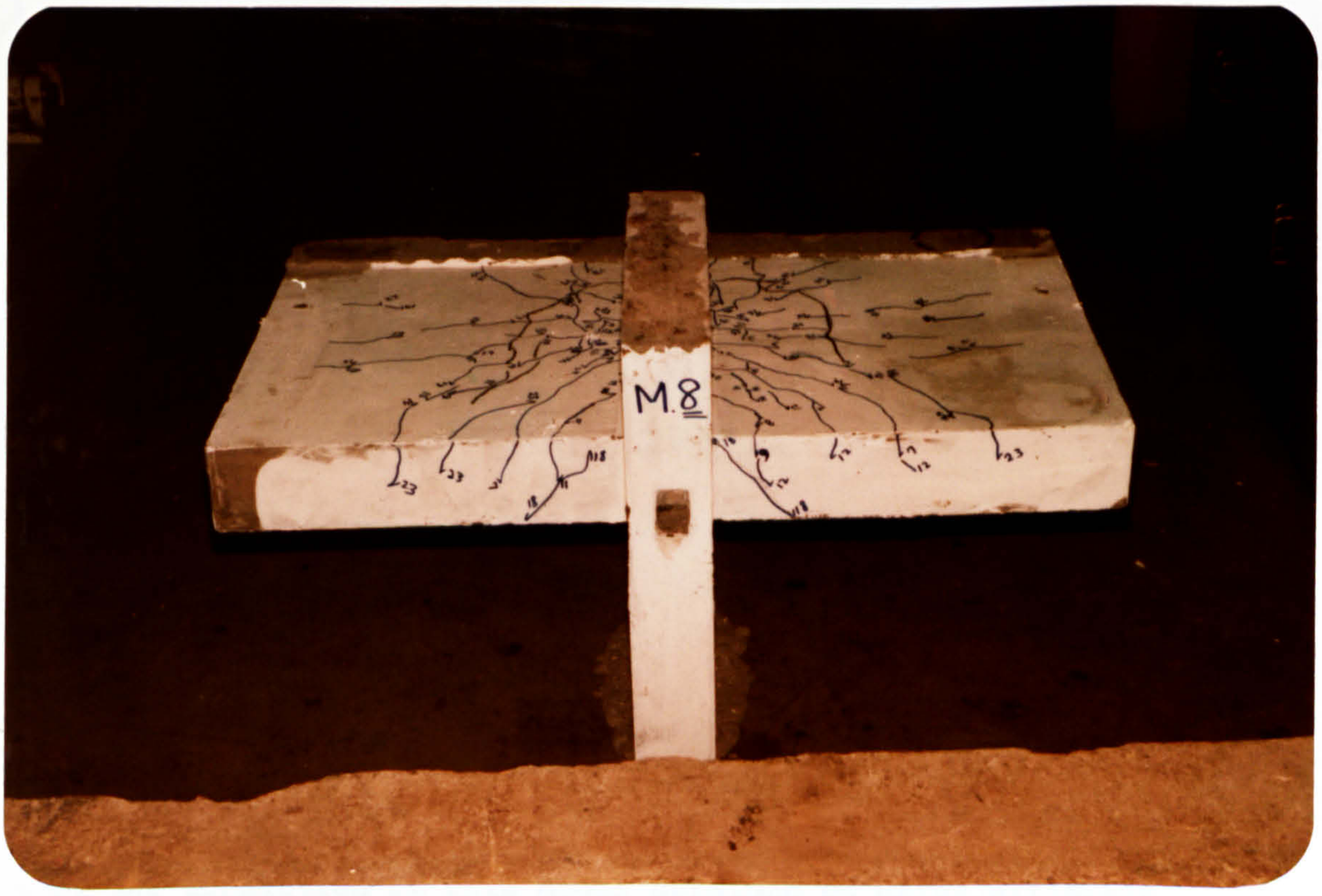

Figure (6.120) : Crack pattern after failure at the back of model MT8.

6.4.7.1 Model MT9

Model MT9 was similar to MT3 except that the slab of this model was doubly reinforced. The arrangement of the reinforcement in the slab of this model is shown in Figure (6.121). Other experimental data are shown in Figures (6.122) to (6.127). The total gravity load applied to this model was 18 kN.

Behaviour of the model: The first crack perpendicular to the inner face of wall as shown in Figure (6.128) appeared at a load of 34% of the ultimate wind load at failure. Very fine cracks in the slab at the back of the model were detected when the load was approximately 62% of the ultimate load. The crack pattern of this model was also similar to that of MT3. The location of shear cracks in the slab at the back of the model after failure is shown in Figure (6.129). The photographs showing the cracking pattern after failure are presented in Figures (6.130) and (6.131). The wind load at failure for this model was 147.2 kN. Wind load-displacement curves for this model and MT3 are shown in Figure (6.132).

6.4.7.2 Comparison and discussion

The behaviour of the measured compressive strain in concrete and tensile strain in steel in the slab of model MT9 was not much different from the previous models. However at higher stages of loading the measured compressive strain in concrete at the bottom of the slab of this model near the inner edge of wall was relatively very low. The calculated ultimate strength of the connection of this model obtained by using different methods is compared with the experimental wind load at failure in table 6.11.

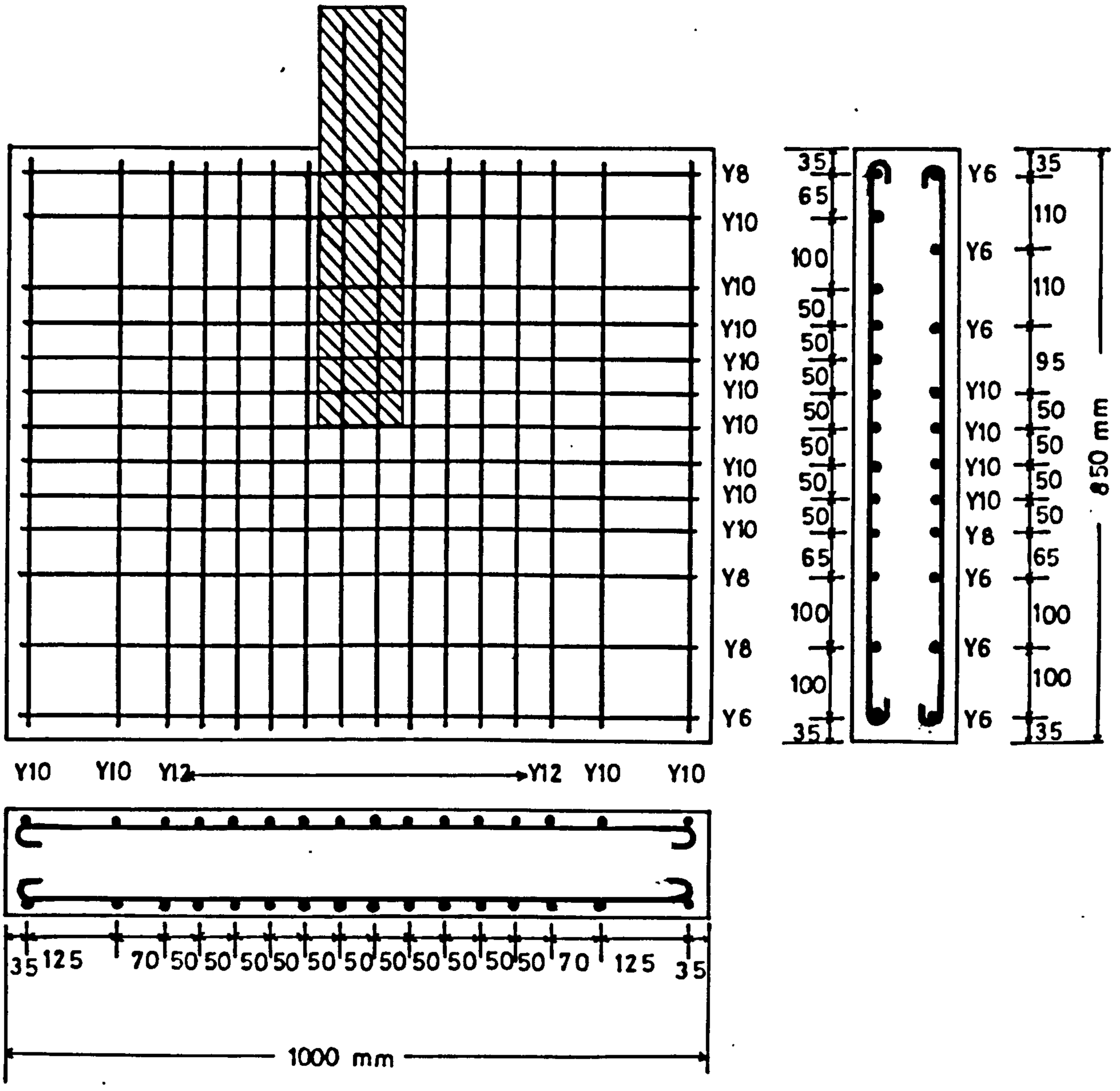

Figure (6.121). Arrangement of reinforcing bars in the slab of model MT9.

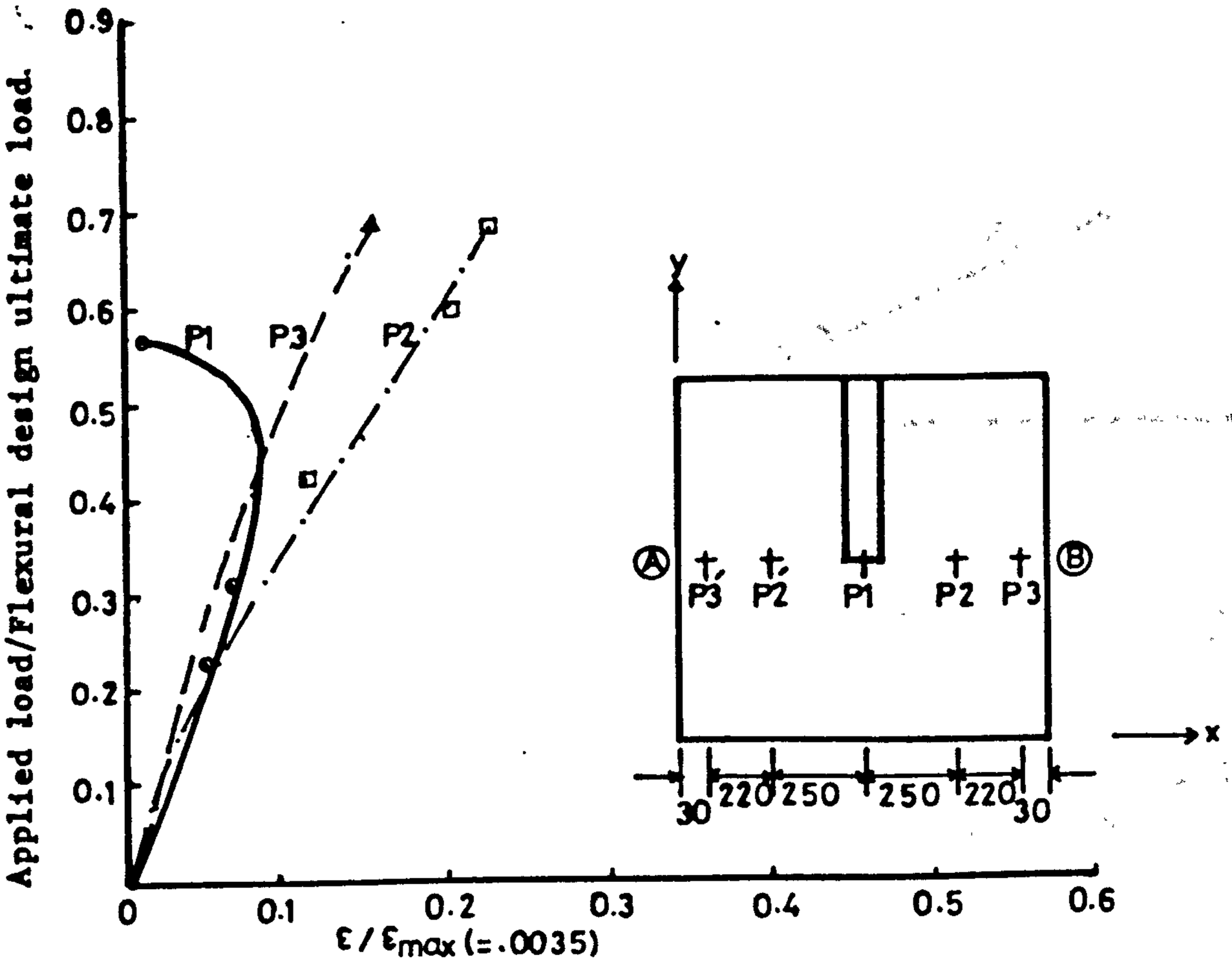

Figure (6.122) : Comp. strain in concrete at different points along transverse section AB in the slab of MT9.

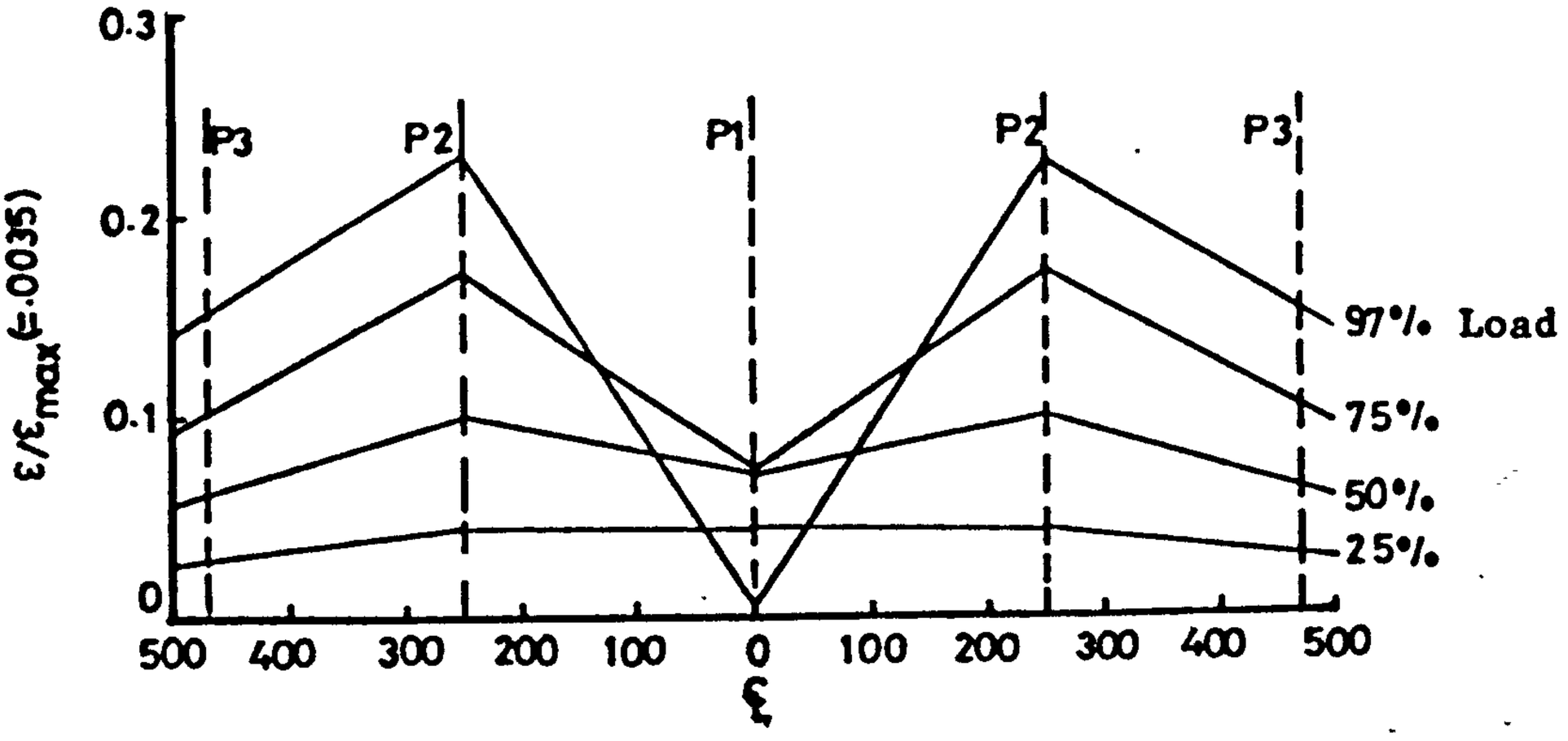

Figure (6.123) : Variation of comp.strain in concrete in windward direction along transverse critical section at different stages of loading, in the slab of MT9.

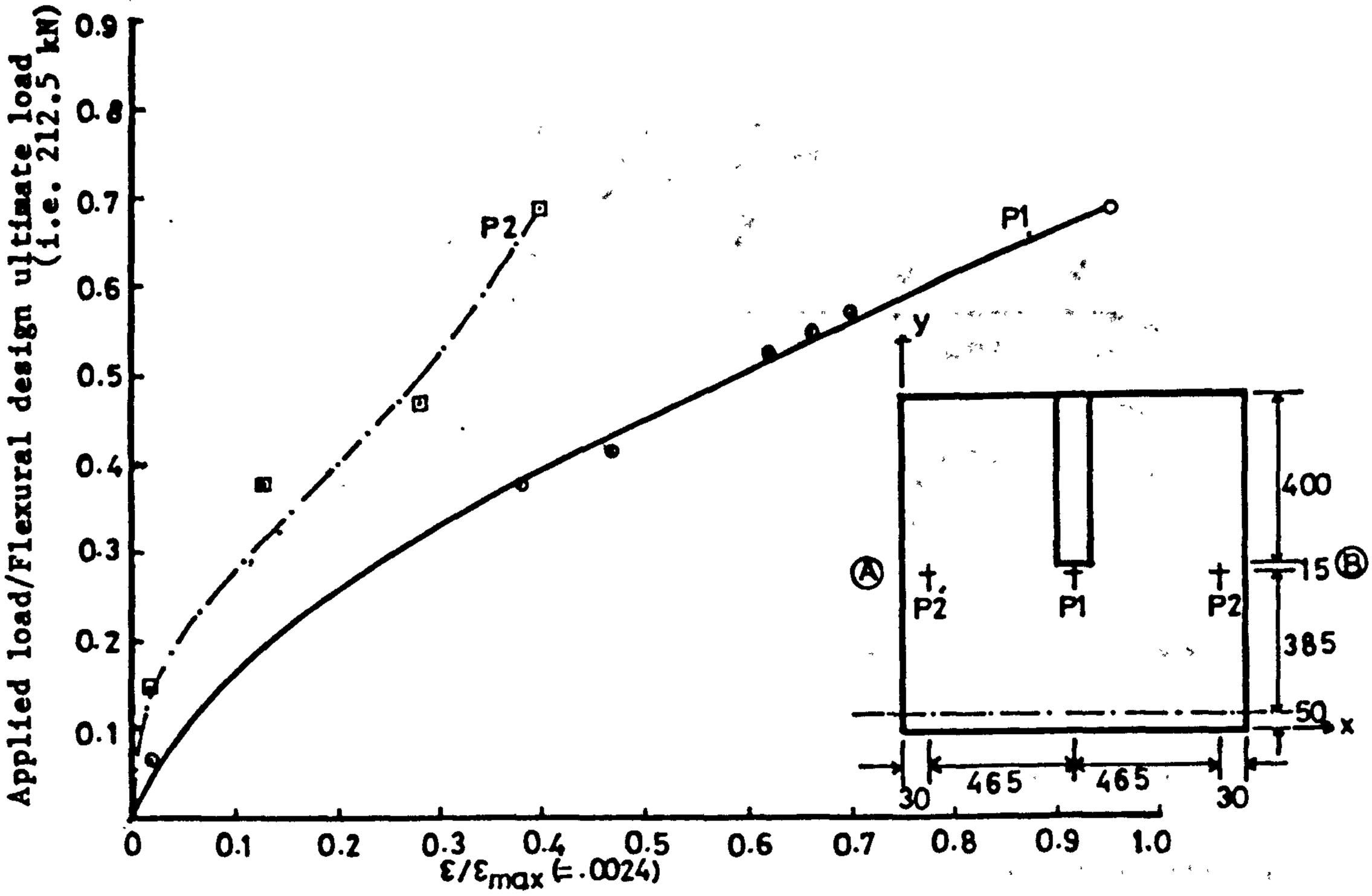

Figure (6.124) : Tensile strain in steel at different points along transverse section AB, in windward direction, in the slab of MT9.

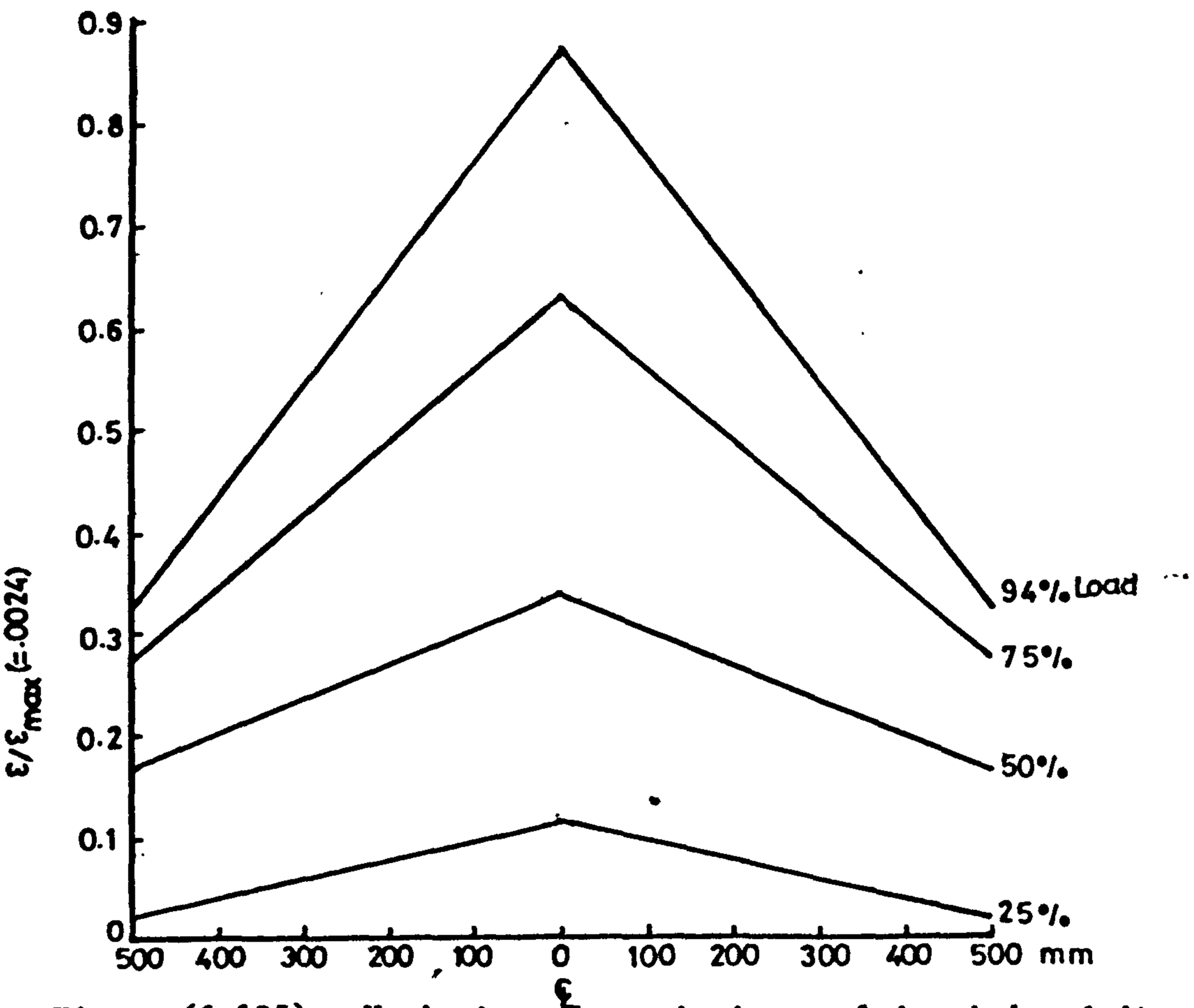

Figure (6.125) : Variation of strain in steel in windward direction along transverse critical section at different stages of loading in the slab of MT9.

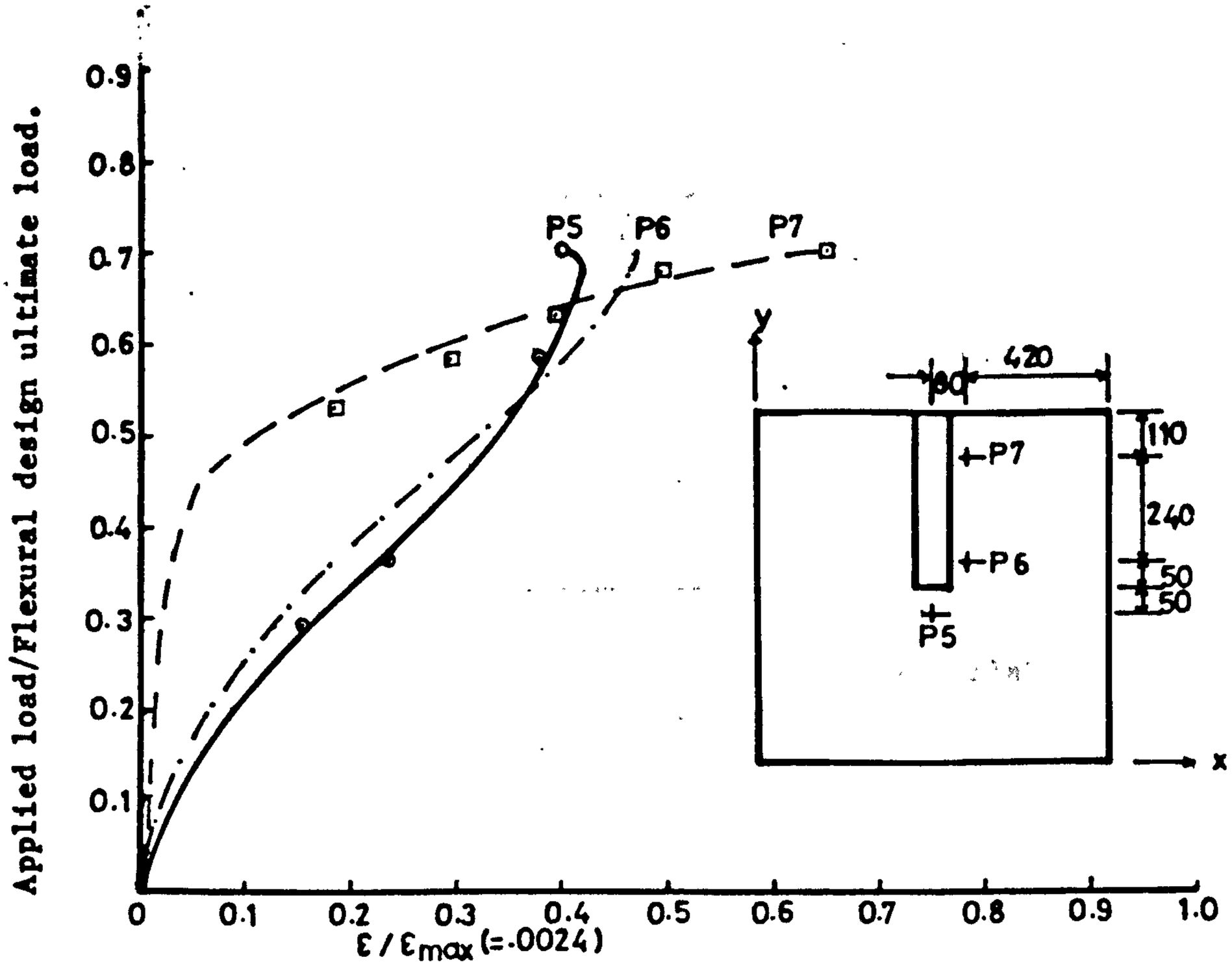

Figure (6.126) : Tensile strain in steel at different points in transverse direction along the side of wall, in the slab of MT9.

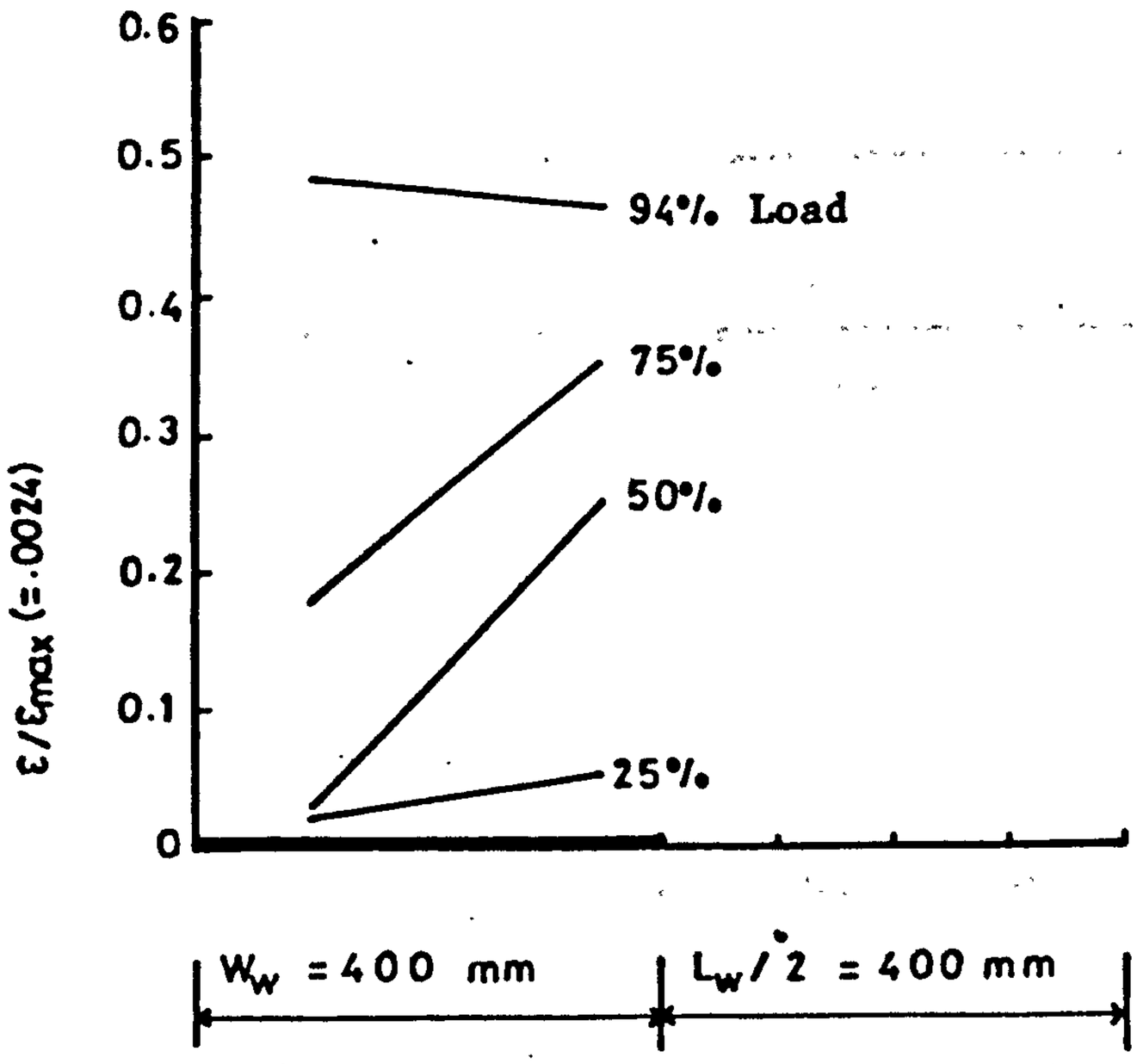

Figure (6.127) : Variation of strain in steel in transverse direction along the side of wall, in the slab of MT9.

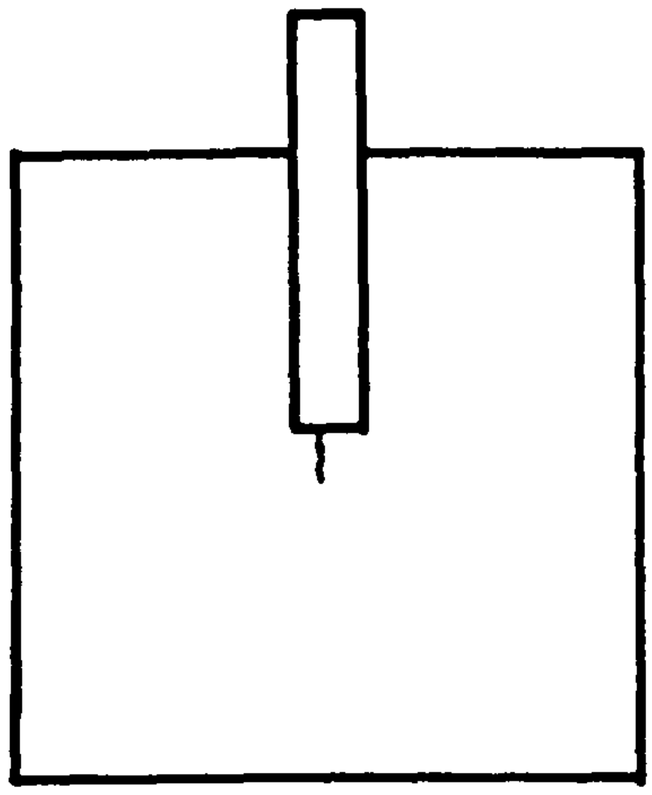

Figure (6.128) : Initiation of cracks in the slab of model MT9.

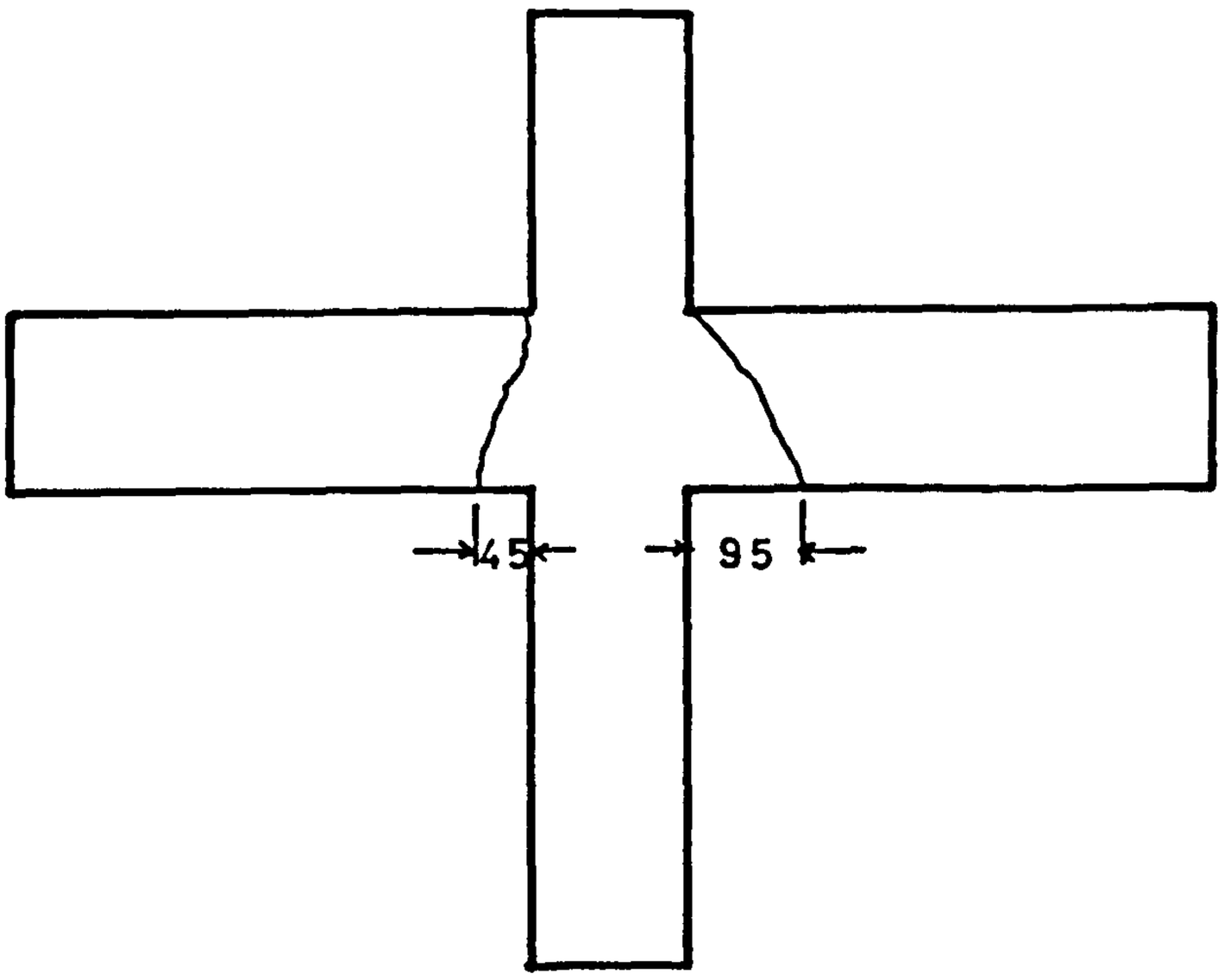

Figure (6.129) : Shear cracks in the slab at the back of model MT9.

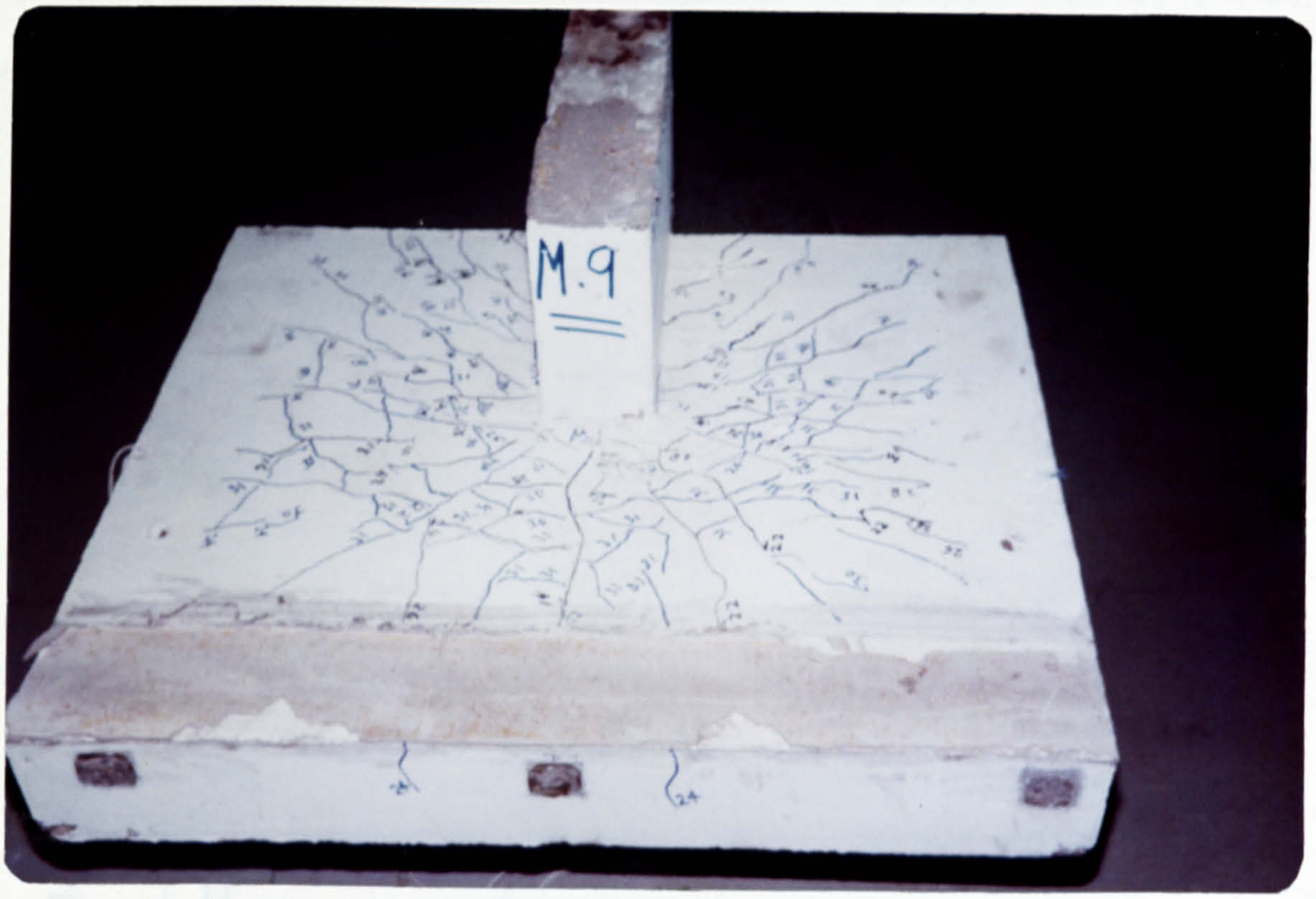

Figure (6.130) : Crack pattern of the slab of model MT9 after failure.

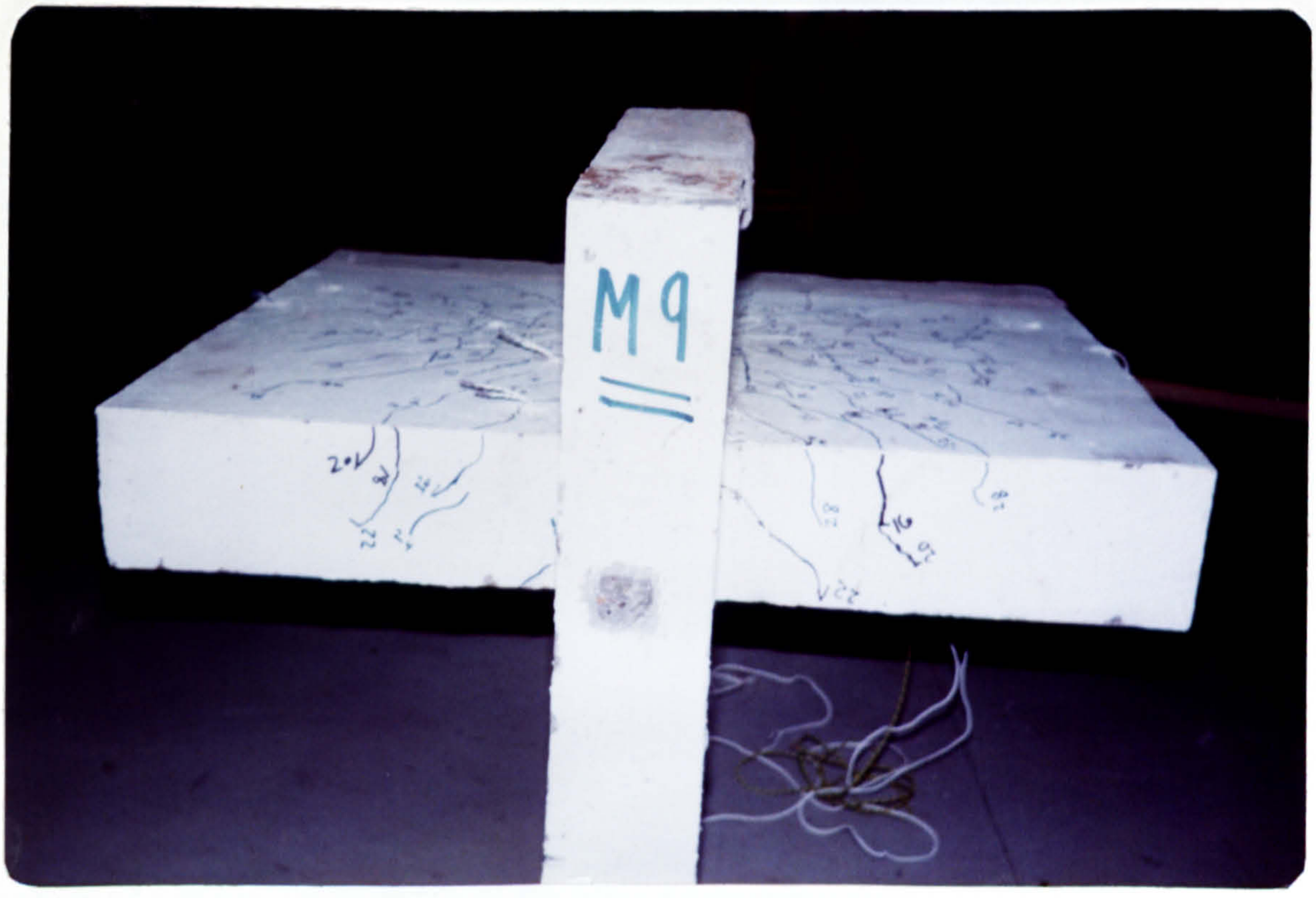

Figure (6.131) : Shear cracks after failure in the slab at the back of MT9.

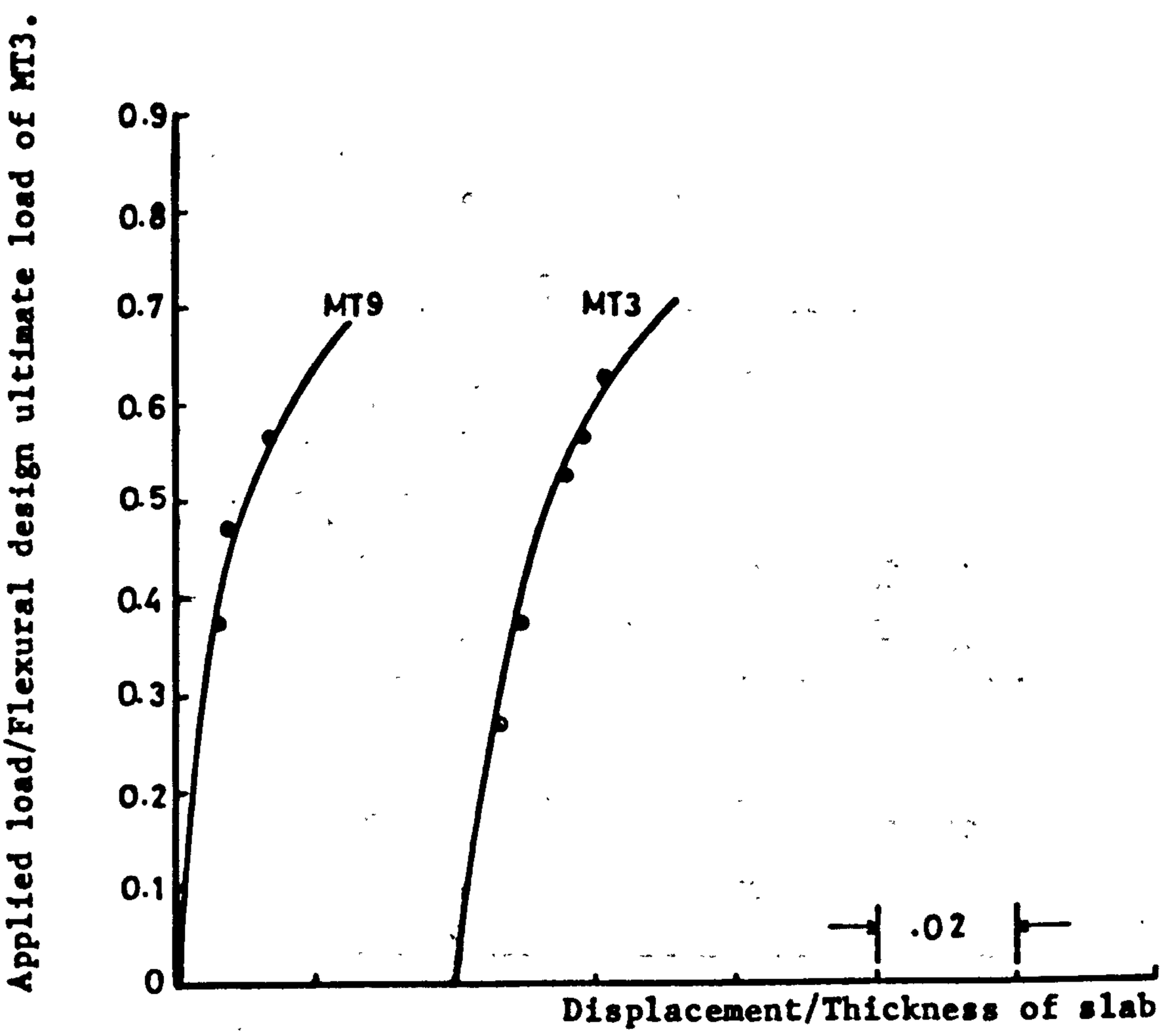

Figure (6.132) : Wind load-displacement relationship for models of Vth group of MT series.

Table 6.11. Comparison of calculated and experimental ultimate loads for models of groups IV & V of MT series.

Model	f_{cu} N/mm^2	Experimental load at failure V_{exp} kN	CP110 without transfer of moment $V_{cal.1}$ kN	CP110 with transfer of moment $V_{cal.2}$ kN	ACI method $V_{cal.3}$ kN	Chang method $V_{cal.4}$ kN	Schwaighofer & Collins $V_{cal.5}$ kN	Coull & Wong $V_{cal.6}$ kN
MT8	32.0	163.65	145.26 (1.13)	30.93 (5.29)	102.11 (1.6)	53.04 (3.09)	154.98 (1.06)	80.25 (2.04)
MT3	42.8	154.2	155.78 (.99)	33.17 (4.65)	119.21 (1.29)	61.83 (2.49)	180.64 (0.85)	85.93 (1.79)
MT9	35.02	147.2	182.1 (0.81)	38.77 (3.8)	107.15 (1.37)	55.64 (2.65)	162.55 (0.91)	100.13 (1.47)

Note. Figures in brackets show the ratio $\frac{V_{exp}}{V_{cal}}$

6.4.8 Models of Group VI (i.e. MT10, MT7 and MT11) (Effect of ratio of flexural steel)

As has already been mentioned, these models were tested to study the effect of the ratio of flexural reinforcement in the slab on the strength of wall-slab connection. Model MT7 is common to this group and group III and its behaviour has already been described. Therefore only the behaviour of models MT10 and MT11 is described here.

6.4.8.1 Model MT10

This model is similar to model MT7 except the steel ratio which was lower by 30% in corresponding strips of model MT10 than that of MT7. The arrangement of reinforcement in the slab of this model is shown in Figure (6.133). The other experimental data are shown in Figures (6.134) to (6.138). The total gravity load applied to this model was 18 kN.

Behaviour of the model: The first three cracks as shown in Figure (6.139) appeared at a wind load of 30% of the load at failure, in addition to gravity load. The ultimate crack pattern was not different from that of model MT7. Although the ratio of flexural reinforcement in the slab of this model was the lowest among all the models of the main test series, the failure was sudden and brittle, implying that it was a shear failure. The shear cracks in the slab at the back of the model appeared when the applied wind load was only 42% of the ultimate load. The photograph showing the crack pattern of this model after failure is shown in Figure (6.140). The wind load at failure was 153.27 kN.

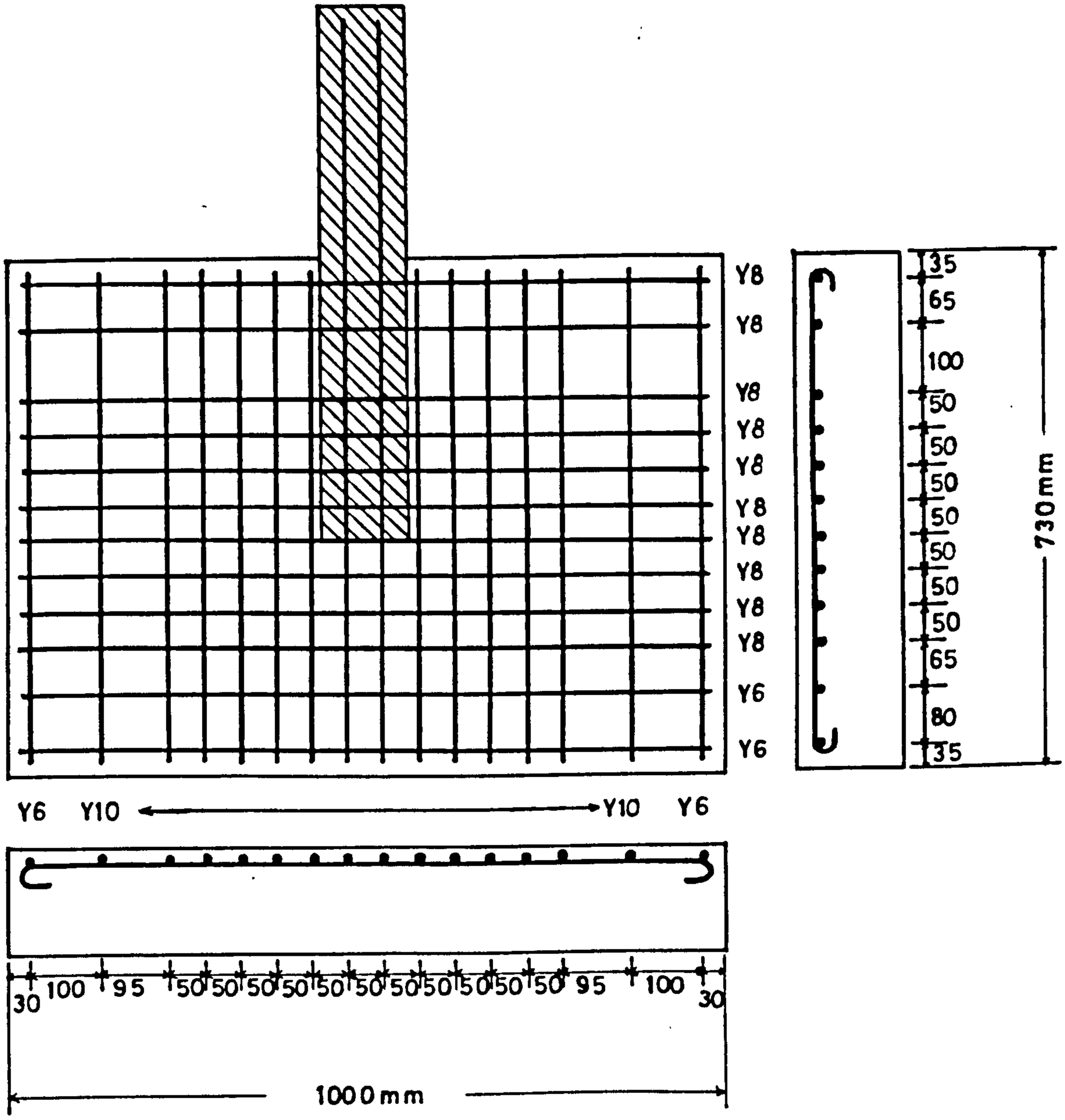

Figure (6.133) : Arrangement of reinforcing bars in the slab of model MT10.

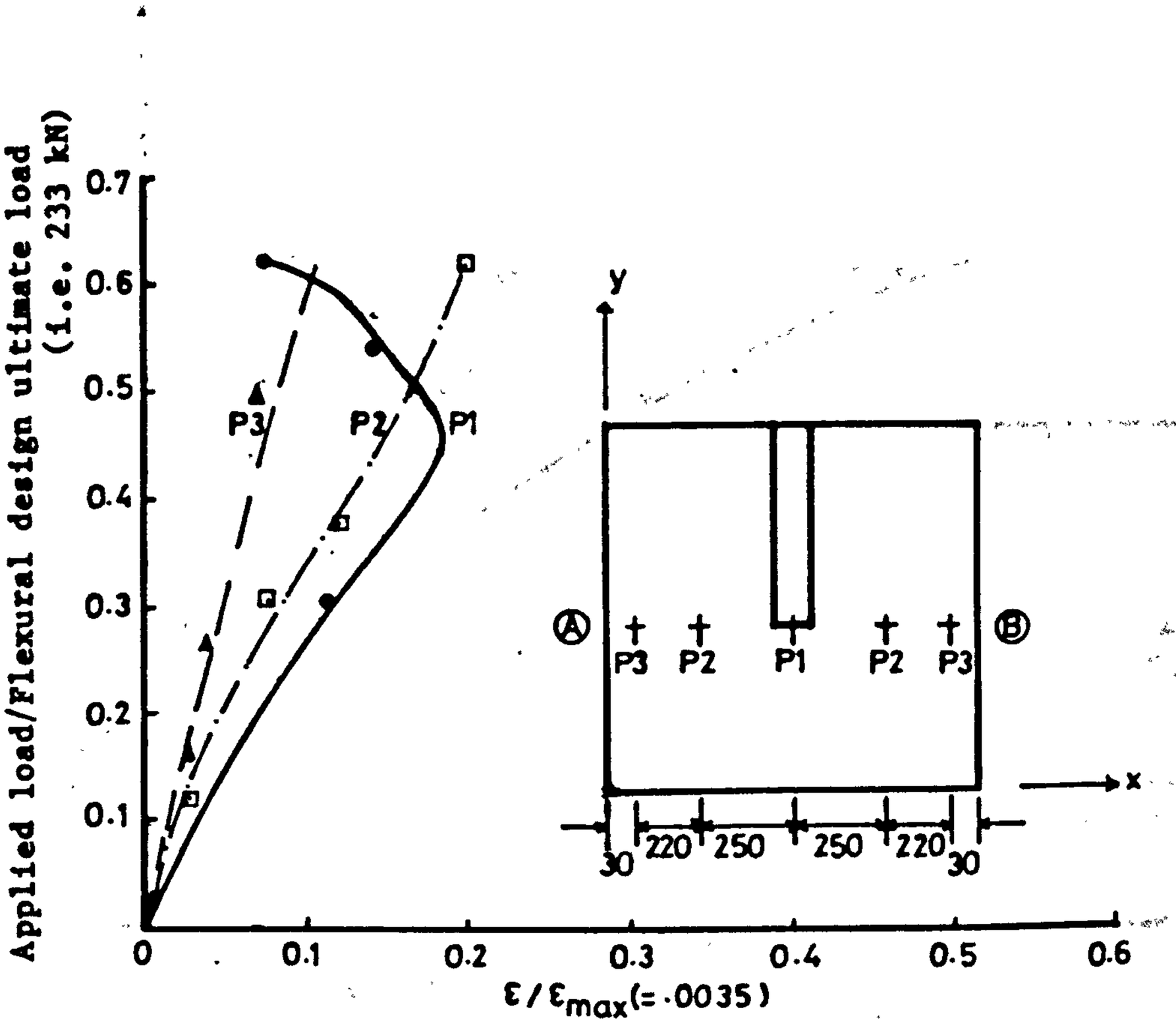

Figure (6.134) : Compressive strain in concrete at different points along transverse critical section AB in windward direction, in the slab of MT10.

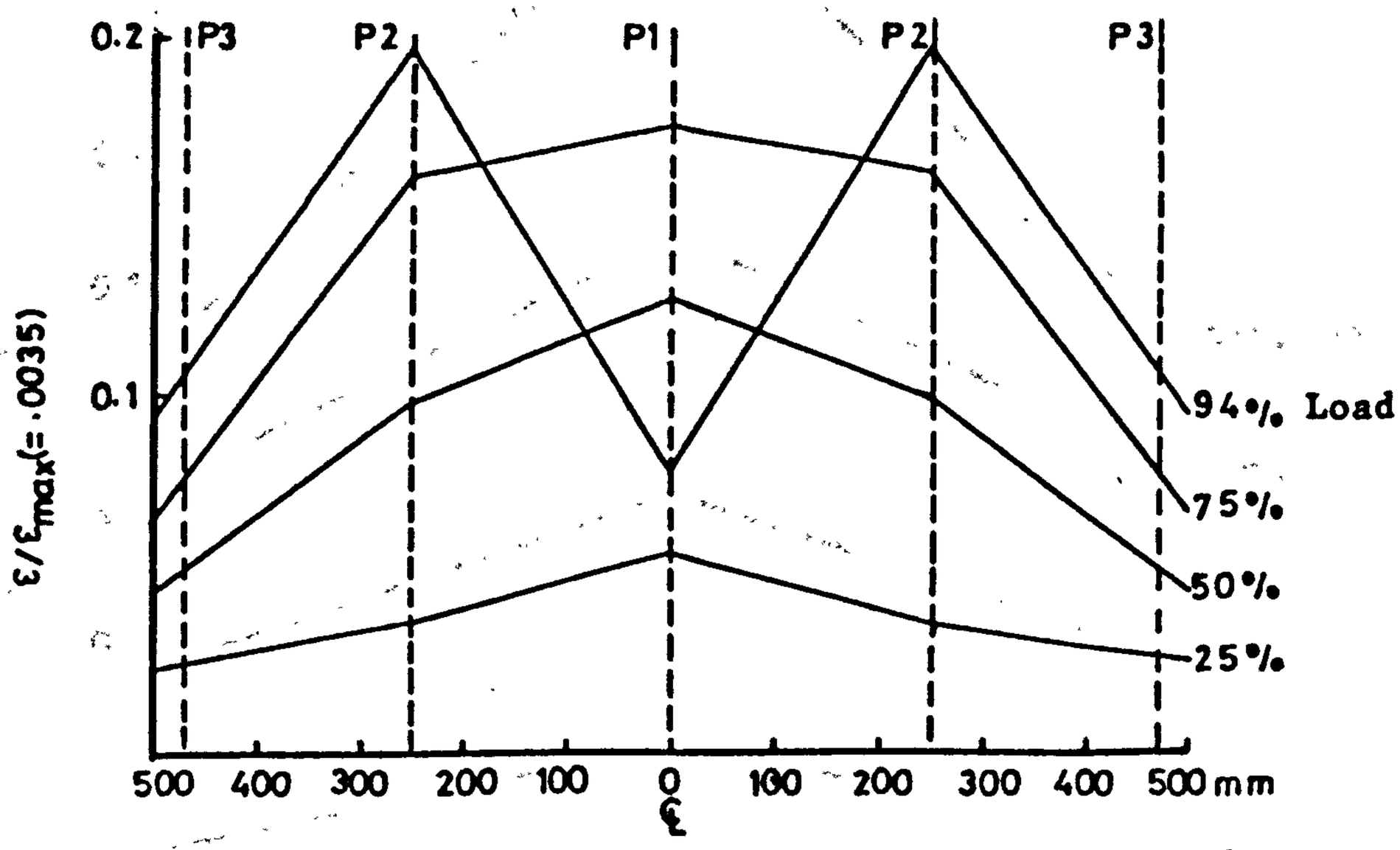

Figure (6.135) : Variation of compressive strain along transverse critical section at different stages of loading, in the slab of MT10.

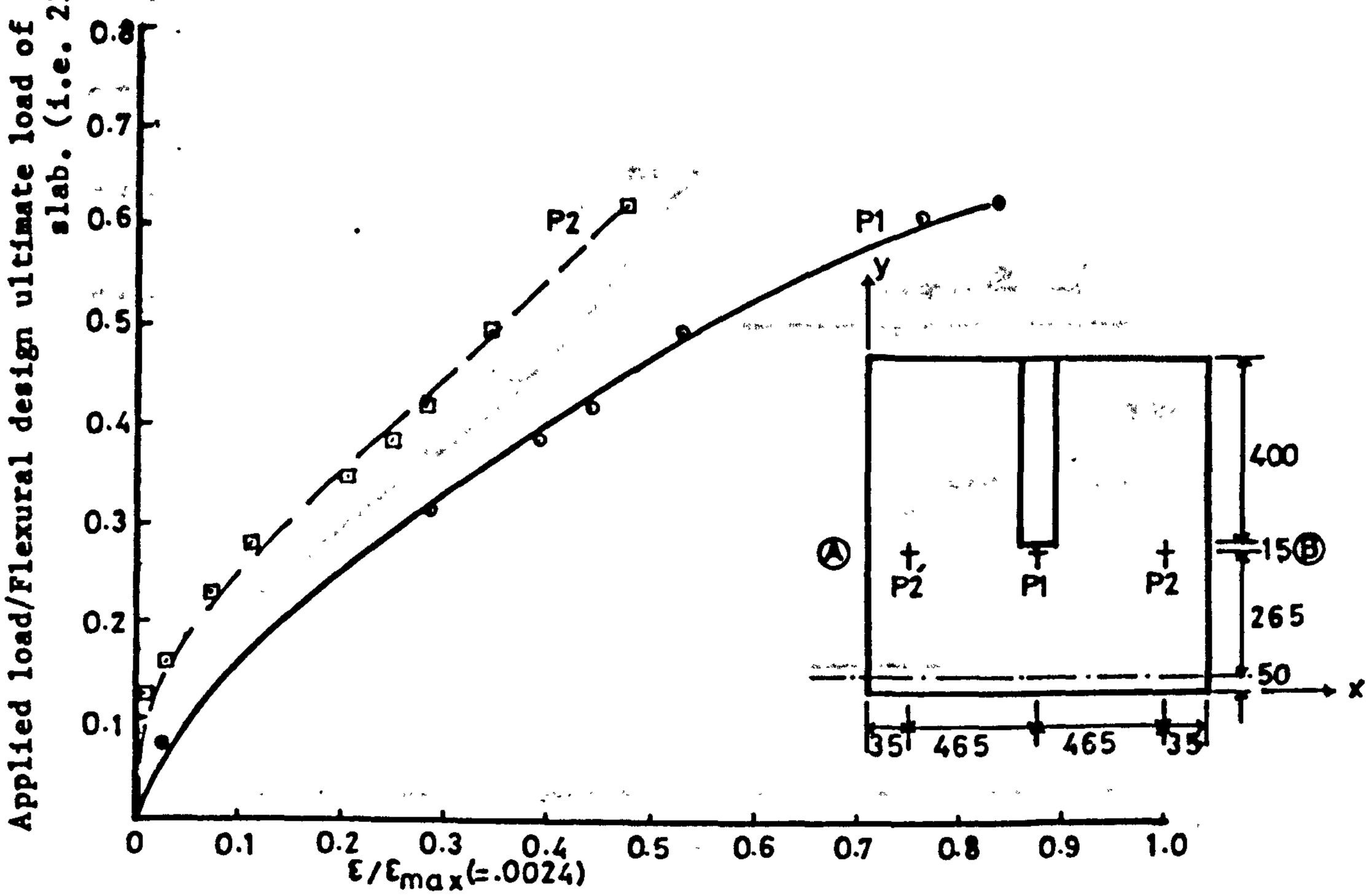

Figure (6.136) : Tensile strain in steel in windward direction at different points along transverse section AB, in the slab of MT10.

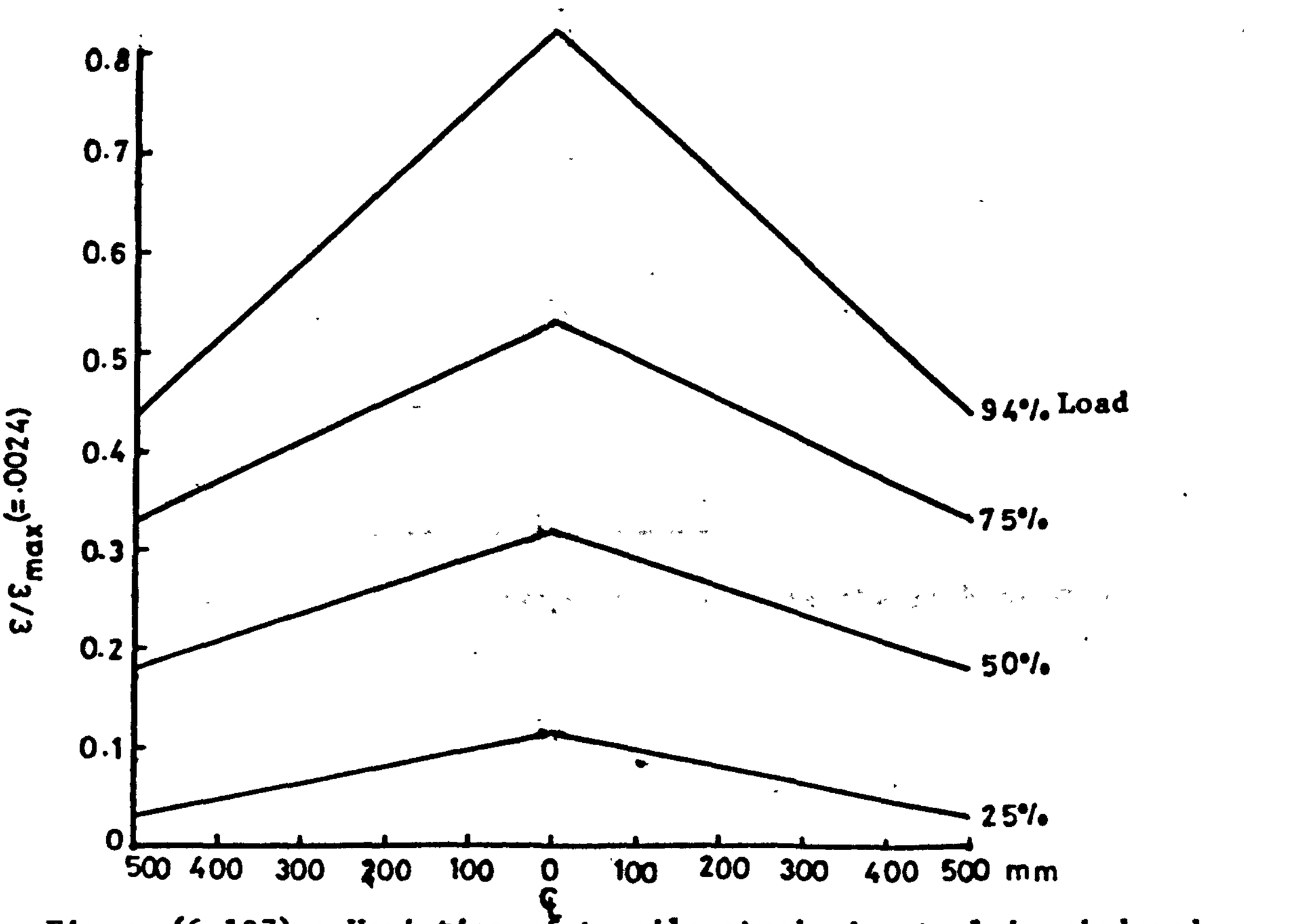

Figure (6.137) : Variation of tensile strain in steel in windward direction along the transverse critical section at different stages of loading, in the slab of MT10.

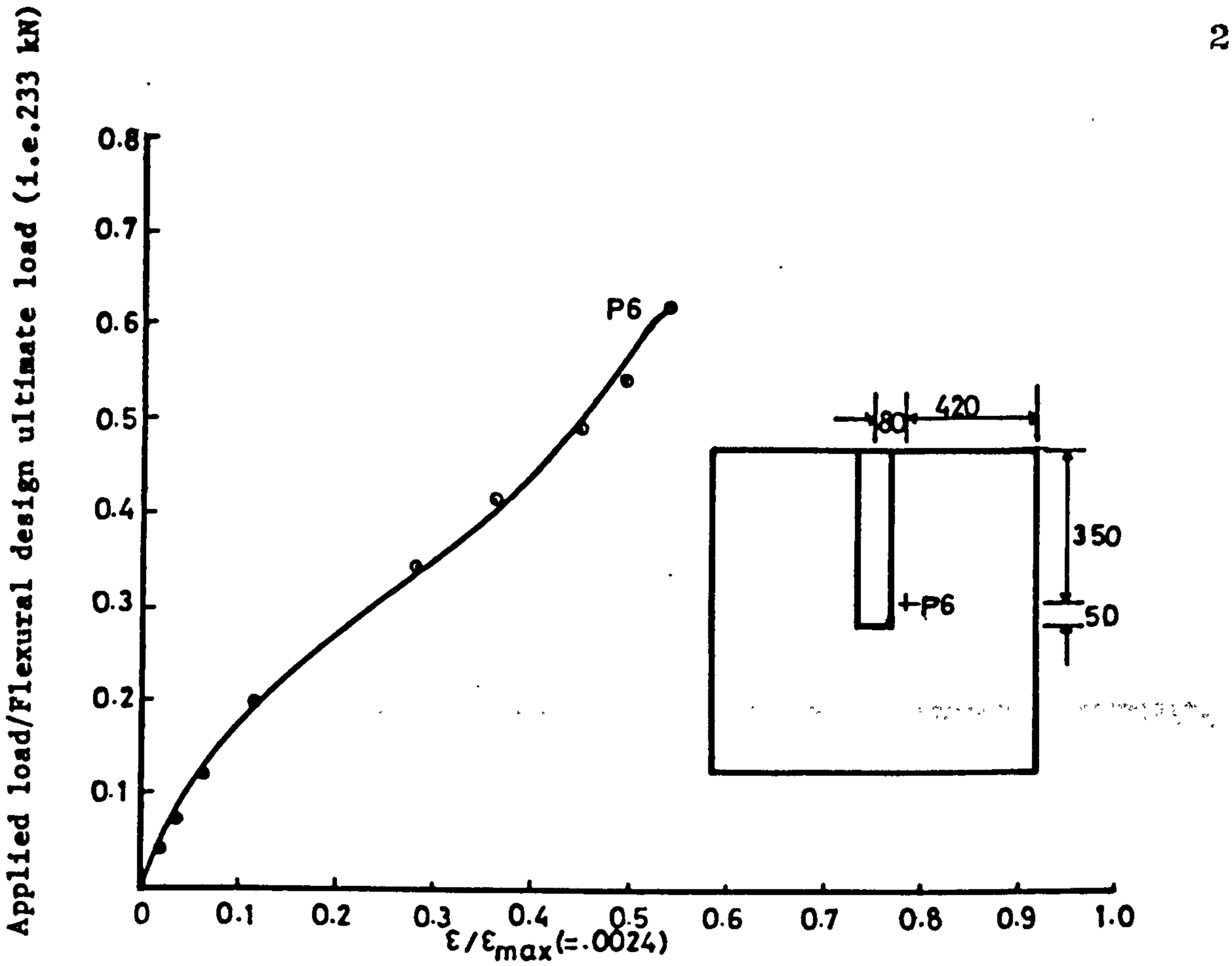

Figure (6.138) : Tensile strain in steel in transverse direction near the inner edge of wall, in the slab of model MT10.

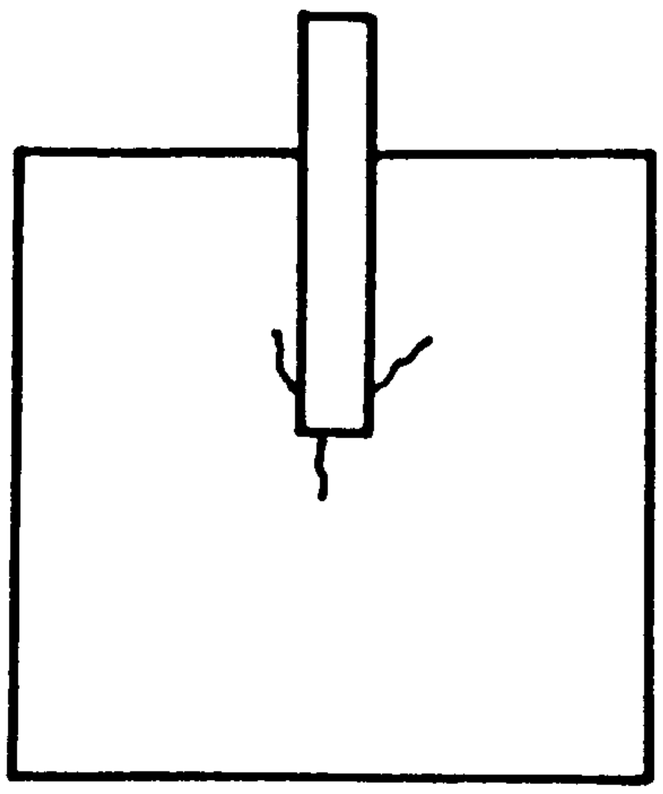

Figure (6.139) : Initiation of cracks in the slab of MT10.

Figure (6.140) : Crack pattern of the slab of MT10 after failure.

6.4.8.2 Model MT11

This model was also similar to model MT7 except the ratio of flexural reinforcement which was higher by 30% in corresponding strips of this model than that of MT7. The arrangement of reinforcement in the slab of this model is shown in Figure (6.141). Other experimental data is shown in Figures (6.142) to (6.147). The total gravity load applied to this model was 18 kN.

Behaviour of the model: In this model the first crack appeared perpendicular to the inner edge of the wall at a wind load of 18.5% of the ultimate load, in addition to gravity load. The first shear crack in the slab at the back of the model appeared at a load of approximately 45% of the load at failure for this model. The ultimate crack pattern was same as that of models MT7 and MT10. The failure took place when the gravity load was being readjusted to its desired value. The wind load at failure was 164.0 kN. Photographs showing the crack pattern of this model are presented in Figures (6.148) and (6.149). A sketch showing the shear cracks in the slab at the back of the model is shown in Figure (6.150). The wind load-displacement curves for models MT10, MT7 and MT11 are presented in Figure (6.151).

6.4.8.3 Comparison and discussion

Table 6.12 compares the experimental ultimate loads for the models of this group with the calculated ultimate loads. From this table it can be observed that ACI318 method seems generally more promising. The value of v_c as recommended by ACI318 is a function/

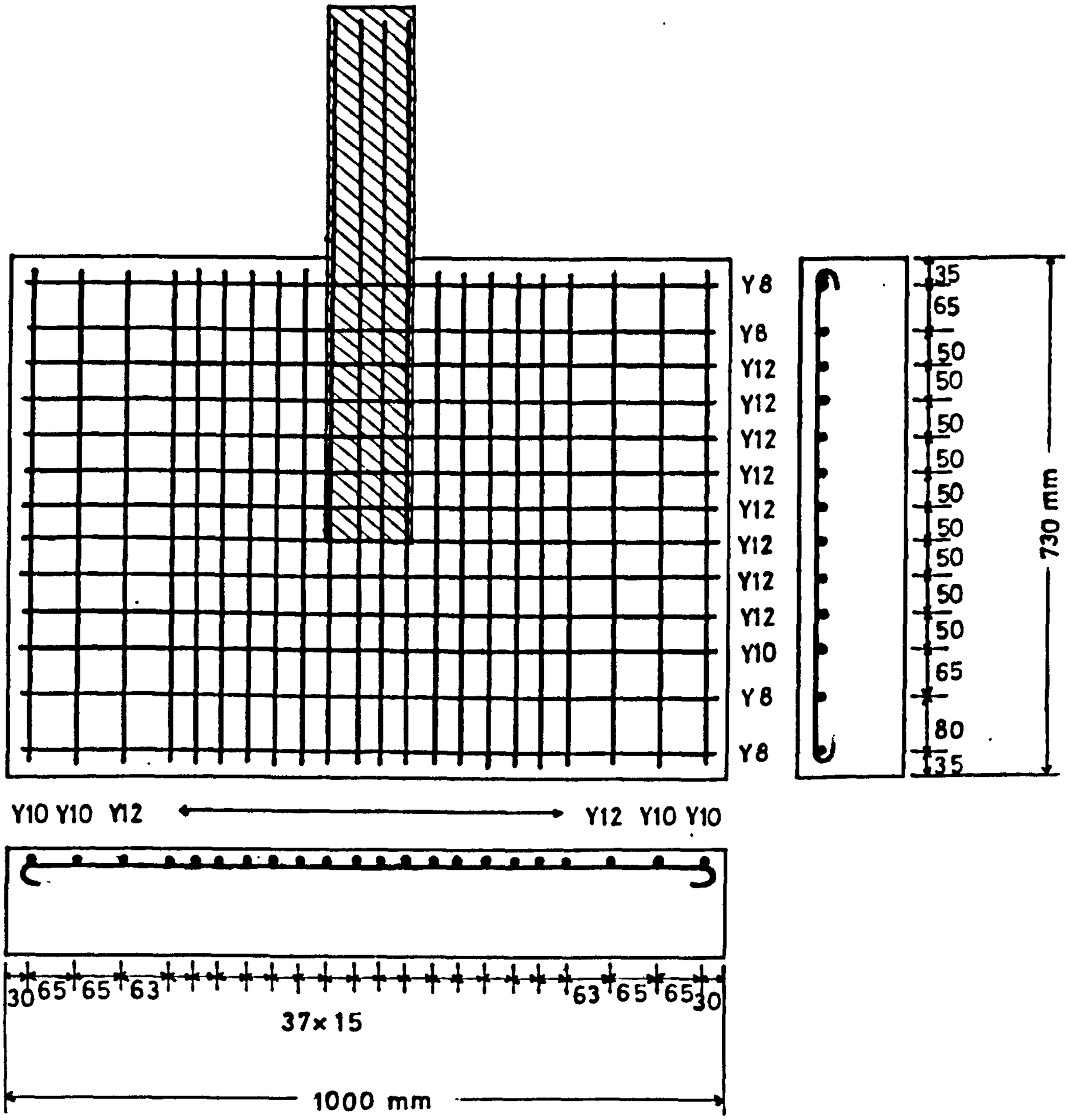

Figure (6.141) : Arrangement of reinforcing bars in the slab of the model MT11.

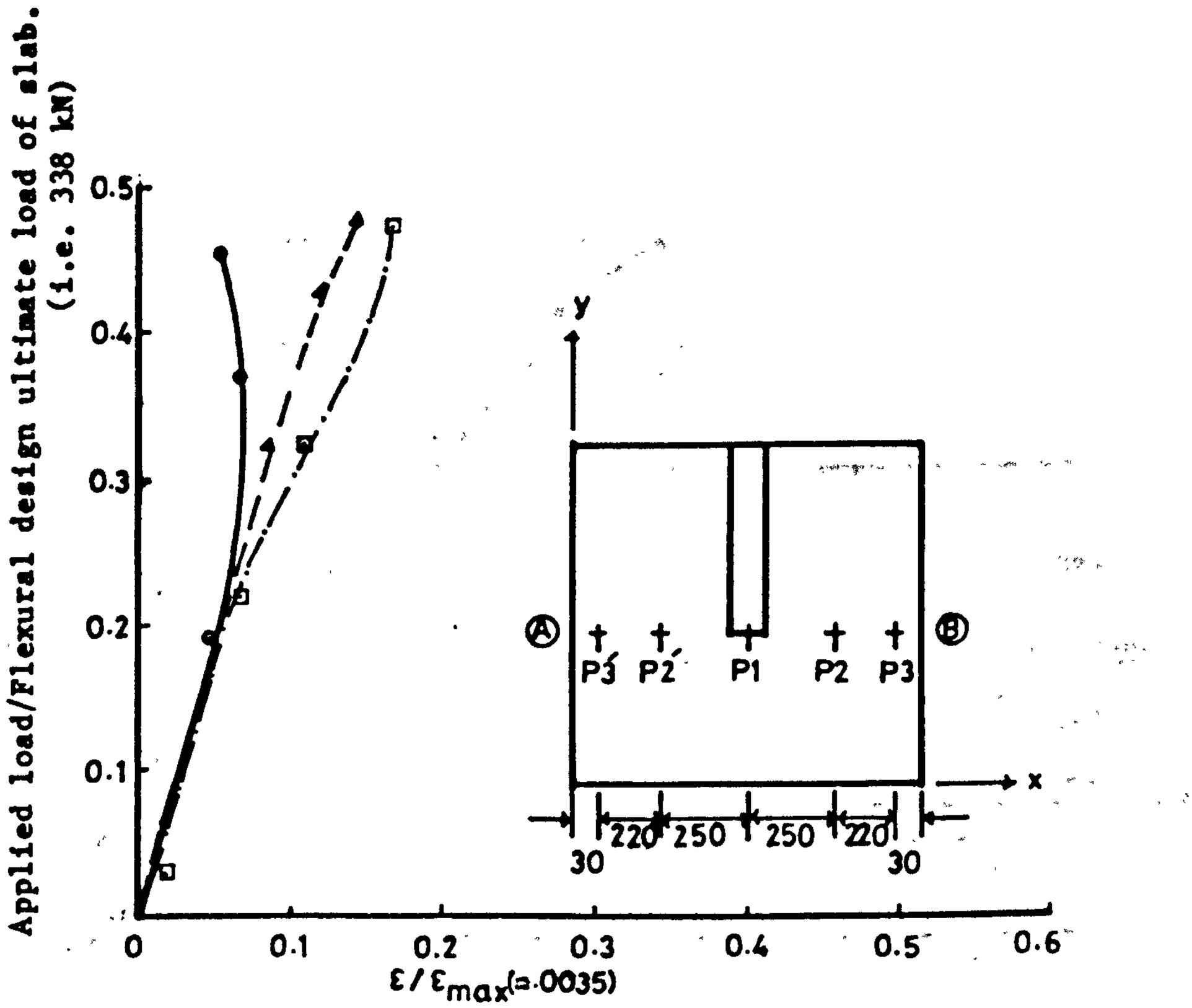

Figure (6.142) : Compressive strain in concrete at different points along transverse critical section AB in windward direction in the slab of model MT11.

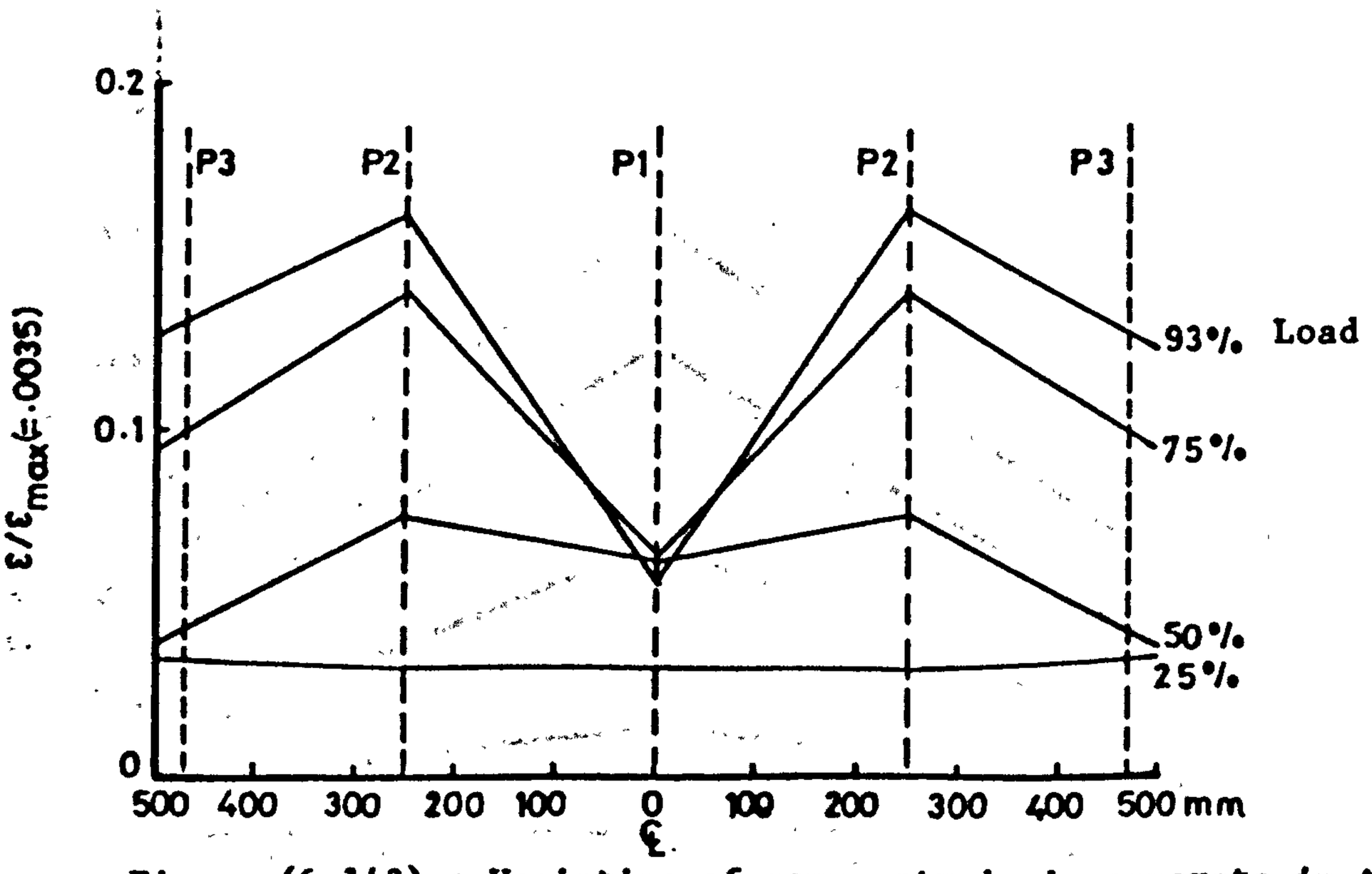

Figure (6.143) : Variation of comp. strain in concrete in the windward direction along transverse critical section in the slab of model MT11.

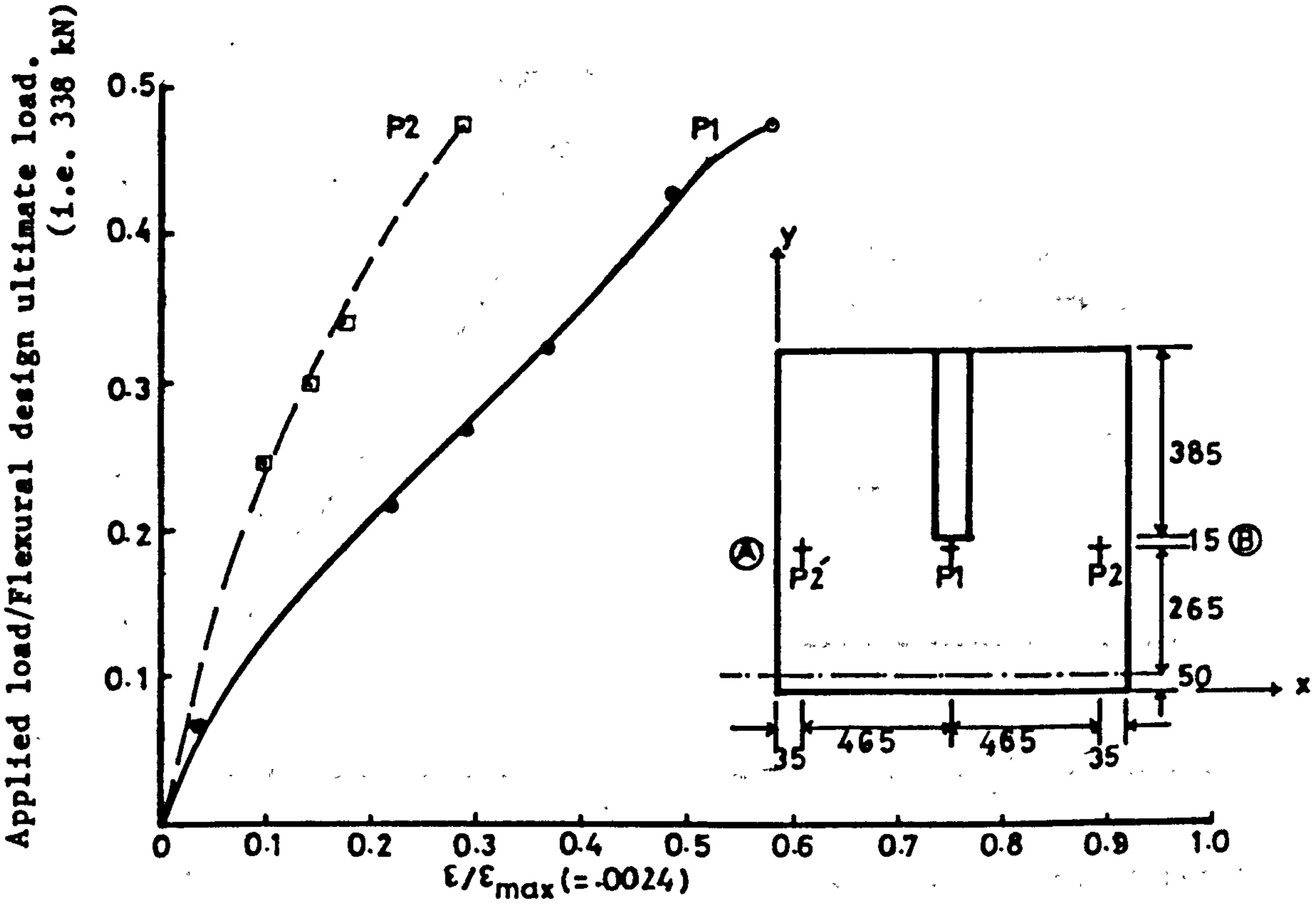

Figure (6.144) : Tensile strain in steel in windward direction at different points along section AB, in the slab of model MT11.

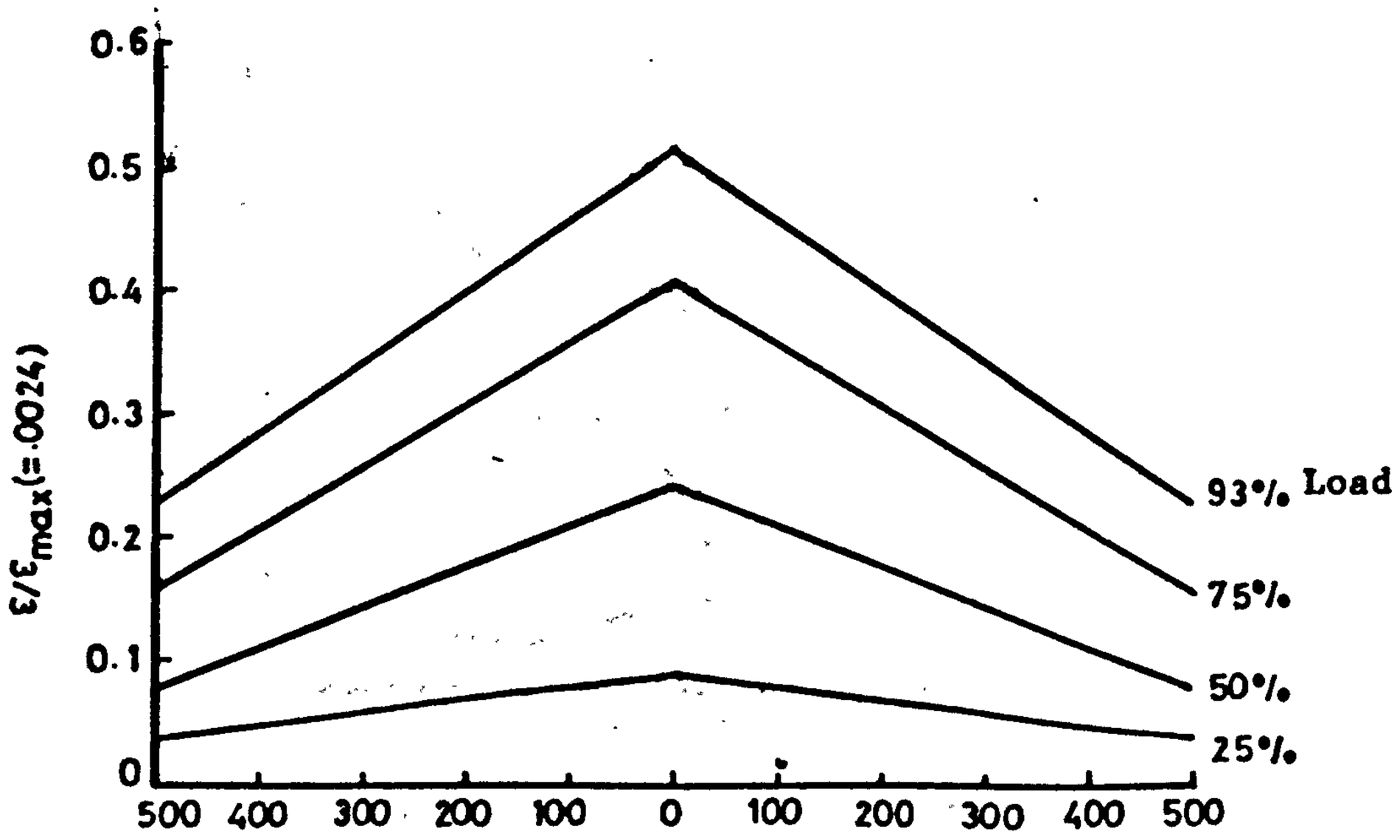

Figure (6.145) : Variation of strain in steel in windward direction along transverse critical section, in the slab of MT11.

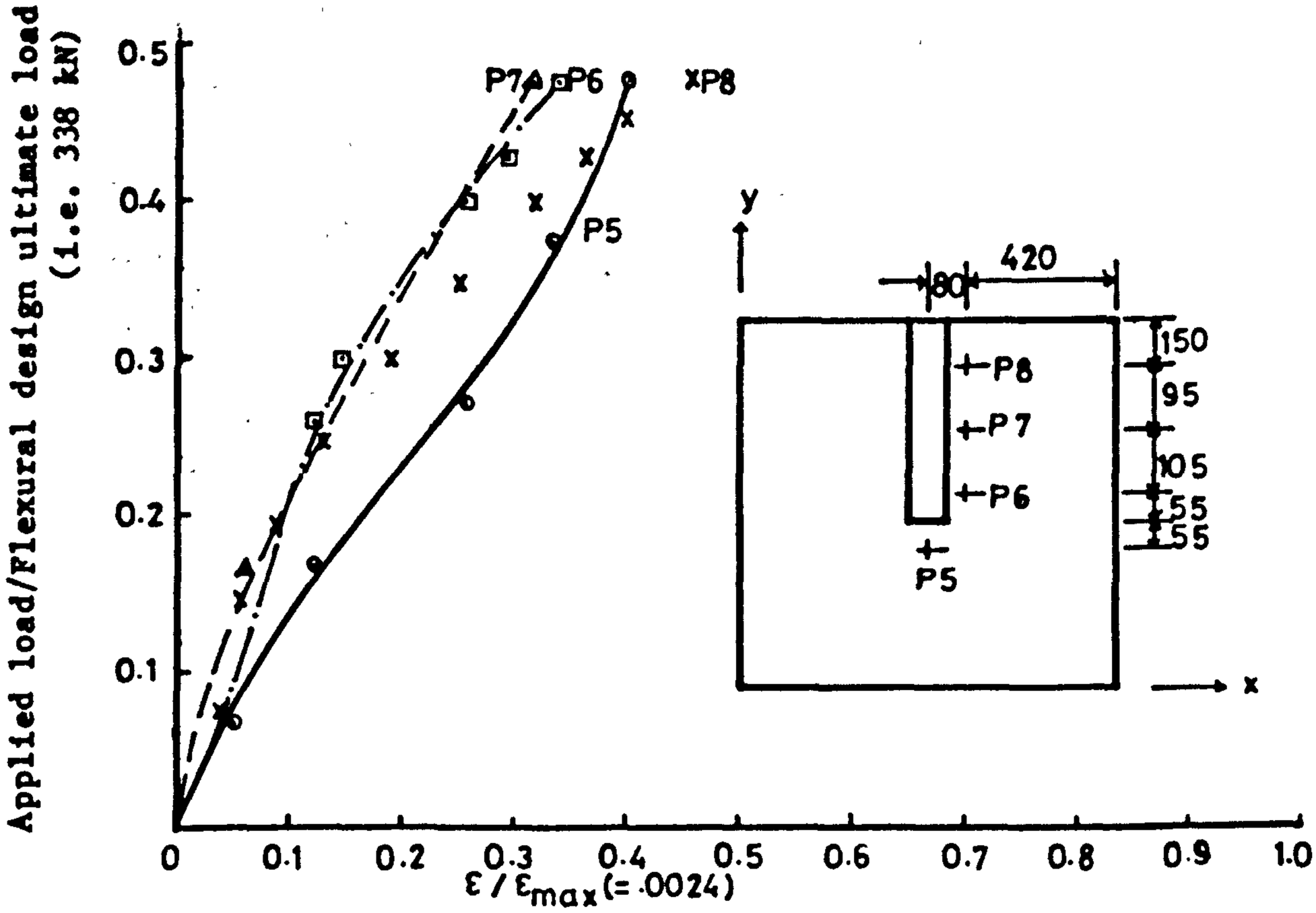

Figure (6.146) : Tensile strain in steel at different points in transverse direction along the sides of the wall, in the slab of MT11.

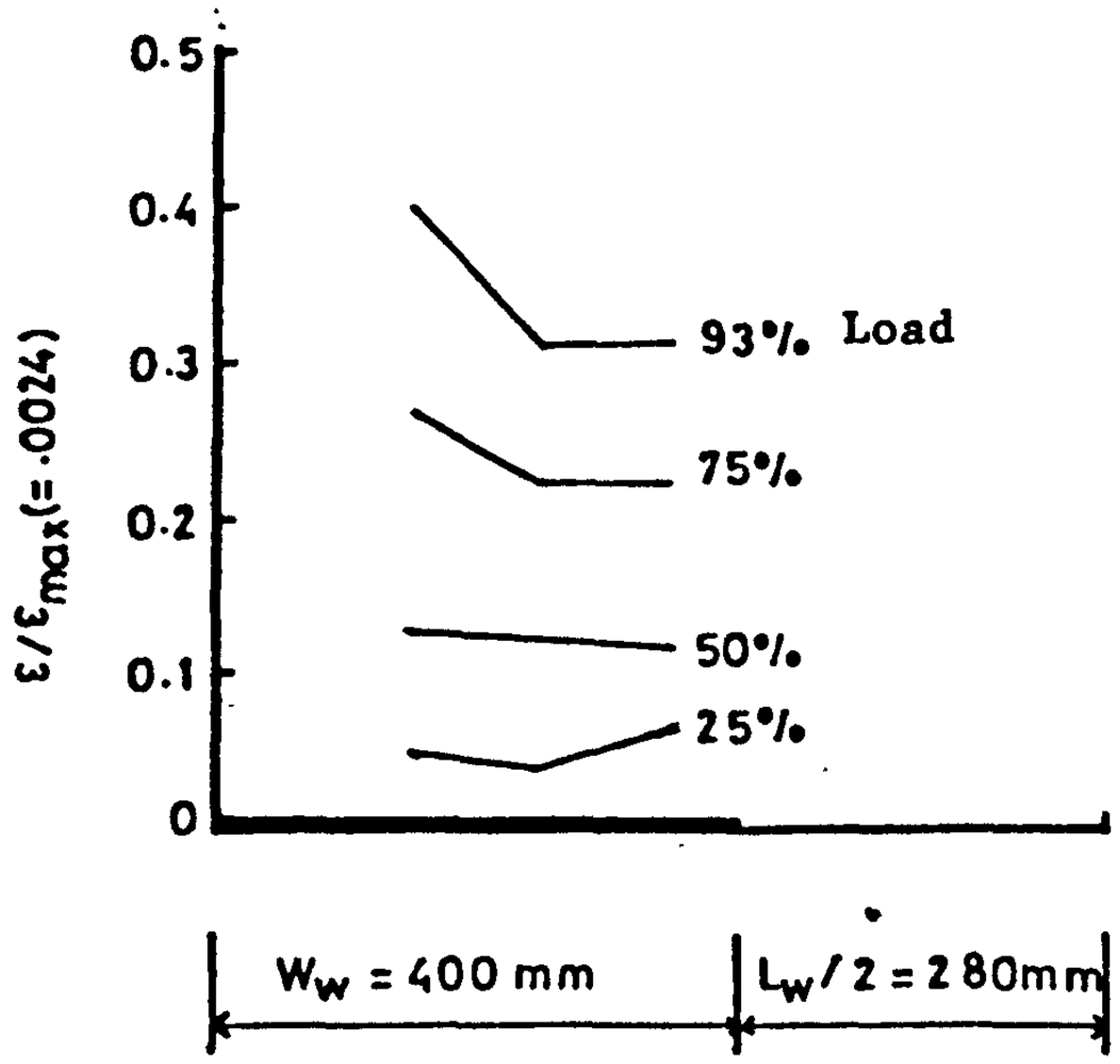

Figure (6.147) : Variation of the strain in steel in transverse direction along the side of the wall, at different stages of loading, in the slab of MT11.

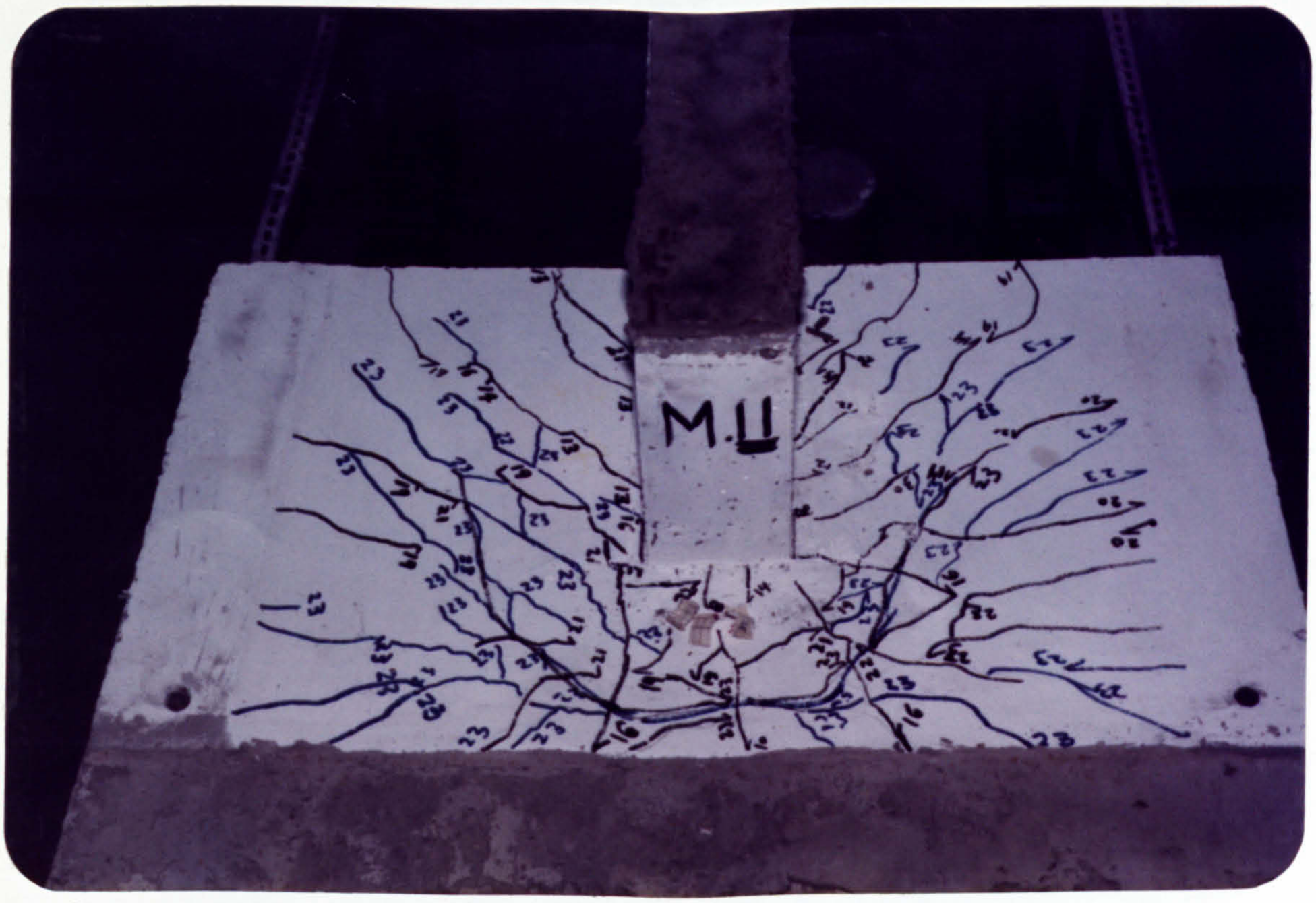

Figure (6.148) : Crack pattern after failure, of the slab of model MT11.

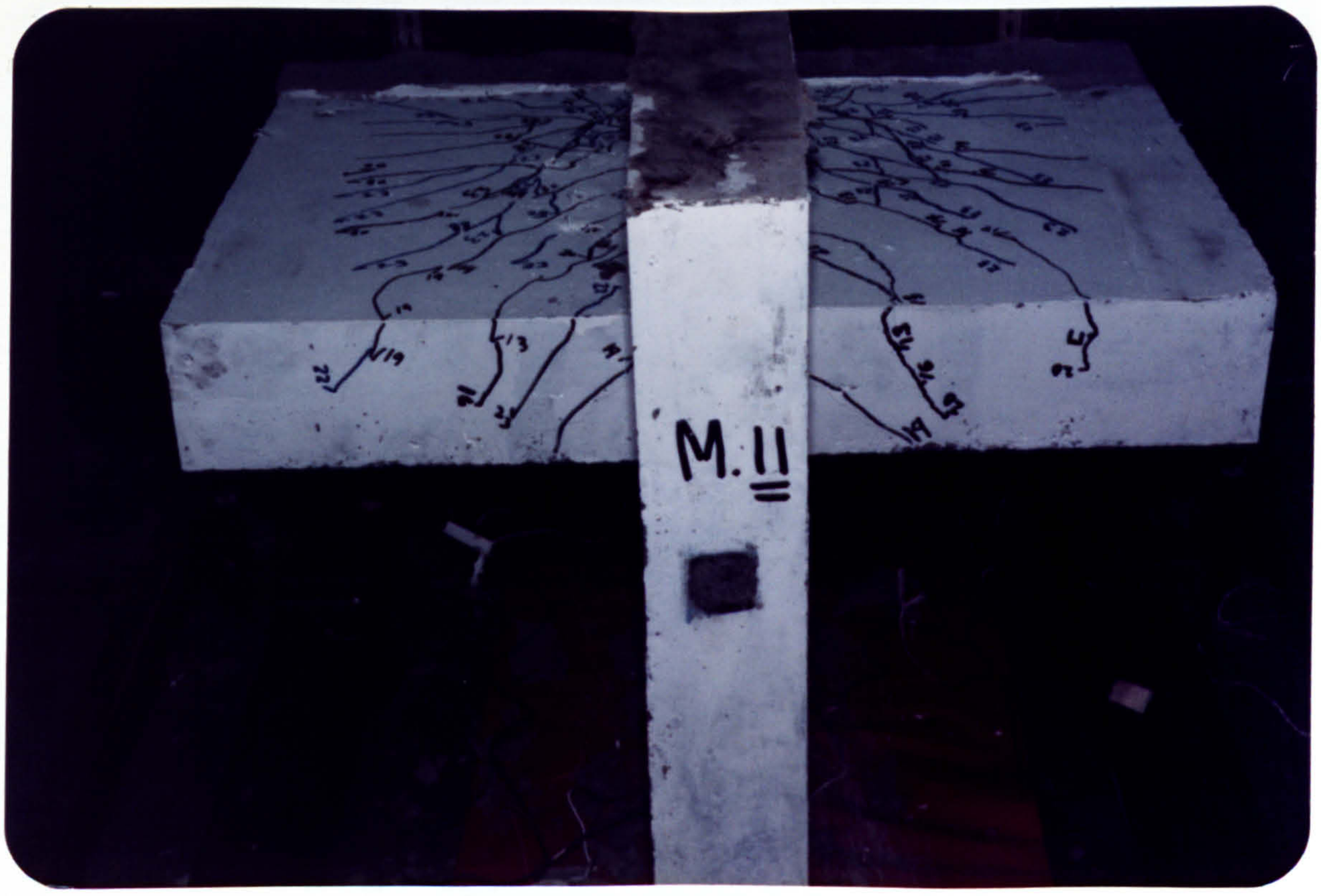

Figure (6.149) : Shear cracks in the slab at the back of model MT11.

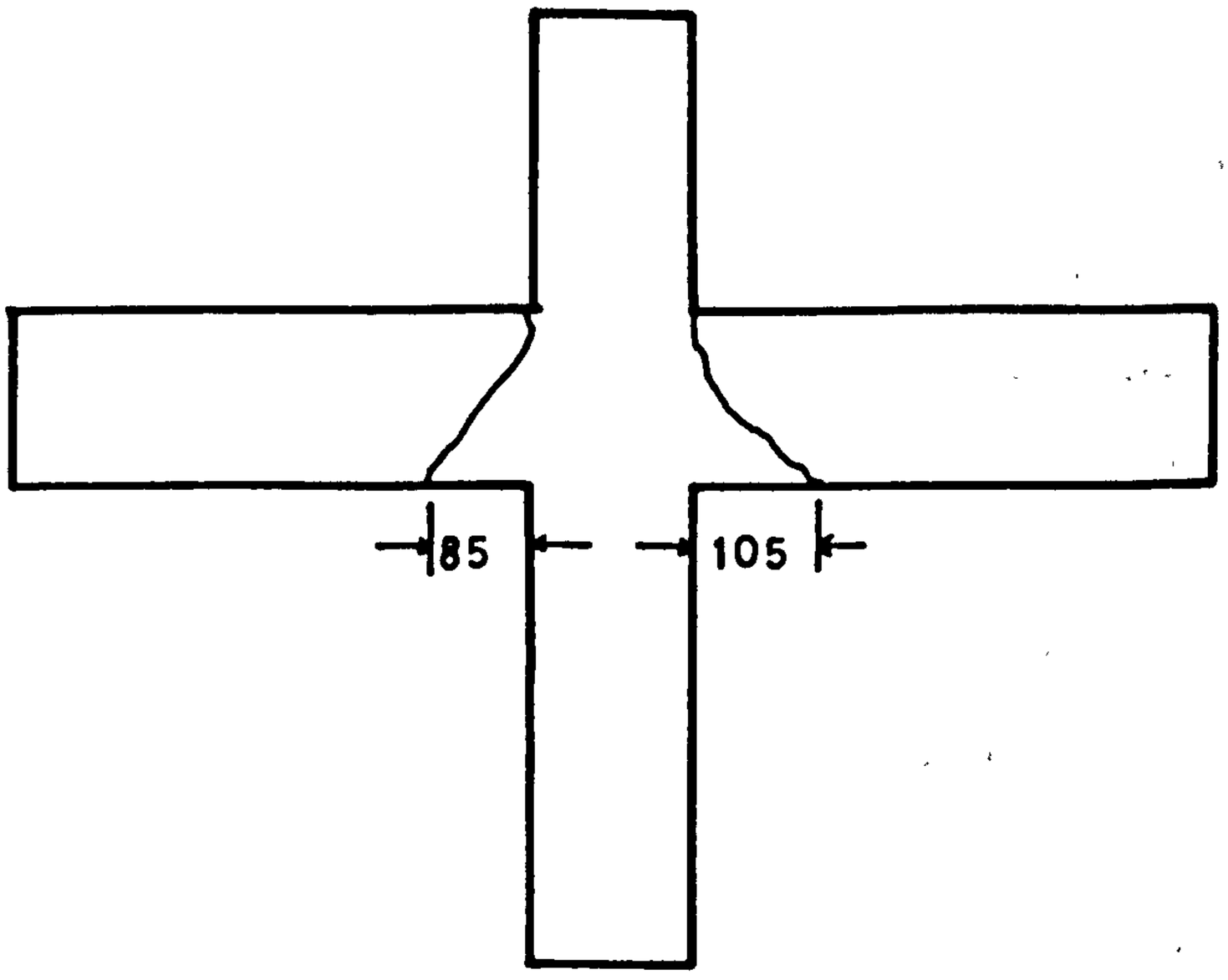

Figure (6.150) : Shear cracks in slab at the back of model MT11

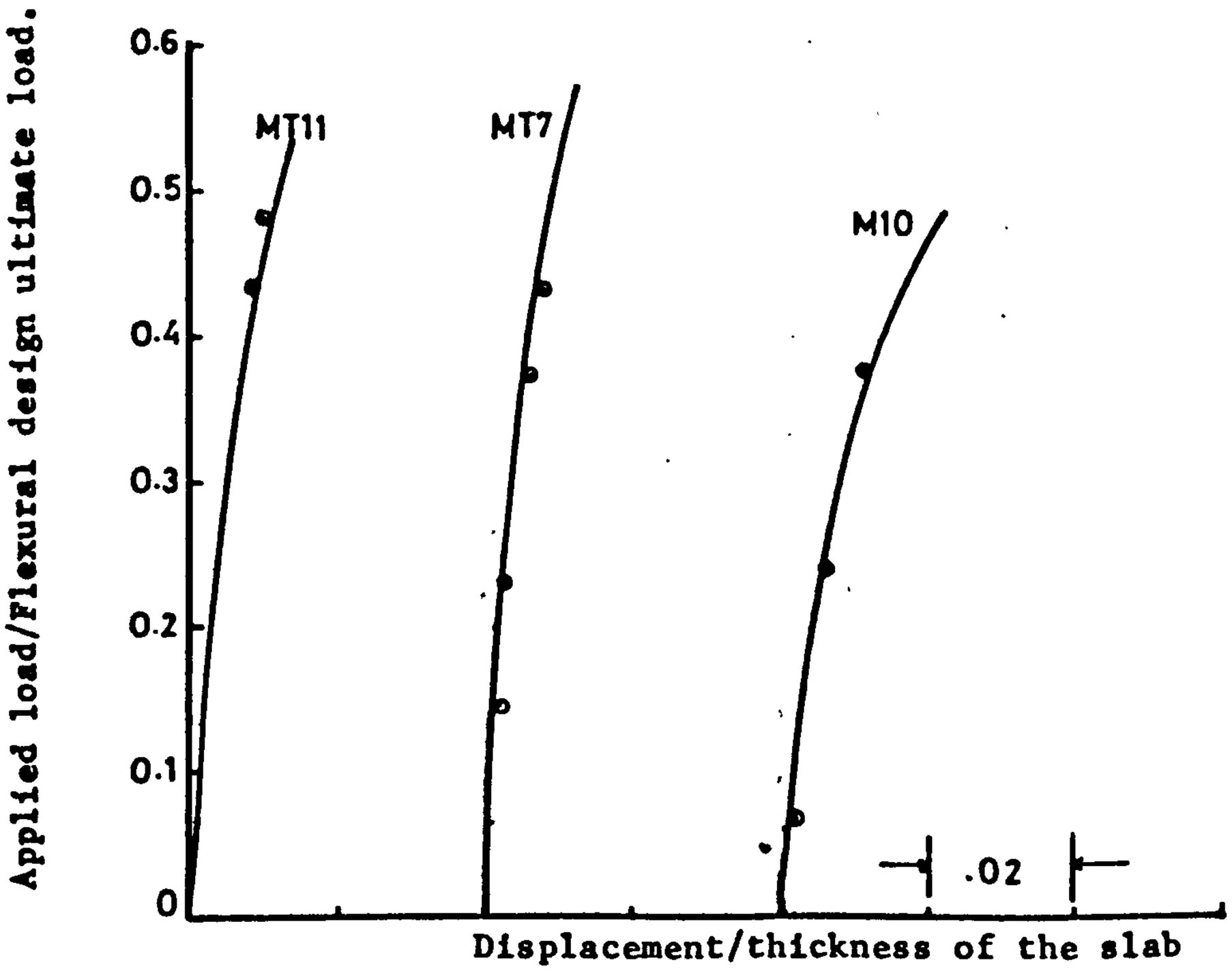

Figure (6.151) : Wind load-displacement relationship for models of VIth group.

of the compressive strength of concrete alone but is insensitive to the ratio of flexural steel. This shows some effect on the ratio $\frac{V_{exp}}{V_{cal}}$, which is highest for MT11 (with the highest ratio of steel) and lowest for MT10 (with lowest ratio of steel).

In previous sections the location of shear cracks in the slabs of all the models have been shown not only by photographs but complete with measurements with the help of sketches. Almost in all the cases these cracks started at the wall-slab junction the top of the slab and propagated diagonally away from the wall. The average distance of the tail from the wall for the models of PT series is 70 mm as compared to the effective depth of the slab i.e. 80 mm. For models of main test series this distance is 121 mm as compared to the effective depth of the slab i.e. 129 mm in this case. Thus it is not unreasonable to assume that the critical perimeter for shear is located at a distance of $\frac{d}{2}$ (where d is the effective depth) from the wall periphery as recommended by Schwaighofer & Collins (8) for shear wall-slab connections and by ACI 318 for slab-column connections.

Table 6.12. Comparison of calculated and experimental ultimate loads for models of VIth group of MT series.

Model No.	f_{cu} N/mm^2	Experimental load at failure V_{exp} kN	CP110 without transfer of moment $V_{cal\ 1}$ kN	CP110 with transfer of moment $V_{cal\ 2}$ kN	ACI method $V_{cal\ 3}$ kN	Chang method $V_{cal\ 4}$ kN	Schwaighofer & Collins $V_{cal\ 5}$ kN	Coull & Wong $V_{cal\ 6}$ kN
MT10	34.85	153.27	129.47 (1.18)	30.65 (5.0)	128.6 (1.19)	59.02 (2.6)	162.1 (0.95)	71.73 (2.14)
MT7	41.8	177.56	155.78 (1.14)	36.89 (4.81)	142.02 (1.25)	64.93 (2.73)	178.41 (1.0)	74.51 (2.38)
MT11	32.1	164.0	169.47 (0.97)	40.12 (4.09)	123.38 (1.33)	56.52 (2.9)	155.21 (1.06)	93.32 (1.76)

Note. The figures in brackets show the ratio $\frac{V_{exp}}{V_{cal.}}$

C H A P T E R S E V E N

THEORETICAL INVESTIGATIONS

7.1 GENERAL

7.1.1 Purpose of theoretical study

This theoretical study was carried out by using nonlinear finite element plate bending programme described in chapter three. The object of theoretical analysis was.

(i) To obtain (theoretical confirmation) the nonlinear flexural behaviour of the models tested as a check on the validity of the direct design method.

(ii) To obtain a better understanding of stress redistribution which might take place at the ultimate limit state.

(iii) To check the validity of assumptions made in simple 'models' to predict failure loads.

(iv) To check the theoretically predicted state of direct stress in concrete in the compression zone along the critical section and the shear transferred through it at experimental load at failure. This should hopefully assist in developing a failure criteria for shears which can be adopted while using two dimensional nonlinear programme.

7.1.2 Procedure adopted for analysis

The mesh and boundary conditions used for this analysis are shown in Figure (7.1). The reasons for selecting this particular size of mesh were already discussed in detail in chapter three. Since all the edges of the actual models were free, bonndary conditions for the analysis also/

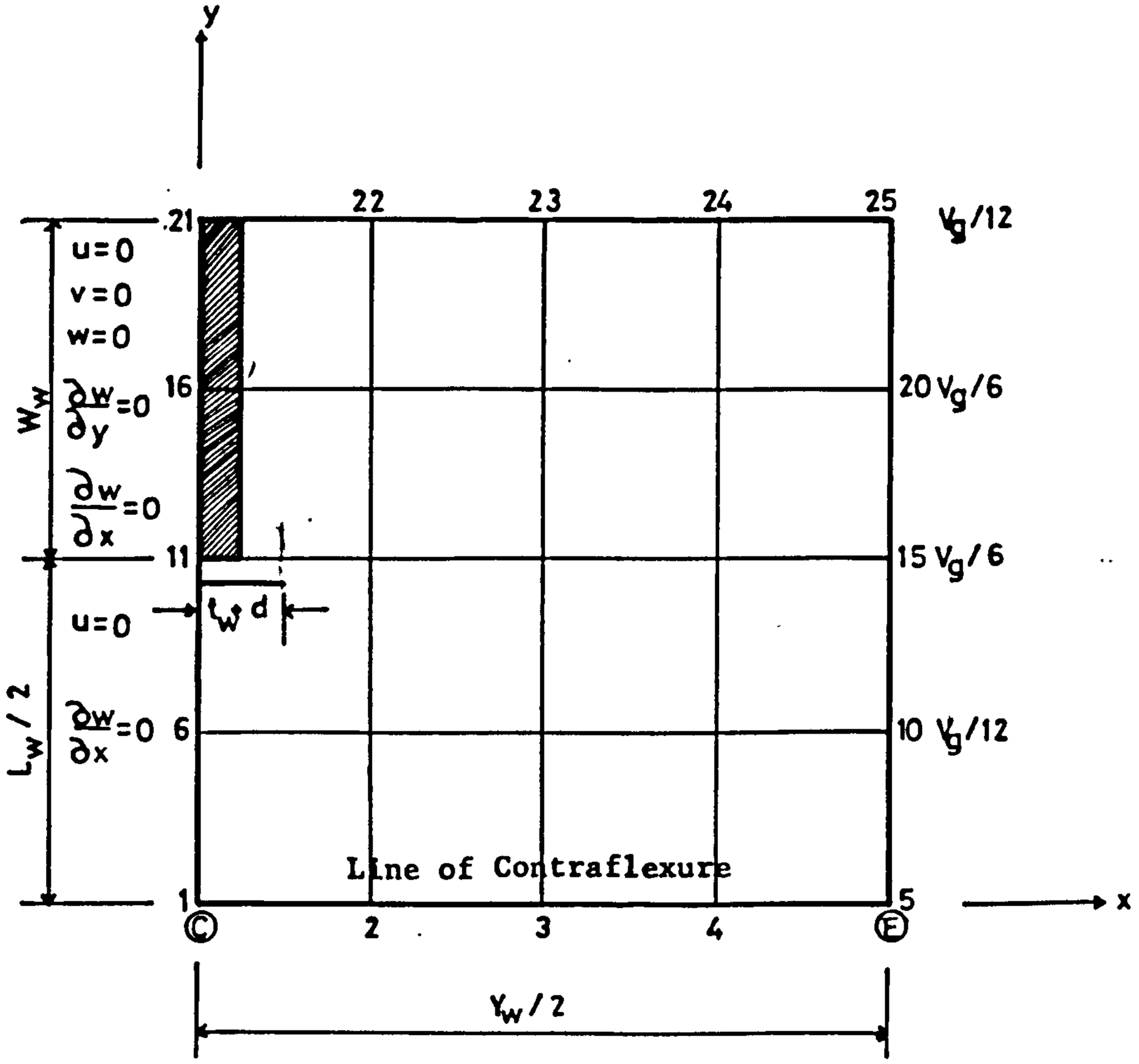

Figure(7.1): Typical mesh with boundary conditions used for nonlinear analysis.

reflect the same feature. As discussed in chapter three, a size of load increment of .25 P_{cr} (where P_{cr} is the cracking load) was adopted and a limit of 15 was imposed on maximum number of iterations. The material properties were those actually measured in the laboratory for each model.

During experiments all the loads were load controlled. The gravity load was applied by means of two side beams, while the wind load was applied through a beam such that the displacement along the line of contraflexure was uniform but the total wind load was load controlled. In the analysis to simulate constant displacement of the line of contraflexure we have to increment displacements for wind loading such that a reasonably small increment of wind load would be obtained. However in the nonlinear range it is almost impossible to predict the wind load for a certain displacement. The problem was further complicated by the fact that both gravity and wind loads had to be applied to the model. Therefore the following scheme of simulating the wind loads was adopted.

In the first instance elastic distribution of the corresponding wind loads along the line of contraflexure, required for the prescribed uniform displacement of .05 mm simulating wind load, was obtained. In the programme to introduce the prescribed displacement at any node, corresponding diagonal term of the stiffness matrix was multiplied by a large number (1×10^4) and the corresponding force was at the same time replaced by this newly formed diagonal term multiplied by the prescribed displacement (i.e. stiff spring approach). In the nonlinear analysis it was assumed that the distribution of the total wind load along the line of contraflexure remained the same as at the elastic /

range. The wind load was thus load controlled as was the gravity load.

Loads V_g (as shown in Figure (7.1)) simulating gravity loads were also applied to the models of main test series. During experimental work all the gravity load was applied during first five load increments. Nonlinear finite element analysis requires that the load be applied in small increments. However to duplicate the experimental condition during analysis, all the gravity load was applied in the first five increments. This greatly affected the theoretical response of models of second group (with the intensity of gravity load as main parameter). This point is discussed later in this chapter. For the sake of convenience, the thickness of the wall was assumed to be zero. However the effect of actual wall thickness was investigated by analysing the model PT2, both with and without wall thickness taken into account. This effect is also discussed in detail later in this chapter. Generally it was observed that slightly better predictions in terms of flexural ultimate load could be obtained from the analysis if the thickness of wall was taken into account. The analysis with zero wall thickness shows somewhat higher torsion along the sides of the wall. However the results are generally satisfactory even when the thickness of wall is taken as zero.

From among the models of preliminary test series only model PT2 was analysed. Distribution of shear along the line of contraflexure corresponding to the uniform displacement of .05 mm for this model is shown in Figure (7.2). This model was tested for wind load alone. It was observed that the displacement of the edge representing line /

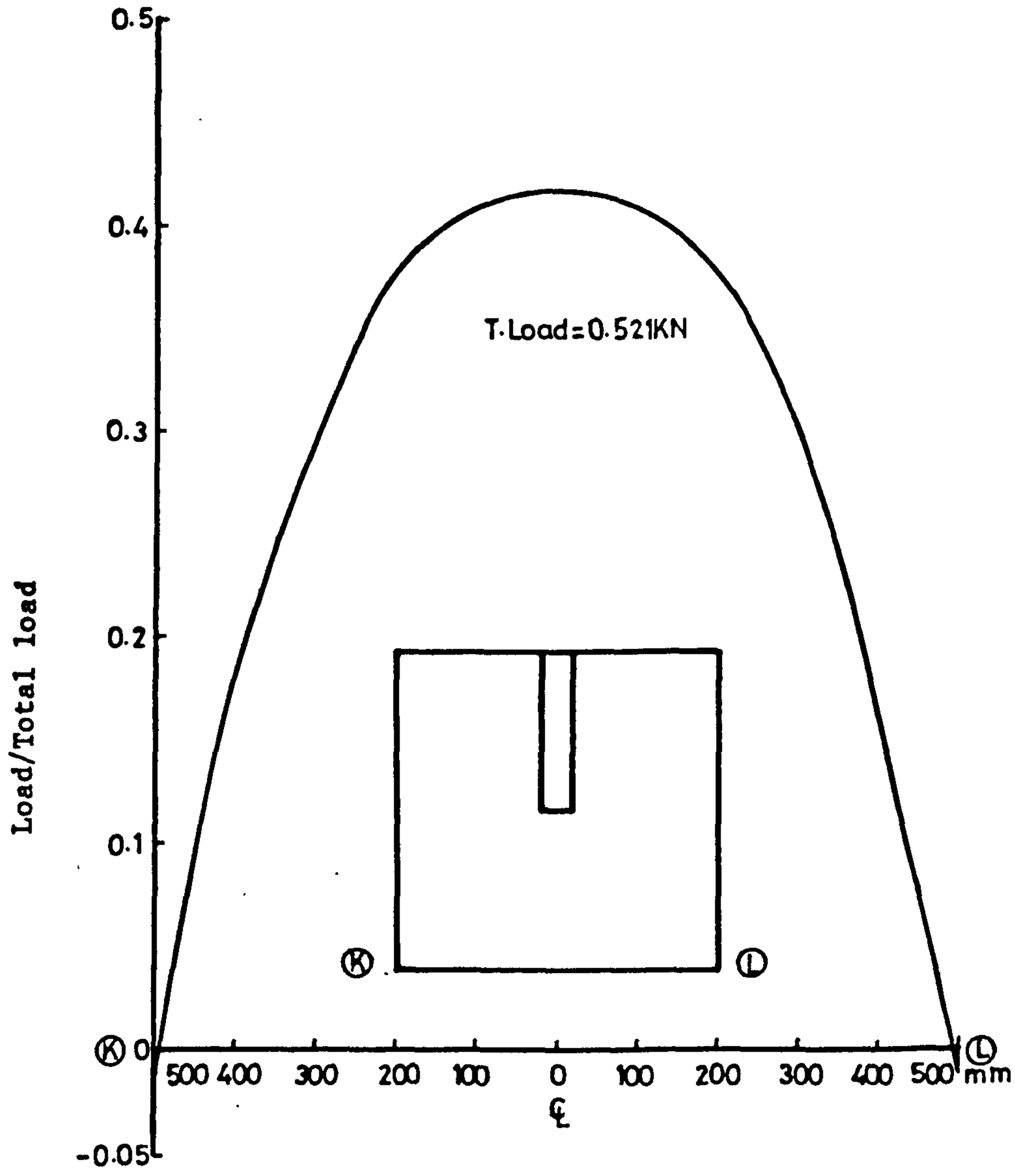

Figure (7.2) showing the nodal forces required to displace uniformly the line of contraflexure KL by ·0.5 mm for the model PT2.

of contraflexure remained uniform for this model up to failure. The elastic distribution of shear along line of contraflexure for different models of main test series is shown in Figure (7.3) to Figure (7.5). It is clear from Figure (7.4) that as the corridor opening width is increased, the curve showing distribution of shear due to wind loads along the line of contraflexure becomes less peaky.

For all the models of main test series, the thickness of steel layer assumed for each element in the x as well as y-direction, depended upon the steel ratio in the corresponding regions of the actual models.

During experimental work it was observed that due to presence of gravity loads the displacement of the line of contraflexure (central line of corridor opening) did not remain uniform. However the difference was not too large even for MT5 for which the intensity of the gravity load was the highest. For this model the displacement at corner point E (Figure (7.1)) was approximately 1.09 times that at central point C. The numerical calculations also exhibited the same behaviour of the slab for all the models of main test series except for models MT4 and MT5. For models MT4 and MT5 the displacement at edge E was 1.4 and 1.67 times that at central point C respectively when the theoretical wind load was equal to the experimental wind load.

7.2 SINGULARITY OF STRESSES

Very large stresses are predicted by finite element method at a point where there is an abrupt change of boundary conditions. This concentration of stresses at a single point is called 'Singularity of stresses'. The problem of singularity of stresses in slabs connecting/

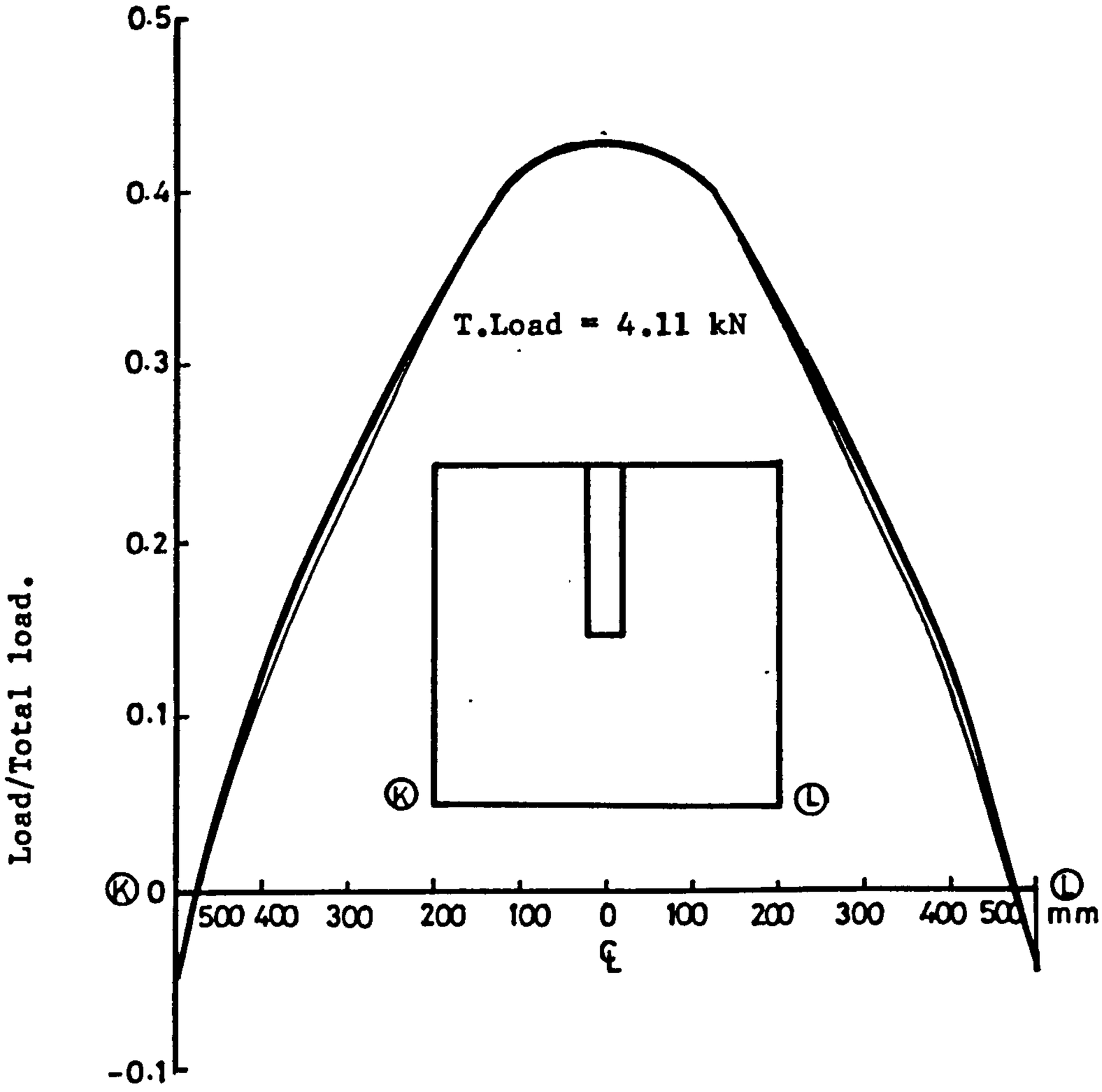

Figure (7.3) showing equivalent nodal forces required to displace the line of contraflexure kL, uniformly, by.0.5 mm, for model MT1, MT2 and MT3.

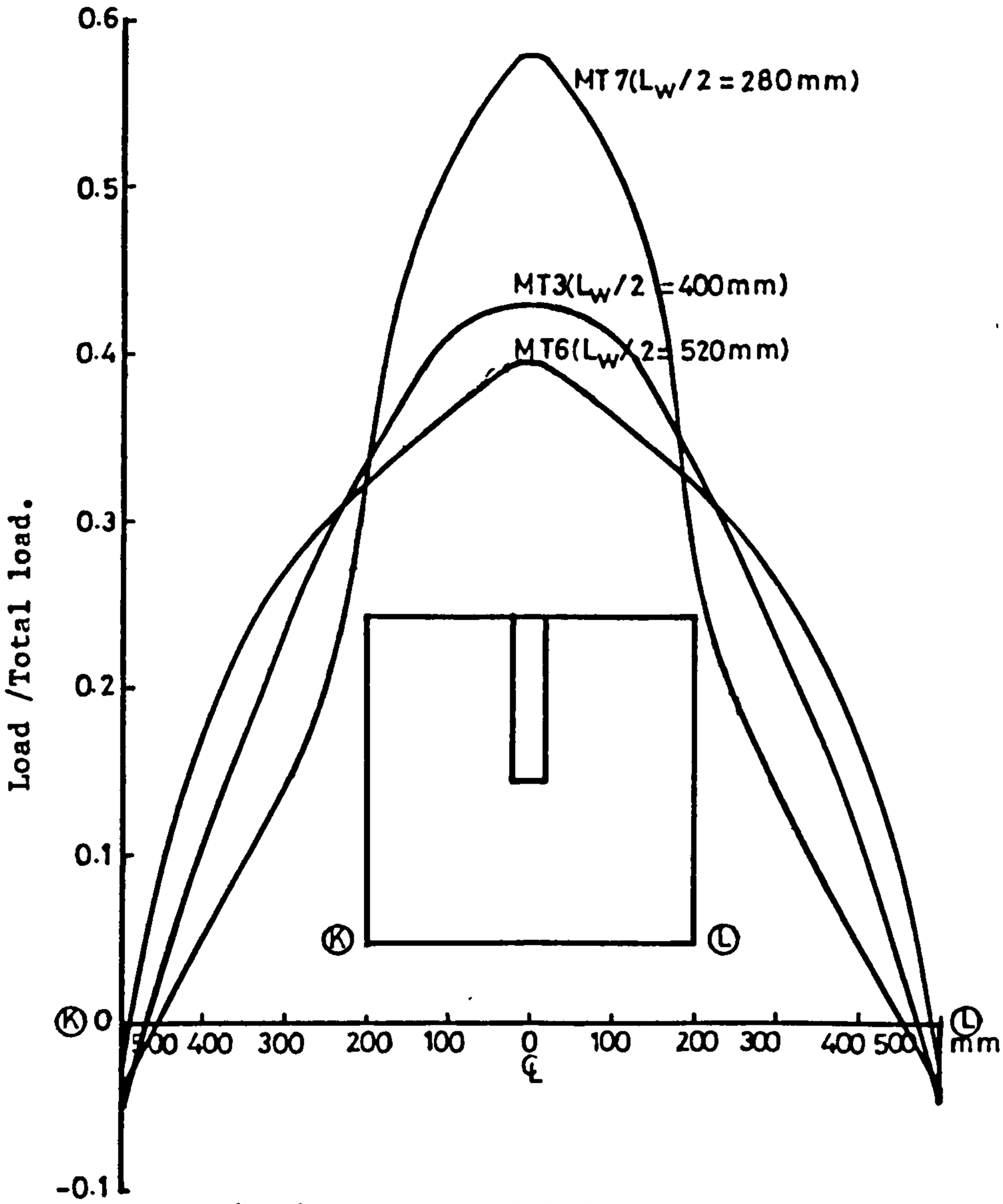

Figure (7.4) showing nodal forces required to displace uniformly the line of contraflexure kL, corresponding to a total applied wind load of 4.11 kN, for models MT6, MT3 and MT7.

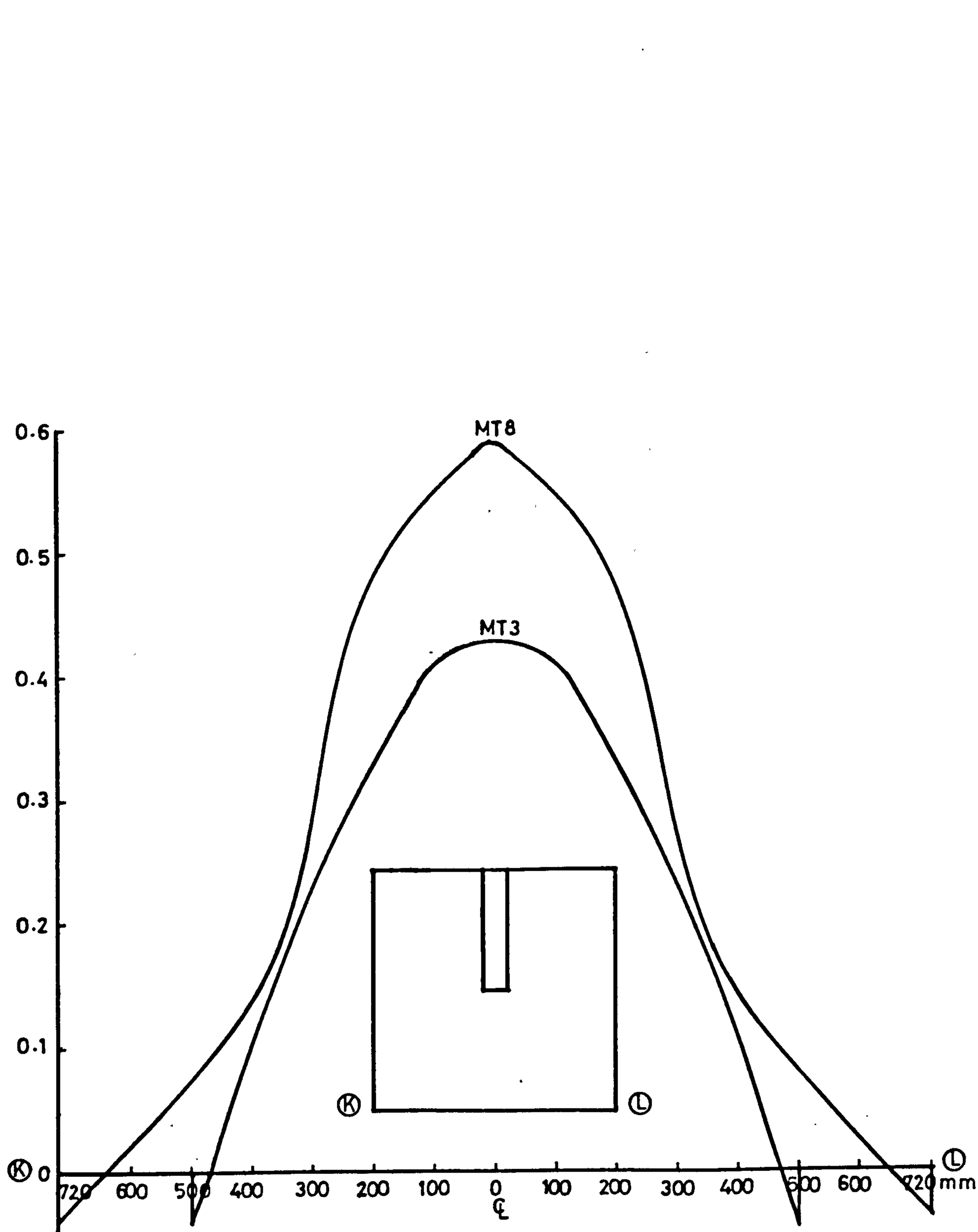

Figure (7.5) showing equivalent nodal forces required to displace the line of contraflexure kL, uniformly, corresponding to a total applied wind load of 4.11 kN, for models MT3 and MT8.

shear walls was recognised by Coull & Wong (10). From the convergence study using mesh refinement they showed that when the thickness of wall is taken zero, except at the tip of the wall, the moments in the windward direction (M_y) along a critical transverse section passing through the inner edge of wall converge to definite values. However the bending moment calculated at the tip of the wall diverges with the mesh refinement. Thus unlike common problems for which the results converge to true solution with the refinement of mesh, here the use of fine mesh results in serious over-estimation of the stresses at the tip of the wall. In other words the theoretical stresses at the tip of the wall cannot be relied upon. It will be shown in the following sections that the mesh size used for this investigation (i.e. 4 x 4 elements) predicts reasonably correct stresses and displacements at all points except at the corners.

Similar results are obtained even when the wall thickness is included in the analysis.

The stress singularity predicted in the slab is due to the use of thin plate theory and boundary conditions associated with an infinitely rigid wall support. The infinitely large stresses predicted will in reality be limited by local elastic deformation, material yielding or stress distribution in the critically stressed areas in the wall and slab. It is therefore more practical to consider the net distributed forces in a small slab strip, rather than the extremely large stresses at a point, as a basis for the design of the slab section. To make the results more meaningful, Coull& Wong (10) have proposed that the calculated peak bending moment (M_y) at the critical node should only be used in conjunction with the calculated value at/

the adjacent node to give an estimate of the net bending moment distributed in the critical strip bounded by the nodes. However in our case the stresses, strains etc. are calculated at sampling points instead of nodes and have been averaged over a width which is equal to (t_w + d) where t_w is the thickness of wall and d is the effective depth of slab (Figure (7.1)). By comparing the theoretical and experimental results it will be shown in the later sections of this chapter that this width is quite reasonable. It has also been proposed by Coull & Wong (10) that the stresses in x-direction along the sides of the wall near its tip should also be averaged in the same way. But in our case this proved to be unnecessary, since they were found to be reasonably correct even without averaging. In their case, for shears they showed that it was not possible to use the same averaging procedure adopted with the moments, since a shear discontinuity always existed between the singular and the adjacent node and that the calculated positive and negative stress resultants at the respective nodes were divergent with refinement of element mesh around the singular point. The apparent finite width over which the critical positive shearing forces were distributed was also arbitrary because in the limit of mesh refinement this would be reduced to a point.

Situation is a little bit different in the present case. With the help of elastic distribution of shear due to wind loading alone, for different models, it will be shown later that the discontinuity of the shear between two consecutive points at the tip of the wall did not exist. Therefore same procedure of averaging used for stresses, strains etc. was adopted while calculating the ultimate shear stress induced along critical section when the applied load was equal to the experimental ultimate load.

7.3 LOAD-DISPLACEMENT RELATIONSHIP

Before presenting the description of the theoretical wind load-displacement behaviour of the models and its comparison with the experimental work, it is worth mentioning here that all the wind load-displacement curves presented in this section are nondimensionalized by dividing the displacement by the thickness of the slab and the loads by the design ultimate flexural loads.

Figure (7.6) shows the comparison between theoretical and experimental curves for model PT2. From this figure it can be observed that at early stages of loading the theoretical curve shows somewhat lower stiffness of the slab. This is possibly due to the fact that in the absence of measured tensile strength of concrete, a slightly conservative value of $f_t = .05\ f_{cu}$ was adopted for the analysis (although tensile strength of concrete should not affect the theoretically predicted ultimate loads, it has appreciable effect on the load-displacement characteristics at early stages of loading). However at higher loads, the theoretical curve exhibits higher stiffness than the experimental value. The maximum difference between the theoretical and experimental displacement is at a load of approximately 93% of the experimental load at failure, when the theoretical displacement is about 85% of the measured displacement. It may therefore be concluded that the analysis predicts reasonably well the load-displacement history for this model, subjected to wind load alone.

Theoretical as well as experimental wind load versus displacement curves for the first group of models of the main test series i.e. (MT1, MT2 and MT3) are presented in Figure (7.7). It can be observed from this figure that in all the cases there is very good agreement between the theoretical and experimental curves up to more than 50%/

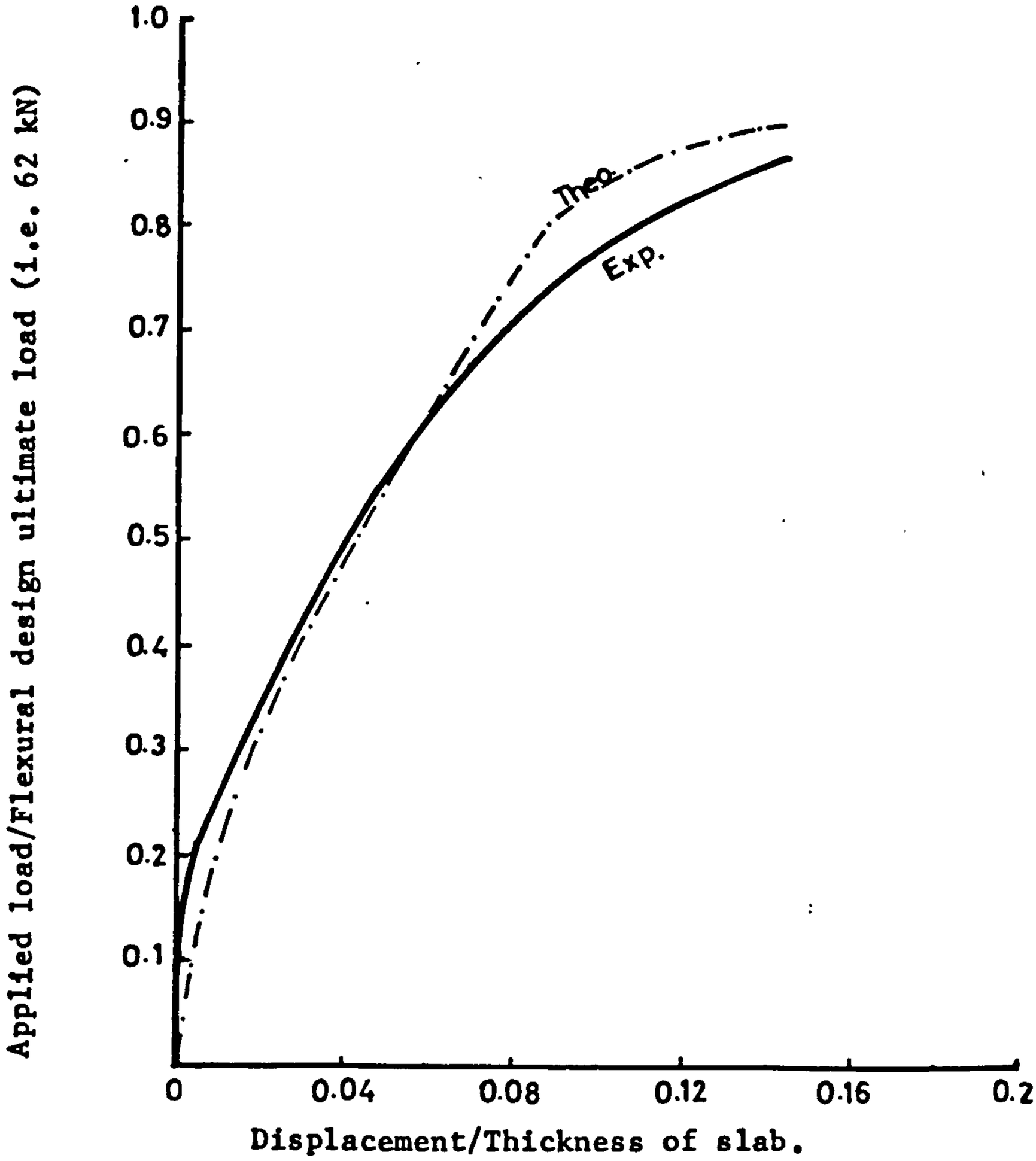

Figure (7.6) : Comparison between theoretical and experimental Load-displacement relationship for model PT2.

of ultimate load. However the experimental displacements are considerably larger than the theoretical one for loads greater than 50% of the experimental ultimate loads. At the experimental load at failure the theoretical displacement for these models is in the range of sixty percent of the experimental one. Since due to equipment failure the test of MT2 was interrupted, two experimental curves are shown for MT2, both virgin and final.

Theoretical and experimental curves for IInd group of models of the main test series (i.e. models MT4 and MT5) are shown in Figure (7.8). It can be observed from this figure that there is a better agreement between the theoretical and the experimental curves for these models than that of the models of first group. The main difference between the models of Ist and II group is the intensity of gravity load. With the applied load approaching experimental ultimate load, the theoretical displacements are larger than the experimental values, the opposite of what happened in the case of first group.

The wind load-displacement curves for models MT6 to MT11 are shown in Figures (7.9) to (7.11). Except model MT6, generally the agreement between theoretical and experimental curves for these models is not much different from that of models of Ist group (i.e. MT1, MT2 and MT3). The agreement is poor for model MT6. For this model the theoretical displacement at experimental ultimate load is less than even half the experimental one. No reason could be found from experimental or theoretical work for this unexpected behaviour.

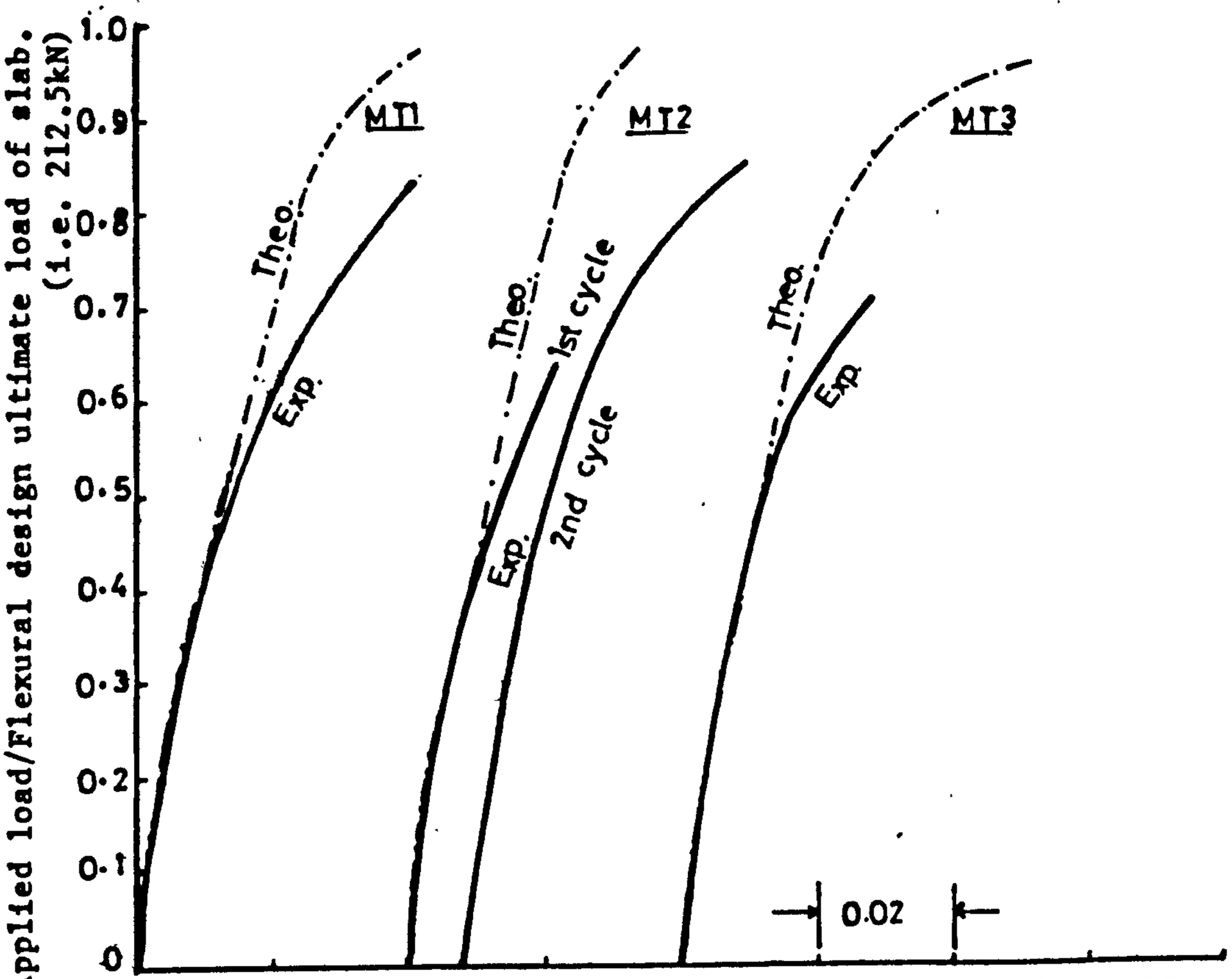

Figure (7.7) : Comparison between theoretical and experimental w.load-displacement relationship for models of Ist group of MT series.

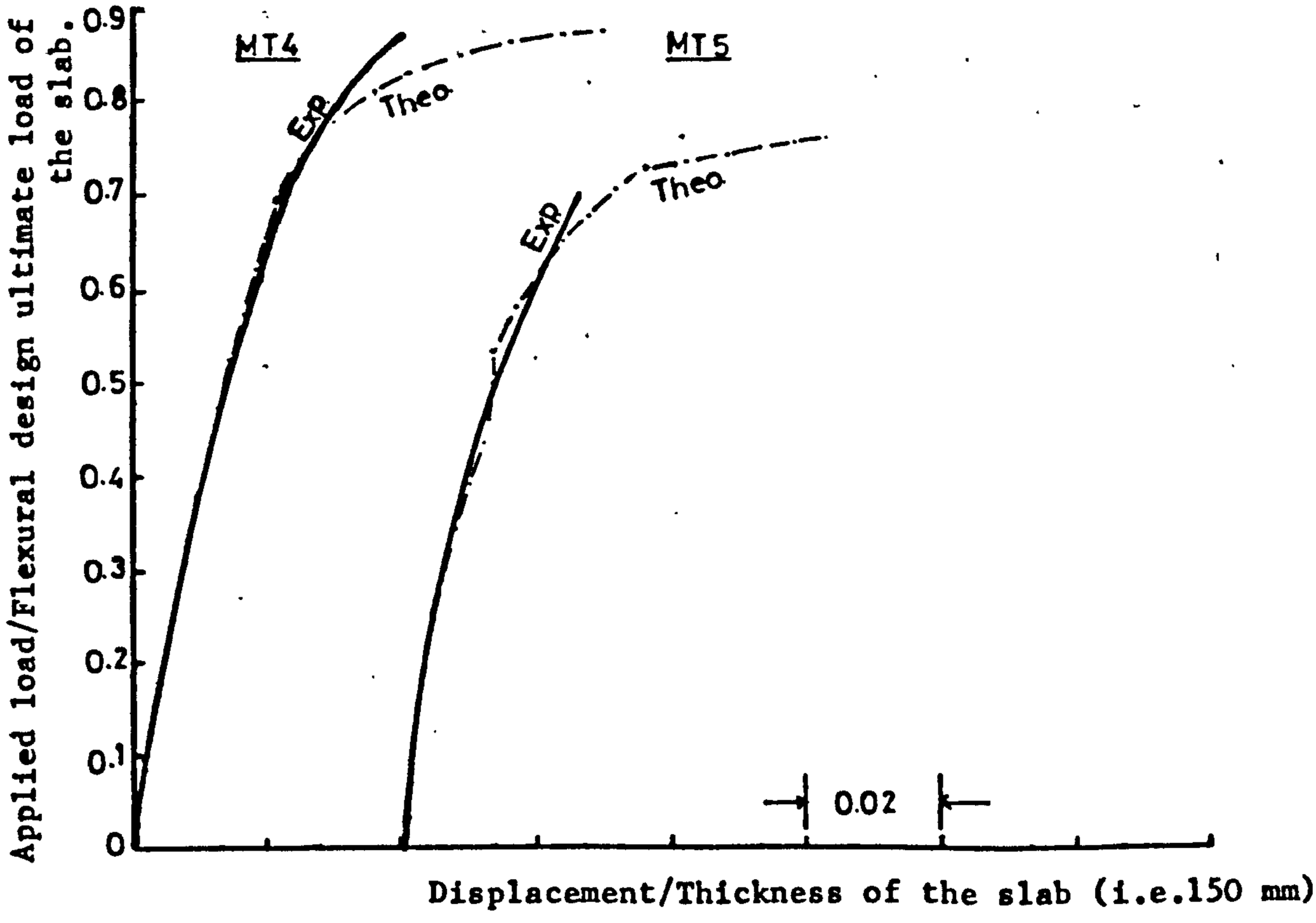

Figure (7.8) : Comparison between theoretical and experimental w.load-displacement relationship for models of IInd group of MT series.

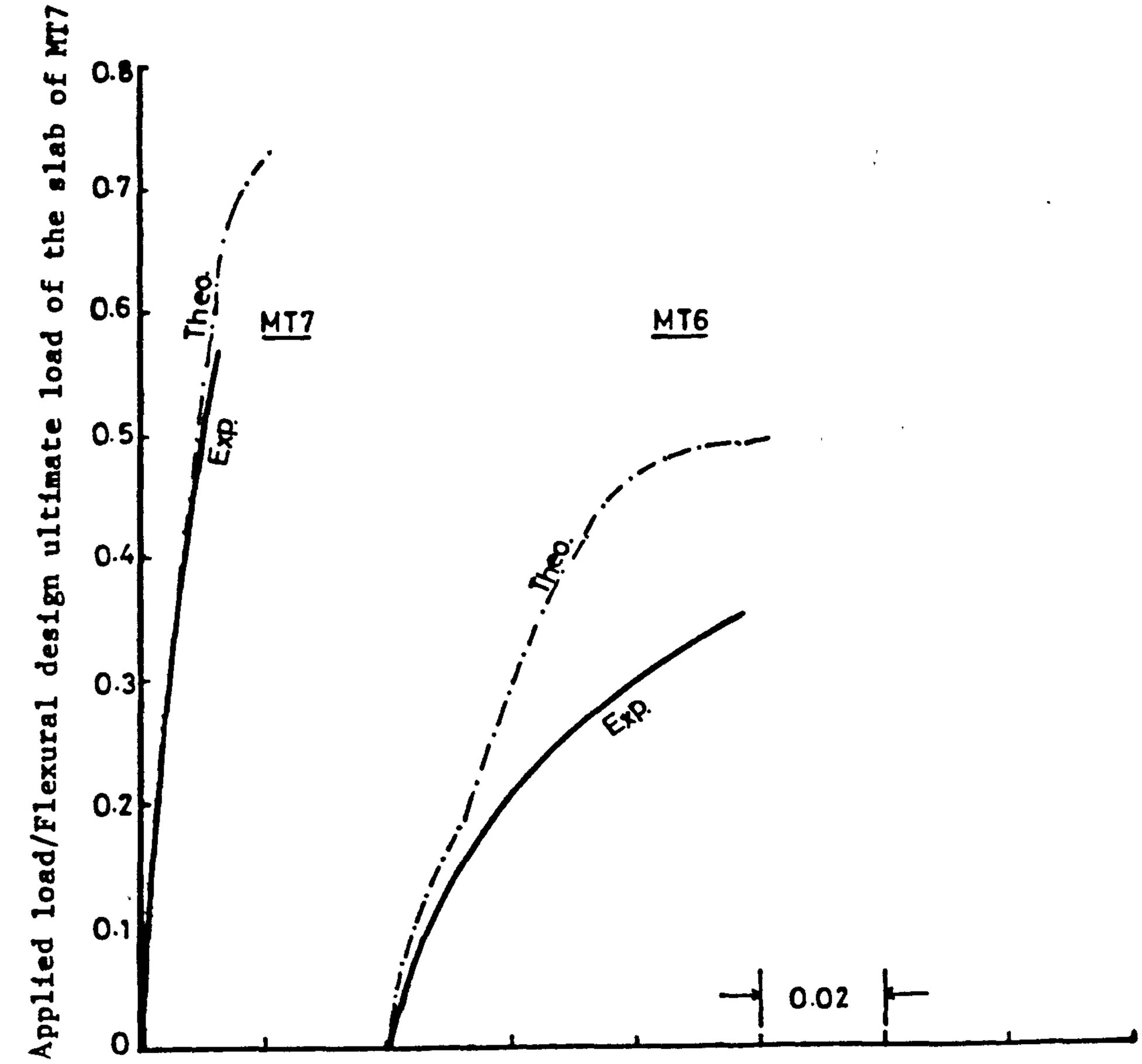

Figure (7.9): Comparison between theoretical and experimental w.load-displacement relationahip for models of IIIrd group of MT series.

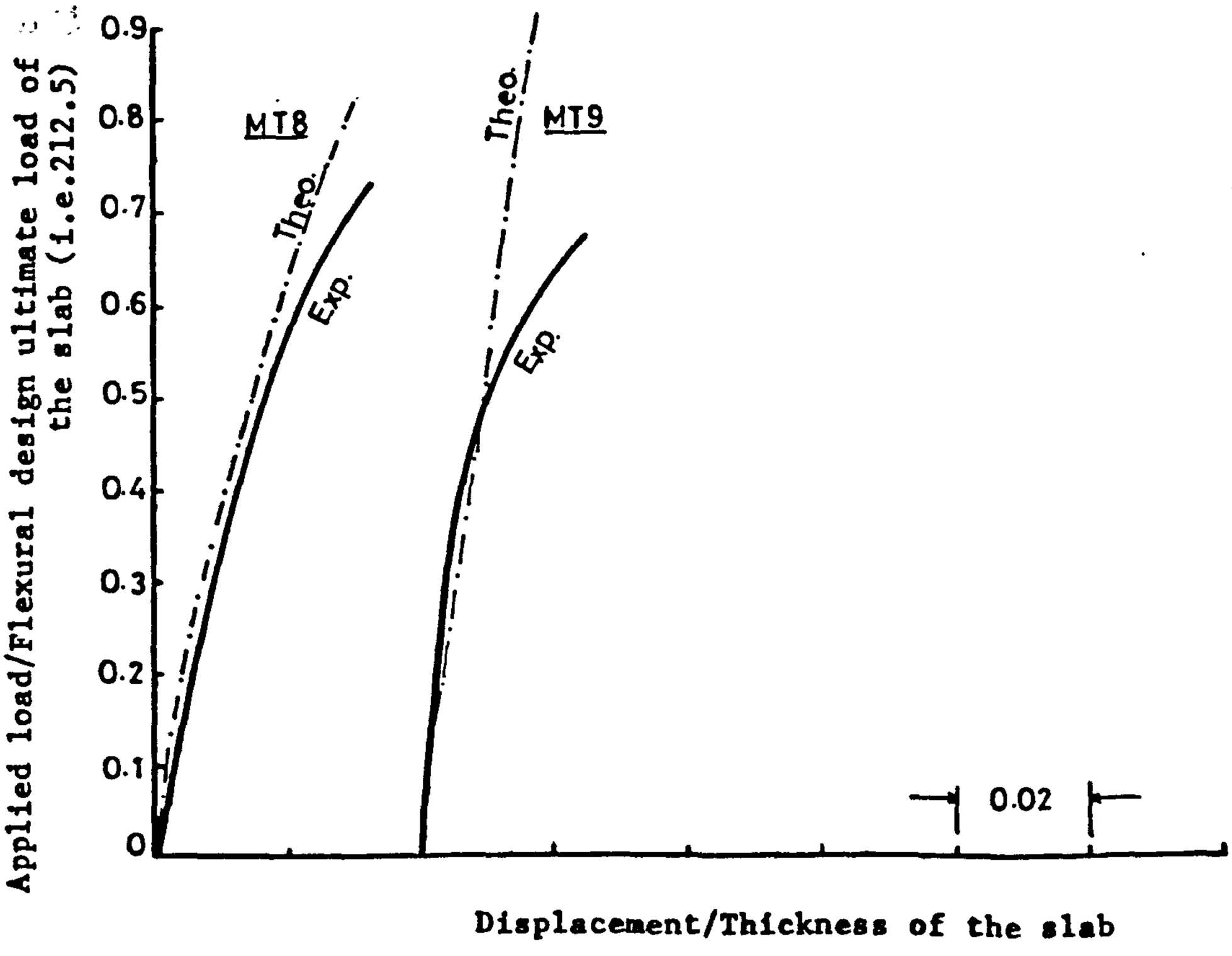

Figure (7.10) : Comparison between theoretical and experimental w. load-displacement relationship for models MT8 & MT9

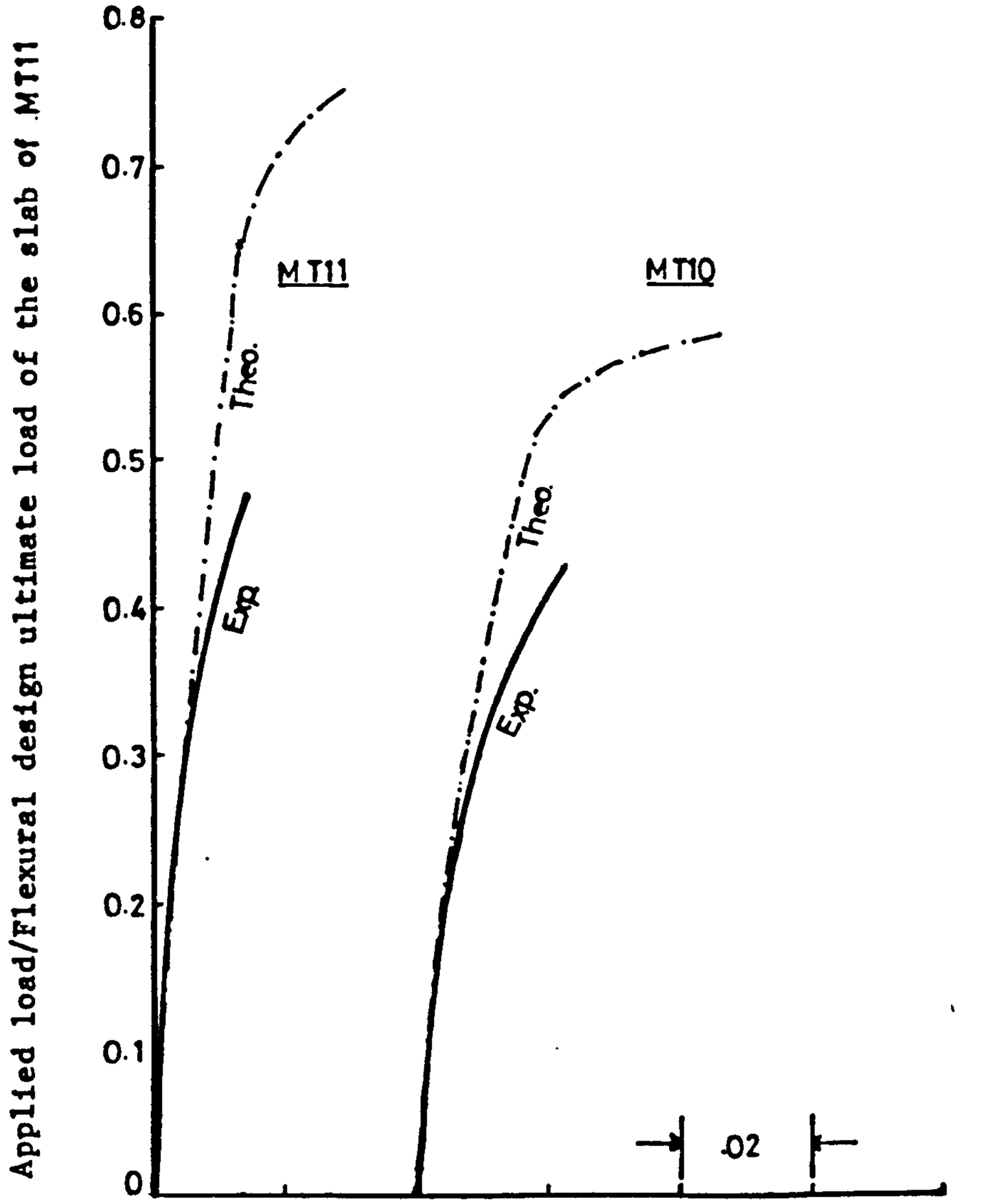

Figure (7.11) : Comparison between theoretical and experimental w.load-displacement relationship for models MT9, MT10 and MT11.

7.4 COMPRESSIVE STRAIN IN CONCRETE

In this section the theoretical compressive strain in concrete is compared with the measured one. Generally due to singularity of stresses, strains much larger than the measured values are predicted in the slab at the inner face of wall, especially if the thickness of wall is taken as zero. However much better agreement between the theoretical and measured strains can be achieved if (as discussed in section (7.2)) the strain at two consecutive sampling points is averaged at the tip of the wall along the transverse critical section for flexure. The compressive strains in the concrete at the bottom of the slab of model PT2 (case of wind loading alone), along transverse critical section, passing through the tip of the wall, are shown in Figure (7.12). From this figure it can be observed that nearer the point is to the tip of the wall, the poorer is the agreement between the measured and theoretical strains.

Figure (7.13) shows the comparison between the theoretical and experimental strain in concrete at the bottom of the slab for model MT1 (case of combined loading). It can be observed that finite element analysis shows higher concentrations of strains in the slab near the tip of the wall and underestimates them near the sides of the slab. Theoretical and experimental compressive strains for all the other models of main test series are compared in Figures(7.14) to Figure (7.23). All these figures depict the same behaviour of strains. In most of the cases there is reasonable agreement between theoretical and experimental strains at points P_2 midway between the wall and the free edge. Near the tip of the wall (Point P_1) the situation is further aggravated by the unexpected behaviour of the measured strains/

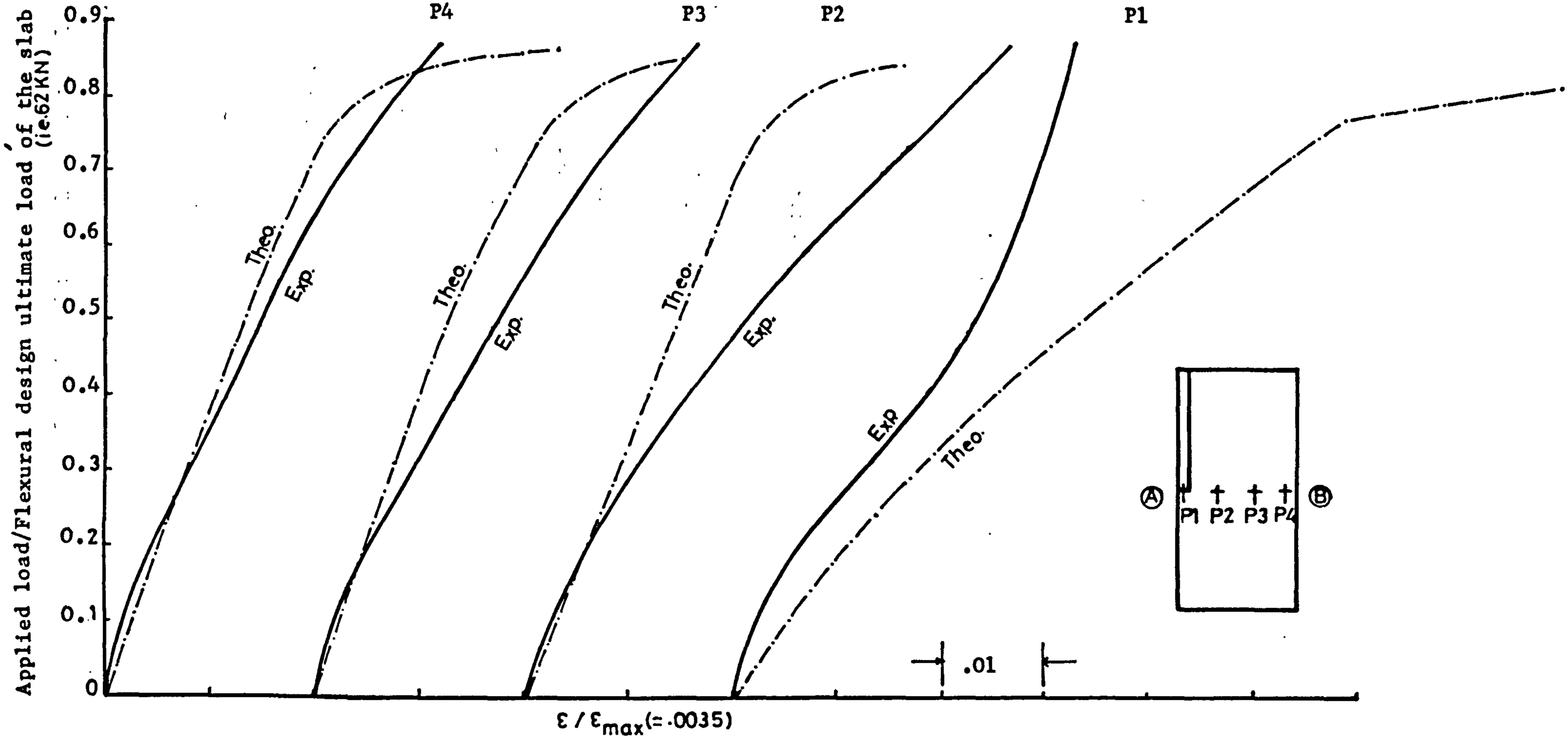

Figure (7.12): Comparison between the theoretical and measured compressive strain in concrete in windward direction along transverse critical section AB in the slab of model PT2.

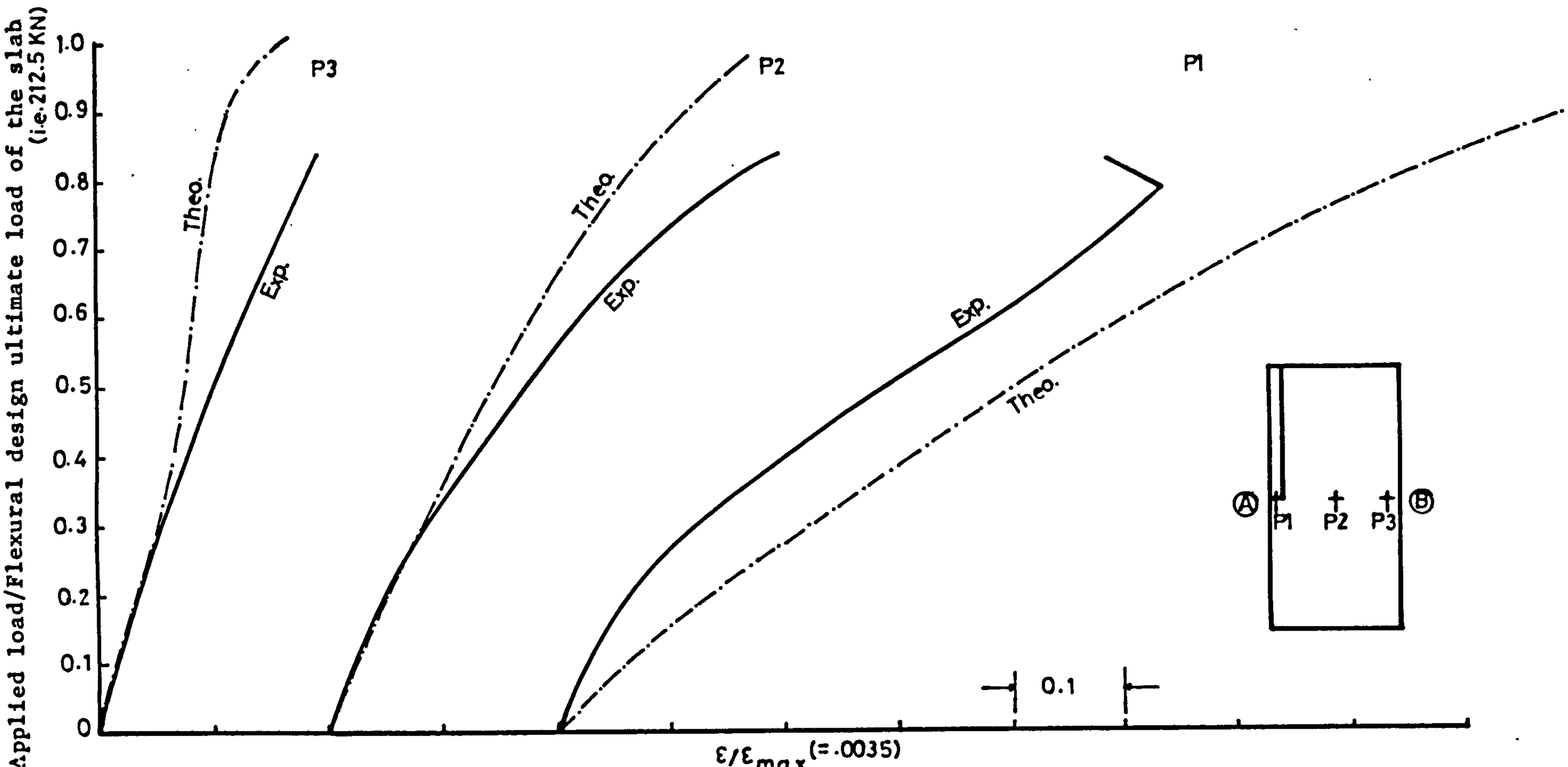

Figure (7.13) : Comparison between theoretical and measured compressive strain in concrete at different points along transverse critical section AB, in the slab of MT1.

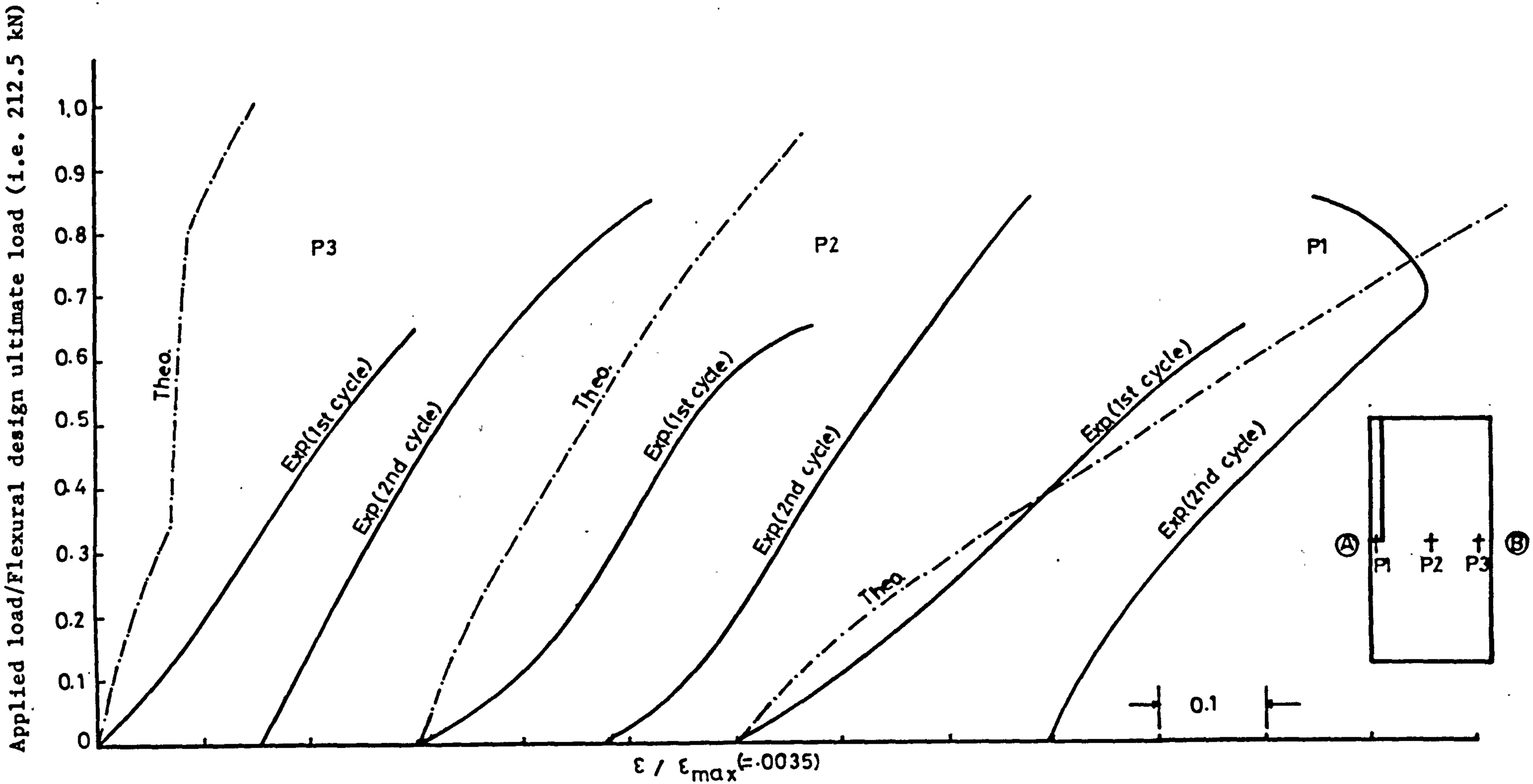

Figure (7.14) : Comparison between theoretical and measured compressive strain in concrete, in windward direction at different points along transverse critical section AB, in the slab of model MT2.

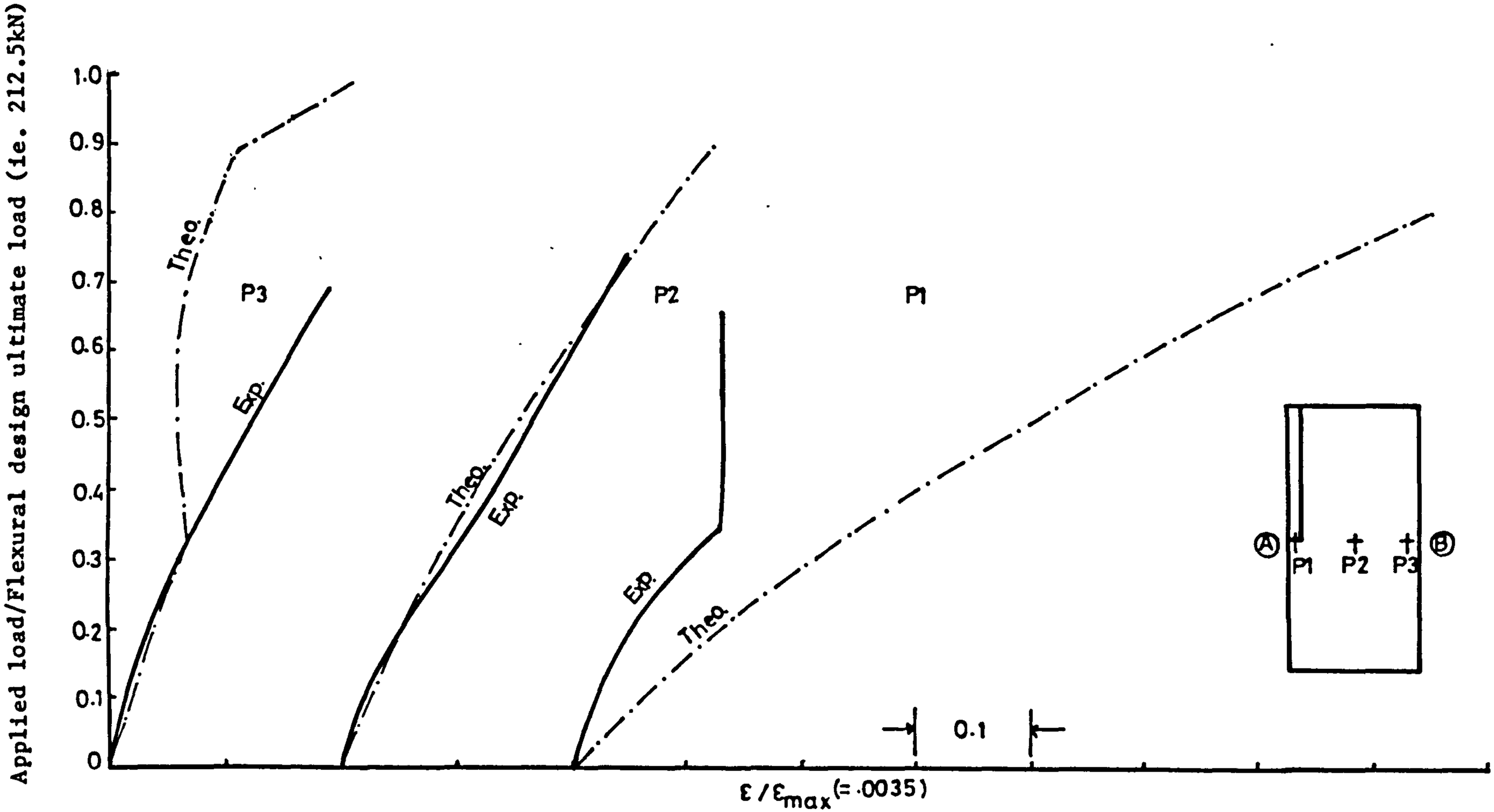

Figure (7.15) : Comparison between theoretical and measured comp. strain in concrete, in windward direction at different points along transverse critical section AB, in the slab of model MT3.

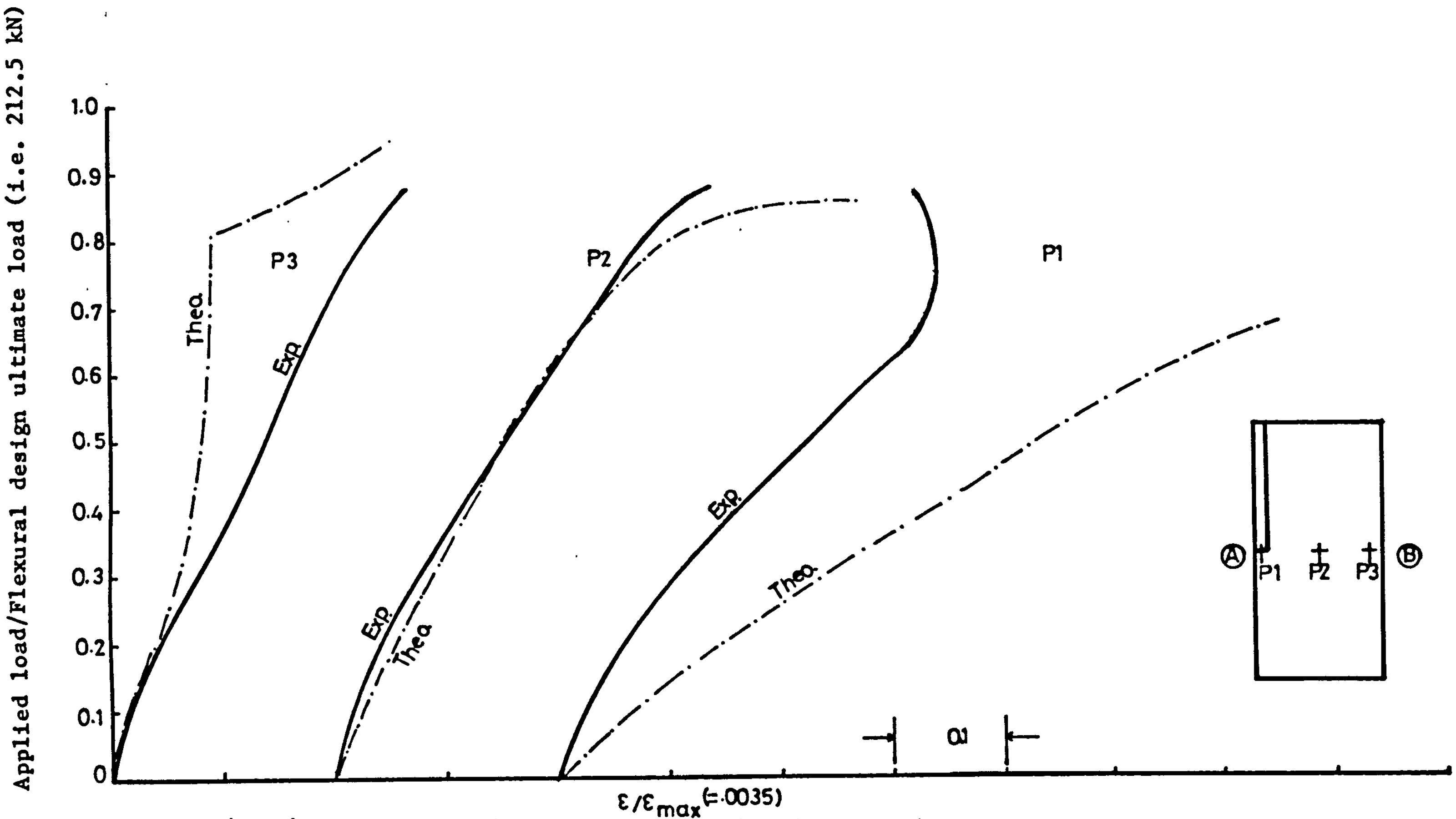

Figure (7.16) : Comparison between theoretical and measured compressive strain in concrete in windward direction at different points along transverse critical section AB, in the slab of MT4.

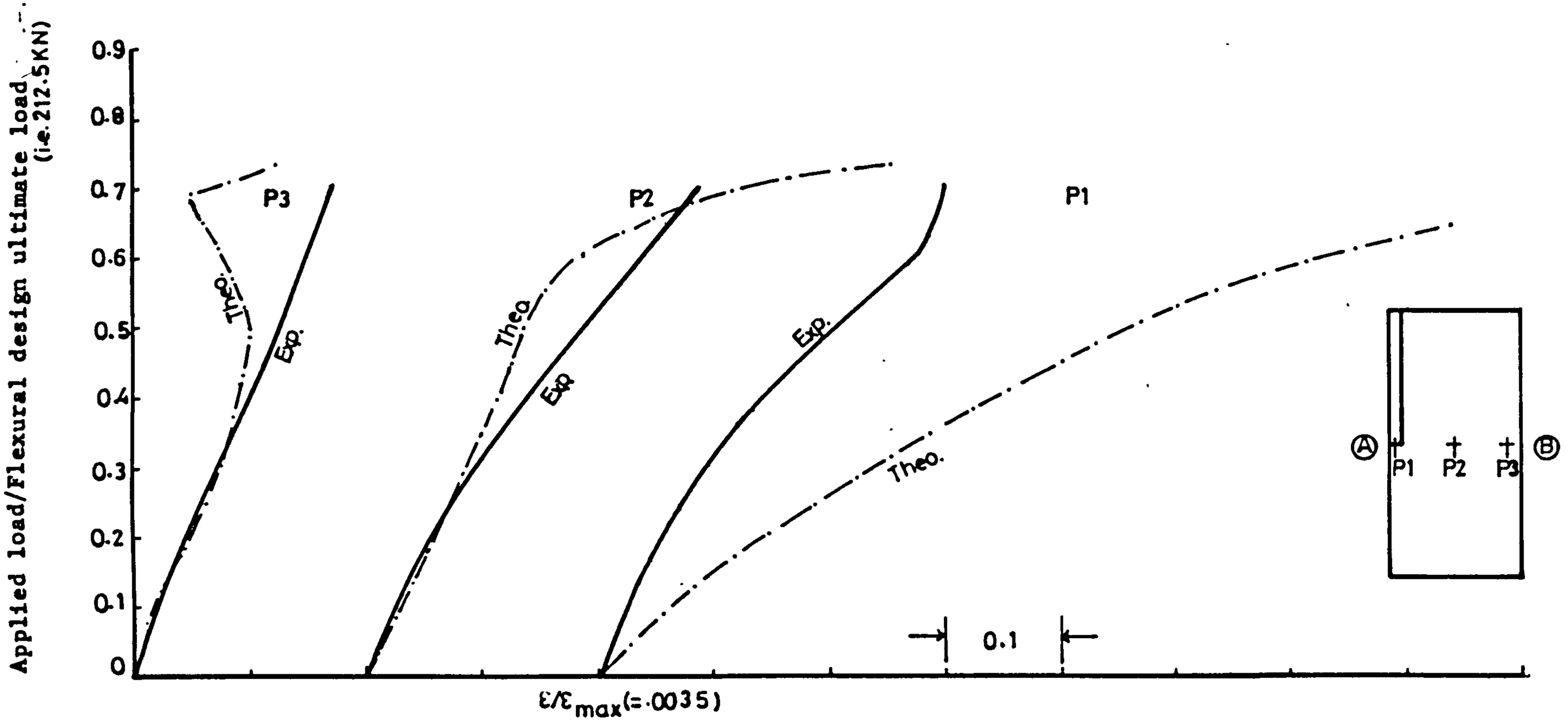

Figure (7.17) : Comparison between theoretical and measured compressive strain in concrete at different points along transverse critical section AB, in the slab of MT5.

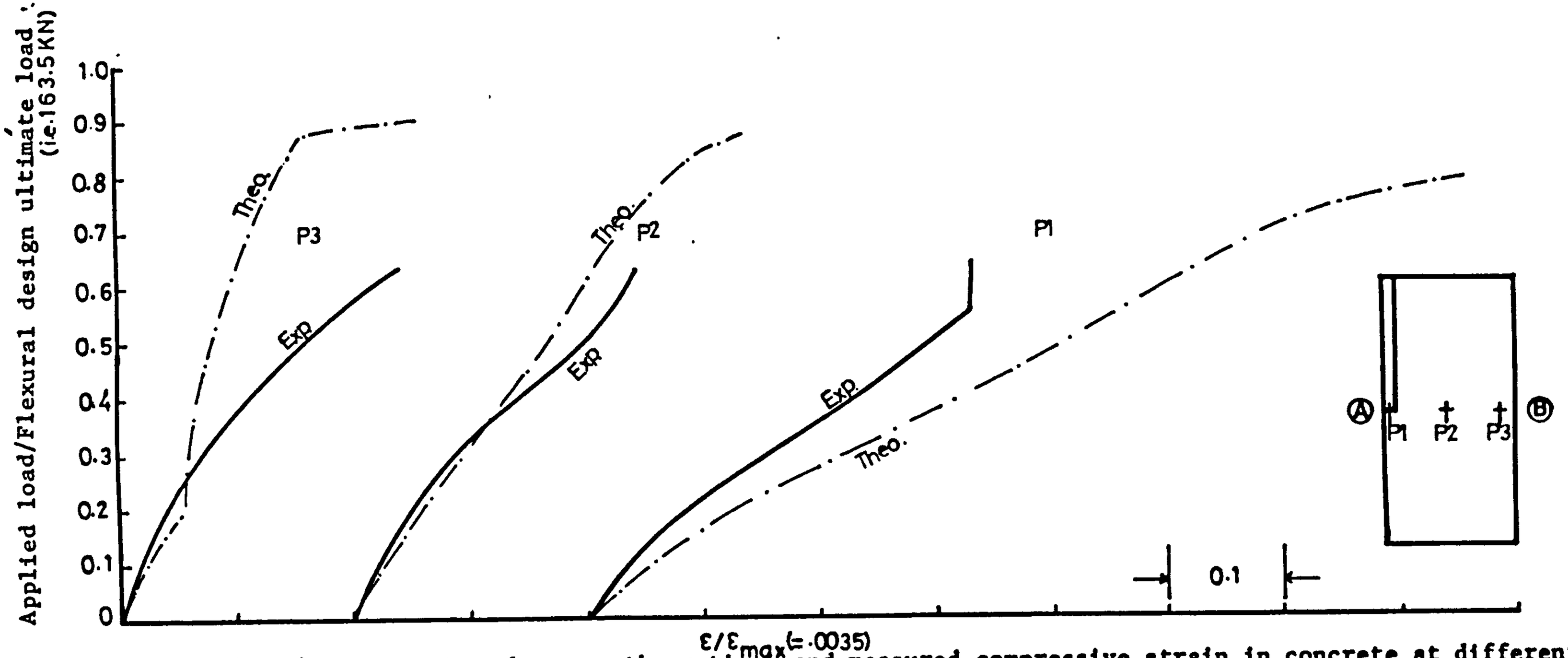

Figure (7.18) : Comparison between theoretical and measured compressive strain in concrete at different points along transverse critical section AB, in the slab of MT6.

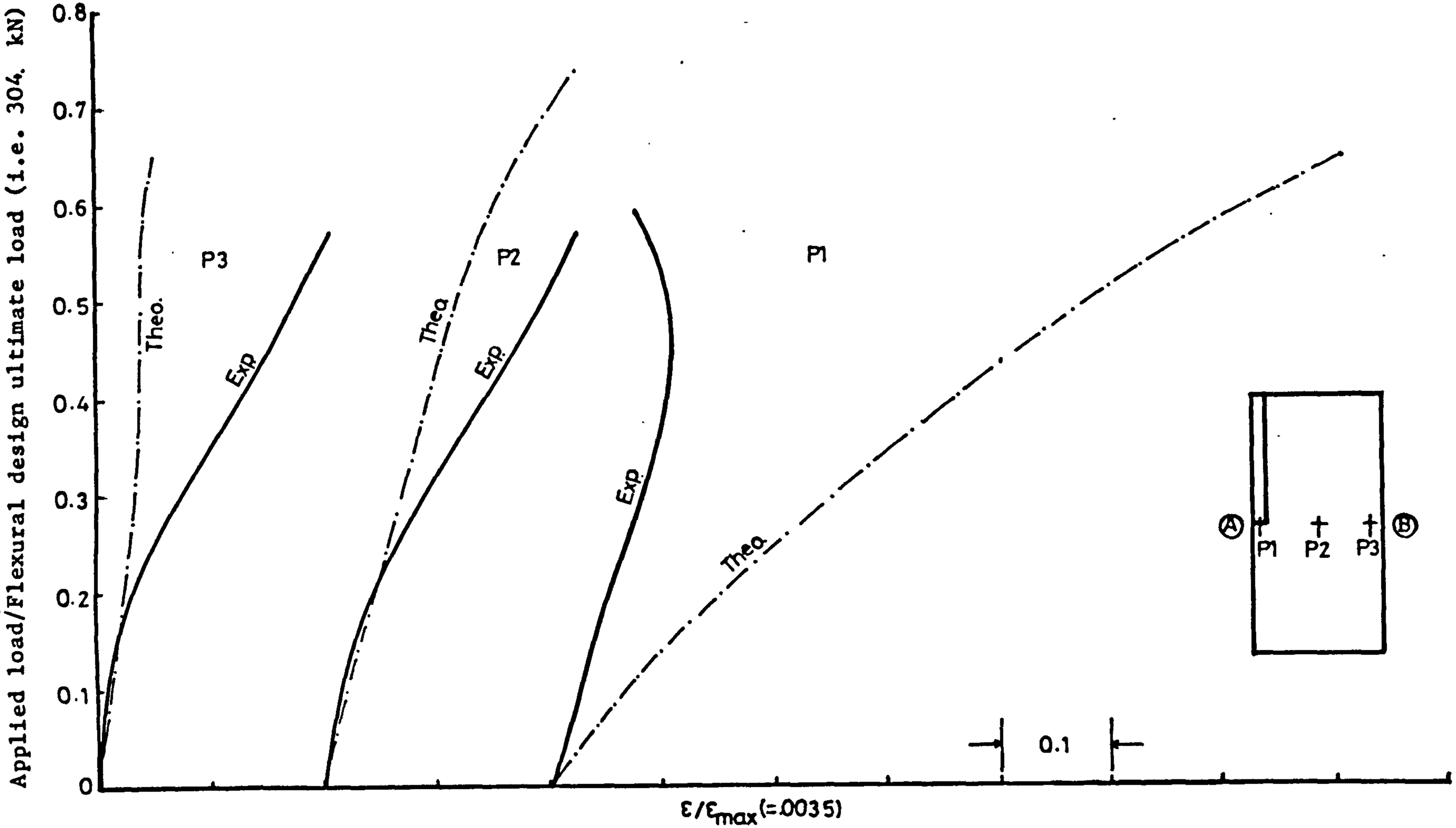

Figure (7.19) : Comparison between theoretical and experimental compressive strain in concrete at different points along transverse critical section AB, in the slab of model MT7.

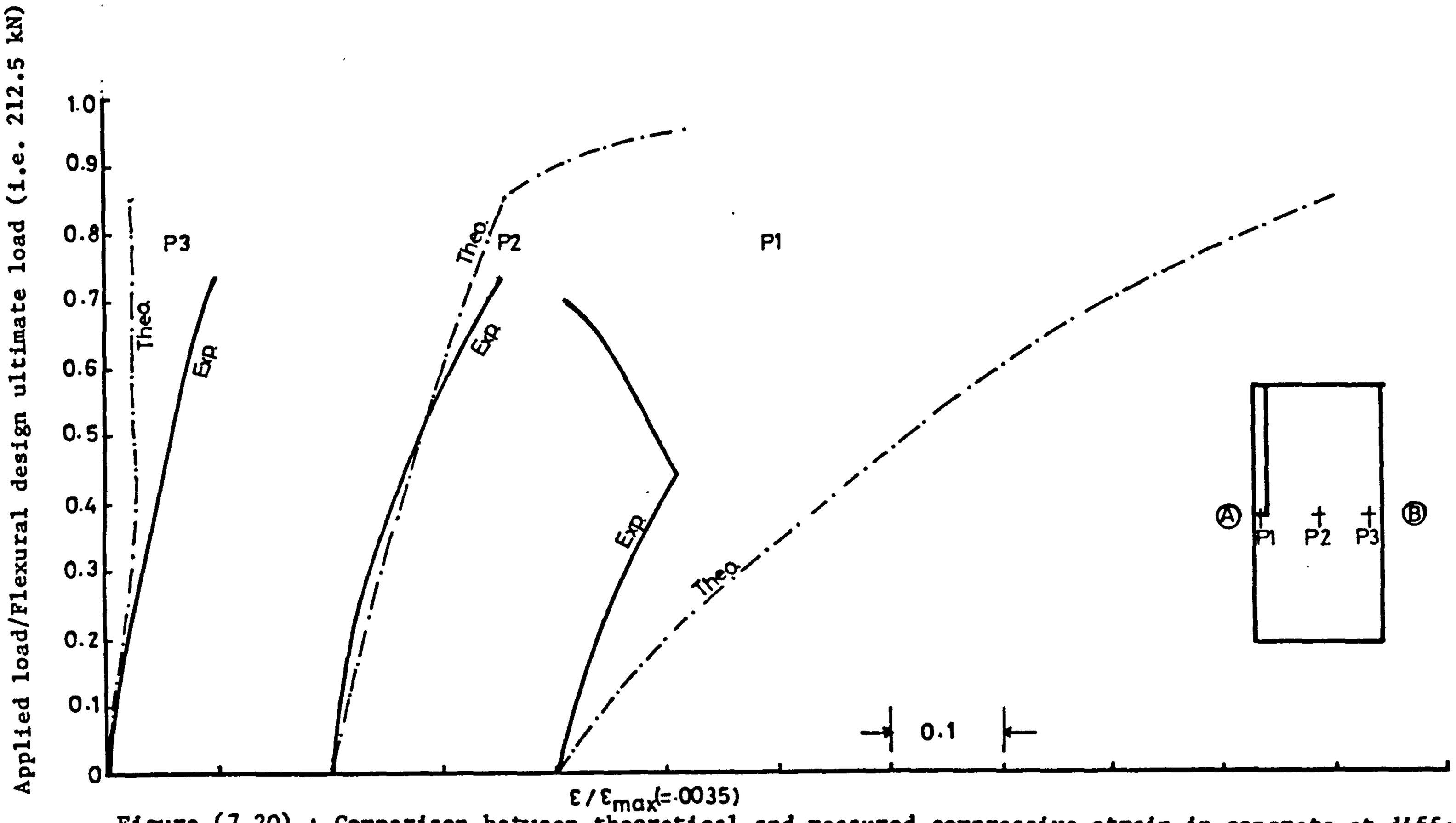

Figure (7.20) : Comparison between theoretical and measured compressive strain in concrete at different points along transverse critical section AB, in the alab of MT8.

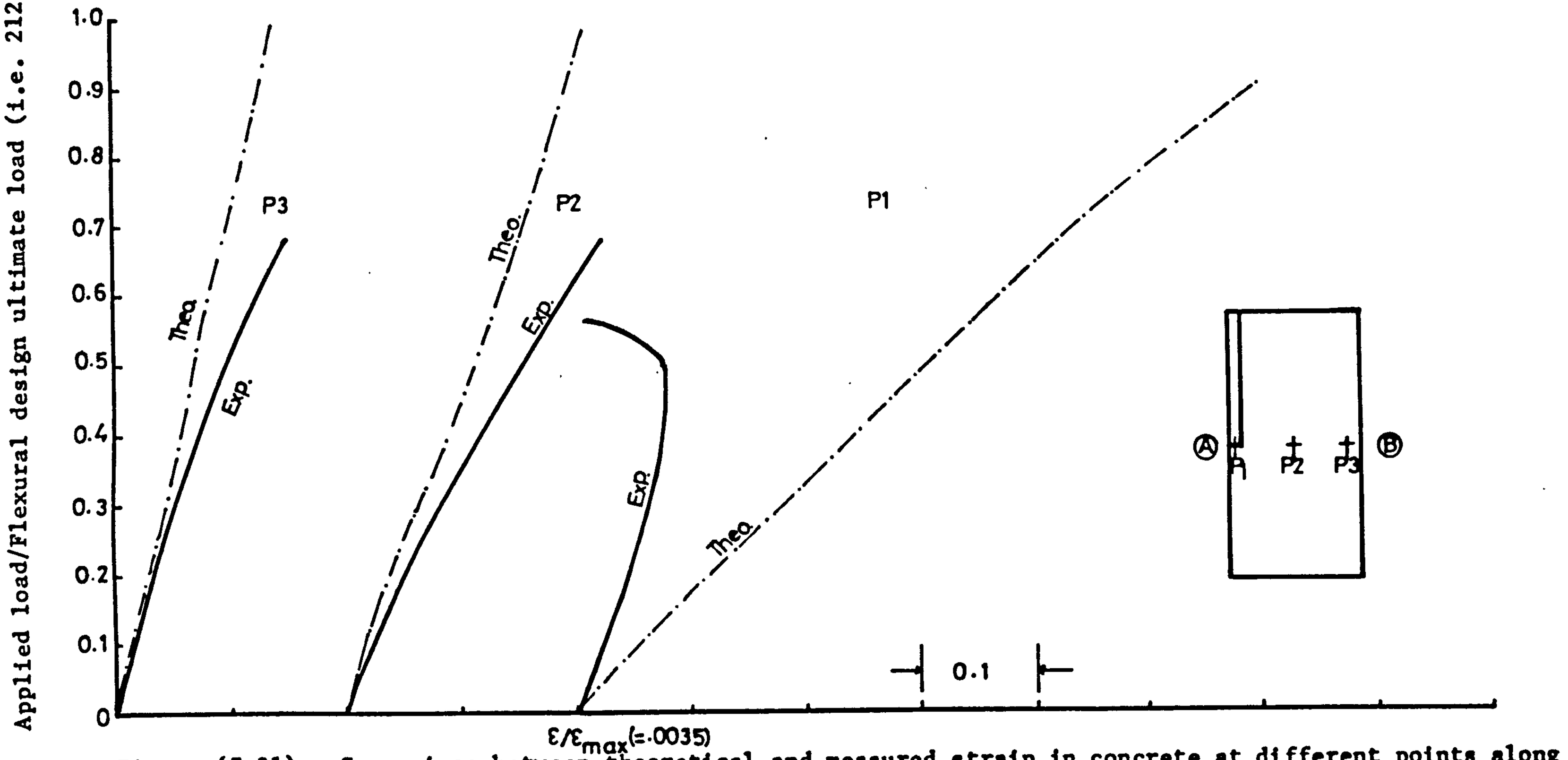

Figure (7.21) : Comparison between theoretical and measured strain in concrete at different points along transverse critical section AB, in the slab of model MT9.

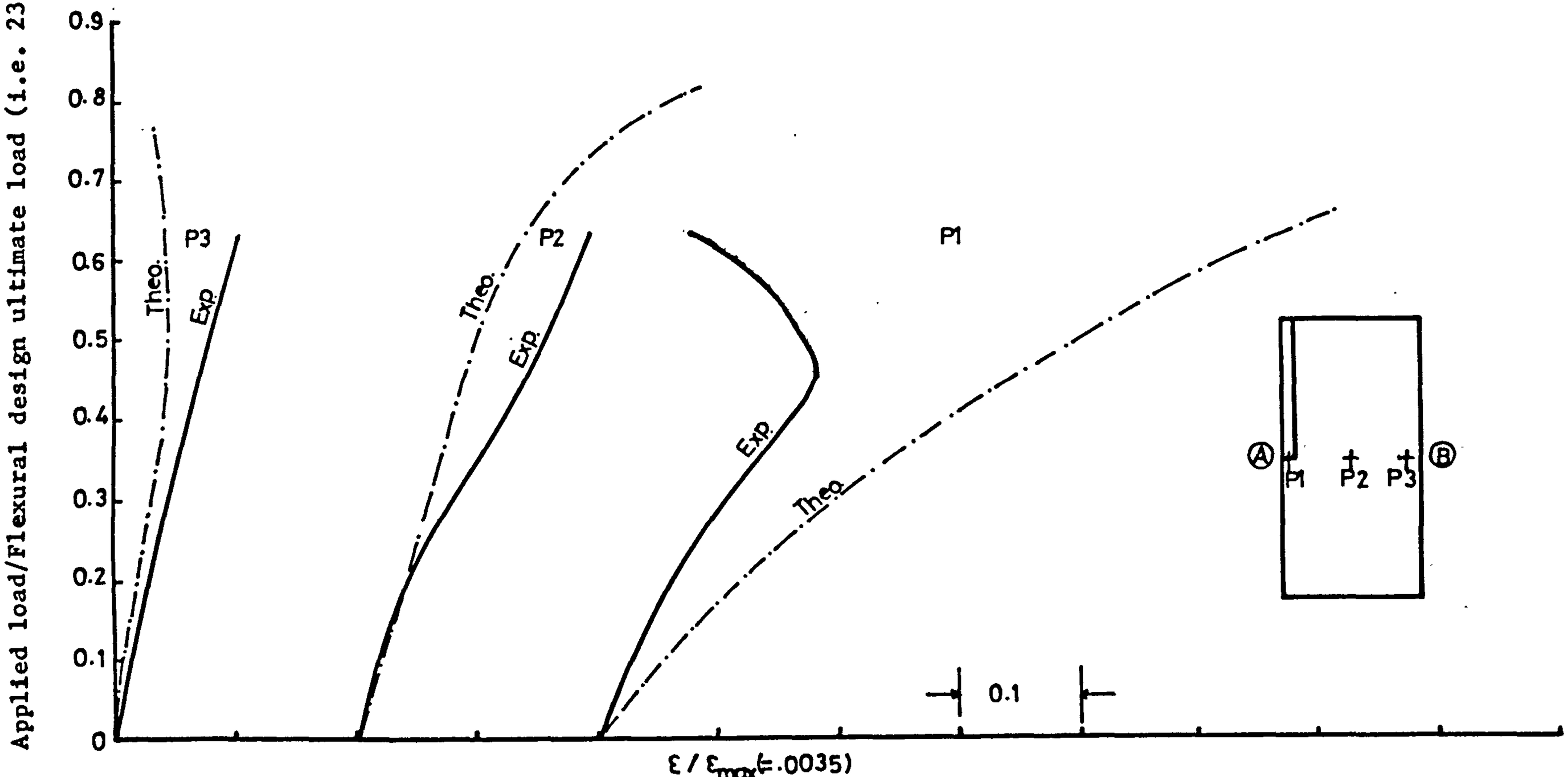

Figure (7.22) : Comparison between theoretical and experimental compressive strain in concrete at different points in windward direction along transverse critical section AB, in the slab of model MT10.

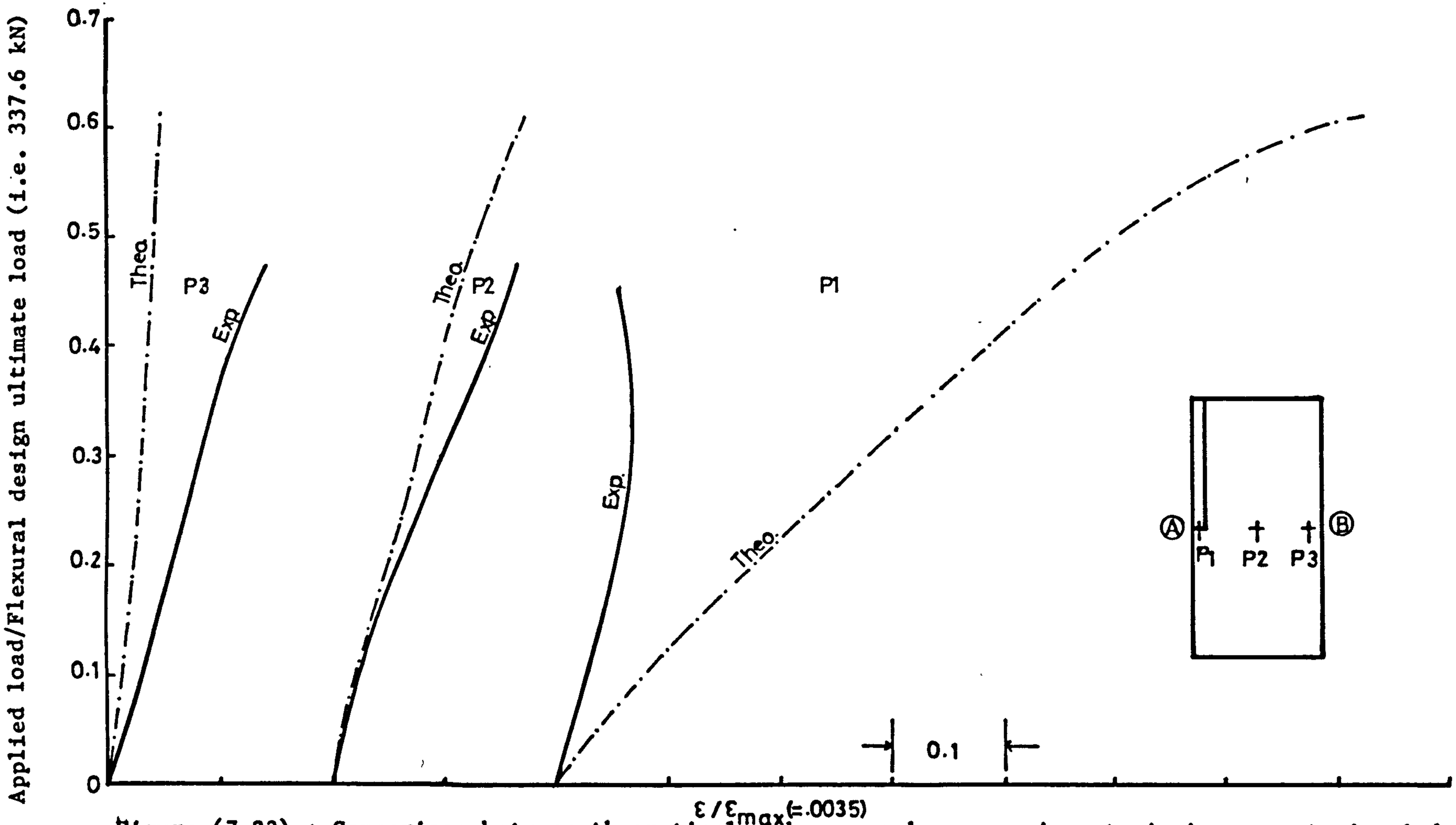

Figure (7.23) : Comparison between theoretical and measured compressive strain in concrete in windward direction at different points along transverse critical section AB, in the slab of MT11.

which, at higher loads, show unloading with the increase in the applied load. During experimentation once this behaviour was detected in model PT2, in all the succeeding tests, this region of the slab was carefully checked after application of each load increment and no cracking or any sign of distress was observed at the bottom of the slab in the area surrounding the strain gauge until failure occurred. As this phenomena repeats in many models, this can not be attributed to experimental arror. The theoretical analysis completely failed to predict this behaviour.

7.5 STRAIN IN STEEL

As has already been mentioned in chapter six of this thesis, strain in steel was not measured in the models of preliminary test series and the models of Ist group of main test series. However comparison of theoretical strain in steel in y-direction at certain points along a transverse section passing through the slab near the inner face for models MT4 to MT11 is presented in Figures (7.2 4) to (7.30). Basically in all the cases the agreement is good at point P1 (opposite of what happened in the case of compressive strains) but poor at the points near the edges.

Theoretical strain in steel in x-direction (transverse direction) along the sides of the wall, in the slabs of models MT4 to MT11, at certain points is compared with measured strain in Figures (7.31) and (7. 36). Basically the agreement is good at point P6 (along the side of wall near the inner face), reasonable at point P5 except for MT4 (wall tip) and generally poor at point P7 (towards the back of the wall).

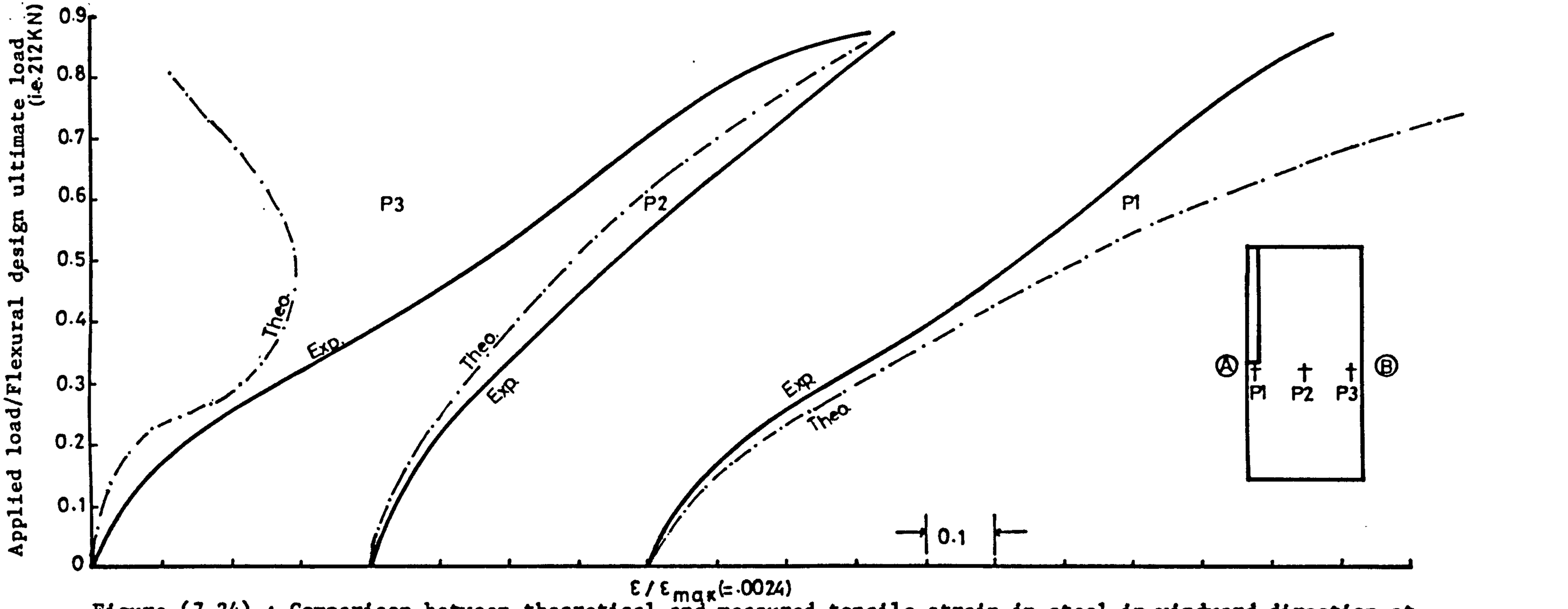

Figure (7.24) : Comparison between theoretical and measured tensile strain in steel in windward direction at different points along transverse section AB in the slab of MT4.

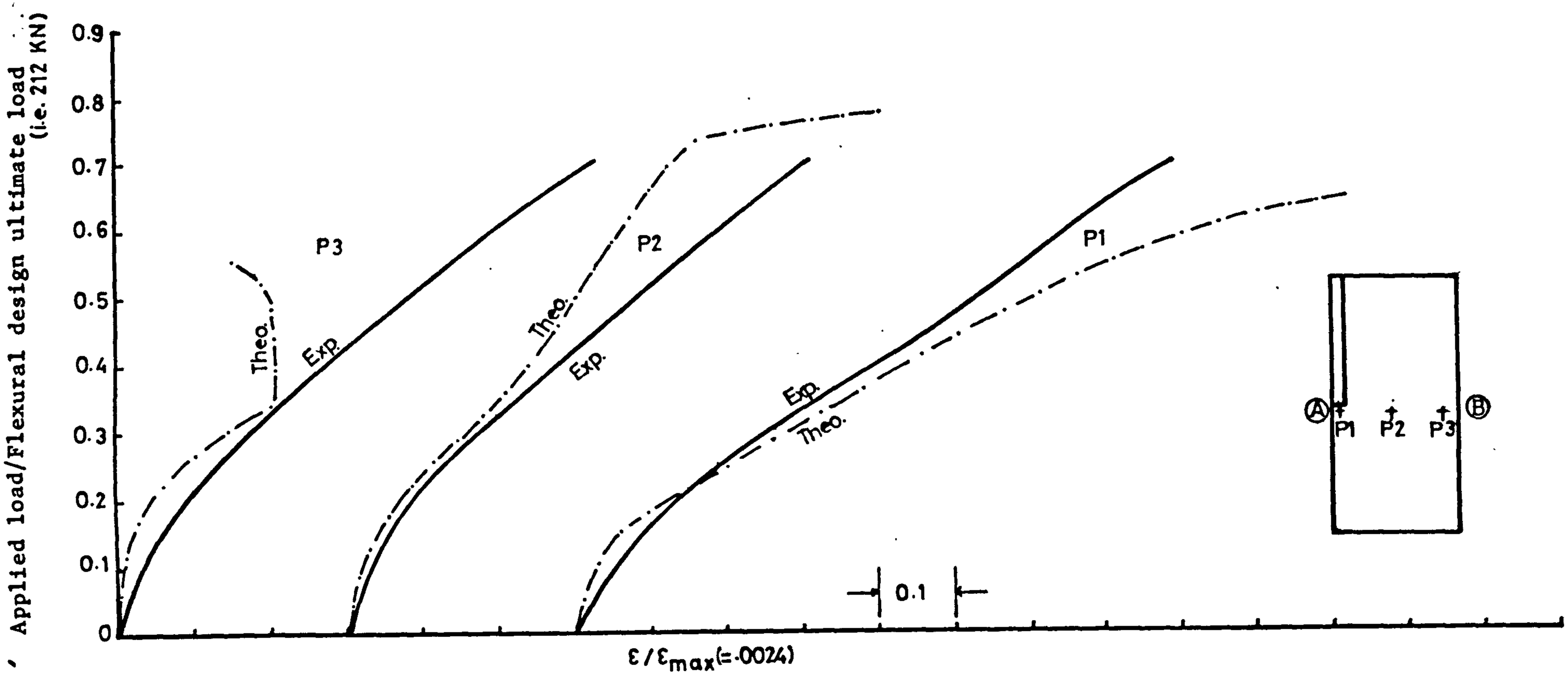

Figure (7.25) : Comparison of theoretical and measured tensile strain in steel in windward direction at different points along transverse critical section AB, in the slab of model MT5.

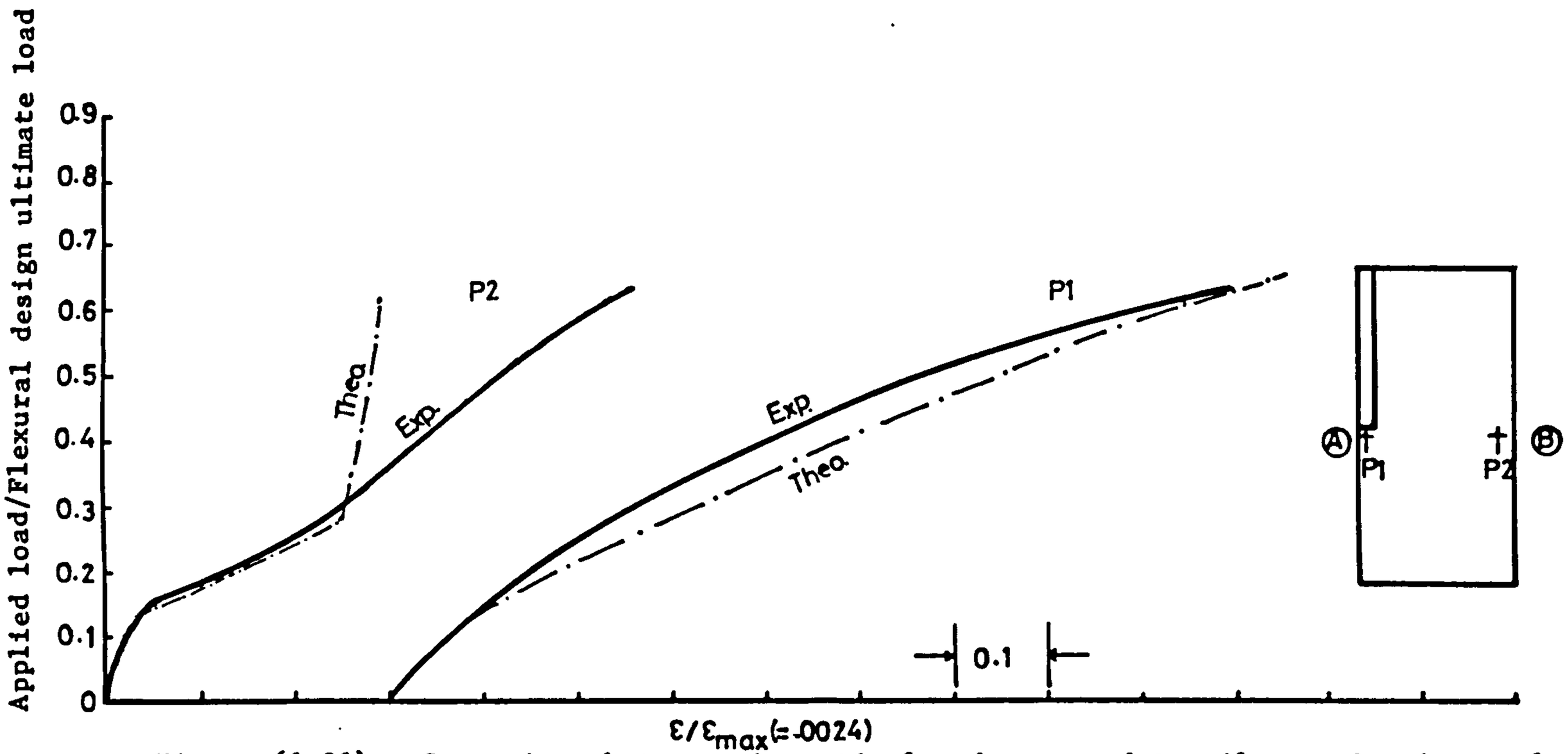

Figure (6.26) : Comparison between theoretical and measured tensile strains in steel in windward direction at different points along transverse section AB in the slab of MI6

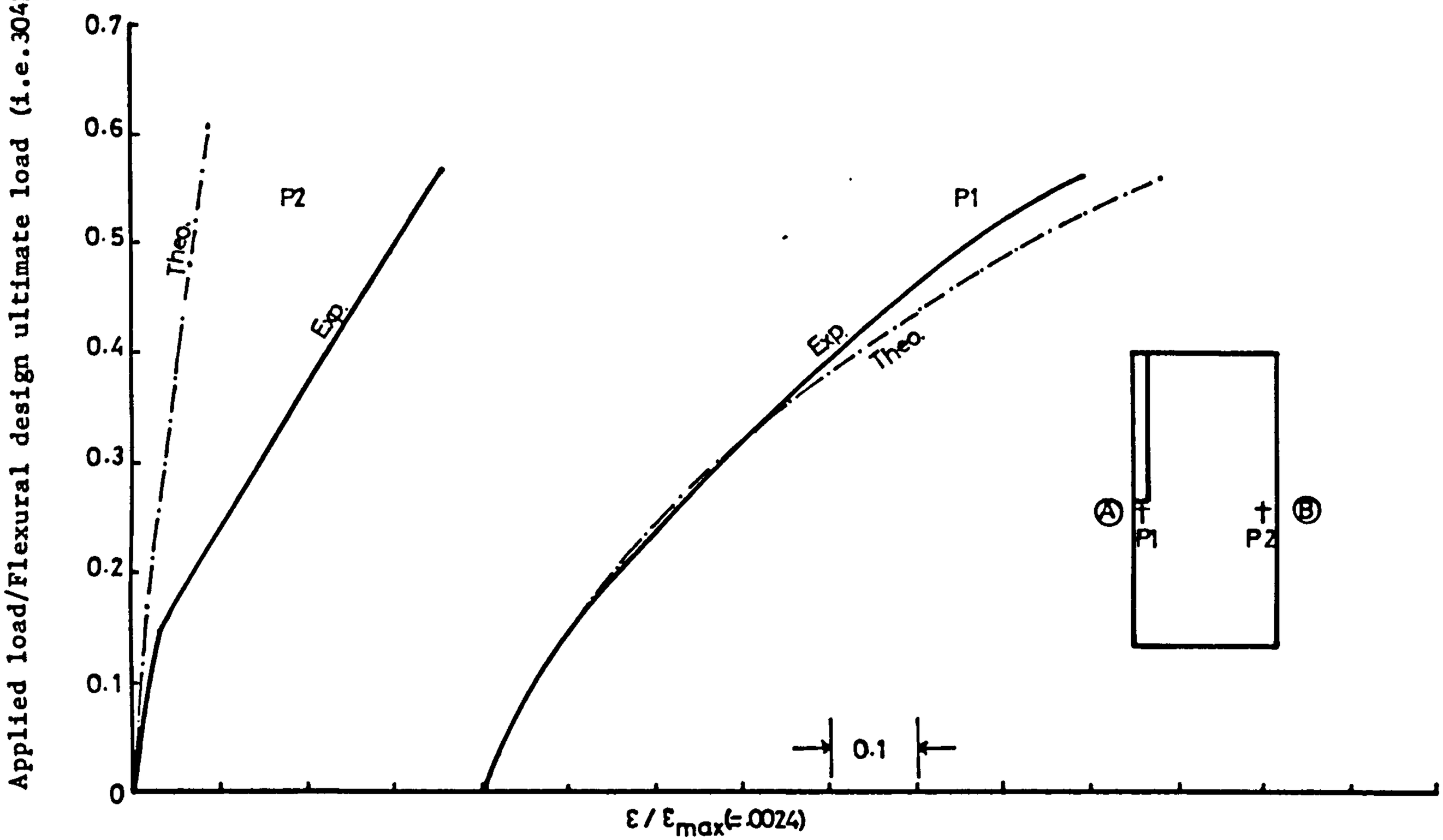

Figure (7.27) : Comparision between theoretical and measured tensile strain in steel in windward direction at different points along transverse section AB in the slab of MI7.

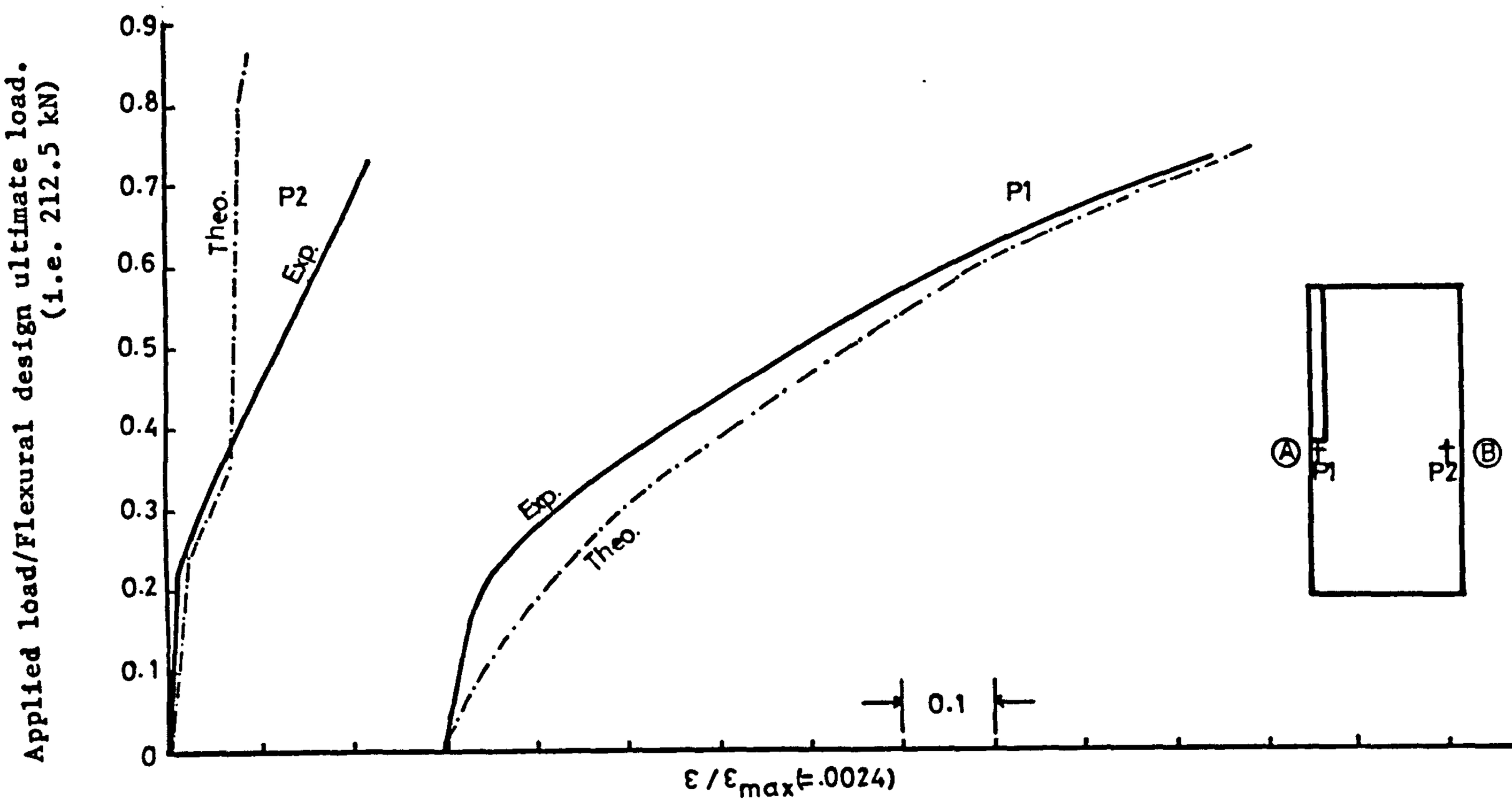

Figure (7.28) : Comparison between theoretical and measured tensile strain in steel in windward direction at different points along transverse section AB in the slab of MT8.

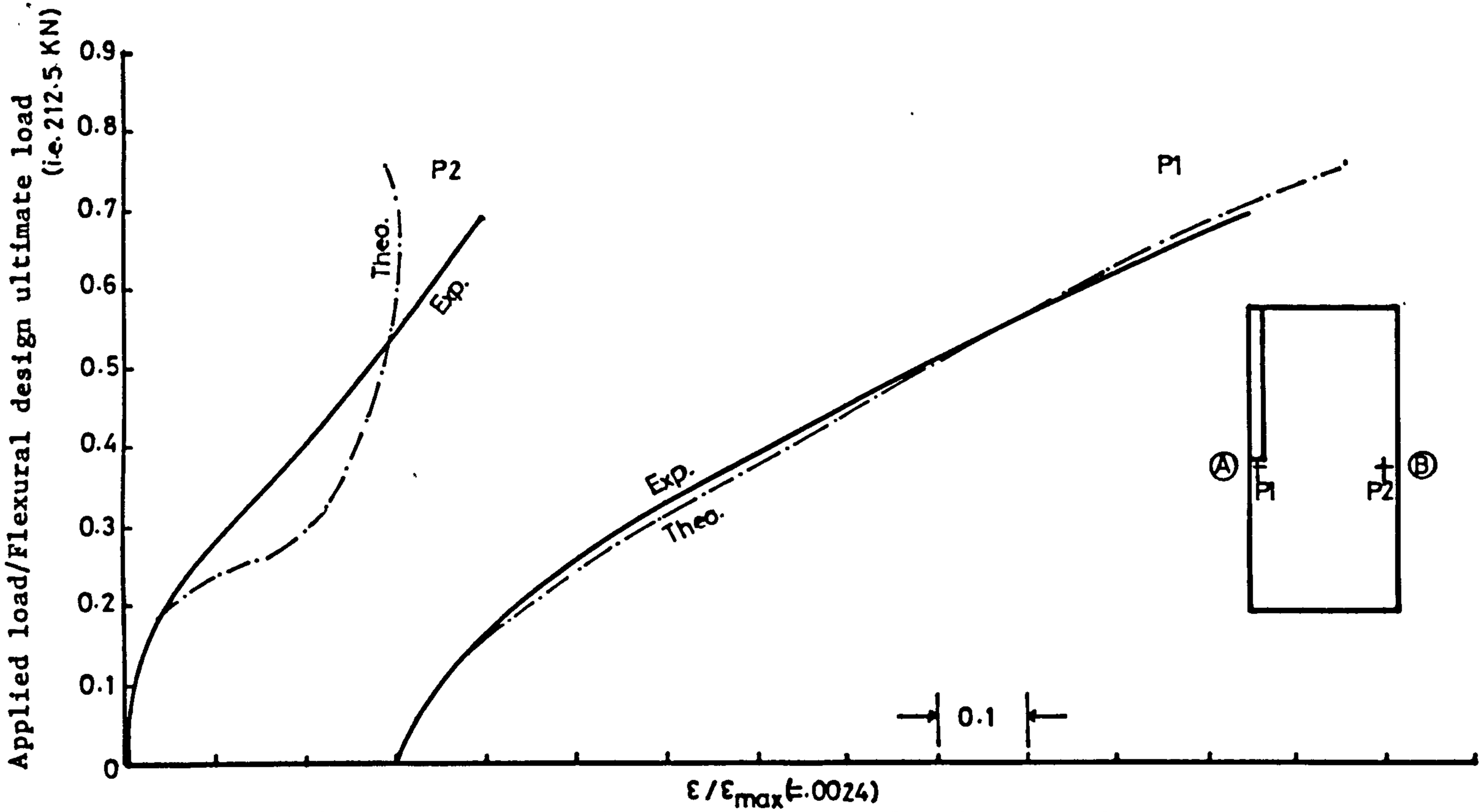

Figure (7.29) : Comparison between theoretical and measured strain in steel at different points in windward direction in the slab of model MT9.

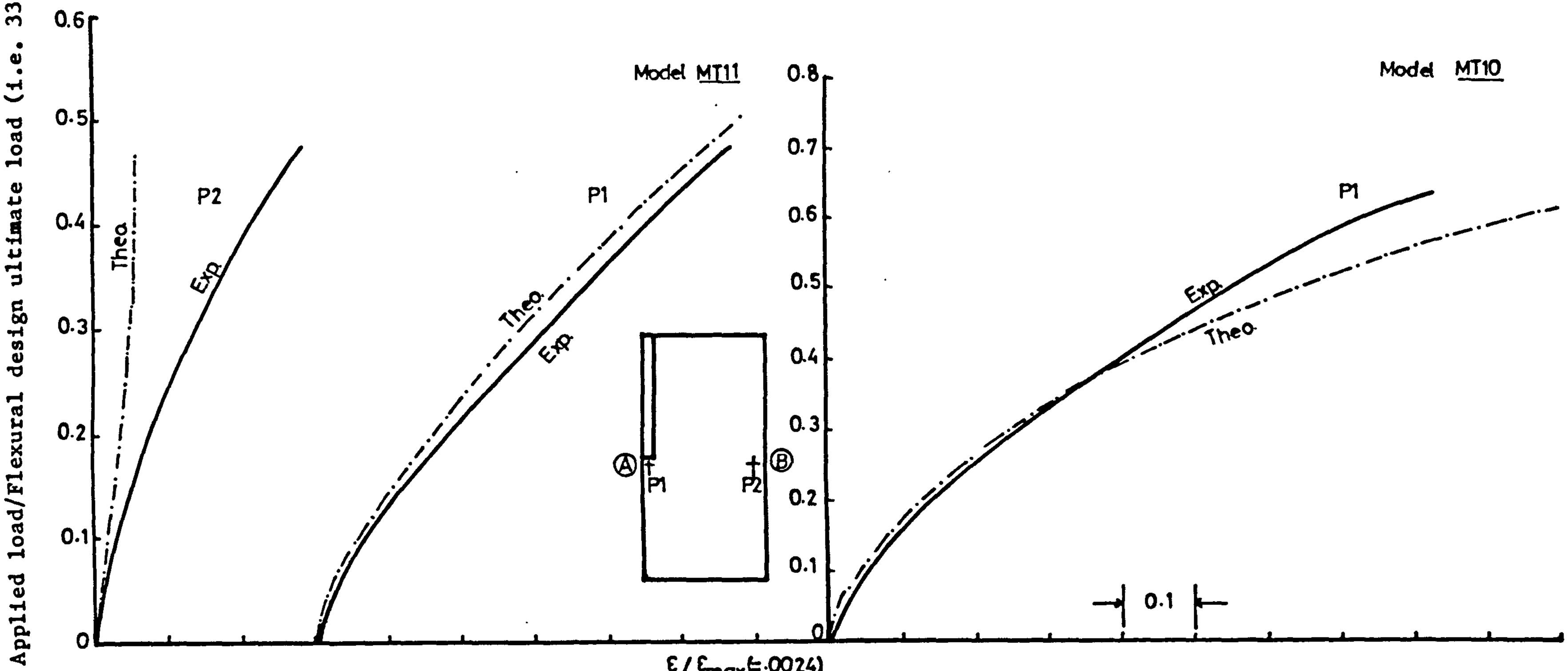

Figure (7.30) : Comparison between theoretical and measured tensile strain in steel in windward direction along transverse section AB in the slabs of models MT10 and MT11

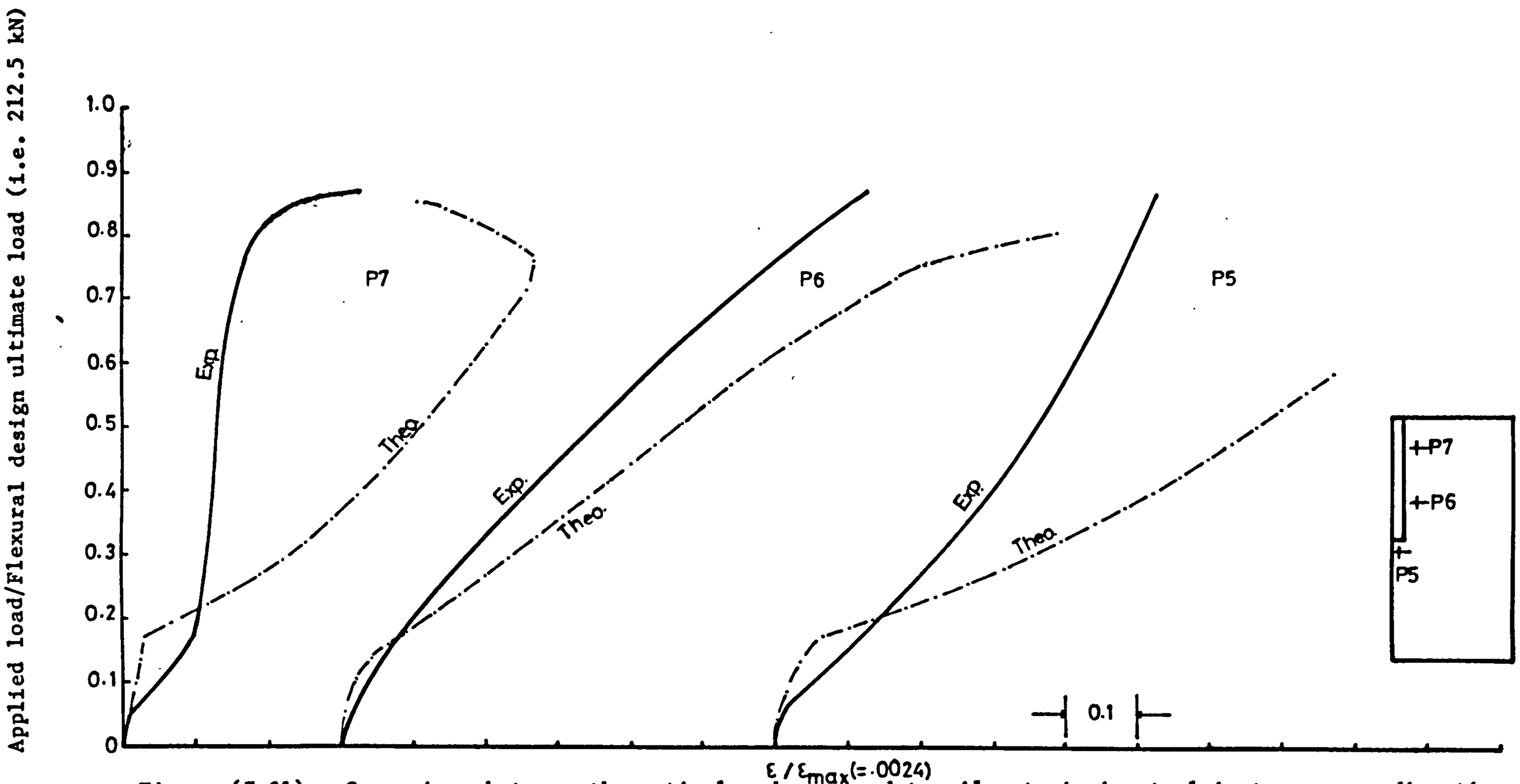

Figure (7.31) : Comparison between theoretical and measured tensile strain in steel in transverse direction at different points along the side of the wall, in the slab of model MT4.

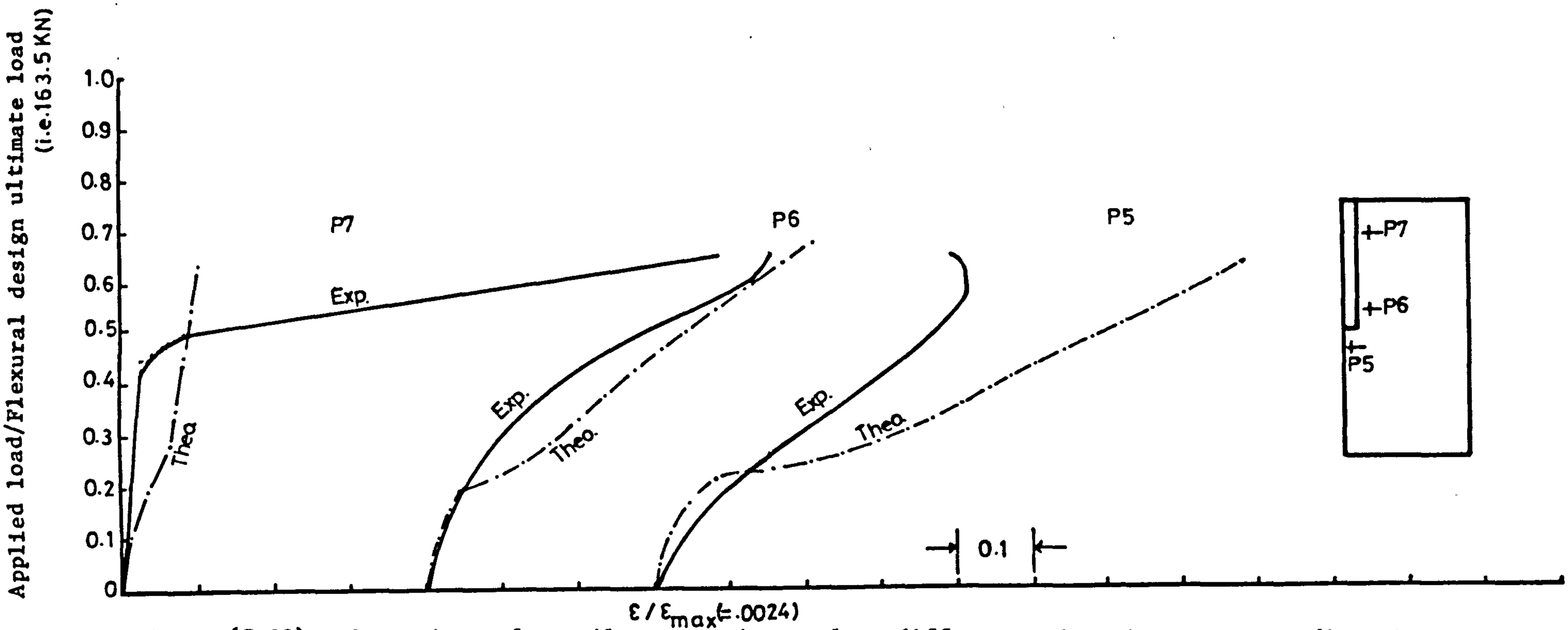

Figure (7.32) : Comparison of tensile strain in steel at different points in transverse direction in the slab of MT6.

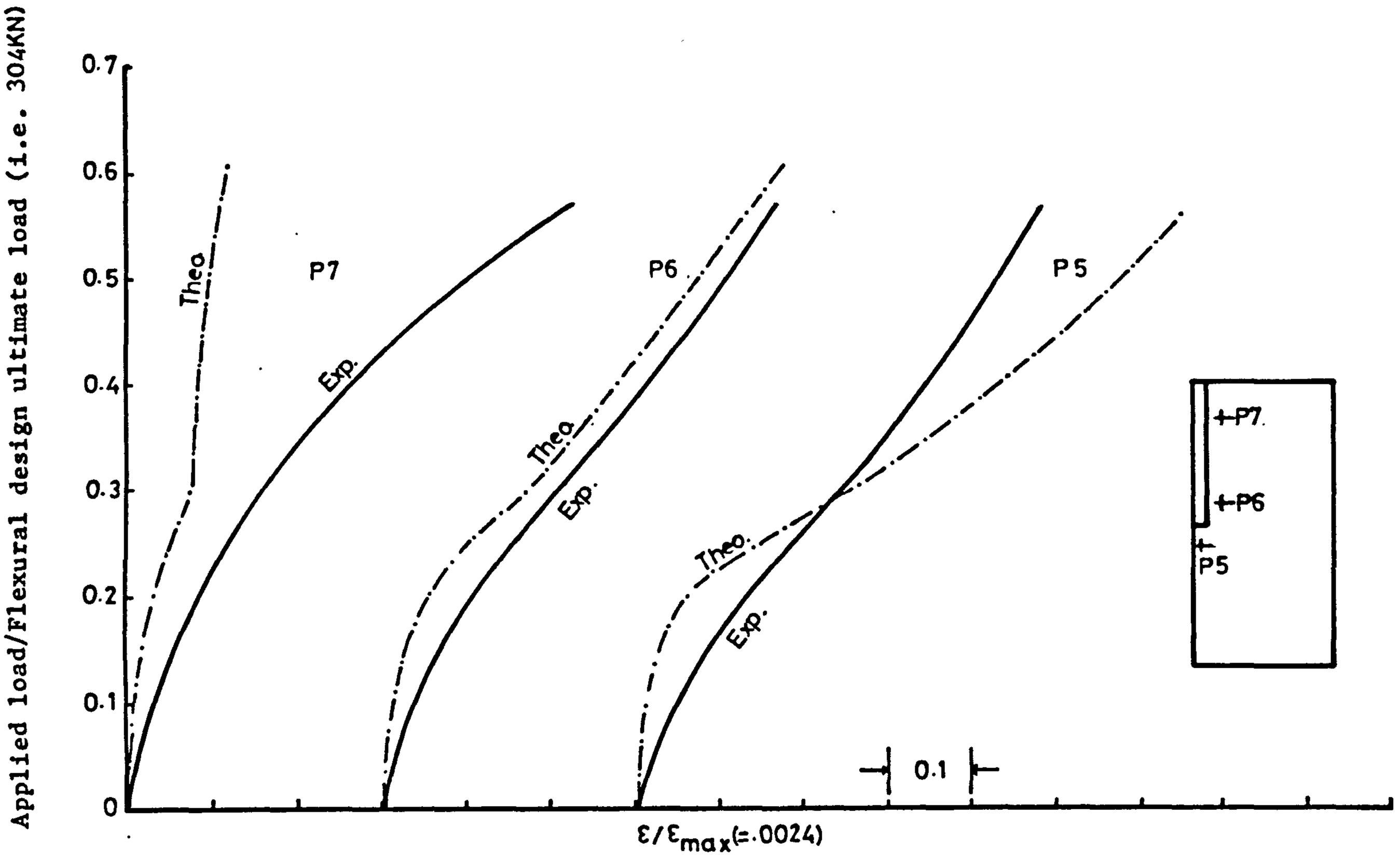

Figure (7.33) : Comparison between theoretical and measured tensile strains in steel in transverse direction at different points along the side of wall, in the slab of model MT7.

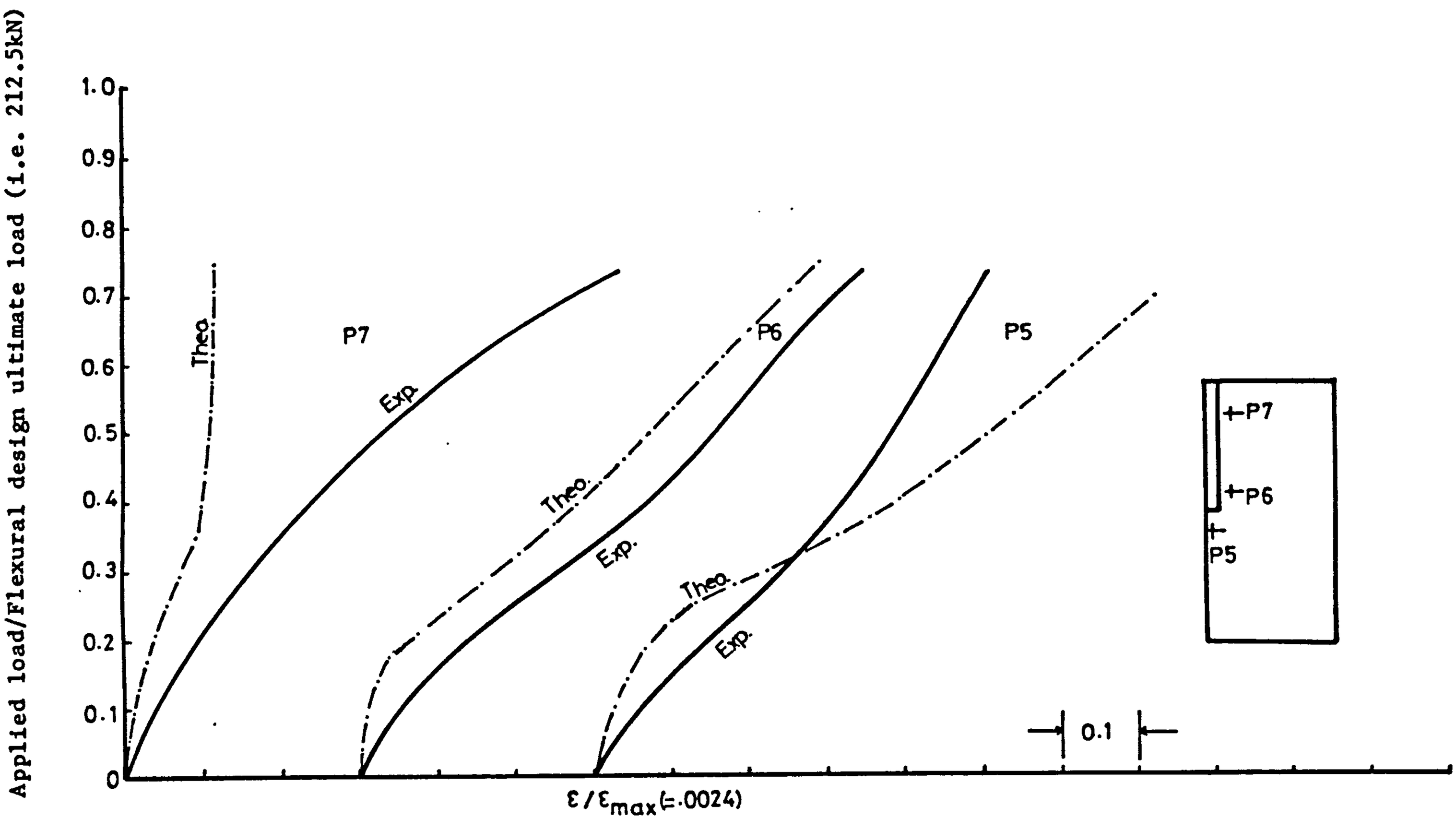

Figure (7.34) : Comparison between theoretical and measured tensile strains in transverse direction at different points, along the side of wall in the slab of model MT8.

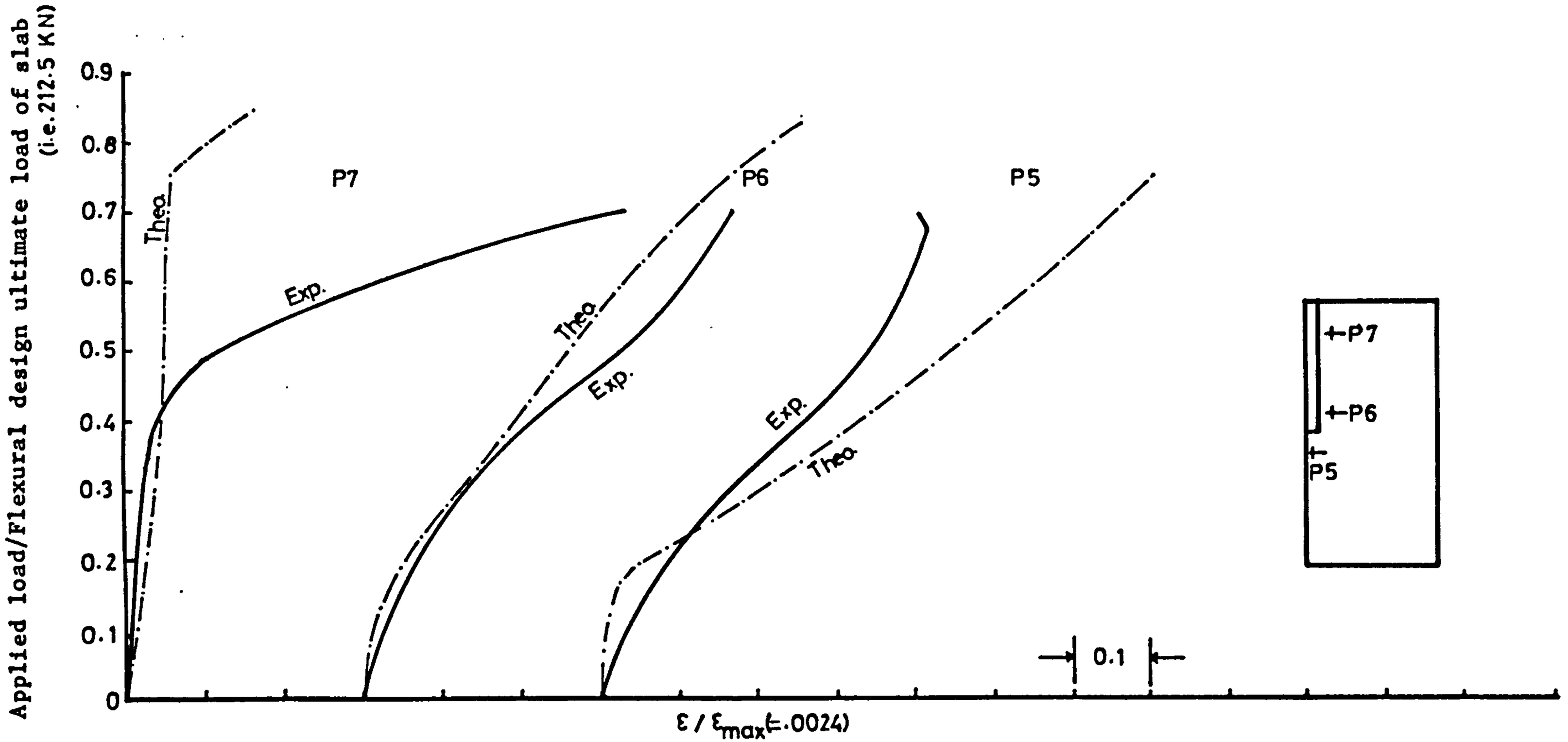

Figure (7.35) : Comparison between theoretical and measured strain in steel at different points in transverse direction in the slab of MT9.

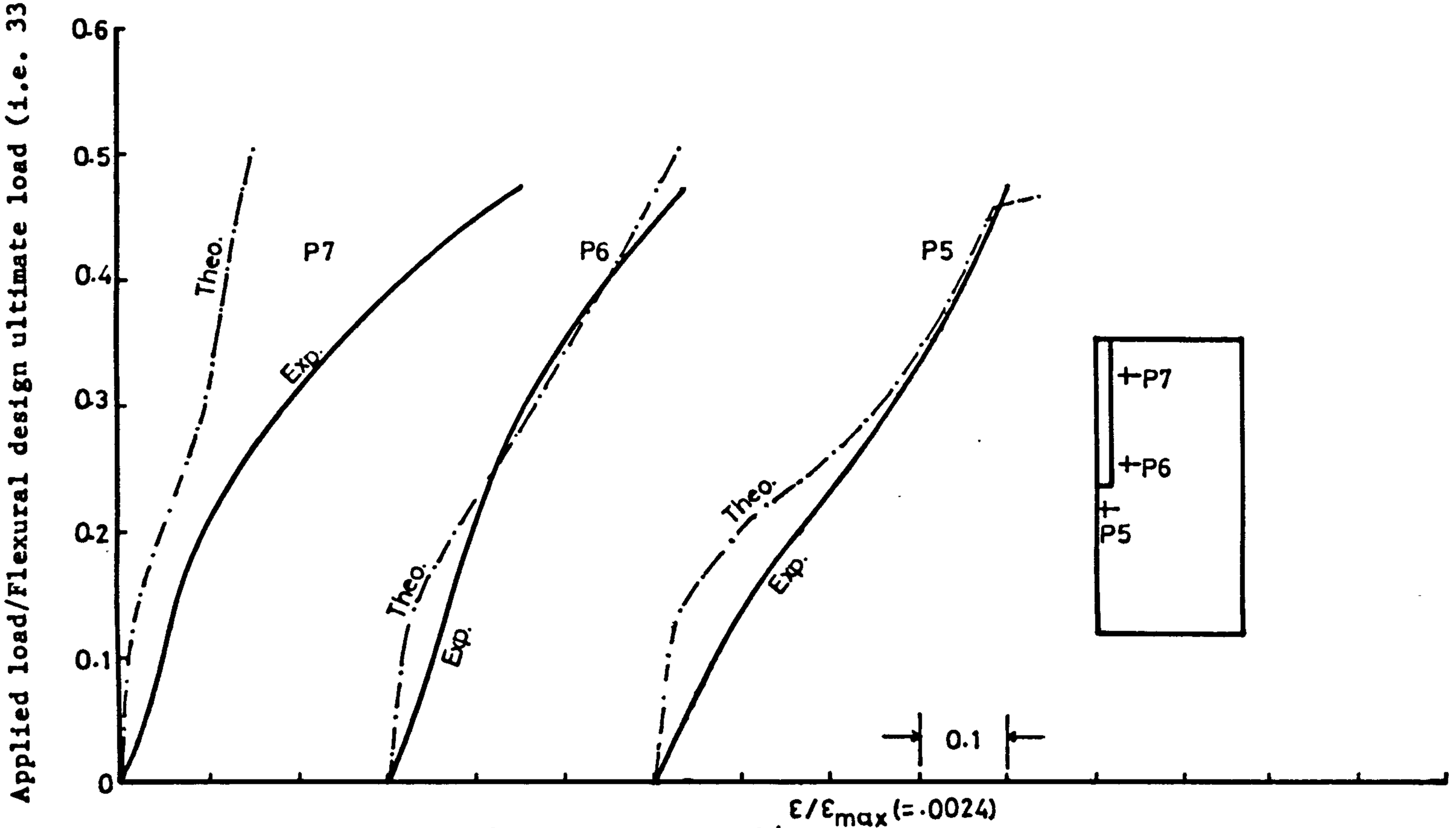

Figure (7.36) : Comparison between theoretical and measured tensile strain in steel in transverse direction at different points along the side of the wall, in the slab of model MT11.

Generally the trend shown by strain in steel is not very much different from the one reported by Hawkins, Bao and Yamazaki (15) in their unpublished paper regarding the experimental and theoretical study of the slab-column connection. A brief review of their work was given in chapter two of this thesis. While comparing the measured strains in steel and concrete, they write, "In general there was reasonable agreement between measured and computed values in the vicinity of the column. Agreement was poorer remote from the column with the analysis predicting strains progressively less than the measured for increasing distances from the column".

7.6 ULTIMATE FLEXURAL LOAD

It was stated in chapter six that the slabs of the models of preliminary test series were not designed using the direct design method but a uniform ratio of steel of 1.03% was provided at the top of the slab in both directions. However the design ultimate load was calculated on the basis of effective width of slab obtained from the design charts produced by Coull & Wong (5). At the design stage the slabs of all the models of the group I, II and III (i.e. MT1 to MT7) were designed for an ultimate moment carrying capacity of 85.0 kN-M along critical section against applied wind-loading in addition to that due to gravity loads using characteristic values of f_{cu} for concrete and measured value of f_y for steel. However the ultimate moment along the transverse critical section for flexure for all the models of main test series was recomputed using the measured values of f_{cu} for concrete and f_y for steel after the models were tested and from it the equivalent ultimate wind loads to be applied along the line of contraflexure were determined. The design ultimate wind/

loads (V_{design}), ultimate loads predicated by finite element nonlinear analysis ($V_{F.E.}$) and the displacement to thickness ratio at which the analysis was stopped are shown in table (7.1). From this table it can be observed that the programme predicts the ultimate loads for the slabs of model PT2 and models of Ist group of main test series (i.e. MT1, MT2 and MT3) with great accuracy. For all the other models except models MT5 and MT9 the ratio of the ultimate wind loads predicted by nonlinear analysis to the design ultimate load is approximately in the range of 82 to 97%.

An average ratio $\frac{V_{design}}{V_{F.E.}} \times 100$ for all models is 94%. Thus it can be concluded that the programme is capable of predicting the flexural ultimate loads for connecting slabs in a shear wall structure.

In general the theoretically predicted ultimate loads are smaller than the design values. The reason for this could be:

(i) As has been shown in previous sections, finite element shows higher concentration of strain in steel and concrete near the inner face of wall. This caused early theoretical yielding of steel and crushing of concrete in this region, consequently leading to earlier failure of this region and lower ultimate loads.

(ii) Since during analysis the thickness of wall was not taken into account, this caused further increase in the concentration of the strains and stresses in the slab around the tip of the wall, leading to lower theoretical ultimate loads. It will be shown later in this chapter that the presence of finite wall thickness in the analysis increases the ultimate load by up to 10% of that with zero wall thickness.

Table 7.1. Comparison of the flexural ultimate loads predicted by finite element method with design ultimate loads.

Model No.	V_{design} kN	$V_{finite\ element}$ kN	$\frac{Displ.}{slab\ thickness}$	$\frac{V_{design}}{V_{F.E.}} \times 100$
PT2	62.0	63.0	.17	102%
MT1	227.4	229.23	.188	101%
MT2	235.7	242.33	.195	103%
MT3	230.0	214.63	.17	93.3%
MT4	222.62	194.24	.164	87%
MT5	219.37	163.0	.138	74.4%
MT6	167.56	158.2	.21	94.4%
MT7	327.5	269.0	.188	82%
MT8	217.54	210.36	.195	97%
MT9	222.0	252.74	.162	114%
MT10	232.71	211.4	.142	91%
MT11	337.56	282.62	.189	84%

Average = 94%

(iii) Nonlinear finite element analysis requires that the load be applied in small increments but to simulate the experimental conditions all the gravity load was applied in the first five increments; this resulted in the prediction of lower ultimate loads for MT4 and MT5 since the gravity load for these models was considerably higher than that of other models.

(iv) It was stated in subsection (7.1.2) of this chapter that different thickness of steel layer both in x and y-direction (which is constant within the element) was assumed for each element depending upon the ratio of steel in the actual model in that particular region of slab. As a typical example Figure (7.37) shows the variation of the steel in y-direction along the transverse critical section AB and the ratio of steel provided in each strip of models of the 1st group. Since the stresses and hence the ratio of steel required vary even within the same element from one sampling point to the other, this could also possibly be one of the reasons of lower theoretical ultimate loads.

7.7 ELASTIC DISTRIBUTION OF SHEAR AT THE WALL PERIPHERY

The elastic distribution of shears due to wind load alone along a section AB parallel to the sides of the wall and along a transverse section BC parallel to the inner face of wall was obtained. For models of Ist group this distribution for a total wind shear of 4.11 kN (corresponding to a uniform displacement of 0.05 mm of line of contraflexure) is shown in Figures (7.38) and (7.39). From Figure (7.38) it can be observed that the wall width has no effect on the distribution of shear Q_y along section BC. However Figure (7.39)

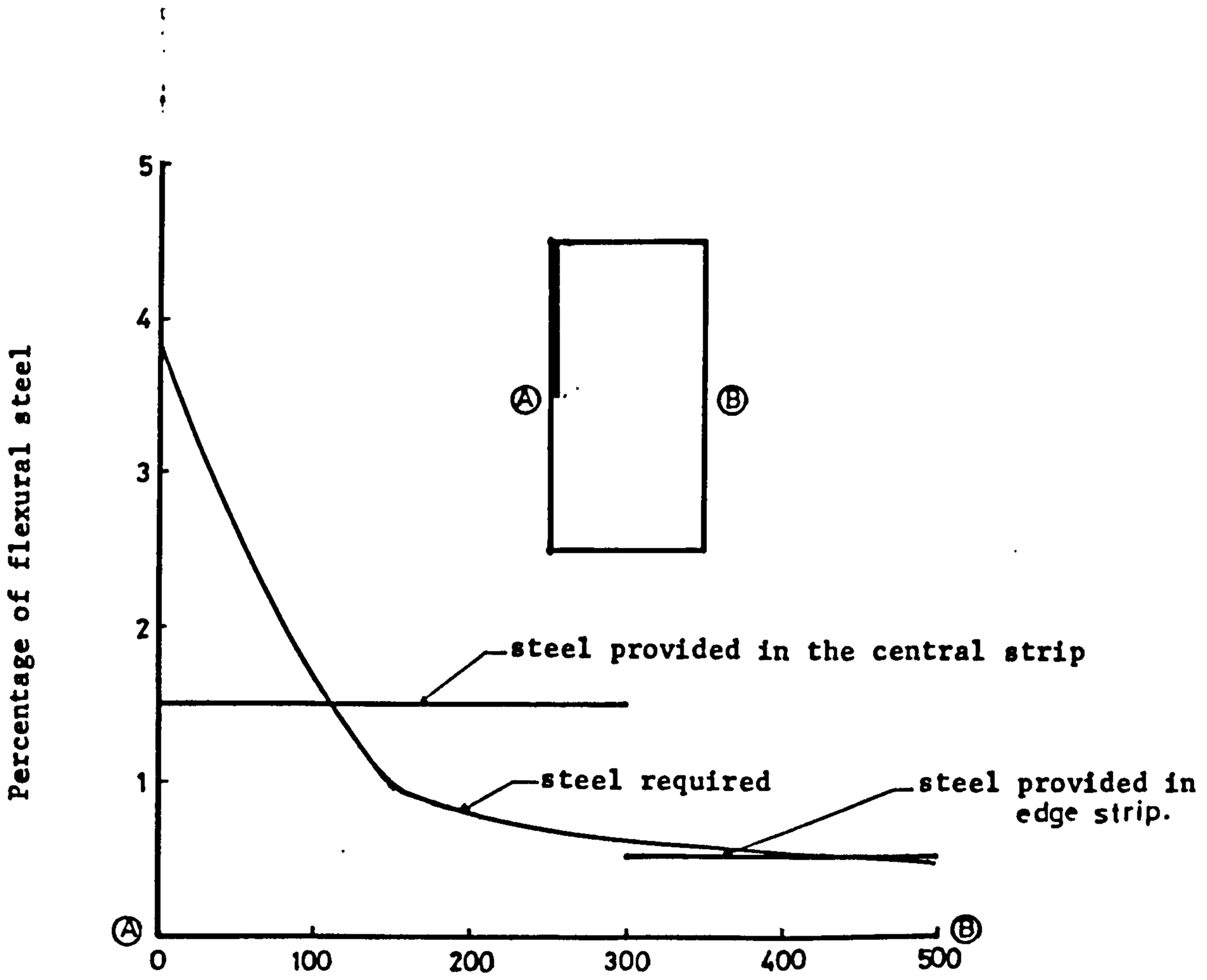

Figure (7.37) : showing the percentage of flexural steel required and percentage of steel actually provided in windward direction along transverse section AB in the slab of model MT1.

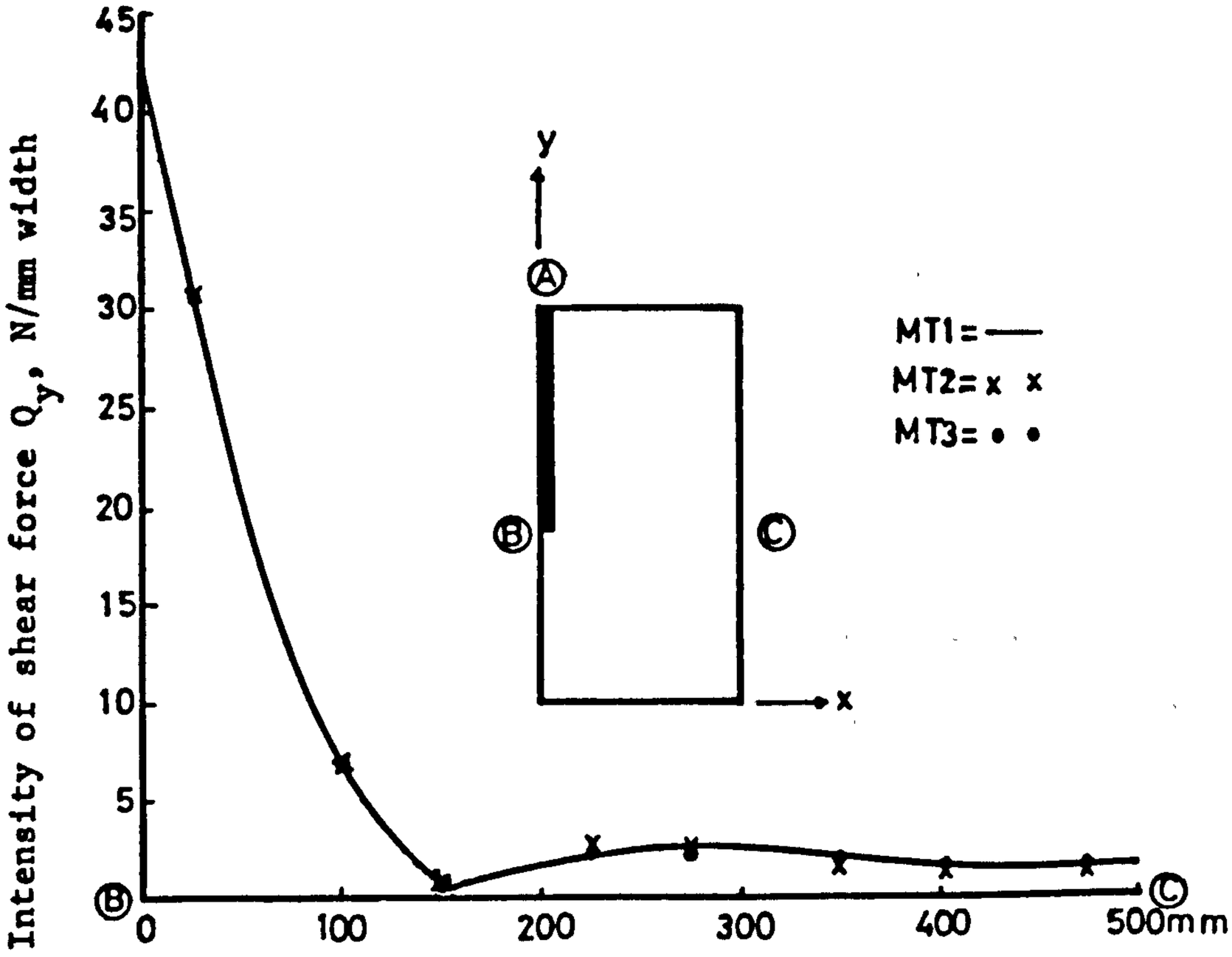

Figure (7.38) : Elastic distribution of shear Q_y along transverse section BC in the slabs of models MT1, MT2 and MT3.

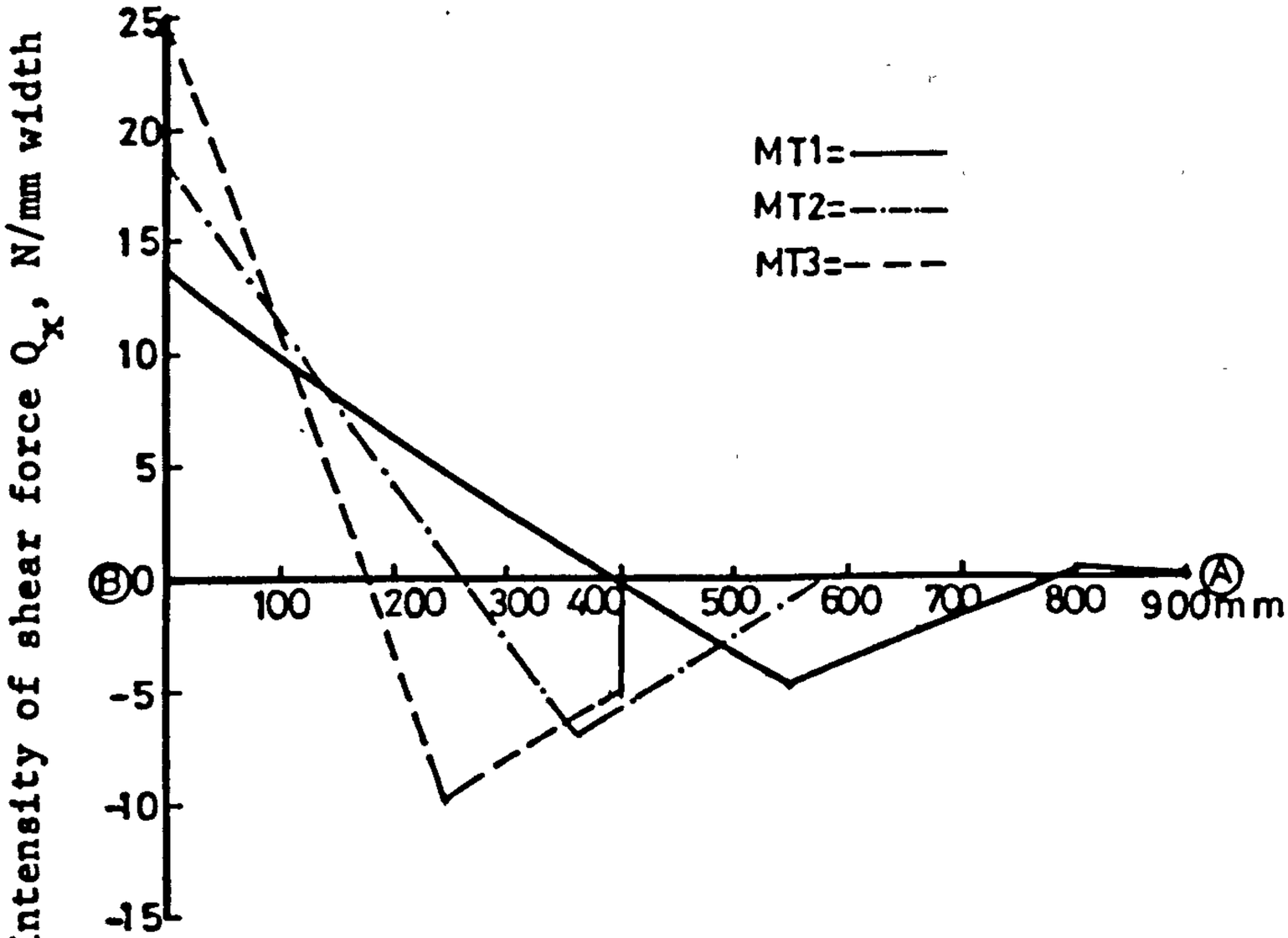

Figure (7.39) : Elastic distribution of shear Q_x along the sides of the wall in the slabs of models MT1, MT2 and MT3.

shows that it has considerable effect on the distribtion of shear Q_x along the sides of the wall (i.e. section AB). The total positive shear Q_x (acting downward) induced along the sides is also affected by the wall length. For model MT2 (with W_w = 600 mm) it is 90% and for MT3 (with W_w = 400 mm) it is 82% of that induced in MT1 (with W_w = 900 mm). The distance from the tip of the wall to the point where shear changes its sign, also changes with the change in wall length but in all the three cases it is approximately .44 of the corresponding wall length. The intensity of shear Q_x at the inner edge of wall is also greatly affected by wall length. For models MT2 and MT3 it is approximately 37% and 80% respectively, more than that of MT1.

The elastic distribution of shear Q_y and Q_x along sections BC and AB for models of IIIrd group i.e. MT3, MT6 and MT7 (due to wind shear of 4.11 kN acting along the line of contraflexure) is shown in Figures (7.40) and (7.41). Though the line of contraflexure is still displaced uniformly but the displacement is different for each model. Although the distribution of both Q_x and Q_y is affected, the effect is more pronounced on the distribution of Q_x along the sides of the wall. Due to the increase in torsion along the sides with the increase of the corridor opening width, the intensity of Q_x at the tip of the wall is the highest for MT6 (with L_w = 520 mm) and lowest for MT7 (with L_w = 280 mm). The intensity of Q_x at this point for models MT3 (with L_w = 400 mm) and MT6 is 22% and 44% respectively higher than that of MT7.

The distribution of Q_y and Q_x for model MT8 is compared with that of MT3 in Figures (7.42) and (7.43). The bay width of MT8 was 1440 mm while that of MT3 it was 1000 mm. It can be seen from the/

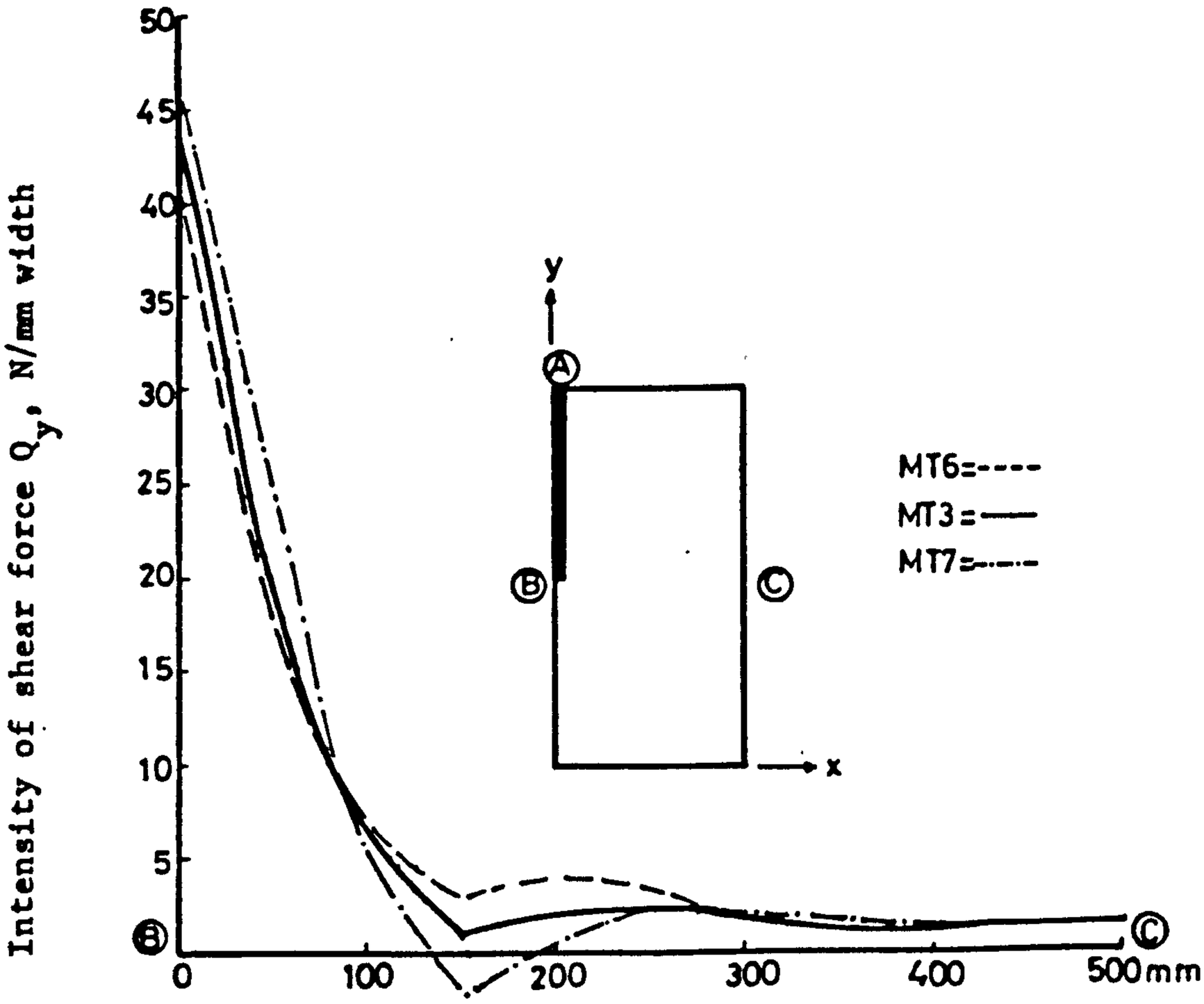

Figure (7.40) : Elastic distribution of shear Q_y along transverse section BC in the slabs of models MT6, MT3 and MT7.

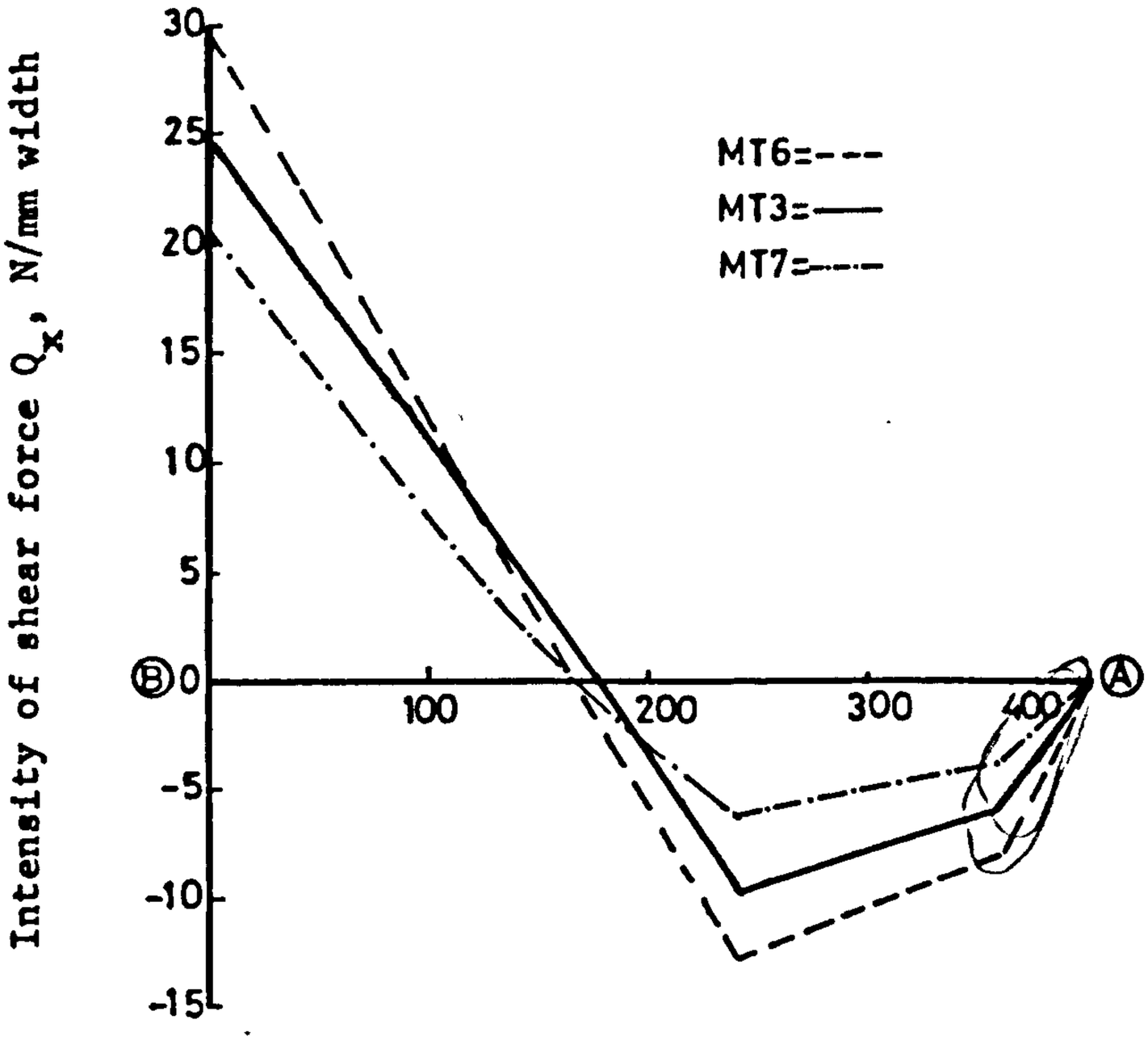

Figure (7.41) : Elastic distribution of shear Q_x along the sides of the wall in the slabs of models MT6, MT3 and MT7.

Figure (7.42) that the effect on the distribution of Q_y is not very much pronounced. But Figure (7.43) shows that the maximum intensity at the tip of the wall and total magnitude of positive shear Q_x induced along the sides of the wall is considerably affected. The intensity of Q_x at the tip of the wall for MT8 is found to be approximately 27% less than that of MT3.

7.8 DISTRIBUTION OF THE SHEAR IN THE POST ELASTIC RANGE

Before discussing the distribution of shear in the post elastic range the method adopted for calculating the shear per unit length (Q_x etc) is discussed with reference to the cantilever shown in Figure (7.44). An overall thickness of slab was assumed to be 100 mm and it was divided in to eight layers as shown in Figure (7.45). An elastic problem was tried first, by applying a small load of 2 kN (Figure (7.44)) and following procedure was adopted to calculate the distribution of shear force Q_x etc.

(i) Referring to Figure (7.46) and from equilibrium considerations

$$Q_x = \int \tau_{xz}\, dz \qquad (7.1)$$

and $$\frac{\partial \tau_{xz}}{\partial z} + \frac{\partial \sigma_x}{\partial x} + \frac{\partial \tau_{xy}}{\partial y} = 0$$

Or approximately

$$\frac{\Delta \tau_{xz}}{\Delta z} + \frac{\Delta \sigma_x}{\Delta x} + \frac{\Delta \tau_{xy}}{\Delta y} = 0$$

Or $$\Delta \tau_{xz} = -\left(\frac{\Delta \sigma_x}{\Delta x} + \frac{\Delta \tau_{xy}}{\Delta y}\right) \Delta z \qquad (7.2)$$

where Δz is the thickness of the layer

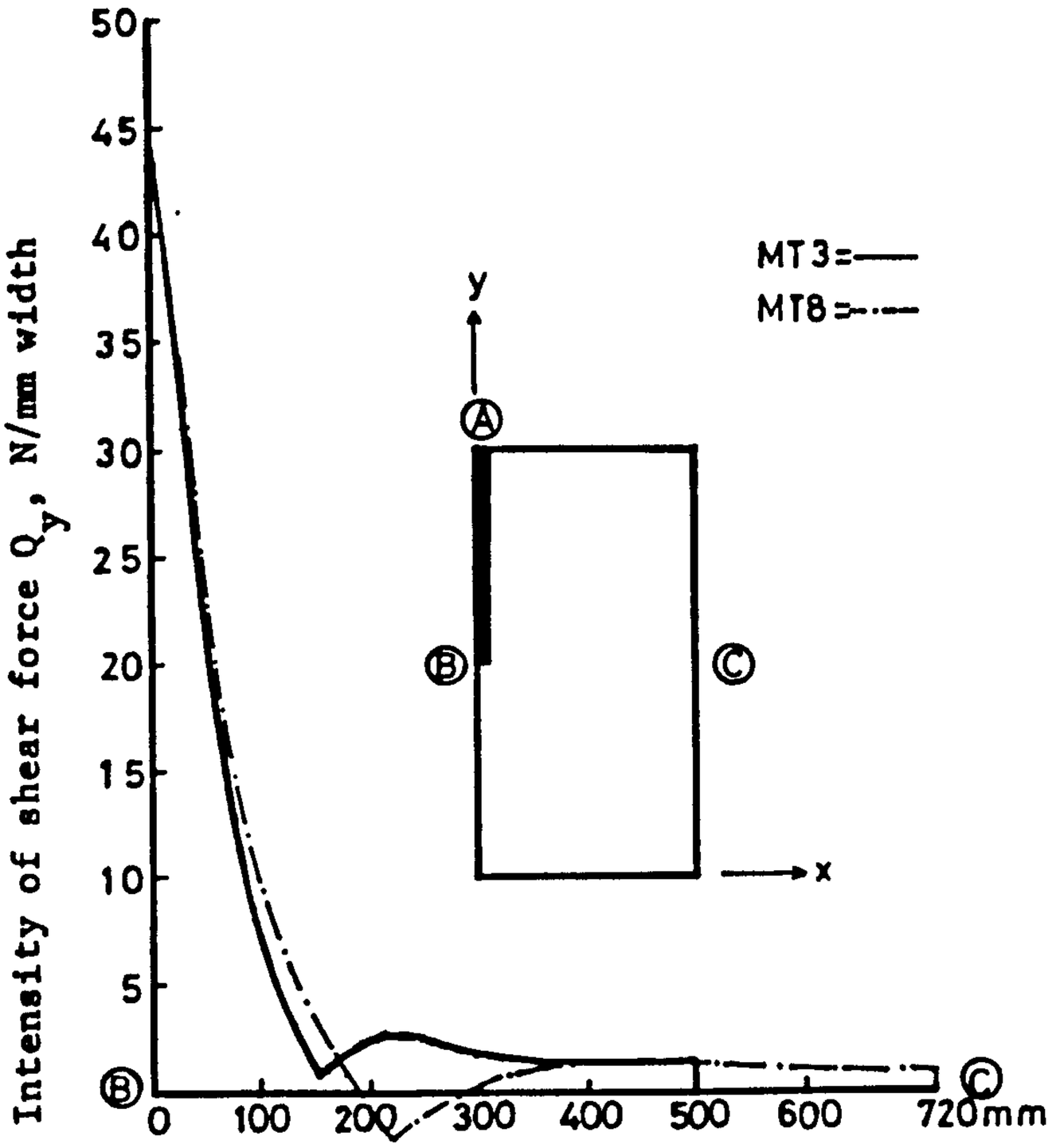

Figure (7.42) : Elastic distribution of shear Q_y along transverse section BC in the slabs of models MT3 and MT8.

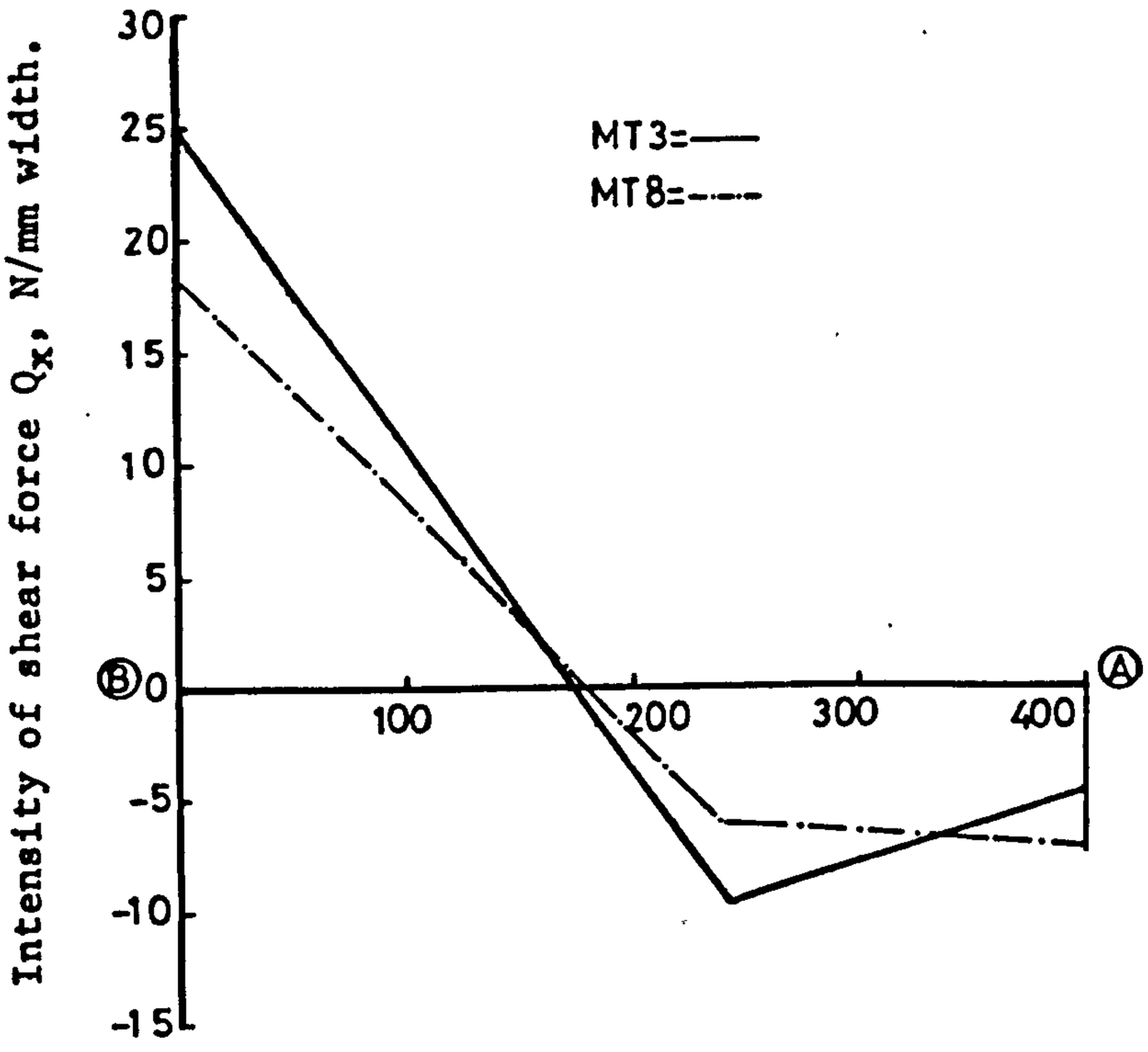

Figure (7.43) : Elastic distribution of shear force Q_x along the sides of the wall in the slabs of models MT3 and MT8.

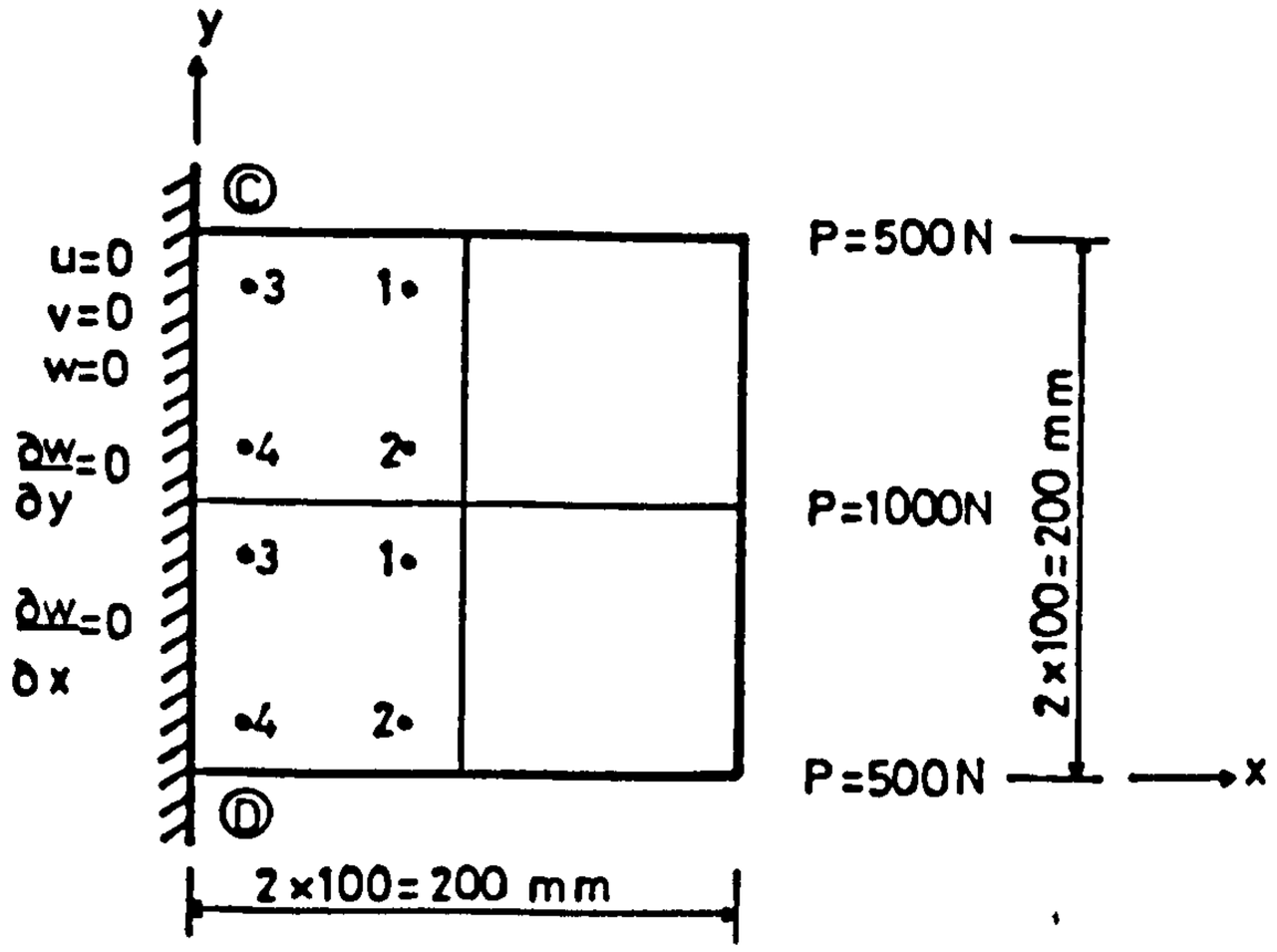

Figure (7.44) : Cantilever slab with mesh boundary conditions and applied loads.

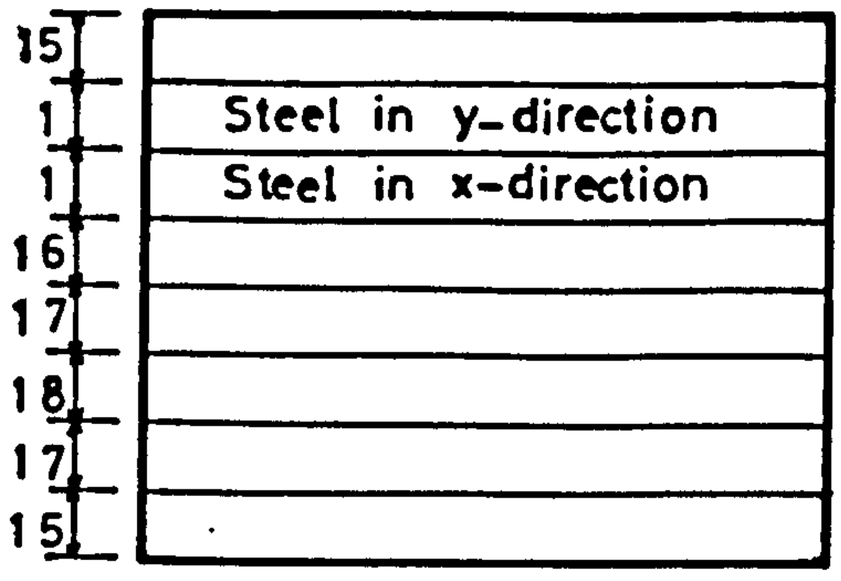

Figure (7.45) : Layer thicknesses for cantilever of Figure (7.44).

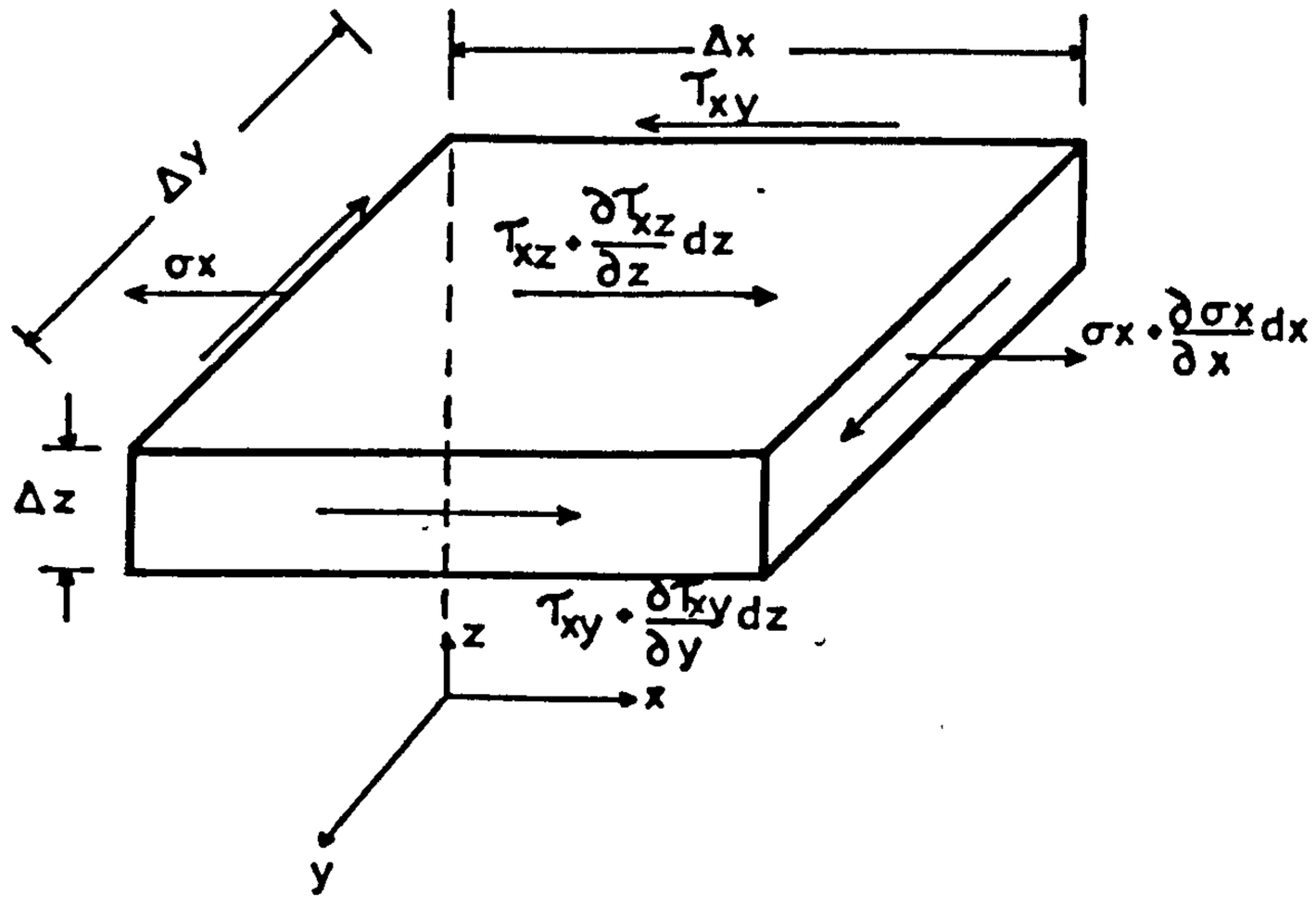

Figure (7.46) : A typical layer under stress field.

Then $\tau_{xz} = -\int_{z}^{h/2} (\frac{\partial \sigma_x}{\partial x} + \frac{\partial \tau_{xy}}{\partial y}) dz$ Or $\int_{-h/2}^{z} (\frac{\partial \sigma_x}{\partial x} + \frac{\partial \tau_{xy}}{\partial y} dz$

(7.3)

Or approximately $\tau_{xz} = -\Sigma(\Delta\tau_{xz})$

The values of $\Delta\tau_{xz}$ at sampling point 4 of element No.1 (Figure (7.44)) calculated using equation (7.2) are presented in table (7.2).

(ii) τ_{xz} for each layer was calculated by performing integration (summation) (a) from top to bottom (i.e. $\tau_{xz} = \int_{z}^{h/2} \Delta\tau_{xz}$) (b) from bottom to top (i.e. $\tau_{xz} = \int_{-h/2}^{z} \Delta\tau_{xz}$) (c) Both from top and bottom to midplane (i.e.) $\tau_{xz} = \int_{z}^{h/2} \Delta\tau_{xz}$ if $z \geq 0$ and $\tau_{xz} = \int_{-h/2}^{z} \Delta\tau_{xz}$ if $z \leq 0$.

τ_{xz} thus calculated for each of the above three cases are shown in Figure (7.47) and the values of τ_{xz} dz in each layer and $\Sigma \tau_{xz} dz$ are presented in Table (7.2).

Similarly Q_x at sampling point 3 of element No. (Figure (7.44)) was also calculated and taking an average value of Q_x for G.P.3 and G.P.4 the total shear transferred along CD was calculated and it was found to be (i) 2.12 kN (ii) 1.54 kN (iii) 2.2 kN, as compared to applied load of 2 kN.

Thus it was concluded that the equilibrium could not be maintained if the summation was carried out from bottom to top.

Table 7.2. $\Delta\tau_{xz}$ and τ_{xz} in different layers of cantilever slab of Figure (7.44) at an applied lof of 2 kN (Elastic range).

layer No.	$\Delta\tau_{xz}$	τ_{xz} (summation from top)	τ_{xz} (summation from bottom)	τ_{xz} (summation from top & bottom)
1	.05866	.05866	-.02789	.05866
2	00	00	00	00
3	.03219	.09085	.03077	.09085
4	.03694	.12779	.06296	.12779
5	.01356	.14135	.0999	.14135
6	-.01448	.12687	.11346	.11345
7	-.0409	.08596	.09898	.09897
8	-.05807	.02789	.05807	.05807
$Q_x = \Sigma \tau_{xz} dz$ =		9.5817	6.9141	10.014

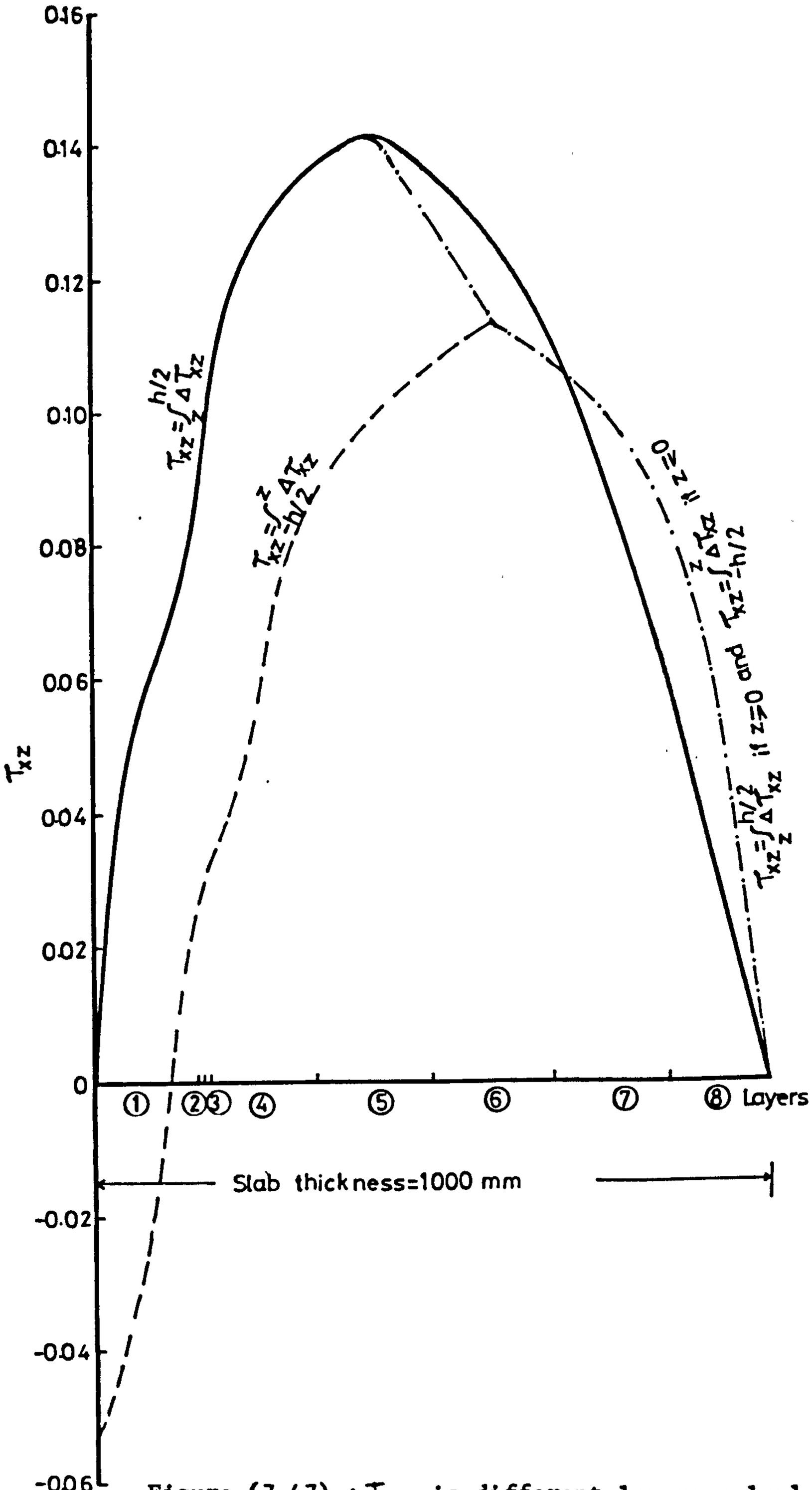

Figure (7.47) : τ_{xz} is different layers calculated by performing integration (a) from top to bottom (b) from bottom to top and (c) both from top and bottom.

The applied load was then incremented and the above procedure was repeated. Table (7.3) shows the values of $\Delta \tau_{xz}$, τ_{xz} and Q_x when the applied load was equal to 25.958 kN. The total shear transferred was found to be (i) 2.29 kN (ii) 48 kN (iii) 28.8 kN.

It was therefore concluded that after cracking the equilibrium between the applied load and induced shear could be maintained only when integration was performed both from top and bottom to the mid plane.

In fact a very large number of cases was studied and in the non-linear range the equilibrium between the applied and induced shear was achieved only when integration was performed from top and bottom to the mid plane. Therefore for all the models this form of integration was adopted in determining the values of Q_x and Q_y.

Figure (7.48) shows the distribution of shear Q_y along transverse section BC passing through the slab at the inner edge of wall for model MT1. From this figure it can be observed that the curve is very steep in the vicinity of the wall up to a load of about 80% of the experimental ultimate load but with further increase of load redistribution of stresses takes place and the curve flattens. Away from the wall region the effect of nonlinearity is insignificant.

Figure (7.49) shows the distribution of shear Q_x in the slab of the same model (i.e. MT1) along the sides of the wall (section AB). It is obvious from this figure that the redistribution of shear takes place along the sides of the wall too. However the/

Table 7.3. $\Delta\tau_{xz}$ and τ_{xz} in different layers of cantilever slab of Figure (7.44) at an applied load of 25.958 kN. (Nonlinear range).

layer No.	$\Delta\tau_{xz}$	τ_{xz} (summation from top)	τ_{xz} (summation from bottom)	τ_{xz} (summation from top & bottom)
1	00	00	-1.7392	00
2	00	00	00	00
3	.7938	.7938	-1.7392	.7938
4	00	.7938	-2.533	.7938
5	00	.7938	-2.533	-2.533
6	00	.7938	-2.533	-2.533
7	-1.046	-.2522	-2.533	-2.533
8	-1.487	-1.7392	-1.487	-1.487
$Q_x = \sum \tau_{xz} dz$ =		10.902	222.376	137.95

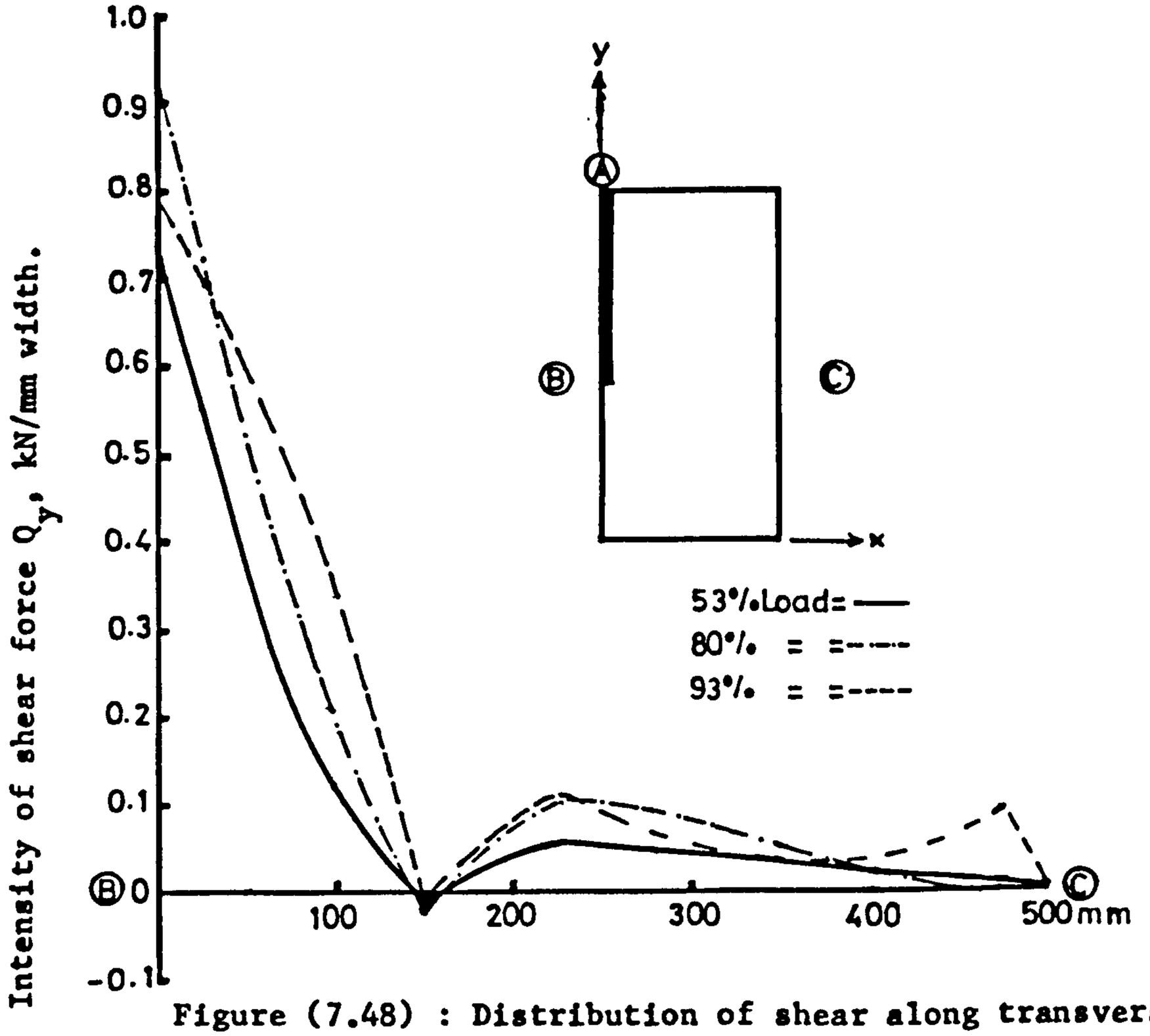

Figure (7.48) : Distribution of shear along transverse section BC at different stages of loading, in the slab of model MT1.

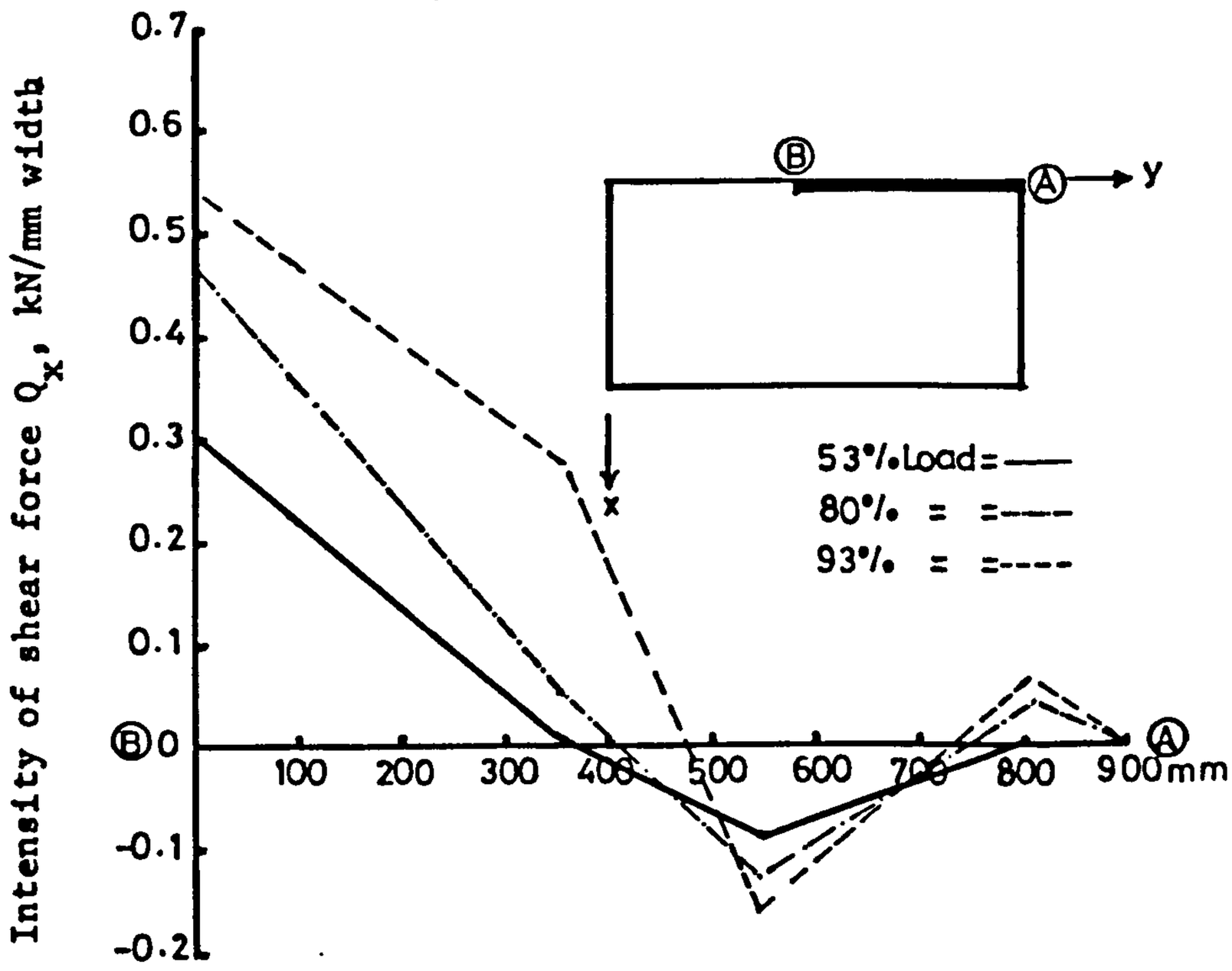

Figure (7.49) : Distribution of shear Q_x along the sides of the wall in the slab of model MT1.

point where shear changes its sign, from the inner face of wall is only slightly affected by this redistribution.

To get some idea about the effective length of the critical perimeter along the sides of the wall, it is probably of more importance to study the distribution of the maximum shear stress along the sides of the wall when the applied theoretical wind load is equal to the experimental ultimate load. This distribution for all the models except MT4 and MT5 is shown in Figures (7.50) to (7.58).

Since strains, stresses etc. were largely overestimated in models MT4 and MT5, the yielding of steel and crushing of concrete occurred well before the applied wind load was equal to the experimental ultimate load. By the time theoretical wind load reached the experimental ultimate value, the induced vertical stresses around the inner edge of wall dropped to zero. Therefore the distribution of shear for these models is not presented here.

7.9 MAXIMUM SHEAR STRESS BY NONLINEAR ANALYSIS

In this section for each model theoretical average shear stress v_{ui}, induced along the critical section at the tip of the wall predicted by the finite element analysis when the theoretical wind load was equal to the experimental ultimate load, is compared with the critical shear stress v_c calculated by using ACI318 formula, viz. $v_c = .33\sqrt{f'_c}$ N/mm^2 (where f'_c is the cylinder crushing strength of concrete.

In the light of the cracking patterns of the models tested, the critical section is assumed to be located at a distance $\frac{d}{2}$ from wall periphery. From the distribution of the shear stress, obtained from the nonlinear analysis, it was observed that due to combined effect of torsion and direct shear, in some cases the shear stress induced along the sides of the wall in the immediate vicinity of the inner face was even higher than the average shear stress at the inner face of critical section. However it may be assumed that before failure some redistribution between this region and inner face will take place and therefore the induced shear stress is averaged at all the three sampling points (i.e. two at the inner face and one along the side of the wall as shown in Figure (7.59)). This shear stress is called v_{ui}.

Table (7.4) shows the comparision between v_{ui} and $v_c(=.33\sqrt{f'_c})$. For all the models of main test series except MT4 and MT5. For calculation purpose the cylinder compressive strength of concrete was taken as 0.8 of the cube crushing stress of the concrete on the day the model was tested. As discussed earlier in this chapter, the shear stress near the inner edge of wall in models MT4 and MT5 was reduced to zero before the theoretically applied wind load reached the experimental ultimate load. Therefore its comparison with v_c could not be presented.

From among the models of preliminary test series only PT2 was analysed. During experiment the strain in steel or concrete along the sides of the wall was not measured. Therefore it was not possible to know whether finite element analysis predicts them satisfactorily or not. However it was observed that shear stress/

at the first sampling point along the side of the wall was reduced to zero before the theoretical load was equal to the experimental ultimate load. Therefore comparison of v_{ui} with v_c for this model could not be presented either.

From the table (7.4) it can be observed that a fairly constant ratio of $\frac{v_{ui}}{v_c}$ is obtained for models of Ist and IVth group of main test series with an average of 2.29.

The ratio $\frac{v_{ui}}{v_c}$ for models of IIIrd group shows that with the increase in corridor opening width there is corresponding decrease in the ratio $\frac{v_{ui}}{v_c}$.

The values of v_c calculated from $.33\sqrt{f'_c}$ are insensitive to the ratio of flexural steel. In practice the ratio of steel affects the value of v_c to some extent. This fact is reflected by the ratio $\frac{v_{ui}}{v_c}$ for the models of Vth and VIth group as well. It can be observed that with the increase in steel ratio, v_{ui}/v_c also shows higher values. The curve showing the ratio $\frac{v_{ui}}{v_c}$ versus the ratio of flexural steel in the central strip of slab of the models of group VI of the main test series is shown in Figure (7.60).

Taking value of v_{ui} from Table (7.4) as the ultimate value for the respective models, the portion of curves in Figures (7.50) to (7.58), showing positive shear is idealized and the equivalent effective length of critical perimeter along the sides of the wall is evaluated. Since except models MT1 (with W_w = 900 mm) and MT2 (W_w = 600 mm) the wall width of all the other models was same (i.e. W_w = 400 mm), the equivalent effective length for all the/

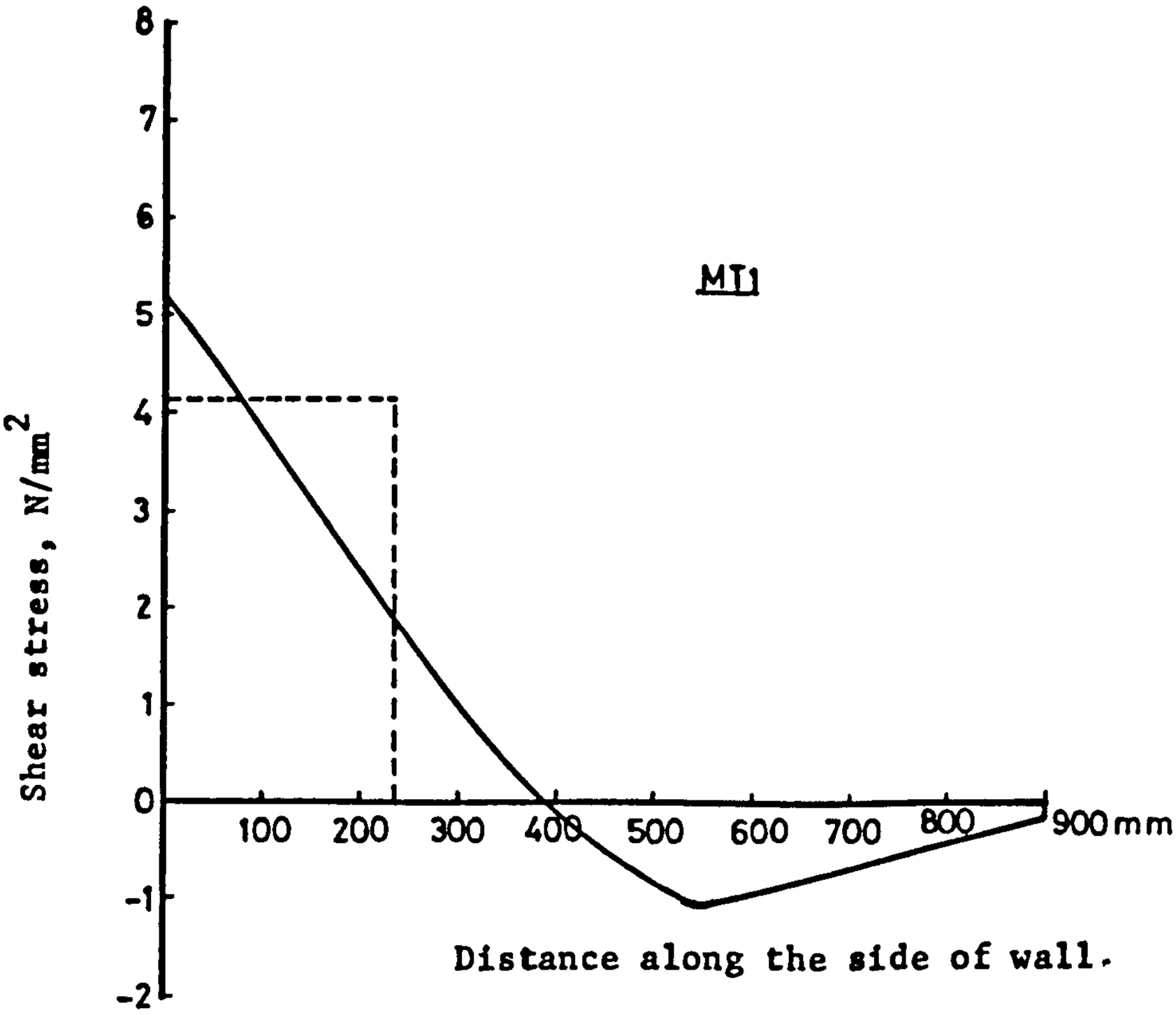

Figure (7.50) : Variation of shear stress along the sides of wall, in the slab of model MT1 at theoretical load equal to the experimental load at failure.

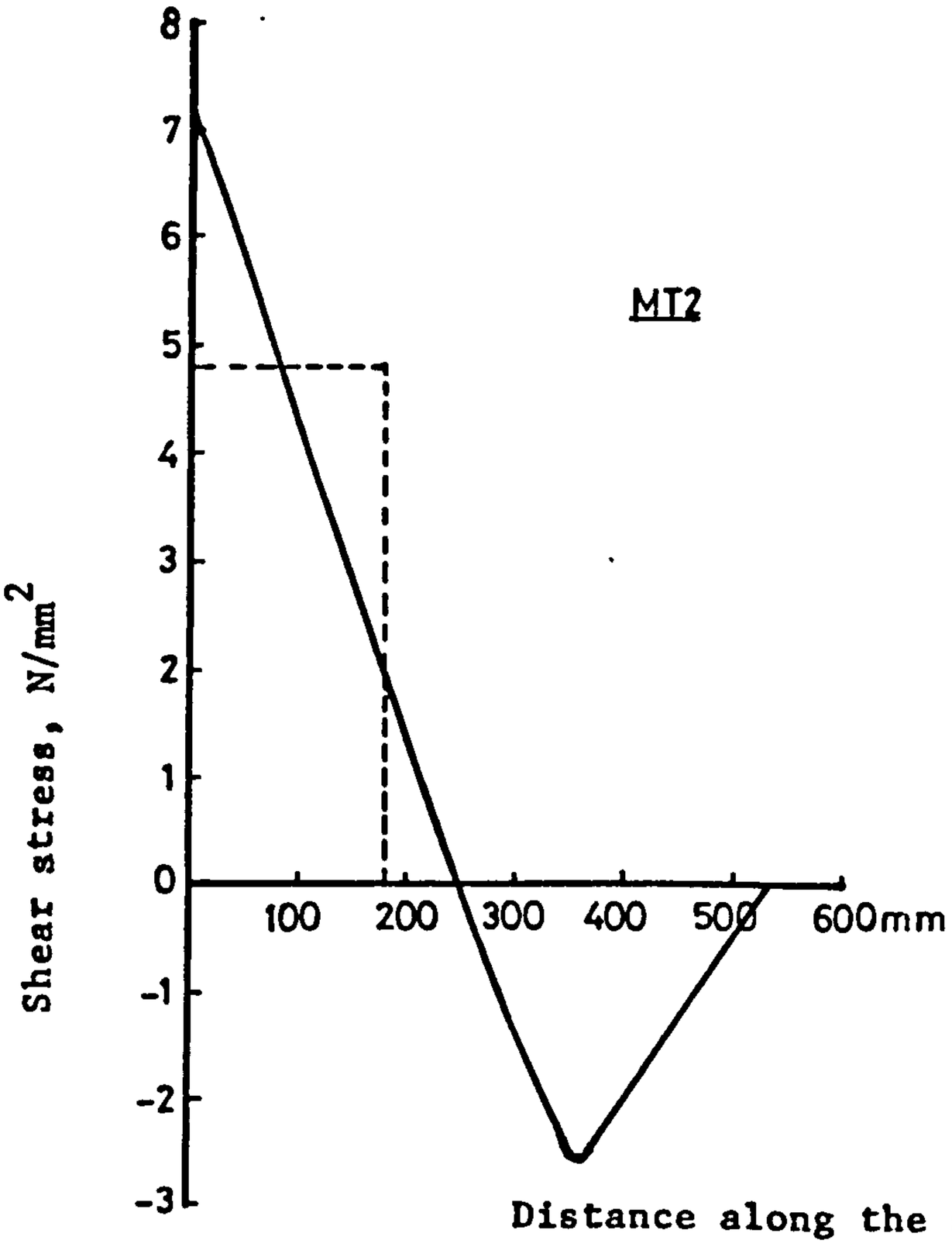

Figure (7.51) : Variation of shear stress along the sides of wall, in the slab of model MT2 at theoretical load equal to the experimental load at failure.

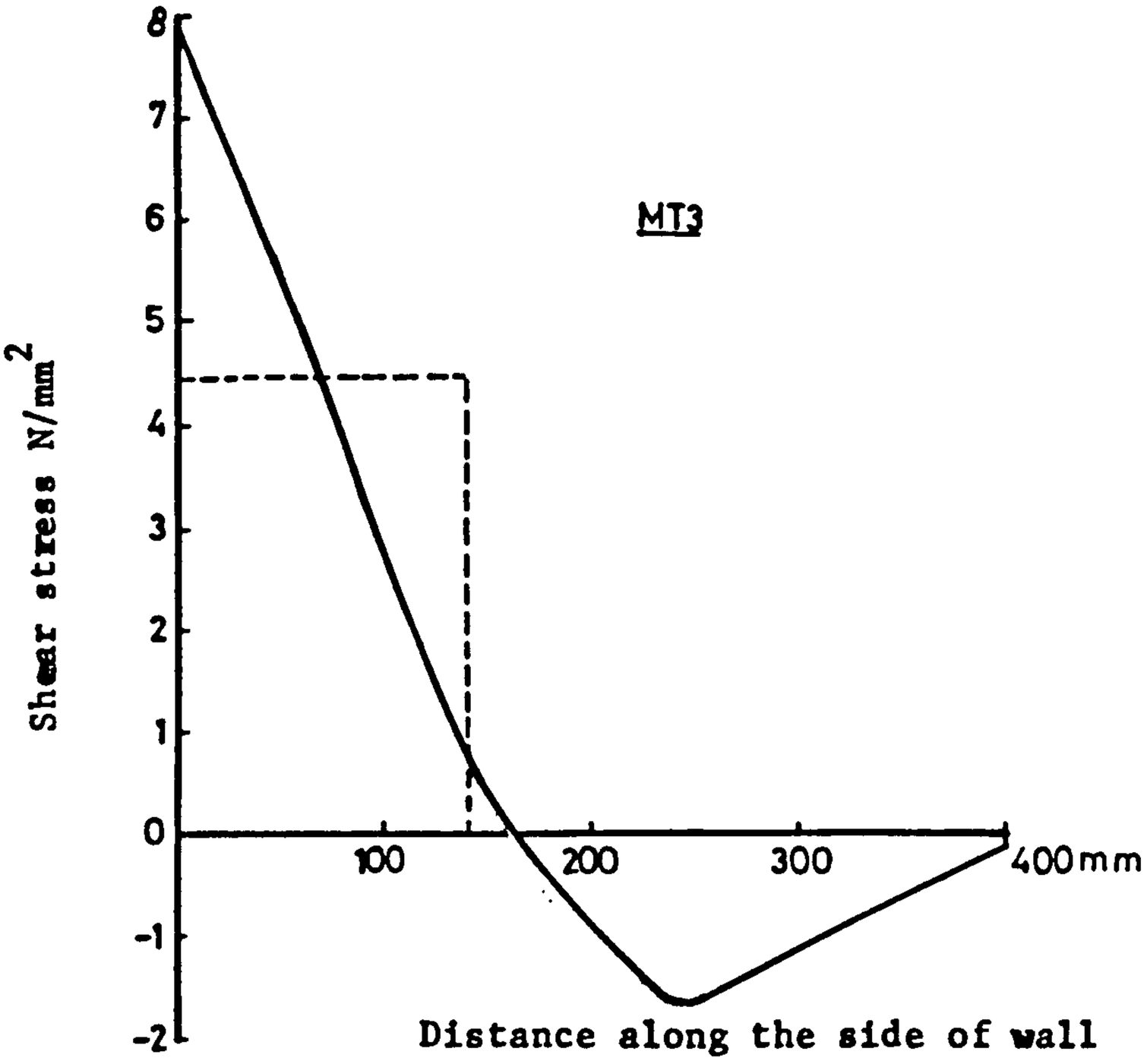

Figure (7.52) : Variation of shear stress along the sides of wall, in the slab of model MT3 at theoretical load equal to the experimental load at failure.

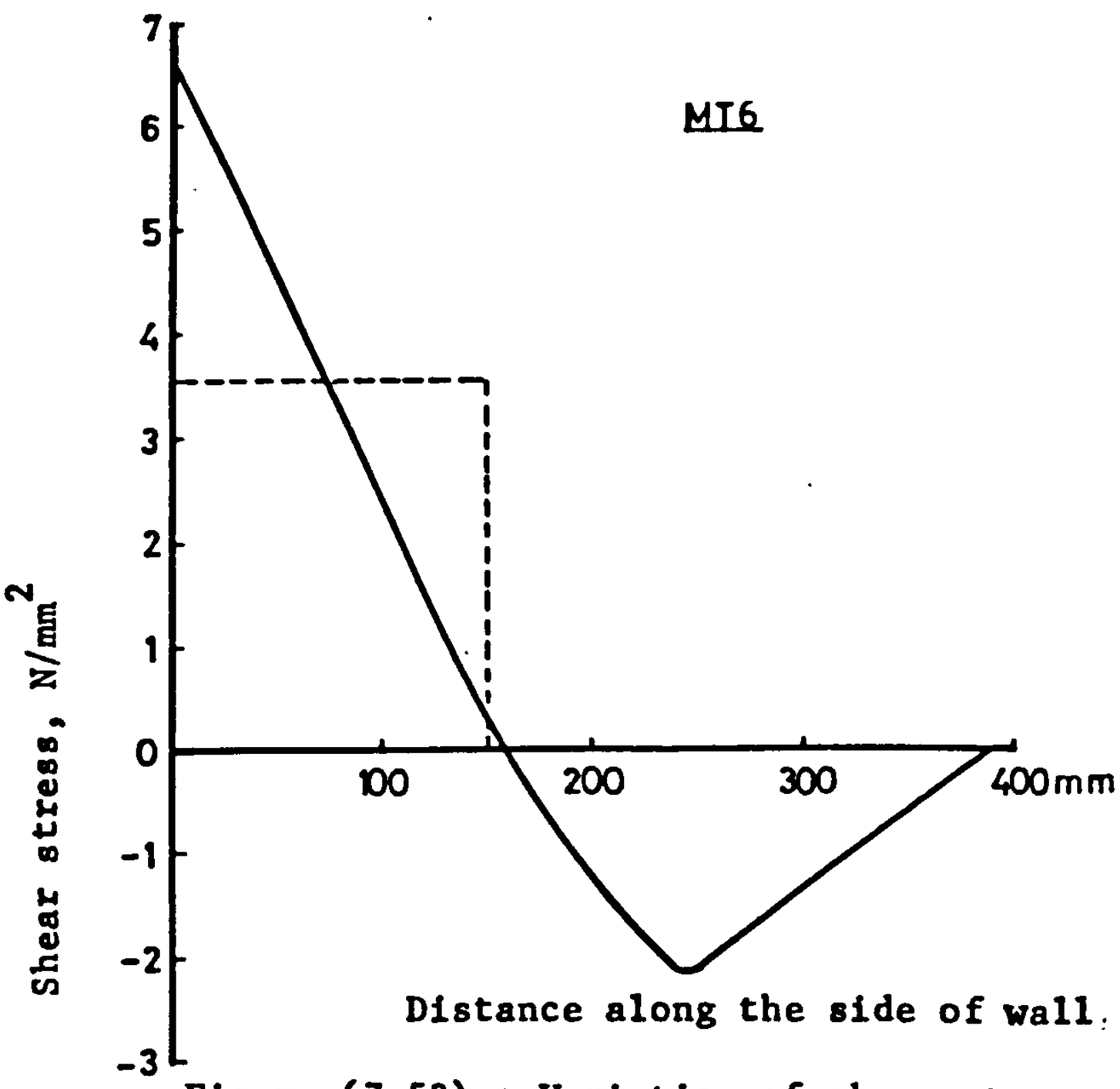

Figure (7.53) : Variation of shear stress along the sides of wall, in the slab of model MT6 at theoretical load equal to the experimental load at failure.

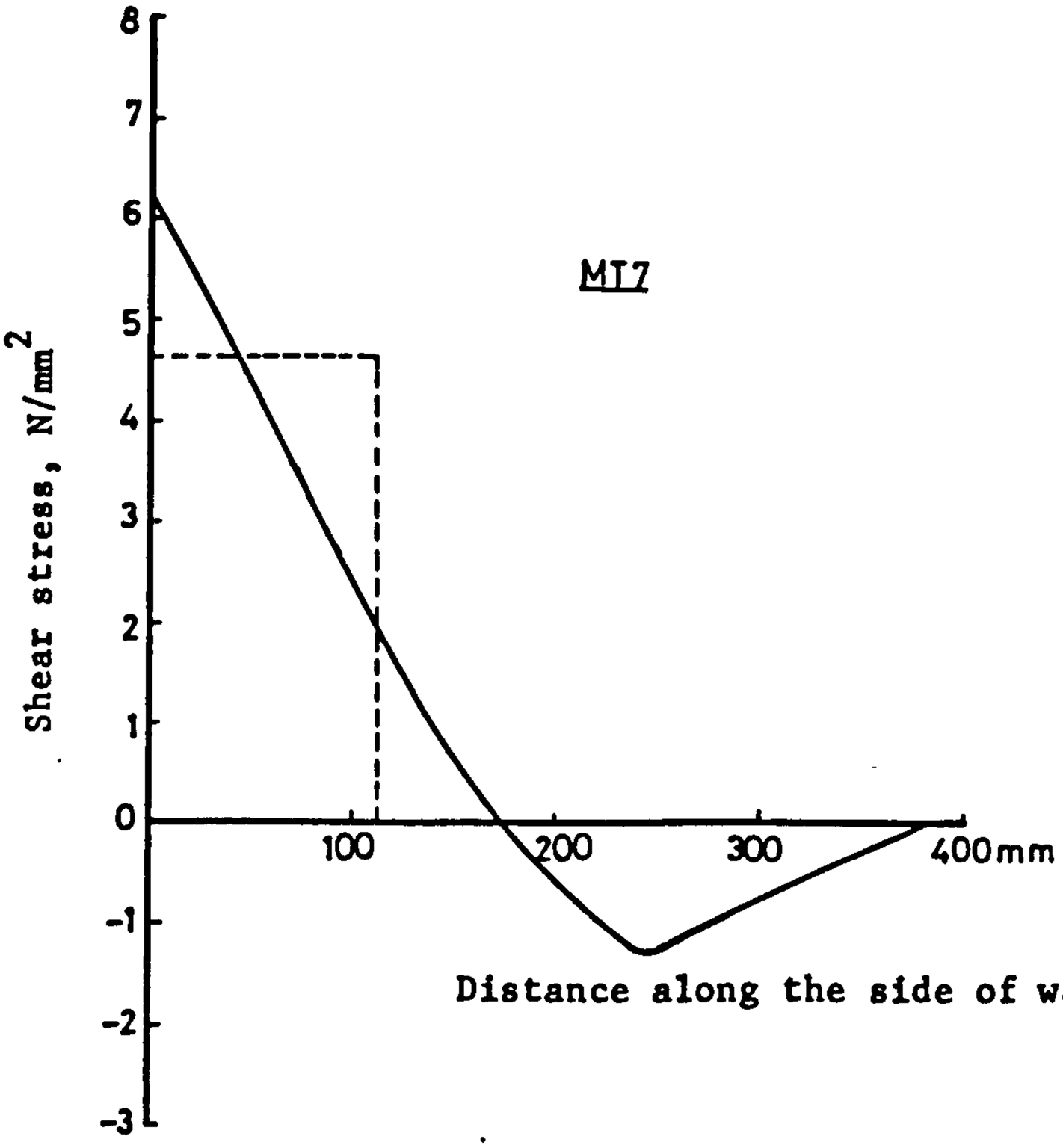

Figure (7.54) : Variation of shear stress along the sides of wall, in the slab of MT7 at theoretical load equal to the experimental load at failure.

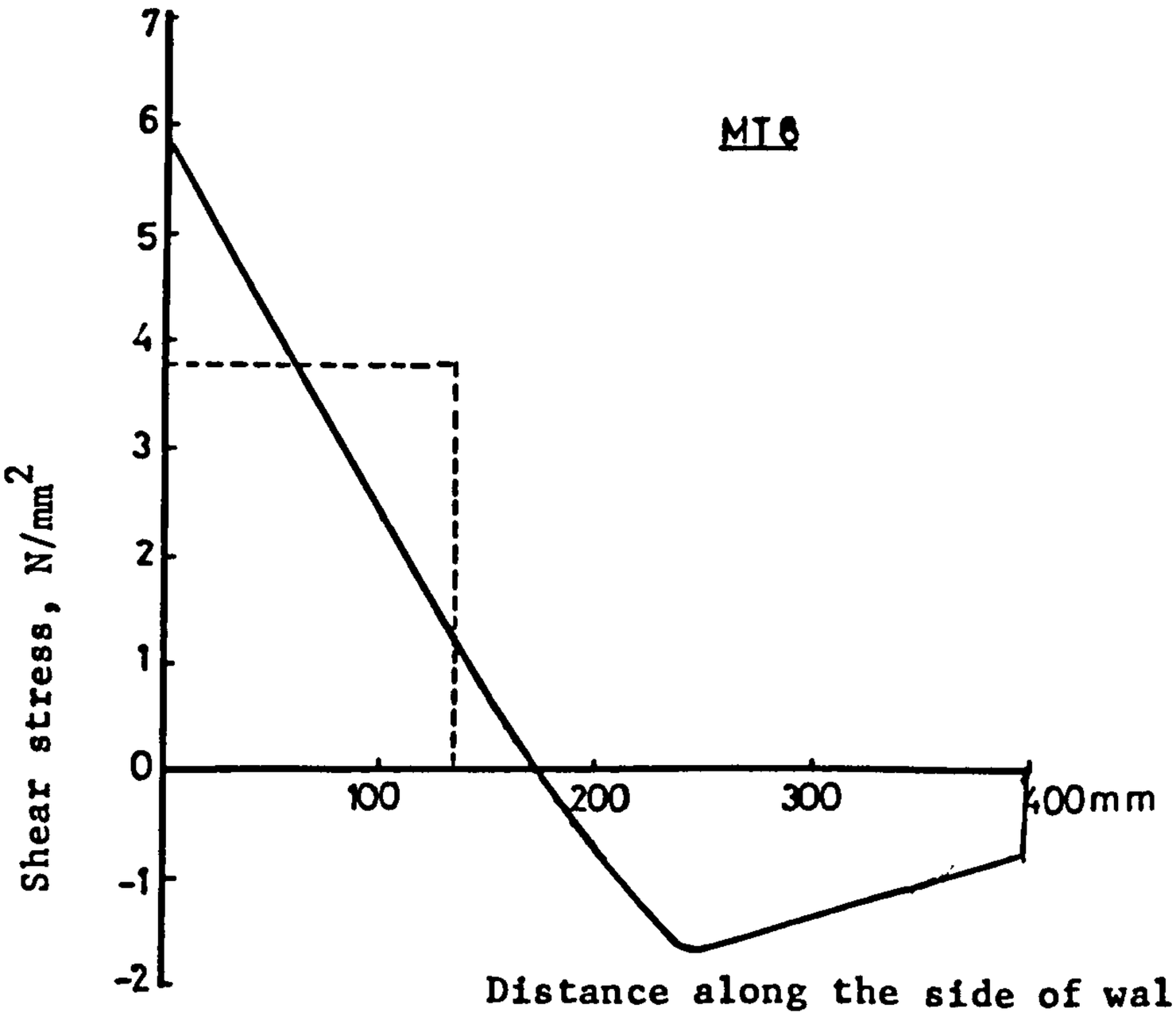

Figure (7.55) : Variation of shear stress along the sides of wall in the slab of MT8 at theoretical load equal to the experimental load at failure.

MT9

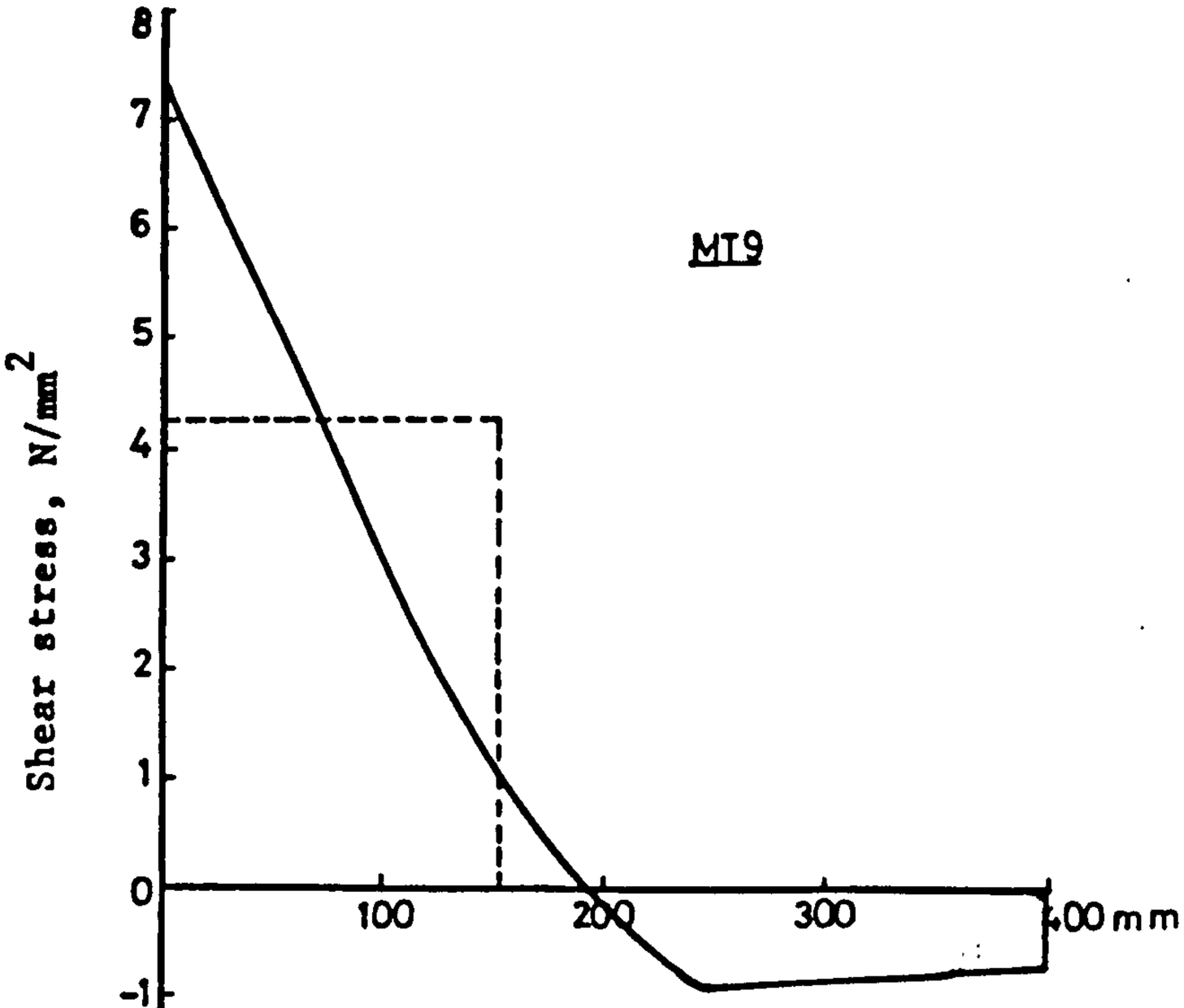

Figure (7.56) : Variation of shear stress along the sides of wall, in the slab of MT9 at theoretical load equal to the experimental load at failure.

MT10

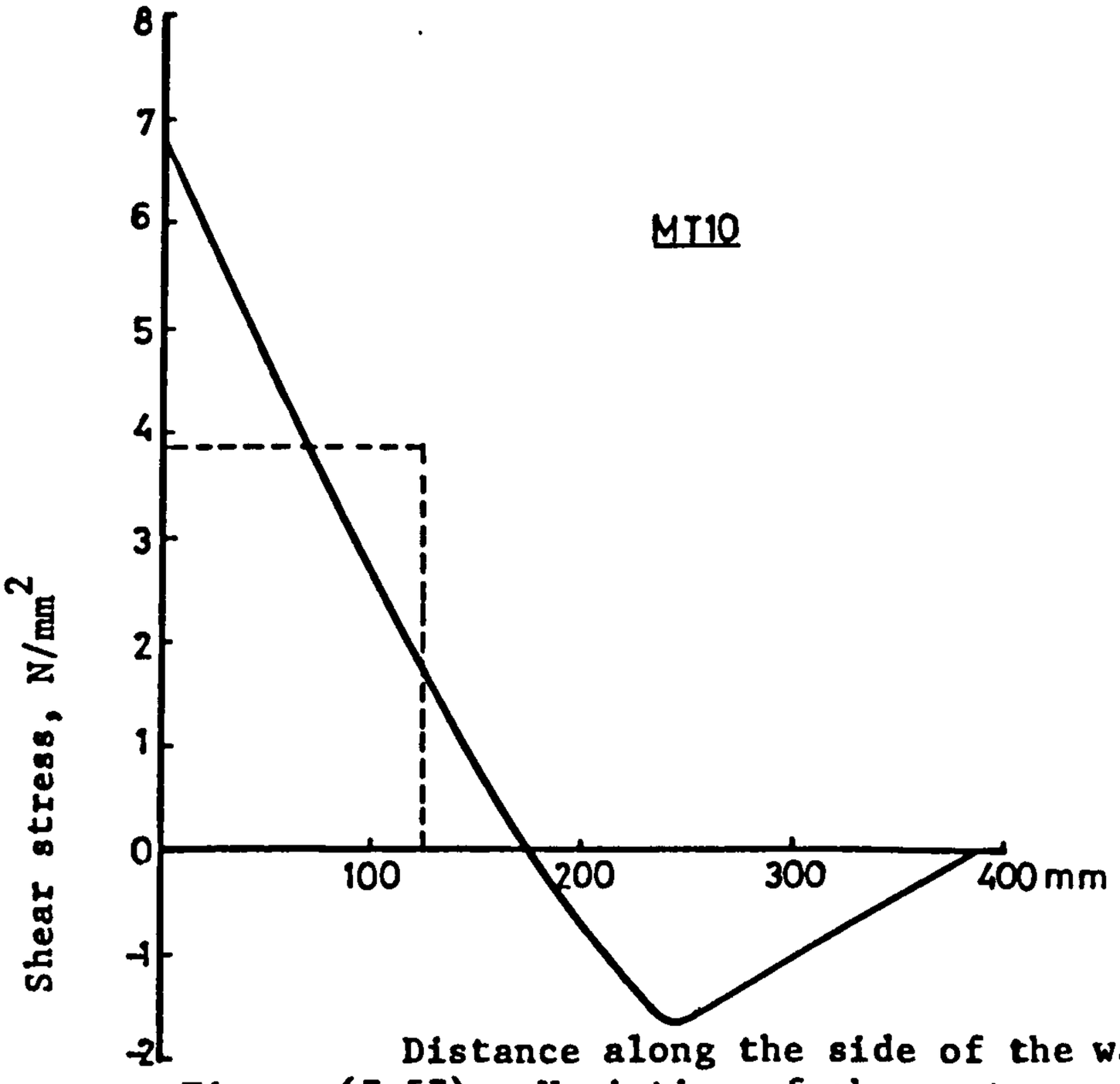

Figure (7.57) : Variation of shear stress along the sides of wall in the slab of MT10 at theoretical load equal to the experimental load at failure.

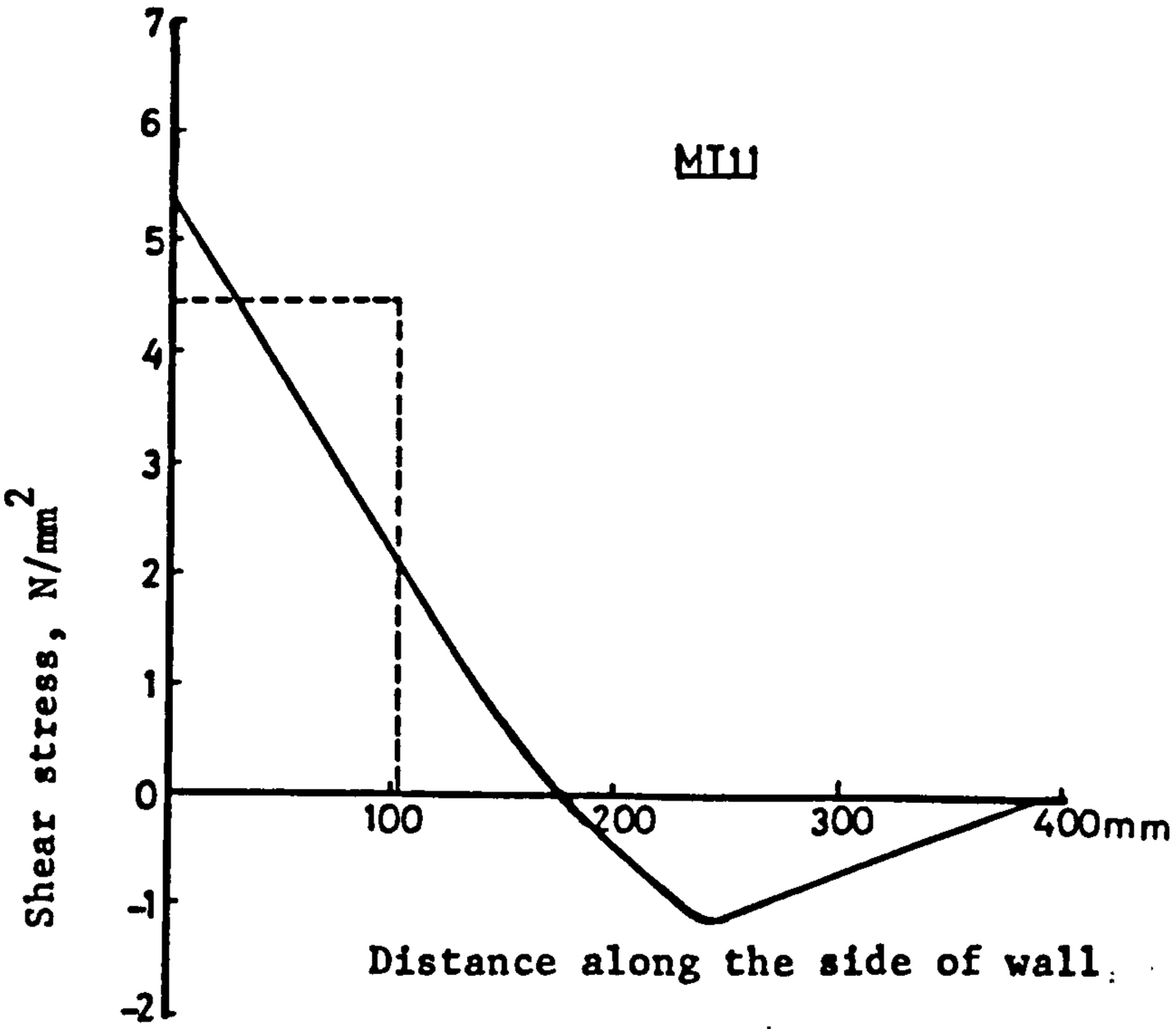

Figure (7.58) : Variation of shear stress along the sides of wall in the slab of MT11 at theoretical load equal to the experimental load at failure.

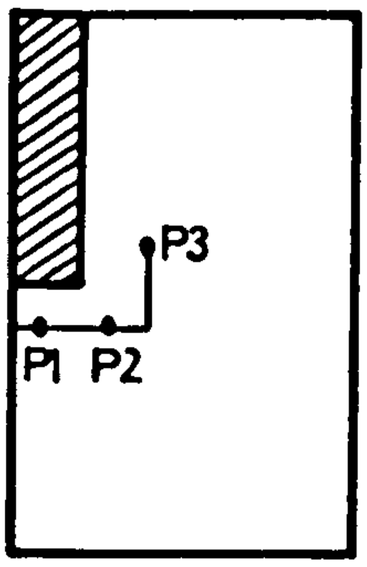

Figure (7.59) showing sampling points at the inner edge of wall, for which the induced shear stress is averaged.

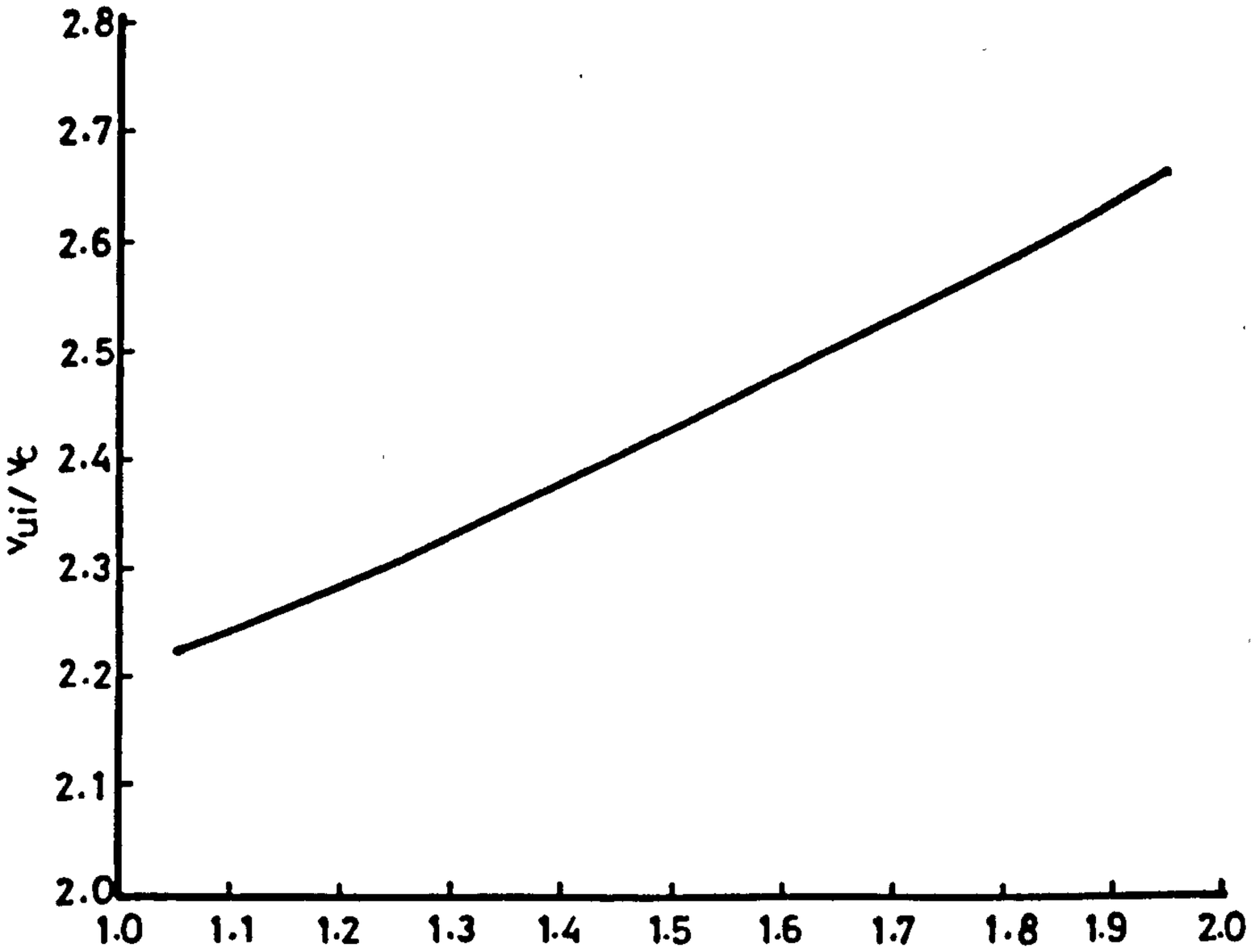

Figure (7.60): Curve showing variation of $\frac{v_{ui}}{v_c}$ versus the percentage of steel in windward direction, in the central strip of the slab.

Table 7.4 Comparison between shear stress in the slab at the inner face of wall predicted by F.E. when theoretical load was equal to experimental load at failure with the critical shear stress calculated from ACI formula.

Group No.	Model No.	Exp: load kN	f'_c N/mm^2 $=.8f_{cu}$	$v_c = .33\sqrt{f'_c}$ N/mm^2	v_{ui} N/mm^2	$\frac{v_{ui}}{v_c}$	Remarks
Group I	MT1	175.33	29.6	1.8	4.2	2.29	Main parameter Wall width, W_w For MT1, W_w =900mm = MT2 = 600mm = MT2 = 400mm
	MT2	192.9	40.16	2.09	4.8	2.30	
	MT3	154.2	34.24	1.93	4.45	2.31	
Group III	MT6	105.8	25.75	1.68	3.53	2.08	Main parameter Corridor opening width, L_w For MT6, $\frac{L_w}{2}$ = 520 MT3, = 400 MT7, = 280
	MT3	154.2	34.24	1.93	4.45	2.31	
	MT7	177.56	33.44	1.91	4.64	2.43	
Group IV	MT3	154.2	34.24	1.93	4.45	2.31	Main parameter bay width, y_w For MT3, Y_w = 1000 MT8, = 1440
	MT8	163.65	25.6	1.67	3.77	2.26	
Group V	MT3	154.2	34.24	1.93	4.45	2.31	Main parameter Flexural steel. Slab of MT9 was double reinforced
	MT9	147.2	28.02	1.747	4.24	2.45	
Group VI	MT10	153.27	27.88	1.74	3.85	2.22	Main parameter, Flexural steel For MT10 = 1.05% = MT7 = 1.5% = MT11 = 1.95% in the central strip.
	MT7	177.56	33.44	1.91	4.64	2.43	
	MT11	164.0	25.68	1.67	4.445	2.66	

models is averaged. The average value is found to be 131 mm which may be compared to effective depth of the slab, d, i.e. 129 mm. The equivalent effective length for model MT2 (i.e. 182 mm) which is nearly equal to $(t_w + \frac{d}{2})$ is greater than that of MT3 (i.e. 141 mm) by 29% and for MT1 (viz. 236 mm which is slightly less than $(t_w + d)$ i.e. 254 mm) it is greater than that of MT3 by 67%.

The equivalent effective length along the sides of the wall which is nearly equal to d(where d is the effective depth of slab) may be compared to that recommended by (i) Chang (9) as $(\frac{L_w}{4} + \frac{d}{2})$ and (ii) Schwaighofer & Collins (8) as $(t_w + d)$.

7.10 SUITABILITY OF DIRECT DESIGN METHOD FOR CONNECTING SLABS

While discussing the direct design method in chapter four it was proposed that the slab should be divided into a number of strips and the reinforcement in each strip should be provided for an average value of moment so that the ratio of steel would vary from strip to strip but remain constant within each strip. Obviously the choice of the width of each strip and total number of strips depends upon the rate of variation of moments. Since in the case of slabs connecting shear walls the intensity of moments due to lateral loads is the highest at the inner face of wall, great care is needed especially while selecting the width of the central strip. In the light of the experience gained from the experimental as well as theoretical study of the behaviour of connecting slabs, in this section the following questions/

are discussed.

(i) What should be the number of strips and the width of each strip?

(ii) What are the major factors affecting the actual intensity of stresses in the central strip?

(iii)Was the number of strips selected for the slabs of the models adequate?

(iv)What was the extent of redistribution?

(v) Was the condition of 'formation of mechanism with minimum amount of redistribution' satisfied?

It was mentioned in chapter four that although the finite element method is not an integral part of the direct design method, it is probably the most suitable method to obtain the elastic moment fields for design. However the problem with the connecting slabs is that when the distribution of moments is obtained using the finite element method, due to singularity of stresses very large moments are induced at the tip of the wall. If the moments are taken as an average of the most highly stressed point at the tip of the wall and that at the adjacent point along the transverse critical section passing through the inner edge of wall (as proposed by Coull & Wong (10)), then a very narrow strip will be required to resist very high moments which it is difficult to satisfy from practical point of view. It was shown in section (7.5) that the theoretically predicted strain in steel in main direction when averaged over a central/

strip of the width (t_w + d) was in reasonable agreement with the measured one, though in some cases calculated strain was still somewhat higher than the measured values. Therefore this could possibly be used as the width of the central strip. However while designing the models the moments had been averaged over a wider central strip (Fig. (7.61)). In fact the width of central strip mainly depends upon the intensity of the stresses at the tip of the wall in real structures which is a function of the nondimensional structural parameteric ratio L_w/Y_w . In chapter six with the help of measured strain in steel along the transverse critical section for models of third group (i.e. MT6, MT3 and MT7) it was shown that the curve showing the distribution of strains becomes steeper as the value of the ratio L_w/Y_w decreases. Similar behaviour was shown by the curves showing theoretical distribution of shear induced along the line of contraflexure and the shear along transverse critical section as discussed earlier in section (7.1 and 7.7) of this chapter. Thus relatively smaller width of central strip shouldbe used when the ratio L_w/Y_w is small. Away from the centre along the critical section, the intensity of stresses is low and its variation is not too steep and therefore there is not much redistribution of stresses involved even at late stages of loading. The choice of the widths and number of strips could be left to the experience and personal judgement of the designer.

The fact that theoretically design ultimate loads for the slabs of all the models were nearly achieved showed that the/

direct design method is quite suitable for the particular type of slabs connecting shear walls in a laterally loaded shear walls-slabs structure as well.

It has already been mentioned in chapter four that the direct design method requires that the steel in slab should yield at sufficient number of points with minimum amount of redistribution of stresses in slab thus converting it into a mechanism. In all the models, due to singularity of stresses in the slab at the inner edge of wall, local yielding of steel started at early stages (when the applied wind load was in the range of 47 to 58% of design ultimate load) leading to lower theoretical ultimate loads than what they were designed for. At ultimate loads in most of the models the steel in the main direction along the transverse critical section yielded only in two out of four elements. Figure (6.62) shows step by step yielding of steel in different elements of the slab of model MT1 as the loading progresses. From this figure it can be observed that the local yielding of the steel in y-direction near the inner edge of wall started when the applied load was only 53% of the flexural design ultimate load. However the average strain in element No.5 reached its yield value when the applied load was equal to 78% of design ultimate load, while in element No.6 steel yielded at 92% of the ultimate load. The steel in element No.7 yielded when the applied wind load was equal to design ultimate load. Thus it can be concluded that large amount of redistribution must have taken place before steel in sufficient number of elements yielded, implying that the slab of the model should have been divided in larger number of strips in windward direction than what it was. The step by step yielding/

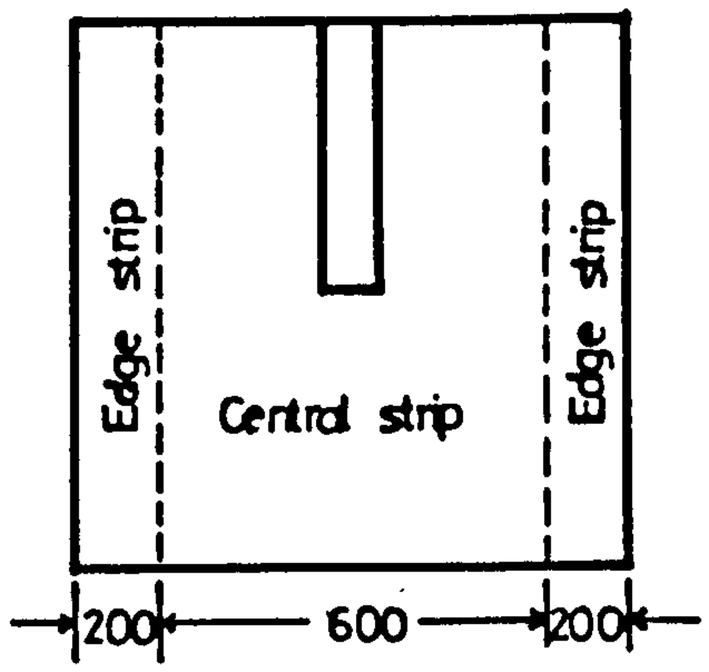

Figure (7.61) : showing different strips in windward direction of the slab of a typical model.

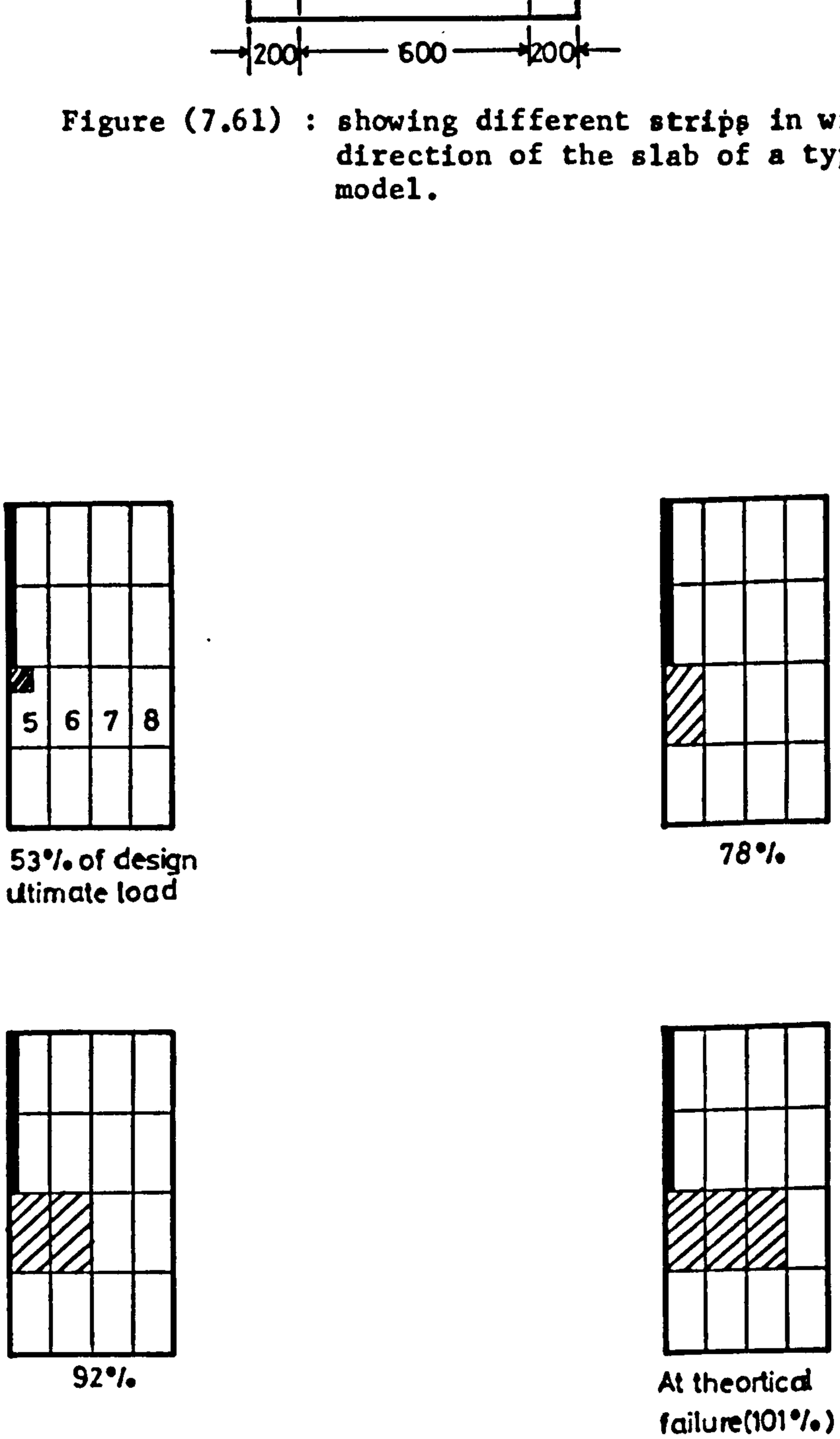

Figure (7.62) : Step by step yielding of steel in different elements of the slab of MT1.

of steel in slabs of models MT2 to MT11 is shown in Figures (7.63) to (7.72).

The method was further investigated by redesigning model PT2 for a critical moment of 26.6 kN-M corresponding to wind shear of 48 kN. Instead of dividing the slab into a certain number of strips and providing an average ratio of steel as proposed in chapter four steel for each element was designed separately according to the intensity of moments obtained from elastic analysis. The full nonlinear analysis of this mathematical model was then performed. It was observed that the yielding of steel in slab near the inner edge of wall started when the applied wind shear was only 58% of the design ultimate load. The induced moment along the critical section attained a maximum value of 26.2 kN-M and then dropped. By this time the strain in steel near the inner edge of wall had already reached a value of 5.5 times yield strain and the displacement of the line of contra-flexure was .133h (where h is overall thickness of slab). From this nonlinear analysis it was observed that at early stages of loading the stresses at the tip of the wall increased at a higher rate than other points. The redistribution took place only at very late stages of loading. Thus the concentration of stresses in this region of the slab was more than the one predicted by elastic analysis. This lead to early yielding of the steel and consequently slightly lower moment carrying capacity than what actually the slab was designed for. Thus it may be concluded that whenever a connecting slab is designed using direct design method, the actual load at failure in practice would be slightly less than the design ultimate load.

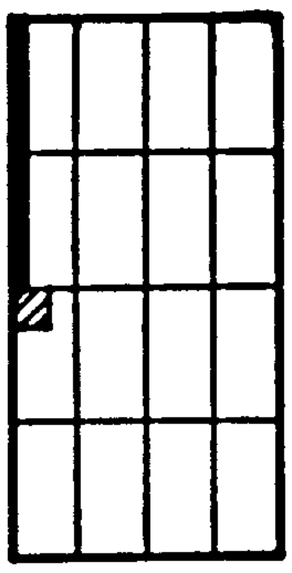

53%of design ultimate load

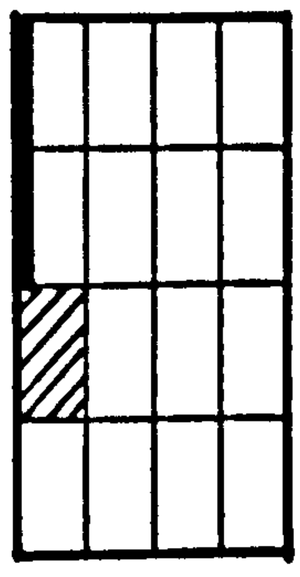

78%

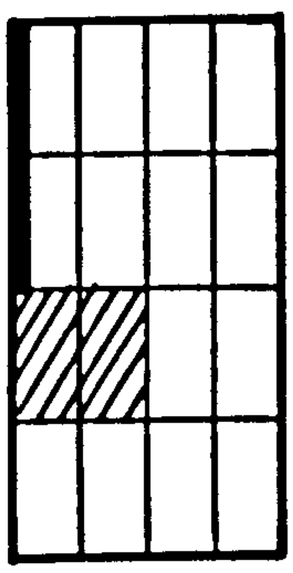

96%

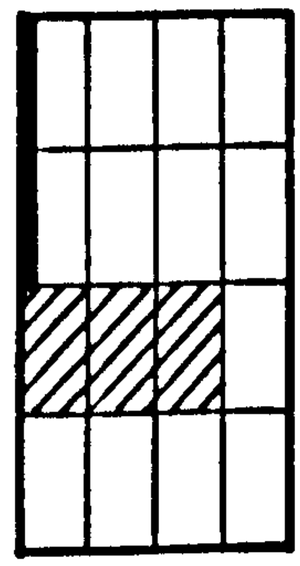

At theortical failure(100%)

Figure (7.63) : Step by step yielding of steel in the slab of MT2.

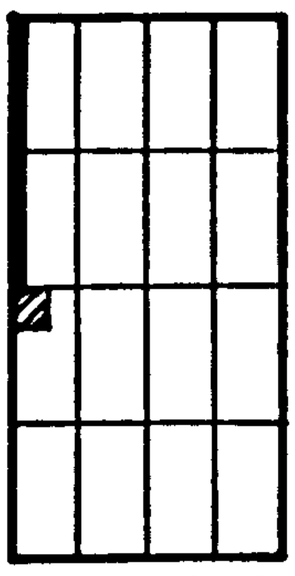

52%of design ultimate load

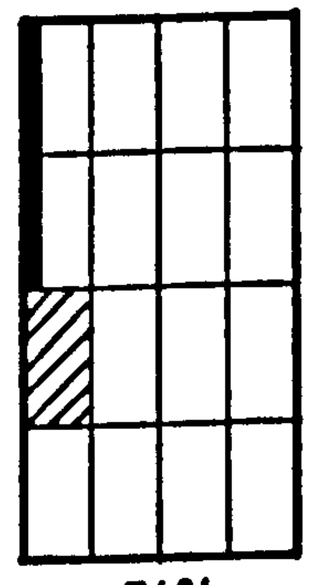

74%

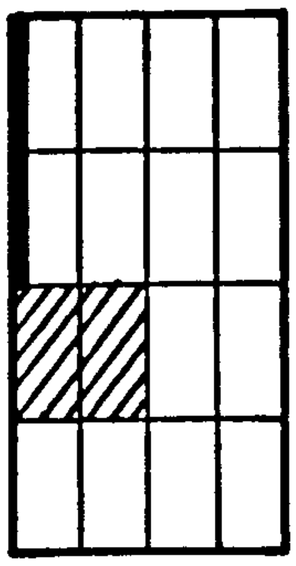

89%

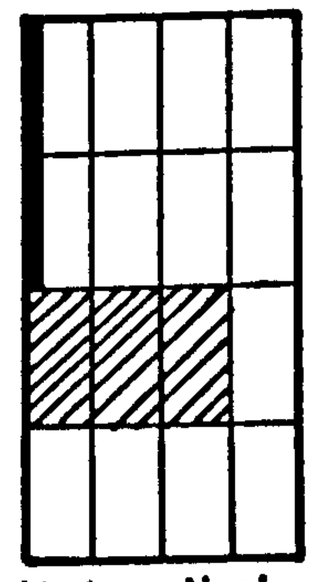

At theortical failure (93%)

Figure (7.64) : Step by step yielding of steel in the slab of MT3.

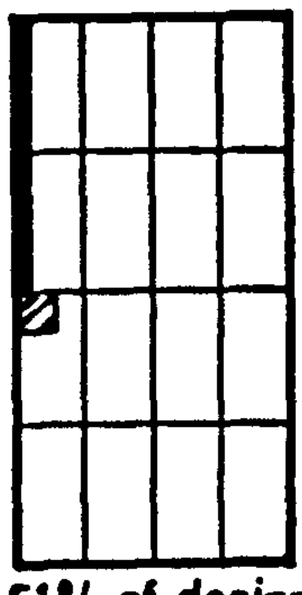

51% of design ultimate load

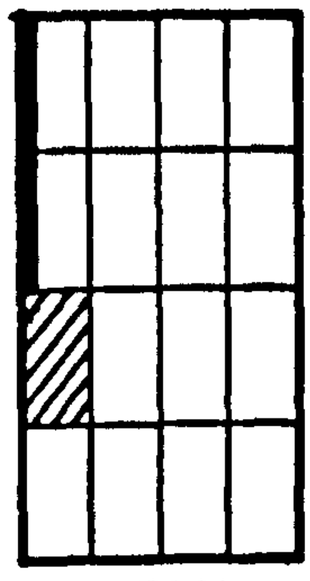

72%

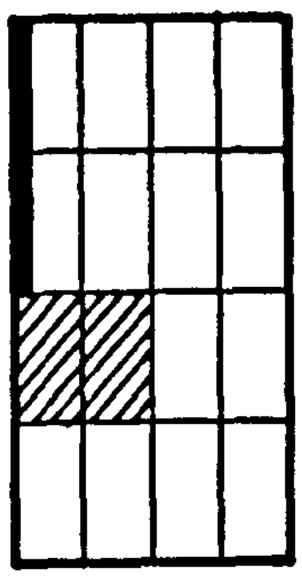

83%

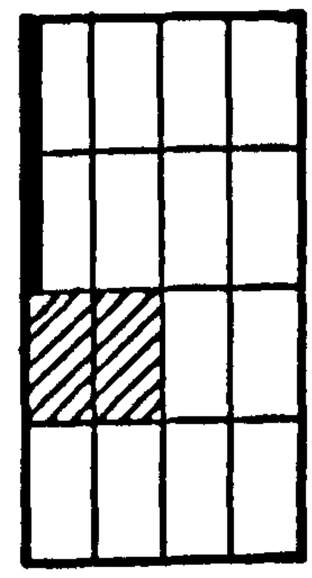

At theortical failure(87%)

Figure (7.65) : Step by step yielding of steel in the slab of MT4.

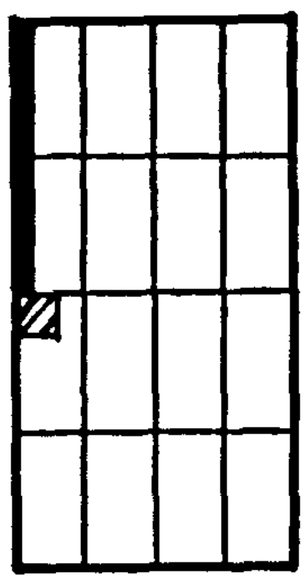

47% of design ultimate load

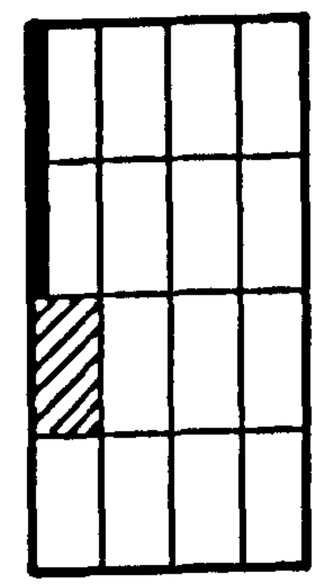

64%

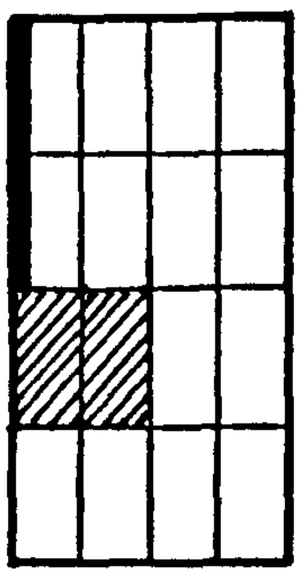

At theortical failure(74%)

Figure (7.66) : Step by step yielding of steel in the slab of MT5.

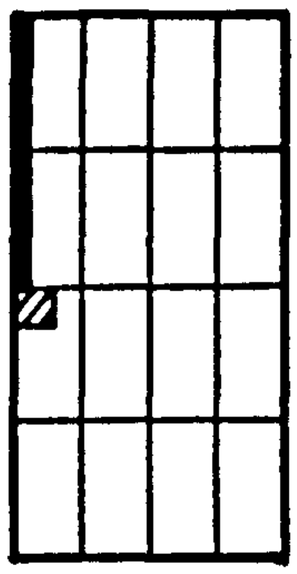

57% of design ultimate load

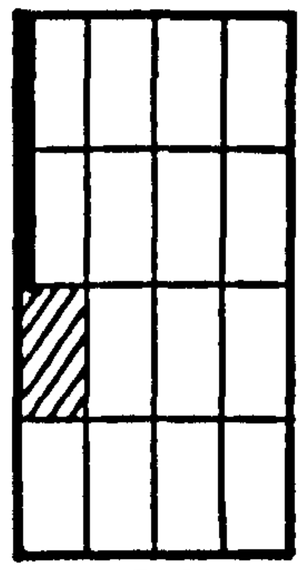

72%

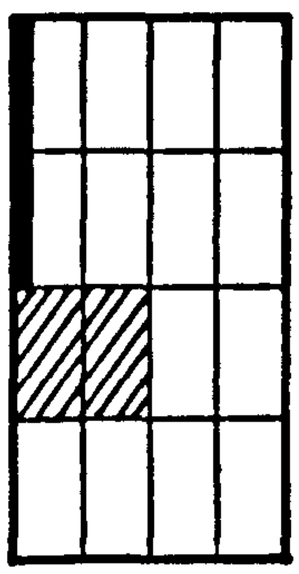

90%

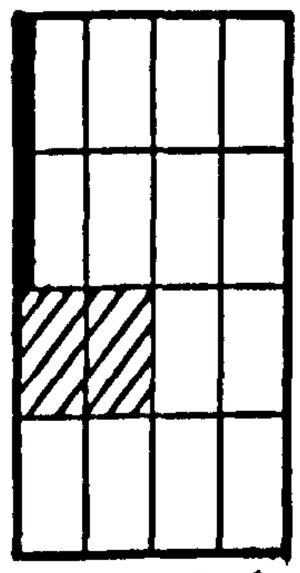

At theortical failure (94.4%)

Figure (7.67) : Step by step yielding of steel in the slab of MT6.

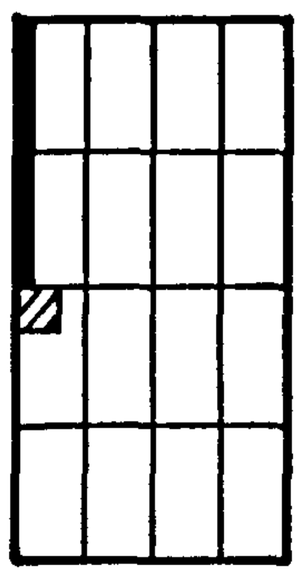

43% of design ultimate load

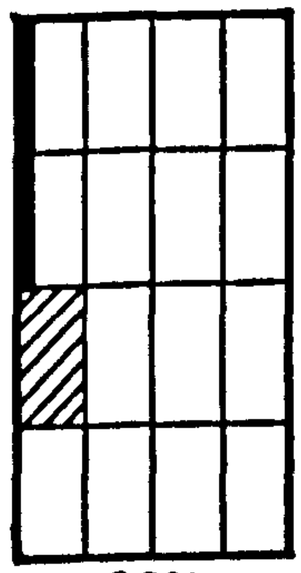

66%

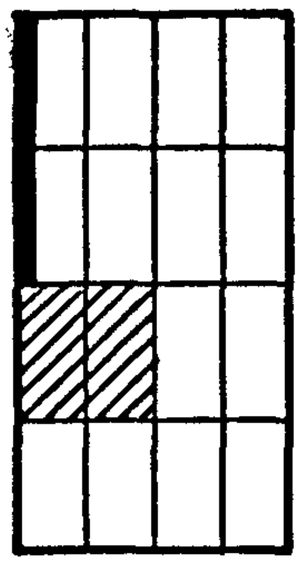

80%

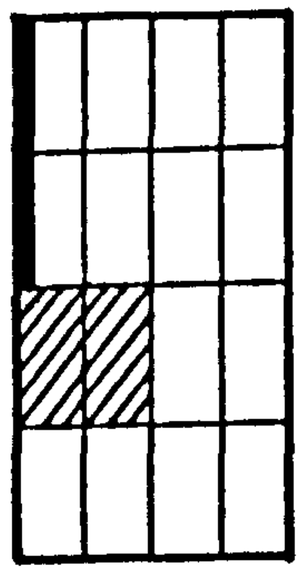

At theortical failure (82 %)

Figure (7.68) : Step by step yielding of steel in the slab of MT7.

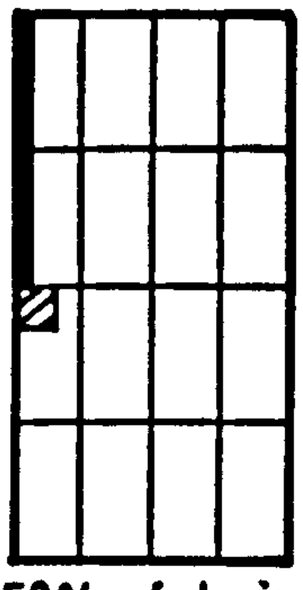

58% of design ultimate load

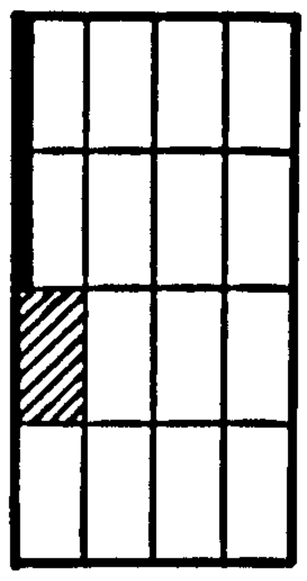

83%

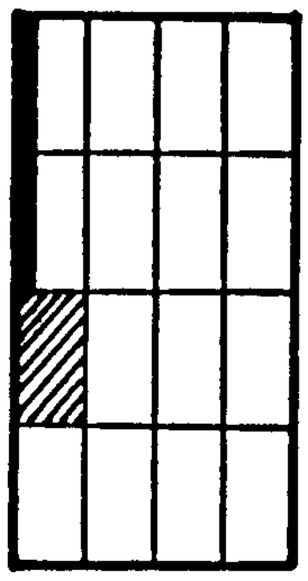

At theortical failure(97%)

Figure (7.69) : Step by step yielding of steel in the slab of MT8.

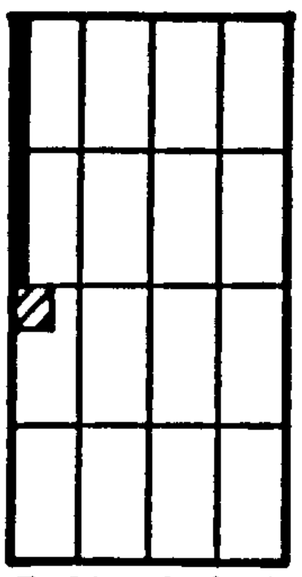

53% of design ultimate load

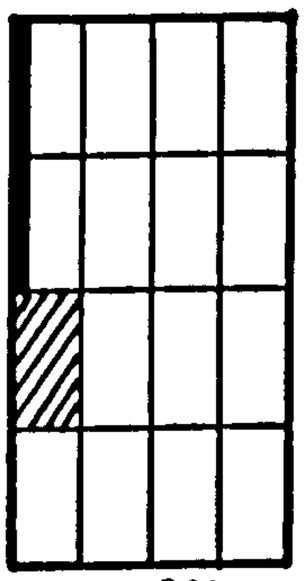

79%

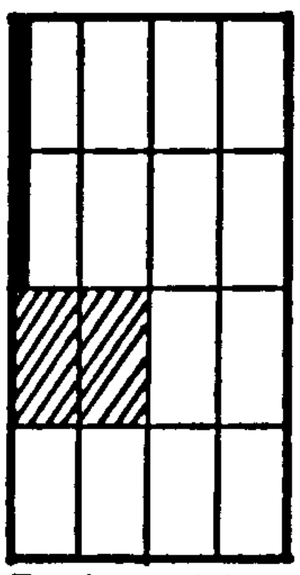

Design ultimate load

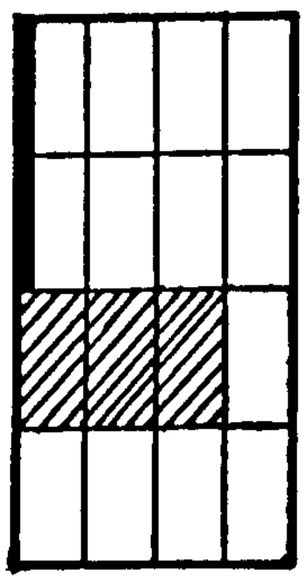

At theortical failure(114%)

Figure (7.70) : Step by step yielding of steel in the slab of MT9.

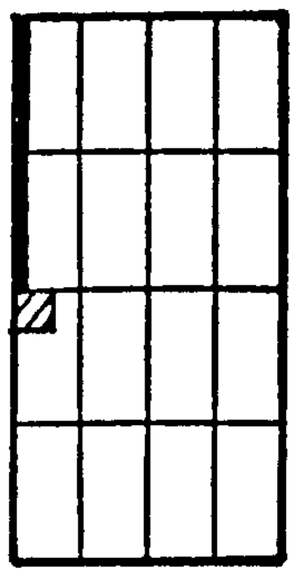

47% of design ultimate load

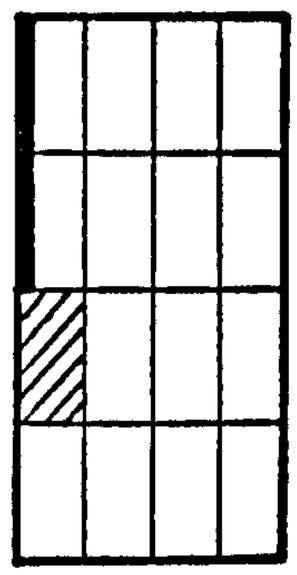

71%

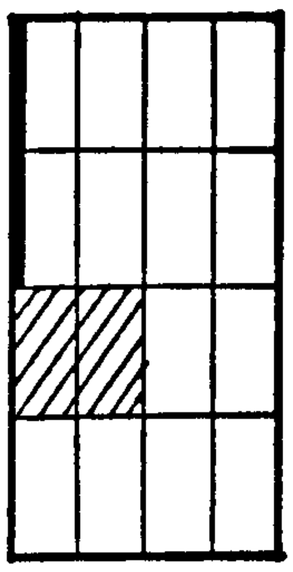

88%

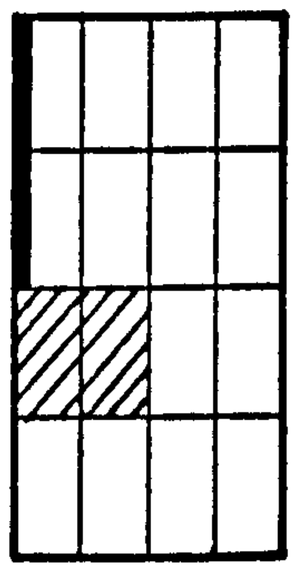

At theortical failure(91%)

Figure (7.71) : Step by step yielding of steel in the slab of MT10.

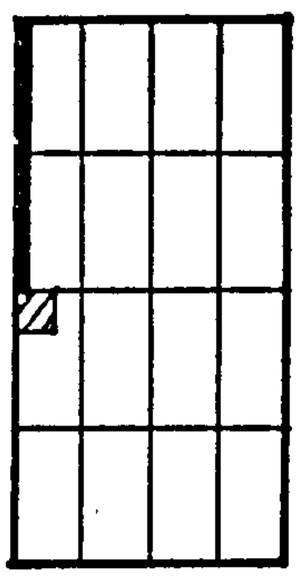

51% of design ultimate load

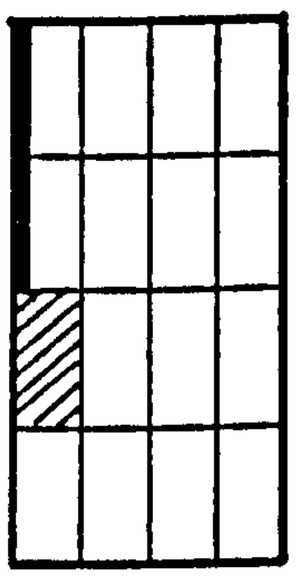

70%

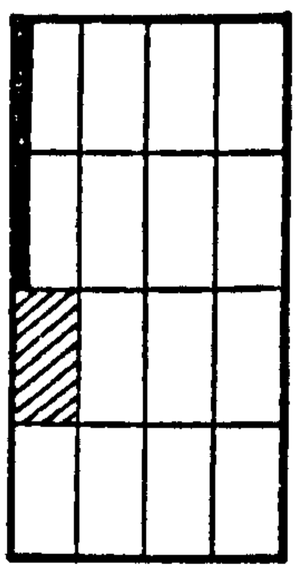

At theortical failure(84%)

Figure (7.72) : Step by step yielding of steel in the slab of MT11.

7.11 THEORETICAL CRACK PATTERN

Only for one model i.e. PT2, the theoretical crack pattern was obtained. For this purpose the original version of nonlinear plate bending programme written by Johnnary (21) was used. Very fine mesh of 10 x 10 elements was selected for this analysis. Stresses were calculated at the centre of each element. Theoretical crack pattern obtained from this analysis is shown in Figure (7.73). Comparing this theoretical crack pattern with the actual one shown in Figure (7.74), it can be concluded that except for the crack perpendicular to the inner edge of wall which developed in the actual model but not detected by the analysis, the theoretical crack pattern obtained from the analysis is reasonably correct.

7.12 EFFECT OF ACTUAL WALL THICKNESS

During the theoretical part of the investigation, all the analysis was carried out with a zero wall thickness. The effect of wall thickness was therefore investigated by reanalysing model PT2 by taking wall thickness into account.

Figure (7.75) shows theoretical and experimental load-displacement curves for this model. From this figure it can be observed that better agreement between the theoretical and experimental load-displacement relationship is obtained if the wall thickness is not taken into account and relatively higher ultimate flexural load is predicted if finite wall thickness is taken into account in the analysis. Ultimate load predicted with wall thickness taken into account is in better agreement with design flexural ultimate load for this model. Theoretical load is 102%/

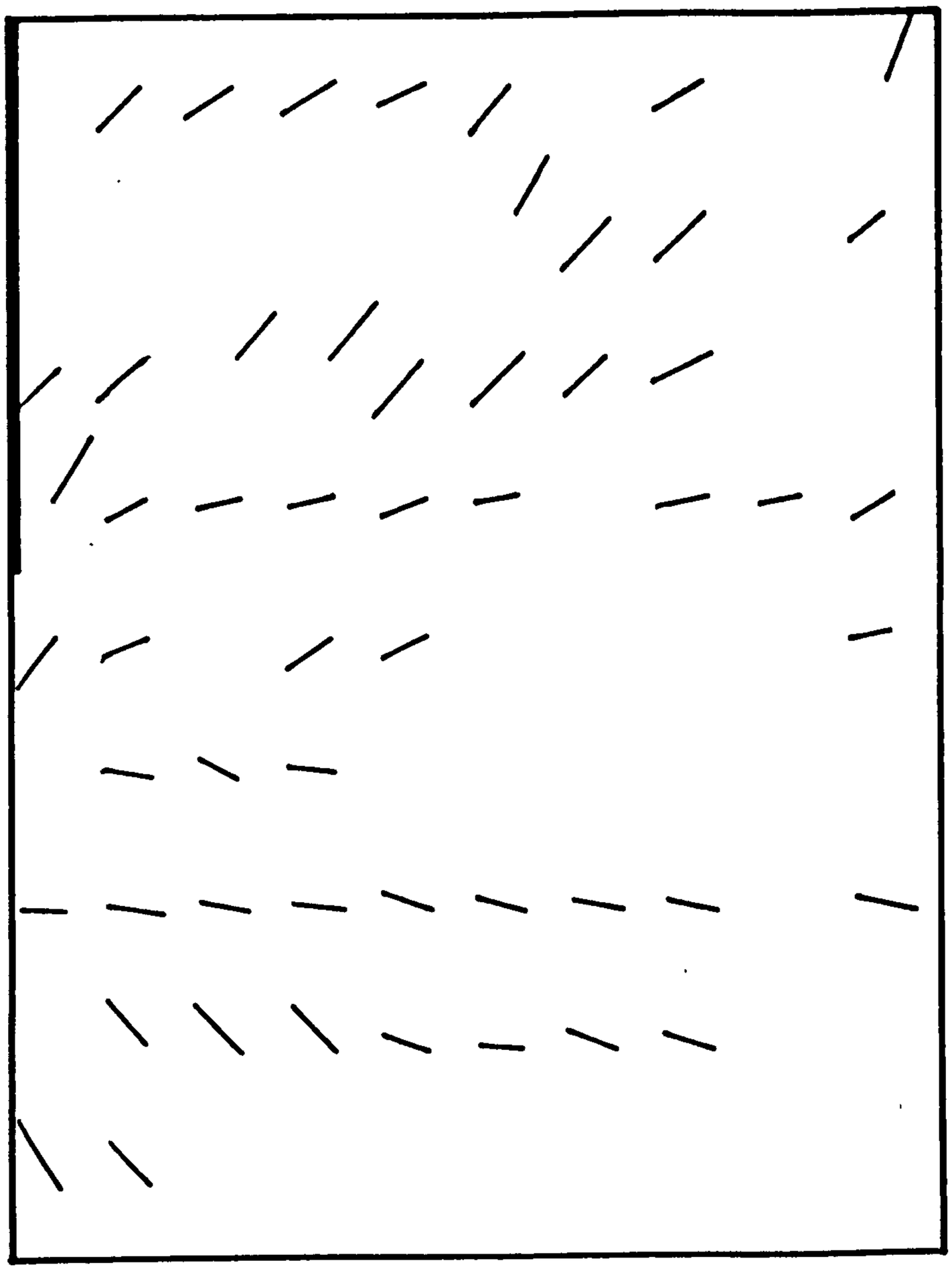

Figure (7.73) : Theoretical crack pattern of the slab of model PT2.

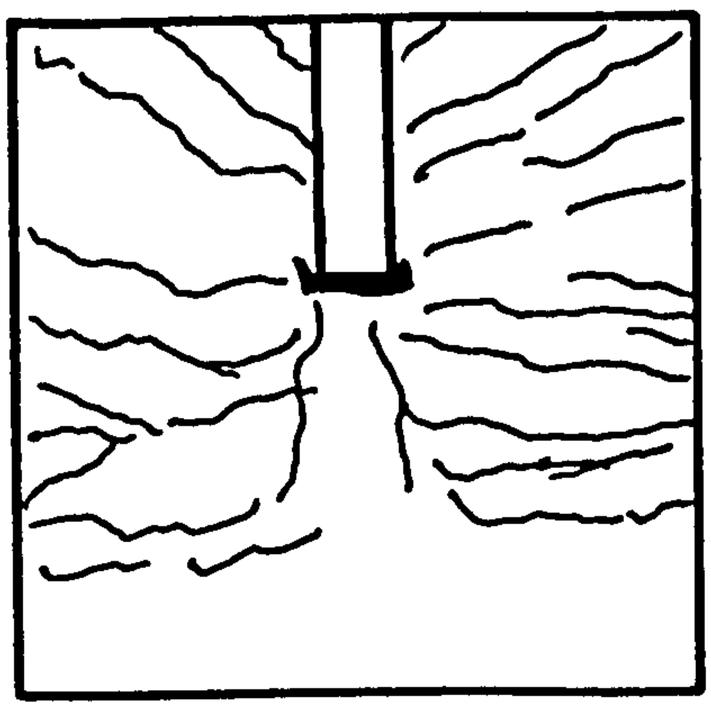

Figure (7.74) : Crack pattern of the slab of model PT2.

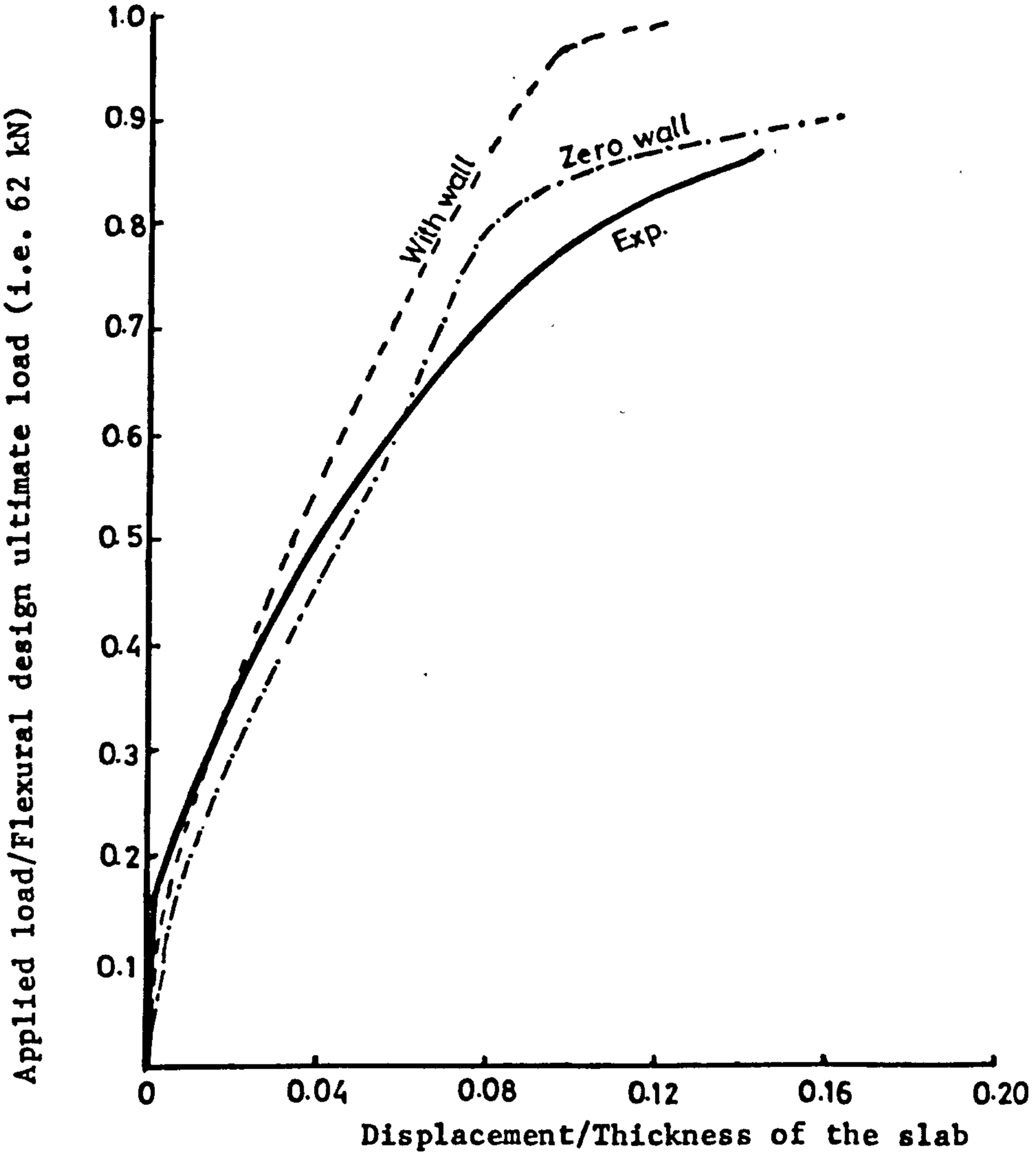

Figure (7.75) : Comparison between experimental and theoretical (both with and without wall thickness taken into account) wind load-displacement relationship for PT2.

with wall thickness taken into account and 91% without wall taken into account, of the design ultimate flexural load.

Theoretical strain for both the cases (i.e. with and without thickness, of wall taken into consideration) are compared with the measured strains in Figure (7.76). From this figure it can be observed that at early stages of loading slightly better agreement between theoretical and experimental strains is obtained at point P1 (near the inner face of wall) if the thickness of wall is taken into account. However at later stages of loading due to the unexpected behaviour of measured strains (discussed in chapter six) which show unloading, the strain is largely overestimated in both the theoretical cases. Agreement is very good at point P2 if wall thickness is taken into account. However at points P3 and P4 there is better agreement between theoretical and measured strains if thickness of wall is assumed to be zero.

The theoretical distributions of shear Q_y along transverse section BC passing through the slab at the inner edge of wall at a load of 32% and 89% of the experimental ultimate load is shown in Figure (7.77). From this figure it can be observed that at early stages of loading the distribution Q_y is slightly affected by the presence of finite wall thickness. The biggest difference is at the tip of the wall. Here the intensity of Q_y is higher if the thickness of wall is assumed to be zero. However since it is always the average value of Q_y (averaged over a width of $(t_w + d)$) at the inner face of wall which is taken into account,/

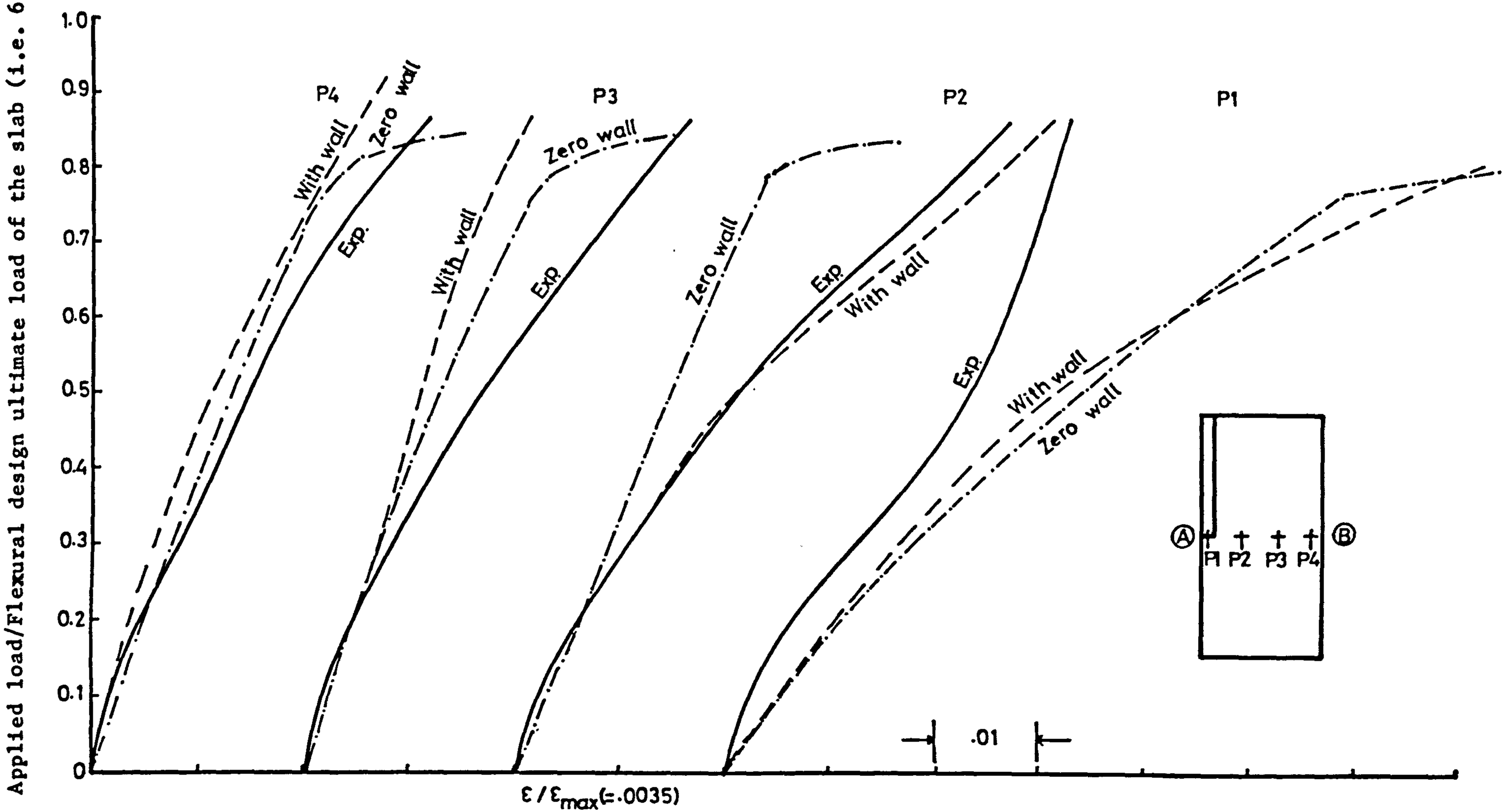

Figure (7.76) : Comparison between measured and theoretical (both with and without wall thickness taken into account) comp: strain in concrete at different points in the slab of PT2.

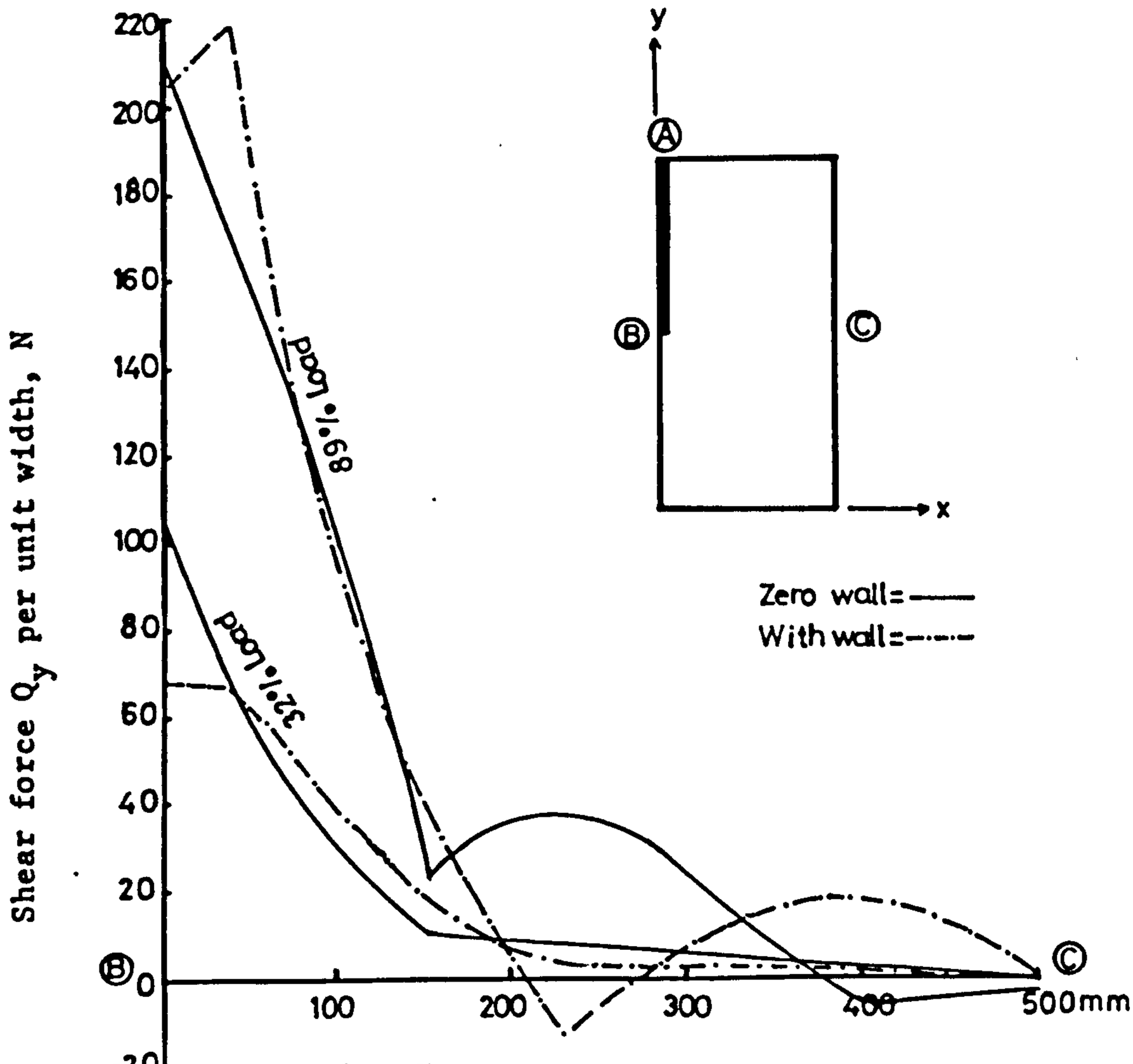

Figure (7.77) : Comparison of shear distribution obtained from nonlinear analysis with and without wall thickness.

this difference becomes negligible. At later stages of loading, away from the wall the distribution shows considerable difference if the wall thickness is taken into consideration. However since it is not a critical region, this difference may safely be disregarded.

It was observed that when the thickness of wall was taken as zero, due to local yielding of steel at the tip of the wall, $\frac{dT_b}{dx}$(the rate of change of tension) in the steel started decreasing, so that when the load was equal to 89% of ultimate experimental load, the total shear Q_y induced along BC was 15% less than the applied load.

Figure (7.78) shows the distribution of shear Q_x along the sides of the wall (section AB). It is obvious from this figure that the presence of finite wall thickness has negligible effect on the positive shear (acting downward) along the sides of the wall, near its inner edge. However the intensity of negative shear (acting upwards) is greatly reduced if wall thickness is taken into account.

In both the cases (with and without wall thickness)all the concrete layers along the sides of wall, near its inner edge were cracked well before the applied load reached the ultimate experimental value. Therefore $A\tau_{xz}$ etc. was also reduced to zero and it was only $\frac{dT_b}{dx}$(the rate of change of tension) in the steel which was showing some value. Thus calculated shear Q_x in this region was negligibly small.

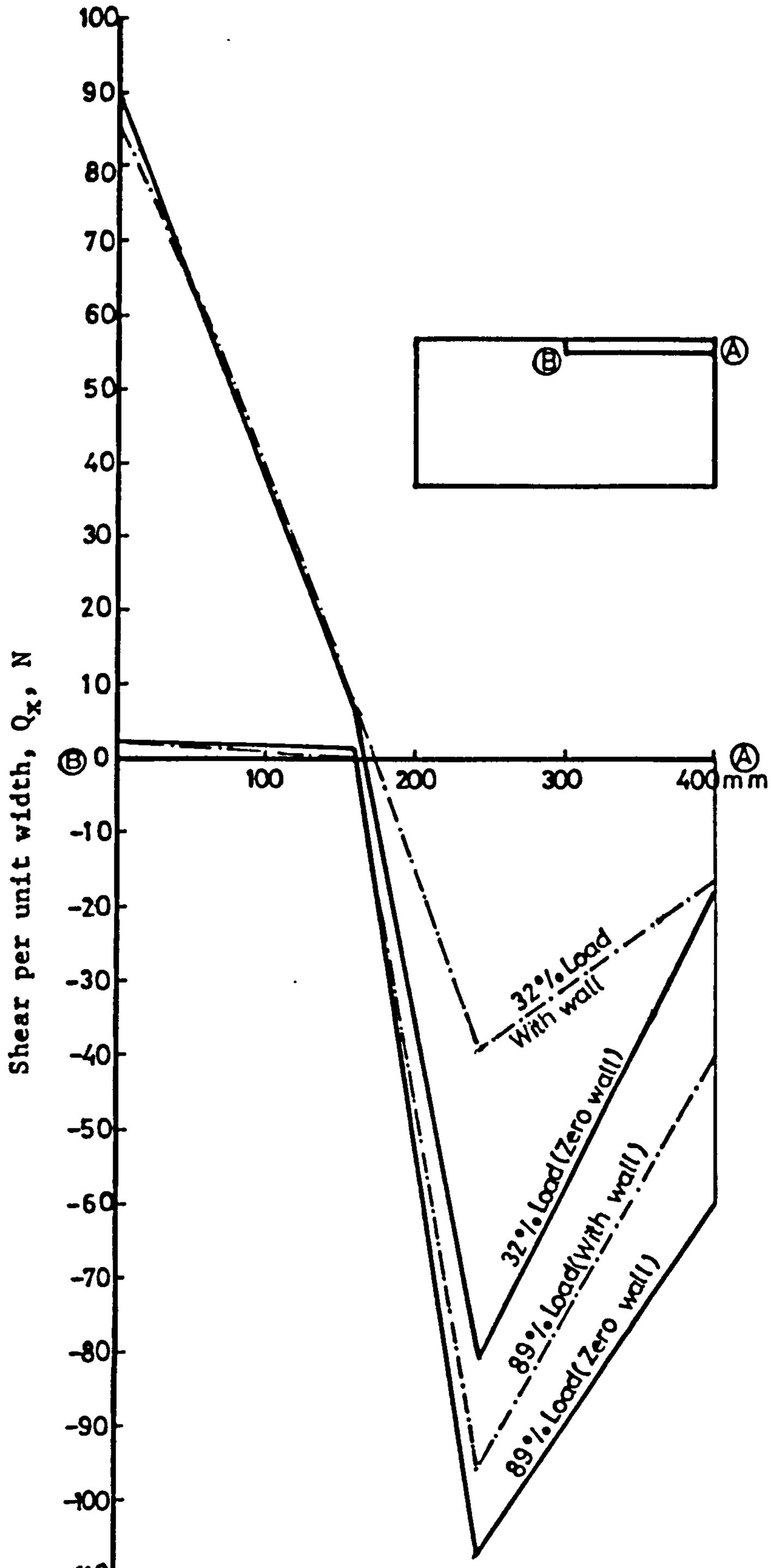

Figure (7.78) : Distribution of shear along the sides of the wall in the slab of model PT2, with and without thickness of wall taken into account.

From the discussion presented in this section it may be concluded that slightly better predictions, especially in terms of ultimate loads can be obtained if wall thickness is taken into account. But generally the results are acceptable even when the thickness of wall is assumed to be zero. For sake of simplicity and the ease with which the "input data" can be prepared and the subsequent saving of time, since long it has been a common practice to assume the thickness of wall to be zero for the purpose of the finite element analysis. Because then it is possible to reduce the number of different types of elements and use a uniform mesh. It was therefore decided not to take finite thickness of wall into consideration for the theoretical study presented in this thesis.

C H A P T E R E I G H T

ANALYSIS OF RESULTS

8.1 GENERAL

Since the actual strength of concrete on the day each model was tested was different for different models, in an effort to compare the ultimate loads of various models on a common concrete strength basis the ultimate loads of all the models are corrected to an average cube strength for the whole series. This is done as follows:

ACI code relates the critical shear stress of concrete with its cylinder crushing strength for slabs by the relation:

$$v_c = .33\sqrt{f_c'} \quad N/mm^2$$

where f_c is the cylinder crushing strength of concrete.

If we have two cylinder strengths f_{c1}' and f_{c2}' then

$$v_{c2}/v_{c1} = .33\sqrt{f_{ci}} \;/\; .33\sqrt{f_{c2}'}$$

$$\text{Or } v_{c2} = v_{c1}\sqrt{f_{c2}'/f_{c1}'}$$

Since ultimate shear strength of slab-wall junction is a function of v_c, provided all the other parameters are same, then the ultimate loads are related by

$$V_{u2} = \sqrt{f_{c2}'/f_{c1}'}\; V_{u1} \qquad (8.1)$$

This formula is used to find the ultimate load at which a model would have failed had the cube crushing strength of its/

concrete been equal to the base value for the whole series, which is 36.8 N/mm^2. Table 8.1 shows the data for uncorrected and corrected ultimate loads for all the models tested.

From the position of the shear cracks in the slab at the back of models, it was proposed in chapter six that for the wall-slab connections the critical section for shear should be assumed to be located at a distance of $\frac{d}{2}$ (where d is the effective depth of the slab) from the wall periphery as recommended by ACI 318(43) for slab-column connections. Thus it seems logical to adopt ACI 318 recommendations for the critical value of shear stress which is given by $v_c = .33\sqrt{f'_c}$ N/mm^2, although this does not take into account the effect of flexural steel on the value of v_c.

By comparing the experimental ultimate loads for all the models with the calculated ultimate loads, it had also been shown in chapter six that from among several methods, ACI 318 method, originally proposed for slab-column connections, seemed more promising. However it can be observed from table 6.8 that this method grossly overestimates the strength of the connection when the wall width, W_w, is relatively large and full wall width is assumed to be effective in resisting the shear due to wind load. The ACI 318 formula could probably predict the strength of connection with sufficient accuracy if a small portion of wall width is taken as effective and entered into calculations. In the following sections the effect of each major parameter will be discussed separately and proposals will be put forward regarding the prediction of the strength of wall-slab connection subjected to uneven shear and unbalanced moment in addition to the shear due to gravity loading.

Table 8.1. The actual and corrected loads for all the models of main test series (corrected against the variation of strength of the concrete).

Group No.	Model No.	Actual f_{cu} N/mm^2	Av. f_{cu} N/mm^2	Actual ultimate load kN	Corrected ultimate load kN	Remarks
Group I	MT1	37.0	36.8	175.33	174.75	Main parameter Wall width W_w; For MT1 = 900 mm " MT2 = 600 " " MT3 = 400 "
	MT2	50.2		192.9	165.06	
	MT3	42.8		154.2	142.9	
Group II	MT2	50.2		192.9	165.06	Main parameter; Gravity load For MT2, .14 N/mm " MT4, .28 " " MT5, .42 "
	MT4	33.1		192.76	203.12	
	MT5	33.2		160.87	169.26	
Group III	MT6	32.2		105.8	113.04	Main parameter; ½ corridor opening width $\frac{L_w}{2}$, For MT6= 520 mm " MT3 = 400 " " MT7= 280 "
	MT3	42.8		154.2	142.9	
	MT7	41.8		177.56	166.5	
Group IV	MT8	32.0		163.65	175.39	Main parameter; Bay width Y_w. For MT8 = 1440 mm " MT3 = 1000 "
	MT3	42.8		154.2	142.9	
Group V	MT9	35.0		147.2	150.83	Main parameter; Flexural steel. MT3 = steel only at the top face. MT9 = Doubly reinforced slab
Group VI	MT10	34.9		153.27	157.29	Main parameter; Flexural steel % of steel in central strip in windward direction For MT10 = 1.05% " MT7 = 1.5% " MT11 = 1.95%
	MT7	41.8		177.56	166.5	
	MT11	32.1		164.0	175.49	

8.2 EFFECT OF WALL WIDTH

Figure (8.1) shows the variation of the strength of the models with variation in wall width. The values are nondimensionalized with respect to the values of MT3. It appears from this figure that the curve is almost asymptotic to the MT1 value.

(46)

Literature reveals that for slab-column connections where the aspect ratio of column is more than 3, the sides of column are not fully effective. Therefore it may not be unreasonable to enter full wall width W_w into the calculations for the prediction of the strength of wall-slab connection if $W_w \leqslant d + \psi t_w$, and $\psi \leqslant 3$ (Here ψ is a constant).

It appears that the experimental data of the models of Ist group fits the following mathematical expression:

$$W_{eff} = 3\, t_w + t_w \left[\frac{1}{2} + \frac{1}{2^2} + \frac{1}{2^3} + \frac{1}{2^4} \cdots\cdots\right] \qquad (8.2)$$

where t_w is the thickness of the wall.

The above equation was used to find the portion of wall length which could be used in the calculation to predict the strength of connection. The number of terms within the brackets was equal to (aspect ratio -3) i.e. $(\frac{W_w}{t_w} - 3)$. There was an additional term for the fractional part of the aspect ratio and this last term was then multiplied by the fractional part.

Using the effective wall width calculated from the above equation, the strengths of wall-slab connections of models of Ist/

group were calculated from ACI 318 formula and are shown in table 8.2. It can be observed from this table that a fairly constant ratio of V_{exp}/V_{cal} is obtained for all these models. The calculated strength of model MT2 is 5% less than that of MT1 which corresponds well to 5.5% decrease in the corrected experimental load at failure of MT2 than that of MT1. Similarly the calculated strength of MT3 is 16% less than that of MT2 as compared to the decrease of 13.4% in the corrected experimental strength.

Generally it can be observed that among the models of Ist group, the value of effective wall width calculated from equation (8.2) is minimum (equal to 3.1 times t_w) for MT3 and maximum (approximately equal to 4 t_w) for MT1. Since further increase in wall width W_w beyond that of MT1 is expected to have no effect on the effective wall width, therefore for sake of simplicity a value of effective wall width equal to 3.5 t_w could probably be used for all the situations.

8.3 EFFECT OF GRAVITY LOAD

It has already been mentioned in chapter six that models of IInd group(i.e. MT2, MT4 and MT5) were tested with the intensity of gravity load as main parameter. Since the intensity of gravity load applied to MT4 was twice that of MT2, it was expected that the ultimate load of MT4 would be lower than that of MT2. However it can be observed from table 8.1 that the corrected experimental ultimate load of MT4 is 23% higher than that of MT2. The intensity of gravity load applied to model MT5 was thrice that of MT2,/

even then as can be observed from table 8.1, the corrected experimental ultimate wind load of this model is 2.5% higher than that of MT2. This appears rather contradictory and possible reasons for this are discussed below.

From Figure (8.2) which shows the experimental shear-compression interaction (40) it can be observed that the shear strength of a concrete section is greatly improved with the increase in the direct compression up to $\sigma/f_c' \leqslant 0.5$. The tension due to bending reduces the shear area but compression due to bending increases the permissible shear stress, so that the final effect is possibly increase in the load carrying capacity.

The state of compression due to bending depends upon the applied moment. The applied moment M_g along the sides of the walls of MT4 and MT5 increased with the increase of gravity load from MT2 to MT4 and MT5. In chapter six it was shown that no flexural cracks parallel to the sides of wall appeared, so that like MT2 full cross section of the slab was still effective in resisting the applied shear stresses. Thus the increased ultimate load carrying capacity of MT4 may be attributed to the improved shear transfer capacity of compression zone due to increased compression caused by the increase in gravity load. However further increase of gravity load from MT4 to MT5 was not only accompanied by improved shear transfer capacity of compression zone but it was also responsible for occurrance of flexural cracks parallel to the sides of the wall causing to some extent a reduction in shear transfer capacity of tension zone. Thus the ultimate strength of MT5 was less than that of MT4 but nearly equal to that of MT2.

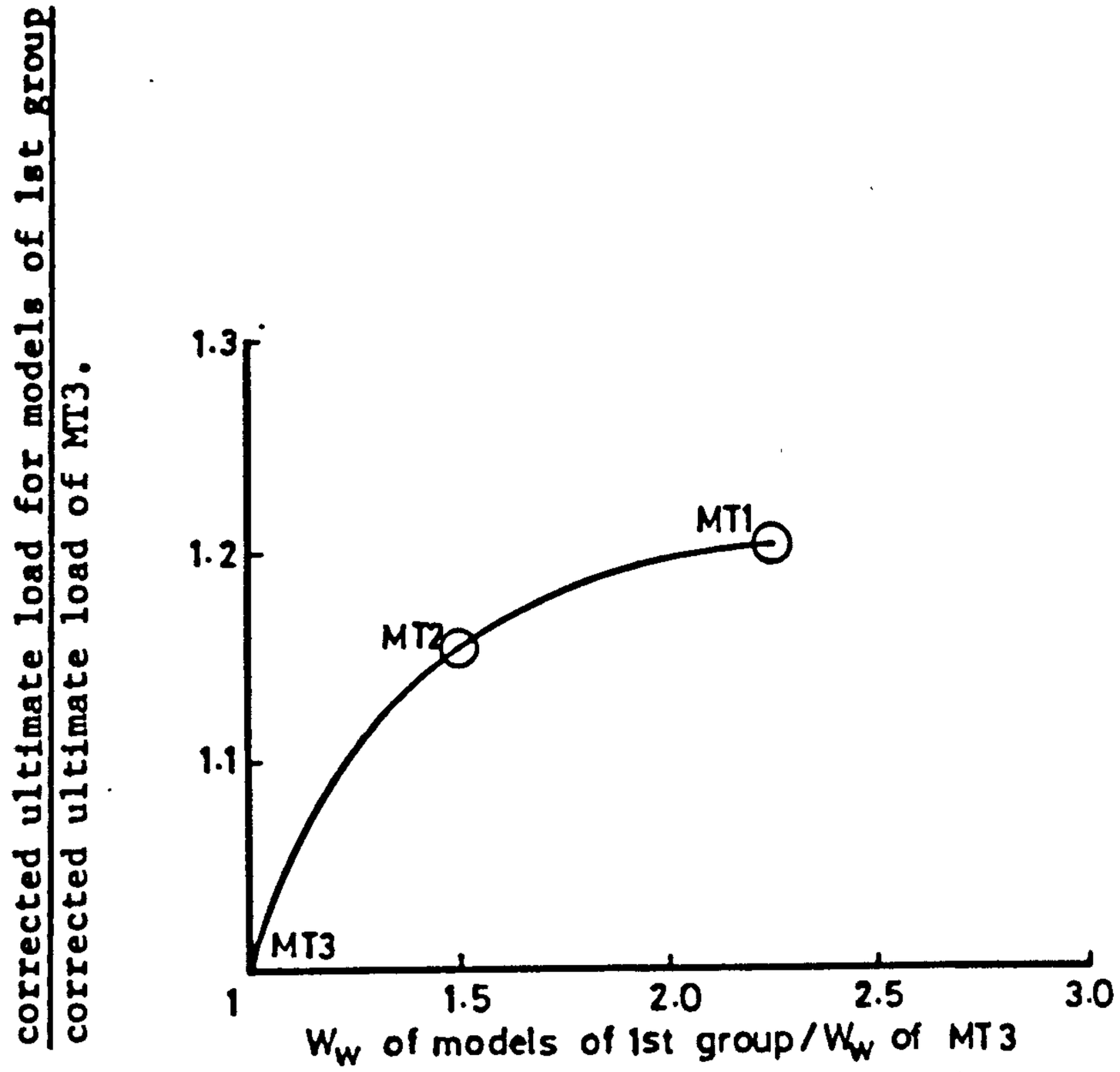

Figure (8.1) : Effect of wall width on ultimate strength of wall-slab connection.

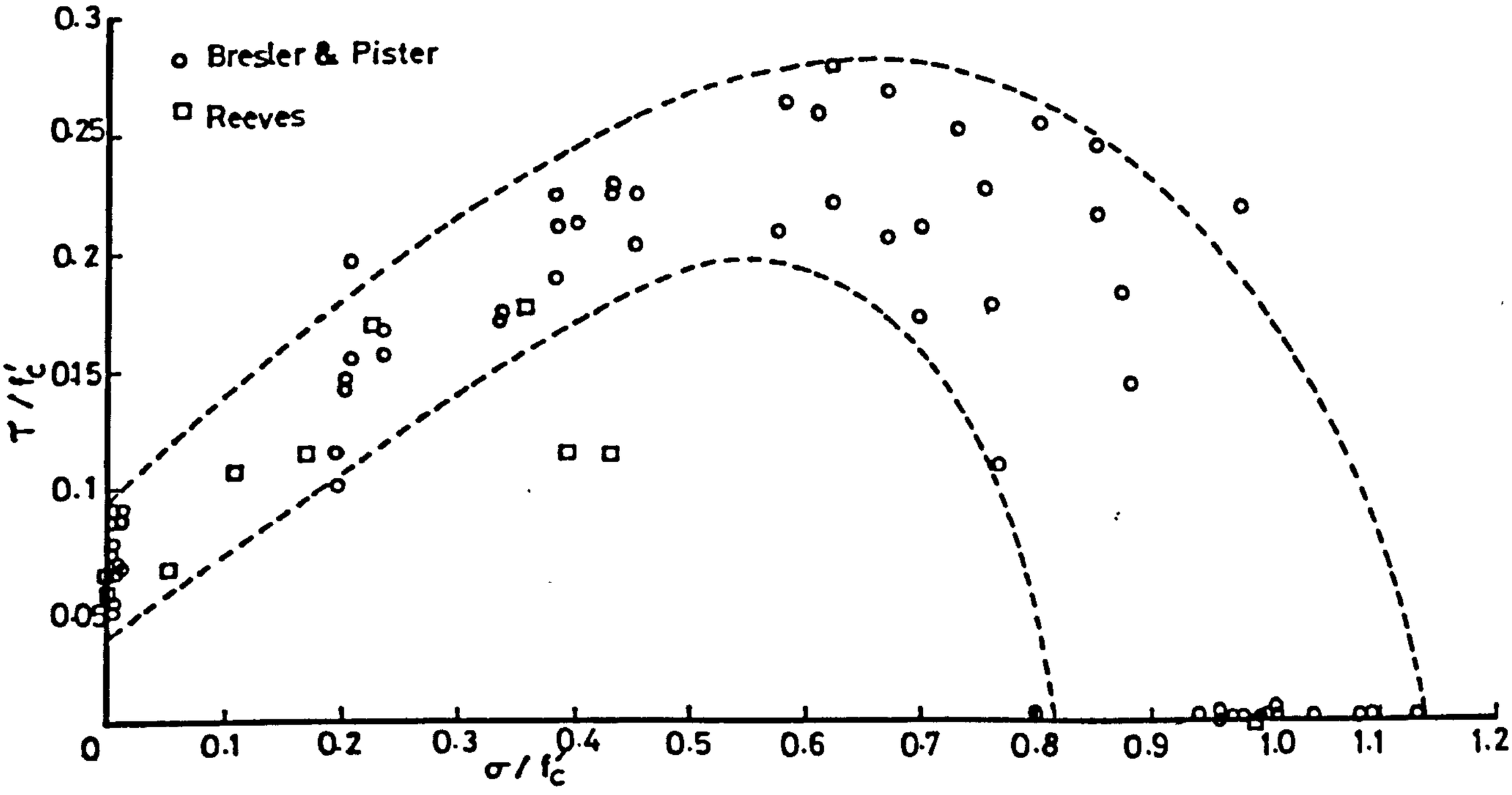

Figure (8.2) : Failure of concrete under compressive and shear stress.

It was mentioned in chapter seven that the stresses, strains etc. were grossly overestimated by finite element method in the slabs of MT4 and MT5 leading to early theoretical failure of models. Therefore no useful information could be obtained from the analysis, regarding the effects of the intensity of gravity load on the overall behaviour of these models.

Although increase of the intensity of gravity load showed some increase in the ultimate wind load transfer capacity of the models, it seems illogical to take this into account in any formula which is to be proposed to estimate the strength of wall-slab connection. It is probably a conservative assumption to assume a linear reduction in the value of critical shear stress v_c, corresponding to the shear stress induced along the critical section by the gravity load.

8.4 EFFECT OF CORRIDOR OPENING WIDTH

It has already been mentioned that models of group III (i.e. MT6, MT3 and MT7) were tested to study the effect of corridor opening width on the strength of wall-slab connection against applied wind shear. Since the moment M_w due to wind shear V_w induced along critical section passing through the inner edge of wall is equal to $\frac{1}{2} L_w V_w$ (where L_w is the corridor opening width) the increase in the corridor opening width causes an increase in the moment M_w. The increase in moment M_w causes an increase in the torsional shear stress along the sides of the wall thus resulting in a decrease in the shear transfer capacity of the connection. It was shown in chapter seven(Figure (7.41)) by /

comparing the curves showing the distribution of shear along the sides of the walls of models of IIIrd group that for the same applied wind shear, corridor opening width has considerable effect on the total shear induced along the sides of the wall. It was also shown in chapter seven (Table 7.2) that the ratio $\frac{v_{ui}}{v_c}$ (where v_{ui} is the shear stress in the slab at the inner edge of wall, predicted by finite element method when theoretical load was equal to experimental load and $v_c = .33\sqrt{f'_c}$) decreased with the increase in the corridor opening width L_w. This imples that the total shear which can be transferred directly at the inner face of critical section is also affected by L_w. It is possible to evaluate these ffects quantitatively but this is useful only when it is required to estimate the moment and shear transferred through each face of wall separately, leading to an approach similar to beam analogies. However it was shown in chapter six (table 6.10) that the ACI 318 method could predict the strength of connections of the models of the IIIrd group with reasonable accuracy. Since the ACI 318 method takes account of the effect of the transfer of unbalanced moment on the strength of connection reasonably well, it is best to use the ACI 318 formula as it stands.

It can be observed from table 8.1 that a decrease of corridor opening width by 30% from MT3 to MT7 caused an increase in the ultimate wind load of MT7 by about 16.5%, while an increase of corridor opening width from MT3 to MT6 by 30% caused a decrease in the ultimate wind load of MT6 of approximately 21% than that of MT3. Taking the ultimate wind load and corridor opening width of model MT7 as base values, curve showing the ultimate wind load versus corridor opening width for models of IIIrd group is shown in Figure (8.3).

The strengths of wall-slab connections of the models MT6, MT3 and MT7 are recalculated using ACI 318 method by entering the effective wall length obtained from equation (8.2) and are presented in table 8.3. From this table it can be observed that the ratio $\frac{V_{exp}}{V_{cal}}$ for model MT7 is slightly less than that of MT3 and corresponds well with that for models of Ist group. However this ratio is somewhat lower for model MT6.

8.5 EFFECT OF BAY WIDTH

Models MT3 and MT8 were tested to study this effect. The increase in bay width Y_w causes an increase in the moment due to gravity load M_g along the sides of the wall. It was shown in chapter seven that the distribution of shear due to wind load induced along the sides of wall is also effected by the bay width and the increase in bay width caused the decrease in the maximum intensity of shear along the sides of the wall near its edge. This must have lead to improved wind load transfer capacity of the connection.

It can be observed from table 8.1 that an increase of Y_w by 440 mm from MT3 to MT8 caused an increase in the corrected ultimate wind load of MT8 of 23% over that of MT3, which is quite considerable. It was shown in chapter six that no flexural cracks parallel to the sides of the wall were detected in model MT8 either. Thus this increase in the ultimate load too could probably be attributed to the improved shear transfer capacity of compression zone of concrete along the sides of the wall due to increase in M_g. This supports the reasoning presented in/

Table 8.2. Comparison of estimated strength of connection for the models of 1st group of MT series, calculated from ACI formula using full wall width and reduced wall width.

Model No.	Av. f_{cu} N/mm^2	W_w mm	W_{eff} mm	$V_{cal.}$ kN	Corrected $\frac{V_{exp.}}{V_{cal.}}$ (reduced wall with ACI)	$V_{exp}/V_{cal.}$ from table (6.8)
MT1	36.8	900	493	130.7	1.34	.75
MT2		600	463	124.28	1.33	1.05
MT3		400	388	107.2	1.33	1.29

Table 8.3. Comparison of estimated strength of connection for models of 111rd group of MT series, calculated from ACI formula using full wall width and reduced wall width.

Model No.	Av. f_{cu} N/mm^2	L_w mm	Corrected $V_{exp.}$ kN	V_{cal}	$\frac{V_{exp.}}{V_{cal.}}$	$V_{exp}/V_{cal.}$ from table (6.8)
MT6	36.8	520	113.04	91.52	1.24	1.21
MT3		400	142.9	107.2	1.33	1.29
MT7		280	166.5	129.47	1.29	1.25

section (8.3) for models MT4 and MT5. It was shown in chapter six (table 6.11) that like models MT4 and MT5, the ratio $\frac{V_{exp}}{V_{cal.3}}$ (where $V_{cal.3}$ is the strength of the connection calculated using ACI 318 method) was relatively higher (equal to 1.6) for model MT8 as well.

8.6 EFFECT OF DOUBLE REINFORCEMENT

Since the wind may blow from any direction, it is a common practice to reinforce the connecting slabs of a shear walls - slabs structureat both their faces. It was expected that due to grid action of this double reinforcement and increased dowel action, the strength of this connection would increase and model MT9 was tested to study this effect. However table 8.1 shows that the increase in the ultimate wind load action strength of MT9 to that of MT3 (with flexural steel in the slab only at its top) was only about 5.5%. This effect may therefore be ignored.

8.7 EFFECT OF RATIO OF FLEXURAL REINFORCEMENT

Models of group VI (i.e. MT10, MT7 and MT11) were tested to study this effect. It can be observed from table 8.1 that decrease in the ratio of flexural steel in windward direction in the central strip of the slab by .45% from MT7 to MT10 caused a decrease in the ultimate windload of MT10 by about 5.5% to that of MT7 and an increase of this ratio by the same amount from MT7 to MT11 caused an increase in the ultimate load of MT11 of about 5.4% to that MT7. This seems to correspond well with CP 110 which assumes an increase in the value of critical stress of .05 N/mm^2 for every increase of .5% of the ratio of flexural reinforcement when $2 \geqslant (\rho) \geqslant 1$.

Hawkins, Bao and Yamazaki (15) from the results of the tests which they performed on slab-column connections, concluded, "ACI 318-77 provisions for determining the strength of slab to interior column connections transferring moment are reasonable for design. They yield results which are conservative when the value within lines 1.5 times slab thickness on either side of the column exceeds .7%. That conservatism increases as the value increases and the warning of impending failure decreases. ACI 318-77 provisions may be non conservative for values less than .7%."

In the light of the test results of the models of group VI (MT10, MT7 & MT11) it may be proposed here that an increase of every .5% in the ratio of flexural steel in the slab in windward direction above 1%, the calculated value of $v_c = .33\sqrt{f'_c}$ N/mm^2 should be increased by .05 N/mm^2 while estimating the strength of wall-slab connection. Thus

$$v_c = .33\sqrt{f'_c} + v_{add} \qquad (8.3)$$

Here v_{add} is the increase in the value of critical shear stress due to increase of ratio of flexural steel above 1%.

8.8 PROPOSED PROCEDURE TO ESTIMATE THE STRENGTH OF CONNECTION

In the light of the study presented in this thesis it is proposed that the following procedure may be adopted to estimate the strength of a wall-slab connection against the applied wind loading:

1. Calculate the effective length of wall W_{eff} from equation (8.2) or assume a value of $W_{eff} = 3.5\ t_w$ and calculate the total length of critical perimeter from,

$$b_p = (2\ W_{eff} + 2d + t_w) \qquad (8.4)$$

2) Calculate the critical shear stress v_c from

$$v_c = (.33\sqrt{f_c'} + v_{add}) - v_g \qquad (8.5)$$

Here f_c' cylinder crushing strength of concrete

v_{add} = the increase in value of v_c due to flexural ratio of steel as discussed in previous section, and

v_g = the shear stress induced along the critical section for shears due to gravity load.

3. Determine the value of factor α_i from

$$\alpha_i = 1 - \frac{1}{1 + \frac{2}{3}\sqrt{\frac{W_{eff} + d}{t_w + d}}} \qquad (8.6)$$

Here t_w is the thickness of wall and

d is the effective depth of slab

4. Calculate the value of J_c from

$$J_c = \frac{d(W_{eff} + \frac{d}{2})^3}{6} + \frac{(t_w + d)d^3}{12} + Y_1^2 (t_w + d)d + 2Y_2^2 (W_{eff} + \frac{d}{2})d \qquad (8.7)$$

Here Y_1 and Y_2 are as shown in Figure (8.4)

5. Calculate ultimate strength of the connection from

$$V_u = \frac{v_c b_p d}{(1 + \alpha_i \frac{M}{V} \frac{Y_1 b_p d}{J_c})}$$

In the above equation $\frac{M}{V}$ may be replaced by $\frac{L_w}{2}$, where L_w is the corridor opening width.

Using the above procedure the strengths of wall-slab connections for models PT1, PT2 and all the models of main test series were calculated and are presented in table 8.4. From this table it can be observed that the proposed method is capable of predicting reasonably correct ultimate strengths of wall-slab connections for all the range of parameters tested in this work.

Finally, a flow chart is presented in Figure (8.5) regarding the complete design procedure for the connecting slabs of a laterally loaded shear wall structure.

Table 8.4 : Comparison of experimental and calculated ultimate loads predicted by using the procedure proposed in Section (8.7).

Model No.	Corrected $V_{exp.}$ kN	$V_{cal.}$ kN	$\frac{V_{exp}}{V_{cal}}$	Remarks
PT1	48.97	36.38	1.35	Preliminary test, case of wind loading alone.
PT2	54.74	45.57	1.20	Case of wind loading alone.
MT1	174.75	134.59	1.30	Main parameter: wall width W_w
MT2	165.06	128	1.29	
MT3	142.9	110.39	1.30	
MT4	203.06	119.63	1.7	Main parameter: Intensity of gravity load.
MT5	169.26	111.27	1.52	V_{cal} underestimated possibly due to high intensity of V_g.
MT6	113.04	94.2	1.20	Main parameter: Corridor opening width L_w
MT7	166.5	133.32	1.25	
MT8	175.39	110.39	1.59	Main parameter: Bay width Y_w.
MT9	150.84	110.39	1.37	Doubly reinforced slab.
MT10	157.29	129.47	1.22	Main parameter: Ratio of flexural steel.
MT11	175.49	137.18	1.28	

Average = 1.35

Standard deviation = 0.15.

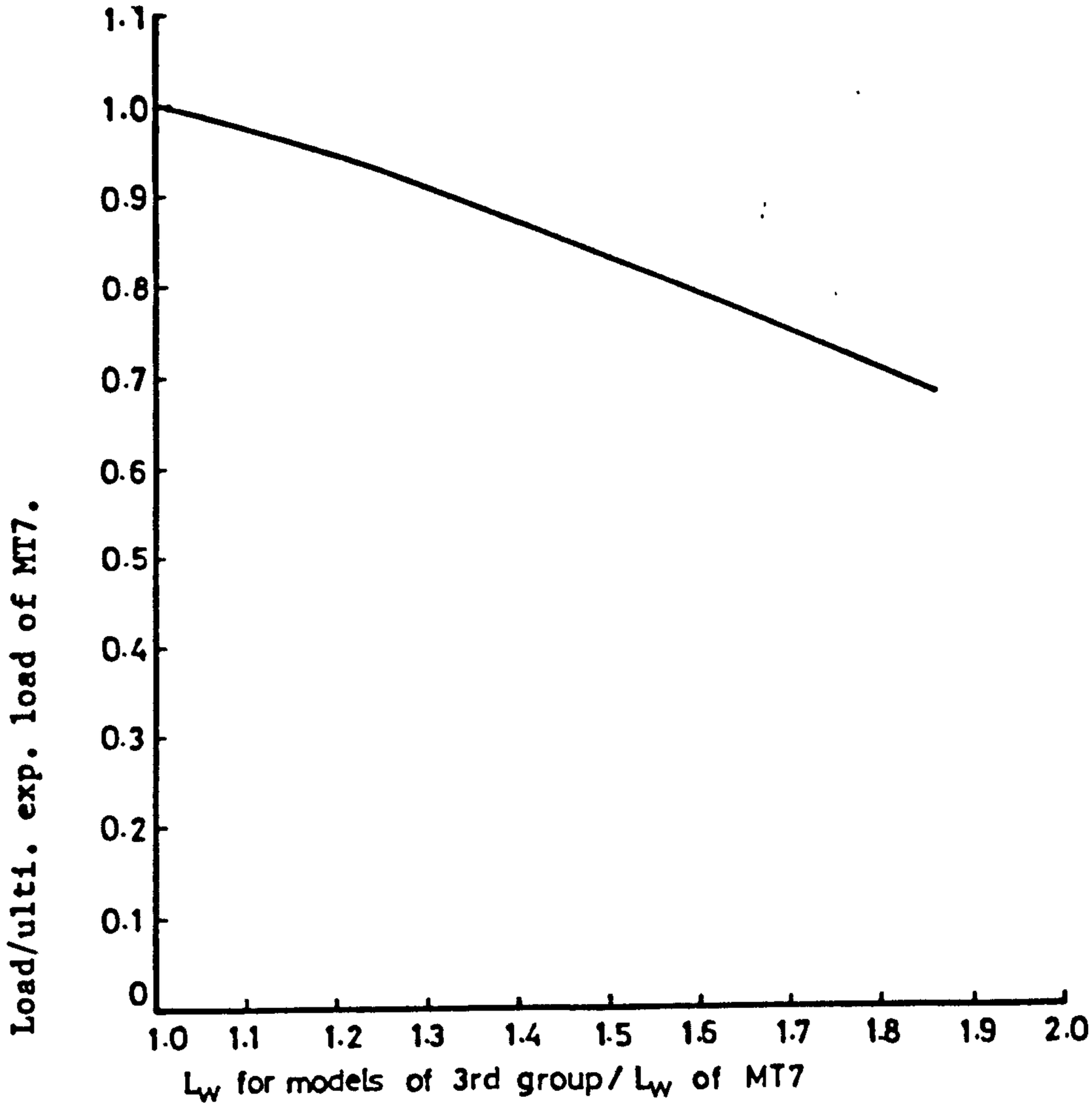

Figure (8.3) : Effect of corridor opening width on ultimate strength of wall-slab connection.

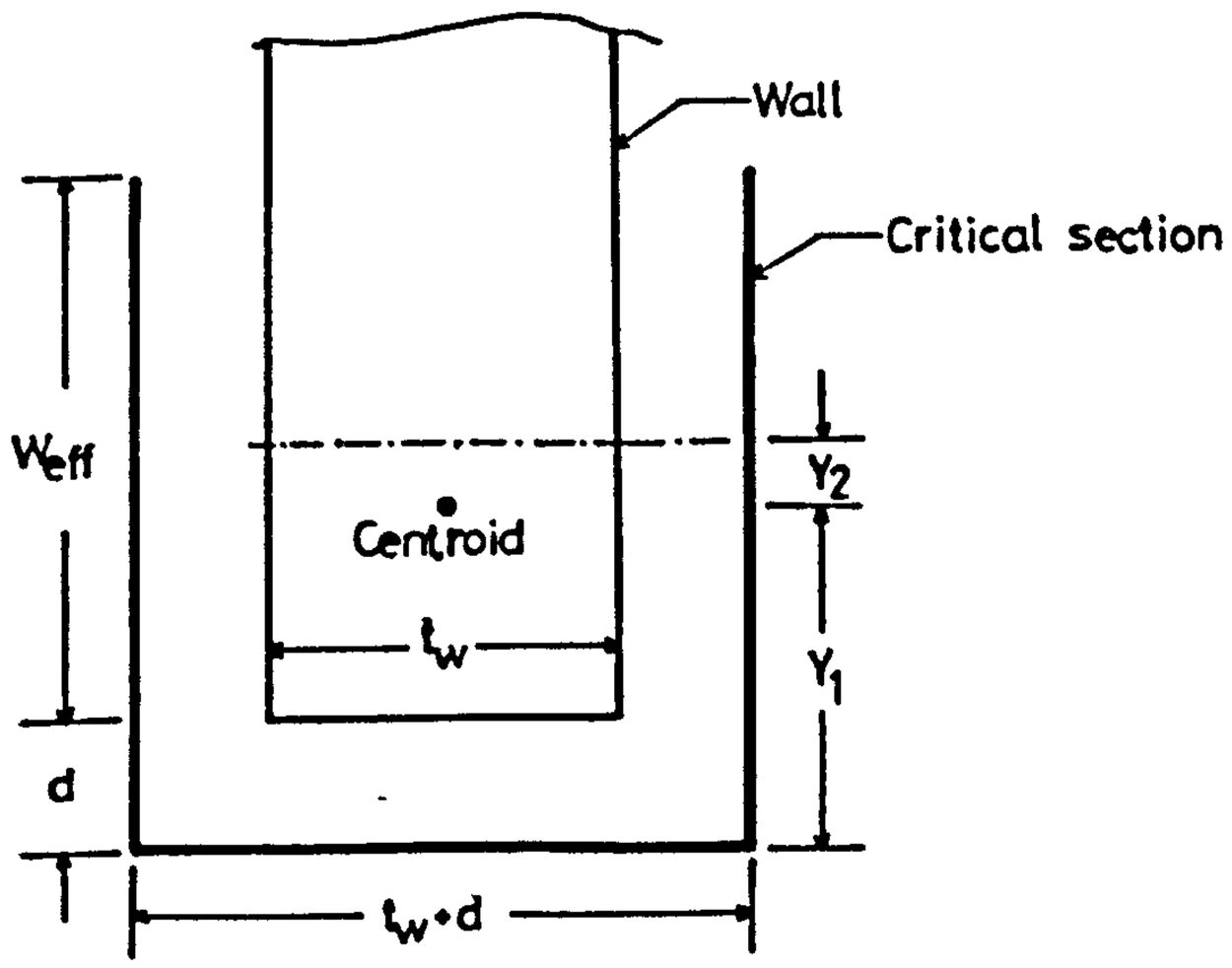

Figure (8.4) : Location of proposed critical section for w. shear around the wall periphery.

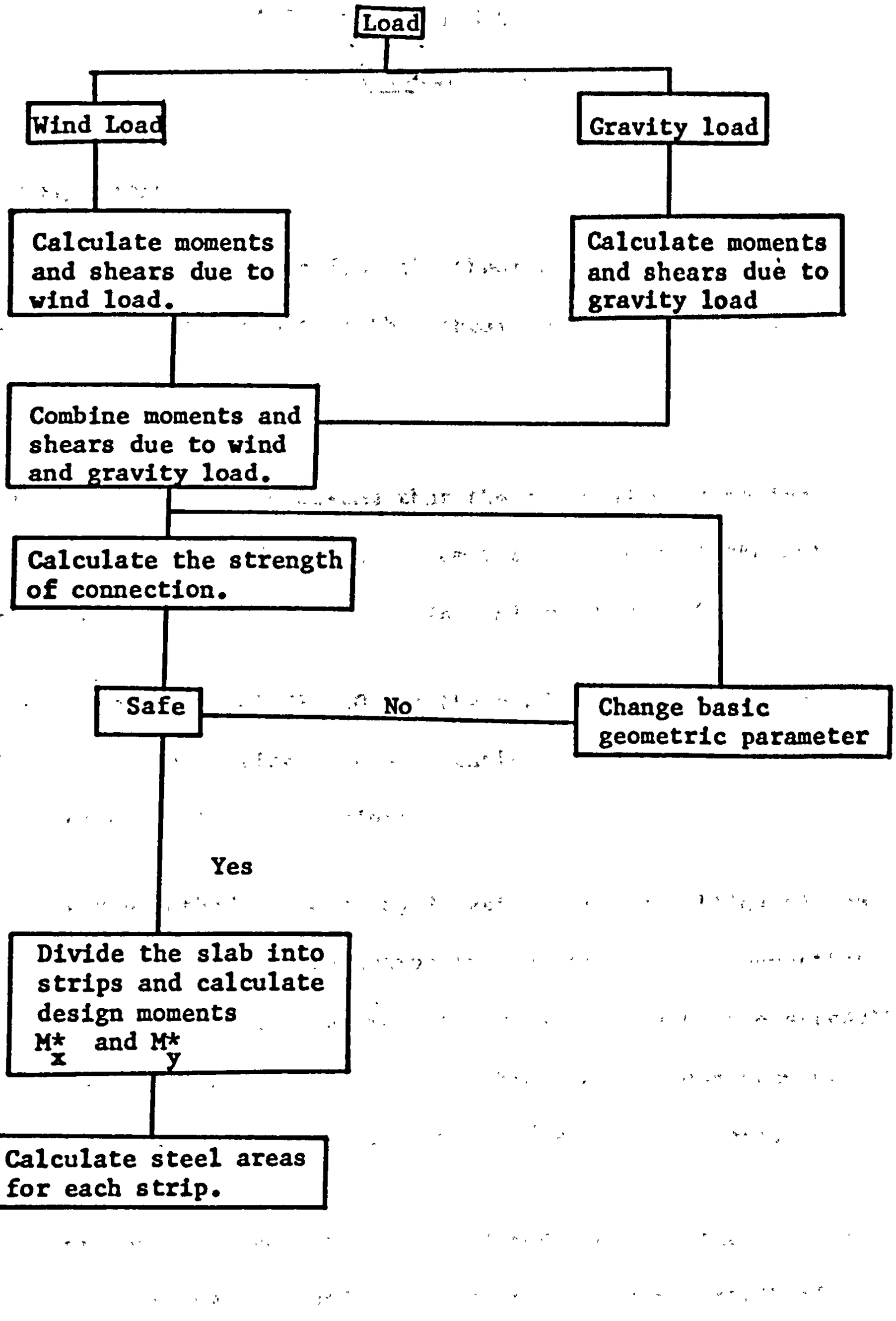

Figure (8.5) : Flow chart for the design of a connecting slab.

CHAPTER NINE

CONCLUSIONS AND RECOMMENDATIONS

9.1 CONCLUSIONS

The conclusions drawn from the theoretical and experimental investigations carried out in this thesis may be summarized as follows:

1. It is reasonable to assume that the critical section for shear is located at a distance $\frac{d}{2}$ from the periphery of the wall, as proposed by Schwaighofer & Collins (8) and Chang (9).

2. Recommendations of CP 110 for the prediction of the strength of slab-column connections are unsuitable for estimating the strength of wall-slab connections.

3. Since the method proposed by Schwaighofer and Collins (8) do not take into account the reduction in the strength of connection due to transfer of unbalanced moment, it overestimates the strength of wall-slab connections particularly when the corridor opening width L_w is relatively large (i.e. when $\frac{M_w}{V_w}$ ratio is large).

The methods proposed by Change (9) and Coull & Wong (10) are based on elastic analysis and do not consider the redistribution of the forces which takes place in the post elastic range. Therefore these methods underestimate the strength of connection.

4. Considerably larger amounts of moment and shear can be transferred by torsion than that calculated on the basis of critical value /

v_{ct} (viz: $0.4\sqrt{f_c'}$ N/mm^2) as recommended by ACI318 when the connection is purely of the torsional type. However for the slab-column or shear wall-slab connections subjected to unbalanced moments, where the failure is governed by the strength of the inner face of critical section for shears, it is unsafe to use higher value of v_{ct} than that recommended by ACI 318-71 (43).

5. Due to singularity of stresses the use of a very fine mesh for nonlinear analysis results in high theoretical concentration of stresses near the tip of the wall causing an early yielding of steel and crushing of concrete in this region, thus leading to an early failure of the slab at the theoretical wind load far less than the design ultimate load.

6. Due to higher concentration of stresses at the tip of the wall, the cracking load P_{cr} for connecting slabs is much lower than that of common slabs. It is therefore recommended that a load increment equal to .25 P_{cr} be used while performing nonlinear analysis of such slabs.

7. Any change in finite value of shear retention factor β has negligible effect on the theoretical load-displacement behaviour of connecting slabs. Slabs subjected to combined loading show slightly lower stiffness when a value of $\beta = 0$ is used.

8. To avoid the effects of singularity of stresses and to make the results more meaningful it is recommended that the stresses and strains etc. in the region near the inner edge of wall in/

windward direction be averaged over a width equal to (t_w + d) where t_w is the thickness of wall and d is the effective depth of slab.

9. The flexural ultimate loads of connecting slabs in terms of wind loading can be predicted with reasonable accuracy with the aid of two dimensional nonlinear plate bending finite element programmes, using layered approach.

10. Generally there is reasonable agreement between the measured and computed strains in steel both in windward and transverse direction in the region of slab near the inner edge of wall. Agreement is poorer remote from the tip of the wall with the analysis predicting strains progressively less than the measured values for increased distance from the tip of the wall.

11. When two dimensional nonlinear finite element programme (with layered approach) is used, the shears Q_x, Q_y may be calculated from $\Delta\tau_{xz}$ and $\Delta\tau_{yz}$ which in turn are calculated in each layer from rate of change of direct stresses (viz. σ_x, σ_y and τ_{xy}). In that case in the post elastic range the equilibrium is maintained only when integration (summation) is performed both from top and bottom to the midplane, i.e.

$$\tau_{xz} = \int_{z}^{h/2} \Delta\tau_{xz} \quad \text{if } z \geqslant 0 \quad \text{and} \quad \tau_{xz} = \int_{-h/2}^{z} \Delta\tau_{xz} \quad \text{if } z \leqslant 0$$

$$\text{Similarly } \tau_{yz} = \int_{z}^{h/2} \Delta\tau_{yz} \quad \text{if } z \geqslant 0 \quad \text{and} \quad \tau_{yz} = \int_{-h/2}^{z} \Delta\tau_{yz}$$

$$\text{if } z \leqslant 0.$$

12. The distribution of shears obtained from finite element analysis when the theoretical wind load was equal to the load at failure for the corresponding model shows that only a small portion of the wall along its sides (with the maximum value equal to t_w + d) can be taken as fully effective in transferring the shear and moment due to lateral loads.

13. Direct ultimate load design method based on elastic distribution of moments is quite suitable for the flexural design of connecting slabs of a shear wall structure subjected to combined loading. However since the concentration of stresses near the inner edge of wall is high and the stress gradient is very steep, special care is needed while choosing the width of the central strip.

14. The crack pattern of the connecting slab of a shear wall structure predicted by finite element analysis is reasonably correct.

15. While performing nonlinear analysis of a connecting slab of a shear wall structure subjected to lateral loads, use of zero wall thickness results in somewhat higher concentration of stresses at the tip of the wall leading to lower theoretical ultimate loads. The presence of finite wall thickness in the analysis increases the ultimate load by up to 10% of that with zero wall thickness. Generally reasonably correct predictions in terms of load-displacement behaviour, stress distribution and ultimate load can be obtained from the analysis by using zero wall thickness as well.

16. When connecting slabs are designed using the direct design method, due to use of average ratios of steel, the ultimate flexural load/

of the slab would be slightly lower than the design ultimate loads.

17. Full wall width W_w is not effective in resisting the applied wind shear. The length of wall along its sides which may be taken as effective seems to follow the mathematical relationship.

$$3t_w + t_w\left[\frac{1}{2} + \frac{1}{2^2} + \frac{1}{2^3} + \ldots\right]$$

where number of terms in brackets is given by (Aspect ratio -3)

Here t_w is the thickness of wall.

However for simplicity a value of effective wall width equal to 3.5 t_w may be adopted.

17. The effect of the percentage of flexural reinforcement on the strength of connection corresponds well with CP 110 which assumes an increase in the value of critical shear stress of .05 N/mm^2 for every increase of 0.5% of the ratio of flexural reinforcement, when $2 \gg \rho \gg 1$.

18. The method recommended by ACI318 for the prediction of strength of slab-column connection subjected to unbalanced moments can be used successfully to predict the strength of wall-slab connection in a shear wall structure subjected to lateral loads as well if it is used in conjunction with the proposals put forward in section (8.8) of this thesis.

9.2 SUGGESTIONS FOR FURTHER WORK

1. All the experimental and theoretical study presented in this thesis pertains only to the connections between inplane parallel/

crosswalls and the slabs. A similar study may be carried out for other wall configurations as well.

2. It may not be practicable to provide shear reinforcement in a connecting slab near the inner edge of wall where it is already heavily reinforced flexurally at the top and bottom, in both directions. However the possibilities of providing some form of special shear reinforcement could be investigated.

3. The effect of repeated horizontal loading and dynamic horizontal forces due to earthquake etc. on the behaviour of connecting slab and the strength of wall-slab connection should be investigated. The recent paper by Paulay and Taylor (41) could probably form the basis of this work.

4. Since all the edges of the slabs of all the models tested were free, it is proposed that the effect of continuity of the slab along its sides on the distribution of forces in the vicinity of the inner edge of wall and on the overall strength of wall-slab connection be investigated.

REFERENCES

1. Rosman, R.
"Approximate Analysis of Shear Walls Subjected to Lateral Loads".
Journal of the American Concrete Institute, June 1964, pp. 717-732.

2. Coull, A. and Irwin A.W.
"Design of Connecting Beams in Coupled Shear Wall Structures".
Journal of American Concrete Institute, March 1969, pp. 205-209.

3. Qadeer A. and Stafford Smith B.
"The Bending Stiffness of Slabs Connecting Shear Walls".
Journal of American Concrete Institute, June 1969, pp. 464-473.

4. Tso W.K. and Mahmoud A.A.
"Effective Width of Coupling Slabs in Shear Wall Buildings".
Journal of the Structural Division, March 1977, pp.573-586.

5. Coull A. and Wong Y.C.
"Structural Behaviour of Floor Slabs in Shear Wall Buildings".
Advances in Concrete Slab Technology, R.K. Dhir and J.G.L. Munday (Editors), Pergamon Press, 1980, pp. 301-312.

6. Coull A. and El Hag A.A.
"Effective Coupling of Shear Walls by Floor Slabs".
Journal of American Concrete Institue, Proc. Vol. 72, August 1975, pp. 429-431.

7. Wong, Y.C.
"Interaction Between Floor Slabs and Shear Walls in Tall Buildings".
Ph.D. Thesis, University of Strathclyde, May, 1979.

8. Schwaighofer J. and Collins M.P.
"Experimental Study of the Behaviour of Reinforced Concrete Coupling Slabs".
Journal of American Concrete Institute, March 1977, pp. 123-127.

9. Chang, Y.C.
"Slabs in Shear Wall Buildings".
A thesis submitted in partial fulfilment for degree of Master of Applied Science to the University of Toronto,September 1969.

10. Coull A. and Wong Y.C.
"Design of Floor Slabs Coupling Shear Walls".
Journal of Structural Engineering, Vol. 109, No. 1, January 1983, pp. 109-125.

11. Regan P.E.
"Design of Punching Shear".
The Structural Engineer, June 1974, No.6, Vol. 52, pp.197-207.

12. Long A.E., Cleland D.J. and Kirk D.W.
"Moment Transfer and the Ultimate Capacity of Slab-Column Structures". The Struct.Eng., Apr.'78, No.4,Vol.56A,pp.95-102.

13. Ghali A., Elmasri M.Z. and Dilger W.
"Punching of Flat Plates Under Static and Dynamic Horizontal Forces".
Journal of American Concrete Institute, October 1976, pp.566-572.

14. Kanoh Y. and Yoshizaki S.
"Strength of Slab-Column Connections Transferring Shear and Moment".
Journal of American Concrete Institute, March 1979, pp. 461-478.

15. Hawkins N.M., Bao A. and Yamazaki J.
"Moment Transfer from Concrete Slabs to Columns".
Unpublished paper, copy of which was obtained by private correspondence in October 1982.

16. Rangan B.V. and Hall A.S.
"Moment and Shear Transfer Between Slab and Edge Column".
Journal of American Concrete Institute, May-June 1983.

17. Rangan B.V. and Hall A.S.
"Forces in the Vicinity of Edge Columns inFlat Plate Floors (V1-Tests on R.C. models), UNICIV Report, No. R-203, Univ. of New South Wales, Kensington, Jan. 83, pp. 240.

18. Park M.R. and Shafiqul Islam.
"Strength of Slab-Column Connections with Shear and Unbalanced Flexure".
Journal of the Structural Division, September 1976,pp.1879-1901.

19. Hawkins N.M.
"Shear Strength of Slabs with Moments Transferred to Columns".
Shear in Reinforced concrete, Vol.2 Publication SP-42,
American Concrete Institute, Detroit, Mich. 1974, pp.817-846.

20. Hawkins N.M. and Corley W.G.
"Transfer of Unbalanced Moment and Shear From Flat Plates to Columns", Cracking, Deflection and Ultimate Load of Concrete Slab Systems, Publication SP30-7, American Concrete Institute, Detroit, Mich. 1971, pp. 147-176.

21. Duncan W. and Johnarry T.
"Further Studies on the Constant Stiffness Method of Nonlinear Analysis of Concrete Structures".
Proc. Instn. Civ. Engrs. Part 2, 1979, 67, Dec. pp. 951-969.

22. Hago A.W.
"Direct Design of Reinforced Concrete Slabs".
Ph.D. Thesis, Department of Civil Engineering, Univ. of Glasgow, May 1982.

23. Liu T.C.Y., Nilson A.H. and Slate F.O.
"Biaxial stress-strain relations for concrete".
Journal of Structural Division, ASCE 98 (ST5), May 1972.

24. Kupfer H. Hilsdorf H.K. and Rusch H.
"Behaviour of Concrete Under Biaxial Stresses".
Journal of American Concrete Institute, August 1969,
pp.656-666.

25. Johnarry T.
"Elastic-Plastic Analysis of Concrete Structures Using Finite Elements".
Ph.D. Thesis, University of Strathclyde, May 1979.

26. Bell J.C. and Elms D.G.
"A Finite Element Approach to Post-Elastic Slab Behaviour".
ACI Special Publications SP30-15, March 1971, pp.325-344.

27. Hand F.R., Pecknold D.A. and Schnobrich W.C.
"Nonlinear Layered Analysis of R.C. Plates and Slabs".
Journal of the Structural Division, ST7, July 1973,pp.1491-1505.

28. Park R. and Paulay T.
"The Principal Mechanisms of Shear Resistance".
From the book "Reinforced Concrete Structures", A. Wiley Interscience Publication, 1975, pp. 278-286.

29. ACI State of-the-Art Report on
"Finite Element Analysis of Reinforced Concrete", 1982.

30. Houde J. and Mirza M.S.
Shear in Reinforced Concrete, Volume 1, Special Publication SP-42.
American Concrete Institute, Detroit, Michigan, 1974.

31. Pauley T. and Loeber P.S.
"Shear Transfer by Aggregate Interlock",
Shear in Reinforced Concrete, Volume 1, Special Publication SP-42,
American Concrete Institute, Detroit, Michigan, 1974.

32. British Standard Code of Practice, CP3, Chapter V, Part II, 1972.
"Basic Data for the Design of Buildings, Loading".

33. Johansen K.W.
"Johansen's 'stepped' yield criteria ".
From the book by Jones L.L. and Wood R.H. Yield-Line Analysis of Slabs, pp. 38-39.

34. Wood R.H.
"The Reinforcement of Slabs in Accordance with a Predetermined Field of Moments".
Concrete Vol.2, No.2, February 1968, pp. 69-76.

35. Armer G.S.T.
Contribution to Discussion on Ref. 34, Concrete,Vol.2, No.8, August 1968, pp. 319-320.

36. British Standard Code of Practice, CP3, Chapter V, Part I, 1967, "Loading".

37. B.S. 882 and 1201, 1965.
"Specification for aggregates from Natural Sources for Concrete".
London, British Standard Institute, 1965.

38. British Standard 1881, Part 5, 1970.
"Methods of Testing Concrete", pp. 12-13.

39. TRRL Supplementary Report No. 254, DOE & DTP, 1977.
"Recommended Standard Practices for Structural Testing of Steel Methods".

40. Taylor H.P.J.
"Shear Stresses in Reinforced Concrete Beams Without Shear Reinforcement".
Technical Report, Cement and Concrete Association, pp.17-18.

41. Paulay T. and Taylor R.G.
"Slab Coupling of Earthquake-Resisting Shear Walls".
Journal of American Concrete Institute, March-April 1981, pp. 130-140.

42. MacLeod I.A., Green D.R.
"Three-Dimensional Analysis of Shear Wall Buildings".
Bulletin of the International Association for Shell and Spatial Structures No.60, Milan, September 1974. pp. 9.

43. ACI 318-71.
Building Code Requirements for Reinforced Concrete,
American Concrete Institute, 1971.

44. British Standard Institution CP110 : The Structural Use of Concrete, Part I, Design, Materials and Workshop, 1972.

45. British Standard Institution CP114: The Structural Use of Reinforced Concrete in Buildings, 1957. (Reprinted 1965).

46. Hawkins N.M., Fallsen H.B. and Hinojosa R.C.
"Influence of Column Rectangularity on the Behaviour of Flate Plate Structures".
SP3P, Cracking, Deflection and Ultimate load of Concrete Slab Systems, American Concrete Institute Detroit, MI, 1971, pp. 127-146.